Gut microbiota-related biomarkers in immuno-oncology

Carolina Alves Costa Silva

THESE DE DOCTORAT

NNT : 2023UPASL068

Gut microbiota-related biomarkers in immuno-oncology

Biomarqueurs liés au microbiote intestinal en immuno-oncologie

Thèse de doctorat de l'université Paris-Saclay

École doctorale n° N°582 : Cancérologie : biologie - médecine – santé (CBMS)
Spécialité de doctorat : Sciences du Cancer
Graduate School : Life, Science and Health. Réferent: Faculté de Médecine.

Thèse préparée dans l'unité de recherche Immunologie anti-Tumorale et Immunothérapie du Cancer (Université Paris-Saclay), sous la direction de **Laurence ZITVOGEL**, PU-PH, la co-direction de **Laurence ALBIGES**, PU-PH et de **Lisa DEROSA**, MCU-PH

Thèse soutenue à Paris-Saclay, le 08 septembre 2023, par

Carolina ALVES COSTA SILVA

Composition du Jury

Membres du jury avec voix délibérative

Eric DEUTSCH PU-PH, Université Paris-Saclay	Président
Stéphane OUDARD PU-PH, Université Paris Descartes	Rapporteur & Examinateur
Antoine TOUBERT PU-PH, Université Paris Cité	Rapporteur & Examinateur
Géraldine SCHLECHT-LOUF MCU, Université Paris-Saclay	Examinatrice
Salima HACEIN-BEY PU-PH, Université Paris Cité	Examinatrice
Leija IMAMOVIC PhD, Sorbonne Université	Examinatrice

“Exu matou um pássaro ontem com uma pedra que só jogou hoje”
Ditado Iorubá

“Andá com fé eu vou, que a fé não costuma faiá”
Gilberto Gil

université PARIS-SACLAY

ÉCOLE DOCTORALE
Cancérologie : biologie - médecine - santé (CBMS)

Titre : Biomarqueurs liés au microbiote intestinal en immuno-oncologie

Mots clés : Immunothérapie; biomarqueurs; microbiota; métagénomique; MAdCAM-1; immunoglobulines.

Résumé : Surpasser la résistance à l'immunothérapie demeure encore un domaine de la recherche inachevé. Les biomarqueurs basés sur le microbiota et les interventions ciblées sur le microbiota sont des stratégies thérapeutiques prometteuses dans l'amélioration de la réponse aux traitements par immunothérapie chez les patients atteints de cancer. Les méthodes standards actuelles d'évaluation de la composition du microbiote intestinal sont couteuses, chronophages et dans le cadre des routines cliniques, nous manquons d'outils de diagnostic pour sélectionner des patients et des donneurs pour des interventions centrées sur le microbiote.

Ici, nous émettons l'hypothèse que les biomarqueurs intestinaux peuvent être traduits en outils faciles à utiliser pour guider les prises de décision des traitements apportés aux patients atteints de cancer. Nous montrons que le cancer induit un ileopathie de stress et une dysbiose intestinale persistante dominée par *Enterocloster* spp., bactéries tolérogènes participant à la progression du cancer. Nous identifions aussi une déviation précoce dans le profil métabolique des patients présentant un mélanome localisé à haut risque, avant récidive, où le métabolisme lipidique pourrait jouer un rôle central dans la progression du cancer.

Les antibiotiques (ABX) ont un effet délétère sur l'immunothérapie et les mécanismes mettant en évidence l'impact délétère des ABX étaient, jusqu'à présent, inconnus. Premièrement, nous avons démontré que les ABX induisent un déséquilibre de la composition microbiotique jusqu'à la dysbiose, dominée par Enterocloster spp. Ensuite, nous avons montré que l'ABX ou la dysbiose intestinale diminuent le MAdCAM-1 iléal, conduisant à la recirculation des cellules immunosupprésives enterotropic T dans la tumeur, ainsi qu'une résistance à l'immunothérapie.

Enfin, on a demontré que la colonisation des tissus par les microbes peut induire des effets anti-tumoraux ainsi qu'une stimulation immunitaire via les structures lymphoïdes tertiaires. La meilleure compréhension des mécanismes et du rôle joué par le microbiote ouvrent des perspectives de développement de nouvelles stratégies de prévention et de traitement de plusieurs types de cancer.

université PARIS-SACLAY

ÉCOLE DOCTORALE
Cancérologie : biologie - médecine - santé (CBMS)

Title : Gut microbiota-related biomarkers in immuno-oncology

Keywords : Immunotherapy; biomarkers; microbiota; metagenomics; MAdCAM-1; immunoglobulins.

Abstract : Surpassing resistance to immunotherapy is an unmet medical need. Increasing evidence show that microbiota-based biomarkers and microbiota-centered interventions (MCI) are promising strategies to improve outcomes of patients under immunotherapy. Current standard methods to evaluate gut microbiota composition are cost- and time-consuming and we lack a diagnostic tool for clinical routine use to select patients and donors to MCI.

Here, we hypothesize that intestinal-based biomarkers can be translated into easy-to-use tools to guide routine treatment-decision in patients with cancer. We show that cancer induced a stress ileopathy and protracted intestinal dysbiosis dominated by tolerogenic *Enterocloster* spp. participating in cancer progression. We also identified early deviations in metabolomics profiling of patients with high-risk localized melanoma before recurrence, where lipid metabolism may play a central role in cancer progression.

Antibiotics (ABX) impairs immunotherapy outcomes and mechanisms underlying the deleterious impact were unknown. First, we demonstrated that ABX shifts the gut microbiota composition towards dysbiosis also dominated by Enterocloster spp. Then, we showed that ABX or gut dysbiosis downregulate the ileal MAdCAM-1, leading to the recirculation of immunosuppressive enterotropic T cells into the tumor and resistance to immunotherapy.

Furthermore, microbial tissue colonization can exert antitumor effects and immune stimulation through tertiary lymphoid structures. Mechanistic insights towards understanding the role of microbiota open opportunities to the development of novel prevention and treatment strategies of various cancer types.

1 INDEX

2 SYNTHESE EN FRANÇAIS

Surpasser la résistance à l'immunothérapie demeure encore un domaine de la recherche inachevé. Le cancer n'est pas seulement une maladie génétique ou épigénétique résultant d'aberrations autonomes des cellules, mais c'est le résultat cumulatif de défaillances fonctionnelles du méta-organisme. Les biomarqueurs basés sur le microbiota et les interventions ciblées sur le microbiota sont des stratégies thérapeutiques prometteuses dans l'amélioration de la réponse aux traitements par immunothérapie chez les patients atteints de cancer. Les méthodes standards actuelles d'évaluation de la composition du microbiote intestinal sont couteuses, chronophages et dans le cadre des routines cliniques, nous manquons d'outils de diagnostic pour sélectionner des patients et des donneurs pour des interventions centrées sur le microbiote.

Ici, nous démontrons que le cancer présente des caractéristiques taxonomiques et métabolomiques qui contribuent à sa progression. Le cancer induit une iléopathie de stress, caractérisée par une prolifération ectopique de cellules entéroendocrines et un déséquilibre entre le système sympathique et cholinergique, ainsi qu'une dysbiose intestinale prolongée dominée par *Enterocloster* spp. tolérogènes. Les antibiotiques modifient la composition du microbiote intestinale en faveur de bactéries tolérogènes (y compris *Enterocloster* spp.) et compromettent les résultats de l'immunothérapie. *Enterocloster* spp induisent des changements métaboliques (perturbation des sels biliaires), entraînant la régulation négative de MAdCAM-1 par des acides biliaires secondaires et la migration des Tr17 intestinales vers les lits tumoraux. De plus, nous avons pu identifier des déviations précoces dans le profil métabolomique des patients atteints de mélanome localisé à haut risque, des mois avant la récurrence, où le métabolisme lipidique, les acides biliaires conjugués et les polyamines acetylées pourraient jouer un rôle central dans la récurrence et la progression du mélanome. En tant que petites molécules agissant comme des intermédiaires ou des produits finaux du métabolisme cellulaire, certains métabolites sont des médiateurs des effets bénéfiques ou nocifs des probiotiques ou de l'alimentation, ouvrant la voie à des interventions thérapeutiques.

Précédemment associé à la réponse à l'immunothérapie dans une cohorte rétrospective de patients porteurs de cancer du rein et du poumon avancés, une validation prospective a confirmé que l'*Akkermansia* muciniphila est indépendamment associée à une amélioration de la survie chez les patients atteints d'un cancer du poumon avancé. En raison des limitations dans la prédiction des résultats cliniques à travers les cohortes et les types de cancer en utilisant une seule espèce métagénomique, nous nous sommes concentrés sur une approche différente, basée sur une distribution écologique des espèces métagénomiques fécales en deux groupes d'interaction d'espèces (« SIG ») opposés. D'un réseau construit à partir des données de métagenomique d'une cohorte de patients porteurs de cancer du poumon, on a pu développer un score unidimensionnel au niveau individuel qui pourrait être utilisé en routine clinique pour sélectionner des patients éligibles ou les donneurs à des interventions basées sur le microbiote. Nous avons aussi démontré que les réponses immunitaires dirigées contre Escherichia coli uropathogène (Tfh ou humorales) dictaient les bénéfices de l'immunothérapie chez les patients atteints de cancer de la vessie. La colonisation tissulaire tumorale par des microbes peut exercer des effets antitumoraux et une stimulation immunitaire par le biais des structures lymphoïdes tertiaires, et ces microbes pourraient être exploités pour de futures stratégies thérapeutiques.
En résumé, nos résultats montrent que des perspectives mécanistiques pour comprendre le rôle du microbiote ouvrent des opportunités pour le développement de nouvelles stratégies de prévention et de traitement de divers types de cancer.

3 ABBREVIATIONS

Anaplastic lymphoma kinase (ALK); Antibiotics (ABX); Antibodies (Abs); Bacillus Calmette-Guérin (BCG); Basal cell carcinoma (BCC); Biologics license applications (BLAs); Body-mass index (BMI); Cancer-associated fibroblasts (CAFs); Cancer testis antigens (CTA); Carcinoma in situ (CIS); Chemoradiotherapy (CRT); Chemotherapy (CT); Colorectal cancer (CRC); Combined positive score (CPS); Complete response (CR); Confidence interval (CI); Cutaneous squamous cell carcinoma (cSCC); Dendritic cells (DCs); Epidermal growth factor receptor (EGFR); Extracellular matrix (ECM); Gastroesophageal junction (GEJ); Gene expression profiles (GEP); Healthy volunteer (HV); Hepatocellular carcinoma (HCC); Immune-checkpoint blockade (ICB); Immunohistochemistry (IHC); Immuno-Oncology (IO); Merkel cell carcinoma (MCC); Liquid chromatography coupled with mass spectrometers (LC/MS); Metabolomics (MB); Metagenomic shot gun (MGS); Microbiota-centered interventions (MCI); Microsatellite instability-high (MSI-H); Microsatellite instability-low (MSI-L); Mismatch repair deficient (dMMR); Mismatch repair proficient (pMMR); Monoclonal antibodies (mAbs); Mutations/megabase (mut/Mb); Natural killer (NK); New molecular entities (NMEs); Next generation sequencing (NGS); Non-muscle invasive bladder cancer (NMIBC); Non–small cell lung cancer (NSCLC); Non-responders (NR); Odds ratio (OR); Overall survival (OS); Partial response (PR); Polymerase chain reaction (PCR); Progression-free survival (PFS); Progressive disease (PD); Radiotherapy (RT); Receptor tyrosine kinases (RTKs); Recurrence-free survival (RFS); Renal cell carcinoma (RCC); Responders (R); Response Evaluation Criteria in Solid Tumours (RECIST); Soluble MAdCAM-1 (sMAdCAM-1); Stable disease (SD); T-cell receptor (TCR); Tertiary lymphoid structures (TLS); Transurethral resection (TURBT); Triple-negative breast cancer (TNBC); Tumor-associated antigens (TAA); Tumor-associated macrophages (TAMs); Tumor-associated neutrophils (TANs); Tumor cells (TC); Tumor-infiltrating immune cells (IC); Tumor microenvironment (TME); Tumor mutation burden (TMB); Tumor mutational burden-high (TMB-H); Tumor proportion score (TPS); Urothelial carcinoma (UC).

4 INTRODUCTION

4.1 THE ADVANCES IN IMMUNOTHERAPY FOR PATIENTS WITH SOLID TUMORS

After the 20th century, an epidemiological transition led to cancer together with cardiovascular diseases as leading causes of death worldwide, superseding infectious diseases (1). In 2020, the global burden of cancer had already risen to 19 million new cases and 10 million deaths and it is predicted to rise about 50% more in 20 years, especially in countries with low human development index (2). Among tumor types, solid ones have high-incidence and mortality in both sexes (2). Fortunately, the global burden of cancer rise was accompanied by an increase of drug approval by regulatory agencies for the most common solid cancers (Fig. 1) (3). Oncologic drugs have evolved from cytotoxic and nonspecific immune cytokines to modern drugs with more precise targets such as receptor tyrosine kinases (RTK) and immune-checkpoint blockade (ICB). Together, these drugs became the backbone of treatment in locally advanced and metastatic cancer in the past 31 years (3). The better understanding of the tumor microenvironment (TME) and the mechanisms of cancer evasion enable the evolution of treatment in oncology.

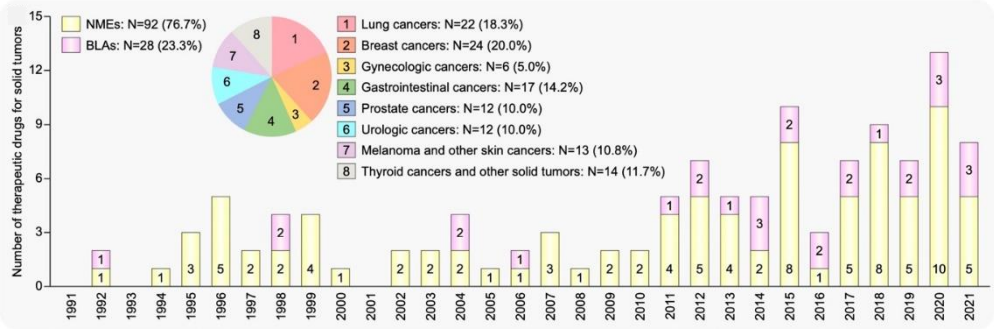

Figure 1 *Number of FDA-approved therapeutic drugs for solid tumors during 31 years (1991-2021). NMEs: New molecular entities; BLAs: Biologics license applications. Adapted from Wu et al. 2022.*

4.2 THE ORCHESTRATED TUMOR MICROENVIRONMENT

TME is a complex and dynamic ecosystem containing not only cancer cells but also resident and recruited non-cancerous cells such as immune (e.g. T cells, B cells, myeloid cells, and others) and stroma cells (e.g. cancer-associated fibroblasts (CAFs) adipocytes, and neurons) immersed in a vascularized extracellular matrix (ECM) (Fig. 2A) (4). Intercellular interactions in the TME are complex and can occur via cell-cell contact (e.g. adhesion molecules, including integrins, cadherins, selectins, and immunoglobulin superfamily members, and also via gap junctions and tunneling nanotubes) and paracrine signaling (e.g. release of cytokines, chemokines, growth factors, proteases, metabolites) (4). TME is decisive in regulating ICB efficacy, whether by physically excluding cytotoxic T cells or increasing the presence of dysfunctional ones (Fig. 2A-B) (4).

T cell infiltration is a key step in the cancer-immunity cycle. Considering physical exclusion of immune cells and the potential to respond to ICB, three basic tumor immune phenotypes are described (Fig. 2C). The immune-inflamed phenotype tumors harbor different markers of inflammation such as immune cell infiltration the tumor parenchyma (e.g., CD4+ and CD8+ T cells), PD-L1 expression (immune but also in tumor cells), and proinflammatory and effector cytokines (type I and type II interferon (IFN), interleukin (IL)-12, IL-23, IL-1β, tumor-necrosis factor (TNF)-α and IL-2) are found (Fig. 2C, red). This phenotype suggests the existence of a pre-existing antitumor immune response that is inhibited, and patients harboring this phenotype have a greater potential to benefit from ICB. The non-inflamed tumors include two phenotypes: immune-excluded and immune-desert. Clinical responses are uncommon in immune-excluded tumors since immune cells are retained in the stroma surrounding the tumor and T-cell do not infiltrate even after activation and proliferation following anti-PD-L1/ PD-1 treatment (Fig. 2C, yellow). In the immune-desert phenotype, there is a paucity of T cell infiltration either into the tumor or the stroma (Fig. 2C, blue).

T cells activation require the release and presentation of neoantigens, where T-cell antigen receptor (TCR) bind to complexes of peptides with major histocompatibility complex (MHC) of antigen-presenting cells (APCs), modulated by co-stimulatory or co-inhibitory molecules, the

immune checkpoints. For example, Programmed Cell Death Protein 1 (PD-1)/ Programmed Cell Death Ligand 1 (PD-L1) pathway enables contact-dependent intercellular interactions that suppress anticancer immune responses (4). PD-1 (CD279) is highly expressed on tumor-infiltrating lymphocytes (TILs) and acts as an inhibitor of both adaptive and innate immune responses. PD-L1 is one of the PD-1 ligands and can be expressed either by cancer or host immune cells. PD-1 expression impact on transcriptional profiles of TILs leading to higher expression of Ki67 and genes involved in the cell cycle regulation and proliferation and these TILs can constitutively release CXCL13. CXCL13 is the prototypic chemokine secreted by T follicular helper cells (Tfh) and involved in tertiary lymphoid structures (TLS) functions. Beyond these immune checkpoints, other intrinsic and extrinsic factors are involved in promoting or suppressing anticancer immune responses such as tumor and germline genetics, exposure to sunlight, infectious agents, microbiota, and pharmacological agents (4,5). The equilibrium between these elements that stimulate or inhibit anticancer immunity characterize the 'cancer–immune set point' (Fig. 2B) (5). Their better characterization and the mechanisms by which they determine the baseline immune profile will allow us to find biomarkers and therapeutic strategies to effectively surpass the 'cancer–immune set point' of a given individual (Fig. 2B).

Rather than a static disease, cancer microenvironment is dynamic and both organ- and cancer cell type-intrinsic features are key determinants to shape TME and tumor progression (Fig. 2A). These features include altered (epi)genetics, metabolic reprogramming, and deregulated signaling. Based on single-cell and multiplexed spatial technologies in cancer of different anatomical sites (lung, breast, and head and neck), recent studies revealed that the evolution from non-invasive or early stages to invasive and later stages lead to an immune infiltrate transition. Adaptive and innate immune cells such as naïve T cells and immunostimulatory neutrophils that sense early cancer lesions are subverted to a tumor-supportive immunosuppressed TME containing fewer cytotoxic natural killer (NK) and CD8+ T cells and rather increased dysfunctional ones, more expression of negative regulators (e.g. PD-L1 and CTLA-4), CD4+FoxP3+ regulatory T cells (Treg) and myeloid cells, such as tissue-resident macrophages (4,6–9). IFN-γ plays an important role in cancer immune surveillance. While

CD8+ T cells can exert anti-tumor activity by releasing IFN-γ, chronic exposure to this cytokine could also upregulate PD-L1 expression in tumor cells and finally lead to immune evasion (10). No wonder that chronic inflammatory conditions such as inflammatory bowel disease (IBD), hepatitis, and obesity predispose to cancer. The chronic inflammation leads to an immunocompromised functional state characterized by an increase of myeloid cells and proinflammatory Th2-type immune responses, releasing reactive oxygen species (ROS), pro-inflammatory cytokines, chemokines, growth factors, and pro-angiogenic factors.

A.

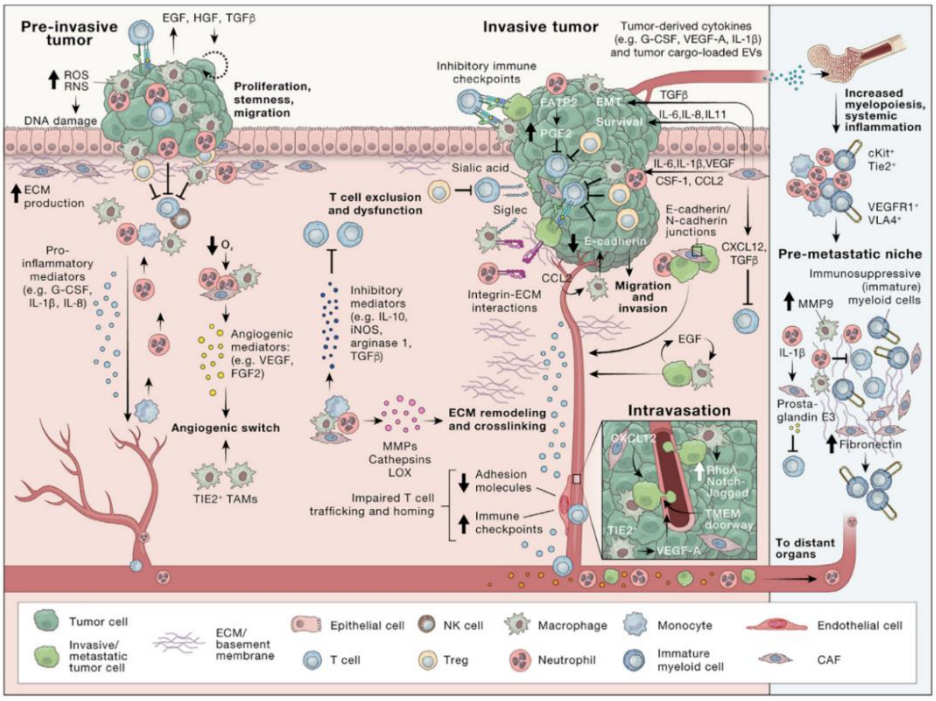
Pre-invasive tumor
EGF, HGF, TGFβ
ROS
RNS
DNA damage
Proliferation, stemness, migration
ECM production
Pro-inflammatory mediators (e.g. G-CSF, IL-1β, IL-8)
O2
Angiogenic mediators: (e.g. VEGF, FGF2)
Angiogenic switch
TIE2+ TAMs
Invasive tumor
Tumor-derived cytokines (e.g. G-CSF, VEGF-A, IL-1β) and tumor cargo-loaded EVs
Inhibitory immune checkpoints
EATP2
EMT
TGFβ
Survival
IL-6,IL-8,IL11
PGE2
IL-6,IL-1β,VEGF
CSF-1, CCL2
Sialic acid
Siglec
T cell exclusion and dysfunction
E-cadherin/ N-cadherin junctions
E-cadherin
CXCL12, TGFβ
CCL2
Integrin-ECM interactions
Migration and invasion
EGF
Inhibitory mediators (e.g. IL-10, iNOS, arginase 1, TGFβ)
ECM remodeling and crosslinking
MMPs
Cathepsins
LOX
Impaired T cell trafficking and homing
Adhesion molecules
Immune checkpoints
Intravasation
CXCL12
RhoA
Notch-Jagged
TMEM doorway
TIE2
VEGF-A
To distant organs
Increased myelopoiesis, systemic inflammation
cKit+ Tie2+
VEGFR1+ VLA4+
Pre-metastatic niche
Immunosuppressive (immature) myeloid cells
MMP9
IL-1β
Prosta-glandin E3
Fibronectin
Tumor cell
Invasive/ metastatic tumor cell
ECM/ basement membrane
Epithelial cell
T cell
NK cell
Treg
Macrophage
Neutrophil
Monocyte
Immature myeloid cell
Endothelial cell
CAF

B.

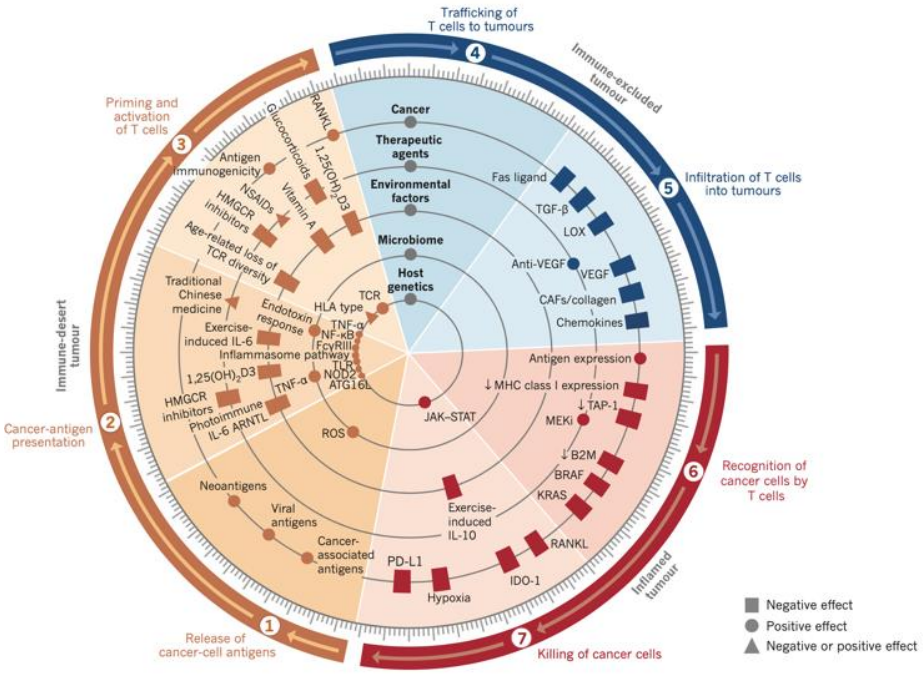
Trafficking of T cells to tumours
Immune-excluded tumour
Infiltration of T cells into tumours
Recognition of cancer cells by T cells
Killing of cancer cells
Release of cancer-cell antigens
Cancer-antigen presentation
Priming and activation of T cells
Immune-desert tumour
Inflamed tumour
Cancer
Therapeutic agents
Environmental factors
Microbiome
Host genetics
Glucocorticoids
RANKL
1,25(OH)2 D3
Vitamin A
NSAIDs
HMGCR inhibitors
Age-related loss of TCR diversity
Antigen immunogenicity
Traditional Chinese medicine
Endotoxin response
Exercise-induced IL-6
Inflammasome pathway
TCR
HLA type
TNF-α
NF-κB
FcγRIII
TLR
NOD2
ATG16L
1,25(OH)2D3
TNF-α
HMGCR inhibitors
Photoimmune IL-6 ARNTL
ROS
Neoantigens
Viral antigens
Cancer-associated antigens
JAK–STAT
Exercise-induced IL-10
PD-L1
Hypoxia
IDO-1
RANKL
KRAS
BRAF
↓B2M
MEKi
↓TAP-1
↓MHC class I expression
Antigen expression
Chemokines
CAFs/collagen
VEGF
Anti-VEGF
LOX
TGF-β
Fas ligand
Negative effect
Positive effect
Negative or positive effect

C.

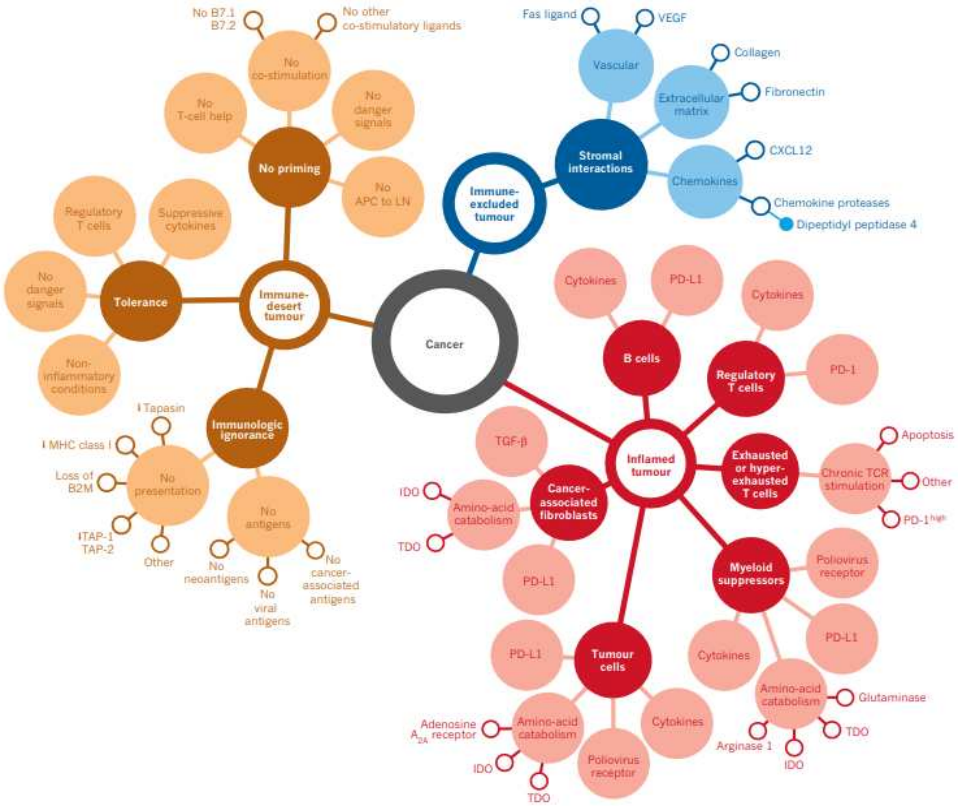

Figure 2 Factors that influence cancer immune tolerance and immunity. **A.** The tumor microenvironment evolves during cancer progression. **B.** Factors regulating the "cancer-immune set point". **C.** Cancer immune phenotypes and causes of immune failure. (De Visser and Joyce 2023; D. S. Chen and Mellman 2017).

4.3 CANCER-CELL INTRINSIC MECHANISMS: GENOME AND EPIGENETICS

In the late 1980s, Boon, Schreiber and colleagues identified the first mutant new antigens (neoepitopes) in murine models, and brought the idea that cancer neoepitopes can be recognized by T cells (11,12). Tumor-associated antigens (TAA) are self-antigens that are over- or abnormally expressed in cancer cells and include glycoprotein antigens, cancer-testis antigens (CTA). The first TAA described, CTA are expressed in cancer cells of different histology in humans but also in

germline cells (testis and placenta) (5,13). Cancer and germline cells share characteristics such as migration, colonization, proliferation and genomic instability. Since the discovery of the CTA MAGE-1, the immunogenicity and cancer-specificity of CTA led to the discovery of other targets with therapeutic function such as cancer/testis antigen 1 (also known as NY-ESO-1) and melanoma-associated antigen 3 (MAGE-A3), and MAGE-C2 (14–16).

The development of novel techniques of DNA sequencing led to the discovery of point, frameshift, insertion or deletion mutations that generate new protein or peptide sequences. The greater the sequence divergence in these proteins or peptides and the number of mutations in a given tumor, the greater the probability of having immunogenic neoantigens (5). These neoantigens can bind MHC class I or class II molecules, and mutant amino acids projected towards the TCR, leading to T cell recognition and protective immunity against cancer. Truncal mutations arise early in carcinogenesis and can be found in almost all of the cancer cells in a given individual. Instead, branch mutations arise later, so they are limited to a subpopulation of cancer cells and may generate less effective antitumoral responses (5). As previously described, carcinogenesis is a complex and multistage process where cancer cells accumulate various somatic mutations over time (Fig. 3A) (4,17). These mutations occur as a result of background mutation rate (shaped by various mutagens, such as smoking and UV light, and repair processes), and natural selection (17). Although most mutations that arise are neutral (or passenger), some of them are considered as driver mutations (Fig. 3A-B), acting to provide a tolerogenic environment and contribute to carcinogenesis (5,17) such as KRAS and BRAF. These mutations activate the MAP kinase pathway , downregulate MHC class I molecules, induce autophagy and reduce apoptosis in TME leading to tumor growth and worse prognosis of patients (5).

Specific driver mutations are potential prognostic and predictive biomarkers (Fig. 3C) (17,18). For example, patients with melanoma BRAF V600E mutation benefit from BRAF kinase inhibitors, while those harboring activating mutations are primary resistant to these therapies (19). Patients with non-small cell lung cancer (NSCLC) harboring EGFR mutations or ALK rearrangements had a dramatic improvement in their outcomes after oncogene drivers-targeted therapy (Fig. 3C right) (20). Modifications in the epigenetic signaling machinery, including

histones and chromatin remodelers, and the expression of microRNAs in tumors influence cytokine profiles also modulate the TME (5,17).
While potentially having immunogenic properties, chronic exposure to antigens can lead to increased expression of PD-1 and effector T cell exhaustion and death (Fig. 3D) (5). 'Hyperexhausted' effector T cells profiles are characterized by high expression of PD-1 but also activation markers such as LAG-3, TIM-3 or TIGIT. These T cells may be committed by chronic TCR stimulation to a pathway of TCR-induced apoptosis. Tumors can also increase immunosuppression through amplification or enhanced transcription of genes that encode negative regulators such as PD-L1, the arachidonate lipoxygenases and IDO-1 and IDO-2 (5). Although CD4+ or CD8+ tumor-infiltrating lymphocytes (TILs) commonly harbor features of memory T cells, that could elicit antitumoral activity, they often have a dysfunctional or exhausted phenotype (5). There is evidence that ICB targeting PD-L1/PD-1 can restore the functionality of these exhausted T cells (Fig. 3D).

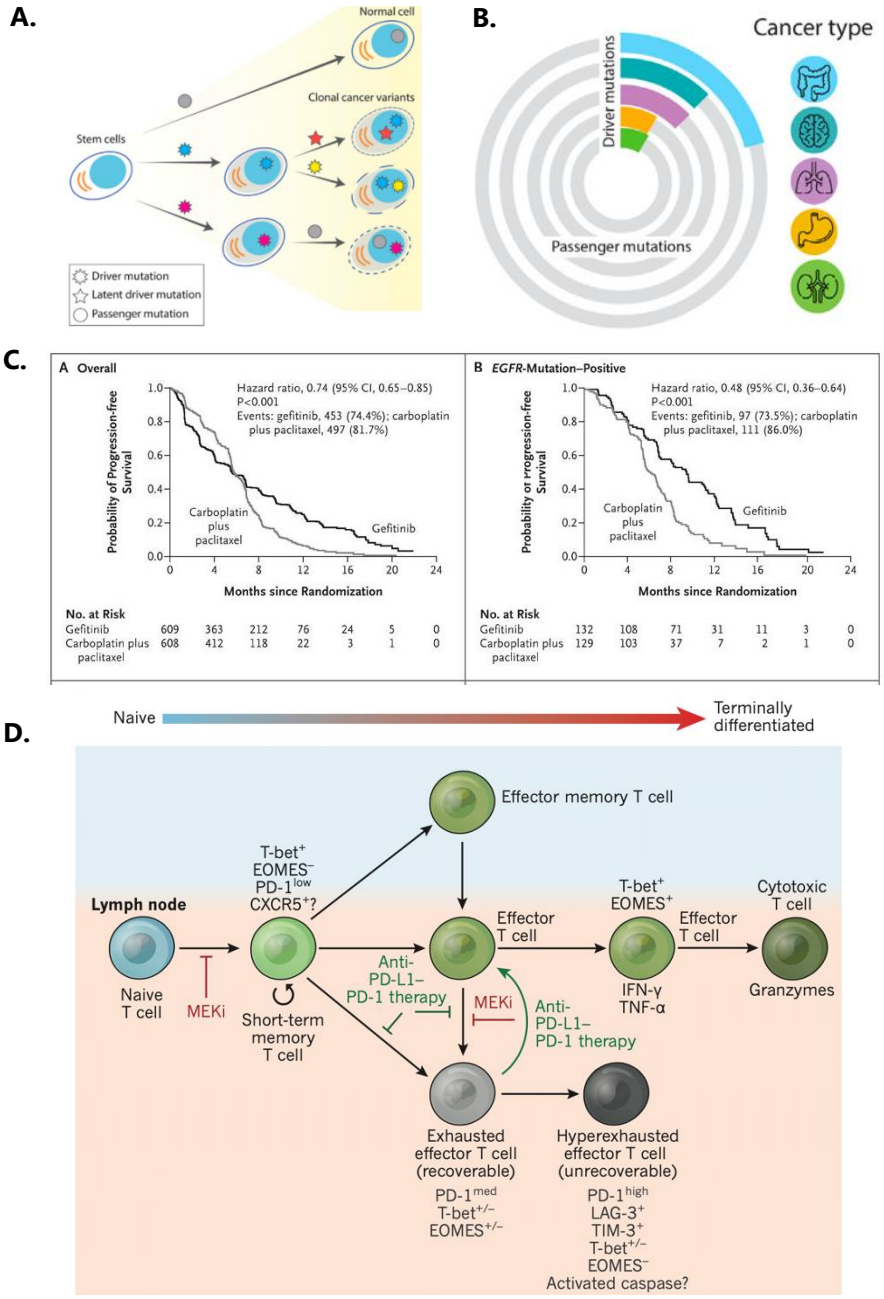

Figure 3 *Cancer genome and epigenetics impact immune surveillance.* ***A.*** *Cancer cells accumulate somatic mutations.* ***B.*** *The proportion of driver (colored) and passenger (grey) mutations per cancer type.* ***C.*** *EGFR mutation predicts response to EGFR-targeted therapy.* ***D.*** *Chronic antigen exposure can lead to effector T cell exhaustion. (Ostroverkhova, Przytycka, and Panchenko 2023; Mok et al. 2009; D. S. Chen and Mellman 2017)*

4.4 CANCER PEPTIDE-BASED VACCINES

Cancer vaccines represent promising strategies modulate the TME by TAA presentation and recognition, triggering T cell activation and anticancer immune responses. They can be used either as preventive or therapeutic strategies. Therapeutic vaccines usually involve exogenous delivery of TAA using antigen-presenting cells (APCs) such as dendritic cells (DCs), viruses, protein or peptides, DNA and RNA, and whole cancer cells (Fig. 4) (3,21). Although DCs-based vaccines present safety profiles and can induce tumor-specific immune responses in clinical trials, there is no robust impact on patients' outcomes (16,21–25). Adotevi and colleagues recently showed promising results with the use of a universal cancer peptide-based vaccine (UCPVax) in patients with solid cancers. UCPVax is a therapeutic vaccine against UCP2 and UCP4, two CD4+ T helper-1 (TH1) peptides derived from telomerase reverse transcriptase (TERT) and bind to most MHC class II molecules. In the clinical trial UCPVax, 59 patients with NSCLC a three-dose schedule (0.25 mg, 0.5 mg, and 1 mg) using a Bayesian-based phase Ib followed by phase IIa de-escalating design (26). Most of the patients developed specific CD4+ TH1 responses after the priming phase (56% after 3 doses and 87.2% after 6 doses). Overall, clinical benefit rate was 39% patients (n=20 SD, and n=1 CR) and the median OS was 9.7 months. The immune-responder patients achieved the greatest benefit: the 1-year PFS and the median OS were 17.2% (95% CI, 7.8 to 38.3) and 11.6 months (95% CI, 9.7 to 16.7) (P = .015) versus 4.5% (95% CI, 0.7 to 30.8) and 5.6 months (95% CI, 2.5 to 10) in non-immune responders (P = .005), respectively (26). Due to the high incidence of TERT promoter mutations in glioblastoma (GBM), the phase 2 UCPVax-Glio evaluated the same therapeutic vaccine in 31 patients with non-mutated *IDH1* and unmethylated *MGMT* GBM after standard therapy with RT and temozolamide (27). Twenty-seven (90%) patients experienced strong and sustained immune responses and the study showed survival benefit when compared to historical data (absence of control arm). There were no dose-limiting toxicity in both studies.

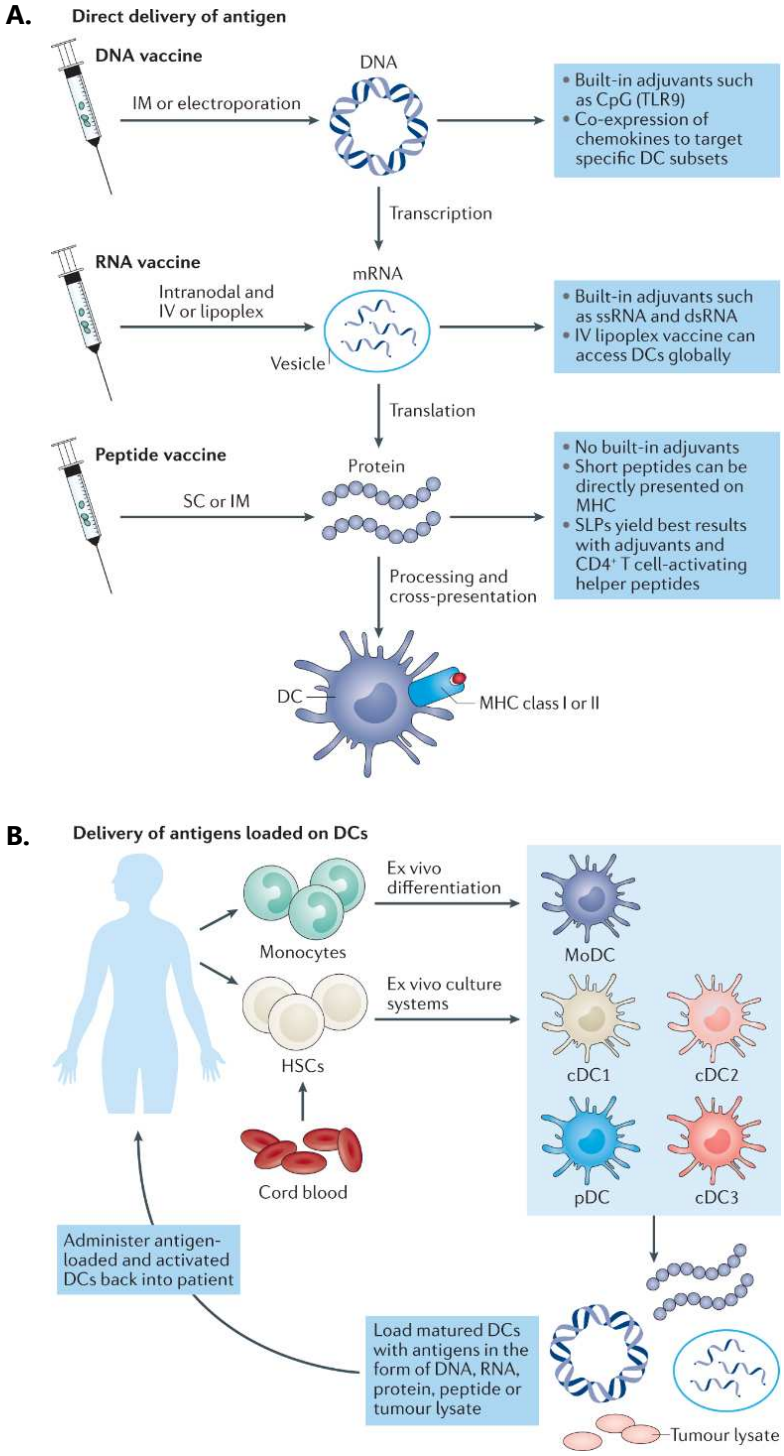

***Figure* 4** Cancer therapeutic vaccines. **A.** Antigen-based cancer vaccines. **B.** Autologous infusion of monocyte-derived dendritic cells loaded with tumor-associated antigens (Saxena et al. 2021).

4.5 CURRENT IMMUNE-CHECKPOINT BLOCKADE AGENTS

ICB represent novel approaches to modulate the TME using monoclonal antibodies (mAbs) that target negative regulators of T cells activation to unleash T-cell immunity and elicit anticancer responses.

4.5.1 CTLA-4 checkpoint

The mAbs targeting CTLA-4 are ipilimumab and tremelimumab. Ipilimumab got the first ICB' FDA approval in 2011. It binds to the counter-receptor CTLA-4 on the cell surface and blocks its interaction with the ligands CD80 (B7.1) and CD86 (B7.2), allowing co-stimulatory molecule CD28 to bind and lead to reactivation of antitumor function of T lymphocytes (3). Tremelimumab was approved by the FDA in 2022. It binds to the same epitope on CTLA-4 and has similar a binding affinity to Ipilimumab (28). Patients treated with anti-CTLA-4 have increased T cell receptor (TCR) diversity (29).

4.5.2 PD-1 and PD-L1 checkpoints

The mAbs targeting PD-L1 are avelumab, atezolizumab and durvalumab. Avelumab binds to the CC' loop of PD-L1. Beyond the PD-L1 CC' loop, atezolizumab also binds to C'C'' and FG loops and durvalumab also binds to the N-terminal region of PD-L1. The Fc fragments of both atezolizumab and durvalumab eliminate the antibody-dependent cellular cytotoxicity (ADCC) effect and complement-dependent cytotoxicity (CDC) and prevent the depletion of activated T cells (3).
Pembrolizumab, nivolumab, cemiplimab and dostarlimab are all mAbs targeting PD-1. Pembrolizumab binds to the C'D loop of PD-1, nivolumab binds to the N-loop of PD-1, and cemiplimab: binds to the BC, C'D, and FG loops of PD-1 with its heavy chain variable domain. Its light chain variable domain sterically inhibits the interaction between PD-1 and PD-L1. With high affinity for both human and cynomolgus monkey PD-1, dostarlimab inhibits both PD-L1 and PD-L2 to interact with PD-1 (3).

4.5.3 LAG-3 checkpoint

LAG-3 is an inhibitory cell surface receptor member of immunoglobulin superfamily expressed in both CD8 and CD4 T cells, Treg and NK cells, firstly described by a french immunologist (30,31). Combining nivolumab (PD-1 Abs) and relatlimab-rmbw (LAG-3 Abs), Opdualag got the first FDA approval for this class of ICB (32).

4.6 BIOMARKERS IN IMMUNO-ONCOLOGY

Although ICB confer durable clinical responses across a wide range of advanced solid and hematologic cancers, the benefit varies considerably between individuals with similar histology. Thus, there is a clear need to identify robust biomarkers of response to ICB. Biomarkers are considered predictive when providing information on the probability to benefit from a particular treatment (e.g. EGFR aberrations predict benefit for EGFR-targeted therapy) (Fig. 3C) (33). Prognostic biomarkers identify the probability of a clinical event (for example, disease progression or death), independently of the therapy. Biomarkers can be either predictive, prognostic or both. Current biomarkers in immuno-oncology (IO) reflect characters of the TME including host factors, sources of antigen, drivers of immune evasion, and markers of immune infiltration (10,34).

4.6.1 Tissue-based biomarkers

Tissue-based biomarkers can be assessed either by whole-exome and whole-transcriptomic techniques, PCR-based assays or immunohistochemistry (IHC) and immunofluorescence (IF) techniques.

4.6.1.1 PD-L1 and PD-1 expression

PD-L1 is a ligand of PD-1 expressed both on tumor and host immune cells such as DCs, macrophages and T cells that inhibit T cell activation (10). PD-L1 expression positively correlates with CD8+ TILs and other markers of active cellular immunity, including IFN-γ, granzymes, CXCL9 and CXCL10. The PD-L1 expression was the first potential predictive biomarker of ICB and patients expressing high PD-L1 are more likely

to benefit from ICB (Table 1) (10). Following the results of some clinical trials, PD-L1 gained FDA approval as a companion diagnostic test for PD-1 or PD-L1 blockade (Table 2).
However, PD-L1 predictive value is not consistent, probably due to variable assays, thresholds, type of cells (immune or cancer) and tissues (fresh versus archive) tested across studies. Between the primary studies that led to ICB approval between 2011-2019, it was predictive in only 28.9% of cases (35). Furthermore, it was not an effective biomarker or even associated with poor prognosis in patients with hepatocellular or urothelial carcinoma (36–38).

4.6.1.2 Tumor mutation burden (TMB)

Since neoantigens are not always effective to load to MHC molecules due to low affinity or lack of mutant amino acids at the appropriate position, higher frequencies of somatic mutations are associated with increased cancer-related antigen burden and ICB benefit (3,10). However, higher heterogeneity of cancer-related neoantigens intratumor can reduce anti-tumor immune responses and PD-L1 expression (10,39). TMB refers to the total number of non-synonymous mutations observed per megabase (10). The higher somatic mutational load, the larger the availability of neoantigen repertoire that can be recognized by T cells (3,10,17). Litchfield and colleagues performed a meta-analysis including 12 studies and 1008 ICB-treated patients with seven different cancer types and available whole-exome sequencing and transcriptomic data (34). Best response (RECIST criteria) was used as the read-out of clinical outcome. Between current published biomarkers, clonal TMB had the strongest effect size associated with ICB response in this pan-cancer meta-analysis (Table 1), highlighting the central role of neoantigens-induced T cell activation and response during ICB (34,40). Importantly, TMB is not a robust predictive biomarker across all cancer types or subtypes, such as acral or mucosal melanoma, Merkel-cell carcinoma and RCC (41–43). As for PD-L1, technique standardization and threshold definition are required.

4.6.1.3 Mismatch Repair Deficiency and Microsatellite Instability

DNA mismatch repair (MMR) pathways are responsible for recognizing

and repairing mismatched bases during DNA replication and gene recombination. Germline mutations or epigenetic silencing in MMR genes (dMMR) lead to the accumulation of errors during DNA replication and genome-wide instability, especially in regions of simple repetitive DNA sequences (known as MSI-H). Cancer harboring MMR deficiency (dMMR) may lead to increased mutations and aberrant neoantigen burden and are more likely to have higher microsatellite instability (MSI-H). It is associated with TMB, increased CD3+ and CD8+ TILs and PD-L1 expression (3,10).
However, dMMR does not always reflect MSI intensity and mutational load, which explains why responses are variable and about half of the patients do not benefit from ICB (10). MSI-H tumors can also arise from inherited germline mutations or epigenetic inactivation of MMR genes and recent evidence show that inactivation of MMR can be pharmacologically-induced, opening a therapeutic opportunity (44). Due to sustained benefit to ICB irrespective of primary site and histology, MSI became the first common predictive biomarker to gain FDA approval (Table 2) (10,45–48). Still not the infallible biomarker, since cannot identify all patients that benefit from ICB.

4.6.1.4 Gene expression profiling

As previously described, genomic subtypes and transcriptomic features can contribute to drive immune evasion and predict targeted-therapy response, including ICB.
Although experiencing great benefit from oncogene drivers-targeted therapy, patients with NSCLC harboring *EGFR* mutations or *ALK* rearrangements benefit less from ICB (20). Inversely, patients with NSCLC harboring *TP53* or *KRAS* mutations, especially *TP53/KRAS* co-mutated, are associated with clinical benefit to ICB (10,49). *TP53* mutation can increase CD8+ TILs and activate effector T cells as well as T cell-inflamed GEP and *TP53/KRAS* co-mutated tumors may have higher TMB. Also, pathogenic *POLE* mutations, gene encode the DNA polymerase epsilon and critical for proofreading and replication, are associated with hypermutated tumors and improved outcomes to ICB (17,50). Nod2 is an innate immunomodulatory protein that recognizes bacterial peptidoglycan through the muramyl dipeptide (MDP) that can lead to tolerogenic immune responses after chronic stimulation

(51). In a prospective cohort of 144 patients with NSCLC treated with anti-PD-1, *NOD2* loss-of-function variants were two times more prevalent in patients considered as exceptional responders (n=40) versus general population and rare in non-responders (n=18): 13.8%, 7.1% and 2.4%, respectively (52). In this study, patients were considered exceptional responders if progression-free survival (PFS) superior to 2 years and at least 1 immune-related adverse event grade 2 or higher and non-responders if progressive disease (PD) as best response.

In patients with melanoma, mutations leading to ineffective MHC-I and MHC-II antigen load and presentation are associated with ICB outcomes in patients with melanoma, such as Beta- 2 microglobulin (*B2M*) mutations (41,53). Polybromo-1 (*PBRM1*) gene is the second most common mutated gene in patients with RCC and may play an important role in its carcinogenesis and immunomodulation. *PBRM1* loss or mutations have been associated with less immunogenic and more angiogenic TME phenotypes and poorer outcomes under ICB (54–56). Between immune infiltration biomarkers, *CXCL9* expression, critical for recruiting antitumoral CD8+ T cell responses (57), had the strongest effect size in the pan-cancer meta-analysis (Table 1) (34). Immune signatures, such as IFN-γ signaling and T-cell–inflamed GEP are related to ICB response in solid tumors (10,34,58). These signatures directly correlate with PD-L1 expression. In transcriptomics-based studies, *CXCL13* expression is associated with improved outcomes and may represent clonal neoantigen-reactive CD8 TILs. (Thommen et al. 2018; Litchfield et al. 2021).

Although the associations with outcomes were relatively homogeneous across cancer types (subtypes were not taken into consideration) and cancer-specific biomarkers were rare (Fig. 5), Litchfield and colleagues showed that current published biomarkers explained only 0.6 of the variance in ICB response (34). In additional analysis of biomarker discovery, 9q34 (TRAF2) loss, that occurs as an evolutionary phenomenon of collateral sensitivity, was associated with ICB response (34). In early carcinogenesis, the whole-chromosome 9 loss is a driver event because it contains tumor suppressor genes such as CDKN2A (9p21.3) (34,59). Cyclin D1 regulates cell cycle and has a central role in carcinogenesis. In fact, *CCND1* amplification was associated with others genome and transcriptome

immunosuppressive hallmarks and comes up as a promising predictive biomarker of resistance to ICB (34,60,61). The potential synergistic interaction between anti-CDK4/6 drugs and ICB opens therapeutical opportunities (62,63). Interestingly, clonal neoantigen-reactive T cells and patients that benefited from ICB shared genes related to chemotaxis (*CCR5*), T cell activation (*CXCL13*, *ICOS*, *NCF1*, *EPSTI1*, *PARP9*, *GBP4*), IFN signaling (*FBX06),* and T cell exhaustion (*SLA2*, *IKZF3*) in the pan-cancer cohort conducted by Litchfield and colleagues (34). Another targetable checkpoint, LAG-3 expression has been associated with prognosis of patients with cancer (64).

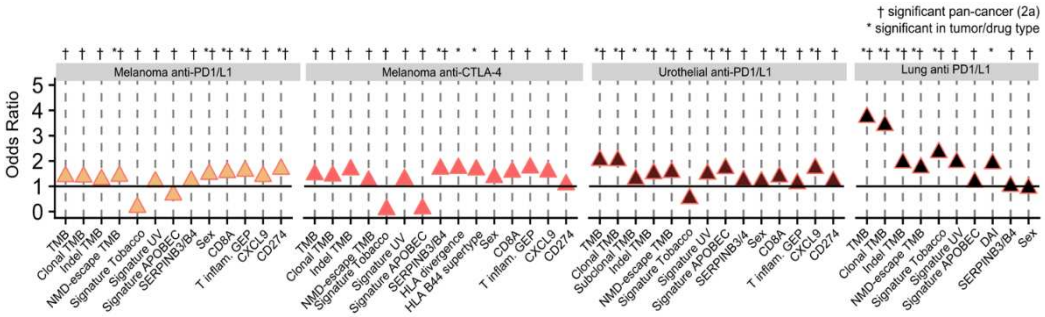

Figure 5 Pan-cancer metanalysis showing odds ratio effect sizes and significant predictive biomarkers of response in the pan-cancer (2a, cross) or independent cohorts (asterisk) from Litchfield et al. 2021.

4.6.1.5 Tumor-infiltrating lymphocytes

High TILs and specifically CD8+ T cell density have been associated with better outcomes to ICB (10). The Immunoscore, a standardized immune assay that quantifies CD3+ and CD8+ T cells in tumor tissue. Firstly used to evaluate the prognosis of localized CRC, where higher scores are related to lower recurrence rates and greater downstaging after CT with or without RT, the Immunoscore has also been associated to outcomes in other cancer types (65–68).

In a metanalysis including 33 studies and 2559 patients treated with ICB, increased CD8+ TILs was associated with better outcomes irrespective of TILs compartments (margin, stroma or intratumoral), cancer type and treatment regimen (monotherapy or combination)

(69). However, alone, CD8+ TILs are not a robust biomarker. Even if highly infiltrated by CD8+ T cells, patients with RCC do not substantially benefit from ICB (70), showing the importance to evaluate also the functional status of these cells. In patients with NSCLC, tumor harboring CD8+ TILs with PD-1 expression >1% were associated with greater outcomes during anti-PD-1 therapy (71). Furthermore, preliminary data show the role of other immune cells such as CD4+ T cells, Tregs, MDSCs, and TAMs as potential biomarkers (10).

4.6.2 Circulating biomarkers

4.6.2.1 Inflammatory markers

Various studies described biological parameters from blood routine sampling as prognostic biomarkers in patients with cancer. Lactate dehydrogenase (LDH) is an enzyme that belongs to the class of oxidoreductases and it has a central role in the anaerobic metabolic pathway. LDH is present in most of the organ tissues and can increase in different acute and chronic diseases, so it is a non-specific marker. In patients with cancer, high lactate dehydrogenase (LDH) is associated with poorer outcomes (41,72,73). Also, higher C reative protein (CRP) levels, a prototypical acute phase reactant, are negatively associated with outcomes (10).
CD27 is a member of TNF-receptor superfamily. Benhamouda et al. showed that CD27+ T cells exhibited a dysfunctional phenotype and CD27-CD70 interaction correlated with levels of soluble CD27 (sCD27) in patients with RCC (74). High level of sCD27, a surrogate of T cell dysfuncton, correlated with improved survival in patients with RCC treated with ICB, but not RTK (74). Not only baseline levels of circulating biomarkers, but also their dynamics during ICB, may predict the clinical benefit to ICB in different cancer types. Lower levels of IL-6 and IL-8 at baseline or decrease in these levels after ICB were associated with longer survival (10). Higher IL-8 levels were associated with immunosupressive TME features (75,76). Differently from tissue-based techniques, high levels of circulating CD8+ TILs were not associated with improved ICB outcomes (69), while some phenotypes of CD8+ and CD4+ T cells were associated with ICB outcomes (77,78). TAAs can induce the production autoantibodies that appear as

potential biomarkers for diagnostic, staging, prognostic and adverse events (79–82). Antibodies (Abs) anti-GM-CSF IgA and IgG have been significantly associated with ipilimumab-induced colitis (80). Interestingly, Rodriguez-Abreu et al. performed baseline autoantibody profiling in patients with NSCLC and prior AID or ICB (group 1) versus control group of patients with NSCLC without prior ICB or AID (group 2) (79). Interestingly, autoantibodies at baseline were identified in both groups. Autoantibodies anti-AQP4 and anti-NCOA1 were associated with the development of immune-related adverse events (irAEs). Autoantibodies to CENPT and SOX5 were related to longer OS in groups 1 and 2, respectively. In the group 1, autoantibodies against IL6, CENPT and the cancer testis antigens NY-ESO-2 and MAGEB2 were associated to benefit and lower risk of irAEs to ICB (79).

4.6.2.2 Immune cells

Also, other studies evaluated the association between blood count parameters from blood routine sampling and outcomes of patients with cancer. Low absolute monocytes and neutrophil-to-lymphocyte ratio (NLR) and, inversely, high relative-lymphocyte count and absolute eosinophils were related to improved outcomes (10,83,84). Using neutrophils/(leukocytes-neutrophils) ratio and LDH level, the Lung Immune Prognostic Index (LIPI) was firstly described as a predictive biomarker in patients with NSCLC (85). Further studies suggest that LIPI has a prognostic rather than predictive value, even in patients with RCC treated either with ICB or RTK (85–87).
There is increasing evidence on the role of B cells and humoral responses in patients with cancer. Carril-Ajuria et al. showed that unswitched memory B cells phenotype were associated with improved outcomes in patients with RCC treated with nivolumab after failure on antiangiogenic therapy (88). These cells positively correlated with with B cell density and TLS into the tumor and also with circulating memory Tfh. Inversely, BAFF and CXCL13, involved in B cell survival and recruitment, negatively correlated with unswitched memory B cells and were associated with poorer outcomes (88).

4.6.2.3 Tumor markers

As indirect markers of tumor burden, the decrease of tumoral markers such as Alpha-Fetoprotein in patients with hepatocellular carcinoma can predict benefit to therapies, including ICB (10,89). Circulating tumor DNA (ctDNA) refers to the fraction of cell-free DNA from tumor detected in the blood of patients and appears as a promising biomarker to ICB (10). In the SAFIR-02 trial, patients with tumor fraction ctDNA were more likely to have liver metastasis and higher tumor burden (90). In this study, the presence of tumor fraction ctDNA was independently associated with poorer survival either with ICB or chemotherapy. Even more, not only the baseline levels, but the dynamics can be used to monitor treatment responses. Undetectable levels at baseline or the drop after anti-PD-1 start was associated with improved response rates and survival in patients with melanoma (91). Unlike, persistently high levels were associated with poorer outcomes. ctDNA is also useful for diagnostic purposes, such as detection of EGFR mutations, including search for resistant mutations during EGFR-targeted therapy (10).

4.6.3 Host-related biomarkers

Host factors have been associated with outcomes in patients with cancer. Although a chronic inflammatory condition and established risk factor for cancer, obesity is associated with greater outcomes in patients with cancer (92). Instead, weight loss and lower muscle mass are associated with poorer outcomes and greater treatment-related toxicity (93) (see Appendix section, Article V). Further, organ-specific differences lead to different tropism for metastasis and both the number of metastatic sites and specific metastatic sites are associated with prognosis or benefit from ICB (4,41). In the pan-cancer meta-analysis for biomarker evaluation, sex appeared as the only significant host-related biomarker (Table 1) (34).

Table 1 Significant biomarkers associated with ICB outcome in a pan-cancer meta-analysis (34).

Category	Biomarker	OR (95% CI)	p-value
Sources of antigens	Clonal TMB	1.74 (1.41–2.15)	2.9×10^{-7}
	Total TMB	1.70 (1.33–2.17)	1.9×10^{-5}
	Frameshift insertion/deletion burden	1.34 (1.12–1.62)	1.6×10^{3}
	NMD-escape TMB	1.38 (1.15–1.66)	5.6×10^{4}
	Tobacco signature	1.39 (1.02–1.88)	3.5×10^{2}
	UV signature	1.34 (1.12–1.60)	1.2×10^{3}
	APOBEC signature	1.39 (1.09– 1.76)	8.1×10^{3}
	SERPINB3 mutations	1.33 (1.12–1.59)	1.2×10^{3}
Host factors	Sex	1.22 (1.03–1.43)	1.9×10^{-2}
Immune infiltration	*CXCL9* expression	1.67 (1.38–2.03)	1.3×10^{7}

	CD8A expression	1.45 (1.20–1.74)	1.0×10^4
	T cell inflamed GEP signature	1.43 (1.05– 1.96)	2.5×10^2
	CD274 (PD-L1) expression	1.32 (1.10–1.58)	3.0×10^3

Confidence interval (CI); gene expression profiles (GEP); nonsense-mediated decay (NMD); odds ratio (OR); tumor mutation burden (TMB).

4.6.4 Integrative models of biomarkers

To date, no biomarker that can robustly predict sensitivity to ICB. To better categorize the patients, recent studies developed predictive models integrating different clinical, genomic and/or transcriptomic characteristics. Litchfield et al. found low correlation between separate biomarker categories, paving the way to combining multiple markers together into a multivariable test in their pan-cancer meta-analysis (34). Using multiple multivariable predictive models for each cohort, clonal TMB and CXCL9 expression were the most relevant biomarkers and were integrated in a 11- (together with indel TMB, NMD-escape TMB, tobacco signature, UV signature, APOBEC signature, sex, T cell inflamed GEP signature, and CD274 and CD8A expression) and 2-marker models. Interestingly, both pan-cancer multivariable models outperformed TMB alone in three independent cohorts, showing that multivariable predictive scores are promising (34). Other studies demonstrated that patients with high expression of both PD-L1 and TILs are more likely to benefit from ICB (94,95). The Tumor Immune Dysfunction and Exclusion (TIDE) is a computational method that integrates a gene expression signatures of T cell dysfunction and exclusion on baseline tumor samples (96). A higher tumor TIDE score predicted worse survival in patients with melanoma, and performed better than other classical biomarkers such as TMB and PD-L1 expression.

Complex biomarkers can work and are already integrated in clinical routine. The 21-gene (Oncoytpe DX®) is well validated to predict recurrence and decide whether adjuvant systemic therapy should be used in patients with node negative, hormone receptor-positive, HER2-negative early breast cancer (97). Other assays have been developed, most of them using different panels of genes such as 70-gene signature (MammaPrint assay), and may also be acceptable (98,99). Integrating both clinical and biological parameters, the International Metastatic renal cell carcinoma Database Consortium (IMDC) risk model predicts survival in patients with renal cell carcinoma (RCC) (100,101). Nowadays, IMDC is used as a treatment-decision criteria in first-line therapy (102).

To date, only three predictive biomarkers have received FDA approval

and have been integrated into clinical routine for treatment decision-making (Table 2). Beyond selection of patients that might benefit from ICB, the discovery of effective biomarkers will decrease socioeconomic burden and avoid undesirable irAEs from ICB use. Although studies advance in the discovery of new biomarkers, their implementation in clinical routine is still challenging. Firstly, validation is required and complex and expensive techniques must be translated into cost-effective tools. Secondly, these tools need independent validation with reliable risk prediction models to support clinical decision-making (103).

Table 2 Immune checkpoint blockade agents with FDA-approval for solid tumors.

Immune checkpoint	Drug	Labeled indications					Trial
		Cancer type	Setting	Therapy line	Biomarker	Combination	
CTLA-4	Ipilimumab	CRC	Metastatic	After fluoropyrimidine, oxaliplatin, and irinotecan schema.	MSI-H or dMMR (assessed by PCR and/or IHC)	Nivolumab	CheckMate-142 (104)
		Esophageal squamous cell carcinoma	Unresectable advanced or metastatic	1st	None	Nivolumab	CheckMate-648 (105)
		HCC	Unresectable	After progression on sorafenib.	None	Nivolumab	CheckMate-040 (106)
		Malignant pleural	Unresectable	1st	None	Nivolumab	CheckMate-743 (107)

		mesothelioma					
		Melanoma	Localized (cutaneous), if pathologic involvement of regional lymph nodes of >1 mm after complete resection, and total lymphadenectomy.	Adjuvant	None	Single-agent	EORTC 18071 (108)
			Unresectable or metastatic	1st	None	± Nivolumab.	NCT00094653, NCT00094653, CheckMate 067 (109–111)

		NSCLC	Metastatic or recurrent	1st	PD-L1 TC ≥1% (Dako® IHC 28-8 pharmDx.), no EGFR or ALK genomic aberrations	Nivolumab	CheckMate 227 (112)
					None	Nivolumab + 2 cycles of platinum doublet CT	CheckMate 9LA (113)
		RCC	Advanced	1st	IMDC intermediate or poor risk	Nivolumab	CheckMate 214 (114)
	Tremelimumab	HCC	Unresectable	1st	None	Durvalumab	HIMALAYA (115)
		NSCLC	Metastatic	1st	No EGFR or ALK genomic tumor aberrations.	Durvalumab and platinum-based CT	POSEIDON (116)

PD-L1	Avelumab	MCC	Metastatic	Any	None	Single-agent	JAVELIN Merkel 200 (117)
		RCC	Advanced	1st	None	Axitinib	JAVELIN Renal 101 (118)
		UC	Locally advanced or metastatic	Maintenance after 1st line platinum-containing chemotherapy. After progression of platinum-based chemotherapy (within 12 months if neoadjuvant or adjuvant).			JAVELIN Bladder 100 and JAVELIN Solid Tumor (119,120)

	Atezolizumab	Alveolar soft part sarcoma	Unresectable or metastatic	Any	None	Single-agent	ML39345 (121)
		HCC	Unresectable or metastatic	without prior systemic therapy	None	Bevacizumab	IMbrave150 (122)
		Melanoma	Unresectable or metastatic		BRAF V600+	Cobimetinib and Vemurafenib	IMspire150 (123)
		NSCLC	Stage II to IIIA	Adjuvant, following resection and platinum-based CT	PD-L1 TC ≥1% (VENTANA SP263)	Single-agent	IMpower010 (124)
			Metastatic	1st	PD-L1 TC ≥50% IC ≥10% (VENTANA SP142), no EGFR or ALK genomic	Single-agent	IMpower110 (125)

					aberrations		
					Nonsquamous, no EGFR or ALK genomic aberrations	Bevacizumab, paclitaxel, and carboplatin	IMpower150 (126)
						Nab-paclitaxel and carboplatin	IMpower130 (127)
				After platinum-containing chemotherapy or approved targeted therapy for EGFR or ALK	None	Single-agent	OAK (128)
		Small cell lung cancer	Extensive stage	1st	None	Carboplatin and	IMpower133 (129)

						etoposide	
	Durvalumab	Biliary tract cancer	Locally advanced or metastatic	1st	None	Gemcitabine and cisplatin	TOPAZ-1 (130)
		HCC	Unresectable	1st	None	Tremelimumab	HIMALAYA (115)
		NSCLC	Unresectable stage III	Maintenance after concurrent platinum-based CT and RT.	None	Single-agent	PACIFIC (131)
			Advanced or metastatic	1st	No EGFR and ALK genomic aberrations	Tremelimumab and platinum-based CT	POSEIDON (116)
		SCLC	Extensive stage	1st	None	Etoposide and either carboplatin	CASPIAN (132)

						or cisplatin	
PD-1	Pembrolizumab	TNBC	High-risk early stage	Neoadjuvant, then adjuvant	PD-L1 CPS ≥10 (IHC 22C3 pharmDx)	CT before surgery, then alone after surgery	KEYNOTE-522 (133)
			Locally recurrent unresectable or metastatic	1st	PD-L1 CPS ≥10 (IHC 22C3 pharmDx)	CT	KEYNOTE-355 (134)
		Cervical cancer	persistent, recurrent, or metastatic	1st	PD-L1 CPS ≥1 (IHC 22C3)	CT ± bevacizumab	KEYNOTE-826 (135)
			recurrent or metastatic	After CT	PD-L1 CPS ≥1 (IHC 22C3)	Single-agent	KEYNOTE-158 (136)
		cSCC	Recurrent, metastatic, or locally advanced	Not curable by surgery or RT	None	Single-agent	KEYNOTE-629 (137)
		Endometrial carcinoma	Advanced	After systemic therapy (in any	pMMR or MSI-L	Lenvatinib	Study 309/KEYNOTE-

				setting), not candidates for curative surgery or radiation.			775 (138)
					dMMR or MSI-H (VENTANA MMR RxDx Panel or FoundationOne CDx)	Single-agent	KEYNOTE-028, KEYNOTE-158, KGOG1041 (46,139,140)
		Esophageal cancer or GEJ	Locally advanced or metastatic	Not candidate to surgical resection or definitive CRT	None	Platinum- and fluoropyrimidine-based CT	KEYNOTE-590 (141)
				after ≥1 prior lines of systemic therapy	Squamous histology with PD-L1 CPS ≥10 (IHC 22C3)	Single-agent	KEYNOTE-059 (142)
		Gastric cancer or GEJ	Locally advanced or metastatic	1st	HER2-positive by IHC (Dako HercepTest™) or	Trastuzumab and fluoropyrimi	KEYNOTE-811 (143)

					FISH (Dako HER2 FISH pharmDx™ Kit)	dine- and platinum-containing CT	
		HNSCC	Recurrent or metastatic	1st	None	Platinum- and fluorouracil-containing CT	KEYNOTE-048 (144)
					PD-L1 CPS ≥1 (IHC 22C3)	Single-agent	
				After platinum-based CT	None		KEYNOTE-012 (145)
		HCC	Advanced	After sorafenib	None	Single-agent	KEYNOTE-224 (146)
		Melanoma	Stage IIB, IIC, or III following complete resection	Adjuvant	None	Single-agent	KEYNOTE-716 and KEYNOTE-054 (147,148)

			Unresectable or metastatic	Any	None		KEYNOTE-001 and KEYNOTE-006 (149,150)
		MCC	recurrent or metastatic	1st	None	Single-agent	KEYNOTE-017 (151)
		Solid tumors	Unresectable or metastatic	After prior treatment, without satisfactory alternate treatment options	MSI-H or dMMR (PCR or IHC) or TMB-H ≥10 mut/Mb (FoundationOneCDx assay)	Single-agent	KEYNOTE-158 (46), KEYNOTE-164 (152), KEYNOTE-051 (NCT02332668)
		CRC	Unresectable or metastatic	1st line	MSI-H or dMMR	Single-agent	KEYNOTE-177 (153)

		NSCLC	Stage III (who are not candidates for surgery or definitive CRT) or metastatic	1st line	PD-L1 TPS ≥1% (IHC 22C3), no EGFR and ALK genomic aberrations.	Single-agent	KEYNOTE-042 (154)
			Metastatic		Nonsquamous histology, no EGFR or ALK genomic aberrations	Pemetrexed and platinum-based CT	KEYNOTE-189 (155)
					Squamous histology	Carboplatin and either paclitaxel or paclitaxel [protein bound])	KEYNOTE-407 (156)
			Stage IB (T2a ≥4 cm), II, or IIIA	Adjuvant, following	None	Single-agent	PEARLS/KEYNOTE-091 (157)

				resection and platinum-based CT			
			Metastatic	After platinum-based CT or EGFR- or ALK-directed therapy	PD-L1 TPS ≥1% (IHC 22C3)	Single-agent	KEYNOTE-010 (158)
		RCC	Advanced	1st	None	Axitinib or lenvatinib	KEYNOTE-426 and CLEAR (138,159)
			Intermediate-high or high risk of recurrence following nephrectomy ± resection of metastatic lesions.	Adjuvant	None	Single-agent	KEYNOTE-564 (160)

		UC	High-risk, NMIBC, BCG-unresponsive with CIS	Ineligible for or have elected not to undergo cystectomy	None	Single-agent	KEYNOTE-057 (161)
			Locally advanced or metastatic	1st, not eligible for platinum-based CT or 2nd after platinum-based CT	None		KEYNOTE-045 and KEYNOTE-052 (162,163)
				1st line, not eligible for platinum-based CT	None	Enfortumab vedotin	EV-103/KEYNOTE-869 {Citation}
	Nivolumab	CRC	Metastatic	Subsequent line, after fluoropyrimidine, oxaliplatin, and irinotecan	MSI-H or dMMR	Ipilimumab	CheckMate-142 (164,165)

				schema			
		Esophageal cancer or GEJ	Following surgery with residual pathologic disease who have received neoadjuvant CT.	Adjuvant	None	Single-agent	CHECKMATE-577 (166)
			Unresectable advanced or metastatic	1st	None	Fluoropyrimidine- and platinum-containing CT (adenocarcinoma and squamous)	CheckMate-649 (167); CheckMate-648 (105)
						Ipilimumab (squamous)	
				After prior		Single-agent	ATTRACTION-3

				fluoropyrimidine- and platinum-based CT		(squamous)	(168)
		Gastric cancer and GEJ	Advanced or metastatic		None	Fluoropyrimidine- and platinum-containing CT	CheckMate-649 (167)
		HNSCC	Recurrent or metastatic	After platinum-based therapy	None	Single-agent	
		HCC	Unresectable	After sorafenib	None	Ipilimumab	CheckMate-040 (106)
		Malignant pleural mesothelioma	Unresectable	1st line	None	Ipilimumab	CheckMate-743 (107)
		Melanoma	Involvement of	Adjuvant	None	Single-agent	CheckMate-238

			lymph nodes or metastatic disease following complete resection				(Weber, Mandala, Del Vecchio, Gogas, Arance, Cowey, Dalle, Schenker, Chiarion-Sileni, Marquez-Rodas, Grob, Butler, Middleton, Maio, Atkinson, Queirolo, Gonzalez, Kudchadkar, Smylie, Meyer, Mortier, Atkins, Long, Bhatia, Lebbé, Rutkowski,

							Yokota, Yamazaki, Kim, De Pril, et al. 2017)
			Unresectable or metastatic	1st line	None	single agent or Ipilimumab	CheckMate 066 and 067 (109,170)
		NSCLC	Localized (tumors ≥4 cm or node positive)	Neoadjuvant	None	Platinum-doublet CT	CheckMate 816 (171)
			metastatic or recurrent	1st line	PD-L1 TC ≥1% (IHC 28-8), no EGFR or ALK genomic aberrations	Ipilimumab	CheckMate 227 (112)
					No EGFR or ALK genomic aberrations	Ipilimumab and 2 cycles of platinum	CheckMate 9LA (113)

						doublet CT	
				Subsequent lines, after platinum-based CT or EGFR- or ALK-directed therapy	None	Single-agent	CheckMate 057 (172)
		RCC	Advanced	1st line	None	Cabozantinib	CheckMate 9ER (173)5
					Intermediate or poor IMDC risk	Ipilimumab	CheckMate 214 (114)
				After anti-angiogenic therapy	None	Single-agent	CheckMate 025 (174)
		UC	Localized, high risk after undergoing radical cystectomy	Adjuvant	None	Single-agent	CheckMate 274 (175)

			Locally advanced or metastatic	Platinum-resistant			CheckMate 275 (176)
	Cemiplimab	BCC	Locally advanced or metastatic	After or not eligible to hedgehog pathway inhibitor	None	Single-agent	Study 1620 (177)
		cSCC	Metastatic or locally advanced	Not eligible for curative surgery or radiation			R2810-ONC-1423 and R2810-ONC-1540 (178)
		NSCLC	Metastatic or locally advanced not eligible for surgery or definitive CRT	1st line	PD-L1 TPS ≥50%, no EGFR, ALK, or ROS1 aberrations.	Single-agent	Study 1624 (179)

					No EGFR, ALK, or ROS1 aberrations	Platinum-based CT	Study 16113 (180)
	Dostarlimab	Endometrial cancer	Recurrent or advanced, not eligible for curative surgery or RT	Platinum-resistant, subsequent lines	dMMR (VENTANA MMR RxDx)	Alone	GARNET (181)
		Solid tumors	Recurrent or advanced	Subsequent lines	dMMR (VENTANA MMR RxDx)	Alone	GARNET (181)
	Retifanlimab	MCC	Metastatic or recurrent locally advanced	Any	None	Alone	POD1UM-201 (182)
LAG-3	Relatlimab	Melanoma	Unresectable or metastatic	1st	None	Nivolumab and relatlimab-rmbw	RELATIVITY-047 (32)

Anaplastic lymphoma kinase (ALK); Bacillus Calmette-Guérin (BCG); Basal cell carcinoma (BCC); Carcinoma in situ (CIS);

Chemoradiotherapy (CRT); Chemotherapy (CT); Colorectal cancer (CRC); Combined positive score (CPS); Cutaneous squamous cell carcinoma (cSCC); Epidermal growth factor receptor (EGFR); Gastroesophageal junction (GEJ); Hepatocellular carcinoma (HCC); Merkel cell carcinoma (MCC); Microsatellite instability-high (MSI-H); Mismatch repair deficient (dMMR); Mutations/megabase (mut/Mb); Non-muscle invasive bladder cancer (NMIBC); Non–small cell lung cancer (NSCLC); Polymerase chain reaction (PCR); Radiotherapy (RT); Renal cell carcinoma (RCC); Triple-negative breast cancer (TNBC); Tumor cells (TC); Tumor-infiltrating immune cells (IC); Tumor mutational burden-high (TMB-H); Tumor proportion score (TPS); Urothelial carcinoma (UC).

5 INTESTINAL-RELATED BIOMARKERS

5.1 THE GUT MICROBIOME

Increasing evidence highlights the important role of the physiology of the intestinal barrier and the microbiota composition in the TME, leading to its recognition as one of the emerging Hallmarks of Cancer (5,183).

5.1.1 Factors shaping the gut microbiome

The taxa of a given individual is mostly explained by environmental factors such as cohabitation over heritability and genetics (184–187). In a three-generational population cohort comprising 8,208 individuals from 2,756 families in Netherlands, Gacesa et al. showed that *A. muciniphila*, *B. longum* and *Bacteriodaceae* were between the small subset of with significant heritable microbiota species (184). Other phenotypes such as technical factors, anthropometrics, medical measurements, exposome, diet, self-reported comorbidities and medication, and socioeconomics were also associated to individual variation of gut microbiome taxonomic composition and function (184,185).

Exposure to smoking, nitrogen dioxide and inhalable small particulate matter, a high-carbohydrate diet were correlated with disease related signatures such as *Clostridia* species. Inversely, healthier diet (such as low carbohydrate and protein intake), living in rural environment and having contact with pets were related with health-related commensals such as butyrate producers *Bacteroides*, *Alistipes* and *Faecalibacterium* (184). Comedications such as proton pump inhibitors (PPIs), antibiotics (ABX), biguanide antidiabetics, osmotic laxatives and intestinal anti-inflammatory agents affect gut microbiota composition (184,188,189). Indeed, Spencer et al. reported that sufficient fiber intake in diet and no probiotic use, associated to better outcomes in patients with melanoma, were related to increased alpha diversity and health-related species belonging to *Ruminococcaceae* family and *Faecalibacterium* genus (190).

5.1.2 The gut microbiome impacts the patients' outcomes under immunotherapy

Here, the impact of the gut microbiota in cancer immunotherapy will be approached based on a four-step proof of concepts: 1) ABX impair ICB efficacy; 2) the Gut OncoMicrobiome Signatures (GOMS) associated with ICB outcomes; 3) human stool composition influences the efficacy of ICB in "avatar" mice; and 4) clinical trials on microbiota-centered interventions.

5.1.2.1 Antibiotics impair ICB efficacy

The negative impact of ABX on ICB efficacy has been firstly demonstrated in a retrospective cohort of patients with RCC and NSCLC. ABX intake within 30 days of ICB start was significantly associated with poorer outcomes (191). Since then, several studies confirmed that ABX derived gut dysbiosis, compromise the efficacy of ICB independently of the tumor histology (192–197). In the largest meta-analysis evaluating the impact of ABX on ICB, 23.4% of the patients took ABX any time during ICB and ABX intake was associated with higher mortality (HR 1.81; 95%CI 1.50-2.17), the deleterious impact being more significant with intake ABX before ICB start (HR 2.26; 95%CI 1.76-2.90; Fig. 6A) (198). The mechanisms underlying the immunosuppressive effect of ABX leading to worse outcomes in patients with cancer were unknown. In a subgroup of patients included in the NIVOREN trial (n=69), ABX intake before ICB start, prior to fecal sampling, affected the gut microbiome composition, leading to a shift towards distinct tolerogenic bacteria (Fig. 6B; see Appendix section, Article XI) (199,200).

5.1.2.2 GOMS associated with ICB outcomes

Metagenomic shot gun (MGS)-based profiling of feces samples showed that gut microbiota composition influences immune responses and therefore the clinical benefit to ICB across countries and cancer types (197,201–205). The presence of regulatory bacteria such as *Akkermansia*

muciniphila, *Ruminococcus* or *Bifidobacterium* genera were associated with improved clinical response to ICB and increased systemic immune tonus (Fig. 7 and Table 3) (197,200,205–207) (see Appendix section, Article X). Spiliopoulou et al. have not found differences in gut microbiota composition of patients with primary versus acquired resistance to ICB in a cohort of patients with cancer of different primary sites (208). The Table 3 depicts specific gut microbial species associated with response to immunotherapy in patients with solid tumors in different studies across the world. Although there are differences regarding specific fingerprint differs between studies, some fingerprints groups such as *Lachnospiraceae* or *Oscillospiraceae* families are usually described as beneficial (198). Confounding variables such as geographical specificities, definition of response and technical factors can contribute to such differences between cohorts (184,198).

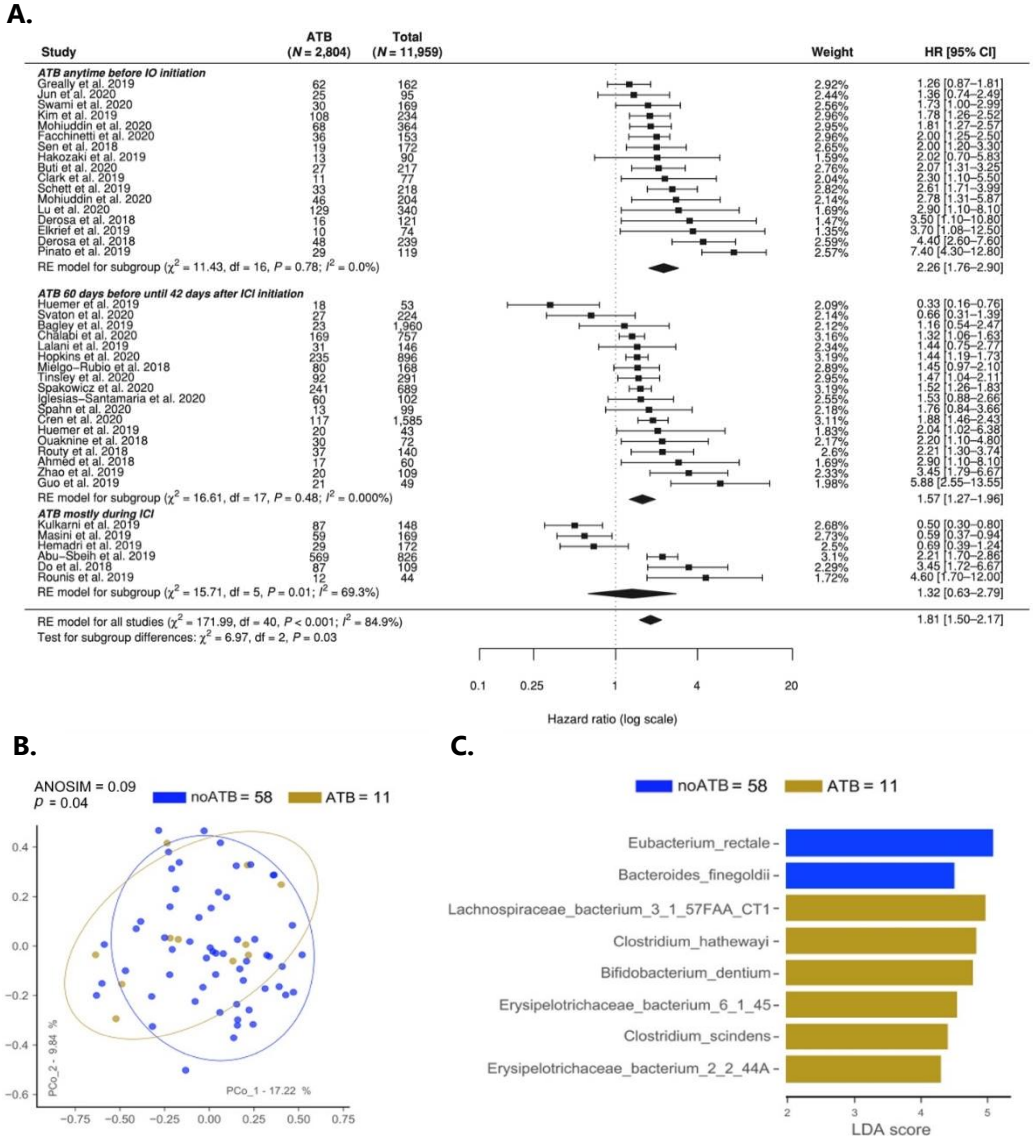

Figure 6 Antibiotics impairs outcomes of patients with cancer treated with immunotherapy. **A.** Meta-analysis of 34 studies evaluating the impact of ABX at different time points on the efficacy of immunotherapy in patients with cancer across different histologies (Lisa Derosa et al. 2021). **B-C.** Beta-diversity (B) differences and LEfSe graph (C) showing the most discriminant species among patients who took antibiotics (ABX, gold) and who did not took ABX (blue) at baseline (n = 69 patients) (Lisa Derosa et al. 2020).

Table 3 *Specific gut metagenomics species are associated with immunotherapy outcomes in patients with solid tumors.*

Country (reference)	Cancer type	Stage	N	ICB	Method	Definition of R	Alpha-diversity	Species
France (209)	Melanoma	IV	26	CTLA-4	16S	SD + CR + PR >6 months	R > NR	R: *Faecalibacterium* spp, *Ruminococcaceae*
USA (210)	Melanoma	Advanced	39	PD-1 ± CTLA-4	MGS	SD + CR + PR	R = NR	R: *F. prausnitzii, D. formicigenerans, B. caccae, S. parasanguinis, H. filiformis, B. thetaiotamicron*
USA (211)	Melanoma	IV	43	PD-1	16S	CR + PR or SD >6	R > NR	R: *F. prausnitzii,*

						months		*Ruminococcaceae*
USA (205)	Melanoma	IV	42	PD-1	16S	CR + PR	R > NR	R: *B. Longum, E. Faecium, C. aerofaciens*
France (197)	NSCLC and RCC	IV	153	PD-1	MGS	CR + PR or SD + CR + PR >3 months	R > NR	R: *A. muciniphila, Eubacterium, Alistipes* spp, *Ruminococcaceae, Lachnospiraceae, Firmicutes*
France (200)	RCC	IV	69	PD-1	MGS	SD + CR + PR >12 months	R > NR	R: *A. muciniphila, Eubacterium sp, B. salyersiae*

								NR: *H. hathewayi, E. clostridioforme*
USA (212)	NSCLC	IV	13	PD-1 + CT	MGS	CR + PR >3-6 months	R = NR	R: *Firmicutes* NR: *Bacteroidetes*
USA (213)	Melanoma	IV	94	PD-1	MGS	SD + CR + PR	R = NR	R: *E. rectale, Blautia* spp, *R. torques, R. gnavus, A. hadrus, Bifidobacterium*
China (214)	NPC	Recurrent or IV	50	PD-1	MGS	PR	R = NR	R: *Clostridiales* order NR: *R. bacterium,*

								Ruminococcus sp., *Ruminiclostridium* genus
UK, Spain, NLD (215)	Melanoma	IV	175	PD-1 + CTLA-4	MGS	SD + CR + PR	R = NR	R: *A. muciniphila, Roseburia, L. vaginalis*
USA (216)	NSCLC	IB and IIIA	37	PD-1 + CT ± CTLA-4	16S	MPR	R = NR	R: *Akkermansia, Lachnospiraceae, Rhodospirillales* NR: *Holdemanella, Megasphaera, Haemophilus* and *Sellimonas*

Hungary (217)	NSCLC	IIIB and IV	62 + 60 V	PD-1	MGS	SD + CR + PR >6 months	R = NR	R: *A. shahii, B. visceriola, B. faecalis, Bacteroides sp. A1C1 and A. finegoldii* NR: *S. salivarius, S. vestibularis, S. parasanguinis, B. longum, B. adolescentis and B. breve*
Croatia (218)	Melanoma	IV	15	PD-1 ± CTLA-4	MGS	CR>12 months. Early if CR	Early R = late R	Early R: *Barnesiella intestinihominis*, *Sutterella*

						achieved <9 months.		*wadsworthensis*, *Bacteroides finegoldii* Late R: *Coprococcus comes*, *Bifidobacterium pseudocatenulatum*

Chemotherapy (CT); Complete response (CR); Immune-checkpoint blockade (ICB); Major pathologic response (MPR) ; Metagenomics shotgun sequencing (MGS); Nasopharyngeal carcinoma (NPC); Netherlands (NLD); Non-responder patient (NR); Number of patients (N); Partial response (PR); Renal cell carcinoma (RCC); Responder patients (R); Stable disease (SD); United Kingdom (UK); Validation (V).

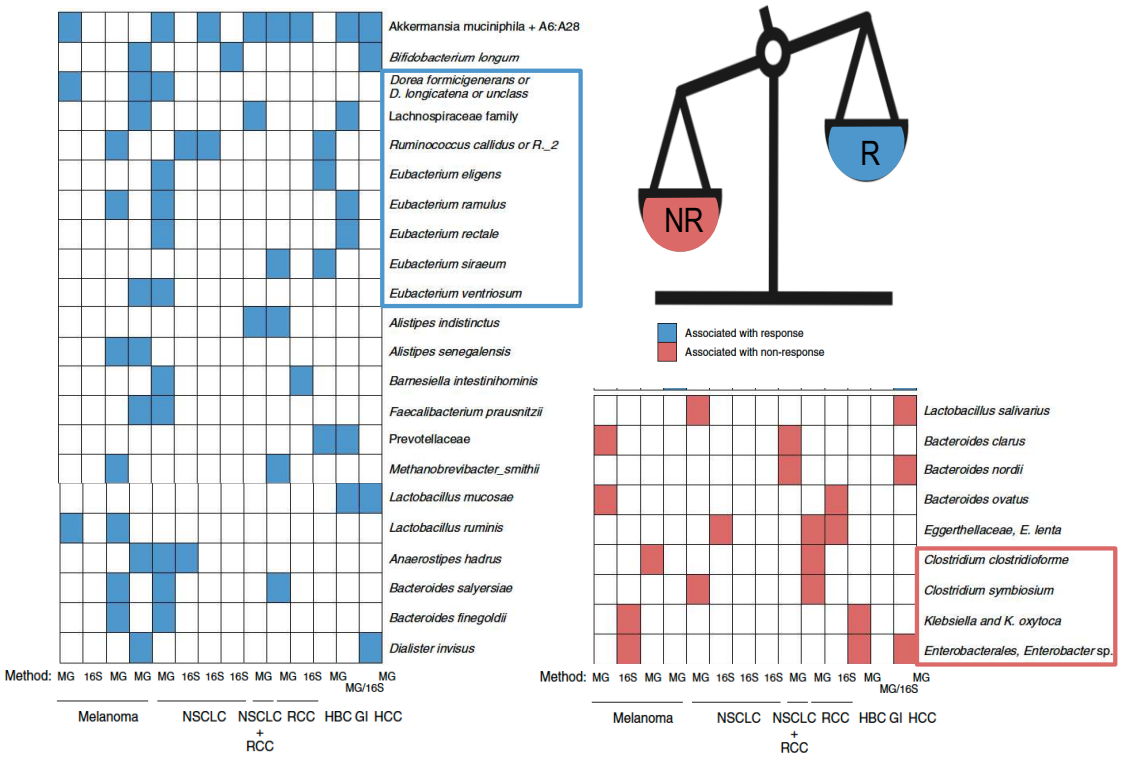

Figure 7 Metagenomics species associated with responders (R, blue) and non-responders (NR, red) to immunotherapy, adapted from (Park et al. 2022).

5.1.2.3 Human stool composition influences the efficacy of ICB in "avatar" mice

In order to establish the causal relationship between gut microbiota composition and ICB efficacy, mice models were used. The fecal microbiota transplantation (FMT) consists on the administration of biological material from a donor to a recipient. The FMT of patients' intestinal microbiota into mice could humanize the gut microbiota of these mice, creating a human microbiota "avatar". The FMT of feces from patients who did not respond to ICB lead to non-responder "avatar" mice. Then, either the FMT from patients that responded to ICB or the oral gavage with specific gut microbial species associated with response to ICB (Table 3) could restore the efficacy of ICB in these non-responder "avatar" mice (197,200,211) (see Appendix section, Article XI).

5.1.2.4 Clinical trials on microbiota-centered interventions (MCI)

MCI consist of therapies based on the modulation of gut microbiota in order to restore a healthier and immunogenic flora. Conditioning of the immune system by the MCI may improve the efficacy of anticancer treatments. MCI include different strategies: FMT, live biotherapeutic products (probiotics), prebiotics, diet, and co-medications (198).

Clinical trials using FMT evaluated the transfer of fecal material from patients with cancer that achieved persistent complete (CR) or partial (PR) responses to ICB ("responder") or healthy individuals either by endoscopy or oral capsules. In two pioneer articles, Baruch and Davar brought up the evidence of the feasibility, safety and efficacy of FMT in patients with cancer (219,220). In the setting of patients with metastatic melanoma primary resistant to ICB, the use of FMT from a responder patient before rechallenge to ICB could restore the efficacy in around 30% of the patients (Fig. 8A-B). Interestingly, IgG responses directed against the allogeneic microflora introduced into melanoma patients by FMT were associated with efficient colonization of the exogenous ecosystem and benefit from rechallenge to ICB (Fig. 8C) (220). Furthermore, upfront FMT from healthy individuals seems to ameliorate response rates in 20 patients with metastatic melanoma treated with ICB in first-line, leading to a disease control rate of 75% (15/20) and overall response rate of 65% (13/20) (Fig. 8D) (221). Park et al. demonstrated that FMT may be a promising strategy in non-melanoma cancer (222). In patients with gastrointestinal cancers with primary (46.2%) or secondary (53.9%) resistance to ICB, the transfer of fecal material from responder patients led to disease control rate in 46.2% of patients after ICB rechallenge, with evidence of immune activation (222). Importantly, FMT was well tolerated in these studies.

Recently, two phase 1 clinical trials have demonstrated the promising efficacy of the live biotherapeutic product CBM588 (containing a strain of *Clostridium butyricum*) in combination with either Nivolumab plus Ipilimumab or Cabozantinib in patients with metastatic RCC treated in first line (223,224). Both trials did not meet their primary endpoint, the change in *Bifidobacterium spp*. relative abundance in the feces of the patients after the use of CBM588.

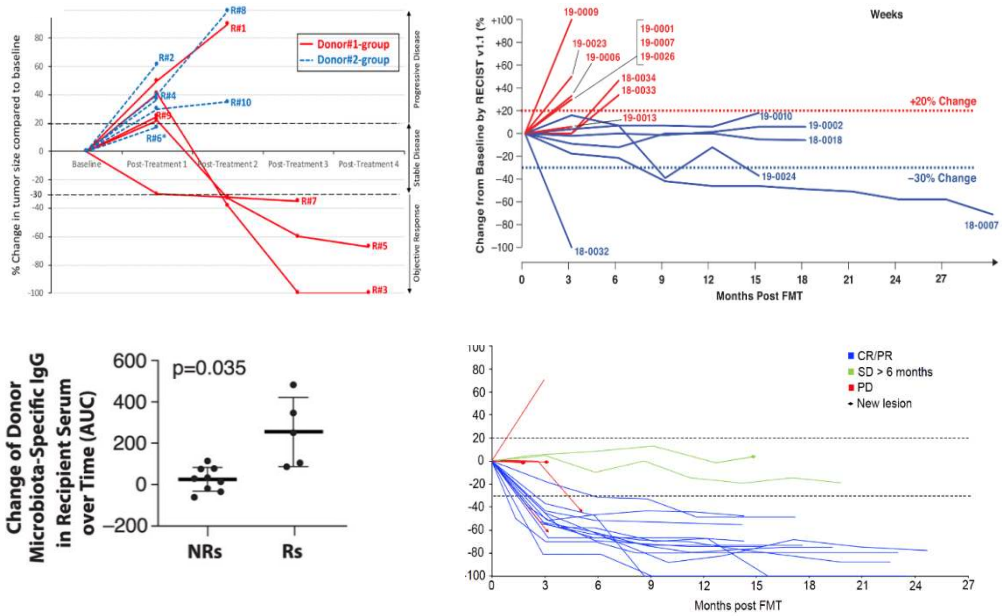

Figure 8 Fecal microbiota transplantation (FMT) circumvents primary resistance to anti-PD-1 blockade. **A.** Ten patients with anti-PD-1-refractory metastatic melanoma: 1CR+ 2PR after FMT (Baruch et al. 2021). **B.** Fifteen patients with anti-PD-1-refractory metastatic melanoma: 1CR + 2PR + 3SD after FMT (Davar et al. 2021). **C.** FMT induced recipient IgG response against donor microbiota (Davar et al. 2021). CR: complete response ; PR: partial response ; SD: stable disease.

5.1.2.5 Definition of health-related microbiome

Rather than a cancer-specific signature, recent evidence shows that different inflammatory diseases such as cardiovascular, metabolic and inflammatory bowel diseases share consistent microbiome–disease patterns (184). As previously described, gut specific MGS species in the feces samples at ICB start have been associated with outcomes in patients with cancer (Table 3), but there are variations at the levels of order, genera, or species between studies. In a three-generational cohort comprising 8208 individuals in Netherlands, Gacesa et al. analyzed the gut microbiota composition related to self-reported health and 81 diseases ($\geq$ 20 cases/disease) using MGS. *Anaerotruncus*, *Ruminococcus*, *Bacteroides*, *Holdemania*, *Flavonifractor*, *Eggerthella*

and *Enterocloster* species comprised the gut signature shared between diseases, whereas *Faecalibacterium*, *Bifidobacterium*, *Butyrivibrio*, *Subdoligranulum*, *Oxalobacter*, *Eubacterium* and *Roseburia* species were associated with self-reported health (184).
Gupta et al. proposed the predictive index Gut Microbiome Health Index (GMHI), a biologically-interpretable mathematical formula using 50 MGS species, and could stratify groups into health and disease status with an accuracy of 73.7% (225). Later, Gacesa et al. applied the GMHI in their three-generational dutch cohort and found significantly difference between individuals with self-reported health and diseases (184). This evidence opens an opportunity to the development of microbiota-based predictive scores for a healthy status and its use as an interception strategy (226).

5.1.3 Cancer-associated microbiota

Accumulating evidence demonstrates that bacteria colonize human cancers, and these microorganisms can be found intracellularly either in cancer and immune cells into the TME (227,228). Methods based on molecular biology, microbiology and histology are currently used to evaluate the cancer-associated microbiota (Fig. 9) (228). To date, there is no standard technique and combining different techniques enables more accurate characterization.

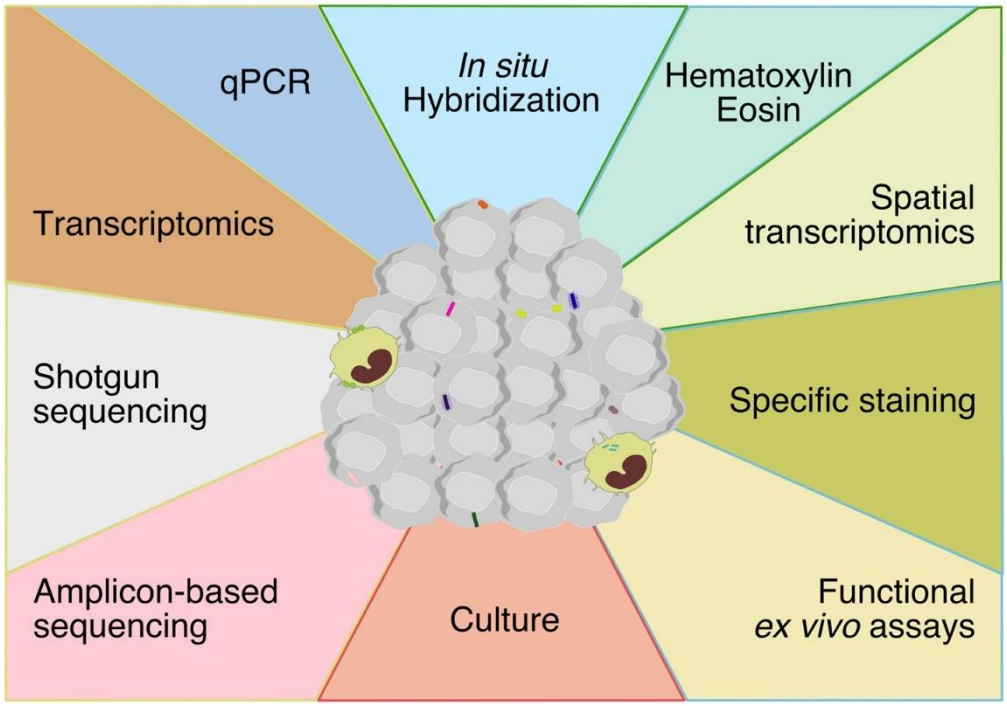

Figure 9 Techniques to assess cancer-associated microbiota (Goubet 2023).

Together with tobacco and UV radiation, it is well known that microorganisms can be procarcinogen to humans. Nowadays, only 11 microorganisms (including seven viruses, three platyhelminthes, and one bacterium) are recognized as pro-carcinogenic agents to humans: the Epstein-Barr (EBV), Hepatitis B (HBV), Hepatitis C (HCV) viruses, Kaposi sarcoma herpesvirus (KSV), human immunodeficiency virus-1 (HIV), human papilloma viruses (HPV), and human T cell lymphotropic virus type 1 (HTLV) viruses, the platyhelminthes Opisthorchis viverrine, Clonorchis sinensis, and Schistosoma haematobium, and the bacterium Helicobacter pylori (229,230). Beyond integration of the genome into host cells and pro-carcinogenic properties, studies have evolved to demonstrate the Janus-face of the microbiome and its impact on immune-surveillance in even more complex and multifactorial mechanisms. Microbial peptides are sources of neoantigens (bacteria-derived or homologous epitopes) and can reveal cancer cells and trigger T cell immunity (227,231). Therefore,

cancer-associated microbial neoantigens are promising targets for therapeutic or preventive strategies.

Surpassing resistance to immunotherapy is an unmet medical need. Microbiota-based biomarkers and MCI are promising strategies to improve outcomes of patient under ICB. Current standard methods to evaluate gut microbiota composition are cost- and time-consuming and we lack a diagnostic tool for clinical routine use to select patients and donors to MCI. Here, we hypothesize that intestinal-based biomarkers can be translated into easy-to-use tools to guide routine treatment-decision in patients with cancer.

6 RESEARCH CONTEXT AND OBJECTIVES

During my thesis, I had the chance to work in different projects that led to the development of intestinal-based biomarkers, both fecal and circulating biomarkers. Fecal biomarker discovery using standard taxonomy MGS profiling could be translated into PCR-based test. The circulating biomarkers include the soluble form of the microbiota-modulated checkpoint mucosal addressin cell adhesion molecule-1 (MAdCAM-1), specific humoral responses against commensals and metabolomics hallmarks.

6.1 FECAL BIOMARKERS

To address the causal link between cancer and dysbiosis, assessing whether gut dysbiosis promotes tumorigenesis and how it controls tumor progression (see Results section, Article I). In parallel, we explored taxonomic fingerprints biomarkers and development of a taxonomic-based score assessing dysbiosis translated into an easy-to-use tool for clinical routine use (see Results section: Articles II & III; Appendix section: Article XI, Abstracts III-VI).

6.2 CIRCULATING BIOMARKERS

6.2.1 Soluble MAdCAM-1

Gut-derived integrin α4β7 can mediate pathologic inflammatory conditions of the gut and traffic of immune cells to extra intestinal sites. Lymphocytes primed in the mesenteric lymph nodes or homing to the intestinal lamina propria express the α4β7 integrin interacting with its counter-receptor, MAdCAM-1, expressed in intestinal high endothelial venules (HEVs). Whether the α4β7–MAdCAM-1 axis controls anticancer immunity is unknown. We investigated the impact of ABX-related dysbiosis and gut-derived immune responses via the α4β7–MAdCAM-1 axis. Then, we aimed to evaluate soluble MAdCAM-1 (sMAdCAM-1) as a proxys of dysbiosis and biomarker in IO (see Results section: Article IV, Appendix section: Abstract VII).

6.2.2 Specific humoral responses against commensals

B cells and TLS have a determinant role in the cancer immune-surveillance and the development of humoral responses directed against specific microbiota species may be associated with effective systemic immunity. We aimed to investigate the impact of specific humoral responses against commensals and T cell responses against commensals on the outcomes of patients with muscle-invasive bladder cancer (MIBC) treated in the PANDORE single-arm, phase II trial (NCT03212651; see Results section, Article V).

6.2.3 Metabolomics profiling

We have previously demonstrated that ketogenic diet (KD) induced a gut microbiota shift towards immunogenic commensals and accumulation of the metabolites ketone bodies (KB) in different organs in preclinical studies (see Appendix section, Article IX). Interestingly, both KD and KB enhance the anticancer effects of PD-1 blockade. We aimed to further investigate metabolomics hallmarks in patients with cancer that can be developed as biomarker or therapeutic strategies (see Results section, Article VI).

7 MATERIAL AND METHODS

7.1 PRECLINICAL RESEARCH

7.1.1 Cell Culture, Reagents, and Tumor Cell Lines.

MC38, MCA-205, B16F10 (syngeneic from C57BL/6J mice), and 4T1 cell lines (syngeneic from BALB/c mice) were purchased from the American Type Culture Collection, whereas the AT3 breast cancer cell line (syngeneic from C57BL/6J mice) was kindly provided by Dr. Mark Smyth (QIMR Berghofer, Brisbane, Australia). The RET melanoma cell line, generated by transgenic expression of the RET proto-oncogene under the control of the metallothionein-1 promoter driving spontaneous melanogenesis, was provided by Viktor Umansky (DKFZ—German Cancer Research Center; syngeneic from C57BL/6J mice). The luciferase-transfected RENCA cell line (syngeneic for BALB/c mice) was provided by Transgene. Cells were cultured at 37°C with 5% CO2 in RPMI 1640 containing 10% FCS, 2 mmol/L l-glutamine, 1% penicillin/streptomycin, and 1% sodium pyruvate and nonessential amino acids. All reagents were purchased from Gibco-Invitrogen. Dead RET cells were created by repeating freezing and thawing of the RET cell line three times continuously, and viability of the cell line was evaluated by the Vi-CELL Cell Viability Analyzer. Cell lines were regularly tested for Mycoplasma contamination and were not used after more than 10 passages.

7.1.2 Ethics, Guidelines, and Providers.

All animal experiments were carried out in compliance with French and European laws and regulations. The local institutional animal ethics board and French Research Ministry approved all mouse experiments (permission numbers: 2020_035_25416). Experiments were performed in accordance with government and institutional guidelines and regulations. Female C57BL/6 mice were purchased from Harlan. Mice were used between 7 and 12 weeks of age. All mouse experiments were performed at the animal facility of Gustave Roussy Cancer Campus

where animals were housed in specific pathogen-free conditions.

7.1.3 Subcutaneous Transplantable MCA-205 sarcoma, MC38, B16F10, and RET Melanoma.

Mice were implanted with 0.8 × 10^6 MCA-205 sarcoma, 1.0 × 10^6 MC38, 0.3 × 10^6 B16F10, or 0.5 × 10^6 live or dead RET melanoma, 0.5 × 10^6 AT3 breast cancer, and 0.3 × 10^6 4T1 cells subcutaneously. Tumor-inoculated mice were treated intraperitoneally when tumors reached a 20 to 40 mm^2 size with anti–PD-1 mAb (250 µg/mouse; clone RMP1-14 purchased from Bio X Cell), anti-CTLA4 (100 µg/mouse, clone 9D9 purchased from Bio X Cell) or isotype controls (clones 2A3 and MPC11, respectively) three times at three-day intervals. Tumor length and width were routinely monitored every three days with a caliper.

7.1.4 The RENCA-luc Orthotopic Tumor Model.

BALB/c mice were anesthetized with isoflurane. A lateral incision was made on the dorsolateral right flank of each mouse. Then, 10^4 Renca-Luc cells resuspended in 30 µL PBS were injected into the subcapsular space of the right kidney. The skin incision was then closed with surgical clips. Tumor growth was monitored after 15 days of tumor injection using an IVIS Imaging System 50 Series (Analytic Jenap). At day 15 post tumor injection, mice were euthanized to harvest small intestines and perform ileum Swiss roll.

7.1.5 Orthotopic Luciferase-Engineered TC1 Lung Cancer Model.

TC1 cells stably expressing firefly luciferase (TC1-Luc, 4 × 10^5 in 100 µL PBS) were percutaneously injected into the right lung of wild-type C57BL/6 mice. Tumor incidence and development were regularly monitored by the in vivo photonic imaging of tumor cells' luciferase activity. In brief, mice received a percutaneous injection of luciferase substrate (Beetle Luciferin potassium salt, Promega) at a dose of 150 mg/kg, and 8 minutes after luciferin inoculation, photons were acquired on a Xenogen IVIS 50 bioluminescence in vivo imaging system (Caliper Life Sciences Inc.). Tumor-bearing mice were sacrificed at days 7, 14, and 21 after tumor injection.

7.1.6 TC1 Intravenous (IV) Model.

To establish the non–small cell lung carcinoma IV model, TC1 cells stably expressing firefly luciferase (TC1-Luc, 5 × 105 in 100 µL PBS) were intravenously injected into wild-type C57BL/6 mice. Tumor incidence and development were regularly monitored by in vivo photonic imaging of tumor cells' luciferase activity. In brief, mice received an i.p. injection of luciferase substrate (Beetle Luciferin potassium salt, Promega) at a dose of 150 mg/kg, and 8 minutes after luciferin inoculation, photons were acquired on a Xenogen IVIS 50 bioluminescence in vivo imaging system (Caliper Life Sciences Inc.). Two weeks after cell injection (day 14), tumor incidence in the lung was detected at an exposure time of four minutes. In vivo imaging was conducted every four to five days with an exposure time starting with four minutes, which was then gradually decreased to three, two, and one minute when photon saturation occurred. Tumor-bearing mice showing photon saturation within less than one minute of exposure were euthanized.

7.1.7 Antibiotic Treatments.

Mice were treated with antibiotic solution containing ampicillin (1 mg/mL), streptomycin (5 mg/mL), and colistin (1 mg/mL; Sigma-Aldrich), or colistin alone (1 mg/mL), or vancomycin alone (0.25 mg/mL) added in autoclaved drinking water. Antibiotic solutions were refreshed and bottles were replaced three times a week.

7.1.8 Cohousing Experiments.

The same number of RET-injected mice (C57BL/6J females) were cohoused as littermates with naïve (non–tumor-bearing) mice (C57BL/6J females) in the same cage from the day of tumor injection until sacrifice. As for methylcholanthrene-induced sarcoma, MCA inoculated and noninoculated mice were admixed in the same cage in a 1:1 ratio or left alone in separate cages. Groups of wild-type C57BL/6 mice were injected subcutaneously in the flank with 100 µg of 3-MCA in 0.10 mL of corn oil. Mice were monitored every 7 days for tumor development 90 to 100 days after 3-MCA treatment. Animals bearing nodules

>0.5 cm2 in area and demonstrating progressive growth were considered as “tumor” nodules, as previously described (232).

7.1.9 DNA extraction and 16S rRNA sequencing of mouse stools.

Preparation and sequencing of mouse fecal samples were performed at IHU Méditerranée Infection, Marseille, France. Briefly, DNA was extracted using two protocols. The first protocol consisted of physical and chemical lysis, using glass powder and proteinase K, respectively, then processing using the Macherey-Nagel DNA Tissue Extraction Kit (233). The second protocol was identical to the first protocol, with the addition of glycoprotein lysis and deglycosylation steps (234). The resulting DNA was sequenced, targeting the V3–V4 regions of the 16S rRNA gene as previously described (235). Raw FASTQ files were analyzed with Mothur pipeline v.1.39.5 for quality check and filtering (sequencing errors, chimerae) on a Workstation DELL T7910. Raw reads were filtered and clustered into Operational Taxonomic Units (OTU), followed by elimination of low-populated OTUs (until five reads) and by de novo OTU picking at 97% pairwise identity using standardized parameters and SILVA rDNA Database v.1.19 for alignment. Sample coverage was computed with Mothur and resulted to be on average higher than 99% for all samples, thus meaning a suitable normalization procedure for subsequent analyses. Bioinformatic and statistical analyses on recognized OTUs were performed with Python v.2.7.11. The most representative and abundant read within each OTU (as evidenced in the previous step with Mothur v.1.39.5) underwent a nucleotide Blast using the National Center for Biotechnology Information (NCBI) Blast software (ncbi-blast-2.3.0) and the latest NCBI 16S Microbial722 database accessed at the end of April 2019 (ftp://ftp.ncbi.nlm.nih.gov/). A matrix of bacterial relative abundances was built at each taxon level (phylum, class, order, family, genus, and species) for subsequent multivariate statistical analyses. Raw data were first normalized and then standardized using Quantile-Transformer and StandardScaler methods from Sci-Kit learn package v0.20.3. Normalization transforms each variable to a strictly Gaussian-shaped distribution, whereas the standardization results in each normalized variable having a mean of zero and variance of one. These two steps of normalization followed by

standardization ensure the proper comparison of variables with different dynamic ranges, such as bacterial relative abundances, tumor size, or colonic infiltrate score. Measurements of α diversity (within sample diversity), such as observed_otus and Shannon index, were calculated at the OTU level using the SciKit learn package v.0.4.1. Exploratory analysis of β-diversity (between sample diversity) was calculated using the Bray–Curtis measure of dissimilarity calculated with Mothur and represented in PCoA, whereas for hierarchical clustering analysis, the "Bray–Curtis" metrics and "complete linkage" method were implemented using custom scripts (Python v.2.7.11). We implemented PLS-DA and the subsequent variable importance plot (VIP) as a supervised analysis in order to identify the most discriminant bacterial species among the different cohorts of mice according to various therapies. When needed, univariate/multivariate statistics and correlation analyses were performed with Python v2.7 and related packages (Scipy, SciKit-learn). All p-values were considered statistically significant if less than or equal to 0.05.

7.2 CLINICAL RESEARCH

7.2.1 Patients' eligibility.

For feces and serum collection, ancillary studies were conducted at Gustave Roussy (GRCC), France according to the ethical guidelines and approval of the local CCPPRB.

7.2.1.1 ONCOBIOTICS trial (NCT04567446)

The ONCOBIOTICS trial (NCT04567446), a multicentric prospective observational study was designed to evaluate the impact of the microbiome composition in the clinical outcome of patients with advanced cancer across different histologies amenable to ICB. We enrolled patients across 12 academic centers in France and 2 centers in Canada. Full eligibility criteria are listed in the trial protocol (236). Fecal samples were prospectively collected at different time points (V1: pre-ICI, V2: before the second ICI injection, V3: at 3 months post-ICI and V4: at 6 months post-ICI) at each center following the International Human Mi-

crobiome Standards (IHMS) guidelines. Each center entered the baseline characteristics including detailed listing of concurrent medications received the last two months prior to ICB initiation, and date of last follow-up in an electronic case report form.

7.2.1.2 PREMIS trial (NCT03984318)

Patients enrolled in PREMIS were above 18-year-old, with histologically proven solid malignancy and at least one tumor evaluation by imaging after immunotherapy onset. The PREMIS study was approved by an ethical committee (Comité de Protection des Personnes Sud-Ouest et Outre Mer I; N°ID-RCB: 2018-A01257-48) and the institutional review board (CSET #2018/2728). All enrolled patients provided a signed informed consent. Serum samples were prospectively collected prior anti-PD(L)1 immunotherapy.

7.2.1.3 NIVOREN trial (NCT03013335)

The GETUG-AFU 26 NIVOREN phase II trial (N° EudraCT: 2015-004117-24) is a multicentric study that assessed the activity and safety of Nivolumab in pts with metastatic clear cell RCC after anti-angiogenic therapy. We measured serum sMAdCAM-1 levels in the available baseline plasma (n=212).

7.2.1.4 IOPREDI trial (NCT03084471)

IOPREDI (EudraCT Number: 2016-005068-33) is the French cohort of the STRONG phase IIIb trial (237). Patients with bladder cancer who progressed on previous chemotherapy were treated with durvalumab 1500 mg every 4 weeks. Baseline plasma samples were used for validation of sMAdCAM-1 (n=79).

7.2.1.5 PANDORE trial (NCT03212651)

PANDORE is a prospective, single-arm phase II trial testing the antitumor activity of preoperative pembrolizumab monotherapy in patients with histologically confirmed (T2–T4aN0M0) transitional cell carcinoma of the bladder. Pembrolizumab was given at the recommended

dose of 200 mg every 3 weeks for three cycles followed by cystectomy with appropriate lymph node dissection. Patients were 18 years of age or older, ineligible for cisplatin or refused cisplatin-based chemotherapy, had diagnostic transurethral resection (TURBT) blocks available, and had adequate hematologic and end-organ function. Key exclusion criteria included documented severe autoimmune disease, chronic infectious disease, use of systemic immunosuppressive medications, and prior use of ICB. Surgery was scheduled 1 to 3 weeks after the last pembrolizumab infusion. Baseline workup included thorax/abdomen/pelvis CT and standard blood analyses (hematology, biochemistry, and coagulation parameters). Neither PET-CT nor MRI was required for baseline imaging. There was no dose modification of pembrolizumab. Patients with grade 2 to 4 pembrolizumab-related toxicity (except for grade 2 infusion reaction) were required to permanently discontinue pembrolizumab administration and to proceed with radical cystectomy. The trial was conducted by the French Genitourinary Group (GETUG) and funded by MSD, which provided the drug. This study was approved by the ethics committee CPP Est-III in December 2017 and the French National Agency for the Safety of Medicines and Health Products (ANSM) in November 2017, and was conducted in accordance with the protocols and Good Clinical Practice Guidelines defined by the International Conference for Harmonisation of Technical Requirements for Pharmaceuticals for Human Use and the principles of the Declaration of Helsinki. Humoral responses against bacteria was evaluated in baseline serum samples (see Results section, Article III).

7.2.1.6 NABUCCO trial (NCT03387761)

The NABUCCO study enrolled 24 patients with stage III UC treated with ipilimumab (cycle 1), ipilimumab and nivolumab (cycle 2), and nivolumab (cycle 3) followed by resection (24). A baseline serum sample was available for 23 patients who defined the validation cohort 2 for the evaluation of humoral responses against bacteria (see Results section, Article III).

7.2.1.7 MATCH-R trial (NCT02517892)

MATCH-R is a prospective trial studying the evolution of the clonal architecture of tumors from patients with advanced cancer and treated with molecular targeted agents to identify mechanisms of acquired resistance. The design of the study has been reported previously (238). Briefly, the primary objective of this study is to characterize molecular mechanisms of resistance to targeted therapies and immunotherapy by next-generation sequencing and the development of patient-derived xenografts and cell lines. The cohor of patients with metastatic bladder cancer treated with pembrolizumab were enrolled in our ancillary study and define the validation cohort 3. Humoral responses against bacteria was evaluated in baseline serum samples (see Results section, Article III).

7.2.1.8 The Melanoma Patients Immunized With Natural DenDritic Cells (MIND-DC) trial (NCT02993315)

The MIND-DC trial involves human participants, was approved by the Dutch Central Committee on Research Involving Human Subjects, and is in concordance with the Declaration of Helsinki. Written informed consent was obtained from all patients. Double-blind, randomized, placebo-controlled phase III clinical trial performed in 2 centers in the Netherlands. Patients with resected stage IIIB and IIIC cutaneous melanoma were randomized in a 2:1 ratio to nDC treatment or placebo (Figure S1A). Patients received either intranodal injections of nDC (3-8x10^6/injection) or placebo every 2 weeks for 3 doses, repeated after 6 and 12 months. The primary endpoint was the 2-year recurrence-free survival (2Y-RFS) rate. Treatment was stopped in case of disease recurrence (including both loco-regional and distant metastases), unacceptable toxicity, or withdrawn from the study. Patients in the DC treatment arm were vaccinated with autologous DC loaded with tumor peptides and overlapping peptide pools. Cells were harvested by apheresis and conventional and plasmacytoid DC were isolated with the fully automated and enclosed immunomagnetic CliniMACS Prodigy® isolation system (Miltenyi Biotec). DC were pulsed with MACS® GMP-grade PepTivators®, overlapping peptide pools of the CTA MAGE-A3 and NY-ESO-1 (Miltenyi Biotec) covering the sequence of the entire antigen, and a mix of fourteen peptides of TAA gp100 and tyrosinase and CTA MAGE-C2, MAGE-A3 and NY-ESO-1 (all Leiden

University Medical Center, Leiden, the Netherlands) and matured with protamine/mRNA (Meda Pharma, Amstelveen, the Netherlands) and Universitätsklinikum Erlangen, Erlangen, Germany). Stool samples were prospectively collected at different time points (T1: pre-treatment, T2: 4 weeks after treatment start (before the 3rd injection), Figure S1A) at each center following the International Human Microbiome Standards (IHMS) guidelines. Both T1 and T2 samples were considered for this analysis. Blood samples were collected at the same timepoints.

7.2.2 Metagenomics analysis of patient stools.

7.2.2.1 Gut OncoMicrobiome Signatures (Results section, Article I)

We conducted a shotgun MG-based analysis of fecal material available in the curated Metagenomic Data package by considering both newly acquired and publicly available data sets (239). More specifically, we collected the stools from patients harboring kidney cancer (N = 69; (200)), breast cancer (N = 83; (240)), lung cancer (N = 368;), prostate cancer (N = 47), ovarian cancer (N = 29), and chronic myelomonocytic leukemia (N = 17). This collection of cancer metagenomes was integrated to 108 melanoma and 705 colon cancer samples from the publicly available database (241) and compared in terms of species-level taxonomic profiles (generated using MetaPhlAn3) with 5,570 healthy volunteers (HV) coming from multiple publicly available data sets (242). We found discriminative species between cancer and healthy samples by considering LEfSe coupled to a pairwise comparison of relative taxonomic abundances (for species having a prevalence equal to or greater than 5%) using bootstrapping of two-tailed Mann–Whitney U tests (with 1,000 permutations and correction for continuity and ties). To limit possible batch effects as much as possible, we kept in the analysis only metagenomes with at least 10M reads. Due to the well-recognized effect of lifestyle on microbiome composition, we considered only samples coming from westernized subjects. Similarly, no ATB use was associated with all publicly available samples.

7.2.2.2 Correlation with sMAdCAM-1 levels (Results section, Article IV)

For MGS analysis, the stools were processed for total DNA extraction and sequencing with Ion Torrent technology following MetaGenoPolis (INRAE) France (243). The gene abundance table was processed using the MetaOMineR (momr R) package. We conducted PERMANOVA using the function adonis from the vegan R package (v2.5-7) with the Atchinson distance on centered log ratios using species-level abundances and 1000 permutations. We employed an ensemble of univariate and multivariate differential abundance methods that included age, gender and cohort in the models, using either species-level relative abundances or count data, where absolute raw counts were estimated from species-level relative abundances by multiplying these values by the total number of reads for each sample. These differential abundance methods included; DESeq2 (v.1.30.0) (244) with the poscounts estimator (DESeq2_poscounts); DESeq2 with the poscounts estimator and a zero-inflated negative binomial model (DESeq2_poscounts_zb); DESeq2 with trimmed mean of M values (TMM; DESeq2_TMM); limma (v3.46.0) (245) with TMM values (limma_voom_TMM); limma with TMM values and a zero-inflated negative binomial model (limma_voom_TMM_zb); ANCOM-BC (v.1.0.1) (246); Maaslin2 (v.1.4.0) (247) and LeFsE (248).

7.2.2.3 Ancillary study of MIND-DC trial (Results section, Article VI)

Overall, 185 fecal samples from 93 patients were sequenced with whole genome sequencing technology. Aliquots of stool samples were stored with DNA/RNA Shield Buffer (Zymo) at –20 °C until use. DNA was extracted from aliquots of fecal samples using the DNeasy PowerSoil Pro Kit (Qiagen) following the manufacturer's instructions. Sequencing libraries were prepared using the Illumina® DNA Prep, (M) Tagmentation kit (Illumina), following the manufacturer's guidelines. A cleaning step on the pool with 0.7x Agencourt AMPure XP beads was implemented. Sequencing was performed on a Novaseq600 S4 flow cell (Illumina) at the internal sequencing facility at University of Trento, Trento, Italy. Libraries were multiplexed using dual indexing and sequenced for 150bp paired-end reads using the Illumina NovaSeq6000 platform according to manufacturer's protocols. Subsequently, sequenced metagenomes were QCed using the pre-processing pipeline implemented by Segata's lab and available on

https://github.com/SegataLab/preprocessing. This preprocessing pipeline consists of three steps: i) Initial quality control by removing low-quality reads (quality score Q20), fragmented short reads (75 bp), and reads with 2 or more ambiguous nucleotides; ii) contaminant DNA removal by using Bowtie 2 with the --sensitive-local parameter, for both the phiX174 Illumina spike-in and human-associated reads (hg19); iii) Sorting and splitting for the creation of paired forward and reverse output files and the unpaired reads in a separate output file for each metagenome. After preprocessing, we obtained an average of 48M reads per sample. Microbial relative abundances were then generated using MetaPhlAn-4 (249), while functional profiles were obtained applying HumanN-3.6 (242). For alpha and beta-diversity, we computed the per-sample Shannon index (250) and the between-samples Bray-Curtis dissimilarities using the implementation available in the Vegan R package (251). Differences in the distributions of alpha and beta diversity for samples collected at diagnosis with respect to recurrence at 2 years were then evaluated using an unpaired two-sample Wilcoxon test (252). For the comparisons concerning response variables (recurrence, 2-year recurrence-free survival) and treatment arms, we fitted a generalized linear model for each feature for each considered task (2 year relapse) via the MaAsLin2 R package (247). Microbial features are first arcsin-sqrt transformed or centered-log-ratio transformed after being converted to pseudo-counts. FDR correction is applied via Benjamini-Hochberg procedure. Only features with at least 30% prevalence have been considered in the analysis for 2-year relapse and 2-year death to guarantee at least 10 positive samples for each feature. A threshold of 20% prevalence is used when comparing DC vs PL samples at baseline.

7.2.3 Metabolomics analyses

7.2.3.1 Plasma sample preparation and targeted detection by LC-MS (Results section, Article VI).

Fifty (50) µl of collected sera were mixed with 500 µl of ice-cold extraction mixture (methanol/water, 9/1, -20°C, with labelled internal standard). To facilitate endogenous metabolites extraction, samples were then completely homogenized (vortexed 5 minutes at 2500 rpm)

and then centrifuged (10 min at 15000 g, 4°C). Supernatants were collected and several fractions were split to be analyzed by different Liquid chromatography coupled with mass spectrometers (LC/MS) (253). Polyamines and biliary acids analyses were performed by LC-MS/MS with a 1260 UHPLC (Ultra-High Performance Liquid Chromatography) (Agilent Technologies) coupled to a QQQ 6410 (Agilent Technologies) and were previously described (254). Pseudo-targeted analysis by UHPLC-HRAM (Ultra-High Performance Liquid Chromatography – High Resolution Accurate Mass) was performed on a U3000 (Dionex) / Orbitrap q-Exactive (Thermo) coupling, previously described (254,255). All targeted treated data were merged and cleaned with a dedicated R (version 4.0) package (@Github/Kroemerlab/GRMeta).

7.2.3.2 Data processing and statistical analysis (Results section, Article VI).

Raw data were preprocessed and analyzed with R using the GRMeta package (@Github/Kroemerlab/GRMeta). This software included statistical analysis using a multivariate method approach, as PCA, Heatmap and data visualization, as volcano plots. Area intensity levels were corrected with a quality control pooled sample based algorithm and normalized area were then log2-transformed prior to heatmaps, boxplots and volcano plots visualizations. A total of 152 metabolites were finally analyzed for sera samples at T1 and at T2. The best significant metabolites were presented with boxplots with metabolite levels log scaled. Mann-Whitney U-test with no adjustment were conducted on data gathered by two groups on processed data with R. In cases when data treatments were performed on more than two groups of patients, Kruskal-Wallis test followed by a Dunn's test with no adjustment were used on processed data. Pearson correlation analysis was applied on log2 transformed data from metabolite normalized profiles and *F. prausnitzii* SGB15318 and 15322 abundances. Relevant metabolites correlating with F. prausnitzii strains were selected and analyzed by enrichment functional analysis with Metaboanalyst (https://www.metaboanalyst.ca) using the KEGG Database(256) for significant metabolites annotation and visualization.

7.2.4 Soluble MAdCAM-1 quantification in patients' serum or plasma samples (Results section, Article IV)

sMAdCAM-1 was quantified in patients sera with Bio-Plex 200 systems (Bio-Rad) and sMAdCAM-1 kit from R&D system (Human Luminex Discovery Assay LXSAHM).

8 RESULTS

8.1 THE GUT ONCOMICROBIOME SIGNATURES

8.1.1 Article I

Title: Cancer Induces a Stress Ileopathy Depending on β-Adrenergic Receptors and Promoting Dysbiosis that Contributes to Carcinogenesis.

Published on: Cancer Discov (2022) 12 (4): 1128–1151.
https://doi.org/10.1158/2159-8290.CD-21-0999.

Satoru Yonekura#, Safae Terrisse#, **Carolina Alves Costa Silva**#, Antoine Lafarge, Valerio Iebba, Gladys Ferrere, Anne-Gaëlle Goubet, Jean-Eudes Fahrner, Imran Lahmar, Kousuke Ueda, Gibrail Mansouri, Eugénie Pizzato, Pierre Ly, Marine Mazzenga, Cassandra Thelemaque, Marine Fidelle, Fanny Jaulin, Jérôme Cartry, Marc Deloger, Marine Aglave, Nathalie Droin, Paule Opolon, Angélique Puget, Fanny Mann, Michel Neunlist, Anne Bessard, Laetitia Aymeric, Tamara Matysiak-Budnik, Jacques Bosq, Paul Hofman, Connie P.M. Duong, Sophie Ugolini, Valentin Quiniou, Sylvie Berrard, Bernhard Ryffel, Oliver Kepp, Guido Kroemer, Bertrand Routy, Leonardo Lordello, Mohamed-Amine Bani, Nicola Segata, Fjodor Yousef Yengej, Hans Clevers, Jean-Yves Scoazec, Edoardo Pasolli, Lisa Derosa#, and Laurence Zitvogel#.
# contributed equally

Gut dysbiosis has been associated with intestinal and extraintestinal cancer, but whether and how it promotes carcinogenesis and cancer progression remains unknown. We demonstrated that tumor injection triggered an early release of REG3γ by ileal cells, transient ileal mucosa atrophy, increased epithelial barrier permeability and apoptosis, and reduction of the villous microvascular thickness, with dominance of sympathetic over cholinergic signaling in the gut. These processes culminated in persistant dysbiosis dominated by gram-positive *Enterocloster* spp, (Fig. 10A). Interrupt the sympathetic signaling either by pharmacologic blockade of β-

adrenergic receptors or *Adrb2*$^{-/-}$ mice, or gut microbiota modulation with gram-positive-targeted ABX (vancomycin) or cohousing with tumor-free mice prevented ileopathy and slowed tumor growth (Fig. 10B-D). Also, we showed that tolerogenic *Enterocloster* spp impairs ICB efficacy (Fig. 10E). Together, these results reinforce the causal role of microbiota on cancer immunosurveillance.

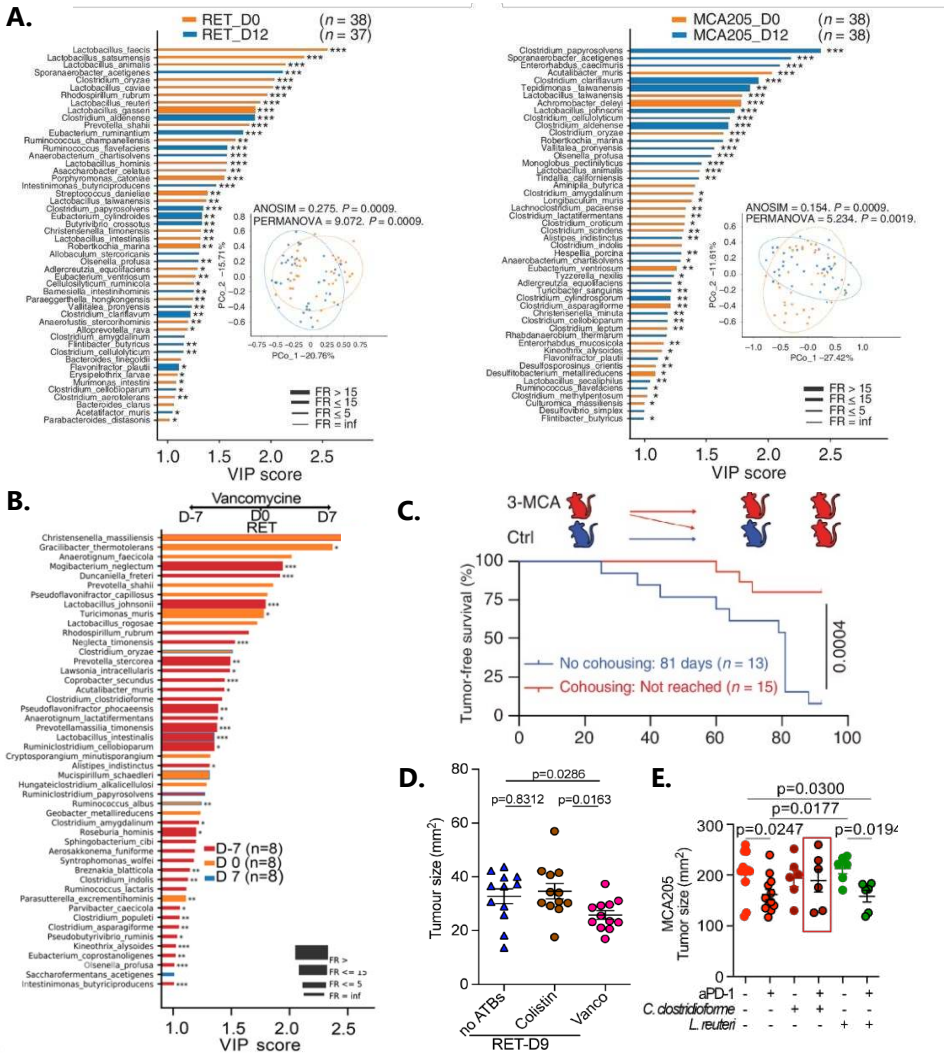

Figure 10 The causal link between cancer and dysbiosis. **A-B.** PCoA of the taxonomic composition of feces (inset) in a paired manner in non-tumor bearers versus RET (A, left) or MCA205 (A, right) tumor-bearers and between different timepoints with vancomycin in RET tumor-bearers (B): before (D−7) start and after 7 (D0) or 14 (D7) days. **C.** Tumor-free survival after 3-Methylcholanthrene (3-MCA) injection in naïve mice that were cohoused or not with non-injected mice. **D.** Tumor size 7 days after inoculation under different antibiotic (ATB) regimen. ANOVA (Kruskal–Wallis test) were used for multiple comparisons. **E.** Animals were treated with vancomycin for 7 days (D0 up to Day 7) and then treated with 10^9 CFU of Clostridium clostridioforme or Lactobacillus reuteri before each intraperitoneal administration of anti-PD-1 antibody every other 3 days for 4 injections. Mann-Whitney test was used.

Then, we demonstrated that patients with cancer also harbor distinct hallmarks of this stress ileopathy, including increased markers of gut permeability and dysbiosis dominated by tolerogenic *Enterocloster* spp (Fig. 11A). Inversely, healthy volunteers harbored species previous described as related to benefit to ICB such as *Lachnospiraceae* and *Oscillospiraceae* family members.

8.1.1.1 Complementary results: unpublished data (see Appendix: Abstract III).

Interestingly, in a longitudinal analysis of gut microbiota composition shift under ICB, we observed that patients with durable responses to ICB (complete + partial responses with progression-free survival >12 months and OS >24 months) lost these tolerogenic *Enterocloster* spp (Fig.11B), while non-responders lost health-related bacteria such as *F. prausnitzii* from *Oscillospiraceae* family (Fig. 11C).

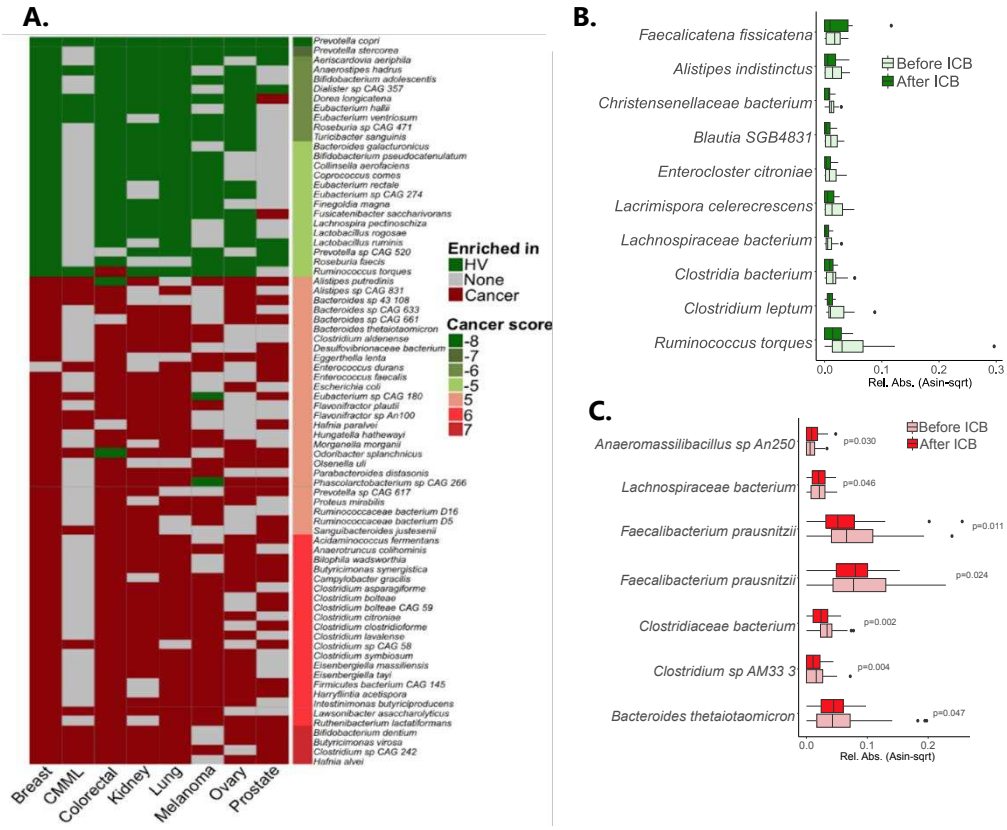

Figure 11 Gut dysbiosis in patients with cancer. **A.** Heat map shows the most relevant gut microbiota species across eight cancer types (n=1637) versus HV (n=5570) using metagenomis shot gun. **B.** Patients with durable responses (complete response + partial response with progression-free survival >12 months and overall survival >24 months, n=17). **C.** Patients with progressive disease as best response (n=61). HV: healthy volunteers. ICB, immune-checkpoint blockade.

RESEARCH ARTICLE

Cancer Induces a Stress Ileopathy Depending on β-Adrenergic Receptors and Promoting Dysbiosis that Contributes to Carcinogenesis

Satoru Yonekura[1,2,3], Safae Terrisse[1,2,3], Carolina Alves Costa Silva[1,2,3], Antoine Lafarge[4], Valerio Iebba[1,2,5], Gladys Ferrere[1,2], Anne-Gaëlle Goubet[1,2,3], Jean-Eudes Fahrner[1,2,3], Imran Lahmar[1,2,3], Kousuke Ueda[6], Gibrail Mansouri[2], Eugénie Pizzato[1,2], Pierre Ly[1,2], Marine Mazzenga[1,2], Cassandra Thelemaque[1,2], Marine Fidelle[1,2,3], Fanny Jaulin[7], Jérôme Cartry[7], Marc Deloger[8], Marine Aglave[8], Nathalie Droin[9], Paule Opolon[10], Angélique Puget[11], Fanny Mann[11], Michel Neunlist[12,13], Anne Bessard[12,13], Laetitia Aymeric[13,14], Tamara Matysiak-Budnik[12,13,14,15], Jacques Bosq[16], Paul Hofman[17], Connie P.M. Duong[1,2,18], Sophie Ugolini[19], Valentin Quiniou[20], Sylvie Berrard[21], Bernhard Ryffel[22], Oliver Kepp[4,23], Guido Kroemer[4,23,24,25,26], Bertrand Routy[27,28], Leonardo Lordello[1,2,29], Mohamed-Amine Bani[10], Nicola Segata[30,31], Fjodor Yousef Yengej[32,33,34], Hans Clevers[32,33,34], Jean-Yves Scoazec[3,10], Edoardo Pasolli[35], Lisa Derosa[1,2,3,36], and Laurence Zitvogel[1,2,3,29]

ABSTRACT Gut dysbiosis has been associated with intestinal and extraintestinal malignancies, but whether and how carcinogenesis drives compositional shifts of the microbiome to its own benefit remains an open conundrum. Here, we show that malignant processes can cause ileal mucosa atrophy, with villous microvascular constriction associated with dominance of sympathetic over cholinergic signaling. The rapid onset of tumorigenesis induced a burst of REG3γ release by ileal cells, and transient epithelial barrier permeability that culminated in overt and long-lasting dysbiosis dominated by Gram-positive *Clostridium* species. Pharmacologic blockade of β-adrenergic receptors or genetic deficiency in *Adrb2* gene, vancomycin, or cohousing of tumor bearers with tumor-free littermates prevented cancer-induced ileopathy, eventually slowing tumor growth kinetics. Patients with cancer harbor distinct hallmarks of this stress ileopathy dominated by *Clostridium* species. Hence, stress ileopathy is a corollary disease of extraintestinal malignancies requiring specific therapies.

SIGNIFICANCE: Whether gut dysbiosis promotes tumorigenesis and how it controls tumor progression remain open questions. We show that 50% of transplantable extraintestinal malignancies triggered a β-adrenergic receptor–dependent ileal mucosa atrophy, associated with increased gut permeability, sustained *Clostridium* spp.–related dysbiosis, and cancer growth. Vancomycin or propranolol prevented cancer-associated stress ileopathy.

INTRODUCTION

During the last decade, the gut microbiome has garnered much attention in the context of evolving immuno-oncology, with compelling evidence of the role of intestinal dysbiosis in primary resistance to immune checkpoint blockade across a large range of advanced malignancies (1–4). This contention was supported by numerous epidemiologic studies pointing out the deleterious impact of broad-spectrum antibiotics in the clinical outcome of anti–PD-1/anti–PD-L1 antibodies in stage III and IV melanoma and lung, kidney, and bladder cancers (5, 6). Of note, the decreased richness of the intestinal ecosystem was associated with a tumor microenvironment poor in T-cell infiltrates.

The increased awareness of the potential contribution of gut dysbiosis in treatment failure led many investigators to describe metagenomics (MG)-based intestinal blueprints associated with resistance to immunotherapy (1–3, 7, 8). However, to what extent cancer-associated dysbiosis precedes the tumorigenic process and therefore is causatively linked to neoplasia

[1]Gustave Roussy, ClinicObiome, Villejuif, France. [2]INSERM U1015, Equipe Labellisée – Ligue Nationale contre le Cancer, Villejuif, France. [3]Université Paris-Saclay, Le Kremlin Bicêtre, France. [4]INSERM U1138, Equipe labellisée par la Ligue contre le cancer, Université de Paris, Sorbonne Université, Centre de Recherche des Cordeliers, Paris, France. [5]Department of Medicine, Surgery and Health Sciences, University of Trieste, Trieste, Italy. [6]Department of Urology, Kurume University School of Medicine, Kurume, Japan. [7]INSERM U1279, Gustave Roussy Cancer Campus, Villejuif, France. [8]Bioinformatics Platform, Gustave Roussy Cancer Campus, Villejuif, France. [9]Genomics Platform, Gustave Roussy Cancer Campus, Villejuif, France. [10]Departement of Biology and Medical Pathology, PETRA Platform, Gustave Roussy, Villejuif, France. [11]Aix Marseille University, CNRS, IBDM, Marseille, France. [12]Nantes Université, The Enteric Nervous System in Gut and Brain Disorders (TENS), Institut des Maladies de l'Appareil Digestif (IMAD), Nantes, France. [13]UMR Inserm U1235, TENS, Nantes, France. [14]Department of Biology, Université d'Angers, 44045 Angers, France. [15]Hépato-Gastroentérologie & Oncologie Digestive, IMAD, Hôtel Dieu, CHU de Nantes, Nantes, France. [16]JBO Consultant, Paris, France. [17]Laboratoire de Pathologie Clinique et Expérimental, FHU OncoAge et Biobanque BB-0033-00025, CHU de Nice, Université Côte d'Azur, Nice, France. [18]Department of Medical Biology, University of Melbourne, Melbourne, Victoria, Australia. [19]Centre d'Immunologie de Marseille-Luminy, Université de la Méditerranée, Marseille, France. [20]Parean Biotechnologies, Saint-Malo, France. [21]Université de Paris, Neuro-Diderot, Inserm, Paris, France. [22]UMR 7355, Molecular Immunology and Embryology, CNRS, University of Orleans, Orléans, France. [23]Cell Biology and Metabolomics Platforms, Gustave Roussy Cancer Campus, Villejuif, France. [24]Pôle de Biologie, Hôpital Européen Georges Pompidou, Assistance Publique-Hôpitaux de Paris, Paris, France. [25]Suzhou Institute for Systems Medicine, Chinese Academy of Medical Sciences, Suzhou, China. [26]Department of Women's and Children's Health, Karolinska University Hospital, Karolinska Institute, Stockholm, Sweden. [27]Centre de Recherche du Centre hospitalier de l'Université de Montréal (CRCHUM), Division of Oncology, Department of Medicine Montréal, Quebec, Canada. [28]Centre Hospitalier de l'Université de Montréal (CHUM), Hematology-Oncology Division, Department of Medicine, Montréal, Quebec, Canada. [29]Center of Clinical Investigations in Biotherapies of Cancer (CICBT) 1428, Villejuif, France. [30]Department CIBIO, University of Trento, Trento, Italy. [31]European Institute of Oncology IRCCS, Milan, Italy. [32]Hubrecht Institute-Royal Netherlands Academy of Arts and Sciences and University Medical Center Utrecht, Utrecht, the Netherlands. [33]Department of Nephrology and Hypertension, University Medical Center Utrecht, Utrecht, the Netherlands. [34]Oncode Institute, Utrecht, the Netherlands. [35]Department of Agricultural Sciences, University of Naples Federico II, Portici NA, Italy. [36]Departement of Medical Oncology, Gustave Roussy Cancer Campus, Villejuif, France.

S. Yonekura, S. Terrisse, and C. Alves Costa Silva are the co–first authors of this article.

L. Derosa and L. Zitvogel are the co–last authors of this article.

Corresponding Author: Laurence Zitvogel, ClinicObiome, Gustave Roussy, 114 rue Edouard Vaillant, Villejuif 94805, France. Phone: 33-1-42-11-50-41; Fax: 33-1-42-11-60-94; E-mail: laurence.zitvogel@gustaveroussy.fr

Cancer Discov 2022;12:1128–51

doi: 10.1158/2159-8290.CD-21-0999

development or is merely its direct consequence remains unknown. Here we show in mice and humans that the tumorigenic process triggers a sustained dysbiosis (in favor of species belonging to the *Clostridium* genus) associated with a stress ileopathy, characterized by ileal mucosa atrophy, constriction of the microvascular villous circulation, and increased expression of tyrosine hydroxylase concomitant with a drop in parasympathetic signaling in the mucosa. Transient amplifying cells and Paneth cells lose their defensins while producing antimicrobial peptides in response to catecholamines. *Clostridia*-killing vancomycin and genetic or pharmacologic inhibition of β-adrenergic receptors interfered in the natural tumor growth kinetics, suggesting that cancer-induced ileopathy should be viewed as a critical corollary of tumorigenesis.

RESULTS

Cancer Can Cause a Terminal Ileopathy

Inflammatory processes distal from the intestine, such as traumatic or ischemic brain injuries, may cause gastrointestinal dysfunction, increased epithelial barrier permeability, and dysbiosis in experimental models and patients (9, 10). Given that cancers are chronic inflammatory lesions, we assessed potential changes in gut permeability following tumor implantation. Transgene-enforced expression of the *Ret* proto-oncogene under control of the metallothionein 1 promoter drives spontaneous melanomagenesis mimicking the human melanoma progression. We took advantage of a *Ret* transgenic melanoma cell line that reaches a surface of 25 to 35 mm^2 within seven days after the subcutaneous inoculation of the minimal tumorigenic dose, leading to tumor outgrowth in 100% cases. We gavaged FITC-labeled dextran (FITC–dextran) into mice at various time points after the inoculation of a sublethal dose of RET melanoma cells (vs. PBS) and determined serum levels of FITC–dextran dye. We observed its transient elevation at 9 days, but not at day 12 after tumor injection, yet less impressive than colitis-induced FITC leakage (Fig. 1A). We also detected blood FITC within six days after inoculation of the transplantable MC38 colon cancer (Supplementary Fig. S1A). Moreover, we found the serum hallmarks of the "leaky gut" syndrome described earlier (11) with elevation of soluble ST2 (IL33R) and/or CD14 at day 20 of RET and/or MCA205 sarcoma tumor bearers (Fig. 1B; Supplementary Fig. S1B) in the absence of weight loss (Supplementary Fig. S1C). This transient gut permeability was accompanied by morphologic changes of the mucosa, starting at day 3, peaking at days 6 to 9, and resolving by day 12 (Fig. 1C). Indeed, a careful examination of tissue sections in light microscopy by four independent pathologists concluded a patchy, partial, or subtotal thickness reduction of the mucosa, characterized by villus atrophy and, in some cases, abrasion of villus extremities, resulting in a significant decrease of the villus/crypt height ratio, bereft of inflammatory infiltrates, in the proximal and terminal ileum (Fig. 1C; Supplementary Fig. S1D). Conversely, IHC staining of $CD8^+$ and $Gr1^+$ cells within the ileal lamina propria (LP) showed reduced intra- and extravascular $CD8^+$ T-cell numbers and LP infiltration by $Gr1^+$ cells following RET inoculation (Supplementary Fig. S1E and S1F). Concomitant changes in the $CD34^+$ villous microvasculature were observed by day 3 (up to day 7), with a significant reduction of the vascular thickness in the distal ileum of RET tumor bearers (Fig. 1D). These morphologic abnormalities spared the duodenum, the jejunum, and colon mucosae (Supplementary Fig. S1G) and were not observed following the injection of killed RET cancer cells (Fig. 1C). The reduction of villus/crypt height ratios coincided with the apoptosis of ileal crypt cells stained with antibodies against cleaved caspase-3 (Fig. 1E), as well as defects in Ki-67^+ proliferative cells at the junction between the transit amplifying compartment and the villus (Fig. 1F). Intestinal epithelial and endothelial cells are normally tightly bound together by intercellular junctional complexes that regulate the paracellular permeability. We stained the ileum of tumor bearers for the tight junction protein Zonula occludens-1 (*Zo1*) and the adherens junction protein E-cadherin but failed to identify an altered distribution during the first three days after RET inoculation (Supplementary Fig. S1H and S1I). In addition, qRT-PCR assessing ileal *Mylk*, *Jam1*, *Ocln*, and *Zo1* gene transcription at day 3 did not show any influence of the tumor establishment (Supplementary Fig. S1J). Of note, tumor inoculation induced a significant decrease of eosinophil numbers in the ileum of RET-bearing mice by day 3 after tumor implantation (Supplementary Fig. S1K). Importantly, this dramatic decrease of the villus/crypt height ratio and occurrence of crypt apoptosis were not only observed by day 3 and up to day 9 after implantation of RET melanoma but were also evidenced after the subcutaneous administration of MCA205 fibrosarcomas and MC38 colon cancers (syngeneic of C57BL/6 mice), but not B16F10 melanoma, nor AT3 or 4T1 breast cancer implantation (Fig. 1G–J). Moreover, orthotopic renal RENCA in the subcapsular area of the kidney of BALB/c mice or lung TC1 within the lung parenchyma both induced the mucosal atrophy at later time points (>day 15), whereas an intravenous model of lung metastases of TC1 failed to do so (Fig. 1G–J).

Altogether, we unveiled that 57% ($n = 4/7$) of mouse transplantable tumors could trigger a cancer-associated ileopathy characterized by a transient (starting at day 3, peaking at days 6–9, and resolving by day 12) epithelial atrophy of the terminal ileum.

Cancer Can Promote Intestinal Dysbiosis in Mice

Intrigued by this cancer-associated ileopathy, we concomitantly analyzed compositional shifts of the fecal microbiota longitudinally in these tumor bearers at different time points of tumor progression across five tumor models. We used high-throughput amplicon sequencing of the gene encoding 16S rRNA and the relevant bioinformatics tools to analyze differences in taxonomic composition in a paired manner, before (D0) and at day 7 (D7) following subcutaneous tumor inoculation across five tumor subtypes (RET, MCA205, RENCA, MC38, and AT3), and we pursued until day 12 (D12) and day 19 (D19) for RET and MCA205 tumors (Fig. 2A and B; Supplementary Fig. S2). There were no differences in any of the alpha diversity metrics inspected (richness, evenness, Shannon index, and Simpson diversity index) at any time point in any of the six tumor types (not shown). However, the principal coordinate analyses (PCoA) of microbial β-diversity distances identified significant shifts in the microbiome composition over time in RET [Fig. 2A for D0 vs. D12; Supplementary Fig. S2A for D0 vs. D7 (top) and

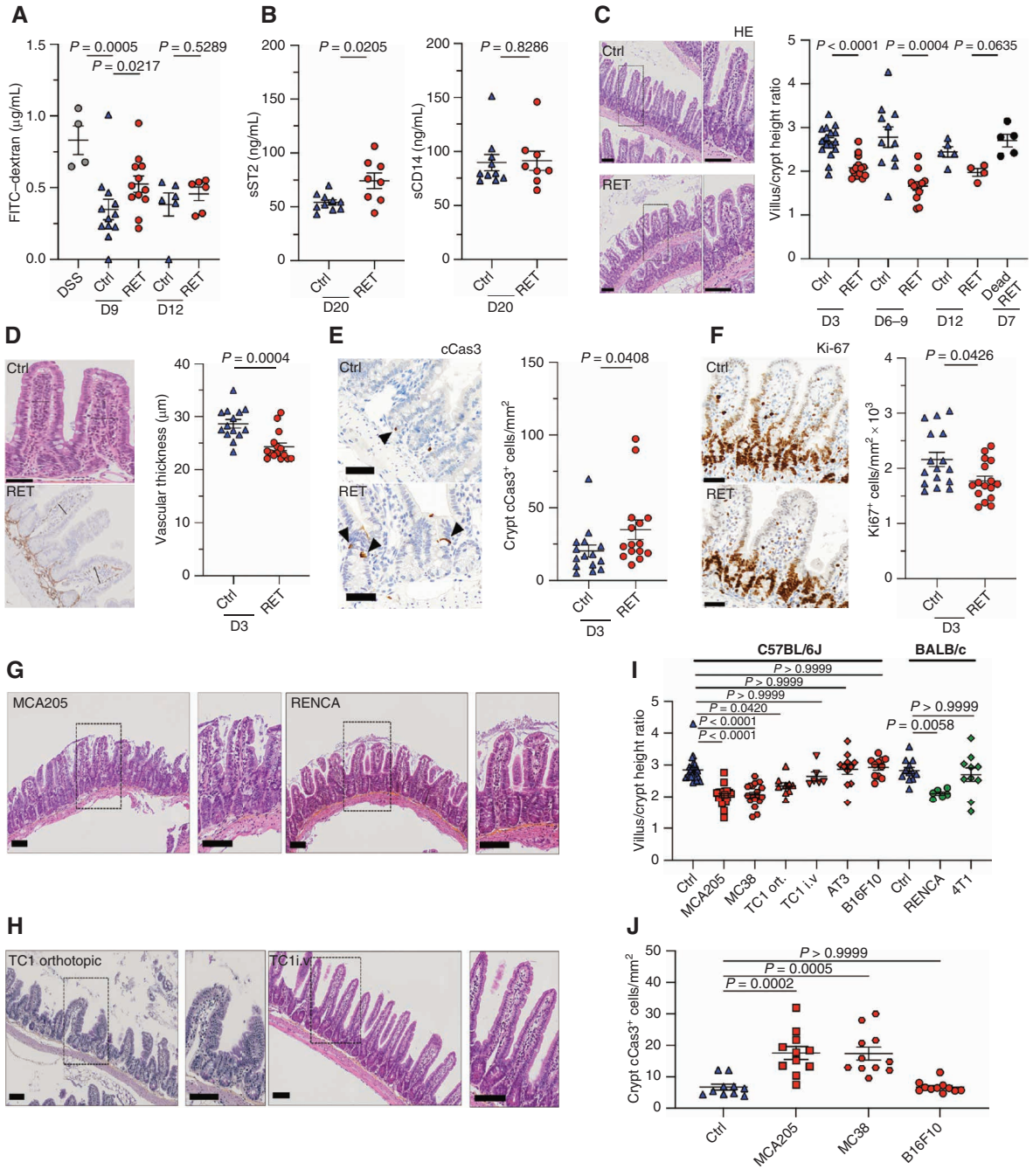

Figure 1. Prototypic pathologic features of cancer-associated ileopathy. **A,** RET-induced (right) or DSS-induced (left) intestinal permeability monitored by FITC–dextran oral administration at day 9 or 12 and translocation in the bloodstream 4 hours later. Each dot represents one mouse; one representative experiment out of two is depicted. Mann–Whitney test was used for comparison with the control group. DSS, dextran sulfate sodium. **B,** Plasma levels of soluble CD14 and ST2 at day 20 in naïve versus RET tumor bearers. Two concatenated experiments are plotted. Each dot represents one mouse. Mann–Whitney test was used for comparison with the control group. **C,** Morphologic changes. Left, typical micrograph of hematoxylin/eosin/saffron-stained ileal tissue visualized in light microscopy. Scale bar, 100 m (Ctrl: PBS injection, RET: tumor injection). Right, manual calculation of the villus/crypt height ratio in the distal ileum, at day 3, days 6–9, and day 12, after subcutaneous tumor implantation of live or dead RET (day 7) versus PBS. Each dot represents one mouse in two concatenated independent experiments of 4–6 mice/group. Mann–Whitney test was used for comparison with the control group. **D,** CD34 staining to monitor villous vascular thickness. A prototypic micrograph picture is shown followed by precise measurement of vascular thickness in RET- and PBS-injected mice at day 3. Each dot represents the mean of 30 ileal villi/animals. Mann–Whitney test was used for comparison with the control group. **E** and **F,** Typical micrograph picture of ileal crypts (**E**) or whole epithelia (**F**) stained with anti–cleaved caspase-3 (cCas3) Ab (**E**) or anti-Ki-67 Ab (**F**; positivity outlined in black arrows) in naïve Ctrls (PBS injection) or RET tumor bearers at day 3, and manual calculation for cCas3 and automated quantification of Ki-67–positive cells/mm^2 were performed. Scale bar, 50 m. Mann–Whitney test was used for comparison with the control group. **G–J,** The same as **C** and **E**, but subcutaneous implantation of different tumor cell lines (MCA205, MC38, B16F10, AT3, orthotopic or intravenous (i.v.) TC1, syngeneic of C57BL/6 mice, or orthotopic RENCA, 4T1 syngeneic of BALB/c mice). Each graph assembles results from 1to 3 independent experiments containing groups of 5–6 mice sacrificed at day 7 after subcutaneous tumor implantation or days 15–21 for orthotopic or i.v. TC1 or RENCA. ANOVA statistical analyses (Kruskal–Wallis test) were used for multiple comparisons. Numerical *P* values are indicated.

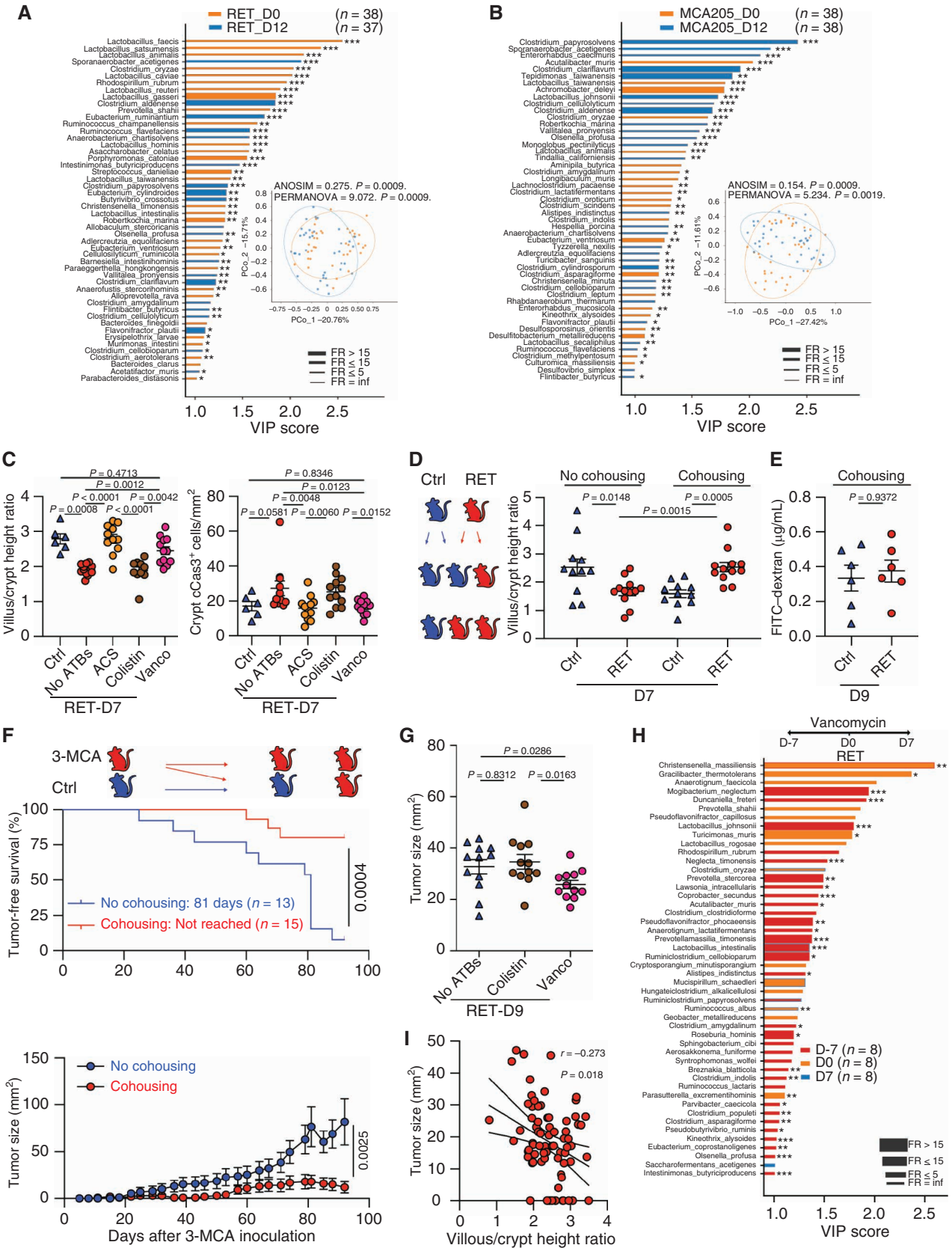

D0 vs. D19 (bottom)], MCA205 [Fig. 2B for D0 vs. D12; Supplementary Fig. S2B for D0 vs. D7 (top), D0 vs. F4 (bottom)], and RENCA tumor models (between D0 and D7; Supplementary Fig. S2C), coinciding with ileal atrophy. In contrast, no significant compositional modulations of the stools could be observed in AT3 tumor bearers (between D0 and D7; Supplementary Fig. S2D) in accordance with the absence of ileopathy. To determine the relative contribution of the abundance of each bacterial species at D0 to the observed group separation at D12, bacterial species were ordered according to their variable importance (VIP) score [which relies on the supervised analysis of partial least square discriminant analysis (PLS-DA); Fig. 2A (RET) and Fig. 2B (MCA205)]. We found a common relative dominance of the Clostridiales order (including *Clostridiaceae* family members, i.e., *Clostridium papyrosolvens*, *C. clariflavum*, *C. cellulolyticum*, *C. aldenense*, and *C. cellobioparum*; *Ruminococcaceae* family members, such as *R. flavefaciens* and *F. plautii*; *Sporanaerobacter* genus, such as *S. acetigenes* and *Vallitaleaceae* family members such as *V. pronyensis*) at the expense of *Lactobacillus* genus (relative loss of *L. animalis* and *L. taiwanensis*) across the three ileopathy-promoting tumor types (RET, MCA205, and RENCA; Fig. 2A and B; Supplementary Fig. S2E–S2G). Importantly, in contrast to the transient nature of the cancer-associated ileopathy, cancer-induced gut dysbiosis persisted for a prolonged period (until animal sacrifice at day 19), with the relative overrepresentativity of distinct taxonomic species such as *F. plautii*, *C. papyrosolvens*, *C. clariflavum*, *C. cellulolyticum*, and *S. acetigenes* and the consistent loss of *Lactobacilli* spp. and *C. oryzae* or *E. ventriosum* (Supplementary Fig. S2E and S2F).

Hence, we conclude that in one model out of two, cancer could trigger a transient ileopathy associated with a protracted intestinal dysbiosis favoring families and species from the *Clostridium* genus until death.

Significance of Intestinal Dysbiosis in Cancer

To parse out the biological significance of these microbial shifts observed right after tumor inoculation and persisting overtime, we used three orthogonal experimental strategies. First, we analyzed the effects of various antibiotic (ATB) regimens on the RET-induced epithelial atrophy observed at day 7. The broad-spectrum ATB cocktail ampicillin, colistin, and streptomycin (ACS) as well as vancomycin (expected to kill most Gram-positive bacteria) completely prevented the reduction of the ileal villus/crypt height ratio and crypt cell apoptosis (Fig. 2C, left and right plots), whereas colistin (only killing Gram-negative commensals) failed to do so, supporting a role for Gram-positive *Clostridium spp.* in this ileopathy. Second, the cohousing of RET tumor bearers with tumor-free mice together for six to nine days (Fig. 2D, left) revealed transmission patterns because it created an ileopathy of the distal ileum in "healthy" animals while significantly protecting the RET tumor–bearing littermates from ileum epithelial damage (Fig. 2D, right). Moreover, cohousing also prevented the transient increase of gut permeability to FITC–dextran dye at nine days after RET tumor implantation (Figs. 1A and 2E). Third, to show the causal link between gut dysbiosis and tumor incidence, we inoculated the 3-methycholanthrene (3-MCA) chemical carcinogen capable of inducing fibrosarcoma in 100% naïve C57BL/6 mice at a dosing of 100 g (12) and compared the incidence and severity of tumor development in 3-MCA recipients maintained alone or together with healthy littermates that did not receive the carcinogen (Fig. 2F, top). Surprisingly, fibrosarcoma formation was significantly retarded and exhibited slower growth kinetics (Fig. 2F, bottom) in animals reared with healthy controls as compared with 3-MCA–isolated animals. Finally, we concluded the preclinical significance of ileopathy-associated dysbiosis in cancer by showing a transient tumor growth retardation induced by the prophylactic oral administration of vancomycin (Fig. 2G). Vancomycin coincided with the relative underrepresentation of six *Clostridia spp*. (*C. clostridioforme*, *C. asparagiforme*, *C. indolis*, *C. populeti*, *C. ihumi*, and *C. amygdalinum;* Fig. 2H; Supplementary Fig. S2H) and with the relative reemergence of distinct Lactobacilli (such as *Lactobacillus rogosae)*. Finally, the cause–effect relationship

Figure 2. Microbiota-dependent cancer-induced ileopathy and biological significance. **A** and **B,** PCoA of the taxonomic composition of feces (inset) in a paired manner in naïve versus RET (**A**) or MCA205 (**B**) tumor-bearing mice at day 12 after tumor implantation. β-Diversity of fecal microbiota (bacterial relative abundance) according to time [before (orange) and 12 days after (blue) tumor inoculation]. ANOSIM and PERMANOVA define the separation of the groups; *P* values define the significance of group separation after 999 permutations of the samples. Bar plot of fecal species that discriminate between pre– and post–tumor inoculation in mice, ordered by their variable importance (VIP) score. For each species, the bar color depicts the cohort with the highest mean relative abundance for a defined species, whereas the border color indicates the cohort with the lowest mean relative abundance. An absent border indicates mean relative abundance of zero in comparator cohort(s). Mann–Whitney test was used. Bar thickness reports the fold ratio (FR) value of the mean relative abundances for each species among the two cohorts. **C,** Effects of various types of antibiotics (ATB) regimen on cancer-induced ileal atrophy and apoptosis in ileal crypts. Calculation of the villus/crypt height ratio (left) or crypt apoptosis (right) at day 7 after subcutaneous RET implantation (vs. PBS) was performed. ANOVA statistical analyses (Kruskal–Wallis test) were used for multiple comparisons. Numerical *P* values are indicated. **D** and **E,** Effects of cohousing of tumor bearers with tumor-free mice on ileal morphology and permeability. Calculation of the villus/crypt height ratio in the distal ileum at days 6–9 after RET implantation (vs. PBS) in isolated versus cohoused mice (middle). Each dot represents one mouse. Gut permeability assessed using the same procedure as the one described in Fig. 1A (**E**). Mann–Whitney test was used for comparison with the control group. **F,** Effects of cohousing of tumor bearers with tumor-free mice on tumor incidence and growth kinetics. Experimental setting of 3-MCA–induced tumorigenesis (**F**, top). MCA was injected in isolated mice or mice doomed to be littermates for >90–100 days with naïve C57BL/6 mice in the same cage. Time to tumor incidence (**F**, middle) and tumor growth kinetics over time (**F**, bottom). Survival curves were estimated using the Kaplan–Meier product limit method. **G,** Effects of various types of ATB regimen on tumor size 7 days after tumor inoculation. Each graph assembles results from two independent experiments containing groups of 5–6 mice. ANOVA statistical analyses (Kruskal–Wallis test) were used for multiple comparisons. Numerical *P* values are indicated. **H,** 16S rRNA-based MG sequencing of fecal amplicons before (D −7) and after 7 (D = 0) or 14 (D7) days of vancomycin. Using PLS-DA VIP plot, coupled to a pairwise comparison of relative taxonomic abundances (for species having a prevalence equal to or greater than 5%), we analyzed taxonomic composition differences between the groups treated or not with oral vancomycin. Bar plot of fecal species that discriminate between pre- and post–tumor inoculation in mice, ordered by their VIP score. For each species, the bar color depicts the cohort with the highest mean relative abundance for a defined species, whereas the border color indicates the cohort with the lowest mean relative abundance. An absent border indicates mean relative abundance of zero in comparator cohort(s). Bar thickness reports the FR value of the mean relative abundances for each species among different groups. **I,** Spearman correlation between villus/crypt height ratio in the distal ileum at days 6–9 after RET implantation and tumor size. Each dot represents one mouse/tumor. Four experiments comprising 5–6 mice/group are concatenated.

between the RET-induced overrepresentation of *Clostridia spp*. and reduced tumor immunosurveillance was brought to us by gavaging tumor-bearing mice treated with anti–PD-1 mAb with distinct *Clostridia spp*. associated with antibiotics- and tumor-induced immunosuppression such as *C. hathewayi* and *C. clostridioforme* (5). This oral feeding with cancer-associated *Clostridia spp*. significantly compromised the efficacy of the immunotherapy, whereas *Lactobacillus reuteri* failed to do so (Supplementary Fig. S2I, left and right). Finally, there was a strong correlation between tumor size at day 7 and villus/crypt height ratios (Fig. 2I), supporting the contention that ileopathy is a corollary syndrome of the tumorigenic process.

Hence, cancer-associated ileopathy coincides with a rapid and durable intestinal dysbiosis dominated by Gram-positive *Clostridium s*pecies participating in the aggressiveness of tumor outgrowth.

Cancer Induced Severe Perturbations of Secretory Cells from the Ileum

Using single-cell RNA sequencing, we profiled 44,807 individual epithelial cells from mouse small intestine harvested in naïve and RET tumor bearers at 24 hours after tumor implantation and characterized the gene signatures associated with melanoma inoculation (Fig. 3A). Unsupervised clustering of the leukocytic and epithelial cells partitioned the data into 20 and 25 groups, respectively (Supplementary Fig. S3A and S3B), which we visualized using *t*-stochastic neighborhood embedding and labeled *post hoc* by the expression of reported marker genes (13). Each cluster was associated with a distinct cell type, including epithelial [stem cells, enterocytes, goblet, Paneth, enteroendocrine (EEC) secretory cells, and tuft cells] and immune cells (T, B, dendritic, and macrophages). Although absorptive enterocytes were partitioned across several clusters representing distinct maturation stages, the EECs, transit amplifying (TA) cells, Paneth, goblet, stem, and tuft cells were each represented by a single distinct cluster (Supplementary Fig. S3A). The proportions of most differentiated ileal cell types were consistent with expected abundances (13) and weakly varied between tumor bearers and naïve animals (Supplementary Fig. S3A–S3C; Supplementary Fig. S4A and S4B), except for nondividing $CD4^+$ T cells ($IL7R^+$, $ICOS^+$, and $RORA^+$), and granzyme A–producing γδ T cells ($CD8a^+$, $CCR6^+$, $KLRD1^+$, and $CCL5^+$) that increased by day 1 after RET inoculation (Supplementary Fig. S4B–S4D), whereas stem and secretory cells were markedly reduced (Fig. 3B). The volcano plot indicating significance versus fold changes of overall versus cell-specific gene expression between naïve and tumor bearers highlighted the relative overexpression of antimicrobial peptides [such as regenerating islet-derived protein 3 beta or gamma (*Reg3β*, *Reg3γ*)] at the expense of defensins (*Defa 5*, *21*, *22*, *23*, *24*, *36*, and *38*) across many clusters of cells (including TA and Paneth cell clusters; Fig. 3C and D), as well as γδT cells and macrophages (Supplementary Fig. S4D and S4E). IHC confirmed the degranulation of distinct crypt cells that encompass Paneth cells and EECs, only in mice bearing tumors triggering the epithelial atrophy (Fig. 3E). Here again, crypt degranulation was a proxy of ileal villus atrophy and prevented by vancomycin (Fig. 3F). We corroborated by qPCR analysis that lectin *Reg3γ* transcription was upregulated at day 7 in the ileal epithelium of RET tumor bearers (Fig. 3G, left) but that antibiotics (broad spectrum and vancomycin but not colistin) could blunt *Reg3γ* gene expression, in line with the capacity of this antimicrobial peptide to bind the peptidoglycan layer of Gram-positive bacteria (14). Lectin *Reg3γ* correlated with epithelial villus atrophy and crypt apoptosis (Fig. 3G, middle and right). In fact, after a transient loss at day 1, EECs defined as chromogranin A–positive (CgA^+) cells were significantly increased by day 3 in the ileal crypts of animals inoculated with tumor cells inducing ileopathy (RET, MCA205, and MC38; Supplementary Fig. S3C; Fig. 4A) but not in animals inoculated with tumors that did not induce crypt damage, such as B16F10 (Fig. 4A, right). Crypt CgA^+ cell numbers correlated with ileal villus atrophy, crypt apoptosis (Fig. 4B), and *Reg3γ* expression (Fig. 4C). Once again, RET-induced early accumulation of EECs capable of overexpressing serum amyloid A gene product (associated with acute inflammation) in ileal crypts was abrogated by vancomycin (Fig. 4D and E) and correlated with tumor size at day 7 (Fig. 4F).

Cancer Induces Catecholamine-Associated Stress Ileopathy

Stress generated by psychological or pathologic disorders can induce most of the features described in this cancer-associated ileopathy (such as increased gut permeability, dysbiosis, and pathophysiologic exacerbation; refs. 10, 15). Despite the potential relevance of the hypothalamic–pituitary–adrenal axis in intestinal permeability (16), we ruled out a role for cancer stress-induced corticosteroids in our symptomatology in as much as corticosterone levels remained stable over time during tumor progression (Supplementary Fig. S5A).

Figure 3. Single-cell transcriptomics analyses reveal acute reactivities of secretory cells. **A,** Single-cell transcriptomics of the CD45-negative component of the terminal ileal epithelial layer overlapping PBS versus RET-injected mice. Uniform manifold approximation and projection (UMAP) plots of $N = 36{,}891$ single cells (points) colored by clusters annotated *post hoc* (refer to Supplementary Fig. S3A) for three naïve and three RET tumor bearers at day 1 after inoculation. Refer to Supplementary Fig. S3A for overlapping representation of the concatenated results for the CD45-positive component of the terminal ileal epithelial layer for the two groups of mice. **B,** Relative proportions of stem cells, neuroendocrine and Paneth cells, and TA cells (according to clusters defined in Supplementary Fig. S3A) in controls (PBS) versus RET-inoculated mice within the CD45-negative fraction. **C** and **D,** Volcano plots of differential gene-expression patterns between pre- and 24 hours after RET inoculation according to $\log_{10}$ adjusted *P* values and $\log_2$ fold ratios for the cluster related to TA cells (**C**, $N = 305$ cells "Ctrl without tumor" vs. $N = 263$ cells "RET") and Paneth cell subsets (**D**, $N = 86$ cells "Ctrl without tumor" vs. $N = 35$ cells "RET") identified from the droplet-based data sets for regional (distal ileum) samples. Significant differences are annotated in red. **E** and **F,** Representative images of degranulating crypts in MCA205 tumor bearers and effects of ATB. Scale bars, 50 m. Cell degranulation analyzed in hematoxylin/eosin/saffron staining in the ileal crypts of naïve or RET, MCA205, or AT3 tumor bearers at day 7 after tumor inoculation without ATB (**E**) and with ATB (**F**). Each dot corresponds to the enumeration of the percentages of degranulated crypts/5–6 fields/animal (**F**). Symbols represent individual mice. Mann–Whitney test. **G,** Quantitative PCR determination of *Reg3γ* gene transcription in the terminal ileum of RET tumor bearers treated with 7 days of various ATB regimen and correlations with morphologic changes. Spearman correlations between the villus crypt height ratio (middle) and crypt apoptosis (right) and *Reg3γ* gene expression. Each dot represents one ileum. The graph depicts two experiments of 5–6 mice/group, each dot representing one ileum. ANOVA statistical analyses (Kruskal–Wallis test) were used for multiple comparisons. Numerical *P* values are indicated between individual ATB groups versus nontreated controls.

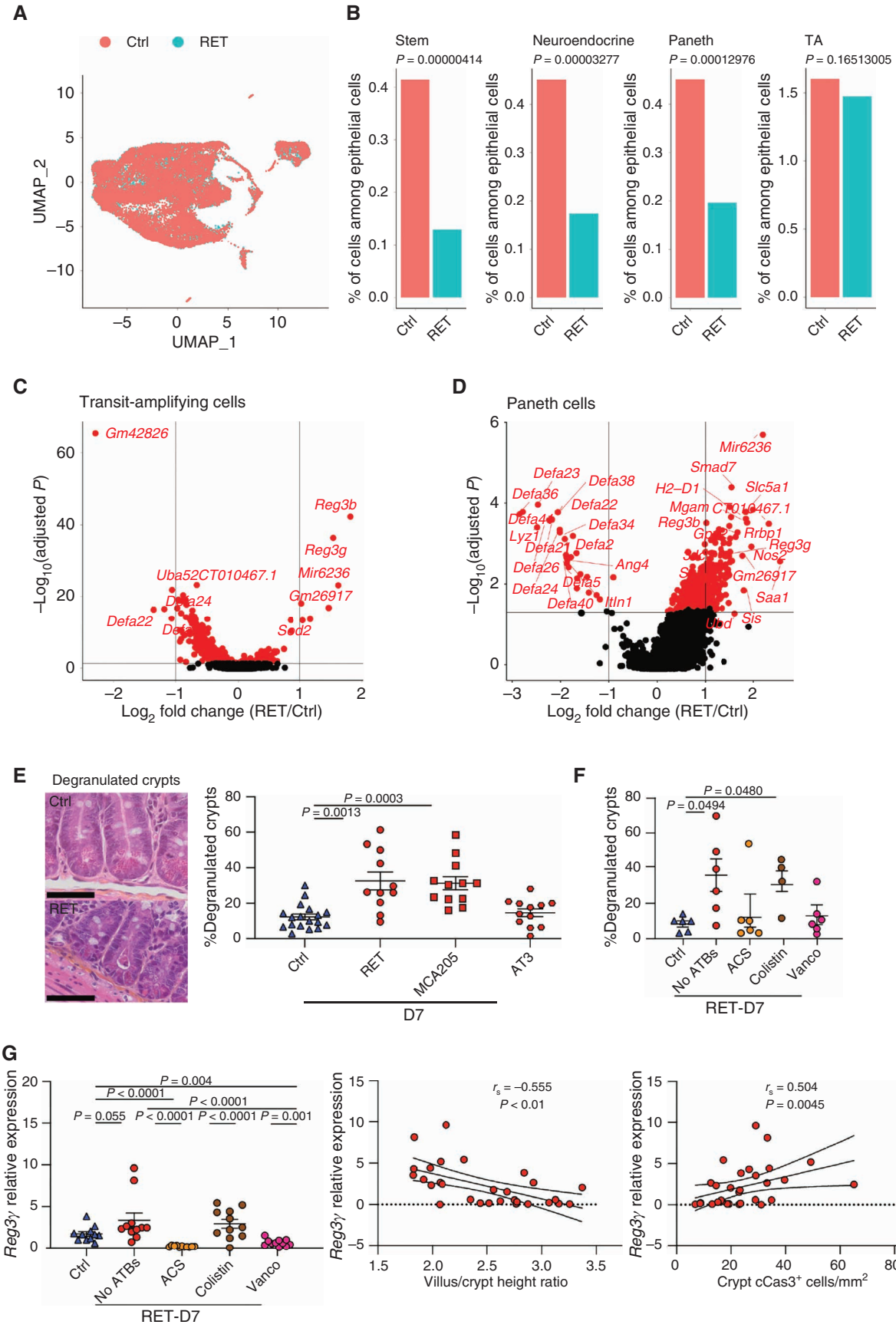

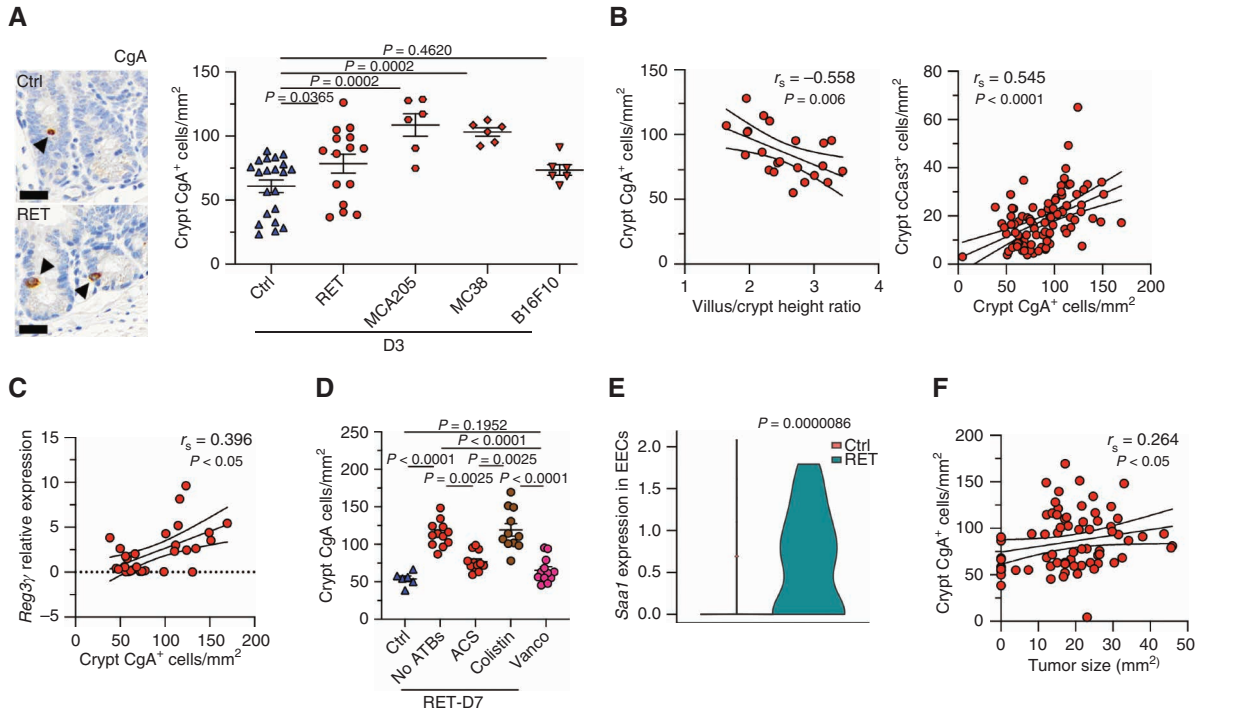

Figure 4. Cancer-induced hyperplasia of EECs in the ileal crypts. **A,** IHC of crypt cells using a CgA-specific staining. Representative micrographs of CgA$^+$ cells in the RET model (left) and enumeration of CgA$^+$ cells/mm^2 in the distal ileum at day 3 after tumor inoculation of different transplantable murine cancers inducing or not inducing ileopathy (right). Scale bar, 25 m. Mann–Whitney test was used for comparison versus control group. **B** and **C,** Spearman correlations between crypt CgA$^+$ cells and villus/crypt height ratio (**B**, left) or cCas3 (**B**, right) in the RET tumor model or with *Reg3γ* ileal gene expression in qPCR at day 3 after RET implantation (**C**). **D,** Enumeration of ileal crypt CgA$^+$ cells according to various regimens of antibiotics at day 7 in the RET model. ANOVA statistical analyses (Kruskal–Wallis test) were used for multiple comparisons. Numerical *P* values are indicated. **E,** Selective overexpression of the *Saa1* gene product in ileal EECs post–RET inoculation identified in single-cell RNA sequencing of the cluster 22 corresponding to EECs (Supplementary Fig. S3A). **F,** Spearman correlations between crypt CgA$^+$ cells and tumor size at day 7. Each dot represents one mouse. Each graph assembles results from 1 to 3 independent experiments containing groups of 5–6 mice.

The gastrointestinal tract is highly innervated by both intrinsic (enteric) and extrinsic nerve fibers, which provide control of gut functions (17). The intrinsic enteric nervous system is organized in two distinct networks, the submucosal and the myenteric plexuses (17). We performed a quantitative analysis of the densities of nerve fibers of the sympathetic and parasympathetic nervous systems of ileal plexus, submucosae, and mucosae after RET tumor inoculation, using IHC staining with anti–tyrosine hydroxylase (TH), anti–choline acetyltransferase (ChAT), or anti–vesicular acetylcholine transporter (VAChT) antibodies. TH catalyzes the rate-limiting step in the synthesis of catecholamines, whereby L-tyrosine is converted into L-DOPA and then dopamine, which is the precursor of the biogenic amines norepinephrine and epinephrine, all three being important neurotransmitters. In the nervous system, TH is a specific marker of catecholaminergic neurons, whereas ChAT, the ACh-synthesizing enzyme, and VAChT are specifically expressed in cholinergic neurons. ChAT staining was not reliable in IHC. So, we took advantage of the ChAT-eGFP mouse model (18), allowing the fluorescence identification of ileal parasympathetic nerves, as well as cells from the villi, crypts, and stroma of the mucosa. ChAT expression was decreased in the stroma at day 3 after RET inoculation (Fig. 5A). VAChT-immunoreactive nerve fibers that extend into LP inside each villus were clearly reduced by RET injection by day 3 up to days 6 to 9 (Fig. 5B). Of note, ChAT$^+$ cell bodies and fibers were not affected in the ileal myenteric plexus (Supplementary Fig. S5B). Although we failed to observe any changes of TH staining in fibers of the submucosae and myenteric plexus (Supplementary Fig. S5C), we noticed an increase in the density of TH$^+$ cells at the bottom of the ileal crypts that were not bona fide neuronal cells in RET and MCA205 tumor bearers (Fig. 5C). Publicly available transcriptomics data sets reveal selective TH expression in EECs (Supplementary Fig. S5D; ref. 13). TH and CgA single stainings markedly correlated (Fig. 5D). Once again, the RET-induced accumulation of TH-positive cells was abrogated by vancomycin but not colistin (Fig. 5E). Of note, the intrinsic innervation of melanoma tumors associated or not with an ileopathy did not differ (Supplementary Fig. S5E).

Transcription patterns of various genes encoding defensins, antimicrobial peptides, innate interferons, ChAT, and adrenergic receptor signaling suggested a coordination between REG3γ and catecholamine pathways (Supplementary Fig. S5F). Hence, we surmised that biogenic amine neurotransmitters could participate in ileal damage. We incubated mouse 3-D crypt stem cell–derived ileal enteroids with physiologic concentrations of dopamine, noradrenaline, and adrenaline for 24 hours and observed a clear reduction of enterocyte proliferation (Fig. 5F and G), concomitant to an increased secretion of the antimicrobial peptide REG3γ (Fig. 5G). Using human ileal enteroids derived in culture medium allowing the differentiation of secretory

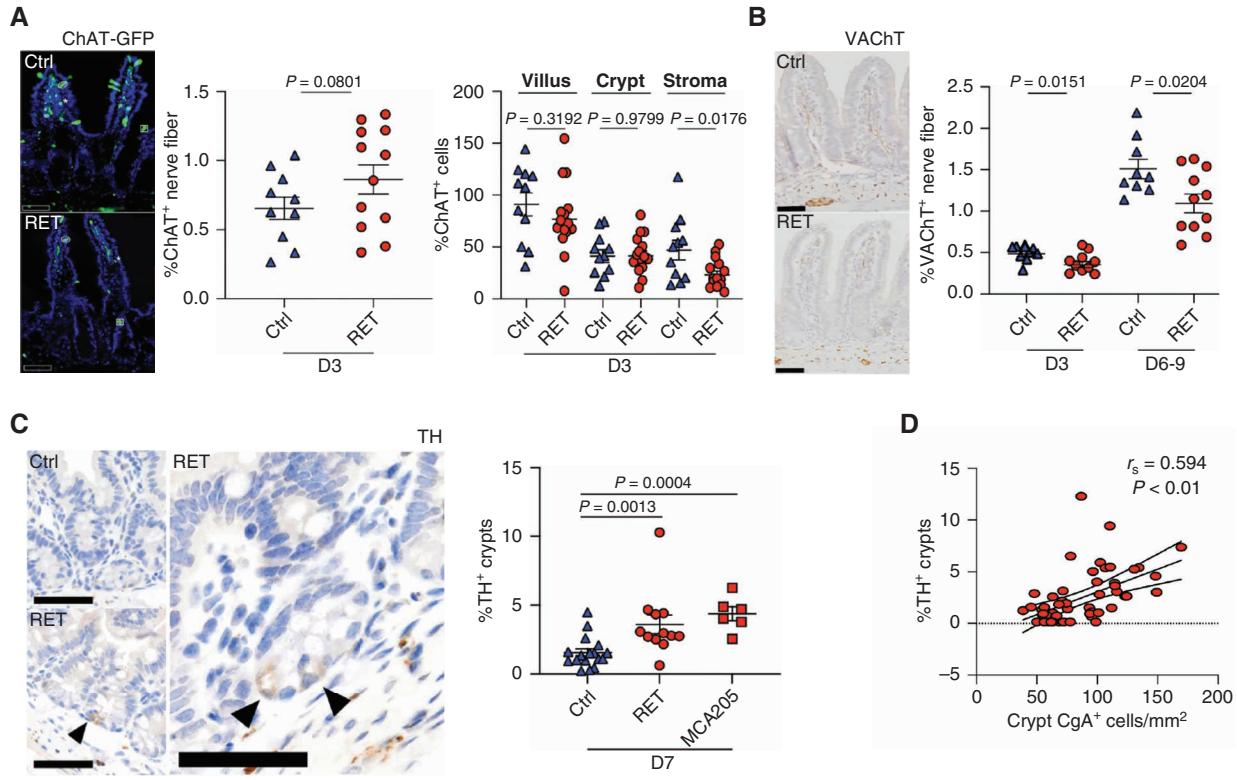

Figure 5. Imbalance between the sympathetic and parasympathetic tonus in ileal mucosa during tumor growth. **A,** ChAT assessment by fluorescence microscopy in the various cell types of the ileal mucosa in eGFP-ChAT transgenic mice after RET (or PBS) inoculation at day 3. ChAT+ nerve fibers (GFP+) were evaluated in the mucosa and submucosa of distal ileum. Also, ChAT+ cells identified in the lining of villi (circle) or crypts (square) and scattered in the stroma "endothelial and immune cells" (star) were counted. Submucosal ganglion cells were excluded from evaluation of ChAT+ nerve fibers and cells. Mann–Whitney test was used for comparison versus control group. **B,** VAChT IHC staining of the ileal mucosa and submucosa using specific antibodies in PBS or RET-injected mice at day 3. One representative micrograph picture (scale bar, 50 m; **A**, **B**) and counting of positive area/total area in the distal ilea at day 3 (**B**). Each dot represents one mouse. A representative experiment out of two yielding similar conclusions is shown. Mann–Whitney test was used for comparison versus control group. **C,** IHC staining of crypt cells with anti-tyrosine hydroxylase (TH)–specific antibodies with two representative micrograph pictures at two different field of magnification (scale bars, 50 m), showing that TH+ cells might correspond to Paneth cells or EEC. Enumeration of TH+ cells in ileal crypts at day 3 after tumor inoculation (RET, MCA205; **C**, right). Mann–Whitney test was used for comparison versus control group. **D,** Spearman correlation between % TH+ crypts and CgA+ cells in the ileal crypts in RET-bearing hosts. (*continued on next page*)

cells, we could recapitulate the capacity of epinephrine (and to some extent norepinephrine) to induce the transcription of *REG3G* gene (but not that of defensin genes; Fig. 5H). Of note, *DEFA5* gene expression remained equal or decreased in similar conditions. Incidentally, the RNA sequencing of all LP leukocytes unveiled that the nondividing CD4+ T-cell subset expressing *Icos* and *Rora* gene products contained signal transduction modules compatible with catecholamine stimulation post–RET inoculation (Supplementary Fig. S4C).

Altogether, an imbalance between catecholamine and cholinergic signaling within the ileal mucosa of tumor bearers was a hallmark of cancer-induced ileal damage that may be apostrophed "stress ileopathy."

Cancer-Induced Ileopathy Is Reduced by Pharmacologic Inhibition or Genetic Ablation of β-Adrenergic Receptors and Contributes to Tumor Growth

Previous studies using models of stroke (10), acute kidney ischemia (19), and sepsis (20) have implicated gut-derived norepinephrine as a key mediator of hepatic and systemic inflammation, with a role of α- or β-adrenoreceptors in the pathology exacerbation. We utilized pharmacologic inhibitors of various receptors of the autonomous nervous and endocrine systems (Fig. 6A) as well as gene-deficient mice to nail down which neuroepithelial circuitry could be involved in the cancer-induced ileopathy. Although pharmacologic inhibition of α1- or α2-adrenergic receptors did not interfere in the RET-induced atrophy of the ileal epithelial layer (Fig. 6B), metyrosine that inhibits the enzymatic capacity of TH to transform L-tyrosine in L-DOPA, β1- or β2-specific or nonspecific pan-β-adrenoreceptor blockade, as well as reserpine, which irreversibly inhibits the vesicular monoamine transporter of catecholamines involved in their release in the synaptic cleft, all prevented RET-induced reduction of the villus/crypt height ratios (Fig. 6B). Accordingly, the use of the β-adrenergic receptor agonist clenbuterol tended to exacerbate the cancer-associated ileopathy (Fig. 6B). In contrast, the anticholinergic agent atropine, which competitively antagonizes the actions of acetylcholine and other muscarinic agonists on all muscarinic receptors within exocrine glands, ganglia, and intramural neurons, could not reverse the effects of tumor progression on the

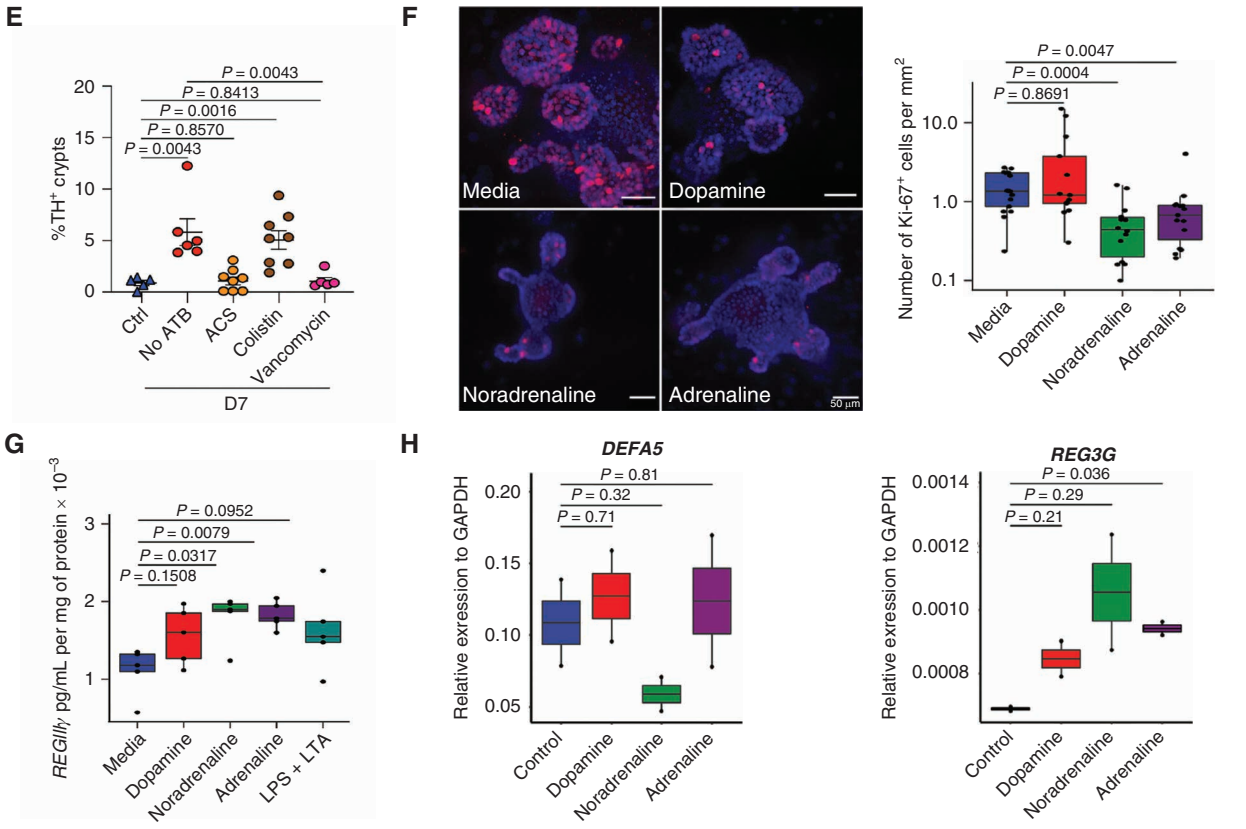

Figure 5. ***(Continued)*** **E,** IHC staining specific for TH expression in ileal crypts of RET tumor bearers that were treated with various regimens of antibiotics during 7 days. The graphs depict a pool of two independent experiments comprising 5–6 mice/group. Mann–Whitney test was used for comparison versus control group. **F–H,** Mouse (**F–G**) and human (**H**) 3-D ileal crypt stem cell–derived enteroids stimulated with catecholamines (**F–H**) or LPS + LTA (**F–G**) 24 hours at day 5 after enteroid dissociation (**F–G**) or for three days (**H**). **F,** z-stacks projection of confocal microscopy images of immunofluorescent staining of Ki-67 and nuclei (with DAPI) in mouse intestinal organoids and ELISA assessment of REG3γ protein normalized to total proteins in the enteroid lysates (**G**). A representative experiment showing raw data for each individual well (out of two yielding similar results) is depicted. **H,** PCR determination of the expression levels of antimicrobial peptide and defensin gene products in human enteroids exposed to various catecholamines. Normalized transcriptional expression of the *REG3G* gene (and *DEFA5*) in human ileal organoids that were differentiated for 4 days and then stimulated with 100 mol/L adrenaline, noradrenaline, or dopamine for 3 days ($n = 2$). Similar conclusions were drawn when stimulating the organoids for 24 hours ($n = 2$). Of note, expression levels of the *DEFA5* gene (left) did not change in similar conditions. Mann–Whitney test was used for comparison versus control group.

ileum (Fig. 6C). Similarly, the steroidal antiprogestogen mifepristone, which prevents binding of cortisol to the glucocorticoid receptor, did not interfere in the tumor-induced ileopathy (Fig. 6C). Prophylactic intake of the β1/β2 adrenergic receptor antagonist propranolol could prevent crypt degranulation and apoptosis, as well as the accumulation of CgA^+ cells (Fig. 6D), when administered at the time of tumor implantation. The pharmacologic inhibition of β-adrenoreceptors phenocopied the effects of the *Adrb2* gene deficiency. The epithelial atrophy could no longer be observed in *Adrb2*$^{-/+}$ or *Adrb2*$^{-/-}$ mice (Fig. 6E). The RET-induced reduction of the villous microvascular thickness that may be related to vasoconstriction was also dependent on the sympathetic tonus (Fig. 6F). However, the pan-β-adrenoreceptor blockade failed to significantly interfere in cancer-induced deviations of the taxonomic composition of the microbiota. Although propranolol and metoprolol could somehow prevent the imbalance between *Ruminococaceae* and *Lactobacillaceace* family members induced by RET implantation at day 8, the β-diversity of the whole intestinal ecosystem was not different in RET tumor bearers treated or not with propranolol (Supplementary Fig. S6A and S6B).

Based on our rationale and former work showing that pan-β blockers affect the immune system and benefit patients and mice bearing melanoma treated with immunomodulators such as rIL2, anti–PD-1 antibodies, or combination-based therapies (21), we addressed whether β-blockade could interfere in the tumor growth kinetics alone or combined with anti–PD-1 antibodies (Supplementary Fig. S6C). The pan-β-blocker propranolol but neither the β2 adrenergic receptor antagonist ICI118551 nor the β2 adrenergic receptor agonist clenbuterol could slow RET and MCA205 outgrowth (Fig. 6G and H), eventually boosting the effects of PD-1 and CTLA4 co-blockade (Supplementary Fig. S6C).

Altogether, cancer-induced ileopathy is a corollary syndrome of distinct malignancies, compromising the epithelial barrier and immune fitness, eventually contributing to cancer progression.

The Gut Oncomicrobiome Signature of Patients with Cancer

We next addressed whether cancer-associated ileopathy has clinical significance in humans. Pioneering reports dating

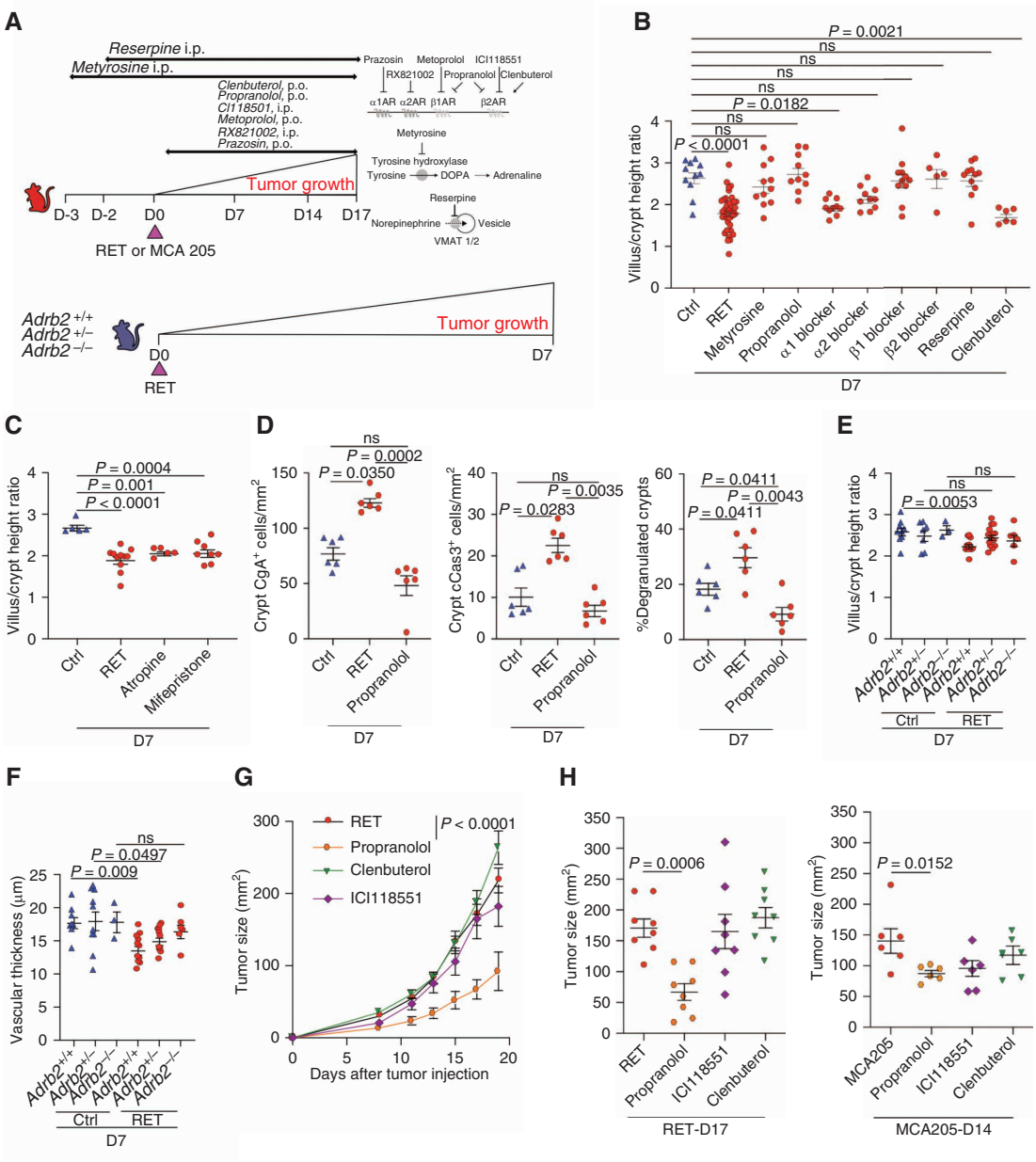

Figure 6. β-Adrenoreceptor signaling controls cancer-induced ileal atrophy. **A,** Graphical scheme of molecular pathways relevant for the catecholamine release or adrenergic receptor signaling and pharmacologic inhibitors (or agonist) used in the following experiments and experimental setting to investigate the effects of various pharmacologic inhibitors or agonist (clenbuterol) of the sympathetic nervous system on RET or MCA205 tumor growth kinetics. **B** and **C,** Villus/crypt height ratio in RET melanoma bearers treated with various pharmacologic inhibitors or agonist (clenbuterol) of the sympathetic nervous system (**B**) or the glucocorticoid or muscarinic receptors (**C**) during 7 days from at least two independent concatenated experiments comprising 5–6 animals/group, each dot representing one ileum. ANOVA statistical analyses (Kruskal–Wallis test) were used for multiple comparisons. Numerical *P* values are indicated. **D,** Modulation of ileal crypt EEC hyperplasia (left), cell apoptosis (middle), and degranulation (right) with propranolol at day 7 in RET-inoculated animals. A representative experiment out of two is depicted, each dot representing one distal ileum. ANOVA statistical analyses (Kruskal–Wallis test) were used for multiple comparisons. Numerical *P* values are indicated. **E** and **F,** The same as in **B**, but using *Adrb2* gene–deficient mice (homozygous or heterozygous littermates) to enumerate villus/crypt height ratio (**E**) and the villous microvasculature thickness at day 7 (**F**). ANOVA statistical analyses (Kruskal–Wallis test) were used for multiple comparisons. Numerical *P* values are indicated. **G** and **H,** Effects of various pharmacologic inhibitors or agonist (clenbuterol) of the sympathetic nervous system on RET or MCA205 tumor growth kinetics, longitudinal RET melanoma growth (**G**, survival curves were estimated using the Kaplan–Meier product limit method), and cross-sectional assessment at sacrifice for RET (**H**, left) and MCA205 (**H**, right) depicted by means ± SEM of tumor sizes, over time or at sacrifice for 6–8 animals/group. Mann–Whitney test was used for comparison versus control group.

from the 1960s already described morphologic abnormalities observed in ileal mucosae of patients diagnosed with advanced malignancies, but this contention was disputed as "spurious" due to numerous confounding factors such as performance status alterations and cachexia that blurred the interpretation of this corollary disease (22–25). Owing to the regulatory constraints limiting endoscopy/biopsy of the distal ileal epithelium in patients recently diagnosed with extraintestinal malignancy, we limited our study to patients diagnosed with proximal colon cancers who underwent surgical resection of terminal ileum.

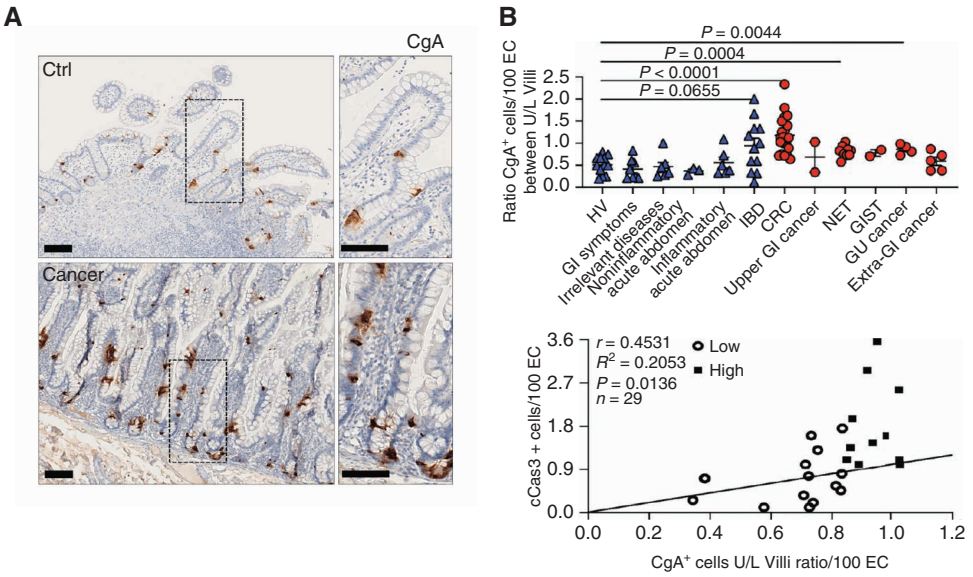

Figure 7. Gut oncomicrobiome MG-based signature across 8 different human malignancies. **A** and **B,** IHC assessment of CgA+ and cleaved caspase-3+ cells in the ileum of "healthy" cancer-free volunteers (HV), patients suffering from colorectal cancers (CRC) or cancers distant from the digestive tract (melanoma, ovarian cancer, kidney or bladder cancer, and Burkitt lymphoma) or inflammatory bowel disease (IBD) or irrelevant diseases [tumor-free individuals without gastrointestinal (GI) tract–related disorders]. Quantification of CgA (top) and Spearman correlation with cleaved caspase-3 (bottom) at diagnosis (refer to Supplementary Table S1 for description of patient characteristics), each dot representing one patient's sample. Numerical *P* values are indicated for Mann–Whitney test versus HV. EC, epithelial cells; GIST, gastrointestinal sarcoma; NET, neuroendocrine tumors; GU, genitourinary cancer. A representative micrograph picture of the ectopic hyperplasia of EEC (**A**) and enumeration (**B**, top) of CgA+ cells in the upper (U) and lower (L) part of the villus in five independent fields/individual, each dot representing the ratio U/L between these two values in one ileum sample (biopsy or surgical resection; **B**). Scale bar, 100 m. (*continued on following page*)

As described in mice, two independent pathologists observed increased proportions of CgA+ EECs in the crypts, often harboring an ectopic distribution reaching the villi tips in patients diagnosed with colon cancer, genitourinary tumors, or neuroendocrine tumors compared with cancer-free individuals (Fig. 7A and B), whereas Paneth cell numbers did not differ (Supplementary Fig. S7A). This EEC accumulation did not appear to be cancer-specific and could be observed in patients suffering from inflammatory bowel disease (Fig. 7B; Supplementary Table S1). Moreover, as seen in tumor-bearing mice, the ectopic accumulation of EEC at the top of the villi correlated with ileal crypt apoptosis in patients (Fig. 7B, bottom). However, in contrast to mice, there were no abnormalities in the proliferative capacities of ileal enterocytes in cancer bearers (Supplementary Fig. S7B). As described in mice, 145 patients with advanced-stage cancer also harbored the specific serum hallmarks of gut permeability (such as soluble CD14 and ST2) compared with healthy individuals (Fig. 7C; Supplementary Table S2).

Based on the premise that cancer might be associated with a corollary gut dysbiosis, we prospectively carried out a shotgun MG-based analysis of fecal material harvested from the largest series of patients with cancer ever reported so far. In a prospective cohort of 1,426 patients with cancer across 8 different malignancies and disease staging, we collected the stools from patients harboring kidney cancer ($n = 69$), breast cancer ($n = 83$), lung cancers ($n = 368$), melanoma ($n = 108$), prostate cancers ($n = 47$), ovarian cancers ($n = 29$), and chronic myelomonocytic leukemia ($n = 17$). These samples were integrated to 705 colon cancers from the publicly available database (26). This collection of cancer metagenomes was compared in terms of species-level taxonomic profiles with 5,570 healthy individuals. Baseline characteristics of patients with cancer in each cohort are presented in Supplementary Table S3. Based on prior studies demonstrating a higher diversity of the gut microbiome in patients with melanoma responding to anti–PD-1 blockade (2), we first compared the alpha diversity in cancer versus cancer-free individuals, and observed no significant differences across multiple diversity metrics (Shannon index; Supplementary Fig. S7C). We then performed PCoA for microbial β-diversity, which provides a measure of the overall relatedness between samples. Significant differences separated bacterial species from feces of individuals with cancer versus those without cancer ($P < 0.01$; Fig. 7D). Using linear discriminant analysis of effect size (LEfSe; ref. 27), coupled to a pairwise comparison of relative taxonomic abundances (for species having a prevalence equal to or greater than 5%) using bootstrapping of two-tailed Mann–Whitney *U* tests (with 1,000 permutations and correction for continuity and ties), we concluded that selected bacterial taxa [$N = 25$; such as Prevotella genus (*P. copri*, *P. stercorea*, and *P. sp CAG520*), Lachnospiraceae family members (*Eubacterium hallii*, *E. ventriosum*, *E. rectale*, *Eubacterium sp CAG 274*, *D. longicatena*, *Roseburia sp CAG 471*, *R. faecis*, *C. comes*, and *Anaerostipes hadrus*), *Actinobacteriaceae* (*Collinsella aerofaciens*, *Bifidobacterium adolescentis*, *B. pseudocatenulatum*, and *Aeriscardovia aeriphila*), *Lactobacillaceae* (*L. rogosae* and *L. ruminis*); Fig. 7E] were overrepresented in healthy individuals. Conversely, distinct bacterial species were overrepresented in patients with cancer across 6 of 8 cancer types, such as 10 Gram-positive commensals, belonging to the *Clostridia* class or Clostridiales order (such as *Clostridium boltae*, *C. citroniae*, *C. clostridioforme*, *C. asparagiforme*, *C. lavalense*, *C. sp CAG242*, *C. symbosium*, and *Ruthenibacterium lactatiformans*), gamma- and delta-proteobacteria (*Bilophila wadworthia* and *Hafnia alvei*),

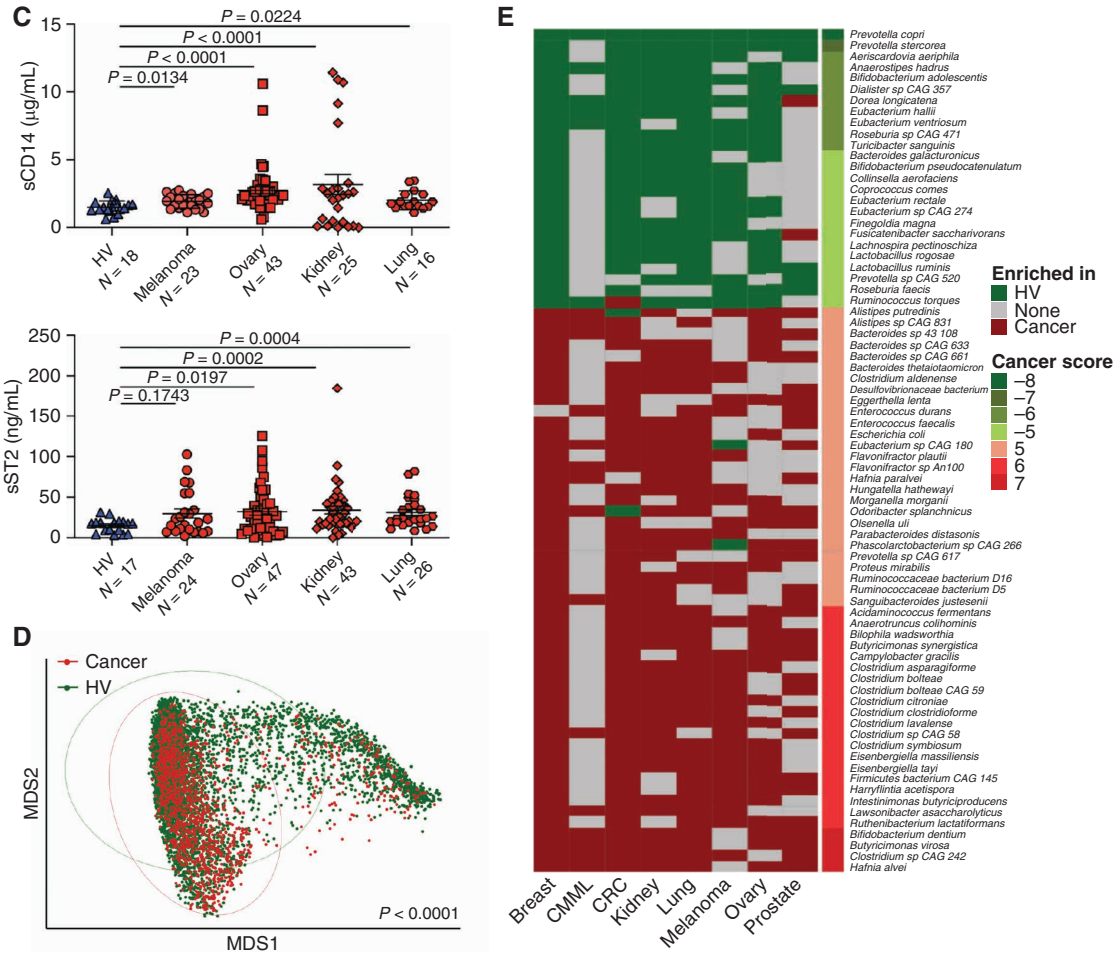

Figure 7. ***(Continued)*** **C,** Quantification of CD14 (top) and soluble ST2 (bottom) in the serum of healthy volunteers (HV) and patients with cancer (melanoma, ovarian cancer, kidney cancer, and non–small lung cell carcinoma) at diagnosis (refer to Supplementary Table S1 for description of patient characteristics), each dot representing one patient's sample. Numerical *P* values are indicated for Mann–Whitney test versus HV. Statistical analyses were performed comparing HV and each cancer histologic type using Student *t* test. **D,** Shotgun MG-based analysis of fecal material harvested from 1,637 patients with cancer (refer to Supplementary Table S2 for description of patient characteristics) and 5,570 HVs. Pairwise comparison on relative taxonomic abundances highlighting species that are over- or underrepresented in multiple cancer types. **E,** The heat map shows the most relevant species as those significant in at least five out of eight cancer categories.

Bifidobacterium dentium, and *Butyricimonas virosa*, as described in rodents and reported in patients with kidney cancer who took antibiotics or failed to respond to immune checkpoint inhibitors (ref. 28; Fig. 7E). We conclude about the prominence of a gut oncomicrobiome fingerprint shared across several tumor types and mammalian species (rodents and humans) where commensals associated with ATB-induced dysbiosis and immunoresistance (mostly Gram-positive bacteria belonging to the Clostridiales order or Proteobacteria) take over beneficial microbes associated with a healthy status.

Altogether, we show a protracted intestinal dysbiosis, most likely associated with stress-induced ileopathy, as a new pathologic feature of cancer progression independent of cachexia in patients with cancer and rodents.

DISCUSSION

Our findings highlight for the first time ileal epithelial dysfunction as a corollary to carcinogenesis initiation that contributes to its pathogenesis and causes a protracted gut dysbiosis. First, the pathologic hallmarks of cancer-associated ileopathy, characterized by mucosal atrophy (abrasion of villi tips), are unexpected in that they occurred rapidly after tumor implantation and are orchestrated in a coordinated manner. This pathogenesis involves defects in endoplasmic reticulum (ER) stress response and autophagy activation, as well as apoptosis of crypt cells accompanied by decreased proliferation in the maturation zone, loss of lymphocytes, granulocytes, and eosinophils, Paneth cell degranulation (with increased REG3γ/defensins ratios), and EEC accumulation in the crypts with ectopic distribution to the villus tip. They are more pronounced in the terminal ileum, reaching the proximal ileum with a short lag, but spared the upper small and large intestine. Following these criteria, the hallmark characteristics of the cancer-associated ileopathy differ from bona fide gut disorders characterized by inflammation or immune-related pathologies or Th2-associated infectious diseases (29–31). However, they are reminiscent of the "cancer enteropathy" first

observed by physicians in 1965 (22–24). Authors described frequent partial (in 10%–29% cases) or subtotal (1%–2% cases) villus atrophy of duodenum, jejunum, or ileum in patients with cancer independent of metastases, treatments, interval to death, or steatorrhoeae, but proportional to duration of the malignancy and weight loss (23, 24).

In mice, the hallmark characteristics of the cancer-associated ileopathy were transient, starting at day 3, peaking at day 8, and resolving at day 12 (when tumors reached a surface of about 20 mm^2), followed by a long-lasting intestinal dysbiosis where Gram-positive bacteria (mostly belonging to the Clostridiales order) prevail in the ecosystem. Owing to its rapid onset, cancer-associated ileopathy did not coincide with body-weight loss nor systemic inflammation due to cachexia. However, it shared with cachexia-associated microbial dysbiosis the relative loss of Lactobacillus genus, the increased gut permeability, and endotoxemia (25, 32, 33). We excluded a role for mucosal T-cell activation in this process (because they were reduced within and outside blood vessels, maybe due to vasoconstriction), as well as a dysregulation of tight junctions, but uncovered a biologically significant imbalance between sympathetic and parasympathetic signals in specific areas of the mucosa. ChAT-producing cells were reduced in the stroma, whereas tyrosine hydroxylase–expressing cells accumulated in the crypts to potentially release biogenic amines (such as epinephrine) that may be, at least in part, a source of the villous microvascular constriction and ileal damage (reduced Ki-67 and increased REG3γ secretion). EEC and Paneth cells were previously reported to express TH, either constitutively for the former ones, or after kidney injury for the latter ones (13, 19, 34). Hence, although the mechanisms by which ileopathy is triggered or maintained during cancer progression remain largely unclear, our findings allow us to speculate that the deviated repertoire of the gut microbiota with the predominance of *Clostridium spp.* may induce EEC production of biogenic amines that in turn signal in and stimulate Paneth cell neighbors to produce and release antimicrobial peptides to control ileal dysbiosis.

Blockade of β-adrenoreceptors limited the growth of extra-intestinal tumors, mostly in those generating the cancer enteropathy. In that regard, Stanley and colleagues showed that ischemic brain injuries caused gut barrier dysfunction and increased permeability, allowing the translocation of ileal bacteria to peripheral organs, paving the way to Gram-positive lung infections. These authors unveiled a biologically significant imbalance between adrenergic and cholinergic signaling within the submucosal plexus in the ileum post-stroke. Indeed, reduction in cholinergic signaling stimulated the proinflammatory immune response (35), whereas its activation prevented the brain injury–induced increase in both intestinal and cerebral vascular permeability (36, 37). Adrenergic-mediated systemic immunosuppression was shown to be beneficial after stroke (38). The pan-β-blocker propranolol could decrease gut permeability post-stroke and reduce bacterial translocation to the lung parenchyma. Moreover, neutralizing β3 adrenoreceptors after stroke could block the bone marrow exodus of inflammatory monocytes (39), which can also be a source of biogenic amines, and contribute to a feedback-positive loop of systemic inflammation (40). Of note, our data indicate that there was no myeloid cell recruitment in ilea post–tumor implantation. Catecholamines mediate numerous functions in the intestine. At the level of epithelial dynamics, noradrenaline release from the sympathetic nervous system appears to stimulate crypt cell proliferation in both the small and large intestines through signaling via α2 adrenoceptors (41). Conversely and in accordance with our findings, adrenaline inhibits cell division in both normal and neoplastic intestinal epithelial cells (IEC) through β-adrenoreceptors (42).

The intestinal immune and nervous systems are intertwined, sensing and integrating luminal cues to regulate motility. The involvement of catecholaminergic neurons in anti-inflammatory responses has been demonstrated in different tissues and is attributed to the broad sympathetic innervation in peripheral lymph nodes associated with expression of β2-adrenergic receptors in immune cells. Recent evidence suggested that intestinal resident macrophage populations play a role in the normal functioning of enteric neurons in homeostatic conditions (43, 44). Specifically, muscularis macrophages (MM), located within and surrounding the myenteric plexus, were shown to regulate the activity of enteric neurons and peristalsis via secretion of bone morphogenetic protein 2 in a microbiota-dependent manner (44). Moreover, MMs displayed a tissue-protective gene-expression profile, a signature that was enhanced following enteric infection, and involved β2-adrenergic receptor signaling (45). While not affecting pathogen load, β-blockade by salbutamol protected mice from enteric nerve loss through a mechanism involving arginase 1 and polyamines (46).

The circuitry connecting luminal sensing to enteric neurons remains largely unknown (47, 48). Recent work directly connected the microbiota to transcription factors in enteric neurons (47, 49) regulating their function. Some lines of evidence suggest that sensing of luminal pathogens, or associated changes in the bowel environment, could be mediated by an intermediate cell type, the EEC (50) or mucosal-associated pain sensory afferents (51), both with the capacity to affect enteric neuron survival and/or activation. Although EECs can synapse with vagal neurons to transduce gut luminal signals in milliseconds by using glutamate as a neurotransmitter, our data suggest that EEC may also express TH and produce catecholamines, as already reported (13).

Interestingly, not all tumorigenic processes trigger this ileopathy. Heterotopic (MC38) or orthotopic (RENCA, fibrosarcoma, RET melanoma) cancers could do so, but even within the same histology (i.e., melanoma), we observed major differences between cell types (B16F10 and RET). It was not a peculiarity of mouse genetic background because RENCA, syngeneic of BALB/c, and all the others (syngeneic of C57BL/6) could elicit ileal dysfunctions. Our findings strongly suggest that soluble products secreted from cancer cells may be transferred to and sensed by distinct epithelial and/or neuronal and/or immune components of the ileal mucosae. Previous work documented that extracellular vesicles from p53-deficient (but not proficient) cancer cells could shuttle tumor miRNA capable of reprogramming the transcriptional profile of existing nerves, resulting in axonal sprouting and emergence of adrenergic nerves indispensable for tumor development (52). In fact, the biological significance of the sympathetic nervous system in tumor progression has already been reported in prostate

and head and neck tumors (52, 53). However, our data do not support this scenario, as we failed to observe any exacerbated innervation of subcutaneous tumors and differences between tumors associated or not with enteropathy. Plasma proteomics and metabolomics as well as bone marrow chimeras could help disentangle stromal versus tumoral cues inducing stress ileopathy.

Our findings rather support the notion that the sympathetic nervous system (or the imbalance within the autonomous nervous system circuitries) indirectly affects natural tumor immunosurveillance. Indeed, β-blockade boosted the efficacy of anti–PD-1 antibodies in MCA205 and RET tumor models. In fact, previous work has already reported that patients with melanoma or breast cancer who took pan-β-blockers presented a greater benefit to immunotherapy or chemotherapy, respectively, as a consequence of increased accumulation of tumor-infiltrating lymphocytes within the tumor microenvironment (21, 54). Indeed, intestinal dysbiosis favoring the dominance of short chain fatty acid–producing immunosuppressive bacteria and/or the translocation of *Lactobacilli* spp. endowed with tolerogenic properties may compromise several of the tumor immunosurveillance mechanisms (2, 8, 28).

Regardless of the precise molecular cues underlying the connections between cancer enteropathy and β2 adrenergic signaling, our data illustrate that the cancer-associated ileopathy is a debilitating corollary syndrome of the tumorigenic process, inducing a long-lasting dysbiosis perturbing the delicate host–tumor balance. Novel diagnosis tools and specific interceptive therapeutics are needed to interfere in this negative feedback loop.

METHODS

Cell Culture, Reagents, and Tumor Cell Lines

MC38, MCA-205, B16F10 (syngeneic from C57BL/6J mice), and 4T1 cell lines (syngeneic from BALB/c mice) were purchased from the American Type Culture Collection, whereas the AT3 breast cancer cell line (syngeneic from C57BL/6J mice) was kindly provided by Dr. Mark Smyth (QIMR Berghofer, Brisbane, Australia). The RET melanoma cell line, generated by transgenic expression of the *RET* proto-oncogene under the control of the metallothionein-1 promoter driving spontaneous melanogenesis, was provided by Viktor Umansky (DKFZ—German Cancer Research Center; syngeneic from C57BL/6J mice). The luciferase-transfected RENCA cell line (syngeneic for BALB/c mice) was provided by Transgene. Cells were cultured at 37 C with 5% CO_2 in RPMI 1640 containing 10% FCS, 2 mmol/L L-glutamine, 1% penicillin/streptomycin, and 1% sodium pyruvate and nonessential amino acids. All reagents were purchased from Gibco-Invitrogen. Dead RET cells were created by repeating freezing and thawing of the RET cell line three times continuously, and viability of the cell line was evaluated by the Vi-CELL Cell Viability Analyzer. Cell lines were regularly tested for *Mycoplasma* contamination and were not used after more than 10 passages.

Mice Experiments

Ethics, Guidelines, and Providers. All animal experiments were carried out in compliance with French and European laws and regulations. The local institutional animal ethics board and French Research Ministry approved all mouse experiments (permission numbers: 2020_035_25416). Experiments were performed in accordance with government and institutional guidelines and regulations. Female C57BL/6 mice were purchased from Harlan. Mice were used between 7 and 12 weeks of age. All mouse experiments were performed at the animal facility of Gustave Roussy Cancer Campus where animals were housed in specific pathogen-free conditions.

Subcutaneous Transplantable MCA-205 Sarcoma, MC38, B16F10, and RET Melanoma. Mice were implanted with 0.8×10^6 MCA-205 sarcoma, 1.0×10^6 MC38, 0.3×10^6 B16F10, or 0.5×10^6 live or dead RET melanoma, 0.5×10^6 AT3 breast cancer, and 0.3×10^6 4T1 cells subcutaneously. Tumor-inoculated mice were treated intraperitoneally when tumors reached a 20 to 40 mm² size with anti–PD-1 mAb (250 g/mouse; clone RMP1-14 purchased from Bio X Cell), anti-CTLA4 (100 g/mouse, clone 9D9 purchased from Bio X Cell) or isotype controls (clones 2A3 and MPC11, respectively) three times at three-day intervals. Tumor length and width were routinely monitored every three days by means of a caliper.

Pharmacologic Treatment

α- and β-Blockade. We conducted intraperitoneal (i.p.) injection of prazosin (purchased at the local pharmacy of Gustave Roussy) at a concentration of 1.5 mg/kg of mice twice a week for α1 blockade, RX821002 (Tocris) at a concentration of 10 mg/kg of mice daily for α2 blockade, metoprolol (purchased at the local pharmacy of Gustave Roussy or Sigma) at a concentration of 10 mg/kg of mice daily for β1 blockade, and ICI118551 (Tocris) at a concentration of 10 mg/kg of mice daily for β2 blockade. For pan-β-blocker or agonist experiments, mice were treated from the day of tumor inoculation with autoclaved drinking water containing propranolol (Sigma or purchased at the local pharmacy of Gustave Roussy) at a concentration of 0.5 mg/mL and filtered through a 0.22- m membrane or clenbuterol (Sigma) at a concentration of 9 g/mL, which was refreshed twice a week.

Catecholamine Depletion. Metyrosine (α-Methyl-D, L-p-tyrosine; CliniSciences) at a concentration of 60 mg/kg of mice was injected i.p. three days before and daily after tumor injection. Reserpine (Sigma) was injected i.p. 48 hours before tumor inoculation at a concentration of 5 mg/kg of mice.

Anticholinergic Agent and Steroidal Antiprogestogen. Atropine (purchased at the local pharmacy of Gustave Roussy or Sigma) and mifepristone (Sigma) at a concentration of 30 mg/kg and 4 mg/kg of mice, respectively, were injected i.p. daily.

The RENCA-luc Orthotopic Tumor Model. BALB/c mice were anesthetized with isoflurane. A lateral incision was made on the dorsolateral right flank of each mouse. 10^4 Renca-Luc cells resuspended in 30 L PBS were injected into the subcapsular space of the right kidney. The skin incision was then closed with surgical clips. Tumor growth was monitored after 15 days of tumor injection using an IVIS Imaging System 50 Series (Analytic Jenap). At day 15, mice were euthanized to harvest small intestines and perform ileum Swiss roll.

Orthotopic Luciferase-Engineered TC1 Lung Cancer Model. TC1 cells stably expressing firefly luciferase (TC1-Luc, 4×10^5 in 100 L PBS) were percutaneously injected into the right lung of wild-type C57BL/6 mice. Tumor incidence and development were regularly monitored by the *in vivo* photonic imaging of tumor cells' luciferase activity. In brief, mice received a percutaneous injection of luciferase substrate (Beetle Luciferin potassium salt, Promega) at a dose of 150 mg/kg, and 8 minutes after luciferin inoculation, photons were acquired on a Xenogen IVIS 50 bioluminescence *in vivo* imaging system (Caliper Life Sciences Inc.). Tumor-bearing mice were sacrificed at days 7, 14, and 21 after tumor injection.

TC1 Intravenous (IV) Model. To establish the non–small cell lung carcinoma IV model, TC1 cells stably expressing firefly luciferase (TC1-Luc, 5×10^5 in 100 L PBS) were intravenously injected into wild-type C57BL/6 mice. Tumor incidence and development were regularly monitored by *in vivo* photonic imaging of tumor cells' luciferase

activity. In brief, mice received an i.p. injection of luciferase substrate (Beetle Luciferin potassium salt, Promega) at a dose of 150 mg/kg, and 8 minutes after luciferin inoculation, photons were acquired on a Xenogen IVIS 50 bioluminescence *in vivo* imaging system (Caliper Life Sciences Inc.). Two weeks after cell injection (day 14), tumor incidence in the lung was detected at an exposure time of four minutes. *In vivo* imaging was conducted every four to five days with an exposure time starting with four minutes, which was then gradually decreased to three, two, and one minute when photon saturation occurred. Tumor-bearing mice showing photon saturation within less than one minute of exposure were euthanized.

Antibiotic Treatments. Mice were treated with antibiotic solution containing ampicillin (1 mg/mL), streptomycin (5 mg/mL), and colistin (1 mg/mL; Sigma-Aldrich), or colistin alone (1 mg/mL), or vancomycin alone (0.25 mg/mL) added in autoclaved drinking water. Antibiotic solutions were refreshed and bottles were replaced three times a week.

Cohousing Experiments. The same number of RET-injected mice (C57BL/6J females) were cohoused as littermates with naïve (non–tumor-bearing) mice (C57BL/6J females) in the same cage from the day of tumor injection until sacrifice. As for methylcholanthrene-induced sarcoma, MCA inoculated and noninoculated mice were admixed in the same cage in a 1:1 ratio or left alone in separate cages. Groups of wild-type C57BL/6 mice were injected subcutaneously in the flank with 100 g of 3-MCA in 0.10 mL of corn oil. Mice were monitored every 7 days for tumor development 90 to 100 days after 3-MCA treatment. Animals bearing nodules >0.5 cm^2 in area and demonstrating progressive growth were considered as "tumor" nodules, as previously described (12).

RNA Extraction and PCR to Determine Gene Expression

Lysis and extraction protocols were identical for all murine samples. Tumor or intestinal samples were snap-frozen in liquid nitrogen in RLT and buffer containing 0.1% β-mercaptoethanol. On the day of extraction, samples were thawed at 4 C and homogenized on a microtube homogenizer (Benchmark Scientific) in RNA-free glass bead tubes (Dutscher). Total RNA extraction and genomic DNA removal were performed with the RNeasy Mini Kit (Qiagen), following the manufacturer's recommendations. A maximum of 1 g of RNA, measured by using a NanoDropTM Spectrophotometer (Thermo Fisher Scientific), was reverse-transcribed into cDNA with a mix composed of SuperScript III Reverse Transcriptase (Life Technologies), RNaseOUT Recombinant Ribonuclease Inhibitor (Life Technologies), Random primers (Promega), and Deoxynucleoside Triphosphate Set, PCR grade (Roche Diagnostics).

Quantitative Gene Expression Assay. Expressions of murine Ppia (Mm02342430_g1), Ang4 (Mm03647554_g1), Lyz2 (Mm01612741_m1), Reg3γ (Mm00441127_m1), α Defensin-5 (Mm00651548_g1), defensin β1 (Mm00432803_m1), IFNα1 (Mm03030145_gH), IFNβ1 (Mm00439552_s1), IFNλ2 (Mm04204157_gH), Th (Mm00447557_m1), ChAT (Mm01221880_m1), Adrb1 (Mm00431701_s1), and Adrb2 (Mm02524224_s1; all from Life Technologies) were analyzed with the TaqMan Gene-Expression Assay using the Universal Master Mix II on a StepOnePlus Real-Time PCR System (Life Technologies). Amplifications were carried out using the following ramping profile: 1 cycle at 95 C for 10 minutes, followed by 45 cycles of 95 C for 30 seconds, 60 C for 1 minute. Quantitative RT-PCR data were normalized to the expression levels of the housekeeping gene Ppia by means of the $2^{-\Delta C_t}$ method.

Pathologic Methods and Analyses

Animal Handling after Sacrifice to Investigate the Digestive Tract. Mice were sacrificed at various time points post–RET (or tumor) inoculation. The intestinal tissues including duodenum, jejunum, ileum, and colon were harvested, and the lumen was flushed with sterile PBS. Each intestinal segment was cut longitudinally, rolled, and fixed in 4% paraformaldehyde (PFA) overnight. After fixation, the intestine tissue was preserved in formalin-fixed, paraffin-embedded or optimum cutting temperature compound.

IHC of Murine Intestinal Tissues. For morphologic analysis, a hematoxylin, eosin, and saffron staining was used. For all biomarker staining, we used Bond Leïca automated immunostainer instruments. For the detection of cleaved caspase-3, Ki-67, TH, VAChT, and CD8, paraffin sections were processed for heat-induced antigen retrieval (either ER1 corresponding citrate buffer pH6 or ER2 corresponding EDTA buffer pH9) for 20 minutes at 100 . Slides were incubated with the antibody for one hour at room temperature. The antibodies used were as follows: cleaved caspase-3 (Cell Signaling Technology, D4W2Z, rabbit, 1:100, ER2), Ki-67 (Cell Signaling Technology, D3B5, rabbit, 1:500, ER2), TH (Millipore, polyclonal, rabbit, 1:300, ER1), VAChT (Synaptic Systems, polyclonal, rabbit, 1:500, ER2), and CD8 (Cell Signaling Technology, D4W2Z, rabbit, 1:400, ER2). The signal was revealed with the Rabbit HRP PowerVision Kit (Leïca Biosystems, #PV6119). The signals were detected with diaminobenzidine (DAB). For the detection of ZO1, CgA, and E-cadherin, paraffin sections were processed for heat-induced antigen retrieval (either ER1 or ER2) for 20 minutes at 100 . Slides were incubated with the antibody for 30 minutes at room temperature. The antibodies used were as follows: ZO1 (Abcam, EPR19945-224, rabbit, 1:1,000, ER2), CgA (Immunostar, 1317001, rabbit, 1:1,000, ER1), and E-cadherin (Cell Signaling Technology, 24E10, rabbit, 1:100, ER2). To reveal the signal, slides were incubated with Bond Polymer Refine Detection Kit (Leïca Biosystems, #DS9390) and red chromogen. For the detection of double markers CD4/FOXP3 simultaneously, antigen retrieval was performed by incubating slides in ER2 buffer (pH 9.0) for 20 minutes at 100 C. Then, the antibodies were successively incubated for one hour at room temperature and detected, respectively, by Bond Polymer Refine Red Detection (Leïca Biosystems, #DS9390) and by Bond Polymer Refine Detection Kit (Leïca Biosystems, #DS9800). The antibodies used were as follows: CD4 (Cell Signaling Technology, D7D2Z, rabbit, 1:50, ER2) and FOXP3 (Cell Signaling Technology, D608R, rabbit, 1:200, ER1). These slides were successively revealed by red chromogen (Leica Biosystems) and HIGHDEF Black HRP chromogen/substrate (Enzo Life Sciences, #ADI-950-171-0030). Finally, the sections were counterstained by hematoxylin (Leica Biosystems). For Alcian Blue special stain, slides were deparaffinized with xylene and rehydrated with alcohol and water. Then, slides were incubated with Alcian Blue solution pH2.5 for 45 minutes at room temperature. Without rinsing, slides were covered with sodium tetraborate solution. Finally, slides were rinsed in distilled water, dried, and mounted with xylene-based media. Images for analysis were acquired as whole slide images (WSI) with a slide scanner Zeiss Axio Scan.Z1 and Olympus VS120 whole-slide imaging system.

Measurement of Villus/Crypt Height Ratio. WSIs of longitudinal sections from adult mouse small intestine (duodenum, jejunum, and ileum) were generated. Five representative areas of distal ileum were randomly selected from each mouse. Measurements of villus and crypt height were performed using QuPath (55), when crypt-villus units were well oriented. The ratio of villus height/crypt height was calculated based on the measurements of each crypt-villus unit. Tangentially cut or less than 3–5 not well-oriented villi or crypts were excluded from the analysis.

Analysis of IHC Biomarkers

Biomarkers in Whole Tissues. QuPath software was used (55). Regions of interest (ROI) were defined first by "Simple tissue detection" function and modified by hand in each WSI to quantify biomarker-positive cells, and "Positive cell detection" or "Object classification" functions were used for detection of Ki-67, CD4/FOXP3, and goblet cells, whereas other biomarkers such as cleaved caspase-3,

CgA, TH, CD8, and GR1 were quantified manually. To quantify biomarker-positive areas such as ZO1, E-cadherin, and VAChT, "Pixel classification" function was used, and the DAB$^+$ area was considered as a biomarker-positive area. Artifacts and other nonspecific structures stained by the biomarkers were manually excluded.

Whole-Mount Immunostaining and Clearing Procedure. Tissue samples were immunostained and cleared following the iDISCO$^+$ protocol. Briefly, samples were dehydrated using graded series of methanol solution and then bleached in methanol/5% hydrogen peroxide overnight at 4 C. Samples were rehydrated using graded series of methanol solution, permeabilized for two days at 37 C and incubated in blocking buffer: PTwH (0.2% Tween-20, 10 mg/L heparin in PBS), 5% DMSO, and 3% donkey serum for three days at 37 C. Tissues were incubated with primary antibodies at 37 C for one week, washed in PTwH, and incubated with secondary antibodies for two to three days. The antibodies used are as follows: rat anti-panendothelial cell antigen monoclonal antibody, unconjugated, clone MECA-32 (rat, 1:10, catalog no. 550563, RRID:AB_393754, BD Pharmingen), anti–tyrosine hydroxylase antibody (rabbit, 1:200, catalog no. AB152, RRID:AB_390204, Merck Millipore), anti-VaChT antibody (rabbit, 1:250, catalog no. 139 103, RRID:AB_887864, Synaptic Systems), Cy3-AffiniPure Donkey Anti-Rabbit IgG (H + L) antibody (Donkey, 1:500, catalog no. 711-165-152 RRID:AB_2307443, Jackson ImmunoResearch Labs), Alexa Fluor 647-AffiniPure Donkey Anti-Rat IgG (R + L) antibody (Donkey, 1:500, catalog no. 712-605-153 RRID:AB_2340694, Jackson ImmunoResearch Labs). Samples were washed in PTwH, dehydrated in graded methanol series, and equilibrated in 66% dichloromethane/33% methanol overnight. Delipidation was completed by immersion in 100% dichloromethane for 20 minutes. Finally, samples were immersed in dibenzyl ether to homogenize the refractive indices between the tissue and the imaging medium.

LSFM and Image Processing. Cleared samples were imaged at 0.63× zoom on a light-sheet fluorescence microscope (LSFM; Ultramicroscope II, LaVision Biotec) using Inspector Microscope controller software (Version 5.1.328, LaVision Biotec). Stack images were converted to Imaris files (.ims) using Imaris File Converter and opened with Imaris ×64 software (version 9.6; Bitplane) to obtain 3-D volume images. 3-D pictures were generated using the "snapshot" tool.

Biomarkers in Villi and Crypts. To calculate the cell density of biomarkers such as cleaved caspase-3 or CgA only in villi or crypts, areas of murine villi and crypts were identified by a deep learning–based method. Briefly, WSIs were cropped into 256 × 256 pixel tiles. Blank tiles and tiles with only debris or uninterpretable pieces of tissue were excluded. The neural network trained by pathologists (S. Yonekura and K. Ueda) performed the semantic segmentation of villi, crypts, LP in murine ileum and colon using Python library "Segmentation model."

Quantification of ChAT$^+$ or VaChT$^+$ Areas in Mucosa and Submucosa of murine ileum. Mice were implanted with 0.5×10^6 RET melanoma cells subcutaneously and sacrificed at day 3. A Swiss-roll tissue of ileum was collected and fixed, and the expression of VAChT was revealed by the IHC using DAB. Images displayed in the figures were acquired as WSIs with a digital slide scanner Olympus VS120. Image analysis was performed using QuPath (20). Briefly, the VAChT$^+$ area was identified by detecting the percentage of DAB$^+$ area within five representative (1.0 mm^2) manually annotated regions, corresponding to the mucosa and submucosa of the ileum, randomly selected for each mouse. Only nerve fibers were quantified, excluding the submucosal plexus.

Quantification of ChAT$^+$ Neurons in Myenteric Plexus. Distal ileum segments were fixed in 0.1 mol/L PBS containing 4% PFA at room temperature for three hours. Whole mounts of longitudinal muscle and myenteric plexus were obtained by microdissection and were permeabilized with PBS containing 4% horse serum (HS) and 0.5% Triton X-100 for one hour at room temperature. Tissues were then incubated with the following primary antibodies sequentially: rabbit anti-ChAT [gift from Prof. Dr. M. Shemann (TUM School of Life Sciences, Technical University of Munich, Freising, Germany), 1/1,000] for 72 hours, and human anti-neuronal marker (gift from CHU Nantes, 1/500) overnight, both containing 4% HS, 0.5% Triton X-100, and 0.02% sodium azide at room temperature. After washing, tissues were incubated for two hours at room temperature with the appropriate secondary antibodies and mounted with Pro-Long Gold Antifade Reagents (Thermo Fisher Scientific). A minimum of 20 ganglia per tissue (animals) was analyzed using an Olympus BX microscope.

Quantification of Immunofluorescence ChAT$^+$ Areas in Mucosa and Submucosa of Murine Ileum. ChAT-GFP transgenic mice were implanted with 0.5×10^6 RET melanoma cells subcutaneously and sacrificed at day 7. A Swiss-roll tissue of distal ileum was collected, fixed, and counterstained with DAPI for the nucleus. Images displayed in the figures were acquired as WSIs with a digital slide scanner Olympus VS120. Image analysis of ChAT$^+$ was performed using QuPath (20). Briefly, the ChAT$^+$ area was identified by detecting the percentage of the GFP$^+$ area within two to five representative (1.0 mm^2) manually annotated regions, corresponding to well-oriented mucosa and submucosa of the ileum, randomly selected from two to four different sections of the ileum from each mouse. Out-of-focus and not well-oriented areas were excluded from the analysis. Areas of ChAT$^+$ cells in the villi, crypts, or stroma (vessels/immune cells) were excluded from ChAT$^+$ nerve fibers area, but were counted separately for each mouse. Cases with less than 30 villi evaluated were excluded from the final analysis.

Quantification of CD8$^+$ Cells in the Ileum. WSIs were used to calculate CD8$^+$ cell density with QuPath. Five to eight representative regions (1.0 mm^2), randomly selected, were evaluated in the distal ileum of each mouse. CD8$^+$ cells were manually counted as intra- or extravascular, according to their location in well-oriented villi. Cases with fewer than 30 villi evaluated were excluded from the final analysis.

Quantification of GR1$^+$ Cells in the Ileum. WSIs were used to calculate GR1$^+$ cell density with QuPath. Due to the low number of cells present in the sample, GR1$^+$ cells were counted in the entire distal segment of the ileum, considering the presence of GR1$^+$ cells in the LP of the villi, among the crypts or total. Total length was determined for the segment of distal ileum of each mouse in order to define a normalized count of GR1$^+$ cells/mm.

Single-Cell RNA Sequencing

Ileum samples from C57BL/6 mice with and without RET melanoma were collected, and fat tissue, Peyer's patches, and feces were removed. Intestines were cut longitudinally, rolled up, and then cut transversally into small pieces into a tube. Pieces were transferred into a new 50-mL tube with 20 mL of IEC medium containing PBS, 5% FCS, 5 mmol/L EDTA, and 1 mmol/L DTT. Tubes were vortexed and shaken at 37 C for 20 minutes. Cell suspensions were filtered with a 40- m cell strainer into a new tube, centrifuged, resuspended in a solution of PBS 1× (without EDTA and magnesium) containing 0.04% de BSA (400 g/mL), and counted. Cell suspensions were stored in LoBind tubes at a concentration of 1.0×10^6 cellules/mL and kept on ice until use. Single-cell suspensions were loaded onto a chromium single-cell chip (10X Genomics) according to the manufacturer's instructions for coencapsulation with barcoded gel beads at a target capture rate of ~10,000 individual cells per sample. Captured mRNAs were barcoded during cDNA synthesis using the Chromium Next GEM Single-Cell 3′ GEM, Library and Gel Bead Kit v3.1 (10X Genomics) according to the manufacturer's instructions. The resulting libraries were prepared in parallel in one single batch. We pooled all of the libraries for sequencing in an Illumina

flow cell. All the libraries were sequenced with an 8-base index read, a 28-base Read1 containing cell-identifying barcodes and unique molecular identifiers (UMI), and a 91-base Read2 containing transcript sequences on an Illumina NovaSeq 6000 at Gustave Roussy.

Statistical Assessment of Single-Cell RNA Sequencing

Quality Control, Pseudomapping, and Quantification. Raw binary base call (BCL) files were demultiplexed and converted to Fastq format using bcl2fastq (Illumina). Quality control of reads was performed using fastqc and assignment to the expected genome species evaluated with fastq screen (56). Reads were pseudomapped to the Ensembl reference transcriptome v99 corresponding to the mus musculus GRCm38 build with kallisto using its « bus » subcommand and parameters corresponding to the 10X Chromium 3′ scRNA-Seq v3 chemistry (57). The index was made with the kb-python wrapper of kallisto (57, 58). Barcode correction using whitelist provided by the manufacturer (10X Genomics), and gene-based quantification of reads was performed with BUStools (59).

Quality Control on Each Sample. Cell barcodes by symbol count table were loaded in R (v3.6.3) using the BUSpaRse package (https://github.com/qubvel/segmentation_models). To call real cells from empty droplets, we used the emptyDrops() function from the dropletUtils package, which assesses whether the RNA content associated with a cell barcode is significantly distinct from the ambient background RNA present within each sample (60, 61). Barcodes with $P < 0.001$ (Benjamini–Hochberg-corrected) were considered as legitimate cells for further analysis. The count matrix was filtered to exclude genes detected in fewer than five cells, cells with fewer than 1,500 UMIs, or fewer than 200 detected genes, as well as cells with a mitochondrial transcript proportion higher than 20%. The proportion of ribosomal gene counts and the proportion of mechanical stress-response gene counts were also estimated but not used to filter cells.

Cell-Cycle Scoring. Cell-cycle scoring of each cell was performed using two methods: the cell-cycle scoring function from the Seurat package and the cyclone function from Scran. Barcodes corresponding to doublet cells were identified and discarded using the union of two methods. First, scDblFinder using default parameters except for minClusSize (set to the minimum of 50, or the number of cells divided by 50) and dbr set to (number of cells)²/1E+05). Second, *scds* with its hybrid method using default parameters (62). We manually verified that the cells identified as doublets did not systematically correspond to cells in the G_2–M phase.

Individual Analysis. Seurat was applied for further data processing. The SCTransform normalization method (63) was used to normalize, scale, select 3,000 highly variable genes, and regress out bias factors (number of detected genes, proportion of mitochondrial transcripts, proportion of ribosomal transcripts, and proportion of mechanical stress-response transcripts). Pearson residuals from this regression were used for dimension reduction by principal components analysis (PCA). The number of PCA dimensions to keep for further analysis was evaluated by assessing a range of reduced PCA spaces using 3 to 49 dimensions, with a step of 2. For each generated PCA space, Louvain clustering of cells was performed using a range of values for the resolution parameter from 0.1 to 1.2, with a step of 0.1. The optimal space was manually evaluated as the one combination of kept dimensions and clustering resolution resolving the best structure (clusters homogeneity and compacity) in a uniform manifold approximation and projection (UMAP) space. Additionally, we used the clustree method to assess if the selected optimal space corresponded to a relatively stable position in the clustering results tested for these dimensions/resolution combinations (64).

Detected clusters were mapped to known markers of IECs (13) and immune cells (65). Data sets were divided into two data sets containing either epithelial cells or immune cells based on *Ptprc* (CD45) gene expression prior to integration.

Integration Analysis. Data sets were integrated using canonical correlation analysis to identify pairwise anchors between data sets and using the anchors to harmonize the data sets, as implemented in Seurat. In practice, data sets were normalized independently using SCTransform, as described before (see individual analysis section). The top 3,000 highly variable genes across all samples were selected by the SelectIntegrationFeatures function and used for integration with the PrepSCTIntegration, FindIntegrationAnchors, and IntegrateData functions (with default parameters). After integration, a PCA was performed on the integrated data set.

Louvain clustering was performed as described for individual analysis, using 35 dimensions and a resolution of 0.9. Results were visualized through a UMAP reduction at two dimensions.

The automatic annotation of cell types, cluster marker gene detection, and cerebro visualization steps were performed similarly to the individual analysis.

Grouped analysis: IndivNorm: Each data set was normalized independently by SCTransform, as described in the individual analysis section, and then data were merged using the merge function from Seurat. A common dimension reduction was performed by PCA. Louvain clustering was performed as described for individual analysis, using 35 dimensions and a resolution of 0.9. Results were visualized through a UMAP reduction at two dimensions. The automatic annotation of cell types, cluster marker gene detection, and cerebro visualization steps were performed similarly to the individual analysis.

GlobalNorm: Data sets were merged by merge function from Seurat, and then a normalization by SCTransform and a common dimension reduction by PCA were performed (as described in the individual analysis section). Louvain clustering was performed as described for individual analysis, using 35 dimensions and a resolution of 0.9 (for the epithelial cells data set) and using 30 dimensions and a resolution of 0.9 (for the immune cells data set). Results were visualized through a UMAP reduction at two dimensions. The automatic annotation of cell types, cluster marker gene detection, and cerebro visualization steps were performed similarly to the individual analysis.

Custom differential analysis: Differential expression analyses were performed using the Wilcoxon test implemented in the Seurat package. Resulting *P* values were corrected for false-positive rate using the Bonferroni correction.

Gene set enrichment analysis: Gene set enrichment analysis was performed using fgsea R package. Pathways were retrieved from the Reactome database (https://reactome.org/) using the function Reactomepathway from fgsea package. Pathways that comprised fewer than 15 genes were excluded from the analysis.

Serum Levels of Soluble ST2, CD14, and Corticosteroids

Blood taken from mice was centrifuged for 3 minutes at 12 rcf. The serum was collected and stored at –20 C until analysis. ST2, CD14, and corticosteroid levels were measured using the Duoset murine ST2 and CD14 ELISA Kit (R&D Systems) following the manufacturer's instructions.

DNA Extraction and 16S rRNA Sequencing of Mouse Stools

Preparation and sequencing of mouse fecal samples were performed at IHU Méditerranée Infection, Marseille, France. Briefly, DNA was extracted using two protocols. The first protocol consisted of physical and chemical lysis, using glass powder and proteinase K, respectively, then processing using the Macherey-Nagel DNA Tissue Extraction Kit (66). The second protocol was identical to the first protocol, with

the addition of glycoprotein lysis and deglycosylation steps (67). The resulting DNA was sequenced, targeting the V3–V4 regions of the 16S rRNA gene as previously described (68). Raw FASTQ files were analyzed with Mothur pipeline v.1.39.5 for quality check and filtering (sequencing errors, chimerae) on a Workstation DELL T7910. Raw reads were filtered and clustered into Operational Taxonomic Units (OTU), followed by elimination of low-populated OTUs (until five reads) and by *de novo* OTU picking at 97% pairwise identity using standardized parameters and SILVA rDNA Database v.1.19 for alignment. Sample coverage was computed with Mothur and resulted to be on average higher than 99% for all samples, thus meaning a suitable normalization procedure for subsequent analyses. Bioinformatic and statistical analyses on recognized OTUs were performed with Python v.2.7.11. The most representative and abundant read within each OTU (as evidenced in the previous step with Mothur v.1.39.5) underwent a nucleotide Blast using the National Center for Biotechnology Information (NCBI) Blast software (ncbi-blast-2.3.0) and the latest NCBI 16S Microbial722 database accessed at the end of April 2019 (ftp://ftp.ncbi.nlm.nih.gov/). A matrix of bacterial relative abundances was built at each taxon level (phylum, class, order, family, genus, and species) for subsequent multivariate statistical analyses. Raw data were first normalized and then standardized using QuantileTransformer and StandardScaler methods from Sci-Kit learn package v0.20.3. Normalization transforms each variable to a strictly Gaussian-shaped distribution, whereas the standardization results in each normalized variable having a mean of zero and variance of one. These two steps of normalization followed by standardization ensure the proper comparison of variables with different dynamic ranges, such as bacterial relative abundances, tumor size, or colonic infiltrate score. Measurements of α diversity (within sample diversity), such as observed_otus and Shannon index, were calculated at the OTU level using the SciKit learn package v.0.4.1. Exploratory analysis of β-diversity (between sample diversity) was calculated using the Bray–Curtis measure of dissimilarity calculated with Mothur and represented in PCoA, whereas for hierarchical clustering analysis, the "Bray–Curtis" metrics and "complete linkage" method were implemented using custom scripts (Python v.2.7.11). We implemented PLS-DA and the subsequent variable importance plot (VIP) as a supervised analysis in order to identify the most discriminant bacterial species among the different cohorts of mice according to various therapies. When needed, univariate/multivariate statistics and correlation analyses were performed with Python v2.7 and related packages (Scipy, SciKit-learn). All *P* values were considered statistically significant if less than or equal to 0.05.

16S rRNA Gene Sequence Processing and Analysis in Mice with or without Propranolol (Supplementary Fig. S6A and S6B). Demultiplexed raw sequence data were processed using Qiime2 version 2020.6.0 along with the plugin DADA2 (69). Amplicon sequence variants (ASV) were generated for each sample. Each run was denoised separately. Briefly, sequences were corrected for Illumina amplicon sequence errors, dereplicated, and merged of paired-end reads. Figaro (70) was used to determine the optimal truncation parameters. Thus, sequence lengths were truncated at position 243 for forward reads and at position 239 for reverse reads. Runs were merged together using the qiime2's plugin feature table followed by chimera removal using uchime *de novo* method. The taxonomy assignment was performed against the GreenGenes reference database v13.8 (V3-V4 segment; ref. 71). Qiime's artifact files related to feature and taxonomy tables resp. phylogenetic tree were exported to biom respectively. Newick format in order to use with phyloseq R package v1.32 (72). For alpha-diversity analysis, each sample was downsampled to 10,000 reads (graphically determined through rarefaction curves). Samples for which reads number was below this threshold were excluded. Alpha diversity measures the species richness within each sample, which were assessed by observed ASV, Chao1, Shannon index, and inverse Simpson index. The Wilcoxon test was used to determine significant differences in alpha diversity among the two groups. β-Diversity was analyzed through PCoA with weighted UniFrac distance (73). Permutation multivariate analysis of variance using the distance metrices method (74) was used to test for the differences among communities. The DESeq2 (75) method was used for differential analysis. ASVs detected in less than 30% of samples within one group were excluded from differential analysis. All statistical analyses were performed under R version 4.0.2.

Handling of Patient Specimens

Feces-related translational research was conducted according to the ethical guidelines and approval of the local ethical committee (CCPPRB, Kremlin Bicêtre). Feces (for MG analysis) and serum collection were performed under the study "Oncobiotics," B2M ethics protocol number PP: 15-013. Written informed consent was obtained for all patients in accordance with the Declaration of Helsinki.

Clinical Management. Detailed in Supplementary Tables S1, S2, and S3. Most if not all patients were under routine clinical management outside of clinical protocols.

MG Analyses. Stool DNA extraction and sequencing have been handled by Metagenopolis platform, INRAE, Jouy-en Josas, as previously described (1, 28).

Small Intestine Crypt Isolation and Organoid Culture for Quantification of REG3γ Secretion

Crypt isolation and organoid culture were performed as previously described (76) with the following modifications. Briefly, the ileum of 10- to 13-week-old mice was cut longitudinally and scraped with a cover slip to remove villi. The intestine was cut transversely into 2- to 4-mm pieces and washed four times with cold PBS. Fragments were then incubated in 2 mmol/L EDTA in PBS for 30 minutes on ice. Following the removal of the EDTA medium, fragments were vigorously resuspended in PBS containing 10% FCS (Gibco) and passed through a 70- m strainer (BD Bioscience). This step was repeated three times. Isolated crypts were pelleted and washed in Advanced DMEM/F12 (ADF; Invitrogen). Crypts were then resuspended in 1 mL of Matrigel growth factor reduced basement membrane matrix (Corning), and 50 L drops were placed into prewarmed 24-well plates. Following Matrigel polymerization, crypts were overlaid with ADF supplemented with 100 U/mL penicillin G sodium, 100 g/mL streptomycin sulfate, 2 mmol/L L-glutamine, 10 mmol/L HEPES, 1× N2 15 supplement, 1× B27 supplement, 50 ng/mL mEGF, 100 ng/mL mNoggin (PeproTech), N-acetylcysteine (Sigma; reagents from Invitrogen unless otherwise indicated), and 10% conditioned medium of R-Spondin-1–transfected HEK 293T cells. Media were changed every two to three days. Cultures were split every 7 to 10 days by first dissolving the Matrigel with cold ADF and mechanically disrupting the organoids using a narrowed Pasteur pipette. Media were supplemented five days after splitting with either adrenaline, noradrenaline, or dopamine (kind gift of the pharmacy of Gustave Roussy Institute) at a concentration of 100 mol/L or with LPS 10 ng/mL (Sigma) + LTA 10 ng/mL (Sigma). After six days of culture, media were removed and organoids were extracted from the Matrigel using organoid harvesting solution (Cultrex, catalog no. 3700-100-01). Organoids were then lysed mechanically with narrowed Pasteur pipette to collect intraluminal content, and organoid lysates were immediately frozen at –80 C. REG3γ was quantified in organoid lysates using a commercial ELISA kit (LSBio, catalog no. LS-F6890-1). Whole protein concentration in organoid lysates was assessed using a micro BCA protein assay kit (Thermo Fisher).

Human Enteroid Manufacturing

Materials. DAPT (catalog no. D5942), dopamine hydrochloride (catalog no. H8502), (±)-epinephrine hydrochloride (catalog no.

E4642), and L-(–)-norepinephrine (+)-bitartrate salt monohydrate (catalog no. A9512) were purchased from Sigma. WNT surrogate was purchased from U-Protein Express.

Methods

Human Ileal Organoid Experiments

Human ileal tissue was obtained with written informed consent of the patients and approval of the ethical committee of the University Medical Center Utrecht. Human ileal organoids were established and cultured as previously described (77, 78), with WNT-conditioned medium replaced by WNT surrogate 0.15 nmol/L. For analysis of *REG3G* and *DEFA5* mRNA expression, organoids were first cultured in expansion conditions for four days after dissociation. Organoids were then differentiated for four days using the niche-inspired intestinal organoid culture medium containing insulin-like growth factor-1 and fibroblast growth factor 2 as described by Fujii et al. (79) with the following changes: removal of Gastrin, replacement of WNT-conditioned medium by WNT surrogate 0.15 nmol/L, and addition of 10 mol/L of the NOTCH signaling inhibitor DAPT. This medium enhanced differentiation toward the secretory lineage. Organoids were subsequently treated with this medium without or with 100 mol/L epinephrine, norepinephrine, or dopamine for 24 hours or three days. RNA was harvested and isolated using the RNEasy Kit (Qiagen) according to the manufacturer's protocol. Reverse transcription was performed using M-MLV Reverse Transcriptase, RNase H Minus, and Point Mutant (Promega) according to the manufacturer's protocol. Quantitative PCR was performed using the IQ Sybr Green Supermix (Bio-Rad) and the CFX384 Touch Real-Time PCR Detection System (Bio-Rad). Gene expression was normalized to expression of the housekeeping gene *GAPDH*. The following qPCR primer sequences were used:

GAPDH; Fw (5′ → 3′); GATTTGGTCGTATTGGGCGC
Rv (5′ → 3′); TTCCCGTTCTCAGCCTTGAC
REG3G; Fw (5′ → 3′); GGTGAGGAGCATTAGTAACAGC
Rv (5′ → 3′); CCAGGGTTTAAGATGGTGGAGG
DEFA5; Fw (5′ → 3′); AGACAACCAGGACCTTGCTAT
Rv (5′ → 3′); GGAGAGGGACTCACGGGTAG

Fixed Organoid Immunostaining

Organoids were collected five to seven days after passaging. Matrigel was removed using cold ADF and mechanically disrupted using a narrowed Pasteur pipette. Disrupted organoids were washed once in cold ADF and resuspended in a medium to Matrigel ratio of 1:1 at a concentration of 2,000 organoids per mL. Organoid suspension (5 L) was plated in 96-well plates (ibidi, catalog no. 89646). After Matrigel polymerization, organoids were cultivated for five days in ADF supplemented with 100 U/mL penicillin G sodium, 100 g/mL streptomycin sulfate, 2 mmol/L L-glutamine, 10 mmol/L HEPES, 1× N2 15 supplement, 1× B27 supplement, 50 ng/mL mEGF, 100 ng/mL mNoggin (PeproTech), N-acetylcysteine (Sigma; reagents from Invitrogen unless otherwise indicated), and 10% conditioned medium of R-Spondin-1–transfected HEK 293T cells. Media were changed every two days. After five days of culture, organoid media were supplemented with either adrenaline, noradrenaline, or dopamine at a concentration of 100 mol/L. After six days of culture, organoids were centrifuged at 3,000 rpm for 10 minutes at 4 C prior to fixation. Organoids were fixed in Matrigel using 4% PFA in PBS at room temperature for one hour. Organoids were permeabilized with 0.5% triton X100 (Sigma) in PBS for one hour and blocked using 0.5% triton X100 in PBS supplemented with 10% FCS for one hour. Organoids were incubated with primary antibody solution containing rabbit anti-mouse Ki-67 antibody (1:200, Abcam, ab16667) and incubated for an additional 24 hours at 4 C with secondary antibody solution containing DyLitgth550 goat anti-rabbit antibody (1:200, Abcam, ab96884) and 0.2 g/mL DAPI (Invitrogen). Images were acquired using an sp8 confocal microscope (Leïca).

Image analysis was performed using ImageJ software.

Statistical Analyses

Mouse Models. Data analyses and representations were performed with either the statistical environment R (http://www.R-project.org/), Microsoft Excel (Microsoft Co.), or Prism 8 (GraphPad). Tumor growth in mouse models was analyzed with dedicated software (80). For comparisons of nonparametric two group parameters, the Mann–Whitney *U* test was used. Kruskal–Wallis for multiple groups was used to test differences between groups. Survival curves were estimated using the Kaplan–Meier product limit method. All tests were two-sided, and *P* values <0.05 were considered statistically significant.

MG Analyses of Human Samples. We conducted a shotgun MG-based analysis of fecal material available in the curatedMetagenomicData package by considering both newly acquired and publicly available data sets (81). More specifically, we collected the stools from patients harboring kidney cancer ($N = 69$; ref. 28), breast cancer ($N = 83$; ref. 82), lung cancer ($N = 368$; ref. 83), prostate cancer ($N = 47$), ovarian cancer ($N = 29$), and chronic myelomonocytic leukemia ($N = 17$). This collection of cancer metagenomes was integrated to 108 melanoma and 705 colon cancer samples from the publicly available database (26) and compared in terms of species-level taxonomic profiles (generated using MetaPhlAn3) with 5,570 healthy individuals coming from multiple publicly available data sets (84). We found discriminative species between cancer and healthy samples by considering LEfSe coupled to a pairwise comparison of relative taxonomic abundances (for species having a prevalence equal to or greater than 5%) using bootstrapping of two-tailed Mann–Whitney *U* tests (with 1,000 permutations and correction for continuity and ties). To limit possible batch effects as much as possible, we kept in the analysis only metagenomes with at least 10M reads. Due to the well-recognized effect of lifestyle on microbiome composition, we considered only samples coming from westernized subjects. Similarly, no ATB use was associated with all publicly available samples.

Data Availability

The data generated or analyzed during this study are included within the article, its Supplementary Information files, and public repositories. Raw metagenomic sequences are available in the Sequence Read Archive (SRA) under the Bioproject accession PRJNA785435 (human) and PRJNA785093 (mice), and raw RNA sequencing is available in the ArrayExpress under accession E-MTAB-11242 (mice; https://www.ebi.ac.uk/arrayexpress/).

Code Availability

No unique software or computational code was created for this study. Codes detailing implementation of established tools/pipelines are described in detail in the Methods section and available upon request to the corresponding author.

Authors' Disclosures

J. Fahrner reports other support from Transgene outside the submitted work. O. Kepp is a cofounder of Samsara Therapeutics. G. Kroemer reports grants from Eleor, Kaleido, Lytix Pharma, PharmaMar, Samsara Therapeutics, Sanofi, Sotio, Vascage, and Vasculox/Tioma and other support from EverImmune outside the submitted work; is on the board of directors for the Bristol Myers Squibb Foundation France; and is a scientific cofounder of EverImmune, Samsara Therapeutics, and Therafast Bio. N. Segata reports grants from Oncobiome during the conduct of the study. H. Clevers reports personal fees from Roche outside the submitted work and is an inventor on a

number of patents on an invention from his lab related to adult stem cell–based organoid technology. His employer (Royal Netherlands Academy of Arts and Sciences) has exclusively licensed these patents to an organization with which H. Clevers has no involvement. L. Zitvogel reports other support from EverImmune, grants from 9 Meters, Kaleido, and Daiichi Sankyo, and grants and personal fees from Transgene during the conduct of the study; grants from GlaxoSmithKline, Bristol Myers Squibb, Roche, and PILEJE outside the submitted work; a patent for EP21305846 pending; and is the president of the scientific advisory board for EverImmune and of the IHU Méditerranée Infections. No disclosures were reported by the other authors.

Authors' Contributions

S. Yonekura: Conceptualization, data curation, software, formal analysis, validation, investigation, writing–original draft, project administration. **S. Terrisse:** Conceptualization, data curation, software, formal analysis, investigation, writing–original draft, project administration. **C. Alves Costa Silva:** Data curation, software, formal analysis, validation, investigation, writing–original draft. **A. Lafarge:** Resources. **V. Iebba:** Software, formal analysis, metho-dology. **G. Ferrere:** Formal analysis, methodology, involved in mouse model experiments. **A. Goubet:** Formal analysis, methodology. **J. Fahrner:** Conceptualization, formal analysis, investigation, involved in mouse model experiments. **I. Lahmar:** Software, formal analysis, methodology. **K. Ueda:** Formal analysis, investigation, involved in mouse model experiments. **G. Mansouri:** Formal analysis, involved in pathology analysis. **E. Pizzato:** Formal analysis, investigation, involved in organoid experiments. **P. Ly:** Formal analysis, investigation, involved in mouse model experiments. **M. Mazzenga:** Formal analysis, investigation, involved in mouse model experiments. **C. Thelemaque:** Formal analysis, involved in mouse model experiments. **M. Fidelle:** Resources. **F. Jaulin:** Investigation. **J. Cartry:** Data curation, investigation. **M. Deloger:** Data curation, formal analysis, methodology. **M. Aglave:** Data curation, software, formal analysis, visualization, involved in bioinformatic analysis. **N. Droin:** Software, formal analysis, supervision, visualization, methodology, involved in RNA sequencing and single-cell analysis. **P. Opolon:** Formal analysis, validation. **A. Puget:** Formal analysis, visualization, involved in pathology analysis. **F. Mann:** Formal analysis, supervision, validation, methodology, involved in pathology analysis. **M. Neunlist:** Formal analysis, supervision, validation, and methodology. **A. Bessard:** Formal analysis, validation, visualization, involved in pathology analysis. **L. Aymeric:** Project administration. **T. Matysiak-Budnik:** Data curation. **J. Bosq:** Formal analysis, supervision, validation, visualization, methodology, involved in pathology analysis. **P. Hofman:** Formal analysis, supervision, validation, visualization, methodology, involved in pathology analysis. **C.P. Duong:** Formal analysis, investigation, and visualization. **S. Ugolini:** Formal analysis, supervision, validation, methodology. **V. Quiniou:** Software, formal analysis, visualization, involved in metagenomic analysis. **S. Berrard:** Validation, writing–review and editing. **B. Ryffel:** Investigation and methodology. **O. Kepp:** Writing–review and editing. **G. Kroemer:** Conceptualization, supervision, writing–original draft, writing–review and editing. **B. Routy:** Formal analysis, investigation, writing–review and editing. **L. Lordello:** Software, formal analysis, validation, visualization, involved in pathology analysis: VAChT, ChAT, Gr1, CD8, CD34/vessels analysis. **M. Bani:** Formal analysis. **N. Segata:** Methodology. **F. Yousef Yengej:** Data curation. **H. Clevers:** Resources. **J. Scoazec:** Methodology. **E. Pasolli:** Data curation, software, formal analysis, visualization, involved in human metagenomic analysis. **L. Derosa:** Conceptualization, resources, supervision, validation, investigation, writing–original draft, project administration. **L. Zitvogel:** Conceptualization, resources, supervision, funding acquisition, validation, writing–original draft, project administration, writing–review and editing.

Acknowledgments

L. Zitvogel and G. Kroemer are supported by the Seerave Foundation, Gustave Roussy Odyssea, the Gustave Roussy Foundation, the European Union Horizon 2020 Project Oncobiome (Project Number: 825410); the RHU LUMIERE: ANR-16-RHUS-0008; the Ligue contre le Cancer (équipe labellisée); Agence Nationale de la Recherche (ANR)—Projets blancs; ANR ILEOBIOME, 19-CE15-0029-01, ANR under the frame of E-Rare-2, the ERA-Net for Research on Rare Diseases; AMMICa US23/CNRS UMS3655; Association pour la Recherche sur le Cancer (ARC); Association "Le Cancer du Sein, Parlons-en!"; Cancéropôle Ile-de-France; Chancelerie des Universités de Paris (Legs Poix), Fondation pour la Recherche Médicale (FRM); a donation by Elior; European Research Area Network on Cardiovascular Diseases (ERA-CVD, MINOTAUR); Fondation Carrefour; High-end Foreign Expert Program in China (GDW20171100085), Institut National du Cancer (INCa); Inserm (HTE); Institut Universitaire de France; LeDucq Foundation; the LabEx Immuno-Oncology (ANR-18-IDEX-0001); the SIRIC Stratified Oncology Cell DNA Repair and Tumor Immune Elimination (SOCRATE); and the SIRIC Cancer Research and Personalized Medicine (CARPEM). This work is supported by the Prism project funded by the Agence Nationale de la Recherche under grant number ANR-18-IBHU-0002. F. Mann is supported by INCa, la Ligue contre le cancer, and Fondation ARC (PAIR PANCREAS 186738). S. Terrisse is financially supported by INSERM-PLAN CANCER. S. Yonekura, B. Routy, and L. Derosa were funded by Gustave Roussy Course of Excellence in Oncology–Fondation Philanthropia. O. Kepp is supported by the DIM ELICIT initiative of the Ile de France.

The costs of publication of this article were defrayed in part by the payment of page charges. This article must therefore be hereby marked *advertisement* in accordance with 18 U.S.C. Section 1734 solely to indicate this fact.

Note

Supplementary data for this article are available at Cancer Discovery Online (http://cancerdiscovery.aacrjournals.org/).

Received July 25, 2021; revised November 8, 2021; accepted December 15, 2021; published first December 20, 2021.

REFERENCES

1. Routy B, Le Chatelier E, Derosa L, Duong CPM, Alou MT, Daillère R, et al. Gut microbiome influences efficacy of PD-1–based immunotherapy against epithelial tumors. Science 2018;359:91–7.
2. Gopalakrishnan V, Spencer CN, Nezi L, Reuben A, Andrews MC, Karpinets TV, et al. Gut microbiome modulates response to anti–PD-1 immunotherapy in melanoma patients. Science 2018;359:97–103.
3. Matson V, Fessler J, Bao R, Chongsuwat T, Zha Y, Alegre M-L, et al. The commensal microbiome is associated with anti–PD-1 efficacy in metastatic melanoma patients. Science 2018;359:104–8.
4. Zitvogel L, Ma Y, Raoult D, Kroemer G, Gajewski TF. The microbiome in cancer immunotherapy: diagnostic tools and therapeutic strategies. Science 2018;359:1366–70.
5. Derosa L, Routy B, Desilets A, Daillère R, Terrisse S, Kroemer G, et al. Microbiota-centered interventions: the next breakthrough in immunooncology? Cancer Discov 2021;11:2396–412.
6. Derosa L, Hellmann MD, Spaziano M, Halpenny D, Fidelle M, Rizvi H, et al. Negative association of antibiotics on clinical activity of immune checkpoint inhibitors in patients with advanced renal cell and non-small-cell lung cancer. Ann Oncol 2018;29:1437–44.
7. Daillère R, Derosa L, Bonvalet M, Segata N, Routy B, Gariboldi M, et al. Trial watch: the gut microbiota as a tool to boost the clinical efficacy of anticancer immunotherapy. OncoImmunology 2020;9:1774298.
8. Hakozaki T, Richard C, Elkrief A, Hosomi Y, Benlaïfaoui M, Mimpen I, et al. The gut microbiome associates with immune checkpoint

inhibition outcomes in patients with advanced non–small cell lung cancer. Cancer Immunol Res 2020;8:1243–50.
9. Singh V, Sadler R, Heindl S, Llovera G, Roth S, Benakis C, et al. The gut microbiome primes a cerebroprotective immune response after stroke. J Cereb Blood Flow Metab 2018;38:1293–8.
10. Stanley D, Mason LJ, Mackin KE, Srikhanta YN, Lyras D, Prakash MD, et al. Translocation and dissemination of commensal bacteria in post-stroke infection. Nat Med 2016;22:1277–84.
11. Mehraj V, Jenabian M-A, Ponte R, Lebouché B, Costiniuk C, Thomas R, et al. The plasma levels of soluble ST2 as a marker of gut mucosal damage in early HIV infection: AIDS 2016;30:1617–27.
12. Koebel CM, Vermi W, Swann JB, Zerafa N, Rodig SJ, Old LJ, et al. Adaptive immunity maintains occult cancer in an equilibrium state. Nature 2007;450:903–7.
13. Haber AL, Biton M, Rogel N, Herbst RH, Shekhar K, Smillie C, et al. A single-cell survey of the small intestinal epithelium. Nature 2017;551:333–9.
14. Abreu MT. Toll-like receptor signalling in the intestinal epithelium: how bacterial recognition shapes intestinal function. Nat Rev Immunol 2010;10:131–44.
15. Söderholm JD, Perdue MH. Stress and intestinal barrier function: II. Stress and intestinal barrier function. Am J Physiol Gastrointest Liver Physiol 2001;280:G7–13.
16. Zheng G, Wu S-P, Hu Y, Smith DE, Wiley JW, Hong S. Corticosterone mediates stress-related increased intestinal permeability in a region-specific manner: corticosterone and colon tight junction protein. Neurogastroenterol Motil 2013;25:e127–39.
17. Furness JB. The enteric nervous system and neurogastroenterology. Nat Rev Gastroenterol Hepatol 2012;9:286–94.
18. Tallini YN, Shui B, Greene KS, Deng K-Y, Doran R, Fisher PJ, et al. BAC transgenic mice express enhanced green fluorescent protein in central and peripheral cholinergic neurons. Physiol Genomics 2006;27:391–7.
19. Han SJ, Kim M, D'Agati VD, Lee HT. Norepinephrine released by intestinal Paneth cells exacerbates ischemic AKI. Am J Physiol Renal Physiol 2020;318:F260–72.
20. Yang S, Koo DJ, Zhou M, Chaudry IH, Wang P. Gut-derived norepinephrine plays a critical role in producing hepatocellular dysfunction during early sepsis. Am J Physiol Gastrointest Liver Physiol 2000;279:G1274–81.
21. Kokolus KM, Zhang Y, Sivik JM, Schmeck C, Zhu J, Repasky EA, et al. Beta blocker use correlates with better overall survival in metastatic melanoma patients and improves the efficacy of immunotherapies in mice. OncoImmunology 2018;7:e1405205.
22. Collins JR. Small intestinal mucosal damage with villous atrophy: a review of the literature. Am J Clin Pathol 1965;44:36–44.
23. Wangel AG, Deller DJ. Malabsorption syndrome associated with carcinoma of the bronchus. Gut 1965;6:73–6.
24. Gilat T, Fischel B, Danon J, Loewenthal M. Morphology of small bowel mucosa in malignancy. Digestion 1972;7:147–55.
25. Bindels LB, Neyrinck AM, Loumaye A, Catry E, Walgrave H, Cherbuy C, et al. Increased gut permeability in cancer cachexia: mechanisms and clinical relevance. Oncotarget 2018;9:18224–38.
26. Thomas AM, Manghi P, Asnicar F, Pasolli E, Armanini F, Zolfo M, et al. Metagenomic analysis of colorectal cancer datasets identifies cross-cohort microbial diagnostic signatures and a link with choline degradation. Nat Med 2019;25:667–78.
27. Segata N, Izard J, Waldron L, Gevers D, Miropolsky L, Garrett WS, et al. Metagenomic biomarker discovery and explanation. Genome Biol 2011;12:R60.
28. Derosa L, Routy B, Fidelle M, Iebba V, Alla L, Pasolli E, et al. Gut bacteria composition drives primary resistance to cancer immunotherapy in renal cell carcinoma patients. Eur Urol 2020;78:195–206.
29. Cardoso-Silva D, Delbue D, Itzlinger A, Moerkens R, Withoff S, Branchi F, et al. Intestinal barrier function in gluten-related disorders. Nutrients 2019;11:2325.
30. Moriyama S, Brestoff JR, Flamar A-L, Moeller JB, Klose CSN, Rankin LC, et al. β_2-adrenergic receptor–mediated negative regulation of group 2 innate lymphoid cell responses. Science 2018;359:1056–61.
31. Enaud R, Hooks KB, Barre A, Barnetche T, Hubert C, Massot M, et al. Intestinal inflammation in children with cystic fibrosis is associated with Crohn's-like microbiota disturbances. J Clin Med 2019;8:645.
32. Bindels LB, Neyrinck AM, Claus SP, Le Roy CI, Grangette C, Pot B, et al. Synbiotic approach restores intestinal homeostasis and prolongs survival in leukaemic mice with cachexia. ISME J 2016;10:1456–70.
33. Bindels LB, Neyrinck AM, Salazar N, Taminiau B, Druart C, Muccioli GG, et al. Non digestible oligosaccharides modulate the gut microbiota to control the development of leukemia and associated cachexia in mice. PLoS One 2015;10:e0131009.
34. Bohórquez DV, Shahid RA, Erdmann A, Kreger AM, Wang Y, Calakos N, et al. Neuroepithelial circuit formed by innervation of sensory enteroendocrine cells. J Clin Invest 2015;125:782–6.
35. Pavlov VA, Wang H, Czura CJ, Friedman SG, Tracey KJ. The cholinergic anti-inflammatory pathway: a missing link in neuroimmunomodulation. Mol Med Camb Mass 2003;9:125–34.
36. Bansal V, Costantini T, Ryu SY, Peterson C, Loomis W, Putnam J, et al. Stimulating the central nervous system to prevent intestinal dysfunction after traumatic brain injury: J Trauma Inj Infect Crit Care 2010;68:1059–64.
37. Singh V, Roth S, Llovera G, Sadler R, Garzetti D, Stecher B, et al. Microbiota dysbiosis controls the neuroinflammatory response after stroke. J Neurosci 2016;36:7428–40.
38. Wong CHY, Jenne CN, Lee W-Y, Leger C, Kubes P. Functional innervation of hepatic iNKT cells is immunosuppressive following stroke. Science 2011;334:101–5.
39. Roth S, Singh V, Tiedt S, Schindler L, Huber G, Geerlof A, et al. Brain-released alarmins and stress response synergize in accelerating atherosclerosis progression after stroke. Sci Transl Med 2018;10:eaao1313.
40. Staedtke V, Bai R-Y, Kim K, Darvas M, Davila ML, Riggins GJ, et al. Disruption of a self-amplifying catecholamine loop reduces cytokine release syndrome. Nature 2018;564:273–7.
41. Tutton PJ, Helme RD. Stress induced inhibition of jejunal crypt cell proliferation. Virchows Arch B Cell Pathol 1973;15:23–34.
42. Tutton PJM, Barkla DH. Effect of an inhibitor of noradrenaline uptake, desipramine, on cell proliferation in the intestinal crypt epithelium. Virchows Arch B Cell Pathol Incl Mol Pathol 1989;57:349–52.
43. De Schepper S, Verheijden S, Aguilera-Lizarraga J, Viola MF, Boesmans W, Stakenborg N, et al. Self-maintaining gut macrophages are essential for intestinal homeostasis. Cell 2018;175:400–15.
44. Muller PA, Koscsó B, Rajani GM, Stevanovic K, Berres M-L, Hashimoto D, et al. Crosstalk between muscularis macrophages and enteric neurons regulates gastrointestinal motility. Cell 2014;158:300–13.
45. Gabanyi I, Muller PA, Feighery L, Oliveira TY, Costa-Pinto FA, Mucida D. Neuro-immune interactions drive tissue programming in intestinal macrophages. Cell 2016;164:378–91.
46. Matheis F, Muller PA, Graves CL, Gabanyi I, Kerner ZJ, Costa-Borges D, et al. Adrenergic signaling in muscularis macrophages limits infection-induced neuronal loss. Cell 2020;180:64–78.
47. Muller PA, Schneeberger M, Matheis F, Wang P, Kerner Z, Ilanges A, et al. Microbiota modulate sympathetic neurons via a gut–brain circuit. Nature 2020;583:441–6.
48. Prüss H, Tedeschi A, Thiriot A, Lynch L, Loughhead SM, Stutte S, et al. Spinal cord injury-induced immunodeficiency is mediated by a sympathetic-neuroendocrine adrenal reflex. Nat Neurosci 2017;20:1549–59.
49. Obata Y, Castaño Á, Boeing S, Bon-Frauches AC, Fung C, Fallesen T, et al. Neuronal programming by microbiota regulates intestinal physiology. Nature 2020;578:284–9.
50. Kaelberer MM, Buchanan KL, Klein ME, Barth BB, Montoya MM, Shen X, et al. A gut-brain neural circuit for nutrient sensory transduction. Science 2018;361:eaat5236.
51. Chiu IM, Heesters BA, Ghasemlou N, Von Hehn CA, Zhao F, Tran J, et al. Bacteria activate sensory neurons that modulate pain and inflammation. Nature 2013;501:52–7.
52. Amit M, Takahashi H, Dragomir MP, Lindemann A, Gleber-Netto FO, Pickering CR, et al. Loss of p53 drives neuron reprogramming in head and neck cancer. Nature 2020;578:449–54.
53. Magnon C, Hall SJ, Lin J, Xue X, Gerber L, Freedland SJ, et al. Autonomic nerve development contributes to prostate cancer progression. Science 2013;341:1236361.
54. Hamy A-S, Derosa L, Valdelièvre C, Yonekura S, Opolon P, Priour M, et al. Comedications influence immune infiltration and pathological

response to neoadjuvant chemotherapy in breast cancer. OncoImmunology 2020;9:1677427.
55. Bankhead P, Loughrey MB, Fernández JA, Dombrowski Y, McArt DG, Dunne PD, et al. QuPath: open source software for digital pathology image analysis. Sci Rep 2017;7:16878.
56. Wingett SW, Andrews S. FastQ screen: a tool for multi-genome mapping and quality control. F1000Research 2018;7:1338.
57. Bray NL, Pimentel H, Melsted P, Pachter L. Near-optimal probabilistic RNA-seq quantification. Nat Biotechnol 2016;34:525–7.
58. Melsted P, Booeshaghi AS, Gao F, Beltrame E, Lu L, Hjorleifsson KE, et al. Modular and efficient pre-processing of single-cell RNA-seq. BioRxiv 673285 [Preprint]. 2019. Available from: https://doi.org/10.1101/673285.
59. Melsted P, Ntranos V, Pachter L. The barcode, UMI, set format and BUStools. Bioinformatics 2019;35:4472–3.
60. Lun ATL, Riesenfeld S, Andrews T, Dao TP, Gomes T, participants in the 1st Human Cell Atlas Jamboree, et al. EmptyDrops: distinguishing cells from empty droplets in droplet-based single-cell RNA sequencing data. Genome Biol 2019;20:63.
61. Griffiths JA, Richard AC, Bach K, Lun ATL, Marioni JC. Detection and removal of barcode swapping in single-cell RNA-seq data. Nat Commun 2018;9:2667.
62. Bais AS, Kostka D. scds: computational annotation of doublets in single-cell RNA sequencing data. Bioinformatics 2020;36:1150–8.
63. Hafemeister C, Satija R. Normalization and variance stabilization of single-cell RNA-seq data using regularized negative binomial regression. Genome Biol 2019;20:296.
64. Zappia L, Oshlack A. Clustering trees: a visualization for evaluating clusterings at multiple resolutions. GigaScience 2018;7:giy083.
65. Xu H, Ding J, Porter CBM, Wallrapp A, Tabaka M, Ma S, et al. Transcriptional atlas of intestinal immune cells reveals that neuropeptide α-CGRP modulates group 2 innate lymphoid cell responses. Immunity 2019;51:696–708.
66. Dridi B, Henry M, El Khéchine A, Raoult D, Drancourt M. High prevalence of methanobrevibacter smithii and methanosphaera stadtmanae detected in the human gut using an improved DNA detection protocol. PLoS One 2009;4:e7063.
67. Angelakis E, Bachar D, Henrissat B, Armougom F, Audoly G, Lagier J-C, et al. Glycans affect DNA extraction and induce substantial differences in gut metagenomic studies. Sci Rep 2016;6:26276.
68. Million M, Tidjani Alou M, Khelaifia S, Bachar D, Lagier J-C, Dione N, et al. Increased gut redox and depletion of anaerobic and methanogenic prokaryotes in severe acute malnutrition. Sci Rep 2016;6:26051.
69. Callahan BJ, McMurdie PJ, Rosen MJ, Han AW, Johnson AJA, Holmes SP. DADA2: high-resolution sample inference from Illumina amplicon data. Nat Methods 2016;13:581–3.
70. Weinstein MM, Prem A, Jin M, Tang S, Bhasin JM. FIGARO: An efficient and objective tool for optimizing microbiome rRNA gene trimming parameters [Internet]. Bioinformatics; 2019. Available from: http://biorxiv.org/lookup/doi/10.1101/610394.
71. McDonald D, Price MN, Goodrich J, Nawrocki EP, DeSantis TZ, Probst A, et al. An improved Greengenes taxonomy with explicit ranks for ecological and evolutionary analyses of bacteria and archaea. ISME J 2012;6:610–8.
72. McMurdie PJ, Holmes S. phyloseq: an R package for reproducible interactive analysis and graphics of microbiome census data. PLoS One 2013;8:e61217.
73. Lozupone CA, Hamady M, Kelley ST, Knight R. Quantitative and qualitative β diversity measures lead to different insights into factors that structure microbial communities. Appl Environ Microbiol 2007;73:1576–85.
74. McArdle BH, Anderson MJ. Fitting multivariate models to community data: a comment on distance-based redundancy analysis. Ecology 2001;82:290–7.
75. Love MI, Huber W, Anders S. Moderated estimation of fold change and dispersion for RNA-seq data with DESeq2. Genome Biol 2014;15:550.
76. Sato T, Vries RG, Snippert HJ, van de Wetering M, Barker N, Stange DE, et al. Single Lgr5 stem cells build crypt-villus structures in vitro without a mesenchymal niche. Nature 2009;459:262–5.
77. Sato T, Stange DE, Ferrante M, Vries RGJ, Van Es JH, Van den Brink S, et al. Long-term expansion of epithelial organoids from human colon, adenoma, adenocarcinoma, and Barrett's epithelium. Gastroenterology 2011;141:1762–72.
78. Beumer J, Artegiani B, Post Y, Reimann F, Gribble F, Nguyen TN, et al. Enteroendocrine cells switch hormone expression along the crypt-to-villus BMP signalling gradient. Nat Cell Biol 2018;20:909–16.
79. Fujii M, Matano M, Toshimitsu K, Takano A, Mikami Y, Nishikori S, et al. Human intestinal organoids maintain self-renewal capacity and cellular diversity in niche-inspired culture condition. Cell Stem Cell 2018;23:787–93.
80. Enot DP, Vacchelli E, Jacquelot N, Zitvogel L, Kroemer G. TumGrowth: an open-access web tool for the statistical analysis of tumor growth curves. Oncoimmunology 2018;7:e1462431.
81. Pasolli E, Schiffer L, Manghi P, Renson A, Obenchain V, Truong DT, et al. Accessible, curated metagenomic data through ExperimentHub. Nat Methods 2017;14:1023–4.
82. Terrisse S, Derosa L, Iebba V, Ghiringhelli F, Vaz-Luis I, Kroemer G, et al. Intestinal microbiota influences clinical outcome and side effects of early breast cancer treatment. Cell Death Differ 2021;28:2778–96.
83. Derosa L, Routy B, Thomas AM, Iebba V, Zalcman G, Friard S, et al. Intestinal Akkermansia muciniphila predicts clinical response to PD-1 blockade in patients with advanced non-small-cell lung cancer. Nat Med 2022;28:315–24.
84. Beghini F, McIver LJ, Blanco-Míguez A, Dubois L, Asnicar F, Maharjan S, et al. Integrating taxonomic, functional, and strain-level profiling of diverse microbial communities with bioBakery 3. Elife 2021;10:e65088.

8.1.3 Article II

Title: Intestinal *Akkermansia muciniphila* predicts clinical response to PD-1 blockade in patients with advanced non-small-cell lung cancer

Published on: Nature Medicine 2022 Feb;28(2):315-324.
DOI: 10.1038/s41591-021-01655-5

Lisa Derosa #, Bertrand Routy #, Andrew Maltez Thomas #, Valerio Iebba, Gerard Zalcman, Sylvie Friard, Julien Mazieres, Clarisse Audigier-Valette, Denis Moro-Sibilot, François Goldwasser, **Carolina Alves Costa Silva**, Safae Terrisse, Melodie Bonvalet, Arnaud Scherpereel, Hervé Pegliasco, Corentin Richard, François Ghiringhelli, Arielle Elkrief, Antoine Desilets, Felix Blanc-Durand, Fabio Cumbo, Aitor Blanco, Romain Boidot, Sandy Chevrier, Romain Daillère, Guido Kroemer, Laurie Alla, Nicolas Pons, Emmanuelle Le Chatelier, Nathalie Galleron, Hugo Roume, Agathe Dubuisson, Nicole Bouchard, Meriem Messaoudene, Damien Drubay, Eric Deutsch, Fabrice Barlesi, David Planchard, Nicola Segata, Stéphanie Martinez, Laurence Zitvogel, Jean-Charles Soria, Benjamin Besse
# contributed equally

Based on previous retrospective studies, we performed MGS taxonomic profiling in a prospective cohort of patients with advanced NSCLC to validate the predictive value of *Akkermansia muciniphila* (*Akk*) to ICB treatment (see Appendix, Article VI). Our cohort was composed of 338 patients with advanced NSCLC treated with ICB in first line or further. We showed that patients harboring *Akk* at baseline had a richer gut microbiota composition and experienced greater benefit to ICB: increased objective response rates and OS. Intriguinly, we observed that patients harboring higher levels of *Akk* relative abundance (above 77th percentile 4.8%, *Akk* ^{high}) were associated with reduced survival (OS inferior to 12 months) (Fig. 12A). Interestingly, *Akk* ^{high} coincided with ABX intake and the presence of tolerogenic *Enterocloster* genus. Overall, the prevalence of *Akk* was about 40%. Upon trichotomic stratification, 9% of the patients were considered *Akk* ^{high} and most of them were negative (*Akk* $^{-}$) (Fig. 12B, left). Patients into *Akk*^{low} group experienced improved survival when compared to

Akk $^{-}$ and *Akk* ^{high} (Fig. 12B, right). The OS benefit sustained after adjustment to other prognostic factors such as PD-L1 expression, antibiotics, and performance status in multivariate analyses (Fig. 12C).

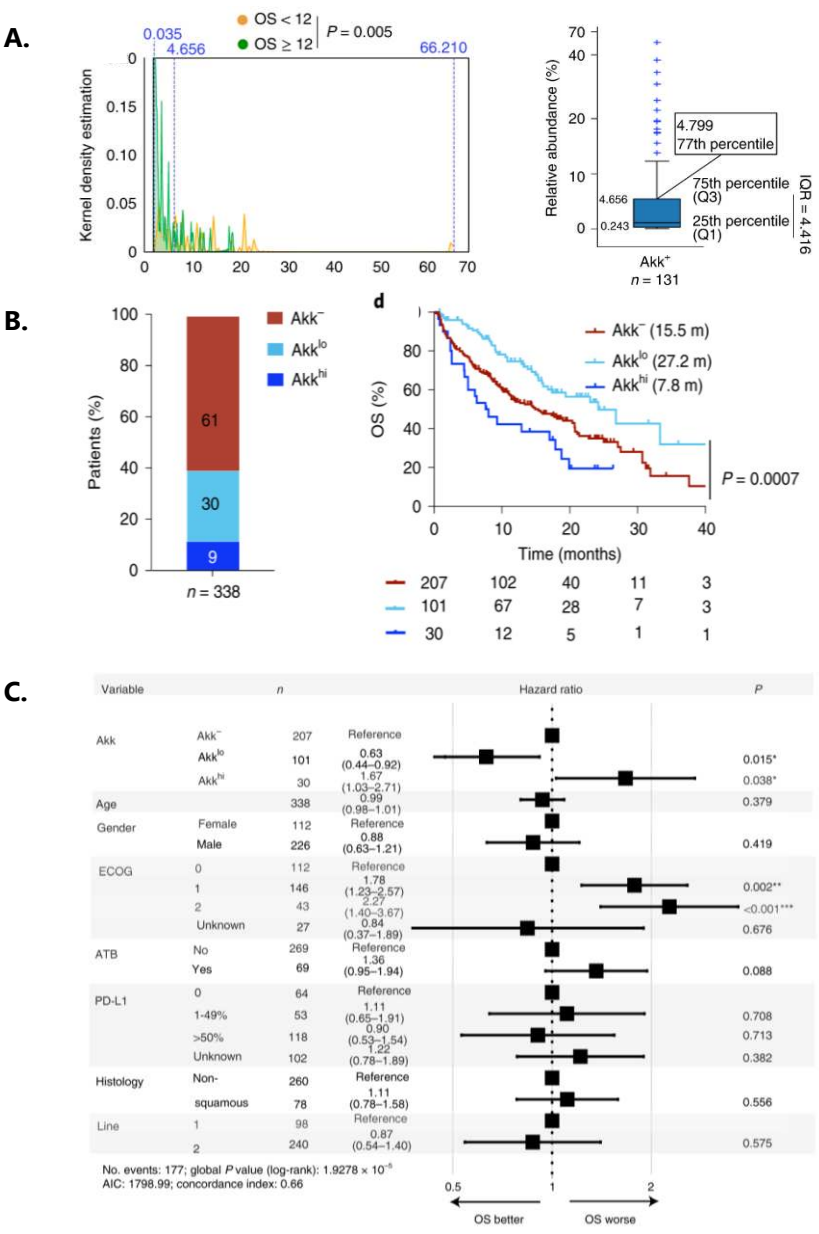

Figure 12 Akkermansia muciniphila (*Akk*) as a potential biomarker. **A.** Kernel density estimation aligning overall survival (OS) and relative abundance of Akk (left) and its distribution according to 77th percentile (right). B. Distribution of patients to Akk trichotomic stratification (left) and kaplan-Meier curve of OS (right). **C.** Cox logistic regression multivariate analysis of OS according to Akk trichotomic stratification (Akk $^{-}$, Akk ^{low} and Akk ^{high}).

nature medicine

ARTICLES

https://doi.org/10.1038/s41591-021-01655-5

Intestinal *Akkermansia muciniphila* predicts clinical response to PD-1 blockade in patients with advanced non-small-cell lung cancer

Lisa Derosa[1,2,3,4,35], Bertrand Routy[5,6,35], Andrew Maltez Thomas[7,8,35], Valerio Iebba[9], Gerard Zalcman[10], Sylvie Friard[11], Julien Mazieres[12], Clarisse Audigier-Valette[13], Denis Moro-Sibilot[14], François Goldwasser[15,16,17], Carolina Alves Costa Silva[1,2], Safae Terrisse[1], Melodie Bonvalet[1], Arnaud Scherpereel[18], Hervé Pegliasco[19], Corentin Richard[5,6], François Ghiringhelli[20,21,22], Arielle Elkrief[5,6], Antoine Desilets[5,6], Felix Blanc-Durand[1], Fabio Cumbo[7], Aitor Blanco[7], Romain Boidot[23], Sandy Chevrier[23], Romain Daillère[24], Guido Kroemer[1,15,25,26,27], Laurie Alla[28], Nicolas Pons[28], Emmanuelle Le Chatelier[28], Nathalie Galleron[28], Hugo Roume[28], Agathe Dubuisson[1], Nicole Bouchard[29], Meriem Messaoudene[5,6], Damien Drubay[30], Eric Deutsch[1,4,31,32], Fabrice Barlesi[1,2], David Planchard[1,2], Nicola Segata[7,8], Stéphanie Martinez[33], Laurence Zitvogel[1,3,4,34] ✉, Jean-Charles Soria[1] and Benjamin Besse[1,2,4]

Aside from PD-L1 expression, biomarkers of response to immune checkpoint inhibitors (ICIs) in non-small-cell lung cancer (NSCLC) are needed. In a previous retrospective analysis, we documented that fecal *Akkermansia muciniphila* (Akk) was associated with clinical benefit of ICI in patients with NSCLC or kidney cancer. In the current study, we performed shotgun-metagenomics-based microbiome profiling in a large cohort of patients with advanced NSCLC ($n = 338$) treated with first- or second-line ICIs to prospectively validate the predictive value of fecal Akk. Baseline stool Akk was associated with increased objective response rates and overall survival in multivariate analyses, independent of PD-L1 expression, antibiotics, and performance status. Intestinal Akk was accompanied by a richer commensalism, including *Eubacterium hallii* and *Bifidobacterium adolescentis*, and a more inflamed tumor microenvironment in a subset of patients. However, antibiotic use (20% of cases) coincided with a relative dominance of Akk above 4.8% accompanied with the genus *Clostridium*, both associated with resistance to ICI. Our study shows significant differences in relative abundance of Akk that may represent potential biomarkers to refine patient stratification in future studies.

The development of ICIs targeting the PD-1–PD-L1 interaction has transformed the therapeutic landscape of patients with advanced NSCLC[1–6]. Landmark trials performed on previously treated patients with advanced NSCLC demonstrated superior overall survival (OS) following PD-1–PD-L1 blockade treatment compared with standard chemotherapy[1–3]. Following randomized phase III trials on patients with previously untreated advanced NSCLC, ICIs were approved in the first-line setting, either as monotherapy for patients with tumor PD-L1 expression $\geq$ 50% on tumor cells or in combination with platinum-doublet chemotherapy irrespectively of PD-L1 expression[4–6]. However, only a minority (35%) of patients benefit from sustained response to ICI[7]. Most patients with NSCLC develop primary or secondary resistance or occasional rapid acceleration of the disease, called hyper-progression[8]. Therefore, an understanding of mechanisms of resistance to ICI to identify novel and robust biomarkers of resistance is urgently needed.

Primary resistance has been attributed to low tumor mutational burden and poor intrinsic antigenicity of tumor cells[9,10], defective antigen presentation[11], limited intratumoral lymphocyte infiltration related to T cell exhaustion[12], and metabolic immunosuppressive pathways[13,14]. High-dimensional omics technologies are currently being developed to decipher the main regulators of the "cancer immune set-point"—the threshold beyond which an effective immune response can occur in the tumor bearer[15].

Recent lines of evidence point to the biological significance of the composition of the gut microbiota in influencing peripheral immune tonus and effectiveness of ICIs in patients with cancer[16]. The human gut microbiome, composed of 1×10^{13} micro-organisms, modulates many host processes, including metabolism, inflammation, peristalsis, elimination of pathogens and xenobiotics, maturation of immune functions to maintain tolerance to microbial and food antigens, and maintenance of intestinal epithelial barrier fitness. More recently, the gut microbiome has unexpectedly been shown to influence the effectiveness of ICIs[17]. First, in preclinical models, experiments with germ-free or antibiotic (ATB)-treated mice revealed that the antitumor activity of ICIs requires the presence of gut microbial components[18]. Similarly, ATB treatment prior to ICI initiation drastically reduced the clinical benefit in several cohorts of patients across various cancer types (melanoma,

A full list of affiliations appears at the end of the paper.

advanced NSCLC, renal cell carcinoma (RCC), and urothelial cancer)[17,19–21]. This observation was confirmed in prospective trials and large meta-analyses, suggesting that gut microbiota may be instrumental for the immunostimulatory mode of action of ICIs[16].

Supporting this contention, we and others reported that primary responses to anti-PD-1–PD-L1 antibodies in patients with epithelial tumors and melanoma could, at least in part, be attributed to the taxonomic composition of the gut microbial ecosystem[17,19,22]. A diverse microbiota and the presence of specific bacteria, such as Akk or the *Ruminococcus* or *Bifidobacterium* genera, were associated with improved clinical response to ICI, correlating with increased systemic immune tonus[17,19,22]. We previously reported the stool metagenomic profiling of 100 patients diagnosed with refractory NSCLC or RCC who were receiving second- or third-line anti-PD-1 antibodies, and we concluded that the prevalence of Akk was increased in patients presenting partial response or stable disease, compared to patients in progressive disease (61% versus 34%, respectively, $P = 0.007$)[17]. Akk was also over-represented in patients with progression-free survival (PFS) > 3 months in an analysis of a subgroup of 60 patients with NSCLC[17]. Another group performed 16S ribosomal RNA (rRNA) gene amplicon sequencing of feces from 37 patients with NSCLC patient, confirming that Akk was enriched in patients who responded to ICI treatment[23]. In patients treated with abiraterone acetate, an inhibitor of androgen biosynthesis approved to treat metastatic castration-resistant prostate cancer, intestinal Akk also correlated with therapeutic responses[24]. Intestinal prevalence of Akk has also been associated with low body mass index (BMI), fitness, and successful aging (as indicated by its presence in disease-free centenarians)[25]. In animal models, Akk supplementation reduces obesity[26] and its co-morbidities, palliates neurodegenerative disorders[27], and counteracts progeria[28]. However, there are some epidemiological associations between this bacterium and inflammation-related pathologies (such as Parkinson disease[29], colitis during graft-versus-host disease[30], or diet-induced susceptibility to pathogenic *Citrobacter rodentium*[31]). Despite these reports, Akk may be viewed as a potential master regulator of homeostasis in the metaorganism.

Altogether, our earlier results obtained in small cohorts overlooking confounding factors allow us to surmise that the gut microbiome composition, and more specifically the presence of Akk at diagnosis, could become a biomarker predicting objective responses and 12-month survival rates in advanced NSCLC treated with first- and second-line ICIs. To validate this hypothesis, we performed a prospective multicentric study and analyzed baseline microbiome profiles using two metagenomic taxonomic pipelines in 338 patients with advanced NSCLC to predict the clinical benefit to anti-PD-1 antibodies in multivariate analyses.

Results

Association between *A. muciniphila* and clinical outcome. From December 2015 to November 2019, a total of 493 patients were screened for enrollment in this study, and 338 met inclusion criteria. Participants provided at least one baseline (V1 and/or V2) fecal sample for profiling (Extended Data Fig. 1). Using shotgun metagenomic sequencing, we determined that Akk was detectable in 131 (39%) and absent in 207 (61%) patients, and we used MetaPhlAn profiling expanded to identify the main Akk species-level genome bin (SGB9226 spp.[32], Supplementary Table 1). Baseline characteristics were well balanced between patients with detectable Akk (Akk^+) and undetectable Akk (Akk^-) with respect to sex, Eastern Cooperative Oncology Group (ECOG) performance status, smoking history, tumor histology, BMI, PD-L1 expression, and line of therapy (Supplementary Table 2a). However, there was a non-statistically-significant trend for older age in the Akk^+ group (66 years versus 64 years, $P = 0.08$). A total of 69 patients (20%) received ATBs 60 days prior to ICI initiation, with similar frequencies ($P = 0.68$) and regimen in Akk^+ and Akk^- groups (Supplementary Table 2a). Among ATB classes, beta-lactams were the most commonly prescribed in both groups (Supplementary Table 2b, 80% in Akk^+ versus 64% in Akk^-, $P = 0.33$).

For the Akk^+ and Akk^- groups in our cohort, objective response rates (ORRs) were 28% and 18%, respectively (Fig. 1a, $P = 0.04$). Partial response (PR), stable disease (SD), and progressive disease (PD) rates were 28%, 28%, and 44%, respectively, for the Akk^+ group versus 18%, 31%, and 50% for the Akk^- group. When considering the subgroup of patients who received immunotherapy alone as front-line treatment (1L IO, $n = 86$), ORRs were 41% and 19% in the Akk^+ and Akk^- groups, respectively (Fig. 1b, $P = 0.016$). Of note, for the whole cohort of patients (irrespective of the line of treatment), the median OS (mOS) was 18.8 months for the Akk^+ group, compared with 15.4 months in the Akk^- group (hazard ratio (HR) = 0.72; 95% confidence interval (CI) = 0.73–1.62; $P = 0.03$, Fig. 1c and Supplementary Table 2a). The median OS of patients who received immunotherapy as second-line treatment and beyond (≥2L) was 18.8 months in the Akk^+ group compared with 13.4 months in the Akk^- group (HR = 0.70; 95% CI = 0.50–0.98; $P = 0.04$, Fig. 1d and Supplementary Table 2a). For the 1L IO patients, 59% of Akk^+ patients were still alive after 12 months (OS ≥ 12), while only 35% of Akk^- individuals were long-term survivors (Fig. 1e, $P = 0.04$). We draw the same conclusions when using the MetaOMineR pipeline[33] (Extended Data Fig. 2a,b, left).

To establish cause–effect relationships between the presence of Akk (and its ecosystem) and response to ICIs, we retrospectively performed a preclinical meta-analysis by gathering 29 experiments

Fig. 1 | Stool Akk is associated with ICI clinical benefit. a,**b**, Correlations between stool Akk and ORR in 1L + 2L ($n = 338$) (**a**) and 1L ($n = 86$) (**b**) patients. CR; complete response. PR; partial response. SD; stable disease. PD; progressive disease. Data were analyzed using Chi-square test. *P* values are two-sided, with no adjustments made for multiple comparisons. **c**,**d**, Kaplan–Meier curves and Cox regression analyses of OS of 1L + 2L ($n = 338$) (**c**) and 2L ($n = 243$) (**d**) patients, according to Akk status. Akk status was compared using the stratified log-rank test. *P* values are one-sided with no adjustment. m; months **e**, Difference of the intestinal prevalence of Akk between patients with OS < 12 months *v* versus OS ≥ 12 months in 1L immunotherapy (IO), analyzed using Chi-square test. *P* values are two-sided, with no adjustments made for multiple comparisons. **f**–**h**, RNA sequencing of tumor biopsies in a subgroup of 44 patients (17 non-metastatic and 27 metastatic, Supplementary Table 4). **f**, Principal component analysis (PCoA) of the differentially expressed genes according to intestinal prevalence of Akk, using the 395 immune-related gene selection of the Oncomine Immune Response Research Assay, indicating significant differences using a Mann–Whitney $P < 0.10$ through PERMANOVA test with Euclidian distance. **g**, Heatmap of the differentially expressed gene products after normalization (between Akk^+ and Akk^- patients), classified by category. **h**, Boxplot of selected gene expression values according to Akk groups: Akk^+ ($n = 22$) and Akk^- (n = 22) patients (Supplementary Table 4). Differences between groups were assessed with Mann–Whitney tests. C-X-C motif chemokine ligand 10 (CXCL10), C-X-C motif chemokine ligand 9 (CXCL9), guanylate binding protein 1 (GBP1), vascular cell adhesion protein 1 (VCAM1), C-C chemokine receptor type 5 (CCR5), granzyme H (GZMH). The middle line of the box represents the median. The lower and upper hinges correspond to the first and third quartiles (the 25th and 75th percentiles). The upper whisker extends from the hinge to the largest value no further than 1.5 × IQR from the hinge (where IQR is the interquartile range, or distance between the first and third quartiles). The lower whisker extends from the hinge to the smallest value at most 1.5 × IQR of the hinge. Data beyond the end of the whiskers are called "outlying" points and are plotted individually.

in which tumor growth kinetics were followed up in avatar mouse models[34]. These recipients were treated with ATBs and then received fecal microbial transplants (FMTs) from 26 patients with NSCLC (Supplementary Table 3). Next, mice were implanted with syngeneic orthotopic MCA-205 sarcomas (representative tumor model for sensitivity to anti-PD-1 antibodies, as previously described[17,35]) and were later subjected to PD-1 blockade (Extended Data Fig. 2c–e). As observed in our clinical cohort, resistance to therapy in mice was associated with the absence of detectable Akk in the FMT experiments (Extended Data Fig. 2c,d).

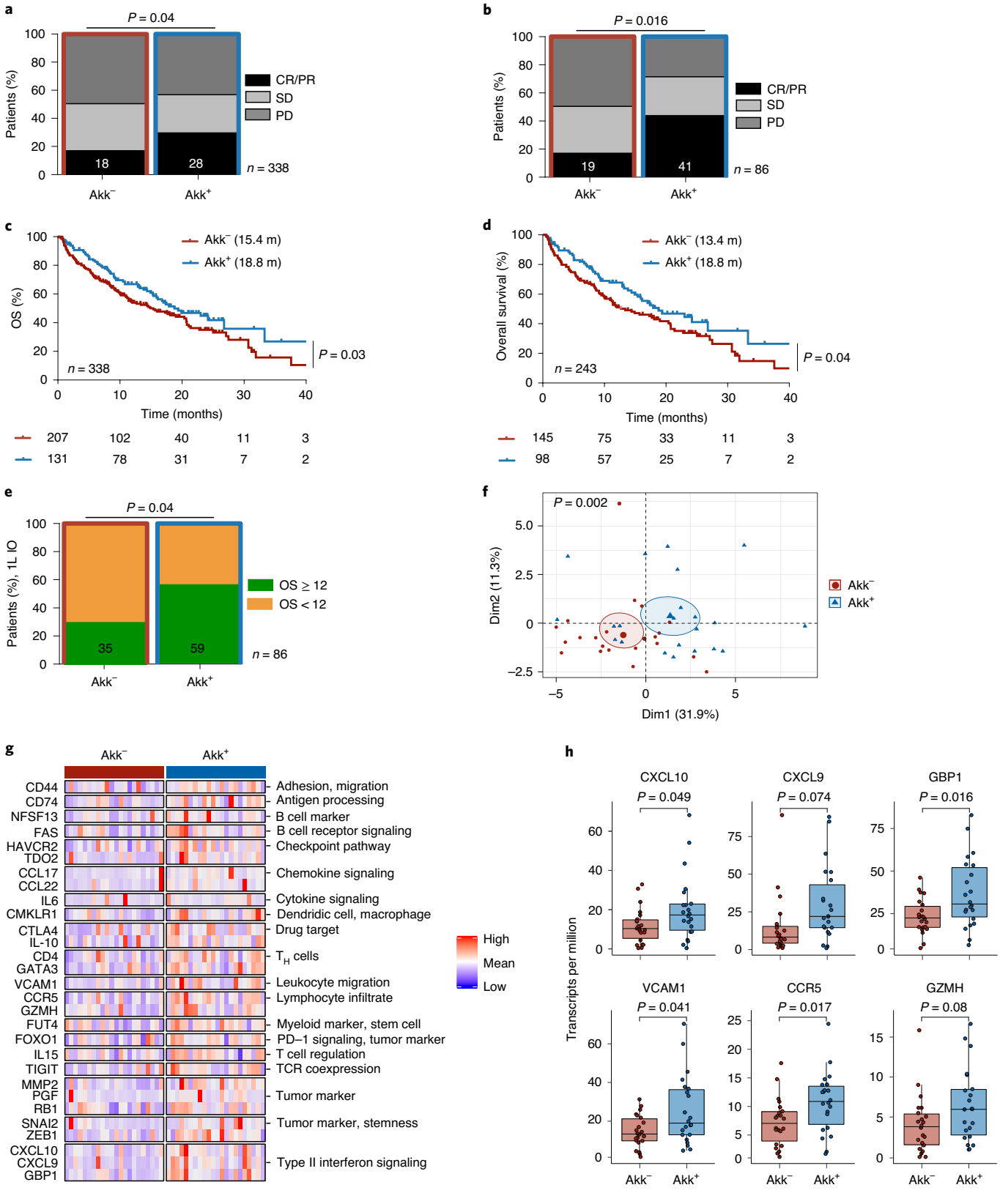

Therefore, in this second independent and prospective study on 338 patients with advanced NSCLC, we validated in humans using two different metagenomics pipelines, as well as in mice, that the presence of Akk is associated with higher ORR and longer OS in patients with NSCLC receiving ICIs.

***A. muciniphila*, the intestinal ecosystem, and the tumor microenvironment.** Given known correlations between compositional differences in the gut microbiota and tumor immune landscape[17,19] that can vary across histological types[36], we addressed the interactions between stool Akk detection and tumor histology (squamous versus non-squamous NSCLC). The presence of Akk in stools at diagnosis had no influence on histology (non-squamous versus squamous NSCLC; for multivariate analysis, $P = 0.556$ in Supplementary Table 2a).

In order to uncover intratumoral transcriptomic differences driven by Akk, we performed tumor RNA sequencing in a subset of patients with available tumor biopsies, which were collected from Akk$^+$ ($n = 22$) and Akk$^-$ ($n = 22$) patients upon diagnosis of locally advanced or metastatic NSCLC (Supplementary Table 4). The supervised analysis of significant gene expression differences between Akk$^+$ and Akk$^-$ groups within a panel of 395 immune-related genes of the Oncomine Immune Response Research Assay[37] revealed a set of differentially expressed genes associated with response to PD-1 blockade in lung cancer (Fig. 1f), such as CD4$^+$ T helper cells (T_H cells) with activation (*CD4*, *CD74*, *Vcam-1*, associated with adhesion and *trans*-migration of T lymphocytes within tumor nests[38]; granzyme H serine protease *Gzmh*, associated with cytolytic activity) and exhaustion (*Ctla4*, *Fas*, *Tigit*, *Havcr2*) markers and the IFN fingerprint (*Ccr5*, *Cxcl9*, *Cxcl10*, *Tdo2*, and IFN-inducible guanylate binding protein 1) (Fig. 1g,h). These results support the possibility that Akk could promote the elicitation or recirculation of T_H1 cells into the tumor microenvironment, as has previously been shown in mouse models[17,18].

Next, we examined compositional taxonomic differences in the gut microbiota in Akk$^+$ and Akk$^-$ patients. We found a significant increase of the Shannon diversity index (Extended Data Fig. 3a, top, $P < 0.0001$) in Akk$^+$ compared with Akk$^-$ patients, as well as differences in the overall microbial community composition (Extended Data Fig. 3a, bottom, $P = 0.0001$). Using LEfSe (linear discriminant analysis effect size) analyses to investigate differences in species relative abundance between the two groups, we found Ruminococcaceae (*Ruminococcus bromii*, *Ruminococcus bicirculans*, *Ruminococcus lactaris*) and Lachnospiraceae (*Eubacterium siraeum*, *Eubacterium eligens*) family members and *Alistipes* spp. (*Alistipes inops*, *Alistipes finegoldii*, *Alistipes indistinctus*, *Alistipes shahii*) to be enriched in Akk$^+$ stools, as has previously been reported[39], whereas *Veillonella parvula*, *Actinomyces* spp., and genus *Clostridium* (*Clostridium innocuum, Hungatella hathewayi*) were overabundant in feces from Akk$^-$ patients (Extended Data Fig. 3b), as has already been described in the lower airway microbiome of patients with NSCLC with poor prognosis[40] as well as patients with kidney cancer resistant to ICIs[35].

Furthermore, within the Akk$^+$ group, we found significant differences in the overall microbial composition between patients with OS $\geq$ 12 months versus OS $<$ 12 months, but this difference was not observed in Akk$^-$ patients (Fig. 2a, $P = 0.009$ versus $P = 0.07$). LEfSe analysis within the participants in the Akk$^+$ group with OS $\geq$ 12 months versus those with OS $<$ 12 months unveiled an increased relative abundance of Lachnospiraceae family members (*Dorea formicigenerans*, *Dorea longicatena*, *Eubacterium rectale*, *Eubacterium hallii*, *Roseburia intestinalis*, *Coprococcus comes*) in patients with OS $\geq$ 12 months. Conversely, species belonging to the Gammaproteobacteria (*Escherichia coli*), the Clostridia class (*R. lactatiformans*), or the Bacilli class (such as *Lactobacillus gasseri, Lactobacillus paragasseri, Lactobacillus oris, Lactobacillus vaginalis*, *Streptococcus parasanguinis*) and *Veillonella parvula* were dominant in patients with OS $<$ 12 months (Extended Data Fig. 3c).

Taken together, these results indicate that the presence of Akk is associated with important, potentially prognosis-relevant shifts in the intestinal microbiota and tumor microenvironment of patients with NSCLC.

Stratification of clinical outcome on the basis of the relative abundance of *A. muciniphila*. We unexpectedly found an over-representation of Akk in patients with OS $<$ 12 months within the Akk$^+$ group, suggesting that the relative abundance of Akk may influence prognosis more than its absolute presence or absence. We next examined an ordinal, rather than a categorical (Akk$^+$ versus Akk$^-$), variable to analyze the clinical significance of Akk. Indeed, the relative abundance of Akk within the Akk$^+$ population ranged from 0.035% to 66.210%. Using a kernel density estimation of the relative abundance of Akk in patients with OS $\geq$ 12 or OS $<$ 12 months, we noticed that patients harboring Akk^{high}, at a relative abundance greater than the 75th percentile (4.656%), did cluster within the OS $<$ 12 months group (Fig. 2b,c, left, $P = 0.005$). To confirm this observation adjusting for other risk factors, we used a supervised approach to statistically define an optimal cutoff for Akk to discriminate two hypothetical groups of Akk$^+$ patients with different prognoses. We utilized a grid search algorithm, based on the multivariable Cox model (adjusted for age, sex, ECOG performance status, ATB exposure, histology, PD-L1, and line of treatment), with the Akaike information criterion as a performance index to determine the finest cutoff that corresponded to 4.799 (the 77th percentile of this cohort) (Fig. 2c, left). Among the whole cohort

Fig. 2 | Akk relative abundance represents a prognostic marker of ICI. a, Beta diversity measured by the Bray–Curtis Index, represented by PCoA, between Akk$^-$ versus Akk$^+$ groups and between OS $<$ 12 months or $\geq$ 12 months within each subgroup. *P* values were calculated using PERMANOVA with 999 permutations. **b**, Kernel density estimation aligning two variables, OS $<$ or $\geq$ 12 months and relative abundance of Akk (range: 0.035-66.210; 75th percentile: 4.656) in the entire cohort of 338 patients. The test used was the two-sided Fisher exact test on a 2 × 2 contingency table. No adjustments were required for this test. **c**, Distribution of the relative abundance of Akk in patients with detectable Akk (left) and percentages of patients within each of the three groups of Akk relative abundance (right). Akk$^-$, undetectable Akk; Akk^{low}, Akk relative abundance between 0.035-4.799%, Akk^{high}, >4.799% (77th percentile). The lower and upper hinges of boxplots correspond to the 25th and 75th percentiles, respectively. The midline is the median. The upper and lower whiskers extend from the hinges to the largest (or smallest) value no further than ×1.5 interquartile range from the hinge, defined as the distance between the 25th and 75th percentiles. **d**–**f**, Kaplan–Meier curve and Cox regression multivariate analysis of OS in 338 patients according to Akk relative abundance, segregated in 3 groups (Akk$^-$, Akk^{lo}, and Akk^{hi}) (**d**) and considering PD-L1 expression (**f**). Median OS of each group is indicated in round brackets. Akk status was compared using the stratified log-rank test. *P* values are one-sided with no adjustment. Cox logistic regression multivariate analysis of overall survival in 338 patients according to Akk relative abundance, segregated in 3 groups (Akk$^-$, Akk^{low}, and Akk^{high}) and all the other relevant clinical parameters (**e**). *P* values were calculated using the Wald test including all covariates in the Cox proportional hazards regression model. Exact *P* values are in Supplementary Table 6. m; months. **g**, Distribution (n (%)) of patients according to Akk relative abundance, segregated in two groups (Akk^{lo} and Akk^{hi}), and ATB use (no ATB, no exposure to ATB; ATB, exposure to ATBs within 2 months prior to ICI initiation). **h**, Kaplan–Meier curve and Cox regression multivariate analysis of OS in 338 patients segregated in 3 groups according to Akk relative abundance (Akk$^-$, Akk^{lo}, and Akk^{hi}) and ATB use (no ATB $n = 269$, left, and ATB $n = 69$, right). Akk status was compared using the stratified log-rank test. *P* values are one-sided with no adjustment. m; months.

of 338 patients, we observed that only 9% of patients (23% of Akk^{+} subgroup) fell into the category of "relative overabundance" of Akk (>4.799%), called Akk^{high} henceforth (Fig. 2c, right).

Moreover, we found a significant increase in Shannon diversity in specimens from Akk^{low} ("normal levels" of Akk in the gut) compared with Akk^{-} or Akk^{high} participants (Extended Data Fig. 4a,

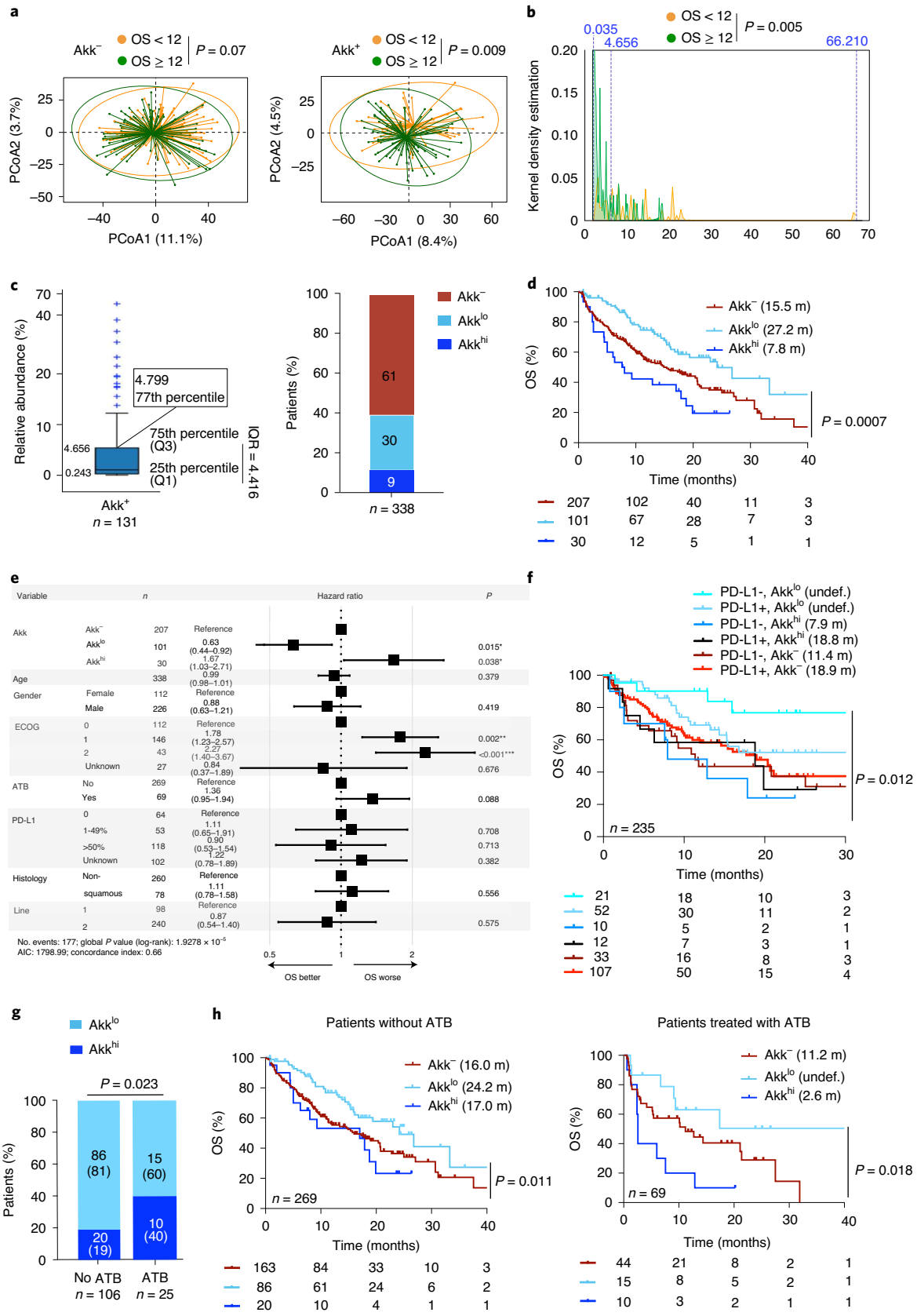

$P = 0.00003$), with the overall microbial community showing clear separation between Akk^{-} versus Akk^{low} as well as between Akk^{low} and Akk^{high} patients (Extended Data Fig. 4b,c, $P = 0.0001$ and $P = 0.0003$, respectively). Variable importance plot (VIP) discriminant analysis of taxonomic stool composition revealed that the ecosystem abnormally enriched in Akk (Akk^{high}) was over-represented by species of the genus *Clostridium* (*Clostridium symbosium*, *Clostridium innocuum*, *Clostridium scindens*, *Clostridium boltae*, *Clostridium clostridioforme*) at the expense of healthy commensals (*Faecalibacterium prausntzii, C. comes, E. rectale, D. formicigenerans, D. longicatena, Ruminococcus torques*, Extended Data Fig. 4d,e).

Kaplan–Meier survival curves, using the trichotomic stratification according to Akk relative abundance, diverged (log-rank test $P = 0.0007$, Fig. 2d and Supplementary Table 5a,b, with a significantly longer median OS for Akk^{lo} patients than for Akk^{hi} (27.2 months versus 7.8 months, Cox-adjusted HR = 0.38; 95% CI = 0.22–0.65, $P = 0.0005$) and Akk^{-} patients (27.2 months versus 15.5 months, adjusted HR = 0.63; 95% CI = 0.44–0.91, $P = 0.0150$). The HR for the other risk factors considered in the multivariate Cox regression analysis are presented in Fig. 2e and Supplementary Table 6. Not surprisingly, ECOG performance status ≥ 1 was another independent prognostic factor for this cohort[31]. The proportionality hazard assumption was questionable only for the ATBs (Schoenfeld residuals trend test, $P = 0.016$), but no statistically significant interaction with time could be identified. In addition, ATB exposure was associated with shorter OS in univariable analysis ($P = 0.009$; Supplementary Tables 5b and 6) and multivariate analysis ($P = 0.088$; Supplementary Table 6).

We also analyzed the interaction between Akk and PD-L1 in 235 patients with advanced NSCLC with available data on tumor expression of tumor PD-L1 (Supplementary Table 2a and Extended Data Fig. 1). We split the cohort into six groups according to PD-L1 expression and Akk fecal detection. The multivariate Cox regression analysis indicated that Akk dictated NSCLC prognosis, more than PD-L1 did ($P = 0.012$ in 235 patients, Fig. 2f).

Overall, we conclude that a trichotomic stratification of patients into Akk^{-}, Akk^{low}, and Akk^{high} may be a more accurate independent prognostic factor of OS than the dichotomous (Akk^{-} versus Akk^{+}) division (likelihood ratio test of multivariable Cox models: $P = 0.0009$). Akk^{low} may be considered as a surrogate of host intestinal fitness. Akk overruled PD-L1 as a predictive biomarker of response to ICIs in patients with NSCLC.

The impact of ATB use on *A. muciniphila* relative abundance and survival outcome. Akk^{high} levels as well as ATB exposure were considered standalone variables associated with shorter OS in patients with NSCLC treated with ICIs. Given these observations, we first combined the dichotomous classification of patients with respect to Akk (Akk^{-} versus Akk^{+}) with history of prior ATB exposure to segregate patients into four groups. The Akk^{+} group without ATB exposure showed the strongest clinical benefit (median OS of 23.0 months) compared with the three other groups (Extended Data Fig. 5a). The next favorable prognostic group was Akk^{-} without ATB exposure, with a median OS of 16.0 months. In contrast, exposure to ATB showed the shortest OS (mOS around 9 months, Extended Data Fig. 5a, $P = 0.017$). Accordingly, ATB tended to reduce the alpha diversity of the Akk^{+} group (Extended Data Fig. 5b,c). Moreover, ATB exposure enriched the Akk^{+} group in Gammaproteobacteria (*E. coli*), Clostridia class (*Clostridium bolteae, Ruthenibacterium lactatiformens*), and H2S-producing bacteria (*Bilophila wadsworthia*) (Extended Data Fig. 5d), as has already been described[35], at the expense of health-associated bacteria (*Collinsella aerofaciens*, *D. longicatena*, *D. formicigenerans*, *Eubacterium* spp. *CAG 38*)[34,41] also over-represented in the Akk^{+} group without ATB exposure (Extended Data Fig. 5e).

In an attempt to establish an association between ATB treatment and the relative overabundance of Akk, we compared the percentages of patients with Akk^{hi} stools between the ATB-treated and ATB-free groups (Fig. 2g) and generated a Kaplan–Meier OS curve using the trichotomic classification (Akk^{-}, Akk^{low}, and Akk^{high}) in two subgroups according to ATB exposure before the first ICI administration (Fig. 2h). We found a drastic increase of the proportion of Akk^{high} patients among ATB users (40% versus 19%, $P = 0.023$, Fig. 2g). We confirmed that the overabundance of stool Akk at diagnosis in patients exposed to ATBs was associated with lower OS despite ICI therapy (Extended Data Fig. 5c and Fig. 2h, right). Among ATB-free participants, Akk^{high} patients exhibited reduced benefits from ICIs compared with Akk^{low} individuals, but their benefits were not worse than for the Akk^{-} subgroup (Fig. 2h, left).

Altogether, these results demonstrate that ATB exposure is a negative predictor of survival following ICI and is associated with overabundance of Akk (Akk^{hi}) and the relative dominance of *Clostridium* spp. (*C. bolteae*) and *Lachnoclostridium*.

Stratification of outcome on other components of *A. muciniphila*-associated ecosystem. We used various statistical methods, such as linear discriminant analysis effect size (Extended Data Fig. 3), volcano plot from analysis of variance (ANOVA) model (Fig. 3a), and the MaAsLin multivariate statistical framework (Supplementary Table 7), to compare taxonomic compositional variations between Akk^{+} versus Akk^{-} stools to identify 16 bacterial species, among which 14 were positively and 2 were negatively associated with Akk fecal prevalence independently of other confounding factors, such as age, gender, BMI, lines of therapy (Fig. 3a and Supplementary Table 7). Next, we performed Cox logistic regression multivariate analyses to determine the impact of each bacterium on patient clinical outcome using a trichotomic distribution of their respective relative abundances (according to the cutoff defined above). Apart from Akk, very few bacteria (except *Eubacterium hallii*, *B. adolescentis*, *Parasutterella excrementihominis*, *Intestinimonas butyriciproducens*, and *C. innocuum* already described to mediate immunomodulatory functions[43–45]) were also associated with prolonged (Fig. 3b,d) or reduced (Fig. 3f and Supplementary Table 7) survival following ICI therapy. These bacteria had a "linear dose–response" relationship, in contrast to what was observed for Akk. The presence of Akk along with *E. hallii* or *B. adolescentis* was found to accurately predict ORR and/or mOS in this cohort of 338 patients

Fig. 3 | Stratification of clinical outcome based on other components of the Akk-associated ecosystem. a, Volcano plot (indicating fold change (FC) and *P* values in MaAsLin2 statistical analyses) to segregate taxonomic species (with a prevalence > 2.5%) according to their relative abundance in baseline fecal specimen of 338 patients based on their association with Akk: species significantly associated with or excluded from Akk-enriched ecosystems (Akk^{+}, blue dots, Akk^{-}, red dots). *P* values were calculated testing the null hypothesis and using a two-sided test. **b**,**d**,**f**. Kaplan–Meier OS curves in 338 patients, according to the trichotomic distribution of the relative abundance of beneficial or harmful bacteria retained in the LEfSe model, MaAsLin2, and the Volcano plot/ANOVA (Supplementary Table 7. The trichotomic distribution was compared using the stratified log-rank test. *P* values are one-sided, with no adjustment. **c**,**e**,**g**, Influence of collateral bacteria associated with Akk (retained in Supplementary Table 7) in the Akk-associated impact on ORR and OS in a dichotomic pattern (presence/absence) using the Chi-square test (for ORR, left, *P* values are two-sided, with no adjustments made for multiple comparisons). Cox regression multivariate analysis for Kaplan–Meier curves (right). The trichotomic distribution was compared using the stratified log-rank test. *P* values are one-sided with no adjustment.

with NSCLC (Fig. 3c,e). Hence, these findings suggest that Akk and its collateral commensalism may participate in the clinical benefit mediated by ICI.

***A. muciniphila* rescued response to PD-1 blockade by shifting the microbiome.** To establish a link between Akk and/or its collateral ecosystem and patient clinical outcome, we turned to our

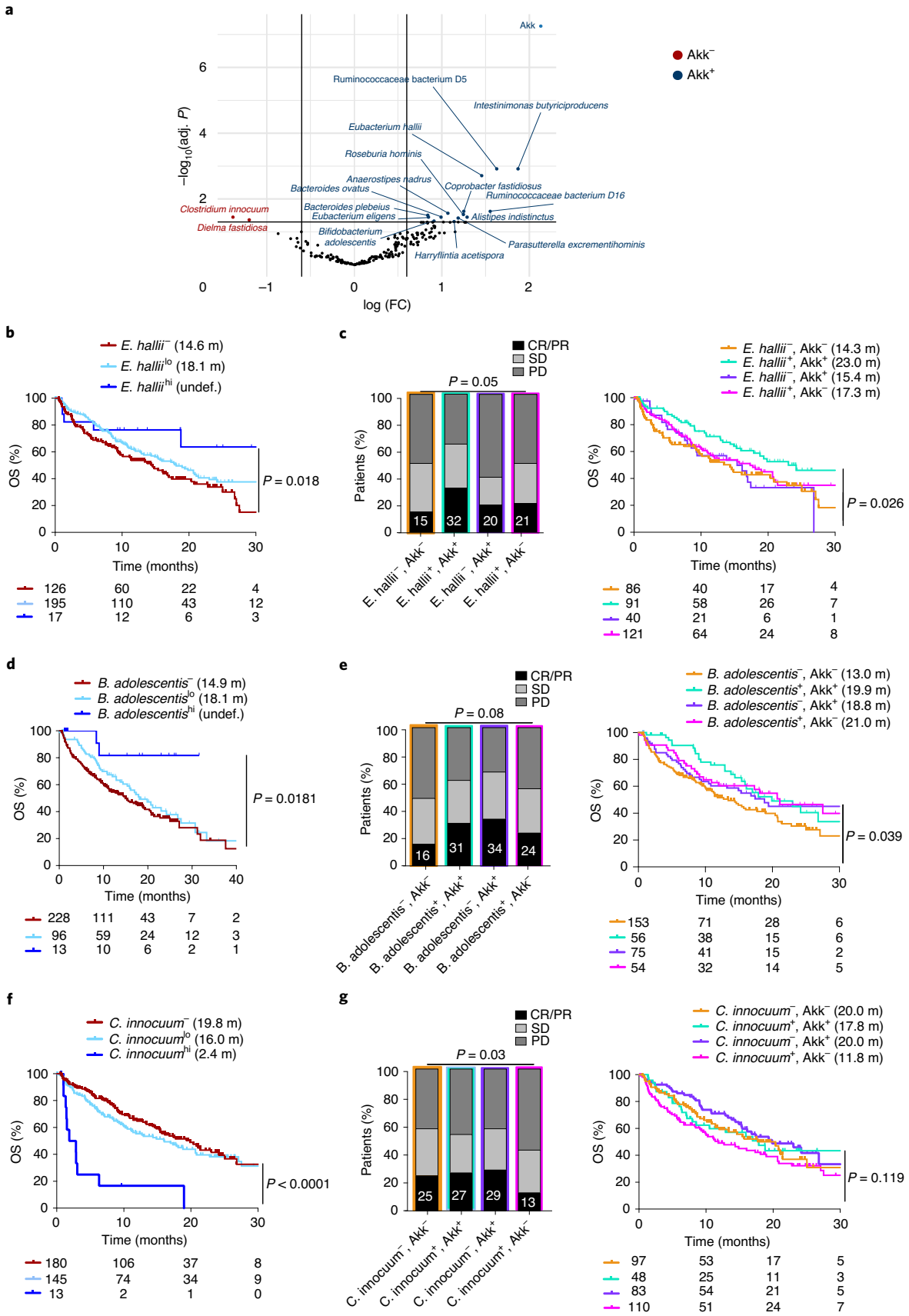

avatar tumor-bearing mouse models with humanized microbiota, described above. As depicted and commented on above (Extended Data Fig. 2c–e), mouse resistance to anti-PD-1 antibodies was associated with FMT bereft of Akk. Next, we analyzed the compensatory effects brought up by oral supplementation with an immunogenic strain of Akk, Akkp2261 (ref. [17]) in both groups of animals, recipients of Akk$^+$ or Akk$^-$ FMTs. Mice reared in specific pathogen-free conditions (SPF) (indicated as FMT– in Extended Data Fig. 6a,b) and inoculated with the same tumor cell line were used as controls of "murine eubiosis". Indeed, we could restore responsiveness to PD-1 blockade only in the setting of Akk$^-$ FMT (Extended Data Fig. 6b,c). Next, our objective was to analyze whether oral supplementation with Akkp2261 would change the host microbiome of the recipient mice and whether remodeling of the host ecosystem would correlate with preclinical benefit to exogenous Akkp2261. For this purpose, we concatenated all tumor models syngeneic of BALB/c (CT26, 4T1) and C57BL/6 (B16F10, MCA-205, MC38) mice that first received stools from 29 patients with NSCLC (Supplementary Table S3) and then were treated with anti-PD-1 antibodies (Extended Data Fig. 6a), and we next collected recipient feces before and after oral feeding with Akkp2261. The non-supervised hierarchical clustering of the ratios between the tumor growth kinetics with anti-PD-1 antibodies with or without exogenous Akkp2261 normalized on the effect of PD-1 blockade in eubiotic conditions (SPF versus FMT) revealed that exogenous Akkp2261 was effective in about 50% of cases (Extended Data Fig. 6d,e, left). We detected taxonomic differences in the recipient microbiota in responders (R) versus non responders (NR) to exogenous Akkp2261 (Extended Data Fig. 6e, right). Compared with NR mice, R mice harbored a relative over-representation of metagenomics species (namely *I. butyriciproducens* and *Parasuterrella excrementihominis*), annotated in Fig. 3a, in stools from humans harboring Akk$^+$. In contrast, NR mice tended to be enriched in *Bacteroides* spp. (Extended Data Fig. 6e, right).

Altogether, avatar mice that received Akk$^-$ human fecal material exhibited a phenotype of tumor resistance to PD-1 blockade but were rescued by *Akkp2261* when *Akkp2261* could shift the microbiome toward the favorable Akk-associated collateral ecosystem.

Discussion

Here, we report the results of a prospective, multicentric study based on the profiling of the gut microbiota of patients with advanced NSCLC treated with PD-1 blockade. The relative abundance of Akk was associated with clinical benefit, defined by an increase in ORR and survival, taking into accounting the main microbiota-relevant confounding factors (age, gender, BMI, lines of therapy). The prognostic significance of this gut bacterium was validated by multivariate analyses and interaction studies, which indicated that Akk is markedly associated with response of NSCLC to treatment with ICIs, independently of age, gender, ECOG performance status, ATB use, and PD-L1. The intestinal residence of Akk was a proxy for richness of the gut ecosystem, as shown by the association of Akk, at a relative abundance within the 77th percentile (Akk^{low}, <4.799%), with stool alpha diversity (Shannon diversity index). These results expand on previous observations that have been made in smaller cohorts of patients with NSCLC[17,39] and provide evidence that gut microbiome diversity and composition, specifically the relative abundance of Akk, offer relevant information to predict survival of patients with NSCLC amenable to ICIs.

Our study is the largest metagenomics prospective analysis that attempted to validate Akk as a new prognostic factor for patients treated with ICIs. Our study results met the pre-specified criterium of statistical significance, which was set as a 10% ORR increase between Akk$^-$ and Akk$^+$ patients when considering all (mostly 2L) 338 patients with NSCLC (from 18.2% to 28.2% in ORR, Fig. 1a). Moreover, we also observed a >10% ORR increase between Akk$^-$ and Akk$^+$ (from 19% to 41% ORR, Fig. 1b), with a mOS advantage in 1L patients (Fig. 1e). Moreover, our study linked the gut microbiota composition to the tumor microenvironmental landscape, highlighting increased transcription of gene products of adaptive immunity and the IFN fingerprint. Finally, we validated in mice that Akk$^-$ stools conferred resistance to PD-1 blockade.

In addition to prospectively validating the hypothesis in a larger and homogeneous cohort, we report that Akk was associated not only with increased alpha diversity but also with a distinct bacterial community associated with health or immunogenic status, represented by Ruminococcacae (*F. prausnitzii*, *R. lactaris*) and Lachnospiraceae (*D. formicigenerans*, *D. longicatena*, *E. rectale*, *E. hallii*, *Roseburia faecis*, *R. intestinalis*) family members, as well as *B. adolescentis*, *I. butyricyproducens*, and others. These findings reconcile the results across several works, geographical distributions, and sequencing technologies, as *Faecalibacterium*, *Ruminococcus*, and *Bifidobacterium* have previously been reported to be enriched in North American, Japanese, and South Korean patients with melanoma and NSCLC cancers who had favorable outcomes[19,34,39,42]. Moreover, even in avatar gut-humanized mouse models, the microbiomes of responders to exogenous Akkp2261 shifted toward an over-representation of some of the above mentioned species belonging to the Akk$^+$ ecosystem.

Confirming the clinical significance of bacterial diversity and commensals associated with responses, our results validate the growing body of evidence linking ATB use and poor clinical outcome[43]. In addition to depleting favorable genera associated with survival (such as Ruminococcus)[39], ATB use tends to deviate the gut microbiome composition toward harmful bacteria that have previously been associated with proinflammatory or immunoregulatory pathways (such as *E. coli* and *C. bolteae*)[44], supporting previous findings in renal cell carcinomas amenable to ICIs[35]. Surprisingly, in addition to acting as an independent negative prognostic factor, ATBs promoted an overabundance of Akk above the 77th percentile level, associated with poor prognosis. Indeed, ATB use doubled the proportion of individuals presenting a stool Akk^{high} phenotype. This phenotypic trait of overabundance of Akk >4.799% was associated with a dominance of the *Clostridium* species (*C. bolteae*, *C. innocuum*, *C. asparagiforme*, *C. scindens*, *C. symbosium*) belonging to clusters IV and XIVa of the genus *Clostridium*, known to maintain IL-10-producing regulatory T cells in colonic lamina propria[45].

Aside from ATB use, overabundance of Akk (>4.799%) was associated with a shorter OS than was a "normal" relative abundance of Akk (<4.799%), possibly reflecting an underlying pathophysiological disorder of the intestinal barrier in patients with advanced cancer. High relative proportions or subdominance of Akk in the ecosystem has been associated with pathophysiological failures (such as anorexia nervosa[46], GVHD[30], aging[47], dysmetabolism[48], HIV infection[49], pathobionts[50], and liver injury[51]). Hence, in the context of gut injury by, or conducive to, ATB use, Akk might constitute a biomarker of ongoing but imperfect intestinal repair. Of note, we failed to observe a similar trichotomic distribution correlating with opposite clinical outcome investigating other bacteria (Fig. 3).

Hence, we conclude that Akk's relative abundance could represent a reliable biomarker of favorable or dismal prognosis for patients receiving immunotherapy with PD-1 blockade. It may be of utmost importance to IO patients, risk-stratified on the basis of shot-gun metagenomics (rather than by 16S rRNA) sequencing, to precisely quantify the relative abundance of Akk in addition to ATB use and PD-L1 expression in patients with NSCLC in prospective trials designed to discover optimal biomarkers.

Therapeutic strategies modulating the microbiome, such as FMT or commensals, are currently being evaluated to boost ICI responses or circumvent primary resistance to ICI, though without patient stratification based on degree of dysbiosis[52]. Here we provide

preclinical data suggesting that Akk could therapeutically bypass the resistance to anti-PD-1 blockade conferred by FMT bereft of endogenous Akk (Extended Data Fig. 6 and refs. [17,34]). The oral supplementation with exogenous Akk (Akkp2261) was particularly effective when Akk shifted the recipient microbiome toward a healthy status (Extended Data Fig. 6d,e). A recent preclinical study indicates that the anticancer effects of recombinant interleukin-2 could be improved by Akk in a Toll-like receptor-2-dependent fashion[53]. In patients, food supplementation with Akk is safe and reduces insulin resistance and dyslipidemia in the context of pre-diabetes[48]. Altogether, we surmise that therapeutic supplementation with a lyophilized encapsulated Akkp2261 would benefit the subgroups of patients not exposed to ATB and devoid of endogenous Akk. In contrast, complex polymicrobial consortia or fecal microbial transplantation may be best suited for patients with prior ATB exposure.

The limitations of this study are the following. First, it did not evaluate the predictive value of Akk in 1L chemo-immunotherapy combinations (only considering 1L IO presenting with >50% PD-L1 tumor expression). Second, it could not consider the interactions between the tumor mutational burden and stool Akk prevalence. Moreover, this study failed to investigate the functional and clinical relevance of rarer *Akkermansia* spp.[54] different from the SGB9226 monitored in this study using MetaPhlAn 3 pipeline with a custom marker database (see Methods). Nevertheless, our study provides a strong rationale for the development of diagnostic tools for assessing gut dysbiosis for routine oncological management, as well as a framework for the design of microbiota-centered interventions to circumvent primary resistance to ICI in patients with NSCLC.

Online content

Any methods, additional references, Nature Research reporting summaries, source data, extended data, supplementary information, acknowledgements, peer review information; details of author contributions and competing interests; and statements of data and code availability are available at https://doi.org/10.1038/s41591-021-01655-5.

Received: 15 December 2020; Accepted: 6 December 2021;
Published online: 3 February 2022

References

1. Herbst, R. S. et al. Pembrolizumab versus docetaxel for previously treated, PD-L1-positive, advanced non-small-cell lung cancer (KEYNOTE-010): a randomised controlled trial. *Lancet* **387**, 1540–1550 (2016).
2. Brahmer, J. et al. Nivolumab versus docetaxel in advanced squamous-cell non–small-cell lung cancer. *N. Engl. J. Med.* **373**, 123–135 (2015).
3. Borghaei, H. et al. Nivolumab versus docetaxel in advanced nonsquamous non–small-cell lung cancer. *N. Engl. J. Med.* **373**, 1627–1639 (2015).
4. Gandhi, L. et al. Pembrolizumab plus chemotherapy in metastatic non-small-cell lung cancer. *N. Engl. J. Med.* **378**, 2078–2092 (2018).
5. Paz-Ares, L. et al. Pembrolizumab plus chemotherapy for squamous non–small-cell lung cancer. *N. Engl. J. Med.* **379**, 2040–2051 (2018).
6. Reck, M. et al. Pembrolizumab versus chemotherapy for pd-l1–positive non–small-cell lung cancer. *N. Engl. J. Med.* **375**, 1823–1833 (2016).
7. Gadgeel, S. et al. Updated analysis from KEYNOTE-189: pembrolizumab or placebo plus pemetrexed and platinum for previously untreated metastatic nonsquamous non-small-cell lung cancer. *J. Clin. Oncol.* **38**, 1505–1517 (2020).
8. Ferrara, R. et al. Hyperprogressive disease in patients with advanced non-small cell lung cancer treated with PD-1/PD-L1 inhibitors or with single-agent chemotherapy. *JAMA Oncol.* **4**, 1543–1552 (2018).
9. Riaz, N. et al. Tumor and microenvironment evolution during immunotherapy with nivolumab. *Cell* **171**, 934–949.e16 (2017).
10. Rizvi, N. A. et al. Cancer immunology. Mutational landscape determines sensitivity to PD-1 blockade in non-small cell lung cancer. *Science* **348**, 124–128 (2015).
11. Spranger, S., Bao, R. & Gajewski, T. F. Melanoma-intrinsic β-catenin signalling prevents anti-tumour immunity. *Nature* **523**, 231–235 (2015).
12. Smyth, M. J., Ngiow, S. F., Ribas, A. & Teng, M. W. L. Combination cancer immunotherapies tailored to the tumour microenvironment. *Nat. Rev. Clin. Oncol.* **13**, 143–158 (2016).
13. Koyama, S. et al. Adaptive resistance to therapeutic PD-1 blockade is associated with upregulation of alternative immune checkpoints. *Nat. Commun.* **7**, 10501 (2016).
14. Young, A. et al. Co-inhibition of CD73 and A2AR adenosine signaling improves anti-tumor immune responses. *Cancer Cell* **30**, 391–403 (2016).
15. Chen, D. S. & Mellman, I. Elements of cancer immunity and the cancer–immune set point. *Nature* **541**, 321–330 (2017).
16. Derosa, L. et al. Microbiota-centered interventions: the next breakthrough in immuno-oncology? *Cancer Discov.* **11**, 2396–2412 (2021).
17. Routy, B. et al. Gut microbiome influences efficacy of PD-1-based immunotherapy against epithelial tumors. *Science* **359**, 91–97 (2018).
18. Vétizou, M. et al. Anticancer immunotherapy by CTLA-4 blockade relies on the gut microbiota. *Science* **350**, 1079–1084 (2015).
19. Gopalakrishnan, V. et al. Gut microbiome modulates response to anti-PD-1 immunotherapy in melanoma patients. *Science* **359**, 97–103 (2018).
20. Derosa, L. et al. Negative association of antibiotics on clinical activity of immune checkpoint inhibitors in patients with advanced renal cell and non-small-cell lung cancer. *Ann. Oncol.* **29**, 1437–1444 (2018).
21. Derosa, L. & Zitvogel, L. Antibiotics impair immunotherapy for urothelial cancer. *Nat. Rev. Urol.* **17**, 605–606 (2020).
22. Matson, V. et al. The commensal microbiome is associated with anti-PD-1 efficacy in metastatic melanoma patients. *Science* **359**, 104–108 (2018).
23. Jin, Y. et al. The diversity of gut microbiome is associated with favorable responses to anti-programmed death 1 immunotherapy in Chinese patients with NSCLC. *J. Thorac. Oncol.* **14**, 1378–1389 (2019).
24. Daisley, B. A. et al. Abiraterone acetate preferentially enriches for the gut commensal Akkermansia muciniphila in castrate-resistant prostate cancer patients. *Nat. Commun.* **11**, 4822 (2020).
25. Santoro, A. et al. Gut microbiota changes in the extreme decades of human life: a focus on centenarians. *Cell. Mol. Life Sci.* **75**, 129–148 (2018).
26. Zhou, Q. et al. Gut bacteria *Akkermansia* is associated with reduced risk of obesity: evidence from the American Gut Project. *Nutr. Metab.* **17**, 90 (2020).
27. Blacher, E. et al. Potential roles of gut microbiome and metabolites in modulating ALS in mice. *Nature* **572**, 474–480 (2019).
28. Bárcena, C. et al. Healthspan and lifespan extension by fecal microbiota transplantation into progeroid mice. *Nat. Med.* **25**, 1234–1242 (2019).
29. Romano, S. et al. Meta-analysis of the Parkinson's disease gut microbiome suggests alterations linked to intestinal inflammation. *NPJ Parkinsons Dis.* **7**, 1–13 (2021).
30. Shono, Y. et al. Increased GVHD-related mortality with broad-spectrum antibiotic use after allogeneic hematopoietic stem cell transplantation in human patients and mice. *Sci. Transl. Med.* **8**, 339ra71 (2016).
31. Desai, M. S. et al. A dietary fiber-deprived gut microbiota degrades the colonic mucus barrier and enhances pathogen susceptibility. *Cell* **167**, 1339–1353.e21 (2016).
32. Karcher, N. et al. Genomic diversity and ecology of human-associated *Akkermansia* species in the gut microbiome revealed by extensive metagenomic assembly. *Genome Biol.* **22**, 209 (2021).
33. Le Chatelier, E. et al. Richness of human gut microbiome correlates with metabolic markers. *Nature* **500**, 541–546 (2013).
34. Routy, B. et al. The gut microbiota influences anticancer immunosurveillance and general health. *Nat. Rev. Clin. Oncol.* **15**, 382–396 (2018).
35. Derosa, L. et al. Gut bacteria composition drives primary resistance to cancer immunotherapy in renal cell carcinoma patients. *Eur. Urol.* **78**, 195–206 (2020).
36. Meng, X. et al. Immune microenvironment differences between squamous and non-squamous non-small-cell lung cancer and their influence on the prognosis. *Clin. Lung Cancer* **20**, 48–58 (2019).
37. Hwang, S. et al. Immune gene signatures for predicting durable clinical benefit of anti-PD-1 immunotherapy in patients with non-small cell lung cancer. *Sci. Rep.* **10**, 643 (2020).
38. Nakajima, K. et al. IAP inhibitor, Embelin increases VCAM-1 levels on the endothelium, producing lymphocytic infiltration and antitumor immunity. *Oncoimmunology* **9**, 1838812 (2020).
39. Hakozaki, T. et al. The gut microbiome associates with immune checkpoint inhibition outcomes in patients with advanced non-small cell lung cancer. *Cancer Immunol. Res.* **8**, 1243–1250 (2020).
40. Tsay, J.-C. J. et al. Lower airway dysbiosis affects lung cancer progression. *Cancer Discov.* **11**, 293–307 (2020). https://doi.org/10.1158/2159-8290.CD-20-0263
41. Benevides, L. et al. New insights into the diversity of the genus *Faecalibacterium*. *Front. Microbiol.* **8**, 1790 (2017).
42. Lee, S.-H. et al. *Bifidobacterium bifidum* strains synergize with immune checkpoint inhibitors to reduce tumour burden in mice. *Nat. Microbiol.* **6**, 277–288 (2021).
43. Elkrief, A., Derosa, L., Kroemer, G., Zitvogel, L. & Routy, B. The negative impact of antibiotics on outcomes in cancer patients treated with immunotherapy: a new independent prognostic factor? *Ann. Oncol.* **30**, 1572–1579 (2019).

44. Seo, S. W., Kim, D., Szubin, R. & Palsson, B. O. Genome-wide reconstruction of OxyR and SoxRS Transcriptional regulatory networks under oxidative stress in *Escherichia coli* K-12 MG1655. *Cell Rep.* **12**, 1289–1299 (2015).
45. Atarashi, K. et al. Induction of colonic regulatory T cells by indigenous *Clostridium* species. *Science* **331**, 337–341 (2011).
46. Ruusunen, A., Rocks, T., Jacka, F. & Loughman, A. The gut microbiome in anorexia nervosa: relevance for nutritional rehabilitation. *Psychopharmacol.* **236**, 1545–1558 (2019).
47. van der Lugt, B. et al. *Akkermansia muciniphila* ameliorates the age-related decline in colonic mucus thickness and attenuates immune activation in accelerated aging Ercc1−/Δ7 mice. *Immun. Ageing* **16**, 6 (2019).
48. Depommier, C. et al. Supplementation with *Akkermansia muciniphila* in overweight and obese human volunteers: a proof-of-concept exploratory study. *Nat. Med.* **25**, 1096–1103 (2019).
49. Ouyang, J. et al. The bacterium *Akkermansia muciniphila*: a sentinel for gut permeability and its relevance to HIV-related inflammation. *Front. Immunol.* **11**, 645 (2020).
50. Huck, O. et al. *Akkermansia muciniphila* reduces *Porphyromonas gingivalis*-induced inflammation and periodontal bone destruction. *J. Clin. Periodontol.* **47**, 202–212 (2020).
51. Wu, W. et al. Protective effect of *Akkermansia muciniphila* against immune-mediated liver injury in a mouse model. *Front. Microbiol.* **8**, 1804 (2017).
52. Baruch, E. N. et al. Fecal microbiota transplant promotes response in immunotherapy-refractory melanoma patients. *Science* **371**, 602–609 (2020).
53. Shi, L. et al. Combining IL-2-based immunotherapy with commensal probiotics produces enhanced antitumor immune response and tumor clearance. *J. Immunother. Cancer* **8**, e000973 (2020).
54. Cani, P. D. & de Vos, W. M. Next-generation beneficial microbes: the case of *Akkermansia muciniphila*. *Front. Microbiol.* **8**, 1765 (2017).

[1]Gustave Roussy Cancer Campus, Villejuif, France. [2]Cancer Medicine Department, Gustave Roussy, Villejuif, France. [3]Institut National de la Santé Et de la Recherche Médicale (INSERM) U1015, Equipe Labellisée, Ligue Nationale contre le Cancer, Villejuif, France. [4]Université Paris-Saclay, Ile-de-France, France. [5]Department of Medicine, Centre Hospitalier de l'Université de Montréal (CHUM), Hematology-Oncology Division, Montréal, Quebec, Canada. [6]Centre de Recherche du CHUM (CRCHUM), Montréal, Quebec, Canada. [7]Department CIBIO, University of Trento, Trento, Italy. [8]European Institute of Oncology (IEO) IRCCS, Milan, Italy. [9]Department of Medical, Surgical and Health Sciences, University of Trieste, Trieste, Italy. [10]Thoracic Oncology Department-CIC1425/CLIP2 Paris-Nord, Hospital Bichat-Claude Bernard, AP-HP, Université Paris-Diderot, Paris, France. [11]Pneumology Department, Foch Hospital, Suresnes, France. [12]Department of Pneumology, Toulouse University Hospital, Toulouse, France. [13]Pneumology Department, Centre Hospitalier Toulon Sainte-Musse, Toulon, France. [14]Department of Thoracic Oncology, Centre Hospitalier Universitaire, Grenoble, France. [15]UPR 4466, Paris Descartes University, Sorbonne Paris Cité, Paris, France. [16]Department of Medical Oncology, Cochin Hospital, Assistance Publique-Hôpitaux de Paris, Paris, France. [17]Immunomodulatory Therapies Multidisciplinary Study Group (CERTIM), Paris, France. [18]Department of Pulmonary and Thoracic Oncology, University of Lille, University Hospital (CHU), Lille, France. [19]Pulmonary Department, European Hospital, Marseille, France. [20]Cancer Biology Transfer Platform, Centre Georges-François Leclerc, Dijon, France. [21]Centre de Recherche INSERM LNC-UMR1231, Dijon, France. [22]Department of Medical Oncology, Centre Georges-François Leclerc, Dijon, France. [23]Unit of Molecular Biology, Department of Biology and Pathology of Tumors, Georges-François Leclerc Cancer Center, UNICANCER, Dijon, France. [24]EverImmune, Gustave Roussy Cancer Campus, Villejuif, France. [25]Centre de Recherche des Cordeliers, INSERM U1138, Equipe labellisée—Ligue contre le cancer, Université de Paris, Institut Universitaire de France, Paris, France. [26]Metabolomics and Cell Biology Platforms, Institut Gustave Roussy, Villejuif, France. [27]Pôle de Biologie, Hôpital Européen Georges Pompidou, AP-HP, Paris, France. [28]Université Paris-Saclay, INRAE, MGP, Jouy en Josas, France. [29]Centre Hospitalier de Sherbrooke, Sherbrooke, Quebec, Canada. [30]INSERM U1018, Oncostat, Villejuif, France. [31]Department of Radiation Oncology, Gustave Roussy, Villejuif, France. [32]INSERM U1030, Radiothérapie Moléculaire et Innovation Thérapeutique, Villejuif, France. [33]Service des Maladies Respiratoires, Centre Hospitalier d'Aix-en-Provence, Aix-en-Provence, France. [34]Center of Clinical Investigations in Biotherapies of Cancer (BIOTHERIS) 1428, Villejuif, France. [35]These authors contributed equally: Lisa Derosa, Bertrand Routy, Andrew Maltez Thomas. ✉e-mail: laurence.zitvogel@gustaveroussy.fr

Methods

Study design and treatment. *Ethical issues.* The ancillary studies have been designed according to an IRB approved-study (Oncobiotics Sponsor Protocol N: Center for Security and Emerging Technology (CSET) 2017/2619, Agence nationale de sécurité du médicament et des produits de santé ID-RCB N: 2017-A02010-53, https://clinicaltrials.gov/ct2/show/NCT04567446). The trial was conducted in accordance with Good Clinical Practice guidelines and the provisions of the Declaration of Helsinki. All patients provided written informed consent. General Data Protection Regulation procedures and anonymization rules have been applied according to Oncobiome H2020 model system already in place in the ClinicoBiome, Gustave Roussy. All data and sample collection was performed in compliance with regulatory, ethical, and European GDPR requirements.

Patient eligibility. NCT04567446, a multicentric prospective observational study designed to evaluate the impact of the microbiome composition in the clinical outcome of patients with advanced NSCLC treated with anti-PD-L1–PD-L1. We enrolled across 12 academic centers in France and 2 in Canada. Adult patients with pathologically confirmed advanced non-squamous or squamous NSCLC and an ECOG performance status score of 0–2 who were amenable to ICIs as standard of care and who could provide a stool sample were eligible. Eligible patients received ICIs following progression on platinum-based chemotherapy regimens, either with nivolumab or atezolizumab regardless of PD-L1 expression or with pembrolizumab if PD-L1 was ≥1%. Given the subsequent approval of first-line ICI in the first-line setting during the study accrual period, patients who received pembrolizumab monotherapy or in combination with platinum-based chemotherapy, depending on PD-L1 expression, were also included. Standard-of-care treatment was continued until disease progression, unacceptable adverse effects, or completion as per the protocol (2 years of ICI treatment). Full eligibility criteria are listed in the trial protocol (NCT04567446). Baseline characteristics, including a detailed listing of concurrent medications received the 2 months prior to ICI initiation and the date of last follow-up, were entered at each center in an electronic case report form.

Hypothesis. Sample-size calculation was performed on the basis of the primary end-point, defined as investigator-assessed ORR from the hypothesis proposed in Routy et al.[17] that in a population with metagenomics detectable Akk (Akk$^+$) in the gut microbiome, the response rate would be higher than in the population with undetectable Akk (Akk$^-$). We considered that a meaningful clinical difference would correlate to an ORR incremental from 10% in the Akk$^-$ to 20% in the Akk$^+$ group. Given the superiority hypothesis, power was set at 80% with a two-sided alpha level of 5%, using EAST program. Hence, we determined that at least 292 patients would be necessary to confirm our primary objective.

Study end-point and assessments. Computed tomography scans were performed at baseline and every 8–12 weeks for the first year and every 12–15 weeks thereafter until disease progression. Tumor response was assessed using the Response Evaluation Criteria in Solid Tumors version (RECIST) 1.1 (ref. [55]). The primary end-point was investigator-assessed ORR, which was defined as the number and percentage of patients with a best overall response (BOR) of confirmed complete response or PR. BOR was defined as the best response designation, recorded between the date of first treatment dose and the date of the initial objectively documented tumor progression per RECIST v1.1 or the date of subsequent therapy, whichever occurs first. For patients without documented progression or subsequent therapy, all available response designations contributed to the BOR determination. Secondary end-points included OS and microbiome variables, such as alpha and beta diversity and differential abundance analyses at the genus level. OS was defined as the time from trial inclusion until death from any cause. The follow-up of patients alive at the database lock was censored to the date of last record of contact.

Treatment modalities: the number of pembrolizumab (every other 21 days) or nivolumab (every other 15 days) or atezolizumab (every other 21 days) injections received was 4 ± 2 at 8–12 weeks and was 20 ± 4 at 12 months.

Human stool samples and metagenomics analyses. Fecal samples were prospectively collected (V1: pre-ICI, V2: before the second ICI injection, V3: at 3 months post-ICI, V4: at 6 months post-ICI) at each center following the International Human Microbiome Standards (IHMS) guidelines. Only the baseline V1 sample was considered for this analysis; for patients for whom such timely collection was not feasible, V2 samples were considered "baseline". For metagenomic analysis, the stools were processed for total DNA extraction and sequencing with Ion Proton technology following MetaGenoPolis (INRA) France, as previously reported[17,56,57]. Cleaning, filtering, and classification of reads were performed with two different pipelines: MetaOMineR and MetaPhlAn 3 (ref. [58]). In order to determine Akk presence or absence, we used a total of 463 genetic markers identified from 4 *Akkermansia* candidate species-level genome bins (SGBs) (SGB9223: 38 markers, SGB9224: 54 markers, SGB9226: 171 markers, SGB9228: 200 markers)[32] in MetaPhlAn. As outlined in Supplementary Table 1, the type of strain of *A. muciniphila* (MucT) delineated as SGB9226, was the most prevalent species in our cohort (>80% of *Akkermansia*-positive subset) and was therefore used for the calculation of the relative abundance of Akk in the main figures of this article.

We found msp_0025 to correspond to SGB9226, and used its relative abundance values as a proxy for *A. muciniphila* in MetaOMineR. A full description of both DNA purification and metagenomic pipelines is available in Derosa et al.[35]. Starting from abundance matrices, only taxa that were present in at least 2.5% of all samples were considered, and then raw data were normalized and standardized (SciKit-learn version 0.20.3).

Tumor RNA sequencing. Using a previously published technique[59], total RNA was extracted from formalin-fixed paraffin-embedded (FFPE) tumors from patients with advanced NSCLC included in the main analysis as well as from patients with limited stages (Supplementary Table 5). Libraries were prepared from 12 µl of total RNA with the TruSeq Stranded Total RNA using Ribo-Zero (Illumina) following manufacturer instructions. BBMAP v38.87 was used to trim the sequencing adapters and filtered the low quality and too short reads. Kallisto software[60] was used for quantifying transcript abundance from RNA-seq data against GRCh38 cDNA reference transcriptome from the Ensembl database, release 101. Only protein-coding transcripts and genes were included in the downstream analysis. Transcript Per Million values have been used for downstream analysis. Mann–Whitney tests have been performed to compare gene expression according to *Akkermansia* groups. PERMANOVA test with Euclidian distance has been used to assess the difference between groups on the subset of differentially expressed genes.

Preclinical study details. *Mice.* All animal experiments were carried out in compliance with French and European laws and regulations. The local institutional animal ethics board (Ministère de la Recherche, de l'Ènseignement Superieur er de l'Innovation) approved all mice experiments (permission numbers: 2016-049-4646, 2018-020-510263031v3). Mice avatar studies have been approved by the regulatory animal facility local and national committees (Ministère de la Recherche, de l'Ènseignement Superieur er de l'Innovation) (Everimmune no. 13366-2018020510263031 v3, APAFIS no. 17530-201811413352738 v2 (03/2019-03/2024). APAFIS no. 21378-201907080848483459). Female C57Bl/6 and BALB/c mice were purchased from Harlan and Janvier, respectively. Mice were used between 8 and 16 weeks of age and housed in SPF conditions. All mouse experiments were performed at the animal facility in Gustave Roussy Cancer Campus, where animals were housed in SPF conditions.

Cell culture, reagents, and tumor cell lines. MC38, MCA-205, B16F10 (syngeneic from C57BL/6 mice), and 4T1 cell lines (syngeneic from BALB/c mice) were purchased from ATCC. 4T1, MCA-205, and MC38 cells were cultured in RPMI 1640 containing 10% FCS, 2 mM L-glutamine, 100 UI/ml penicillin–streptomycin, 1 mM sodium pyruvate, and MEM non-essential amino acids. All reagents were purchased from Gibco-Invitrogen. B16F10 and CT26 cells were cultured in DMEM containing 10% FCS with 100 UI/ml penicillin–streptomycin and non-essential amino acids. All cell lines were cultured at 37 °C with 5% CO_2 and were regularly tested to confirm they were free of mycoplasma contamination.

Subcutaneous model of MCA-205, MC38, B16F10, and 4T1. Syngeneic C57BL/6 mice were implanted with 0.8×10^6 MCA-205, 1.0×10^6 MC38/CT26, or 3×10^5 B16F10 cells subcutaneously. Syngeneic BALB/c mice were implanted with 3×10^5 4T1 cells subcutaneously. For tumor growth experiments, tumor-implanted mice were treated intraperitoneally when tumors reached 20–40 mm² in size with anti-PD-1 monoclonal antibodies (250 µg/mouse; clone RMP1-14, lot 695318A1) or isotype control (clone 2A3, lot 686318F1). Mice were injected 4 times at 3-day intervals with anti-PD-1 monoclonal antibodies. Tumor length and width were routinely monitored three times per week using a caliper. All antibodies were purchased from BioXcell.

Antibiotic treatments. Mice were treated with an ATB solution containing ampicillin (1 mg/ml), streptomycin (5 mg/ml), and colistin (1 mg/ml) (Sigma-Aldrich) added in the drinking water of mice. Antibiotic activity was confirmed by cultivating fecal pellets resuspended in BHI + 15% glycerol at 0.1 g/ml on COS (Columbia Agar with 5% sheep blood) plates for 48 hours at 37 °C in aerobic and anaerobic conditions. In brief, in the context of fecal microbial transplantation experiments, mice received 3 days of ATB treatment before undergoing FMT the next day by oral gavage using animal feeding needles.

FMT experiments. FMT was performed by thawing fecal material. Two hundred µl of the suspension was then transferred by oral gavage into ATB pre-treated recipient (as described above). In addition, another 100 µl was applied on the fur of each animal. Two weeks after FMT, tumor cells were injected subcutaneously and mice were treated with anti-PD-1 monoclonal antibodies or isotype control, as previously explained. We used MCA-205 fibrosarcomas because, in SPF eubiotic mice, it is normally sensitive to anti-PD-1 antibodies and has been used as a reference mouse model in our previous avatar experiments reported in refs. [17,35]; both papers show that results obtained with MCA-205 were recapitulated in orthotopic TC1 lung cancer or RENCA models, respectively. So, we can trust the biological relevance and suitability of this MCA-205 model system to probe FMT or taxonomic fecal composition in future experiments.

Murine meta-analysis. We conducted 29 individual experiments over 2 years comprising 6–8 groups (including 6 mice per group). The growth kinetics of orthotopic MCA-205 sarcomas, and other tumors such as MC38 colon cancer (syngeneic from C57BL/6 mice), 4T1 breast or CT26 colon tumors (syngeneic from BALB/c mice), or B16 (melanoma), were monitored in avatar mouse models[34]. These recipients were ATB-treated and then received FMTs from 26 patients with NSCLC (phenotype of R versus NR to PD-1 blockade, and relative abundance of stool Akk, both described in Supplementary Table 6). Then, syngeneic tumors were implanted in mice, which were later subjected to immunotherapy with anti-PD-1 antibodies. FMT could confer sensitivity (when stools were Akk^+) or resistance (when stools were Akk^-) to anti-PD-1 antibodies, when compared with animals in eubiosis reared in SPF conditions (without FMT). Next, we analyzed the benefit and compensatory effects of oral supplementation of Akkp2261, based on presence or absence of Akk in the human donor's stool. Of note, exogenous Akkp2261 was not detectable more than 30 hours in the recipient intestines (as shown by qRT–PCR using *A. muciniphila*-specific probe sets). To better scrutinize whether the exogenous Akkp2261 could shift the microbiome of the recipient tumor-bearers differently in R versus NR mice, we concatanated all tumor models syngeneic of BALB/c mice (CT26, 4T1) and C57BL/6 mice (B16F10, MCA-205, MC38) that were treated by FMT from 29 patients with NSCLC and then treated the mice with anti-PD-1 monoclonal antibodies with or without Akkp2261 prior to stool collection for 16S-rRNA-based-sequencing of fecal amplicons. We calculated the relative benefit of exogenous Akk by dividing the ratio of (tumor size between anti-PD-1+ Akkp2261 /anti-PD-1+ water), normalized on the ratio of tumor sizes between anti-PD-1/control monoclonal antibodies in SPF mice for each time points for the whole kinetics. The non-supervised hierarchical clustering of the ratios between tumor growth kinetics with anti-PD-1 monoclonal antibodies with or without exogenous Akkp2261 normalized on the effect of PD-1 blockade in eubiotic conditions revealed that exogenous Akkp2261 was effective in about 50% cases (heatmap in Extended Data Fig. 3e). To delineate which Akk-associated ecosystem was associated with responses (ratios > mean of the cohort), LEfSe was used to identify the taxonomic changes segregating R versus NR to exogenous Akk. These species were compared with the bacteria in human stools described in Extended Data Fig. 1 and Fig. 3a.

Akk CSUR p2261 was provided by the Institut hospitalo-universitaire Méditerranée Infection, Marseille, France. Akkp2261 was grown on 5% sheep blood enriched Columbia agar (COS) plates in an anaerobic atmosphere created using 3 anaerobic generators (BioMerieux) at 37 °C for at least 72 hours. Identification of the bacterium was performed using a Matrix-Assisted Laser Desorption/Ionization Time of Flight (MALDI-TOF) mass spectrometer (Microflex LT analyzer, Bruker Daltonics). Colonization of ATB pre-treated mice was performed by oral gavage with 100 µl of suspension containing 1×10^8 bacteria obtained from a suspensions of 1×10^9 CFU/ml using a fluorescence spectrophotometer (Eppendorf) at an optical density of 600 nm in PBS. Five bacterial gavages were performed for each mouse: the first 24 hours before the first injection of anti-PD-1 monoclonal antibodies and, subsequently, four times on the same day of ICI.

Mouse fecal DNA extraction and microbiota characterization. Feces were collected from each mouse and group for metagenomics between 7 and 14 days after start of immunotherapy. Samples were stored at −80 °C until processing. Preparation and sequencing of mouse fecal samples was performed at IHU Méditerranée Infection, Marseille, France. Briefly, DNA was extracted using two protocols. The first protocol consisted of physical and chemical lysis using glass powder and proteinase K, respectively, then processing using the Macherey-Nagel DNA Tissue extraction kit (Duren). The second protocol was identical to the first protocol, with the addition of glycoprotein lysis and deglycosylation steps. The resulting DNA was sequenced, targeting the V3–V4 regions of the 16S rRNA gene. Raw FASTQ files were analyzed with Mothur pipeline v.1.39.5 for quality check and filtering (sequencing errors, chimerae) on a Workstation DELL T7910. Raw reads were filtered and clustered into Operational Taxonomic Units (OTUs), followed by elimination of low-populated OTUs (until 5 reads) and by de novo OTU picking at 97% pair-wise identity using standardized parameters and SILVA rDNA Database v.1.19 for alignment. A prevalence threshold of ≥2.5% was implemented for statistical analyses on recognized OTUs, performed with Python v3.8.2. The most representative and abundant read within each OTU (as evidenced in the previous step with Mothur v.1.39.5) underwent a nucleotide blast using the National Center for Biotechnology Information (NCBI) Blast software (ncbi-blast-2.9.0) and the latest NCBI 16S Microbial Database (ftp://ftp.ncbi.nlm.nih.gov/blast/db/). A matrix of bacterial relative abundances was built at each taxon level (phylum, class, order, family, genus, species) for subsequent multivariate statistical analyses.

Statistical analyses. In humans, data matrices were firstly normalized then standardized using QuantileTransformer and StandardScaler methods from Sci-Kit learn package v0.20.3. Normalization using the output_distribution = 'normal' option transforms each variable to a strictly Gaussian-shaped distribution, while the standardization results in each normalized variable having a mean of zero and variance of one. These two steps of normalization followed by standardization ensure the proper comparison of variables with different dynamic ranges, such as bacterial relative abundances. For microbiota analysis, measurements of α diversity (within-sample diversity) such as Richness and Shannon index, were calculated at species level using the SciKit-learn package v.0.4.1. Exploratory analysis of β-diversity (between-sample diversity) was calculated using the Bray–Curtis measure of dissimilarity and represented in Principal Coordinate Analyses (PCoA), along with methods to compare groups of multivariate sample units (analysis of similarities (ANOSIM), permutational multivariate analysis of variance (PERMANOVA)) to assess significance in data points clustering. ANOSIM and PERMANOVA were automatically calculated after 999 permutations, as implemented in SciKit-learn package v0.4.1. We implemented partial least square discriminant analysis (PLS-DA) and the subsequent variable importance plot (VIP) as a supervised analysis wherein the VIP values (order of magnitude) are used to identify the most discriminant bacterial species. All the analyses were performed within a Python v3.8.2 environment. Univariate differential abundance analysis was performed via linear discriminant analysis of effect size (LEfSe)[61]. We added further support of differentially abundant species using two different multivariate differential abundance methods, ANCOM-BC[62] and MaAsLin2[63], which included covariates such as age, sex, BMI, cohort, and sequencing batch. France's Data Protection Article 8 legislation (Commission Nationale Informatique et Libertés) prohibits the analysis of the racial and ethnic origins. Raw sequencing counts were estimated from species-level MetaPhlAn 3 relative abundances by multiplying these values by the total number of reads for each sample and these were used in ANCOM-BC (v.1.0.1) with default parameters, a library size cutoff of 500 reads and no structural zero detection. Masslin2 (v.1.4.0) was run using Logit-transformed relative abundances that were normalized with total-sum-scaling (TSS) and using the variable of interest as a fixed effect.

Survival curves were estimated using the Kaplan–Meier method and compared with the log-rank test (Mantel–Cox method) in a univariate analysis. Multivariate analyses were performed using Cox regression models to determine HRs and 95% confidence intervals (CIs) for OS, adjusting for other clinicopathologic features. The proportionality hazard assumption was checked testing the trend of the Schoenfeld residuals with the cox.zph R function. When the test was statistically significant for a variable, its interaction with time was introduced in the model and tested using the tt (time transformation) function with different functional forms (linear, exponential, logarithmic, and penalized spline). The optimal cutoff for each bacterial species to define different prognosis groups was obtained with grid search algorithm based on the multivariate Cox model to take into account the potential confounding factors (such as age and sex). The grid was defined for each species by the percentiles of the distribution of the non-zero prevalence values. The cutoff corresponding to the model with the better Akaike information criterion (AIC, lower is better) was selected as the optimal cutoff.

All tests were two-sided and statistical significance was set at $P < 0.05$. Statistical analyses were conducted using the GraphPad Prism 7 and R software (http://www.R-project.org/).

In mice, all tumor growth curves were analyzed using software developed in Kroemer's laboratory: https://kroemerlab.shinyapps.io/TumGrowth/. Between-group comparisons of mice and global comparisons were performed using a Kruskall–Wallis test and post-hoc multiple comparisons using Dunn's test. Finally, natural tumor growth data deriving from mice experiments (6 mice per experiment) were averaged for each timepoint (T0 to T8), then longitudinally normalized on the first timepoint, in order to have a common starting value of 1. All averaged and normalized tumor values were then expressed with fold ratios (FR; Extended Data Fig. 6E), and underwent base 2 logaritmization in order to enhance augmentation (red) or diminution (blue) of the tumor growth. A hierarchical clusterization analysis based on Bray–Curtis distance was implemented on longitudinal FR data in order to define a branch of responder to Akkp2261 (Extended Data Fig. 6E, green cluster) or a group of non-responder to Akkp2261 (Extended Data Fig. 6E, red cluster). A reported P values (i.e., $^*P \leq .05$, $^{**}P \leq .01$, $^{***}P \leq .001$) underwent Benjamini–Hochberg two-stage false-discovery rate (FDR) at 10%.

Reporting Summary. Further information on research design is available in the Nature Research Reporting Summary linked to this article.

Data availability

The data generated or analyzed during this study are included within the paper, its Supplementary Information files and public repositories. Detailed information on the cohort is available in Supplementary Table 8 raw metagenomic sequences are available in the SRA under the Bioproject accession PRJNA751792 (https://www.ncbi.nlm.nih.gov/bioproject/PRJNA751792) and PRJNA782662 (https://www.ncbi.nlm.nih.gov/bioproject/PRJNA782662), and raw RNA sequencing are available in the SRA under accession the NCBI accession GSE182328 (https://www.ncbi.nlm.nih.gov/geo/query/acc.cgi?acc=GSE182328). All BioSample (PATIENTS_Metadata.csv) are also provided as supplementary information. Source data are provided with this paper.

Code availability

No unique software or computational code was created for this study. Code detailing implementation of established tools/pipelines are described in details in the Method section and available upon request to the corresponding author.

References

55. Eisenhauer, E. A. et al. New response evaluation criteria in solid tumours: revised RECIST guideline (version 1.1). *Eur. J. Cancer* **45**, 228–247 (2009).
56. Li, J. et al. An integrated catalog of reference genes in the human gut microbiome. *Nat. Biotechnol.* **32**, 834–841 (2014).
57. Nielsen, H. B. et al. Identification and assembly of genomes and genetic elements in complex metagenomic samples without using reference genomes. *Nat. Biotechnol.* **32**, 822–828 (2014).
58. Beghini, F. et al. Integrating taxonomic, functional, and strain-level profiling of diverse microbial communities with bioBakery 3. *Elife* **10**, e65088 (2021).
59. Fumet, J.-D. et al. Prognostic and predictive role of CD8 and PD-L1 determination in lung tumor tissue of patients under anti-PD-1 therapy. *Br. J. Cancer* **119**, 950–960 (2018).
60. Bray, N. L., Pimentel, H., Melsted, P. & Pachter, L. Near-optimal probabilistic RNA-seq quantification. *Nat. Biotechnol.* **34**, 525–527 (2016).
61. Segata, N. et al. Metagenomic biomarker discovery and explanation. *Genome Biol.* **12**, R60 (2011).
62. Lin, H. & Peddada, S. D. Analysis of compositions of microbiomes with bias correction. *Nat. Commun.* **11**, 3514 (2020).
63. Mallick, R. et al. Subduction initiation and the rise of the Shillong Plateau. *Earth Planet. Sci. Lett.* **543**, 116351 (2020).

Acknowledgements

L. Z. and B. B. were funded by the RHU Torino Lumière (ANR-16-RHUS-0008), while L. Z. was supported by H2020 ONCOBIOME and ANR, French–German Ileobiome, 19-CE15-0029-01. L. Z. and G. K. received a donation from Seerave Foundation. L. Z., L. D., and E. D. were supported by the SIRIC Stratified Oncology Cell DNA Repair and Tumor Immune Elimination (SOCRATE). L. D. and L. Z. were supported by SIGN'IT 2020 ARC foundation. This work was also supported by the Prism project funded by the Agence Nationale de la Recherche under grant number ANR-18-IBHU-0002.
L. Z. and G. K. were supported by the Ligue contre le Cancer (équipe labelisée); ANR Projets blancs; ANR under the frame of E-Rare-2, the ERA-Net for Research on Rare Diseases; Association Pour La Recherche Sur Le Cancer (ARC); Bristol-Myers Squibb (BMS) (International Immuno-Oncology Network), Cancéropôle Ile-de-France; Chancellerie des Universités de Paris (Legs Poix), Fondation pour la Recherche Médicale (FRM); a donation by Elior; the European Commission (ArtForce); the European Research Council (ERC); Fondation Carrefour; Institut National du Cancer (INCa); Inserm (HTE); Institut Universitaire de France; LeDucq Foundation; the LabEx Immuno-Oncology; FHU CARE, Dassault, and Badinter Philantropia, and the Paris Alliance of Cancer Research Institutes (PACRI). B. R. is supported by the Canadian Institutes of Health Research (CIHR), Institut du cancer de Montreal and the Prefontaine family. A. C. is supported by the CPRIT Research Training Program (RP170067). N. S. was supported by the European Research Council (ERC-STG project MetaPG-716575); MIUR 'Futuro in Ricerca' (grant No. RBFR13EWWI_001); the European H2020 program (ONCOBIOME-825410 project and MASTER-818368 project); the National Cancer Institute of the National Institutes of Health (1U01CA230551); by the Premio Internazionale Lombardia e Ricerca 2019 to G. K. A. M. has been or is currently an investigator in clinical trials sponsored by BMS, MSD, GlaxoSmithKline (GSK)/Tesaro, Janssen, Roche/Genentech, Pfizer, AstraZeneca, Amgen. A. M. has been or is currently a member of Clinical Trial Scientific Steering Committee for AstraZeneca and GSK.
A. M. has been or is currently a member of the scientific advisory board of the following companies: Merck Serono, Novartis, BMS, Symphogen, Amgen, Tesaro/GSK, Pfizer, AstraZeneca/Medimmune, Servier, and Sanofi. A. M. has provided scientific and medical consulting to the following companies: Roche, Sanofi. A. M. is a member of the data safety and monitoring board for trial NCT02423863 (TLR3 agonist; Oncovir). A. M. has received research funding and/or drug supply for preclinical and clinical research projects from: BMS, Boehringer Ingelheim, Idera, MSD, Fondation MSD Avenir, and SIRIC (INCa-DGOS-Inserm_12551).

Author contributions

L. Z., L. D., B. R., and B. B. conceived the study. L. D. and B. R. orchestrated the ONCOBIOTICS study. B. B. coordinated the clinical inclusions. L. D., G. Z., S. F., J. M., C. A.-V., D. M.-S., F. Goldwasser, A. S., H. P., F. Ghiringhelli, F. B., D. P., S. M., N. B., B. B., and J. C. S. enrolled patients and managed patient stool collection. L. D., C. A. C. S., M. B., S. T., and B. R. coordinated the ONCOBIOTICS network for stool traceability and data collection and management. F. B.-D. recovered the Tumor Mutational Burden. F. C., A. B., and N. S. worked on the new markers for Akk in MetaPhlAn 3. R. B. and S. C. worked on RNA-seq. A. M. T., V. I., and N. S. interpreted the MG analyses and performed independent statistical analyses. C. R. O. Absilon planned the data management and kept the electronic files. D. D. double checked the statistical analyses. L. D., A. D., B. R., and M. M. designed the figures. R. D. and L. D. managed mice experiments. E. L. C., L. A., N. P., N. G., H. R., managed the sequencing of stool samples G. K. participated in data interpretation and edited the paper. All authors participated in paper editing.

Competing interests

L. Z. received research contract from Kaleido and Innovate Pharma and Pilege. L. D. has consulted for and had an advisory role for BMS and Sanofi and was supported by Philantropia Fondation Gustave Roussy. G. Z. received a research grant from Fondation Roche, received fees from Roche, MSD, BMS, and Astra-Zeneca, and is consultant for Da Volterra and Inventiva. L.Z and R.D. are the scientific cofounders of Everimmune. E. D. reports grants and personal fees from Roche Genentech, grants from Boehringer, grants from AstraZeneca, grants and personal fees from Merck Serono, grants from BMS, and grants from MSD. P. D. has had consulting and advisory roles for AstraZeneca, BMS, Boehringer Ingelheim, Celgene, Daiichi Sankyo, Eli Lilly, Merck, Novartis, Pfizer, prIME Oncology, Peer CME, Roche, and Samsung, as well as honoraria from AstraZeneca, BMS, Boehringer Ingelheim, Celgene, Eli Lilly, Merck, Novartis, Pfizer, prIME Oncology, Peer CME, Roche, and Samsung. P. D. ran clinical trials as principal or co-investigator for AstraZeneca, BMS, Boehringer Ingelheim, Eli Lilly, Merck, Novartis, Pfizer, Roche, Medimmun, Sanofi-Aventis, Taiho Pharma, Novocure, and Daiichi Sankyo, and has received travel or accommodation expenses from AstraZeneca, Roche, Novartis, prIME Oncology, and Pfizer. F. G. received honoraria from Amgen, Sanofi, Merk Serono, MSD, BMS, and AstraZeneca, had a consultancy or advisory role for Roche and Enterome, and received direct research fundings from Roche, Enterome, AstraZeneca, and Servier and traveling support from Servier, Amgen, and Roche. J. C. S. in the last 2 years has received consultancy fees from Relay Therapeutics and Gritstone and holds shares of Hookipa, Gritstone, AstraZeneca, and Daiichi Sankyo, and was a full time employee for AstraZeneca in 2017–2019. The remaining authors declare no competing interests.

Additional information

Extended data is available for this paper at https://doi.org/10.1038/s41591-021-01655-5.

Supplementary information The online version contains supplementary material available at https://doi.org/10.1038/s41591-021-01655-5.

Correspondence and requests for materials should be addressed to Laurence Zitvogel.

Peer review information *Nature Medicine* thanks Christian Jobin, Anna Heintz-Buschart, and the other, anonymous, reviewer(s) for their contribution to the peer review of this work. Javier Carmona was the primary editor on this article and managed its editorial process and peer review in collaboration with the rest of the editorial team.

Reprints and permissions information is available at www.nature.com/reprints.

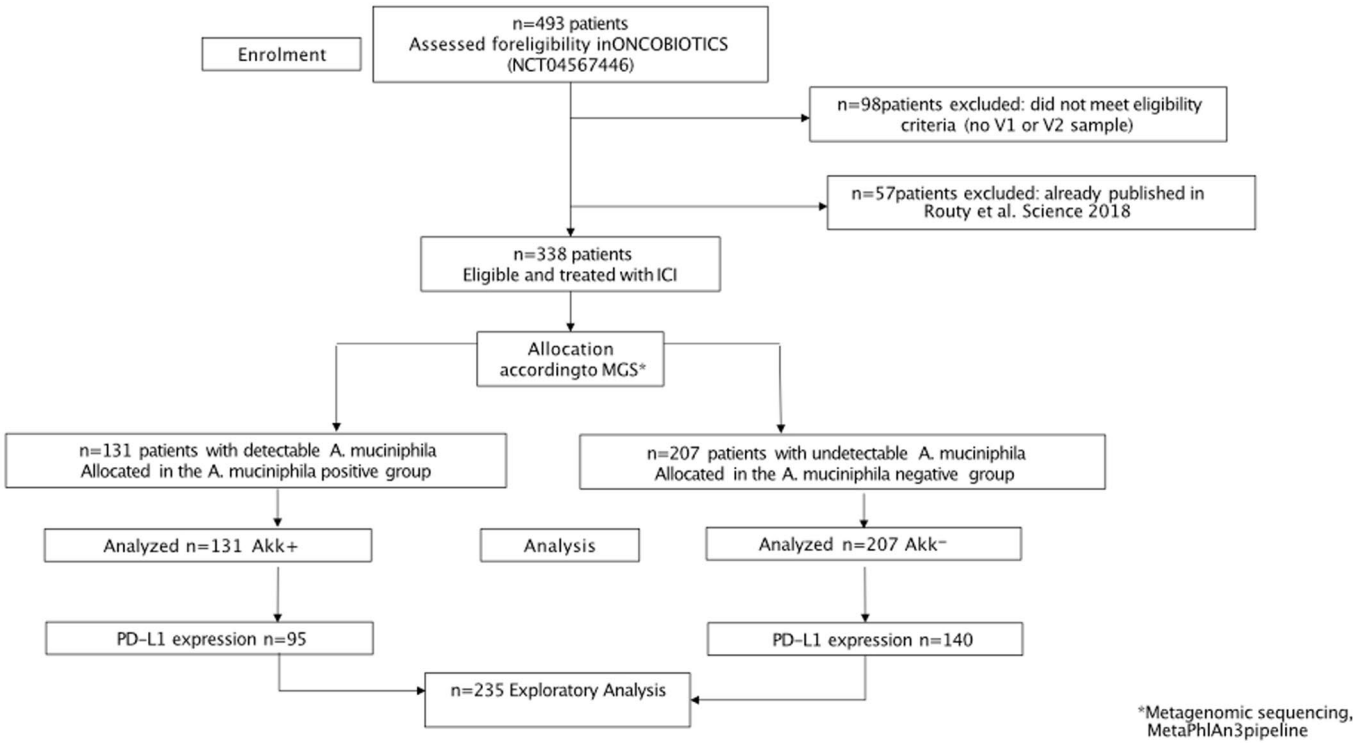

Extended Data Fig. 1 | Consort diagram describing the stool collection in the whole NSCLC ONCOBIOTICS cohort. Consortium diagram for patients enrollment in the ONCOBIOTICS study (n=493) according to stool availability, presence of *Akkermansia muciniphila (Akk)*, and tumor PD-L1 expression levels. V1; baseline fecal sample. V2; before the second injection of the immune checkpoint inhibitor; MGS: Metagenomic Sequencing. Akk^{+}: detection of *Akk;* Akk^{-}: no detection of *Akk* by shotgun metagaenomics sequencing (MGS) analysis at diagnosis.

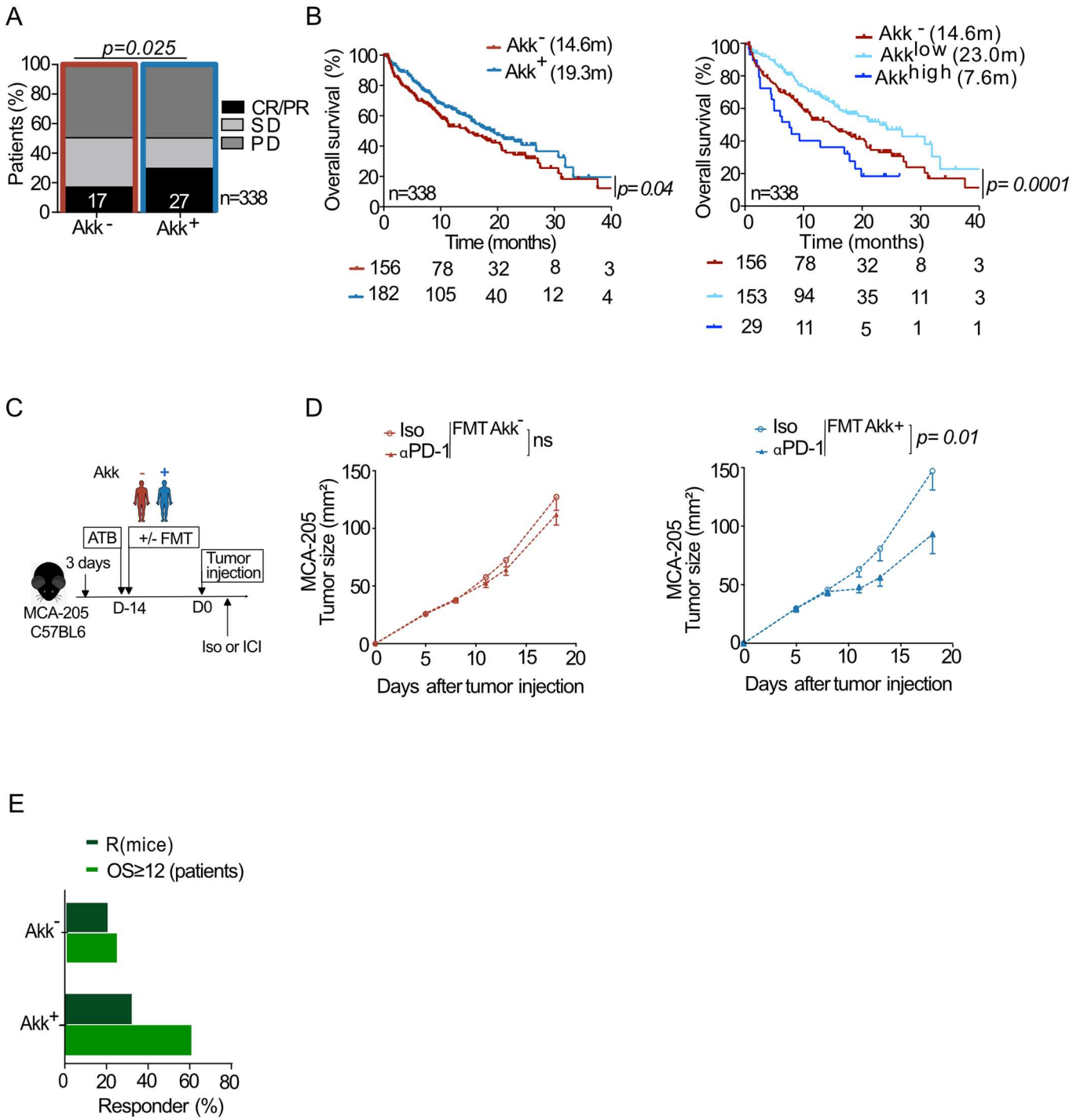

Extended Data Fig. 2 | MetaOMineR-based analysis of the association between stool *A. muciniphila (Akk)* and clinical benefit to ICI in patients. A-B. Correlations between stool prevalence of *Akk* (MetaOMineR pipeline) and ORR **(A)** or OS **(B)** in 1+2L NSCLC patients (N=338, **A-B**) based on MGS identification of Akk in the MetaOMineR algorithm (INRAE). Chi-square test (**A**) and Cox regression analysis for median overall survival (OS) depicted in Kaplan Meier curves according to detectable or undetectable *Akk* (Akk$^+$ or Akk) analyzed in 2 groups (**B**, left panel) or segregated in 3 groups (Akk$^-$, Akk^{low} and Akk^{high}) (**B**, right panel). Chi-square test *P*-values are two-sided, with no adjustments made for multiple comparisons (A). The Akk status was compared using the stratified log-rank test. *P*-values are one-sided with no adjustment (B). **C**. Experimental setting of avatar mice. FMT of NSCLC patients (Supplementary Table S3) segregated according to the presence or absence of *Akk* into MCA-205 tumor bearing C57BL/6 mice. Treatments are indicated by arrows (ATB, FMT, anti-PD-1 (ICI) mAbs, or isotype control mAbs (Iso)). **D**. MCA-205 tumor growth kinetics in each group of FMT according to the prevalence of *Akk*. in isotype Ctl *versus* anti-PD-1 mAbs treated mice. Data are presented as mean values +/-SEM of tumor sizes within 6 animals/group. Concatenation of at least n=8 experiments (using a different stool of NSCLC patient) containing 6 mice/group. Tumor sizes according to FMT Akk$^-$ (**D**, left panel) versus Akk+ (**D**, right panel) are depicted, each dot representing one mouse. Statistics were mixed-effect modeling with specific software ((https://kroemerlab.shinyapps.io/TumGrowth/) for longitudinal tumor growth analysis. *P*-value are indicated. **E**. Percentages of responding mice (tumor reduction of>25 % compared with means of controls in the anti-PD-1 mAbs -treated group) and patients (ORR) in each category of stools used for FMT (derived from patients in Supplementary Table S3). CR; complete response. PR; partial response, SD; stable disease, PD; progressive disease.

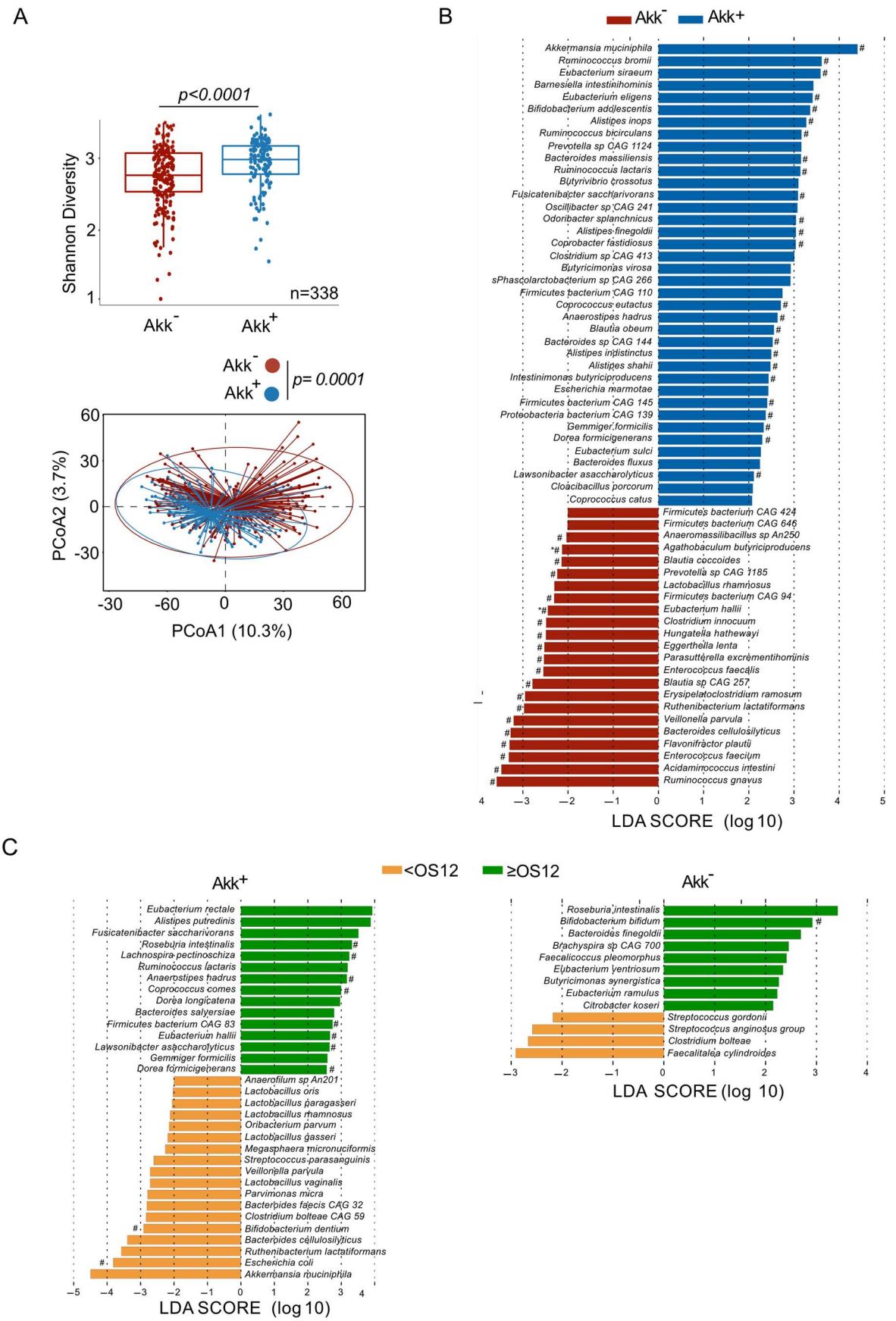

Extended Data Fig. 3 | See next page for caption.

Extended Data Fig. 3 | Metagenomic species characterizing *Akk*$^+$ stools and patient survival. Shannon diversity index representing stool alpha diversity in Akk$^+$ and Akk$^-$ groups of fecal specimens (N=338) (**A**, upper panel). Beta-diversity measured by Bray-Curtis Index represented by Principal Coordinates analysis (PCoA) between Akk$^+$ *versus* Akk$^-$ groups in the whole cohort of 1+2L (**A**, lower panel). *p*-values were calculated using PERMANOVA with 999 permutations. The lower and the upper hinges of boxplots corresponds to the 25th and 75th percentiles, respectively. The midline is the median. The upper and lower whiskers extend from the hinges to the largest (or smallest) value no further than ×1.5 interquartile range from the hinge, defined as the distance between the 25th and 75th percentiles. *P*-values were calculated testing the null hypothesis and using a two-sided test. Exact *p*-value: 3.84573e-05. **B-C**. Differential abundance of metagenomic species measured by linear discriminant analysis of effect size (LEfSe) according to the presence of *A. muciniphila (Akk)* **(B)** and the OS at 12 months **(C)** within Akk+ group (**C**, left panel) and Akk- group (**C**, right panel). LDA; Linear discriminant analysis. OS: overall survival. *P*-values were calculated using a two-sided nonparametric factorial Kruskal-Wallis (KW) sum-rank test. # Multivariate analysis (ANCOM-BC/ Maaslin2) with a false discovery rate (FDR) adjusted *p*-value <0.2.

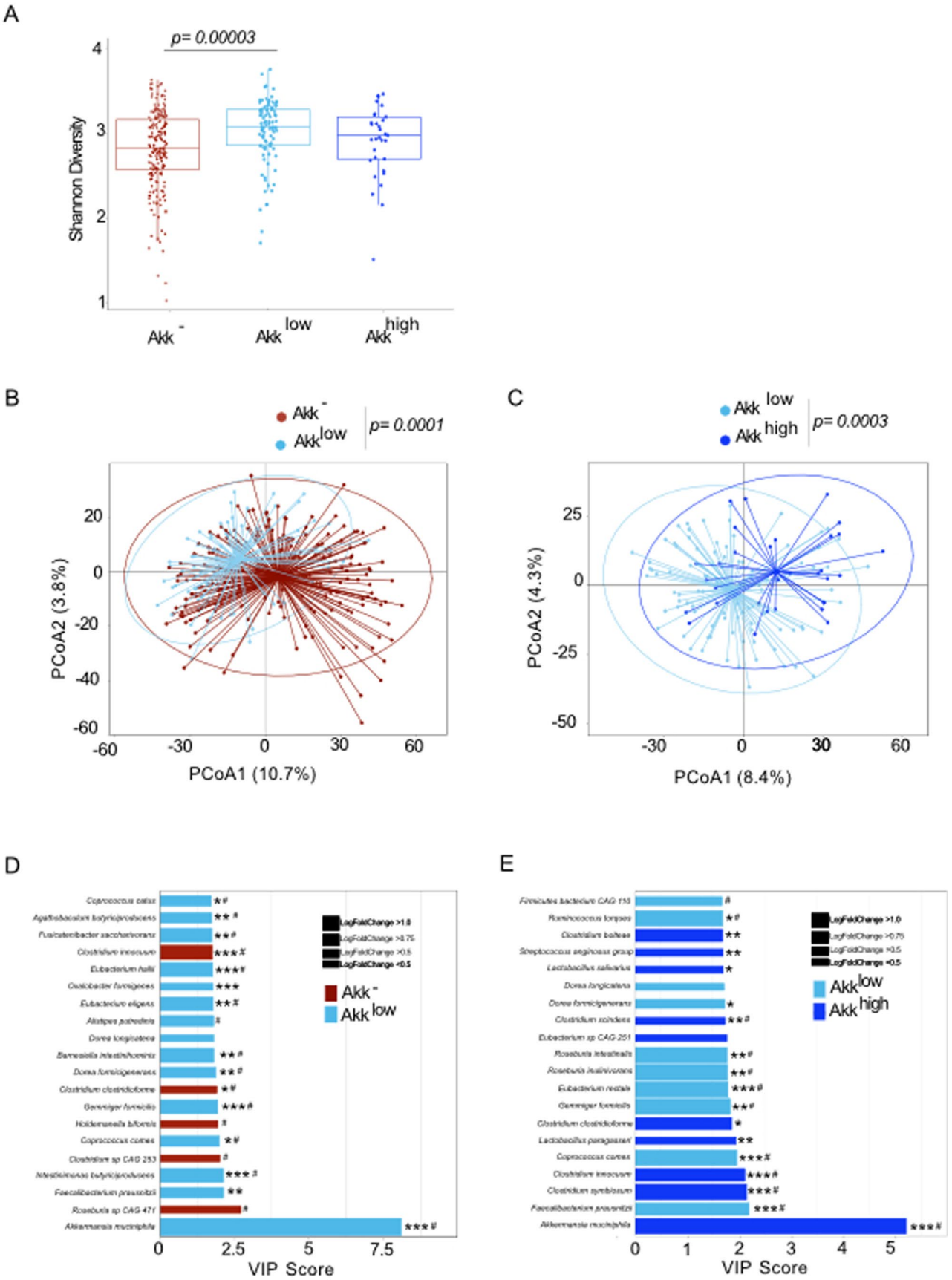

Extended Data Fig. 4 | See next page for caption.

Extended Data Fig. 4 | Compositional taxonomic differences in stools of NSCLC patients segregated according to Akk relative abundance. A. Alpha diversity according to *Akk* relative abundance segregated in 3 groups Akk^{-}: undetectable *Akk*, Akk^{low}: *A. muciniphila* relative abundance between 0.035-4.799% (<77th percentile of positive samples), and Akk^{high}: 4.799% (> 77th percentile) (N=338). The lower and upper hinges of boxplots correspond to the 25th and 75th percentiles, respectively. The midline is the median. The upper and lower whiskers extend from the hinges to the largest (or smallest) value no further than ×1.5 interquartile range from the hinge, defined as the distance between the 25th and 75th percentiles. *P*-values were calculated using a two-sided nonparametric Wilcoxon sum-rank test. **B-C**. Beta-diversity using PCoA between Akk^{-} and Akk^{low} (**B**) and between Akk^{low} and Akk^{high} (**C**) *p*-values were calculated using PERMANOVA with 999 permutations. The PERMANOVA test compares groups of objects and tests the null hypothesis that the centroids and dispersion of the groups are equivalent. The *P*-value is calculated by comparing the actual F test to that gained from (in this case 999) random permutations of the objects between the groups. If p <0.05, the null hypothesis is disregarded and we conclude that the centroids and dispersion between the groups are not equivalent. **D-E**. Variable importance plot (VIP) discriminant analysis of taxonomic stool composition according to Akk relative abundance, between Akk^{-} versus Akk^{low} (**D**) and Akk^{low} versus Akk^{high} (**E**). Differences in bacterial prevalence and abundance in fold ratios are indicated in these VIP plots. VIP: Variable importance plot. * p <0.05,** p <0.01, *** p <0.001. *P*-values were calculated using a two-sided nonparametric Wilcoxon sum-rank test. # Multivariate analysis (ANCOM-BC/Maaslin2) with a false discovery rate (FDR) adjusted *p*-value <0.2.

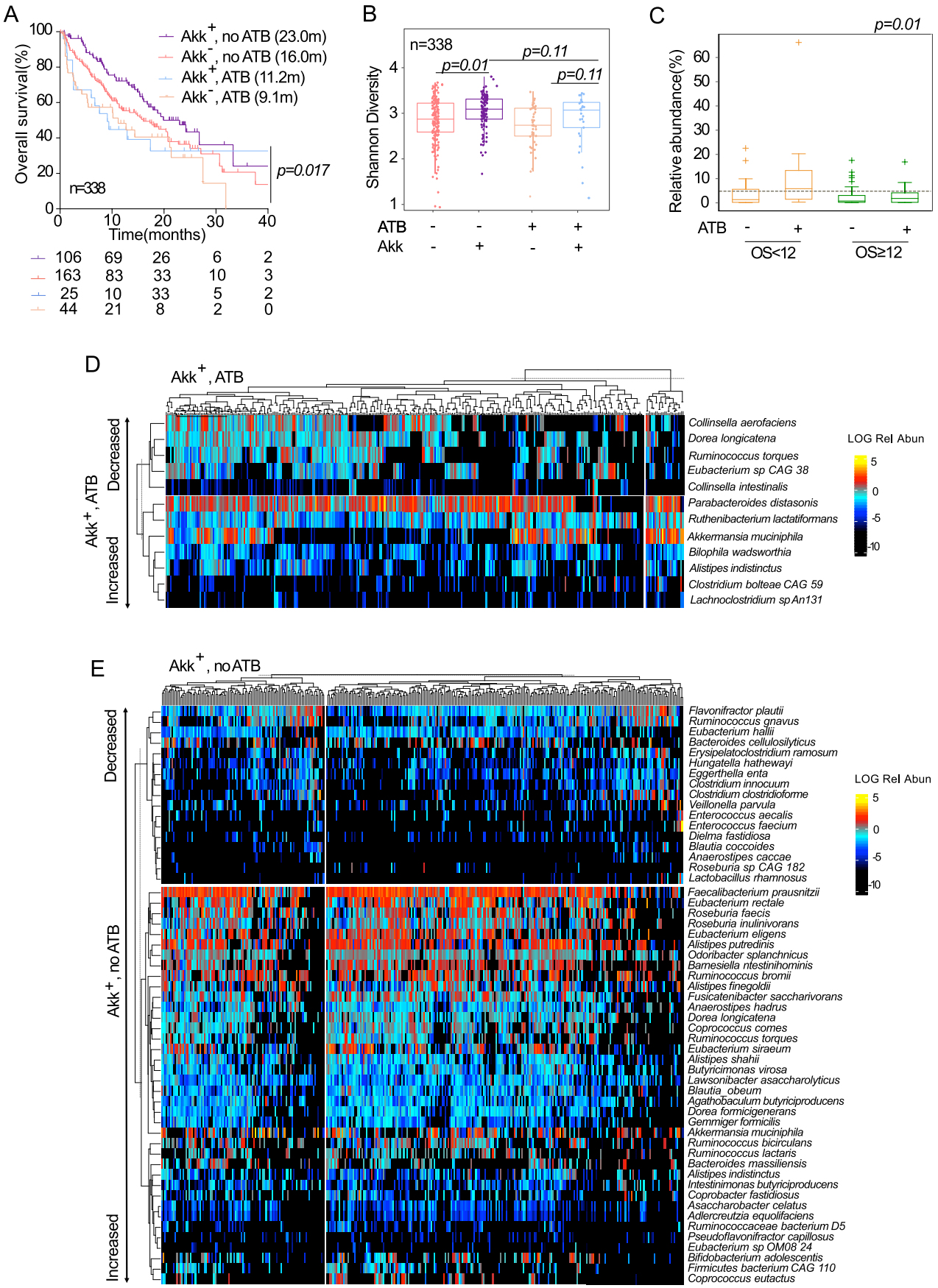

Extended Data Fig. 5 | See next page for caption.

Extended Data Fig. 5 | Interaction between ATB and *A.muciniphila* on survival and microbiome composition. A. Kaplan-Meier curve and Cox regression analysis of overall survival in the n=338 patients according to detectable *versus* undetectable *Akk* (Akk^+ and Akk^-) and ATB use (noATB: no exposure to ATB, ATB: antibiotics exposure within 2 months prior to ICI initiation). The Akk status and ATB use were compared using the stratified log-rank test. *P*-values are one-sided with no adjustment. **B**. Shannon diversity index representing stool alpha diversity in Akk^+ and Akk^- groups of fecal specimen from patients exposed or not to ATB (N=338). The lower and upper hinges of boxplots correspond to the 25th and 75th percentiles, respectively. The midline is the median. The upper and lower whiskers extend from the hinges to the largest (or smallest) value no further than ×1.5 interquartile range from the hinge, defined as the distance between the 25th and 75th percentiles. *P*-values were calculated using a two-sided nonparametric Wilcoxon sum-rank test. **C**. Box Plots representing the relative abundance (mean+/-SEM) of *Akk* according to overall survival at 12 months and exposure or not to ATB in n=338 patients. The lower and upper hinges of boxplots correspond to the 25th and 75th percentiles, respectively. The midline is the median. The upper and lower whiskers extend from the hinges to the largest (or smallest) value no further than ×1.5 interquartile range from the hinge, defined as the distance between the 25th and 75th percentiles. The test used was Kruskal-Wallis, two-sided, 5% level of significance. No adjustments were made for multiple comparisons. **D**. Heatmap showing differentially abundant species identified in stools with detectable *Akk* (Akk^+) in patients exposed to (D) or not exposed to (E) ATB within 2 months prior to ICI initiation. Species were identified using a non-parametric Kruskall-Wallis test comparing 4 groups made up of 2 variables: *Akkermansia muciniphila* presence/absence and antibiotic use. The figure shows species' abundances across samples whose False Discovery Rate (FDR) was <0.2 in the KW test and whose Wilcoxon Rank Sum Test *p*-value was <0.05 when comparing the highlighted group to the rest.

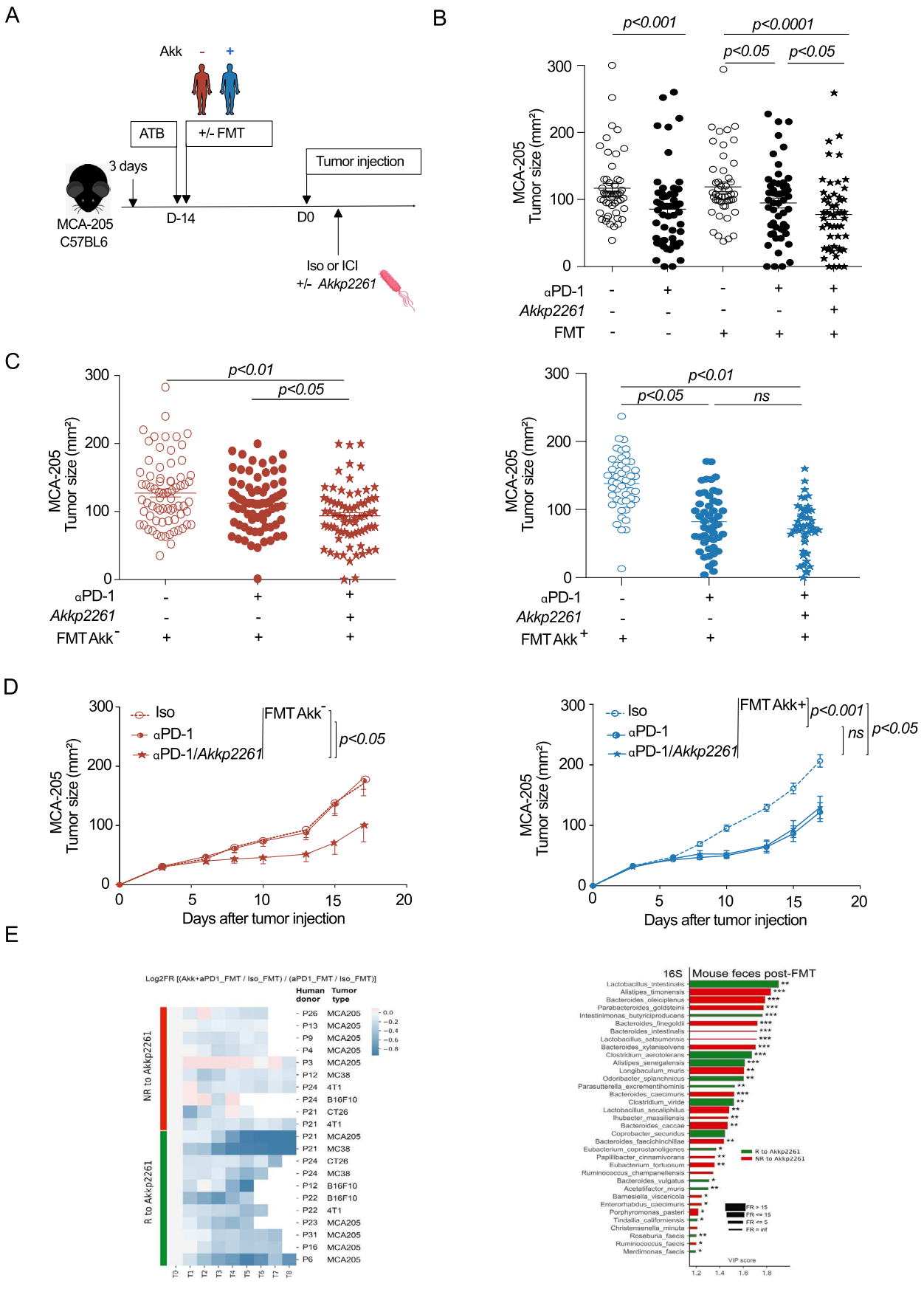

Extended Data Fig. 6 | See next page for caption.

Extended Data Fig. 6 | *Akkp2261* modulated the murine microbiome composition, rescuing responsiveness to PD-1 blockade. A. Experimental setting. After 3 days of ATB, FMT was performed in mice by oral gavage using patient stools classified according to *Akk* (Akk^+ and Akk^-). 14 days later, MCA-205 tumors were i.d inoculated, and mice were treated with anti-PD-1 or iso-control mAbs 4 times every 3 days concomitantly with oral supplementation of *Akkp2261* four times every 3 days. **B-D**. Mean MCA-205 tumor sizes+/-SEM are depicted at day 12 after 4 therapeutic injections of anti-PD-1 mAbs, in each FMT groups (Akk^+ and Akk^-) supplemented or not with *Akkp2261* as well as in animals reared in SPF conditions (FMT-). Concatenation of>25 experiments using n=53 mice in Iso group, n=51 in Iso FMT+ group, n=56 in anti-PD-1 and anti-PD-1 FMT+ groups. Each experiment comprising 6 mice/group and was performed at least 2 times for each FMT (Supplementary Table S6) **(B)**. Tumor sizes according to FMT Akk^- **(C left**, n=72/group; **C right**, n=49 in Iso group and n=48 in other groups) *versus* Akk^+ **(D left**, n=6/group**, D right**, n=12 in Iso and anti-PD-1 groups, n=14 in anti-PD-1 with *Akkp2261***)** are depicted, each dot representing one mouse. Statistics were mixed-effect modeling with specific software ((https://kroemerlab.shinyapps.io/TumGrowth/) for longitudinal tumor growth analysis **(D)** and Mann–Whitney U-test **(B-C)** to compare two independent groups (after Kruskal–Wallis test was implemented using Dunn's test for multiple groups). ns=not significant. **E**. Clustermap of ratios of *Akkp2261*-related tumor reduction at day 12-15 following PD-1 mAbs in FMT normalized onto ratios obtained in SPF mice. The relative tumor size reduction follows a blue color code (the darker the greater; R, Responders)). 29 FMT were performed according to A. N=29-30 mice/group in total. Each experiment contained 6 mice/group and was performed 2-3 times for each tumor model (**E**, left panel). 16S rRNA sequencing of gene amplicons of stools harvested in recipient avatar tumor bearers at day 12 post-4 injections of anti-PD-1 Abs and 4 oral gavages with *Akkp2261* divided into green (R) and red (NR) groups. VIP plot repartition of discriminant metagenomic species segregating groups of mice that responded to oral *Akkp2261* (R, green bars) or not (NR, red bars). (E, right panel). Asterisks represent significant Mann-Whitney U test without FDR at 10%. * p <0.05, ** p <0.01, *** p <0.001. P-values were calculated using a two-sided nonparametric Wilcoxon sum-rank test. Adjustments for multiple comparisons were not made.

8.1.4 Article III (see also Appendix, Abstracts IV and VI).

Title: Custom scoring based on ecological topology of gut microbiota associated with cancer immunotherapy outcome

Submitted to: Cell (August, 2023).

Lisa Derosa#, Valerio Iebba#, **Carolina Alves Costa Silva**#, Bertrand Routy, Gianmarco Piccinno, Guojun Wu, Cassandra Thelemaque, Meriem Messaoudene, Andrew Maltez Thomas, Gerard Zalcman, Sylvie Friard, Julien Mazieres, Clarisse Audigier-Valette, Denis Moro-Sibilot, François Goldwasser, Arnaud Scherpereel, Hervé Pegliasco, François Ghiringhelli, Nicole Bouchard, Cissé Sow, Ines Darik, Silvia Zoppi, Pierre Ly, Anna Reni, Leonardo Lordello, Romain Daillère, Fabrice Barlesi, Eric Deutsch, Karla A. Lee, Laura A. Bolte, Johannes R. Björk, Rinse K. Weersma, Morten Isaksen, Lucas Padilha, Ana Finzel, Bernard Escudier, Laurence Albiges, David Planchard, Fabrice André, Stéphanie Martinez35, Benjamin Besse, Liping Zhao, Nicola Segata, Jérôme Wojcik, Guido Kroemer, Laurence Zitvogel.
# contributed equally

Although specific gut microbial species have been associated with beneficial responses such as *Akkermansia muciniphila*, no consensus exists on a definition and diagnostic tool of dysbiosis to clinical routine use.

Based on fecal MGS data from a retrospective discovery cohort of 245 patients with advanced NSCLC treated with ICB, we constructed co-abundance taxonomic networks that were clustered into species interacting groups (SIG) (Fig. 13, 14A) correlating with overall survival (OS) (Fig 14B). Thirty-seven and fourty five MGS species belonged to the clusters associated with resistance (SIG1) and response (SIG2) to ICB, respectively. For each patient, we calculated the SIG1/SIG2 ratio, considering the number of microbial species in each SIG present in the baseline stool sample (Fig. 14C). When this ratio was poorly discriminant ("grey zone", Fig. 14A), we integrated the *Akk* trichotomic stratification, to obtain a final "TOPOSCORE" (Fig. 14C).

Patients into SIG2+ experience improved OS (Fig. 14D), the benefit was sustained in a validation cohort of 254 patients with NSCLC

and in a third cohort of 216 RCC and UC amenable to ICB. Finally, we translated the 80 MGS-based TOPOSCORE into a 21 bacterial probe set qPCR-based scoring (Fig. 14E) that could become a user-friendly diagnostic tool of gut dysbiosis to select patients for MCI.

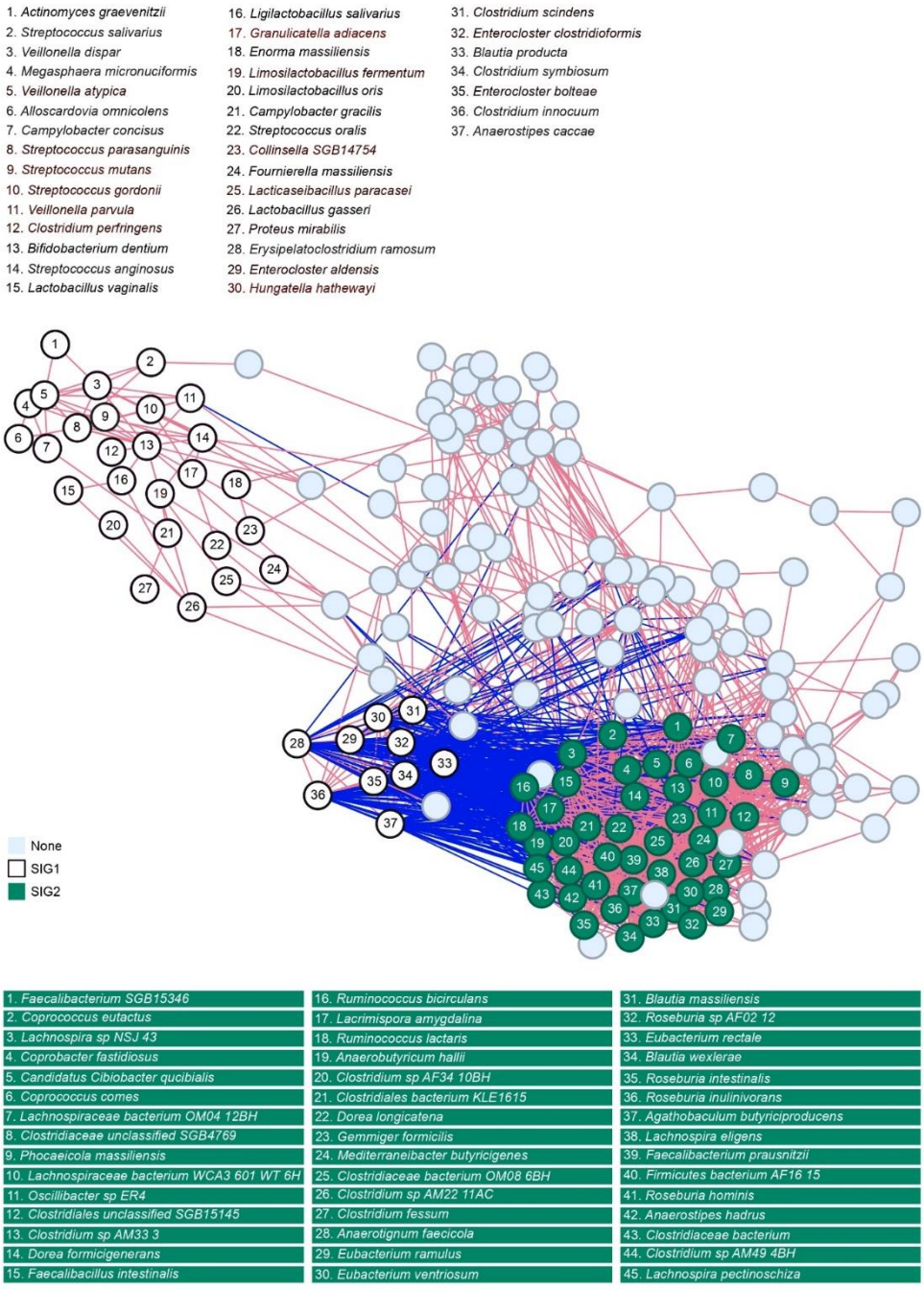

Figure 13 Co-abundance networks and Species Interacting Groups (SIG) associated with response or resistance to ICI.

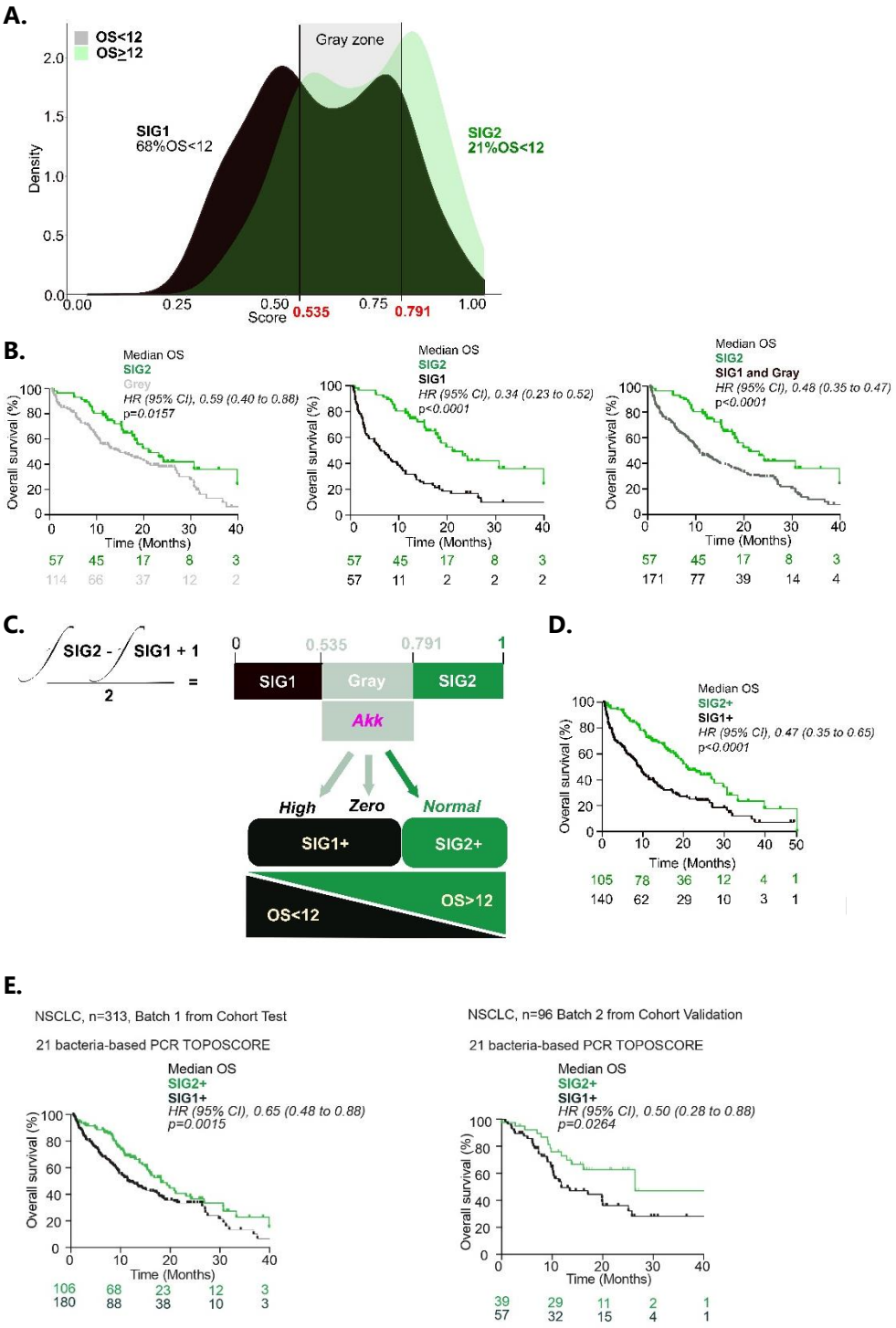

Figure 14 Friendly-user score assessing gut dysbiosis and benefit to immune-checkpoint blockade.

8.2 Soluble MAdCAM-1: a new prognostic biomarker for patients with cancer

8.2.1 Article IV

Title: A microbiota-modulated checkpoint directs immunosuppressive intestinal T cells into cancers.

Published on: Science. 2023 Jun 9;380(6649):eabo2296.
doi: 10.1126/science.abo2296.

Marine Fidelle#, Conrad Rauber#, **Carolina Alves Costa Silva**#, Ai-Ling Tian, Imran Lahmar, Anne-Laure Mallard de La Varende, Liwei Zhao, Cassandra Thélémaque, Isabelle Lebhar, Meriem Messaoudene, Eugenie Pizzato, Roxanne Birebent, Maxime Descartes Mbogning Fonkou, Silvia Zoppi, Anna Reni, Cécile Dalban, Marion Leduc, Gladys Ferrere, Sylvère Durand, Pierre Ly, Aymeric Silvin, Kevin Mulder, Charles-Antoine Dutertre, Florent Ginhoux, Satoru Yonekura, Maria Paula Roberti, Maryam Tidjani-Alou, Safae Terrisse, Jianzhou Chen, Oliver Kepp, Angela Schippers, Norbert Wagner, Javier Suárez Gosálvez, Sebastian Kobold, Jean-Eudes Fahrner, Corentin Richard, Jacques Bosq, Leonardo Lordello, Giacomo Vitali, Nathalie Galleron, Benoît Quinquis, Emmanuelle Le Chatelier, Lucas Blanchard, Jean-Philippe Girard, Anne Jarry, Nadine Gervois, Emmanuelle Godefroy, Nathalie Labarrière, Ronald Koschny, Romain Daillère, Benjamin Besse, Caroline Truntzer, François Ghiringhelli, Nicolas Coatnoan, Vanessa Mhanna, David Klatzmann, Damien Drubay, Laurence Albiges, Andrew Maltez Thomas, Nicola Segata, François-Xavier Danlos, Aurélien Marabelle, Bertrand Routy, Lisa Derosa#, Guido Kroemer#, Laurence Zitvogel#
# contributed equally

We and others showed that ABX deviate the gut taxonomic microbiota composition and have a deleterious impact on survival in patients with cancer treated with ICB across histologies (see Appendix: Article XI and Abstract I). We demonstrate that ABX downregulate the ileal MAdCAM-1, leading to the recirculation of immunosuppressive enterotropic T cells into the tumor leading to resistance to ICB (Fig.

15). Correlating with ileal MAdCAM-1 transcripts, we assessed the impact of soluble MAdCAM-1 (sMAdCAM-1) levels determined by an ELISA assay in four independent cohorts of patients with NSCLC, RCC and bladder cancer treated with ICB. Overall, lower level of sMAdCAM-1 at treatment start was associated with ATB intake, ATB-independent gut dysbiosis and worse outcomes in patients treated with ICB. In multivariate Cox regression analysis, sMAdCAM-1 is an independent prognostic factor in patients from both NSCLC and RCC cohorts (see Appendix section: Abstract VII). Interestingly, higher levels of sMAdCAM-1 was associated with a richer gut microbiota and reduced abundance of species from *Enterocloster* genus. As a proxy for the gut dysbiosis, sMAdCAM-1 might guide the selection of patients amenable to MCI, such as live biotherapeutic products and fecal microbiota transplantation.

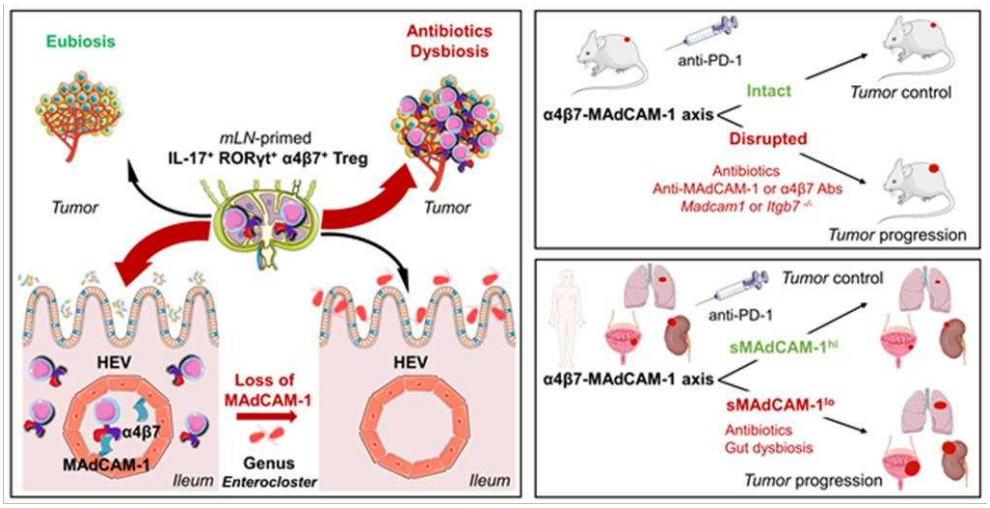

Figure 15 MAdCAM-1 as a gut immune checkpoint for cancer immunosurveillance.

Print Page Summary

Introduction. Resistance of cancers to immune checkpoint blockade (ICB) can result from antibiotic (ABX) treatment, likely as a result of a deviated gut microbiota. ABX compromise clinical outcome when administered prior to, rather than during, ICB administration, suggesting that bacterial recolonization following ABX discontinuation may be deleterious. Gut commensals induce the differentiation of an immunosuppressive subset of FoxP3$^+$ RAR-related orphan receptor gamma t (RORγt$^+$) regulatory (T_R17) cells. Lymphocytes primed in the mesenteric lymph nodes (mLN) or homing to the intestinal lamina propria (LP) express the $\alpha4\beta7$ integrin interacting with its counter-receptor mucosal addressin cell adhesion molecule-1 (MAdCAM-1) expressed in high endothelial venules (HEV).

Rationale. We hypothesized that disruption of the T_R17 cell-retaining MAdCAM-1/$\alpha4\beta7$interaction might cause the migration of T_R17 cells from the gut to tumors and hence compromise the anticancer effects of ICB. We used two complementary methods to visualize the exodus of intestinal T cells to subcutaneous tumors and tumor-draining lymph nodes (tdLNs): (1) Kaede mice expressing a fluorescent protein that is photoconverted upon ultraviolet light illumination of the ileum and (2) the injection of carboxyfluorescein succinimidyl ester (CFSE) into mLNs. Moreover, we used transgene-enforced MAdCAM-1 expression in the liver to locally intercept T_R17 cells during their migration.

Results. Several classes of ABX downregulated MAdCAM-1 expression in ileal venules, Peyer patches and mLNs, coinciding with the ileal exodus of $\alpha4\beta7^+$ T_H17/T_R17 cells towards extraintestinal tumors and tdLNs. This ABX-induced reduction in MAdCAM-1 could be explained by the recolonization of the gut by the genus *Enterocloster* (encompassing the *E. clostridioformis* species, see the figure), as its oral administration was sufficient to downregulate MAdCAM-1 expression. Perturbation of biliary acid metabolism by *E. clostridioformis* downregulated MAdCAM-1. Thus, both ursodeoxycholic acid and lithocholic acid suppressed MAdCAM-1 expression in vitro and in vivo. Genetic or antibody-mediated neutralization of MAdCAM-1 or $\alpha4\beta7$ integrin phenocopied the immunosuppressive effects of ABX, promoting resistance to ICB targeting PD-1, and inducing a surge in gut derived- $\alpha4\beta7^+$ T_R17 cells in tdLNs and tumors (see the figure). Restoration of MAdCAM-1 on ileal HEV by fecal microbial transplantation or blockade of IL-17A reversed the inhibitory effects of ABX. Ectopic expression of MAdCAM-1 in the liver caused the local retention of enterotropic $\alpha4\beta7^+$ T_R17 cells, reducing their accumulation in tumor beds and improving immunotherapy outcome in mice. Finally, low serum soluble MAdCAM-1 was identified as a proxy of intestinal dysbiosis and a robust predictor of shorter overall and progression-free survival of renal, bladder and lung cancer patients under immunotherapy with antibodies targeting PD-1 or PD-L1 (see the figure). In non-small cell lung cancer patients, the prognostic value of soluble MAdCAM-1 was independent from PD-L1 expression.

Conclusion. The relocation of enterotropic and immunosuppressive T_R17 cells to cancer (tumors and tdLNs) is repressed by the molecular interaction between the HEV addressin MAdCAM-1 and the integrin $\alpha4\beta7$ expressed by T_R17 cells. Disruption of the MAdCAM-1 expression by ABX or gut dysbiosis cause the relocation of T_R17 cells into tumors, thus compromising cancer immunosurveillance and the therapeutic efficiency of ICB in mice and patients.

Figure Caption:

MAdCAM-1 as a gut immune checkpoint for cancer immunosurveillance. Bacteria from the genus *Enterocloster* genus, for instance following discontinuation of ABX, induce the downregulation of MAdCAM-1 in the ileal LP and mLNs, inducing the exodus of the immunosuppressive $\alpha4\beta7^{+}$ T_R17 cells, from the gut to cancers and tumor-draining lymph nodes (tdLNs). Disruption of the MAdCAM-1-α4β7 axis compromises the efficacy of immunotherapy in mice and patients.

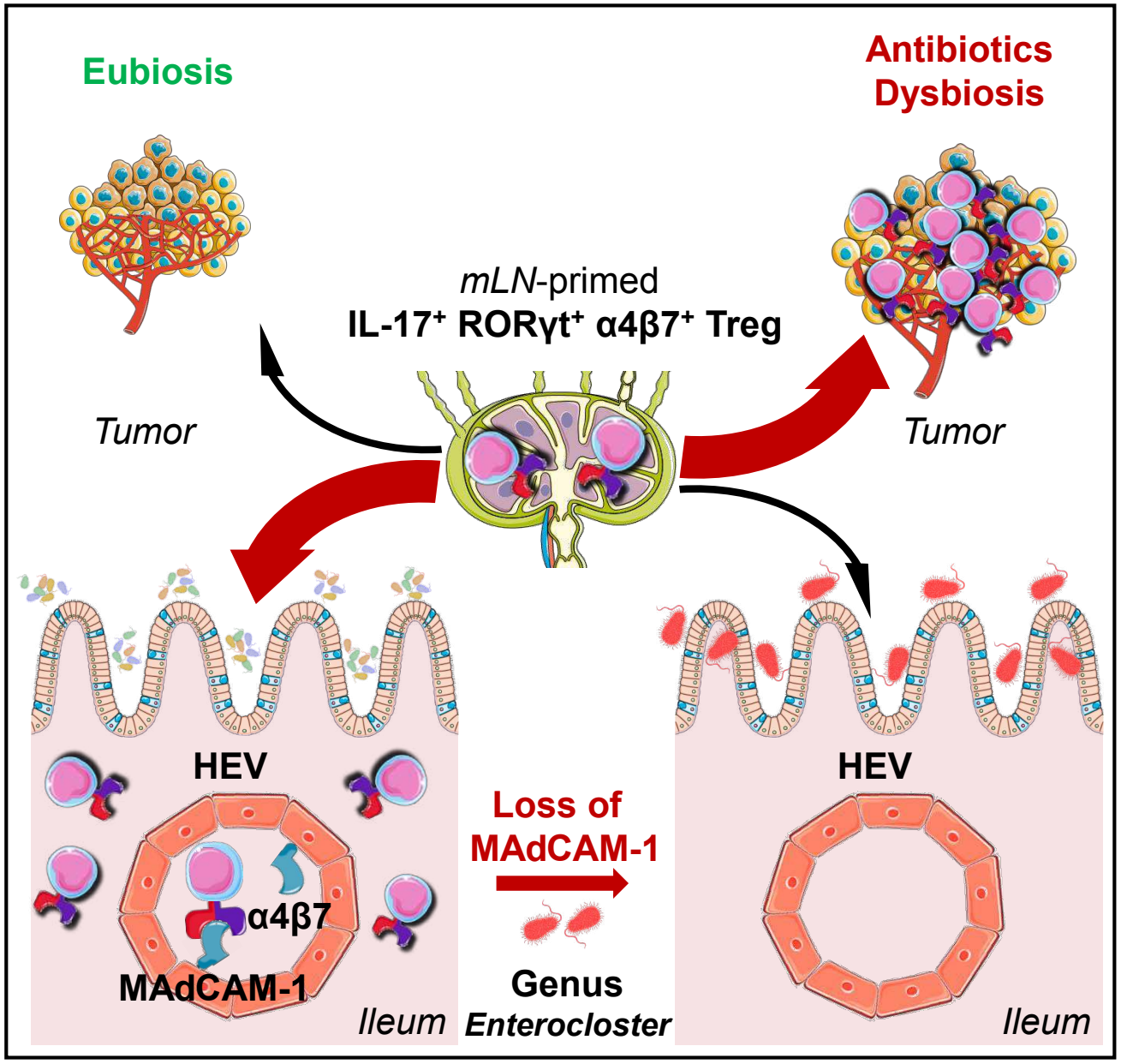
Eubiosis
Antibiotics
Dysbiosis
mLN-primed
IL-17+ RORγt+ α4β7+ Treg
Tumor
Tumor
HEV
α4β7
MAdCAM-1
Ileum
Loss of
MAdCAM-1
Genus
Enterocloster
HEV
Ileum

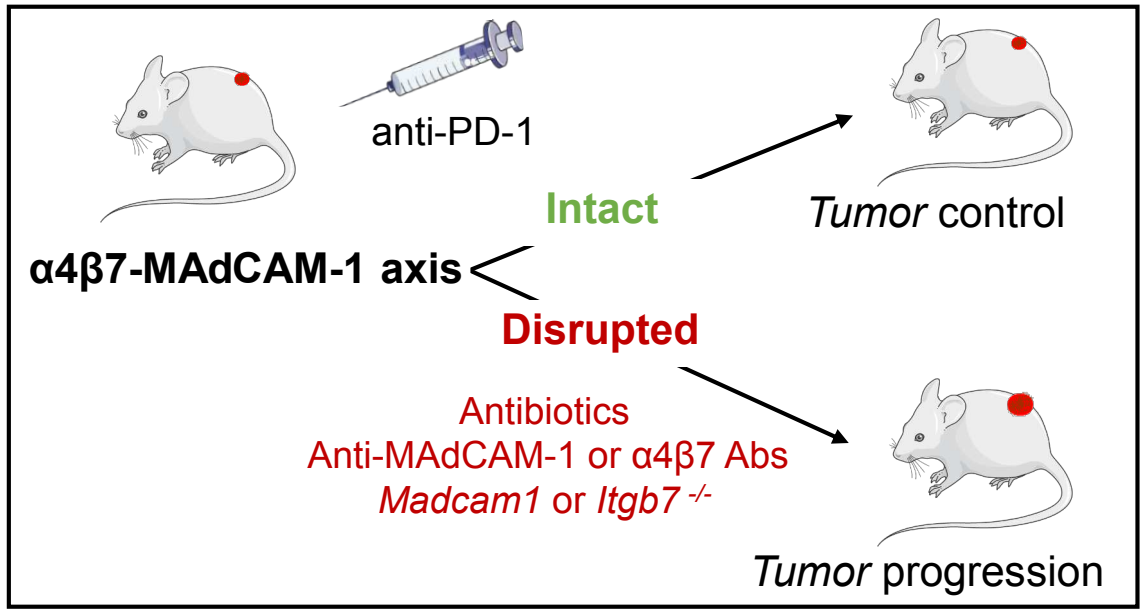
anti-PD-1
Intact
Tumor control
α4β7-MAdCAM-1 axis
Disrupted
Antibiotics
Anti-MAdCAM-1 or α4β7 Abs
Madcam1 or Itgb7 -/-
Tumor progression

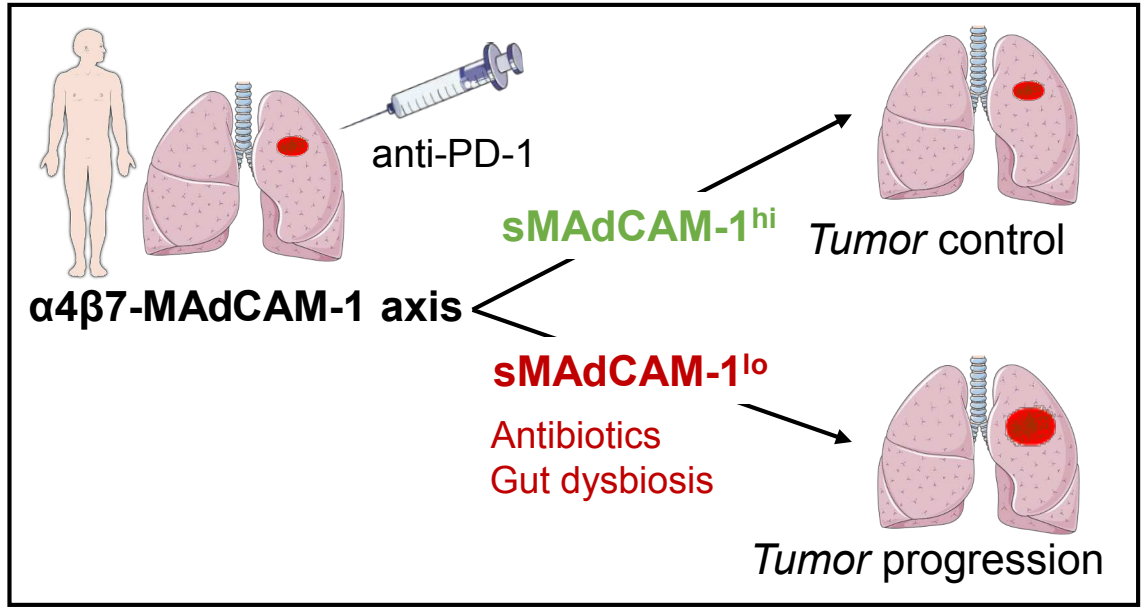
anti-PD-1
sMAdCAM-1hi
Tumor control
α4β7-MAdCAM-1 axis
sMAdCAM-1lo
Antibiotics
Gut dysbiosis
Tumor progression

A microbiota-modulated checkpoint dictating the traffic of intestinal immunosuppressive T cells into cancers

Marine Fidelle†[1,2,3], Conrad Rauber*†[1,2,3,4], Carolina Alves Costa Silva†[1,2,3], Ai-Ling Tian[1,5,6], Imran Lahmar[1,2,3], Anne-Laure Mallard de La Varende[1,2,3], Liwei Zhao[1,5,6], Cassandra Thélémaque[1,3], Isabelle Lebhar[1,3], Meriem Messaoudene[7], Eugenie Pizzato[1,3], Roxanne Birebent[1,2,3], Maxime Descartes Mbogning Fonkou[1,3], Silvia Zoppi[1,2,8], Anna Reni[1,2,9], Cécile Dalban[10], Marion Leduc[1,5,6], Gladys Ferrere[1,3,11], Sylvère Durand[1,5,6], Pierre Ly[1,3,30], Aymeric Silvin[1,3], Kevin Mulder[1,2,3], Charles-Antoine Dutertre[1,3], Florent Ginhoux[1,3], Satoru Yonekura[1,2,3], Maria Paula Roberti[1,3,12,13], Maryam Tidjani-Alou[1,3], Safae Terrisse[1,2,3], Jianzhou Chen[1,3], Oliver Kepp[1,5,6], Angela Schippers[14], Norbert Wagner[14], Javier Suárez Gosálvez[15], Sebastian Kobold[15,16], Jean-Eudes Fahrner[1,2,3], Corentin Richard[7], Jacques Bosq[17], Leonardo Lordello[1,3], Giacomo Vitali[18], Nathalie Galleron[18], Benoît Quinquis[18], Emmanuelle Le Chatelier[18], Lucas Blanchard[19], Jean-Philippe Girard[19], Anne Jarry[20], Nadine Gervois[20], Emmanuelle Godefroy[20], Nathalie Labarrière[20,21], Ronald Koschny[4], Romain Daillère[11], Benjamin Besse[1,2], Caroline Truntzer[22], François Ghiringhelli[22], Nicolas Coatnoan[23,24], Vanessa Mhanna[23,24], David Klatzmann[23,24], Damien Drubay[1,25,26], Laurence Albiges[1,2], Andrew Maltez Thomas[27], Nicola Segata[27,28], François-Xavier Danlos[1,2,3,29,30], Aurélien Marabelle[1,2,3,29,30], Bertrand Routy[7,31], Lisa Derosa††[1,2,3,30], Guido Kroemer†††*[5,6,32], Laurence Zitvogel†††*.[1,2,3,30]

Affiliations:

[1]Gustave Roussy Cancer Campus, Villejuif Cedex, France
[2]Université Paris-Saclay, Faculté de Médecine, Le Kremlin-Bicêtre, France
[3]Institut National de la Santé Et de la Recherche Médicale (INSERM) U1015, Équipe Labellisée - Ligue Nationale contre le Cancer, Villejuif, France
[4]Department of Gastroenterology and Infectious Diseases, University Hospital Heidelberg, Heidelberg, Germany
[5]Centre de Recherche des Cordeliers, INSERM U1138, Équipe Labellisée - Ligue Nationale contre le Cancer, Université Paris Cité, Sorbonne Université, Paris, France.
[6]Metabolomics and Cell Biology Platforms, Gustave Roussy Cancer Campus, Villejuif, France.
[7]Centre de Recherche du Centre Hospitalier de l'Université de Montréal (CRCHUM), Montréal, QC, Canada
[8]Department of Medicine and Surgery, University of Parma, Parma, Italy.
[9]Section of Oncology, Department of Medicine, University of Verona School of Medicine and Verona University Hospital Trust, Verona, Italy
[10]Clinical Research Department, Centre Léon Bérard, Lyon, France
[11]EverImmune, Gustave Roussy Cancer Campus, Villejuif Cedex, France
[12]Clinical Cooperation Unit Applied Tumor Immunity, German Cancer Research Center (DKFZ), Heidelberg, Germany
[13]Department of Medical Oncology, National Center for Tumor Diseases (NCT), Heidelberg University Hospital (UKHD), Heidelberg, Germany
[14]Department of Pediatrics, University Hospital RWTH Aachen, Aachen, Germany
[15]Center of Integrated Protein Science Munich (CIPS-M) and Division of Clinical Pharmacology, Department of Medicine IV, Klinikum der Universität München, LMU Munich, Germany
[16]German Cancer Consortium (DKTK), partner site Munich, Munich, Germany

[17]JBO Consultant, Paris, France
[18]MetaGenoPolis, INRAe, Université Paris-Saclay, Jouy en Josas, France
[19]Institut de Pharmacologie et de Biologie Structurale, IPBS, Université de Toulouse, CNRS, UPS, Toulouse, France
[20]Nantes Université, Université d'Angers, INSERM, CNRS, Immunology and New Concepts in ImmunoTherapy, INCIT, UMR 1302/EMR6001, Nantes, France
[21]LabEx IGO, Université de Nantes, Nantes, France
[22]Université de Bourgogne Franche-Comté, Plateforme de Transfert de Biologie du Cancer, Centre Georges-François Leclerc, Equipe Labellisée Ligue Nationale Contre le Cancer, Centre de Recherche INSERM LNC-UMR1231, Institut Médical de Génétique et d'Immunologie, Dijon, France
[23]AP-HP, Hôpital Pitié-Salpêtrière, Clinical Investigation Center for Biotherapies (CIC-BTi) and Immunology-Inflammation-Infectiology and Dermatology Department (3iD), Paris, France.
[24]Sorbonne Université, INSERM, UMRS959 Immunology-Immunopathology-Immunotherapy Laboratory, Paris, France
[25]Gustave Roussy, Office of Biostatistics and Epidemiology, Université Paris-Saclay, Villejuif, France
[26]Inserm, Université Paris-Saclay, CESP U1018, Oncostat, labeled Ligue Contre le Cancer, Villejuif, France
[27]Department of Computational, Cellular and Integrative Biology, University of Trento, Trento, Italy
[28]Istituto Europeo di Oncologia (IEO), National Cancer Institute (IRCCS), Milan, Italy
[29]Drug Development Department, Gustave Roussy Cancer Campus, Villejuif Cedex, France
[30]Center of Clinical Investigations in Biotherapies of Cancer (BIOTHERIS), Villejuif, France
[31]Hematology-Oncology Division, Department of Medicine, Centre Hospitalier de l'Université de Montréal (CHUM), Montréal, QC, Canada
[32]Institut du Cancer Paris CARPEM, Department of Biology, Hôpital Européen Georges Pompidou, Assistance Publique – Hôpitaux de Paris (AP-HP), Paris, France

*Corresponding authors: Laurence Zitvogel or Guido Kroemer or Conrad Rauber. E-mails: laurence.zitvogel@gustaveroussy.fr or kroemer@orange.fr or conrad.rauber@gmx.de
†Shared co-first authorship
††Shared co-last authorship

Abstract:
Antibiotics (ABX) compromise the efficacy of PD-1 blockade in cancer patients, but the mechanisms underlying their immunosuppressive effects remain unknown. By inducing the downregulation of mucosal addressin cell adhesion molecule-1 (MAdCAM-1) in ileum, post-ABX gut recolonization by species from the genus *Enterocloster* provoked the emigration of enterotropic $\alpha4\beta7^+$ T_R17 $CD4^+$ Treg cells to the tumor. These ABX effects were mimicked by oral gavage of *Enterocloster spp*., genetic deficiency of MAdCAM-1 and its receptor α4β7 integrin, or their antibody-mediated neutralization, while fecal microbiota transplantation or IL-17A neutralization prevented them. In independent cohorts of lung, kidney and bladder cancer patients, low serum levels of soluble MAdCAM-1 had a negative prognostic impact. Thus, the MAdCAM-1/ α4β7 axis constitutes an actionable gut immune checkpoint in cancer immunosurveillance.

Immune checkpoint inhibitors (ICIs) targeting the immunosuppressive interaction between programmed cell death protein 1 (PD-1) and programmed death-ligand 1 (PD-L1) are used in the clinical management of many cancer types (*1*, *2*). Primary resistance to ICIs has been attributed to various molecular or cellular cues (*3–5*). In addition, several studies confirmed the deleterious effect of antibiotics (ABX) on clinical benefit in patients receiving ICIs (*6–8*). Meta-analyses revealed that ABX uptake is more harmful on clinical outcome when administered prior to, rather than during ICIs administration, suggesting that bacterial recolonization following an ABX course may be particularly deleterious (*9–11*). How these new bacterial compositions interfere with the reprograming of the tumor microenvironment (TME) remains a conundrum.

The α4 (CD49d) and β7 integrin subunits interact to form the α4β7 heterodimer. By interacting with its counter-receptor mucosal addressin cell adhesion molecule-1 (MAdCAM-1), α4β7 integrin mediates lymphocyte adhesion and diapedesis from the circulation across the vascular endothelial barrier into gut-associated secondary lymphoid tissue (GALT) or lamina propria (LP). MAdCAM-1 is constitutively expressed in LP venules, as well as in GALT high endothelial venules (HEV), and upregulated by inflammatory cytokines (*12–14*). By preventing the migration of inflammatory $\beta7^+$ T cells from the circulation to the gut, antibodies (Abs) targeting α4β7 or MAdCAM-1 reduce the severity of colitis in patients with inflammatory bowel disease (IBD) (*15–17*).

Intestinal microbiota plays a role in maintaining the homeostatic functions of gut regulatory T (T_{reg}) and interleukin-(IL)-17)-producing T helper 17 (T_H17) cells (*18*, *19*). In fact, gut T_H17 also control extraintestinal inflammation (*20–24*). T_H17 and their lineage-related (forkhead box P3) $FoxP3^+$ RAR-related orphan receptor gamma t ($ROR\gamma t^+$) regulatory (T_R17) cells blunt antitumor immunosurveillance during carcinogenesis (*25*). In human and mice, the expression of the transcription factor RORγt is characteristic of a subpopulation of tumor-infiltrating T_{reg} cells that are induced by gut commensals (*26–28*). Thus, we hypothesized that ABX-induced overgrowth of selected species (*11*, *29*) might affect the trafficking of T_{reg} between the intestinal and tumoral compartments, thereby aggravating cancer immunosuppression and resistance to PD-1 blockade.

ABX downregulate MAdCAM-1 ileal expression in mice and patients

Sterilization of the gut from mice with a cocktail of broad-spectrum ABX (ampicillin, colistin and streptomycin (ACS)) attenuates the anticancer effects of PD-1 blockade (*7*). ACS

reduced the expression of most ileal chemokines and *Madcam1* (**fig. S1A, Fig. 1A**). These effects were specific for the ileum because they were not observed in the colon or in MCA205 fibrosarcomas (**Fig. 1A, fig. S1A**). Ileal *Madcam1* was decreased at the mRNA and protein levels, as determined by RT-qPCR (**Fig. 1A**), immunohistochemistry (**Fig. 1B**), flow cytometry of ileal CD45$^-$ LP cells **(Fig. 1C, fig. S1B**) and ELISA of ileal tissue lysates (**Fig. 1D**). Of note, the integrity of the intestinal architecture and vasculature was preserved upon ACS administration, without any alteration in the density of CD31$^+$ capillaries (**fig. S1C**). Levels of MAdCAM-1 decreased, starting on day 3 of ACS administration and were not even restored on day 4 (ACS+4d) nor day 12 post-ACS cessation (**Fig. 1, C and D**). The ACS cocktail also downregulated *Madcam1* gene expression in Peyer's patches (PP) and in mesenteric lymph nodes (mLN) (**fig. S1, D and E**). Other ABX regimens using β-lactams (ceftazidime and cefepime cephalosporins), aminoglycosides (streptomycin), polymyxins (colistin) and macrolides (erythromycin) also downregulated ileal *Madcam1* (**fig. S1, E and F**). By contrast, piperacillin plus tazobactam, rifaximin or vancomycin had no effect on *Madcam1* expression in two distinct animal facilities located in France (**fig. S1E**) and Canada (**fig. S1F**). *Madcam1* (but not vascular cell adhesion protein *(Vcam1)*) mRNA levels were 10 times lower in tumor- draining LN (tdLN) than in mLN (**fig. S1G**). Mass spectrometry of ileal bacteria cultured from animals treated with various ABX regimens under aerobic and anaerobic conditions identified several species (spp.) belonging to the genus *Enterocloster* (such as *Enterocloster clostridioformis* and *Enterocloster bolteae*) (*29*) that prevailed 4 or 7 days after ACS or erythromycin cessation but not in any other experimental condition (**table S1**). These *Enterocloster* spp. were previously identified in stools of cancer patients resistant to PD-1 blockade (*10*, *11*), as well as in chronic inflammatory disorders (*30*), and mediate resistance to cancer immunotherapy with PD-1 blockade in mice (*31*). Whereas oral gavage of *E. clostridioformis* reduced ileal *Madcam1* mRNA (**Fig. 1E**), administration of immunostimulatory *Akkermansia* strain p2261 (*Akk.*) (*7*, *10*) or *Enterococcus hirae* (*32*) increased basal *Madcam1* expression in ileal tissues from eubiotic mice reared in specific-pathogen-free (SPF) conditions (**Fig. 1E**). Moreover, ACS-induced downregulation of ileal *Madcam1* mRNA was accompanied by that of regulatory cytokines and transcription factors (such as *Foxp3, Il17a*, *Il22, Rorc*), and *Madcam1* mRNA significantly correlated with *Foxp3* and *Il17a* mRNA levels (**fig. S1A, fig. S1, H and I**). Indeed, ACS depleted mucosal CD25$^+$FoxP3$^+$ CD4$^+$ T cells (T_{reg}) and RORγt$^+$ CD4$^+$ T_H17 cells from the ileal LP (**Fig. 1F, fig. S2A**). Finally, ACS phenocopied the ileal

immunomodulatory effects of *Madcam1* knockout or antibody neutralization of MAdCAM-1 (**Fig. 1G**).

We confirmed the coordinated inhibitory effects of several class of ABX on the ileal (but not caecal nor colonic) expression of *MADCAM1* and *RORC* in 31 patients who were treated with ABX (n=10) compared with non-treated patients (n=21) while they underwent intestinal endoscopy and biopsies for various indications (**Fig. 2, A and B, and table S2**). As in mice, we found a correlation between *MADCAM1* and *IL17a* ileal mRNA levels (**Fig. 2C**). In clinical trials, fecal microbial transfer (FMT) from melanoma patients who benefited from PD-1 blockade circumvents primary resistance to ICIs in one third of metastatic melanoma recipients (*33*, *34*). Moreover, FMT from some human donors fails to improve ICIs responses (*7*, *35*). We tested whether random FMT from NSCLC patients to ABX-preconditioned mice would modulate ileal *Madcam1* gene expression. Three out of six FMTs downregulated *Madcam1* mRNA (**Fig. 2D and table S3**). Shotgun metagenomics-based analyses of these three human stools revealed an overrepresentation of *Enterocloster* spp., including *E. clostridioformis* as well as that of *Hungatella hathewayi*, which is phylogenetically close to *Enterocloster* spp. (*29*), in two out of three of these stools compared with the three other human fecal samples (**Fig. 2D**). Mice orally gavaged with stools that downregulated *Madcam1* expression exhibited a relative over-representation of *E. clostridioformis* (**Fig. 2D**). Finally, the longitudinal follow up of cancer patients more than 60 days post- ABX cessation revealed significant decreases of the abundance of *Enterocloster* and *Hungatella* spp. (**Fig. 2E**).

To further elucidate potential molecular cues explaining MAdCAM-1 loss following relative dominance of ileal *E. clostridioformis*, we performed mass spectrometric metabolomics of murine ileal contents 7 days post-gavage with this bacterium. There were significant changes of the biliary acid (BA) levels (**fig. S3A**), in accordance with a previous report (*36*). We screened the effects of various BA (*37*, *38*) and bacteria on *Madcam1* expression in vitro using two murine endothelial cell lines (TSEC and bEnd.3) engineered to express green fluorescent protein (GFP) under the control of the *Madcam1* promoter (**fig. S3B**). Live *E. clostridioformis* directly reduced expression of GFP, whereas the immunogenic *Akk.* failed to do so (**fig. S3C**). Lithocholic acid (LCA) as well as two synthetic farnesoid X receptor (FXR) agonists significantly decreased GFP expression in TSEC and bEnd.3 exposed to IL-1β+TNF-α in a dose-dependent manner (**fig. S3D**). Distinct LCA isoforms reduced GFP expression levels at different dose levels (**fig. S3E**). RT-qPCR confirmed that LCA downregulated *Madcam1* mRNA expression levels in TSEC (**fig. S3F**).

Moreover, LCA (**fig. S3, G and H**) as well as UCDA (**fig. S3I**) dampened *Madcam1* gene expression levels in both ileum and PP or mLN in vivo, in line with a prior report (*39*). Thus, one of the mechanisms by which *Enterocloster* spp. may downregulate MAdCAM-1 in GALT includes the accumulation of distinct BA.

Thus, broad-spectrum ABX downregulate the expression of the ileal mucosal addressin MAdCAM-1, correlating with reduced ileal *Foxp3, Il17a,* and *Rorc*.

ABX induces the exodus of enterotropic α4β7$^+$ CD4$^+$ T cell subsets to tumor- draining lymph nodes

We hypothesized that the loss of ileal MAdCAM-1 might affect the trafficking of enterotropic T cells expressing the MAdCAM-1 receptor α4β7. We took advantage of Kaede mice expressing a fluorescent protein (*40*) that gets photoconverted (PC) upon ultraviolet light (UV) illumination to study the exodus of intestinal cells (*20*, *22*, *23*). To track the fate of ileal, cecal and mLN cells (referred to as "intestine" henceforth) 24 hours after photoconversion of tumor bearers, we performed flow cytometric analyses of PC leukocytes in various organs (**fig. S4A**). Up to 22.8±2.6% of mLN cells remained PC$^+$, and PC$^+$ cells became detectable in the spleen (5.1±0.5%) and tdLN (4.0±0.3%) (**fig. S4A**). UV illumination of the ileum also enabled the visualization of gut leukocyte emigration to tdLN or tumor, albeit to a lower extent than intestine illumination (**fig. S4B**). As a second method of cell tracking, we directly injected carboxyfluorescein succinimidyl ester (CFSE) into the mLN (*41*) and then followed the emigration of CFSE-labeled cells to distant sites at 24 hours (**fig. S4C**). Up to 1.0±0.2% splenocytes, 0.8±0.1% tdLN cells and 0.2±0.02% of tumor infiltrating leukocytes were replaced by mLN-derived leukocytes (**fig. S4C**). Moreover, both methods revealed the selective enrichment of PC$^+$ or CFSE$^+$ α4β7$^+$ CD4$^+$ T cells in the spleen, tdLN, and tumor at 24 hours (**Fig. 3, A and B, fig. S4, D and E)**. Ab-mediated inhibition of MAdCAM-1 in mice led to a more pronounced mLN to tdLN migration of PC or CSFE-labeled cells than in control animals (**fig. S4F**). In contrast, the migration of mLN cells to the contralateral LN (cLN) was not affected (**fig. S4G**).

The bulk-RNA sequencing of α4β7^{hi} CD4$^+$ T cells compared with α4β7$^-$ CD4$^+$ T cells purified from mLN of tumor-bearing mice revealed that α4β7^{hi} CD4$^+$ T cells overexpressed, not only the *Itga4* subunit of α4β7 but also genes involved in T_{reg} functions and T_H17 polarization, but downregulated *Tnfrsf9* (**Fig. 3C, and table S4**).

We investigated how ACS-induced dysbiosis affected the exodus of CSFE-labeled mLN cells to tdLN (**Fig. 3D**). Transient ACS treatment for 14 days, followed by discontinuation of ACS for 4 days facilitated the mLN to tdLN migration of IL-17A secreting $\alpha4\beta7^+$ $CD25^+$ $FoxP3^+$ $CD4^+$ T (T_R17) cells but not that of IL-$17A^+$ $\alpha4\beta7^+$ $FoxP3^-$ $CD4^+$ T (T_{conv}) cells or $\alpha4\beta7^-$ $CD25^+$ $FoxP3^+$ $CD4^+$ T cells (**Fig. 3E, fig. S5A**). Actually, ACS did not increase the bona fide T_{reg} pool of the tdLN constituted by the locally expanded (extraintestinal, CFSE negative) cells (**fig. S5B**). T_R17, which represent up to 40% of intestinal T_{reg} cells, constituted the most mobile $\alpha4\beta7^+$ $CFSE^+$ fraction, accounting for 0.2±0.1% of all $CSFE^+$ $CD4^+$ cells reaching the tdLN 24 hours after injection of CSFE into mLN, after cessation of ACS (**fig. S5B**). These originally enterotropic T_R17 did not only produce IL-17A but also IL-22 (**fig. S5B**). *Madcam1*$^{-/-}$ mice also manifested a similar mLN to tdLN (but not cLN) migration of CFSE-labeled T_{reg} cells (**Fig. 3F, fig. S5C**). Similarly, in Kaede-transgenic mice subjected to UV illumination of the intestine (**fig. S4A**), a neutralizing anti-MAdCAM-1 Ab promoted the gut to tdLN migration of PC $CD25^{hi}$ $\alpha4\beta7^+$ $CD4^+$ T (**Fig. 3G**). Since recolonization post-ACS is accompanied by the emergence of *Enterocloster* spp. (**table S1**) that downregulated ileal *Madcam1* (**Fig. 1E**), we determined whether oral gavage with *E. clostridioformis* would be sufficient to trigger this mLN to tdLN migration. Indeed, this bacterium facilitated the selective intestinal translocation of PC^+ (but not PC^-) $CD25^{hi}$ (but not $CD25^-$) T_H17 cells ($CCR6^+$ $CXCR3^-$) (**Fig. 3H**). These findings suggest that the migrating enterotropic T cells do not use MAdCAM-1- expressing HEV to enter distal tissues. Instead, we observed a role for L/P-selectins in T cell homing to tumor beds during MAdCAM-1 downregulation, as previously described (**fig. S6**) (*42*, *43*).

We next performed Rhapsody-based single cell RNA sequencing of $CFSE^+$ $CD4^+$ T cells recovered from tdLN at 24 hours post-CFSE injection into mLN in mice treated with ACS and oral *E. clostridioformis* (**fig. S7, A and B**). Unsupervised clustering of the $CFSE^+$ $CD4^+$ T cells from tdLN partitioned the data into four cellular clusters (**fig. S7C and table S5**) (*44*). A small cluster featured the prototypic effector T_{reg} phenotype (*26*) (**fig. S7D**). This T_{reg} subset overexpressed *Nrp1*, *CD39* and *CD73* involved in tumor immunosuppression (**fig. S7D)**. This T_{reg} subset also differed from all the other emigrating cells by the overexpression of genes associated with the T_R17 blueprint (*26*) (**fig. S7D**). Another distinctive cluster harbored a follicular T helper/regulatory cell (TFH/TFR)-like transcriptional profile with proliferative/exhaustion hallmarks (*45*) (**fig. S7E**). The two other subsets were characterized by a type I IFN fingerprint

(**fig. S7F**) and a CD8- like regulatory profile defined by immunosuppressive signaling pathways (*46–51*) (**fig. S7G and table S5**).

Most of the mLN emigrating cells to tdLN were T cells and a few were B cells (**Fig. 4A**). To address the clonality of T_{reg} emigrating from the mLN, we performed single cell and deep T cell receptor (TCR) sequencing of $CFSE^+$ T cells harvested from various locations at 24 hours post-mLN CFSE injection. Unsupervised clustering of the $CFSE^+$ T cells partitioned the data into four cellular clusters, one composed of T_{reg}, one of T_{conv}, and two of $CD8^+$ T cells (**Fig. 4B, fig. S8, A and B**). Based on TCR repertoire (*52*), tumor-infiltrating T_{reg} but not T_{conv} cells exhibited higher clonal expansion in mice gavaged with *E. clostridioformis* compared to control mice (**Fig. 4C**). There was a 10-fold increase of TCRs from clusters composed of tumor/tdLN TCRs in mice gavaged with *E. clostridioformis* compared with controls, with a concomitant decrease of TCRs from clusters restricted to mLN (**Fig. 4D**). This recirculation affected preferentially T_{reg} over T_{conv} cells (**Fig. 4C**). Similar clonal expansions were observed in the $CD8^+$ population (**fig. S8C**). The functional profile of mLN-T_{reg} reaching the tumor differed from that of its origin, with an upregulation of genes involved in immunosuppression, cytolysis, and type-I IFN responses (**Fig. 4E**, **fig. S8A**). Oral gavage with *E. clostridioformis* significantly increased the proliferative potential of migratory T_{reg} with the upregulation of genes implicated in cell cycle, chromatin silencing and H3K27 trimethylation, as well as regulatory functions (*Il10*) within tumor beds (**Fig. 4, E and F**). The most striking commonality between mLN emigrating $CD8^+$ and $CD4^+$ T cells reaching the sarcoma was the shutdown of the translation machinery, as previously reported in exhausted $CD8^+$ T cells in chronic infection and cancer (*53–56*) (**fig. S8B, Fig. 4E, and table S5**). Thus, the enterotropic $\alpha4\beta7^+$ $CD4^+$ T cells that translocated from the mLN and PP to the tdLN involved T_{reg}/T_R17 cells exhibiting immunosuppressive functions. These fingerprints further increased when the cells reached the tumor bed, in conditions where the MAdCAM-1/α4β7 axis is compromised by neutralization or knockout of MAdCAM-1, recolonization post-ABX, or *E. clostridioformis*-induced dysbiosis.

The anticancer efficacy of PD-1 blockade relies on the MAdCAM-1-α4β7 axis

Given the immunosuppressive role of T_R17 cells during cancer immuno-surveillance (*27*, *28*, *57*), disruption of the MAdCAM-1/ α4β7 interaction might interfere with ICIs-mediated anticancer effects. Loss of ileal *Madcam1* expression correlated with increased tumor size in tumor- bearing

animals regardless of PD-1 blockade (**fig. S9A**). PD-1 blockade also reduced MCA205 fibrosarcoma growth in wild type (WT) C57BL/6 mice, but failed to do so in *Madcam1*$^{-/-}$ mice and *Itgb7*$^{-/-}$ animals, which lack the β7 chain required for the formation of the α4β7 heterodimer (**Fig. 5A**). Similarly, MCA205 fibrosarcoma, 4T1 breast and orthotopic TC-1 lung cancers normally reduced their growth in response to PD-1 blockade but failed to do so following injection of neutralizing anti-MAdCAM-1 or anti-α4β7 Abs (**Fig. 5B, C and D).** In *Madcam1*$^{-/-}$ mice, there was a constitutive increase of α4β7$^+$ CD4$^+$ T cells in the spleen and in the tumor where they represented approximately 3% of TILs (**Fig. 5E**), as previously described (*58*). Injection of a neutralizing anti-MAdCAM-1 Ab during spontaneous tumor progression reshaped the TME and led to threefold increase in the intratumoral accumulation of RORγt$^+$ T_{reg} (FoxP3$^+$ CD25$^+$) T_R17 cells expressing intestinal T cell markers such as α4β7, CCR9 and CCR6 (**fig. S9B and C)**. Although only 17±0.9% of all MCA205 TILs were α4β7$^+$, 76±1.5% among RORγt$^+$ T_{reg} were α4β7$^+$ (**fig. S9C**). In subcutaneous tumors (MCA205, 4T1), T_{reg} represented 11.7±1.6% of α4β7$^+$ CD4$^+$ TIL and among these T_{reg}, 44.5±5.3% were RORγt$^+$ (**table S6**). Bacterial recolonization of the gut 4 days post-ACS phenocopied *Madcam1* gene deficiency, inducing a three to five-fold increase in the proportion of RORγt$^+$ T_{reg} (T_R17) in tumor beds (**Fig. 5, F and G**). This tumor homing of T_R17 cells was transient and no longer observed by 12 days post-ACS, except when anti-PD-1 Ab was coadministered (**Fig. 5H, fig. S9D**). Indeed, anti-PD-1 Abs facilitated the priming and/or the expansion of T_R17 in the mLN in MCA205 tumor-bearing mice (**fig. S9E**). Anti-PD-1 Ab contributed to the intratumoral accumulation of T_R17 defined as RORγt$^+$ T_{reg} or IL-17A$^+$ IL-22$^+$ T_{reg} in tumors (**Fig. 5H, fig. S9, F and G**). In this context, intratumoral T_{reg} represented 19.1±2.8% of α4β7$^+$ CD4$^+$ TIL, and among these T_{reg}, 51.1±7.7% and 61.3±7% were RORγt$^+$ and IL-17A$^+$ respectively (**table S6**).

The recruitment of T_R17 promoted by PD-1 inhibition was further increased when *E. clostridioformis* (but not *Lactobacillus reuteri*) was supplemented by oral gavage after ACS discontinuation (**fig. S9H**). Blockade of the MAdCAM-1-α4β7 axis during PD-1-targeted immunotherapy impaired the infiltration of tumors by effector CCR5$^+$ CD8$^+$ cells (*59*, *60*) (**Fig. 5I**). Given that the antimicrobial and proinflammatory properties of IL-17, alone or with IL-22 (*61*, *62*), neutralizing these cytokines may circumvent the harmful effects of bacterial recolonization post-ABX during PD-1 inhibition. Indeed, neutralization of IL-17A (but not that of IL-22RA) counteracted the deleterious effects of ACS on PD-1 blockade (**Fig. 5J**). Thus, IL-17A plays a role in the immunosuppressive effects of ABX.

MAdCAM-1 liver expression reduced tumoral accumulation of enterotropic Treg

To strengthen the cause- effect relationship between MAdCAM-1 gut expression and emigration of enterotropic suppressive T cells to tumors, we enforced MAdCAM-1 expression in the liver by hydrodynamic injection of *Madcam1*-encoding cDNA inserted into a vector (*63*). Liver-specific overexpression of the transgene was verified by RT-qPCR and immunohistochemistry (IHC) (**Fig. 6, A and B**). Liver expression of MAdCAM-1 correlated with recirculation of the soluble form of MAdCAM-1 (sMAdCAM-1) (**fig. S9I**). There was a positive correlation between liver *Madcam-1* and *Foxp3* mRNA expression or the local presence of FoxP3$^+$ T cells (**Fig. 6C**). In ACS-treated mice, enforced hepatic MAdCAM-1 expression reduced the frequency of tumoral α4β7$^+$ (but not α4β7$^-$) T_{reg} cells (**Fig. 6, D and E**). Moreover, high hepatic *Foxp3* expression correlated with a reduction of tumor size (**Fig. 6F**). Anti-PD-1 Ab significantly increased liver *Rorc* expression, even more so upon ACS (**Fig. 6G**), with a positive correlation with liver *Madcam1* (**Fig. 6H**). Moreover, ACS-induced resistance to anti-PD-1 Abs could be circumvented when mice ectopically expressed *Madcam1* in the liver to locally retain T_{reg} (**Fig. 6I**). There was a negative correlation between tumor size and liver *Madcam1* mRNA levels in these conditions (**Fig. 6J**). Thus, MAdCAM-1 acts as an immune checkpoint controlling the retention of T_{reg} cells.

Soluble MAdCAM-1 is a strong prognostic factor of cancer patient responses

To investigate the clinical relevance of these findings, we first analyzed TIL infiltrates for the presence of enterotropic α4β7$^+$ T cells in fresh human tumors and ex vivo propagated TILs. The α4β7$^+$ fraction of T_{reg} and CD8$^+$ T cells represented up to 8.3±2.1% and 24.5±6.9% respectively, expressed inhibitory receptors and could electively produce IL-17 (**fig. S10, A and B)**. RORγt$^+$ FoxP3^{hi} cells represented 4.5±0.8% of CD4$^+$ cells in TILs in expansion and expressed the enterotropic marker α4β7$^+$ (**fig. S10C**). Based on previous reports (*64*) and given the correlation between liver or ileal MADCAM-1 and circulating sMAdCAM-1 levels in mice (**fig. S9I-J**), we analyzed the clinical significance of serum sMAdCAM-1 at diagnosis in two independent cohorts of 115 and 187 patients with advanced NSCLC treated with anti-PD-1/PD-L1 antibodies (**table S7**). Patients treated with ABX exhibited lower sMAdCAM-1 levels than

ABX-free patients (**Fig. 7A**). Baseline serum sMAdCAM-1 was a strong independent prognostic factor of survival in NSCLC patients who did not take ABX and to a lesser extent in those who took ABX prior to ICIs (**Fig. 7B**), high baseline levels being associated with prolonged overall survival (OS) and progression-free survival (PFS) (**fig. S10D and E, Fig. 7C**). Low sMAdCAM-1 levels identified the subset of PD1 antibody-refractory patients within PD-L1^{hi} (>50%) NSCLC tumors (**Fig. 7D, fig. S10F**). Multivariate Cox regression analysis taking into consideration clinical variables concluded that sMAdCAM-1 is an independent prognostic factor in NSCLC patients (**table S7**, **fig. S10D**). There was no correlation between sMAdCAM-1 and tumor mutational burden nor RNA detection of MER4 retrotransposon elements (*65*) (**fig. S10G)**. We validated the clinical significance of serum sMAdCAM-1 as a biomarker of OS in 212 metastatic renal cell carcinoma (RCC) patients under second-line nivolumab (*66*) (**Fig. 7E, and table S7**) and in 79 patients diagnosed with metastatic bladder cancer (BC) treated with durvalumab (anti-PD-L1) (*67*) (**Fig. 7F, and table S7**).

To demonstrate the relationship between sMAdCAM-1 and gut dysbiosis in advanced NSCLC patients, we performed supervised hierarchical clustering of metagenomics species (MGS) defining the taxonomic composition of the intestinal microbiota using shotgun MG according to the median of sMAdCAM-1 serum levels (199 ng/ml) in 95 NSCLC patients (**table S8**). MGS richness and Shannon indices were reduced in sMAdCAM-1^{lo} (<median) compared to sMAdCAM-1^{hi} ($\geq$median) patients (**Fig. 8A**). Moreover, the gut composition diverged between sMAdCAM-1^{lo} versus sMAdCAM-1^{hi} patients, as indicated by the ANCOM-based beta-diversity (**Fig. 8B**). Supervised MG analysis revealed two clusters of MGS that were significantly different in relative abundance between the two patient groups (**Fig. 8C**). Importantly, low circulating sMAdCAM-1 levels were associated with an increase in MGS from the genus *Enterocloster* (*E. clostridioformis)* which reduces ileal *Madcam1* expression in mice (**Fig. 1E**), and *E. bolteae*, which are both associated with chronic inflammatory disorders including cancer (*30*, *31*) and poor prognosis in patients treated with immunotherapy (*10*) (**Fig. 8D**). Thus, sMAdCAM-1 is a surrogate marker of intestinal dysbiosis, and is associated with patient overall survival in advanced bladder, lung and kidney cancer.

Discussion

To decipher the mechanisms involved in the immunosuppressive effects of ABX, we studied the emigration of T cells from the gut to distal tumors. We found that the relocation of enterotropic and immunosuppressive T_R17 cells to cancer-relevant compartments is at least partially controlled by the molecular interaction between MAdCAM-1 and α4β7. This demonstration follows prior evidence that gut derived-T_H17 cells control extraintestinal autoimmunity (*20–24*) and inflammation (*68*, *69*). RORγt$^+$ T_{reg} harbor an exacerbated immunosuppressive phenotype compared with T_{reg} (*26*). Recent intestinal T_R17 emigrants found in tdLN exhibit gut-specific T_{reg} features (*70*, *71*), T_H17- related gene expression patterns (*72*) as well as immunosuppressive traits such as *Dusp2*/PCA1 (*47*) and *Pik3ip1* (*73*). In tumors or tdLNs, gut T cell emigrants shut down protein translation and acquire features of exhaustion or lytic functions, perhaps reflecting chronic TCR stimulation (*56*). These data collected in tumor- bearing hosts may be interpreted in the context of IBD, in which the anti-α4β7 Ab vedolizumab increases the recirculation of extraintestinal α4β7$^+$ T_{reg} and central memory T_H17 cells (*74–76*). However, based on our results, α4β7 neutralization may have undesirable systemic immunosuppressive effects in the context of intestinal dysbiosis. Thus, prospective studies should monitor circulating sMAdCAM-1 and α4β7$^+$ T_{reg}, T_R17 and T_H17 cells in cancer patients treated with ICIs alone or in combination with FMT or vedolizumab in order to correlate these parameters with efficacy and toxicity.

Materials and Methods

Patient characteristics and clinical description.

Medical centers and regulatory approvals for translational research. For feces and serum collection, ancillary studies were conducted at Gustave Roussy (GRCC), France according to the ethical guidelines and approval of the local CCPPRB. The ONCOBIOTICS trial (NCT04567446, ID-RCB N°: 2017-A02010-53), a multicentric prospective observational study was designed to evaluate the impact of the microbiome composition in the clinical outcome of patients with advanced NSCLC treated with anti-PD-(L)1 (*10*). We enrolled patients across 12 academic centers in France and two centers in Canada. Adult patients with pathologically confirmed advanced non squamous or squamous NSCLC and an Eastern Cooperative Oncology Group (ECOG) performance-status score of 0-2, amenable to ICI as standard-of-care and compelling to provide a stool sample were eligible. Eligible patients received ICI following progression on platinum-based chemotherapy regimens, either with nivolumab or atezolizumab regardless of PD-L1 expression or with pembrolizumab if PD-L1 $\geq$ 1%. Given the subsequent approval of first-line ICI during the study accrual period, patients who received pembrolizumab monotherapy or in combination with platinum-based chemotherapy, depending on PD-L1 expression were also included. Standard-of-care treatment was continued until disease progression, unacceptable adverse effects, or completion as per protocol (2 years of ICI). Full eligibility criteria are listed in the trial protocol (available at NCT04567446). Baseline characteristics including a detailed listing of concurrent medications received the last 2 months prior to ICI initiation and the date of last follow-up were entered at each center in an electronic case report form. Feces were collected according to the International Human Microbiome Standards (IHMS) guidelines (SOP 03 V1) before the first injection. Serum samples were prospectively collected prior anti-PD(L)1 immunotherapy within the Gustave Roussy sponsored PREMIS study (NCT03984318). Patients enrolled in PREMIS were above 18-year-old, with histologically proven solid malignancy and at least one tumor evaluation by imaging after immunotherapy onset. The PREMIS study was approved by an ethical committee (Comité de Protection des Personnes Sud-Ouest et Outre Mer I; N°ID-RCB: 2018-A01257-48) and the institutional review board (CSET #2018/2728). All enrolled patients provided a signed informed consent. Furthermore, we disposed of one cohort of 45 patients with NSCLC receiving treatment with anti-programmed death 1 (PD-1/PD-L1) checkpoint inhibitors between 2014 and 2020. Patients were treated in the Georges François Leclerc Cancer center. For all patients, abundance of transcripts from RNA-seq data was available, and for some patients, PDL-1 protein expression in tumor cells assessed using immunohistochemistry was also available, as well as tumor mutational burden (TMB) estimated from whole-exome sequencing. We had access to a cohort of patients with advanced renal cell carcinoma (RCC) treated with an anti-PD-1 enrolled in the NIVOREN trial (NCT03013335, N° EudraCT: 2015-004117-24). Finally, additional cohort of patients with bladder cancer treated with an anti-PD-(L)1 alone or together

with anti-CTLA-4 and enrolled in the IOPREDI study (EudraCT Number: 2016-005068-33) was explored. For tumor flow cytometric analyses of fresh or cultivated TILs, all tumor tissues were processed according to the Helsinki Declaration and the guidelines of the French ethics committee for research on human tissues. Tissue biocollection was registered with the French Ministry for Higher Education and Research (DC-2014-2206) with approval from the ethics committee (CPP Ouest IV, Nantes). Each patient included in this study signed an informed consent form. For the four fresh NSCLC tumors examined by flow cytometry, patients over 18 years of age from Gustave Roussy Cancer Campus, Marie Lannelongue, Cochin, Tenon, Foch, Kremlin-Bicêtre, and Saint Joseph hospitals, with primary resectable tumors provided written informed consent according with protocols reviewed and approved by institutional ethics committee including the investigator-sponsored, study "mAb in sitro test", N°ID-RCB: 2016-A00732-49. The experiments conformed to the principles set out in the WMA Declaration of Helsinki and the Department of Health and Human Services Belmont Report. For collection of endoscopic and blood samples, a clinical study "Einfluss von Antibiotika auf das Darm-Chemokinnetzwerk bei Patienten mit soliden Tumoren" was conducted at University Clinics Heidelberg, Germany according to the ethical guidelines and approval of the Regierungspräsisium Karlsruhe.

Collection of endoscopic samples and blood samples. Eligible patients underwent ileocolonoscopy according to clinical standard protocols for non-study related indications (**table S2**) between July 2018 and November 2019. When feasible, endoscopic biopsies of the mucous membranes of the terminal ileum, caecum, and right and left colons were performed in each patient. Tissue samples were either snap frozen in liquid nitrogen and stored at −80°C or immersed into 2% PFA for histology. In addition, two blood samples (10 ml in EDTA tubes) were collected before ileocolonoscopy. All included patients responded to a questionnaire to assess dietary history and baseline clinical data were retrieved from the local clinical information system.

Metagenomic analysis of patient stools. Fecal samples were prospectively collected at different time points (V1: pre-ICI, V2: before the second ICI injection, V3: at 3 months post-ICI and V4: at 6 months post-ICI) at each center following the International Human Microbiome Standards (IHMS) guidelines, but only the baseline V1 sample was considered for this analysis. For metagenomic analysis, the stools were processed for total DNA extraction and sequencing with Ion Torrent technology following MetaGenoPolis (INRAE) France, as previously reported (*7*, *10*, *11*). The gene abundance table was processed using the MetaOMineR (momr R) package. We conducted PERMANOVA using the function adonis from the vegan R package (v2.5-7) with the Atchinson distance on centered log ratios using species-level abundances and 1000 permutations. We employed an ensemble of univariate and multivariate differential abundance methods that included age, gender and cohort in the models, using either species-level relative abundances or count

data, where absolute raw counts were estimated from species-level relative abundances by multiplying these values by the total number of reads for each sample. These differential abundance methods included; DESeq2 (v.1.30.0) (*77*) with the poscounts estimator (DESeq2_poscounts); DESeq2 with the poscounts estimator and a zero-inflated negative binomial model (DESeq2_poscounts_zb); DESeq2 with trimmed mean of M values (TMM; DESeq2_TMM); limma (v3.46.0) (*78*) with TMM values (limma_voom_TMM); limma with TMM values and a zero-inflated negative binomial model (limma_voom_TMM_zb); ANCOM-BC (v.1.0.1) (*79*); Maaslin2 (v.1.4.0) (*80*) and LeFsE (*81*).

Soluble MAdCAM-1 quantification in patients. sMAdCAM-1 was quantified in patients sera with Bio-Plex 200 systems (Bio-Rad) and sMAdCAM-1 kit from R&D system (Human Luminex Discovery Assay LXSAHM).

Cell culture, reagents, and tumor cell lines. MCA-205 fibrosarcoma cells (syngeneic from C57BL/6 mice) and 4T1 WT and 4T1- *Il22ra1*$^{-/-}$ breast cancer cell lines (syngeneic from BALB/c, kindly provided by Dr. Sebastian Kobold (*62*), LMU Klinikum, Germany) were cultured at 37°C in the presence of 5% CO_2 in RPMI 1640 containing 10% FCS, 2 mM L-glutamine, 100 IU/ml penicillin, streptomycin, 1 mM sodium pyruvate, and MEM non-essential amino acids (henceforth referred to as complete RPMI 1640). Luciferase-transfected TC-1 cell lines (syngeneic for C57BL/6 mice, kindly provided by Prof. E. Deutsch (Gustave Roussy Cancer Campus (GRCC)), France) were cultured at 37°C in the presence of 5% CO2 in complete RPMI 1640 and 1 mM HEPES buffer. Cell lines were regularly tested for mycoplasma contamination and were not used after more than 10 passages.

Mice. All animal experiments were carried out in compliance with French and European laws and regulations. The local institutional animal ethics board and French Ministère de la Recherche approved all mouse experiments (permission numbers: 2016-049-4646, 2017_049_99741, 2019_036_21124, 2022_064_40164). Experiments were performed in accordance with Government and institutional guidelines and regulations. Female C57BL/6 and BALB/c were purchased from Harlan or Envigo (France). Mice were used between 7 and 12 weeks of age. *Madcam1*$^{-/-}$ and *Itgb7*$^{-/-}$ mice were a kind gift from A. Schippers (University hospital Aachen, Aachen, Germany). *Madcam1*$^{-/-}$ and *Itgb7*$^{-/-}$ mice and control littermates were backcrossed on the C57BL/6 background and were obtained from an in-house breeding at the local animal care facility at the University Hospital Aachen. The Kaede mice were a kind gift from M. Tomura (Kyoto University, Kyoto, Japan) and were backcrossed and maintained on the C57BL/6 background. All mouse experiments were performed at the animal facility in GRCC where animals were housed in specific pathogen-free conditions.

Antibiotic treatments. If not indicated otherwise, mice were treated with a broad-spectrum antibiotic (ABX) solution containing ampicillin (1 mg/ml), streptomycin (5 mg/ml), and colistin (1 mg/ml) (Sigma-Aldrich) (ACS) added to sterile drinking water. In experiments where single antibiotics were used, the concentrations were identical as stipulated above for ampicillin (A), colistin (C), or streptomycin (S), and was 1 mg/ml for erythromycin, 0.25 mg/ml for vancomycin, 6.15 mg/ml for ceftazidime, 4.1 mg/ml for cefepime, 16.4/2.05 mg/ml for piperacillin/tazobactam and 1.13 mg/ml rifaximin. Solutions and bottles were changed three times weekly. Antibiotic activity, in the experiments where the antibiotic mix was used, was confirmed by cultivating fecal pellets for 48 hours at 37°C in aerobic and anaerobic conditions. To evaluate the impact of antibiotics on MAdCAM-1 expression in the intestine, ACS were administered during 7 to 14 days and discontinued for 4 days (ACS+4d) or for 12 days (ACS+12d) or continued until the end of the experiment in drinking water of naive or MCA-205 tumor-bearing mice.

FMT experiments. In fecal microbial transplantation (FMT) experiments, mice received 3 to 7 days of ACS before undergoing FMT the next day by oral gavage. Fecal microbiota transfer (FMT) was performed by thawing fecal material. Mice were placed in a new cage. Two hundred µl of the suspension was then transferred by oral gavage into each ATB pre-treated recipient using animal feeding needles. In addition, another 100µl was applied on the fur of each animal.

Oral bacterial gavage with commensal species. *Akkermansia p2261* and *Enterococcus hirae* 13144 were provided by everImmune, Villejuif, France. *Enterococcus hirae* 13144 isolates were originally isolated from spleens or mesenteric lymph nodes of SPF mice treated with CTX at GRCC, Villejuif, France. *Enterocloster clostridioformis* was isolated from the ileum of mice that received ACS in drinking water for 7 days followed by 4 days ABX- free at GRCC, Villejuif, France. *Akkermansia p2261, E. clostridioformis* and *Lactobacillus reuteri* were grown on COS plates in an anaerobic atmosphere created using three anaerobic generators (Biomerieux) at 37°C for at least 72 hours. *E. hirae* 13144 was grown in 5% sheep blood enriched Columbia agar for 24 hours at 37°C in aerobic conditions. Colonization of specific-free pathogens (SPF) C57BL/6 mice was performed by oral gavage with 100 µl of suspension containing 1×10^8 to 1×10^9 bacteria. Bacteria concentrations were calculated using a fluorescence spectrophotometer (Eppendorf) at an optical density of 600 nm in NaCl 0.9%. Mice were gavaged once to four times. In experiments concerned, oral gavages were performed concomitantly with anti-PD-1 Ab treatment (four times). The identification of specific bacteria was accomplished using a Matrix-Assisted Laser Desorption/ Ionisation Time of Flight (MALDI-TOF) mass spectrometer (BRUCKER, France).

Oral gavage with biliary acids. Mice were gavaged four times, every two days with 120 mg per kilogram of body weight with lithocholic (LCA) or ursodeoxycholic (UDCA) acids diluted in corn oil.

Subcutaneous cancer mouse models. *MCA-205 sarcoma and 4T1 WT and Il22ra1*$^{-/-}$ *breast cancer.* Syngeneic C57BL/6 mice were implanted with 0.8×10^6 MCA-205 sarcoma cells subcutaneously and treated intraperitoneally (i.p.) when tumors reached 20 to 40 mm² in size with anti-PD-1 mAb (250 μg/mouse; clone RMP1-14) or isotype control (clone 2A3). Syngeneic BALB/c mice were implanted with 0.5×10^5 4T1 WT or *Il22ra1*$^{-/-}$ breast cancer cells subcutaneously and treated i.p. with anti-PD-1 or isotype control mAbs. Mice were injected four times at three-day intervals with anti-PD-1 or isotype control mAbs. Tumor length and width were routinely monitored three times a week by means of a caliper. In experiments using anti-α4β7 mAb (DATK32, 200 μg per mouse) or anti-MAdCAM-1 mAb (MECA-367, 200 μg per mouse), or their isotype controls, clone 2A3 in both cases), monoclonal Abs were injected i.p. every three days starting from day 0 until the final anti-PD-1 injection. In the experiment using anti-IL-17A mAb (clone IL-17F, 100 μg per mouse), mice were injected i.p. concomitantly with anti-PD-1 treatment. All antibodies were purchased from Bio X Cell, NH, USA. In the experiment using anti-CD62L or anti-PSGL-1 mAbs (clone Mel-14 and 4RA10, respectively, 100 μg per mouse), mice were injected i.p. concomitantly with anti-MAdCAM-1 treatment. *Orthotopic luciferase engineered-TC-1.* C57BL/6 mice were anesthetized with isoflurane. Under sterile conditions, a lateral incision was made on the chest wall of each mouse and 6×10^5 TC-1-Luc cells in 10 μl Matrigel (Corning) were injected into the lung. The skin incision was closed with a surgical skin clip. To monitor tumor growth twice weekly, mice received a percutaneous injection of luciferase substrate (Beetle Luciferin potassium salt, Promega) at a dose of 150 mg per kilogram of body weight, and 8 min post-luciferin inoculation, and photons were acquired on a Xenogen IVIS 50 bioluminescence in vivo imaging system (Caliper Life Sciences Inc., Hopkinton, MA, USA).

Construction of liver-specific overexpression vector.

The plasmid pLIVE vector was purchased from Mirus (Cat. #MIR 5420, Madison, WI, USA), and Madcam1 (NM_013591) mouse tagged ORF clone from OriGene (Cat. #MR226268, Rockville, MD, USA). pLIVE vector, which is designed for liver-specific expression and utilizes a chimeric promoter composed of the mouse minimal albumin promoter and the mouse alpha fetoprotein enhancer II, was selected to construct the liver-specific Madcam1 overexpression vector.

The gene encoding mouse Madcam1 was amplified from Madcam1 (NM_013591) mouse tagged ORF clone (pCMV6-Entry-Madcam1) with primers listed below by RT-PCR with OneTaq hot start DNA polymerase (Cat. #M0481, NEB, Ipswich, MA, USA). For more effective expression of Madcam1, Kozak sequence (underlined) were selected and added in forward primer (Madcam1-F-Kozak: 5′-GGCGCGCC<u>GCCACC</u>ATGGAATCCATCCTGGCC-3′; Madcam1-R:5′-CTCGAGTCATAGGTGTGT ACATGAGC-3′). Then, the Madcam1 cDNA was cloned into the AscI and Xho I sites of the pLIVE vector, yielding the pLIVE-Madcam1 plasmid. The huge amount of vector DNAs were prepared by an PureLink™

expi endotoxin-free maxi plasmid purification kit (Cat. #A31231, Invitrogen, Carlsbad, CA, USA) for further hydrodynamic tail vein injection.

Generation of a liver-specific overexpression mouse model. Six-week-old female wild-type C57BL/6 mice were purchased from Envigo, France (Envigo, Huntingdon, UK). All mice were maintained in a temperature-controlled and pathogen-free environment with 12-hour light /dark cycles, with food and water ad libitum. The constructs of pLIVE as a control and pLIVE-Madcam1 vector DNA (250 μg per mouse) were delivered to the mouse liver using the hydrodynamic tail vein injection procedure by using the TransIT®-QR hydrodynamic delivery solution (Cat. #MIR 5240, Mirus, Madison, WI, USA) according to the manufacturer's instructions.

Flow cytometry. ***Mouse.*** Tumors, mesenteric lymph nodes (mLN), draining lymph nodes (tdLN), contralateral lymph nodes (cLN), ilea and spleens were harvested at different time points as indicated in the individual experiments. Excised tumors were cut into small pieces and digested in RPMI medium containing Liberase™ at 25 μg/ml (Roche) and DNase1 at 150 IU/ml (Roche) for 30 minutes at 37°C and then crushed and filtered twice using 100- and 70-μm cell strainers (Becton & Dickinson). Lymph nodes and spleen were crushed in RPMI medium and subsequently filtered twice through a 100-μm cell strainer. Ilea were collected and fat tissue, Peyer's patches and feces were removed. Intestines were cut longitudinally and then cut transversally into small pieces into a tube. Pieces were transferred into a new 50-ml tube with 20 ml of IEC washing medium (PBS, 5% FCS, 5 mM EDTA, and 1 mM DTT), vortexed and shaken at 37°C for 20 min. Tissue and cell suspension were filtered with a cell strainer (100 μm). The filtered cell suspension was discarded. The remaining tissue was incubated for 30 min in LPC medium (RPMI, 5% FCS, 0.25 mg/ml collagenase VIII, and 10 U/ml of DNAse I) and then meshed through a cell strainer (100 μm). The cells obtained from the lamina propria in cell suspension were washed twice with PBS and kept on ice for subsequent analysis. Four million cells, from each sample were pre-incubated with purified anti-mouse CD16/CD32 (clone 93; eBioscience) for 30 min at 4°C, before membrane staining. For intracellular staining, the FoxP3 staining kit (eBioscience) was used. Dead cells were excluded using the Live/Dead Fixable Yellow dead cell stain kit (Life Technologies) or LIVE/DEAD™ Fixable Aqua Dead Cell Stain Kit (Biolegend). For IL-17 and IL-22 staining, cells were stimulated at 37°C during 4 hours with PMA/Ionomycine and Golgi stop cocktail. Anti-mouse antibodies (clone; RRID; μl per 10^6 cells in 100μl) for CD3ε (145-2C11; AB_2629687; AB_893317; 1μl), CD4 (RM4-5; AB_493374; AB_312729; 1μl), CD8α (53-6.7; AB_2564027; 0.5μl), CD25 (3C7; AB_2563060; 1μl), CD44 (IM7; AB_493713; 1μl), CD45 (30-F11; AB_893339; AB_493715; AB_493535; 1μl), CD62L (MEL-14; AB_313093; 1μl), CD127 (A7R34; AB_10897948; 1μl), FoxP3 (FJK-16s; AB_1210557; 1μl), RORγt (B2D; AB_2784671; 1μl), CXCR3 (CXCR3-173; AB_2814078; 1μl), CCR5 (HM-CCR5; AB_2801746; 2μl), CCR6 (29-2L17;

AB_2562513; 1µl), CCR9 (CW-1.2; AB_2889490; 2µl), α4β7/LPAM-1 (DATK32; AB_2811331; 2µl), MAdCAM-1 (MECA367; AB_2629562; 1µl), IL-17A (eBio17B7; AB_11220280; 1µl), IL-22 (1H8PWSR; AB_10598646; 1µl),CD31 (390; AB_830757; 1µl), PNAd (MECA-79; AB_10804391; 1µl), CD62P (RB40.34; AB_2917917; 0.5µl), CD62E (10E9.6; AB_2742835; 0.5µl), CD64 (X54-5/7.1; AB_2629778; 1µl), CD19 (6D5; AB_439718; 1µl) and F4/80 (BM8; AB_893493; 1µl) (all purchased from Thermofisher, Miltenyi, BioLegend, BD and eBioscience) were used to stain cells. Stained samples were acquired on CytoFLEX S 13 colors (Beckman Coulter) and analyses were performed with Kaluza software 2.1 (Beckmann Coulter). TH17 gating depended on the mouse model that was used. The Kaede fluorochrome could not retain its photoconverted state upon fixation with PFA. For Kaede mice, TH17 cells were identified as $CXCR3^{-}$ and $CCR6^{+}$ $CD4^{+}$ T cells and Tregs as $CD127^{-}$ $CD25^{hi}$ $CD4^{+}$ T cells. In other mouse models, TH17 and Tr17 cells were defined after gating on $ROR\gamma t^{+}$ $CD4^{+}$ or $ROR\gamma t^{+}$ and/or IL-$17A^{+}$ $CD25^{+}$ $FoxP3^{+}$ $CD4^{+}$ cells, respectively. ***Human.*** $CD45^{+}$ TILS were sorted according the manufacturer recommendation (CD45 (TIL) MicroBeads, human; Myltenyi; #130-118-780). Anti-human antibodies (clone; RRID) for CD8 (SK1; AB_1645481), TIGIT (741182; AB_2872307), CD25 (BC96; AB_2563807), PD1 (EH12.1; AB_2738425), CD3 (UCHT1; AB_2744387), CD4 (SK3; AB_2870220), CD45 (HI30; AB_2870179), FOXP3 (PCH101; AB_1724125), IL-17 (EIO64dec17; AB_10596502), RORgt (rat (AFKJS-9; AB_2848500), IL-22 (2G12A41; AB_2571931), CTLA4 (BIN3; AB_396176) and α4β7/LPAM-1 (Hu117; MAB100078R-100UG) (all purchased from Thermofisher, BioLegend, BD, R&D and eBioscience) were used to stain cells. For IL-17 and IL-22 staining, cells were stimulated at 37°C during 4 hours with PMA/Ionomycine and Brefeldine A cocktail. Dead cells were excluded using the LIVE/DEAD™ Fixable Aqua Dead Cell Stain Kit (Biolegend). Stained samples were acquired on BD LSRFortessa™ X-20 Cell Analyzer and analyses were performed with FlowJo v10.8.1 software.

Immunohistochemistry. 3-millimeter-thick sections of formalin-fixed, paraffin embedded murine ileum were prepared as "swiss rolls" and were mounted on poly-L-lysine-coated slides, deparaffinized and hydrated through graded alcohols to water. For image analysis and MAdCAM-1 quantification (clone MECA-367, MABF2072 Sigma-Aldrich), QuPath software was used (*82*). ROIs were defined firstly by "simple tissue detection" function and modified by hand in each whole slide image (WSI). To quantify the cell density of biomarker-positive cells, "Positive cell detection" was used.

Histological processing of MadCAM-1 expressing-liver

Murine livers were obtained from the experiments and fixed in buffered formalin for 24-48h, then cut vertically in parallel sections, which were sent to conventional histological processing. For morphological analysis, hematoxylin, eosin & saffron staining (HES) slides were confectioned. Bond Leica automated immunostainer instruments were used to perform immunohistochemistry. Paraffin sections were processed

for heat-induced antigen retrieval (ER2 corresponding EDTA buffer pH9) for 20 min at 100°C. Slides were incubated with the antibody for 1 hour at room temperature. The following antibodies were used: anti-Foxp3 (Cell Signaling, D608R, rabbit, 1:200, ER2) and anti-RORγt (Abcam, EPR20006, rabbit, 1:3000, ER2). The antibodies were detected with di-amino-benzidine-peroxidase (DAB). Finally, the sections were counterstained by hematoxylin (Leica Biosystems).

Quantification of FoxP3 and MadCAM-1 in MAdCAM-1 expressing-liver

Images for analysis were acquired as WSI with a slide scanner Zeiss Axio Scan.Z1 and Olympus VS120 whole-slide imaging system. Image analysis was performed using QuPath, version 0.3.2 (*102*). WSI for FOXP3 were evaluated through multiple steps: (1) simple tissue detection was performed (threshold 220, requested pixel size 20 µm, minimum area 100,000 µm^2, max fill area
100,0000 µm^2, smooth image, cleanup with median filter, smooth coordinates, single annotation); (2) fast cell counts (cell detection channel DAB, Gaussian sigma 1.5 µm, background radius 15 µm, use difference of Gaussians, cell detection threshold 0.5, DAB threshold 0.5); (3) exclusion of detections corresponding to artifacts (folded tissue, dark pigment sedimented, hemorrhage, intravascular lymphocytes) was performed by a pathologist (LL); (4) create density map; (5) select the region of interest (ROI) with 1 mm^2, representing the highest density in the tissue (hotspot). Hot-spot density was then normalized for each experiment based on the control group, then pooled (n=2). WSIs for RORγt were evaluated for hotspot in comparison to the same ROI as indicated for FOXP3. The RORγt positive nuclei were then counted manually, based on morphology, as many nuclei from hepatocytes were also stained in some of the evaluated conditions.

Tracing migration of leukocytes from the gut to the TME. ***Kaede experiments.*** Kaede transgenic mice were anesthetized with 2 to 2.5% isoflurane and administered buprenorphine (0.01 mg per kilogram of body weight) i.p. for analgesia. For photoconversion of ilea, abdominal skin and peritoneum were cut at the midline to access the intraperitoneal terminal ileum. For photoconversion of the caecum, ileum and mesenteric lymph nodes, the cecal pole was identified and the cecal pole including the terminal ileum, the mesenteric lymph nodes and the proximal colon were gently mobilized through the midabdominal incision onto a sterile plastic-coated surgical drape. Non-target structures were covered with aluminum foil. The ventral and dorsal parts of the targeted structures were exposed to ultraviolet light emitted from a 395 nm wave length emitting Diode (Winzwon) light for 30 s each. After illumination, the tissue was moistened with sterile isotonic sodium chloride and gently repositioned into the peritoneal cavity. The peritoneal membrane was closed by continuous stitch with a 5-0 monofil nylon suture (Ethicon). The skin was closed with two 9-mm wound clips (EZ Clip Kit). ***CFSE staining of mesenteric LN cells up to TME or tumor draining lymph nodes.*** C57BL/6 mice were anesthetized with 2 to 2.5% isoflurane and

administered buprenorphine (0.01 mg per kilogram of body weight) i.p. for analgesia. Abdominal skin and peritoneum were cut at the midline to access the mesenteric lymph nodes. The mesenteric lymph nodes were gently mobilized through the midabdominal incision onto a sterile plastic-coated surgical drape. Ileum draining mesenteric lymph nodes were visually identified according to their vasculature. The two most prominent mesenteric lymph nodes were injected with 100 µM CFSE diluted in 5 µl of PBS using a 30G insulin syringe. After repositioning the mesenteric lymph nodes, the peritoneal membrane was closed by continuous stitch with a 5-0 monofil nylon suture (Ethicon).

RNA extraction and RT-qPCR. Lysis and extraction protocols were identical for human and mouse samples. Tumor or intestinal samples were snap frozen in liquid nitrogen in RLT Plus buffer containing 0.1% beta mercaptoethanol. On the day of extraction, samples were thawed at 4°C and homogenized in a microtube homogenizer (Benchmark Scientific) in RNA- free glass bead tubes (Dutscher). Total RNA extraction and genomic DNA removal were performed with the RNeasy Mini kit (Qiagen), following the manufacturer's recommendations. A maximum of 1 µg of RNA, measured using a NanoDrop™ Spectrophotometer (Thermo Fischer Scientific), was reverse transcribed into cDNA with a mix composed of SuperScript III Reverse Transcriptase (Life Technologies), RNaseOUT™ Recombinant Ribonuclease Inhibitor (Life Technologies), Random primers (Promega) and Deoxynucleoside Triphosphate Set, PCR grade (Roche Diagnostics).

Quantitative gene expression assay. The expression of mouse and human *B2m*, *Foxp3*, *Ifng*, *Il10*, *Il17a*, *Il22, Madcam1*, *Vcam1, Ppia*, *Rorc*, *Il18* and *Tbx21* (all from Life Technologies) was analyzed with the TaqMan® Gene Expression Assay using the Universal Master Mix II on a StepOnePlus™ Real-Time PCR System (Life Technologies). Amplifications were carried out using the following ramping profile: one cycle at 95 °C for 10 min, followed by 45 cycles of 95 °C for 30 s and 60 °C for 1 min. Quantitative RT-PCR data were normalized to the expression levels of the housekeeping genes *B2M* or *Ppia*, as indicated in each figure, by means of the $2^{-\Delta Ct}$ method multiplied by 10^6.

Tissue lysis and chemokine analyses. Intestinal and tumoral samples were snap frozen in liquid nitrogen in a non-denaturing cell lysis buffer containing 50 mM Tris HCL pH 7.4, 150 mM NaCl, 300 mM sucrose, 10 mM EDTA ,0.1% Triton 100X and Complete™, Mini, EDTA-free Protease Inhibitor Cocktail (Roche). For subsequent lysis, samples were thawed at 4°C and lysed on a tube homogenizer (Precellys) in ceramic beads lysis tubes (Precellys). Tissue homogenate was centrifuged at 4000*g* for 5 min. The supernatant was used for subsequent analysis. Chemokine concentrations in the tissue lysate were determined according to the manufacturer's recommendation using CCL2, CCL3, CCL4, CCL5, CCL25 and MAdCAM-1 Duoset

ELISA kits (R&D) or using Legendplex Mouse proinflammatory chemokine panel (Biolegend) with cytometric analysis performed on a CytoFLEX S (Beckmann coulter).

Ileum tissue sample preparation and bile acids detection by UHPLC-MS. About 30 mg of collected tissue were weighted and placed in a 2ml homogenizer tube with ceramic beads (Precellys, Bertin Technologies, France) with 1 ml of ice-cold extraction mixture (methanol/water, 9/1, −20°C, with labeled ^{13}C-glycocholic acid as internal standard). To facilitate endogenous metabolites extraction, samples were then completely homogenized (3 cycles of 20 s/ 2380*g*; Precellys 24, Bertin Technologies, Montigny-le-Bretonneux, France) and centrifugated (10 min at 15,000*g*, 4°C). In order to detect bile acids, 300 µl of supernatants were collected and treated following the protocol previously described (*83*). Bile acids analysis was performed by LC-MRM (Multiple Reaction Monitoring) with a 1290 UHPLC (Ultra-High Performance Liquid Chromatography, Agilent Technologies) coupled to a mass spectrometer 6470 TQ (Triple Quadrupole, Agilent Technologies), as previously described (*84*). Targeted data were cleaned with a R (version 4.0) dedicated package (@Github/Kroemerlab/GRMeta).

Bulk RNA sequencing of α4β7$^{+/-}$ CD4$^+$ mesenteric T cells. α4β7$^+$ and α4β7$^-$ CD4$^+$ T cells were isolated from mLN by flow cytometry. Preparation of mRNA-seq libraries and nextseq 75SE run deep sequencing were performed at GeneCore EMBL (Heidelberg, Germany).

Single-cell RNA sequencing by BD Rhapsody. After isolation of CFSE$^+$ CD4$^+$ T cell by flow cytometry, 10.000 cells were washed in cold PBS and loaded onto a BD Rhapsody™ cartridge and processed according to the manufacturer's instructions for targeted single-cell RNA-seq using the predesigned Immune Response Panel (Mouse). The library was clustered at 1.75pM on a NextSeq500 system (Illumina) to generate ~40,000 paired- end reads per cell using High Output v2 chemistry. Sequenced single-cell data was demultiplexed using bcl2fastq2 v2.20.

Single-cell TCR and RNA library construction and sequencing by 10X Genomics Chromium. After isolation of CFSE$^+$CD4$^+$ and CD8$^+$ T cell by flow cytometry from mLN, cLN, tdLN, and tumor, single-cell libraries construction were performed using Chromium Next GEM Single Cell 5′ kits v2 (PN-1000263), Chromium Next GEM Chip K, Single Cell VDJ 5′ Gel Bead, Chromium Single Cell Mouse TCR amplification kit (16 rxns (reactions)) PN-1000254, Library construction kit (16 rxns) PN-1000190 and Dual Index kit TT set A (96 rxns) PN-1000215 kits according to the manufacturer's protocol. Briefly, single cell suspensions from a total of 500 to 20,000 cells with barcoded gel beads and partitioning oil were loaded

to Chromium Next GEM Chip K to generate single-cell gel bead-in-emulsion. Full-length cDNA along with cell barcode identifiers were PCR-amplified to generate 5′Gene Expression (GEX) libraries and V(D)J libraries. Libraries were sequenced using a NovaSeq 6000 (Illumina) to achieve a minimum of 23,000 paired-end reads per cell for GEX and 7000 paired-end reads per cell for V(D)J. Reads were aligned using Cell Ranger v6.1.1 to the GRCm38 mouse references.

Repertoire clonality. TCR sequencing data were processed using the "immunarch" R package. Clonotypes within each population and compartments were then divided into fractions with an occurrence of 1 or >1. The cumulative frequency of each fraction was calculated within the repertoire of each sample.

Sequence similarity analysis. DeepTCR was used to cluster paired TRA-TRB clonotypes based on sequence similarity, using a train Variational Autoencoder (VAE). This generates clusters composed of sequences with a likelihood of shared specificities. The clusters were assigned as being mLN, tumor/dLN or shared based on the percentage of clonotypes composing them. A cluster was considered as specific to a compartment if the log2FC was equal to or higher than 1.5, if else clusters were considered as shared between the compartments (*52*).

Single cell RNA-seq analysis

Expression matrix was analysed using the R environment (version 4.2.1) with the Seurat package (v4.2.1). High-quality cells characterized by fewer than 10% of mitochondrial genes more than 200 UMI features and less than 15,000 unique UMI were selected for further analysis. Count matrix was normalized with regularized negative binomial regression based on the 3000 most variable genes using the SCTransform function. Principal component analysis was used for dimensionality reduction using the RunPCA on the 3000 most variable genes. Contributive components were identified visually using an elbow plot. Nearest neighbors were determined with the FindNeigbhors function using contributive PCA components and cells were clustered using the louvain clustering algorithm with the FindClusters function. Resolution of the clustering algorithm was chose based on a bootstrapping procedure, the resolution giving rise to the maximum number of clusters with co-assignments probabilities superior to 5% was chosen. Differential gene expression (DGE) analysis was performed using the FindMarkers function and p-value were corrected using the p.adj base function with the false discovery rate procedure. Volcano plot visualization was performed using the ggplot2(v3.4.0) R package, Heatmap visualization was performed using the ComplexHeatmap (v2.14.0) R package and Venn Diagram visualization was performed using the ggven R package (v0.1.9).

Cell lines and treatment

Culture media and supplements for cell culture were obtained from Life Technologies (Carlsbad, California, USA) and plastic material came from Greiner BioOne (Kremsmünster, Austria) and Corning (Corning, New York, USA). Mouse transformed endothelial sinusoidal cells (TSECs) were a generous gift from Professor B. P. Fennimore (University of Colorado Anschutz Medical Campus, Aurora, CO, USA) and brain endothelial cells (bEnd.3) were purchased from ATCC. TSECs were cultured in DMEM/F-12 (Dulbecco's Modified Eagle Medium/Nutrient Mixture F-12) plus endothelial growth supplement (Cat. #1052, ScienCell, Carlsbad, CA, USA), supplemented with 10% fetal bovine serum (FBS), 10 U/ml of penicillin sodium and 10 µg/ml of streptomycin sulfate. bEnd.3 cells were cultured in DMEM with 2.5 mM L-glutamine, supplemented with 10% FBS, 10 U/ ml of penicillin sodium and 10 µg/ml of streptomycin sulfate. Both cell lines were cultured in the presence of 5% CO2 at 37°C. Transfected TSEC (TSEC::MAdCAM-1-GFP) and bEnd.3 cells (bEnd.3::MAdCAM-1-GFP) were selected with 500 µg/ml of G418 sulfate (50 mg/mL, Cat. #10131027, Gibco) and stable transformants were maintained under G418 selection pressure. Recombinant murine TNF-α (Cat. #315-01A, PeproTech) and IL-1β (Cat. #211-11B, PeproTech) were diluted in culture media from a stock of 40 µg/mL at the time of treatment. Bile acids (lithocholic acid (LCA) (#700218P-10MG, Sigma-Aldrich), dehydrolithocholic acid (3-oxo-LCA) (#700217P-10MG, Sigma-Aldrich), allolithocholic acid (allo-LCA) (#700330P-5MG, Sigma-Aldrich), isoallo-LCA (#R203424-1MG, Sigma-Aldrich), taurolithocholic acid sodium salt (Tauro-LCA) (#700252P-10MG, Sigma-Aldrich), sodium chenodeoxycholate (CDCA) (#C8261-1G, Sigma-Aldrich), sodium taurochenodeoxycholate (TCDCA) (#T6260-100MG, Sigma-Aldrich), deoxycholic acid (DCA) (#30960-25G, Sigma-Aldrich), ursodeoxycholic acid (UDCA) (#208590250, Thermoscientific), tauroursodeoxycholic acid (TUDCA) (#580549-1GM, Millipore), glycoursodeoxycholic acid (GUDCA) (#06863-1G, Sigma-Aldrich), taurodeoxycholic acid (TDCA) (#580221-5GM, Millipore)) and FXR agonists/antagonists (GW4064 (#G5172-5MG, Sigma-Aldrich), cilofexor (#HY-109083, MCE), tropifexor (#HY-107418, MedChemExpress (MCE)), and (Z)-guggulsterone (#G5168-25MG, Sigma-Aldrich)) dissolved in DMSO were diluted 1:1000, 1:10,000, and 1:100,000 in culture media to a final concentration of 100 µM, 10 µM, and 1µM. Bacteria were cultured (and in some instances pasteurized) before being diluted in culture media to a working concentration with an optical density (OD) of 0.5, 0.25, and 0.1 (*Akkermansia p2261* everImmune strain, *E. clostridioformi*s).

Construction of MAdCAM-1 promoter plasmid

The MAdCAM-1 promoter construct is a PCR product from mouse genomic DNA amplified using 5′-GGAATTCTACCCCCACAGGCCTGCC-3′ as forward primer (EcoRI site is underlined, Eurofins, Nantes, France) and 5′-AGGCCGCGGGGGCCGGCAGCTTCCTAC-3′ as the reverse primer (SacII site is underlined, Eurofins). After digestion by EcoRI-HF and SacII (NEB, Ipswich, MA, USA), the MAdCAM-1 promoter DNA fragment was extracted using a Monarch® DNA gel extraction kit (NEB, Ipswich, MA,

USA). The purified fragments were subcloned into the promoterless pAcGFP1-1 vector (Clontech, Mountain View, CA, USA).

Establishment of MAdCAM-1 promoter reporter cell lines

TSEC and bEnd.3 cells were transfected with the recombinant expression vector pAcGFP1-1-MAdCAM-1 using FuGENE® HD transfection reagent (Cat. # E2312, Promega). Twenty-four hours post-transfection, stable transfectants were isolated by selection with 500 μg/ml of G418. The transfectants (namely TSEC::MAdCAM-1-GFP and bEnd.3::MAdCAM-1-GFP) were maintained in culture medium containing 500 μg/ml of G418 for 2 weeks. The G418-resistant cells were selected and single cell clones were isolated to establish TSEC::MAdCAM-1-GFP and bEnd.3::MAdCAM-1-GFP stable cell lines expressing GFP under the control of the MAdCAM-1 promoter.

High-content microscopy

TSEC::MAdCAM-1-GFP and bEnd.3::MAdCAM-1-GFP were seeded in 384-well/96-well μclear imaging plates (Greiner BioOne) and allowed to adapt overnight. Cells were treated with the indicated agents, then fixed with 3.7% paraformaldehyde (PFA, w/v in PBS) (Cat. #F8775, Sigma-Aldrich) containing 2 μg/ml of Hoechst 33342 at 4°C overnight. Subsequently, the fixative was exchanged with PBS and the plates were analyzed by automated microscopy. Image acquisition was performed using an ImageXpress Micro C automated confocal microscope (Molecular Devices, Sunnyvale, California, USA) equipped with a 20X PlanApo objective (Nikon, Tokyo, Japan), followed by automated image processing with the R software, using the EBImage package (available from the Bioconductor repository https://www.bioconductor.org) and the MorphR package (available from the GitHub repository https://github.com/kroemerlab/MorphR) In short, cytoplasm and nucleus, were segmented and fluorescence intensities were assessed. After exclusion of cellular debris and dead cells, data was normalized, statistically evaluated, and graphically depicted. Also using R software, images were extracted and pixel intensities scaled (to the same extent for all images of a given experiment). At least four view fields were analyzed per well, and each experiment entailed at least quadruplicate assessments.

Data availability. Bulk RNA seq is publicly available (E-MTAB-12787). Single cell Rhapsody RNA seq is publicly available (E-MTAB-12784). Metabolomics is publicly available (MetaboLights Study - MTBLS7364).

A Materials Design Analysis Reporting (MDAR) checklist has been provided.

Statistics. In vitro and in vivo. Data analyses were performed either with the statistical environment R (http://www.R-project.org/) or Prism 6 (GraphPad, San Diego, CA, USA). The standardization of each marker was performed using the z-score (difference of each sample value from the mean/standard deviation). When a control group was available, the data was standardized by dividing the value by the mean of the control group. The non-parametric Mann–Whitney U test was used for comparison of two unpaired groups. The Wilcoxon matched-pairs signed-rank test was used to compare two groups of paired samples. For the comparison of more groups, we used the Kruskal–Wallis test, correcting the statistical significance for multiple comparison and false discovery rate (FDR) using the two-stage step-up method of Benjamini, Krieger and Yekutieli. All reported tests are two-tailed and were considered significant at $P<0.05$. **Patients**. sMAdCAM-1 as a prognostic factor of the patient response in NSCLC, RCC and bladder cancer patients. For each cohort, two groups of patients were defined by the sMAdCAM-1 median. Overall survival and progression-free survival analyses were performed using Kaplan–Meier estimator and the patient groups were compared using the log-rank (Mantel–Cox) test.

References

1. C. Robert, L. Thomas, I. Bondarenko, S. O'Day, J. Weber, C. Garbe, C. Lebbe, J.-F. Baurain, A. Testori, J.-J. Grob, N. Davidson, J. Richards, M. Maio, A. Hauschild, W. H. Miller, P. Gascon, M. Lotem, K. Harmankaya, R. Ibrahim, S. Francis, T.-T. Chen, R. Humphrey, A. Hoos, J. D. Wolchok, Ipilimumab plus dacarbazine for previously untreated metastatic melanoma. *N. Engl. J. Med.* **364**, 2517–2526 (2011).

2. J. Brahmer, K. L. Reckamp, P. Baas, L. Crinò, W. E. E. Eberhardt, E. Poddubskaya, S. Antonia, A. Pluzanski, E. E. Vokes, E. Holgado, D. Waterhouse, N. Ready, J. Gainor, O. Arén Frontera, L. Havel, M. Steins, M. C. Garassino, J. G. Aerts, M. Domine, L. Paz-Ares, M. Reck, C. Baudelet, C. T. Harbison, B. Lestini, D. R. Spigel, Nivolumab versus Docetaxel in Advanced Squamous-Cell Non-Small-Cell Lung Cancer. *N. Engl. J. Med.* **373**, 123–135 (2015).

3. S. Spranger, R. Bao, T. F. Gajewski, Melanoma-intrinsic β-catenin signalling prevents anti-tumour immunity. *Nature*. **523**, 231–235 (2015).

4. J. Gao, L. Z. Shi, H. Zhao, J. Chen, L. Xiong, Q. He, T. Chen, J. Roszik, C. Bernatchez, S. E. Woodman, P.-L. Chen, P. Hwu, J. P. Allison, A. Futreal, J. A. Wargo, P. Sharma, Loss of IFN-γ Pathway Genes in Tumor Cells as a Mechanism of Resistance to Anti-CTLA-4 Therapy. *Cell*. **167**, 397-404.e9 (2016).

5. N. J. Neubert, M. Schmittnaegel, N. Bordry, S. Nassiri, N. Wald, C. Martignier, L. Tillé, K. Homicsko, W. Damsky, H. Maby-El Hajjami, I. Klaman, E. Danenberg, K. Ioannidou, L. Kandalaft, G. Coukos, S. Hoves, C. H. Ries, S. A. Fuertes Marraco, P. G. Foukas, M. De Palma, D. E. Speiser, T cell–induced CSF1 promotes melanoma resistance to PD1 blockade. *Science Translational Medicine*. **10**, eaan3311 (2018).

6. A. Elkrief, L. Derosa, G. Kroemer, L. Zitvogel, B. Routy, The negative impact of antibiotics on outcomes in cancer patients treated with immunotherapy: a new independent prognostic factor? *Ann. Oncol.* (2019), doi:10.1093/annonc/mdz206.

7. B. Routy, E. Le Chatelier, L. Derosa, C. P. M. Duong, M. T. Alou, R. Daillère, A. Fluckiger, M. Messaoudene, C. Rauber, M. P. Roberti, M. Fidelle, C. Flament, V. Poirier-Colame, P. Opolon, C. Klein, K. Iribarren, L. Mondragón, N. Jacquelot, B. Qu, G. Ferrere, C. Clémenson, L. Mezquita, J. R. Masip, C. Naltet, S. Brosseau, C. Kaderbhai, C. Richard, H. Rizvi, F. Levenez, N. Galleron, B. Quinquis, N. Pons, B. Ryffel, V. Minard-Colin, P. Gonin, J.-C. Soria, E. Deutsch, Y. Loriot, F. Ghiringhelli, G. Zalcman, F. Goldwasser, B. Escudier, M. D. Hellmann, A. Eggermont, D. Raoult, L. Albiges, G. Kroemer, L. Zitvogel, Gut microbiome influences efficacy of PD-1-based immunotherapy against epithelial tumors. *Science*. **359**, 91–97 (2018).

8. J. J. Mohiuddin, B. Chu, A. Facciabene, K. Poirier, X. Wang, A. Doucette, C. Zheng, W. Xu, E. J. Anstadt, R. K. Amaravadi, G. C. Karakousis, T. C. Mitchell, A. C. Huang, J. E. Shabason, A. Lin, S. Swisher-McClure, A. Maity, L. M. Schuchter, J. N. Lukens, Association of Antibiotic Exposure With Survival and Toxicity in Patients With Melanoma Receiving Immunotherapy. *JNCI: Journal of the National Cancer Institute*. **113**, 162–170 (2021).

9. L. Derosa, B. Routy, A. Desilets, R. Daillère, S. Terrisse, G. Kroemer, L. Zitvogel, Microbiota-Centered Interventions: The Next Breakthrough in Immuno-Oncology? *Cancer Discov*. **11**, 2396–2412 (2021).

10. L. Derosa, B. Routy, A. M. Thomas, V. Iebba, G. Zalcman, S. Friard, J. Mazieres, C. Audigier-Valette, D. Moro-Sibilot, F. Goldwasser, C. A. C. Silva, S. Terrisse, M. Bonvalet, A. Scherpereel, H. Pegliasco, C. Richard, F. Ghiringhelli, A. Elkrief, A. Desilets, F. Blanc-Durand, F. Cumbo, A. Blanco, R. Boidot, S. Chevrier, R. Daillère, G. Kroemer, L. Alla, N. Pons, E. L. Chatelier, N. Galleron, H. Roume, A. Dubuisson, N. Bouchard, M. Messaoudene, D. Drubay, E. Deutsch, F. Barlesi, D. Planchard, N. Segata, S. Martinez, L. Zitvogel, J.-C. Soria, B. Besse, Intestinal Akkermansia muciniphila predicts clinical response to PD-1 blockade in advanced non-small cell lung cancer patients. *Nat Med*. **28**, 315–324 (2022).

11. L. Derosa, B. Routy, M. Fidelle, V. Iebba, L. Alla, E. Pasolli, N. Segata, A. Desnoyer, F. Pietrantonio, G. Ferrere, J.-E. Fahrner, E. Le Chatellier, N. Pons, N. Galleron, H. Roume, C. P. M. Duong, L. Mondragón, K.

Iribarren, M. Bonvalet, S. Terrisse, C. Rauber, A.-G. Goubet, R. Daillère, F. Lemaitre, A. Reni, B. Casu, M. T. Alou, C. Alves Costa Silva, D. Raoult, K. Fizazi, B. Escudier, G. Kroemer, L. Albiges, L. Zitvogel, Gut Bacteria Composition Drives Primary Resistance to Cancer Immunotherapy in Renal Cell Carcinoma Patients. *Eur Urol*. **78**, 195–206 (2020).

12. G. Gorfu, J. Rivera-Nieves, K. Ley, Role of beta7 integrins in intestinal lymphocyte homing and retention. *Curr. Mol. Med.* **9**, 836–850 (2009).

13. M. Briskin, D. Winsor-Hines, A. Shyjan, N. Cochran, S. Bloom, J. Wilson, L. M. McEvoy, E. C. Butcher, N. Kassam, C. R. Mackay, W. Newman, D. J. Ringler, Human mucosal addressin cell adhesion molecule-1 is preferentially expressed in intestinal tract and associated lymphoid tissue. *Am. J. Pathol.* **151**, 97–110 (1997).

14. H. Ogawa, D. G. Binion, J. Heidemann, M. Theriot, P. J. Fisher, N. A. Johnson, M. F. Otterson, P. Rafiee, Mechanisms of MAdCAM-1 gene expression in human intestinal microvascular endothelial cells. *Am. J. Physiol., Cell Physiol.* **288**, C272-281 (2005).

15. B. G. Feagan, P. Rutgeerts, B. E. Sands, S. Hanauer, J.-F. Colombel, W. J. Sandborn, G. Van Assche, J. Axler, H.-J. Kim, S. Danese, I. Fox, C. Milch, S. Sankoh, T. Wyant, J. Xu, A. Parikh, Vedolizumab as Induction and Maintenance Therapy for Ulcerative Colitis. *New England Journal of Medicine*. **369**, 699–710 (2013).

16. M. Hassan-Zahraee, A. Banerjee, J. B. Cheng, W. Zhang, A. Ahmad, K. Page, D. von Schack, B. Zhang, S. W. Martin, S. Nayak, P. Reddy, L. Xi, H. Neubert, M. Fernandez Ocana, K. Gorelick, R. Clare, M. Vincent, F. Cataldi, K. Hung, Anti-MAdCAM Antibody Increases ß7+ T Cells and CCR9 Gene Expression in the Peripheral Blood of Patients With Crohn's Disease. *J Crohns Colitis*. **12**, 77–86 (2018).

17. W. Reinisch, W. J. Sandborn, S. Danese, X. Hébuterne, M. Kłopocka, D. Tarabar, T. Vaňásek, M. Greguš, P. A. Hellstern, J. S. Kim, M. P. Sparrow, K. J. Gorelick, M. Hoy, M. Goetsch, C. Bliss, C. Gupta, F. Cataldi, S. Vermeire, Long-term Safety and Efficacy of the Anti-MAdCAM-1 Monoclonal Antibody Ontamalimab [SHP647] for the Treatment of Ulcerative Colitis: The Open-label Study TURANDOT II. *J Crohns Colitis*. **15**, 938–949 (2021).

18. D. R. Littman, A. Y. Rudensky, Th17 and regulatory T cells in mediating and restraining inflammation. *Cell*. **140**, 845–858 (2010).

19. P. Pandiyan, N. Bhaskaran, M. Zou, E. Schneider, S. Jayaraman, J. Huehn, Microbiome Dependent Regulation of Tregs and Th17 Cells in Mucosa. *Front Immunol*. **10**, 426 (2019).

20. C. F. Krebs, H.-J. Paust, S. Krohn, T. Koyro, S. R. Brix, J.-H. Riedel, P. Bartsch, T. Wiech, C. Meyer-Schwesinger, J. Huang, N. Fischer, P. Busch, H.-W. Mittrücker, U. Steinhoff, B. Stockinger, L. G. Perez, U. O. Wenzel, M. Janneck, O. M. Steinmetz, N. Gagliani, R. A. K. Stahl, S. Huber, J.-E. Turner, U. Panzer, Autoimmune Renal Disease Is Exacerbated by S1P-Receptor-1-Dependent Intestinal Th17 Cell Migration to the Kidney. *Immunity*. **45**, 1078–1092 (2016).

21. Y. K. Lee, J. S. Menezes, Y. Umesaki, S. K. Mazmanian, Proinflammatory T-cell responses to gut microbiota promote experimental autoimmune encephalomyelitis. *Proc Natl Acad Sci U S A*. **108 Suppl 1**, 4615–4622 (2011).

22. A. M. Magnuson, G. M. Thurber, R. H. Kohler, R. Weissleder, D. Mathis, C. Benoist, Population dynamics of islet-infiltrating cells in autoimmune diabetes. *Proc. Natl. Acad. Sci. U.S.A.* **112**, 1511–1516 (2015).

23. A. M. Morton, E. Sefik, R. Upadhyay, R. Weissleder, C. Benoist, D. Mathis, Endoscopic photoconversion reveals unexpectedly broad leukocyte trafficking to and from the gut. *Proc. Natl. Acad. Sci. U.S.A.* **111**, 6696–6701 (2014).

24. H.-J. Wu, I. I. Ivanov, J. Darce, K. Hattori, T. Shima, Y. Umesaki, D. R. Littman, C. Benoist, D. Mathis, Gut-residing segmented filamentous bacteria drive autoimmune arthritis via T helper 17 cells. *Immunity*. **32**, 815–827 (2010).

25. M. R. I. Young, Th17 Cells in Protection from Tumor or Promotion of Tumor Progression. *J Clin Cell Immunol*. **7**, 431 (2016).

26. E. Sefik, N. Geva-Zatorsky, S. Oh, L. Konnikova, D. Zemmour, A. M. McGuire, D. Burzyn, A. Ortiz-Lopez, M. Lobera, J. Yang, S. Ghosh, A. Earl, S. B. Snapper, R. Jupp, D. Kasper, D. Mathis, C. Benoist, Individual intestinal symbionts induce a distinct population of RORγ+ regulatory T cells. *Science*. **349**, 993–997 (2015).

27. N. R. Blatner, M. F. Mulcahy, K. L. Dennis, D. Scholtens, D. J. Bentrem, J. D. Phillips, S. Ham, B. P. Sandall, M. W. Khan, D. M. Mahvi, A. L. Halverson, S. J. Stryker, A.-M. Boller, A. Singal, R. K. Sneed, B. Sarraj, M. J. Ansari, M. Oft, Y. Iwakura, L. Zhou, A. Bonertz, P. Beckhove, F. Gounari, K. Khazaie, Expression of RORγt Marks a Pathogenic Regulatory T Cell Subset in Human Colon Cancer. *Science Translational Medicine*. **4**, 164ra159-164ra159 (2012).

28. A. Rizzo, M. Di Giovangiulio, C. Stolfi, E. Franzè, H.-J. Fehling, R. Carsetti, E. Giorda, A. Colantoni, A. Ortenzi, M. Rugge, C. Mescoli, G. Monteleone, M. C. Fantini, RORγt-Expressing Tregs Drive the Growth of Colitis-Associated Colorectal Cancer by Controlling IL6 in Dendritic Cells. *Cancer Immunol Res*. **6**, 1082–1092 (2018).

29. K. N. Haas, J. L. Blanchard, Reclassification of the Clostridium clostridioforme and Clostridium sphenoides clades as Enterocloster gen. nov. and Lacrimispora gen. nov., including reclassification of 15 taxa. *Int J Syst Evol Microbiol*. **70**, 23–34 (2020).

30. R. Gacesa, A. Kurilshikov, A. Vich Vila, T. Sinha, M. a. Y. Klaassen, L. A. Bolte, S. Andreu-Sánchez, L. Chen, V. Collij, S. Hu, J. a. M. Dekens, V. C. Lenters, J. R. Björk, J. C. Swarte, M. A. Swertz, B. H. Jansen, J. Gelderloos-Arends, S. Jankipersadsing, M. Hofker, R. C. H. Vermeulen, S. Sanna, H. J. M. Harmsen, C. Wijmenga, J. Fu, A. Zhernakova, R. K. Weersma, Environmental factors shaping the gut microbiome in a Dutch population. *Nature*. **604**, 732–739 (2022).

31. S. Yonekura, S. Terrisse, C. Alves Costa Silva, A. Lafarge, V. Iebba, G. Ferrere, A.-G. Goubet, J.-E. Fahrner, I. Lahmar, K. Ueda, G. Mansouri, E. Pizzato, P. Ly, M. Mazzenga, C. Thelemaque, M. Fidelle, F. Jaulin, J. Cartry, M. Deloger, M. Aglave, N. Droin, P. Opolon, A. Puget, F. Mann, M. Neunlist, A. Bessard, L. Aymeric, T. Matysiak-Budnik, J. Bosq, P. Hofman, C. P. M. Duong, S. Ugolini, V. Quiniou, S. Berrard, B. Ryffel, O. Kepp, G. Kroemer, B. Routy, L. Lordello, M.-A. Bani, N. Segata, F. Y. Yengej, H. Clevers, J.-Y. Scoazec, E. Pasolli, L. Derosa, L. Zitvogel, Cancer Induces a Stress Ileopathy Depending on β-Adrenergic Receptors and Promoting Dysbiosis that Contributes to Carcinogenesis. *Cancer Discovery*. **12**, 1128–1151 (2022).

32. A.-G. Goubet, R. Wheeler, A. Fluckiger, B. Qu, F. Lemaître, K. Iribarren, L. Mondragón, M. Tidjani Alou, E. Pizzato, S. Durand, L. Derosa, F. Aprahamian, N. Bossut, M. Moya-Nilges, D. Derrien, G. Chen, M. Leduc, A. Joseph, N. Pons, E. Le Chatelier, N. Segata, S. Yonekura, V. Iebba, O. Kepp, D. Raoult, F. André, G. Kroemer, I. G. Boneca, L. Zitvogel, R. Daillère, Multifaceted modes of action of the anticancer probiotic Enterococcus hirae. *Cell Death Differ*. **28**, 2276–2295 (2021).

33. E. N. Baruch, I. Youngster, G. Ben-Betzalel, R. Ortenberg, A. Lahat, L. Katz, K. Adler, D. Dick-Necula, S. Raskin, N. Bloch, D. Rotin, L. Anafi, C. Avivi, J. Melnichenko, Y. Steinberg-Silman, R. Mamtani, H. Harati, N. Asher, R. Shapira-Frommer, T. Brosh-Nissimov, Y. Eshet, S. Ben-Simon, O. Ziv, M. A. W. Khan, M. Amit, N. J. Ajami, I. Barshack, J. Schachter, J. A. Wargo, O. Koren, G. Markel, B. Boursi, Fecal microbiota transplant promotes response in immunotherapy-refractory melanoma patients. *Science*. **371**, 602–609 (2021).

34. D. Davar, A. K. Dzutsev, J. A. McCulloch, R. R. Rodrigues, J.-M. Chauvin, R. M. Morrison, R. N. Deblasio, C. Menna, Q. Ding, O. Pagliano, B. Zidi, S. Zhang, J. H. Badger, M. Vetizou, A. M. Cole, M. R. Fernandes,

S. Prescott, R. G. F. Costa, A. K. Balaji, A. Morgun, I. Vujkovic-Cvijin, H. Wang, A. A. Borhani, M. B. Schwartz, H. M. Dubner, S. J. Ernst, A. Rose, Y. G. Najjar, Y. Belkaid, J. M. Kirkwood, G. Trinchieri, H. M. Zarour, Fecal microbiota transplant overcomes resistance to anti–PD-1 therapy in melanoma patients. *Science*. **371**, 595–602 (2021).

35. B. Routy, V. Gopalakrishnan, R. Daillère, L. Zitvogel, J. A. Wargo, G. Kroemer, The gut microbiota influences anticancer immunosurveillance and general health. *Nat Rev Clin Oncol*. **15**, 382–396 (2018).

36. R. Y. Gao, C. T. Shearn, D. J. Orlicky, K. D. Battista, E. E. Alexeev, I. M. Cartwright, J. M. Lanis, R. E. Kostelecky, C. Ju, S. P. Colgan, B. P. Fennimore, Bile acids modulate colonic MAdCAM-1 expression in a murine model of combined cholestasis and colitis. *Mucosal Immunol*. **14**, 479–490 (2021).

37. D. V. Guzior, R. A. Quinn, Review: microbial transformations of human bile acids. *Microbiome*. **9**, 140 (2021).

38. Y. Sato, K. Atarashi, D. R. Plichta, Y. Arai, S. Sasajima, S. M. Kearney, W. Suda, K. Takeshita, T. Sasaki, S. Okamoto, A. N. Skelly, Y. Okamura, H. Vlamakis, Y. Li, T. Tanoue, H. Takei, H. Nittono, S. Narushima, J. Irie, H. Itoh, K. Moriya, Y. Sugiura, M. Suematsu, N. Moritoki, S. Shibata, D. R. Littman, M. A. Fischbach, Y. Uwamino, T. Inoue, A. Honda, M. Hattori, T. Murai, R. J. Xavier, N. Hirose, K. Honda, Novel bile acid biosynthetic pathways are enriched in the microbiome of centenarians. *Nature*. **599**, 458–464 (2021).

39. J. B. J. Ward, N. K. Lajczak, O. B. Kelly, A. M. O'Dwyer, A. K. Giddam, J. Ní Gabhann, P. Franco, M. M. Tambuwala, C. A. Jefferies, S. Keely, A. Roda, S. J. Keely, Ursodeoxycholic acid and lithocholic acid exert anti-inflammatory actions in the colon. *Am J Physiol Gastrointest Liver Physiol*. **312**, G550–G558 (2017).

40. M. Tomura, N. Yoshida, J. Tanaka, S. Karasawa, Y. Miwa, A. Miyawaki, O. Kanagawa, Monitoring cellular movement in vivo with photoconvertible fluorescence protein "Kaede" transgenic mice. *Proc. Natl. Acad. Sci. U.S.A.* **105**, 10871–10876 (2008).

41. V. Singh, S. Roth, G. Llovera, R. Sadler, D. Garzetti, B. Stecher, M. Dichgans, A. Liesz, Microbiota Dysbiosis Controls the Neuroinflammatory Response after Stroke. *J. Neurosci.* **36**, 7428–7440 (2016).

42. C. M'Rini, G. Cheng, C. Schweitzer, L. L. Cavanagh, R. T. Palframan, T. R. Mempel, R. A. Warnock, J. B. Lowe, E. J. Quackenbush, U. H. von Andrian, A novel endothelial L-selectin ligand activity in lymph node medulla that is regulated by alpha(1,3)-fucosyltransferase-IV. *J Exp Med*. **198**, 1301–1312 (2003).

43. J. Mitoma, X. Bao, B. Petryanik, P. Schaerli, J.-M. Gauguet, S.-Y. Yu, H. Kawashima, H. Saito, K. Ohtsubo, J. D. Marth, K.-H. Khoo, U. H. von Andrian, J. B. Lowe, M. Fukuda, Critical functions of N-glycans in L-selectin-mediated lymphocyte homing and recruitment. *Nat Immunol*. **8**, 409–418 (2007).

44. E. Cano-Gamez, B. Soskic, T. I. Roumeliotis, E. So, D. J. Smyth, M. Baldrighi, D. Willé, N. Nakic, J. Esparza-Gordillo, C. G. C. Larminie, P. G. Bronson, D. F. Tough, W. C. Rowan, J. S. Choudhary, G. Trynka, Single-cell transcriptomics identifies an effectorness gradient shaping the response of CD4+ T cells to cytokines. *Nat Commun*. **11**, 1801 (2020).

45. Z. T. Freeman, T. R. Nirschl, D. H. Hovelson, R. J. Johnston, J. J. Engelhardt, M. J. Selby, C. M. Kochel, R. Y. Lan, J. Zhai, A. Ghasemzadeh, A. Gupta, A. M. Skaist, S. J. Wheelan, H. Jiang, A. T. Pearson, L. A. Snyder, A. J. Korman, S. A. Tomlins, S. Yegnasubramanian, C. G. Drake, A conserved intratumoral regulatory T cell signature identifies 4-1BB as a pan-cancer target. *J Clin Invest*. **130**, 1405–1416 (2020).

46. Y. Gao, K. Deason, A. Jain, R. A. Irizarry-Caro, I. Dozmorov, L. A. Coughlin, I. Rauch, B. M. Evers, A. Y. Koh, E. K. Wakeland, C. Pasare, Transcriptional profiling identifies caspase-1 as a T cell–intrinsic regulator of Th17 differentiation. *Journal of Experimental Medicine*. **217**, e20190476 (2020).

47. Dan Lu, L. Liu, Y. Sun, J. Song, Q. Yin, G. Zhang, F. Qi, Z. Hu, Z. Yang, Z. Zhou, Y. Hu, L. Zhang, J. Ji, X. Zhao, Y. Jin, M. A. McNutt, Y. Yin, The phosphatase PAC1 acts as a T cell suppressor and attenuates host antitumor immunity. *Nat Immunol*. **21**, 287–297 (2020).

48. J.-H. Kim, J. Hwang, J. H. Jung, H.-J. Lee, D. Y. Lee, S.-H. Kim, Molecular networks of FOXP family: dual biologic functions, interplay with other molecules and clinical implications in cancer progression. *Molecular Cancer*. **18**, 180 (2019).

49. L. Li, N. Patsoukis, V. Petkova, V. A. Boussiotis, Runx1 and Runx3 are involved in the generation and function of highly suppressive IL-17-producing T regulatory cells. *PLoS One*. **7**, e45115 (2012).

50. L. Belarif, R. Danger, L. Kermarrec, V. Nerrière-Daguin, S. Pengam, T. Durand, C. Mary, E. Kerdreux, V. Gauttier, A. Kucik, V. Thepenier, J. C. Martin, C. Chang, A. Rahman, N. S.-L. Guen, C. Braudeau, A. Abidi, G. David, F. Malard, C. Takoudju, B. Martinet, N. Gérard, I. Neveu, M. Neunlist, E. Coron, T. T. MacDonald, P. Desreumaux, H.-L. Mai, S. Le Bas-Bernardet, J.-F. Mosnier, M. Merad, R. Josien, S. Brouard, J.-P. Soulillou, G. Blancho, A. Bourreille, P. Naveilhan, B. Vanhove, N. Poirier, IL-7 receptor influences anti-TNF responsiveness and T cell gut homing in inflammatory bowel disease. *J Clin Invest*. **129**, 1910–1925 (2019).

51. Y. Chen, J. Wang, X. Wang, X. Li, J. Song, J. Fang, X. Liu, T. Liu, D. Wang, Q. Li, S. Wen, D. Ma, J. Xia, L. Luo, S. G. Zheng, J. Cui, G. Zeng, L. Chen, B. Cheng, Z. Wang, Pik3ip1 Is a Negative Immune Regulator that Inhibits Antitumor T-Cell Immunity. *Clin Cancer Res*. **25**, 6180–6194 (2019).

52. J.-W. Sidhom, H. B. Larman, D. M. Pardoll, A. S. Baras, DeepTCR is a deep learning framework for revealing sequence concepts within T-cell repertoires. *Nat Commun*. **12**, 2309 (2021).

53. T. C. Wirth, H.-H. Xue, D. Rai, J. T. Sabel, T. Bair, J. T. Harty, V. P. Badovinac, Repetitive antigen stimulation induces stepwise transcriptome diversification but preserves a core signature of memory CD8(+) T cell differentiation. *Immunity*. **33**, 128–140 (2010).

54. T. Wu, Y. Ji, E. A. Moseman, H. C. Xu, M. Manglani, M. Kirby, S. M. Anderson, R. Handon, E. Kenyon, A. Elkahloun, W. Wu, P. A. Lang, L. Gattinoni, D. B. McGavern, P. L. Schwartzberg, The TCF1-Bcl6 axis counteracts type I interferon to repress exhaustion and maintain T cell stemness. *Science Immunology*. **1**, eaai8593 (2016).

55. E. J. Wherry, S.-J. Ha, S. M. Kaech, W. N. Haining, S. Sarkar, V. Kalia, S. Subramaniam, J. N. Blattman, D. L. Barber, R. Ahmed, Molecular Signature of CD8+ T Cell Exhaustion during Chronic Viral Infection. *Immunity*. **27**, 670–684 (2007).

56. K. Araki, M. Morita, A. G. Bederman, B. T. Konieczny, H. T. Kissick, N. Sonenberg, R. Ahmed, Translation is actively regulated during the differentiation of CD8+ effector T cells. *Nat Immunol*. **18**, 1046–1057 (2017).

57. C. Voigt, P. May, A. Gottschlich, A. Markota, D. Wenk, I. Gerlach, S. Voigt, G. T. Stathopoulos, K. A. M. Arendt, C. Heise, F. Rataj, K.-P. Janssen, M. Königshoff, H. Winter, I. Himsl, W. E. Thasler, M. Schnurr, S. Rothenfußer, S. Endres, S. Kobold, Cancer cells induce interleukin-22 production from memory CD4+ T cells via interleukin-1 to promote tumor growth. *PNAS*. **114**, 12994–12999 (2017).

58. T. L. Denning, G. Kim, M. Kronenberg, Cutting edge: CD4+CD25+ regulatory T cells impaired for intestinal homing can prevent colitis. *J. Immunol.* **174**, 7487–7491 (2005).

59. D. Dangaj, M. Bruand, A. J. Grimm, C. Ronet, D. Barras, P. A. Duttagupta, E. Lanitis, J. Duraiswamy, J. L. Tanyi, F. Benencia, J. Conejo-Garcia, H. R. Ramay, K. T. Montone, D. J. Powell, P. A. Gimotty, A. Facciabene, D. G. Jackson, J. S. Weber, S. J. Rodig, S. F. Hodi, L. E. Kandalaft, M. Irving, L. Zhang, P. Foukas, S. Rusakiewicz, M. Delorenzi, G. Coukos, Cooperation between Constitutive and Inducible Chemokines Enables T Cell Engraftment and Immune Attack in Solid Tumors. *Cancer Cell*. **35**, 885-900.e10 (2019).

60. A. González-Martín, L. Gómez, J. Lustgarten, E. Mira, S. Mañes, Maximal T Cell–Mediated Antitumor Responses Rely upon CCR5 Expression in Both CD4+ and CD8+ T Cells. *Cancer Res*. **71**, 5455–5466 (2011).

61. A. M. Cooper, IL-17 and anti-bacterial immunity: Protection versus tissue damage. *European Journal of Immunology*. **39**, 649–652 (2009).

62. C. Voigt, P. May, A. Gottschlich, A. Markota, D. Wenk, I. Gerlach, S. Voigt, G. T. Stathopoulos, K. A. M. Arendt, C. Heise, F. Rataj, K.-P. Janssen, M. Königshoff, H. Winter, I. Himsl, W. E. Thasler, M. Schnurr, S. Rothenfußer, S. Endres, S. Kobold, Cancer cells induce interleukin-22 production from memory CD4+ T cells via interleukin-1 to promote tumor growth. *Proceedings of the National Academy of Sciences*. **114**, 12994–12999 (2017).

63. T. Yokoo, K. Kamimura, H. Abe, Y. Kobayashi, T. Kanefuji, K. Ogawa, R. Goto, M. Oda, T. Suda, S. Terai, Liver-targeted hydrodynamic gene therapy: Recent advances in the technique. *World J Gastroenterol*. **22**, 8862–8868 (2016).

64. A. K. Holmer, R. Battat, P. S. Dulai, N. Vande Casteele, N. Nguyen, A. Jain, A. Miralles, J. Neill, H. Le, S. Singh, J. Rivera-Nieves, W. J. Sandborn, B. S. Boland, Biomarkers are associated with clinical and endoscopic outcomes with vedolizumab treatment in Crohn's disease. *Therap Adv Gastroenterol*. **13**, 1756284820971214 (2020).

65. J. Lecuelle, L. Favier, C. Fraisse, A. Lagrange, C. Kaderbhai, R. Boidot, S. Chevrier, P. Joubert, B. Routy, C. Truntzer, F. Ghiringhelli, MER4 endogenous retrovirus correlated with better efficacy of anti-PD1/PD-L1 therapy in non-small cell lung cancer. *J Immunother Cancer*. **10**, e004241 (2022).

66. L. Albiges, S. Negrier, C. Dalban, C. Chevreau, G. Gravis, S. Oudard, B. Laguerre, P. Barthelemy, D. Borchiellini, M. Gross-Goupil, L. Geoffrois, F. Rolland, A. Thiery-Vuillemin, F. Joly, S. Ladoire, F. Tantot, B. Escudier, Safety and efficacy of nivolumab in metastatic renal cell carcinoma (mRCC): Final analysis from the NIVOREN GETUG AFU 26 study. *JCO*. **37**, 542–542 (2019).

67. G. P. Sonpavde, C. N. Sternberg, Y. Loriot, A. Marabelle, J. L. Lee, A. Fléchon, G. Roubaud, D. Pouessel, V. Zagonel, F. Calabro, G. L. Banna, S. J. Shin, F. E. Vera-Badillo, T. Powles, E. Hellmis, P. A. P. Miranda, A. R. Lima, U. Emeribe, S. M. Oh, S. J. Hotte, Primary results of STRONG: An open-label, multicenter, phase 3b study of fixed-dose durvalumab monotherapy in previously treated patients with urinary tract carcinoma. *European Journal of Cancer*. **163**, 55–65 (2022).

68. A. Liesz, E. Suri-Payer, C. Veltkamp, H. Doerr, C. Sommer, S. Rivest, T. Giese, R. Veltkamp, Regulatory T cells are key cerebroprotective immunomodulators in acute experimental stroke. *Nat. Med.* **15**, 192–199 (2009).

69. C. Benakis, D. Brea, S. Caballero, G. Faraco, J. Moore, M. Murphy, G. Sita, G. Racchumi, L. Ling, E. G. Pamer, C. Iadecola, J. Anrather, Commensal microbiota affects ischemic stroke outcome by regulating intestinal γδ T cells. *Nat. Med.* **22**, 516–523 (2016).

70. R. J. Miragaia, T. Gomes, A. Chomka, L. Jardine, A. Riedel, A. N. Hegazy, N. Whibley, A. Tucci, X. Chen, I. Lindeman, G. Emerton, T. Krausgruber, J. Shields, M. Haniffa, F. Powrie, S. A. Teichmann, Single-Cell Transcriptomics of Regulatory T Cells Reveals Trajectories of Tissue Adaptation. *Immunity*. **50**, 493-504.e7 (2019).

71. A. R. Muñoz-Rojas, D. Mathis, Tissue regulatory T cells: regulatory chameleons. *Nat Rev Immunol*. **21**, 597–611 (2021).

72. N. Yosef, A. K. Shalek, J. T. Gaublomme, H. Jin, Y. Lee, A. Awasthi, C. Wu, K. Karwacz, S. Xiao, M. Jorgolli, D. Gennert, R. Satija, A. Shakya, D. Y. Lu, J. J. Trombetta, M. R. Pillai, P. J. Ratcliffe, M. L. Coleman, M. Bix, D. Tantin, H. Park, V. K. Kuchroo, A. Regev, Dynamic regulatory network controlling TH17 cell differentiation. *Nature*. **496**, 461–468 (2013).

73. U. U. Uche, A. R. Piccirillo, S. Kataoka, S. J. Grebinoski, L. M. D'Cruz, L. P. Kane, PIK3IP1/TrIP restricts activation of T cells through inhibition of PI3K/Akt. *J Exp Med*. **215**, 3165–3179 (2018).

74. A. Fischer, S. Zundler, R. Atreya, T. Rath, C. Voskens, S. Hirschmann, R. López-Posadas, A. Watson, C. Becker, G. Schuler, C. Neufert, I. Atreya, M. F. Neurath, Differential effects of α4β7 and GPR15 on homing of effector and regulatory T cells from patients with UC to the inflamed gut in vivo. *Gut*. **65**, 1642–1664 (2016).

75. G. D'Haens, S. Vermeire, H. Vogelsang, M. Allez, P. Desreumaux, A. Van Gossum, W. J. Sandborn, D. C. Baumgart, R. M. Ransohoff, G. M. Comer, A. Ahmad, F. Cataldi, J. Cheng, R. Clare, K. J. Gorelick, A. Kaminski, V. Pradhan, S. Rivers, M. O. Sikpi, Y. Zhang, M. Hassan-Zahraee, W. Reinisch, O. Stuve, Effect of PF-00547659 on Central Nervous System Immune Surveillance and Circulating β7+ T Cells in Crohn's Disease: Report of the TOSCA Study. *J Crohns Colitis*. **12**, 188–196 (2018).

76. G. Calenda, R. Keawvichit, G. Arrode-Brusés, K. Pattanapanyasat, I. Frank, S. N. Byrareddy, J. Arthos, C. Cicala, B. Grasperge, J. L. Blanchard, A. Gettie, K. A. Reimann, A. A. Ansari, E. Martinelli, Integrin α4β7 Blockade Preferentially Impacts CCR6+ Lymphocyte Subsets in Blood and Mucosal Tissues of Naive Rhesus Macaques. *J. Immunol.* **200**, 810–820 (2018).

77. M. I. Love, W. Huber, S. Anders, Moderated estimation of fold change and dispersion for RNA-seq data with DESeq2. *Genome Biol*. **15**, 550 (2014).

78. M. E. Ritchie, B. Phipson, D. Wu, Y. Hu, C. W. Law, W. Shi, G. K. Smyth, limma powers differential expression analyses for RNA-sequencing and microarray studies. *Nucleic Acids Res*. **43**, e47 (2015).

79. H. Lin, S. D. Peddada, Analysis of compositions of microbiomes with bias correction. *Nat Commun*. **11**, 3514 (2020).

80. H. Mallick, A. Rahnavard, L. J. McIver, S. Ma, Y. Zhang, L. H. Nguyen, T. L. Tickle, G. Weingart, B. Ren, E. H. Schwager, S. Chatterjee, K. N. Thompson, J. E. Wilkinson, A. Subramanian, Y. Lu, L. Waldron, J. N. Paulson, E. A. Franzosa, H. C. Bravo, C. Huttenhower, Multivariable association discovery in population-scale meta-omics studies. *PLoS Comput Biol*. **17**, e1009442 (2021).

81. N. Segata, J. Izard, L. Waldron, D. Gevers, L. Miropolsky, W. S. Garrett, C. Huttenhower, Metagenomic biomarker discovery and explanation. *Genome Biol.* **12**, R60 (2011).

82. P. Bankhead, M. B. Loughrey, J. A. Fernández, Y. Dombrowski, D. G. McArt, P. D. Dunne, S. McQuaid, R. T. Gray, L. J. Murray, H. G. Coleman, J. A. James, M. Salto-Tellez, P. W. Hamilton, QuPath: Open source software for digital pathology image analysis. *Sci Rep*. **7**, 16878 (2017).

83. C. Grajeda-Iglesias, S. Durand, R. Daillère, K. Iribarren, F. Lemaitre, L. Derosa, F. Aprahamian, N. Bossut, N. Nirmalathasan, F. Madeo, L. Zitvogel, G. Kroemer, Oral administration of Akkermansia muciniphila elevates systemic antiaging and anticancer metabolites. *Aging (Albany NY)*. **13**, 6375–6405 (2021).

84. S. Durand, C. Grajeda-Iglesias, F. Aprahamian, N. Nirmalathasan, O. Kepp, G. Kroemer, "Chapter 11 - The intracellular metabolome of starving cells" in *Methods in Cell Biology*, O. Kepp, L. Galluzzi, Eds. (Academic Press, 2021; https://www.sciencedirect.com/science/article/pii/S0091679X21000431), vol. 164 of *Monitoring vesicular trafficking in cellular responses to stress - Part A*, pp. 137–156.

Acknowledgments: We would like to particularly thank the animal facility, the Flow cytometry and Pathology Platforms of Gustave Roussy, especially Dr. P. Gonin, L. Touchard, C. Metereau, A. Noel and O. Bawa. We would like to thank the PREMIS operational team, especially S. Farhane (Project leader), S. Messayke (Pharmacovigilance), L. Bedouda (Clinical Research Associate), R. Chaabane (Clinical Research Associate), C. Mohamed-Djalim (Clinical Research Associate) and all investigators. Some figure items were partly generated using Servier Medical Art, provided by Servier, licensed under a Creative Commons Attribution 3.0 unported license.

Funding: This work was supported by SEERAVE Foundation, European Union Horizon 2020, Project Number 825410 and Project Acronym ONCOBIOME, Institut National du Cancer (INCa), ANR Ileobiome - 19-CE15-0029-01, ANR RHU5 "ANR-21-RHUS-0017" IMMUNOLIFE", MAdCAM INCA_ 16698, ANR-IHU Méditerranée-Infections, Ligue contre le cancer, LABEX OncoImmunology, la direction generale de l'offre de soins (DGOS), SIRIC SOCRATE (INCa/DGOS/INSERM 6043), and PACRI network. G.K. was supported by the Ligue contre le Cancer (équipe labellisée); Agence National de la Recherche (ANR) – Projets blancs; AMMICa US23/CNRS UMS3655; Cancéropôle Ile-de-France; Fondation pour la Recherche Médicale (FRM); Equipex Onco-Pheno-Screen; European Joint Programme on Rare Diseases (EJPRD); European Research Council (ICD-Cancer), European Union Horizon 2020 program Crimson; Institut National du Cancer (INCa); Institut Universitaire de France; LabEx Immuno-Oncology (ANR-18-IDEX-0001); a Cancer Research ASPIRE Award from the Mark Foundation; SIRIC Stratified Oncology Cell DNA Repair and Tumor Immune Elimination (SOCRATE); and SIRIC Cancer Research and Personalized Medicine (CARPEM). This study contributes to the IdEx Université de Paris ANR-18-IDEX-0001. M.F. was funded by SEERAVE Foundation. C.Ra. received a fellowship from Immuntrain within the Marie-Slodowska Curie Training network of the European Union (LMU Klinikum). L.D., B.R., S.Y. and F.X.D. were supported by Philantropia at Gustave Roussy Foundation. I.La was funded by Fondation pour la Recherche Médicale (FRM). This work is supported by the Prism project funded by the Agence Nationale de la Recherche under grant number ANR-18-IBHU-0002. This work was funded by the TriPoD European Research Council Advanced EU (322856) and Recherche Hospitalo-Universitaire iMAP (ANR-16-RHUS-0001) grants to D.K. O.K. was funded by INCA and the DIM Elicit. The PREMIS study was funded by Gustave Roussy fondation & Malakoff Humanis. A.Sc. and N.W. were funded by DFG (German Research Foundation) – Project-ID 403324012 – SFB 1382.

Author contributions: Conceptualization: L.Zi., G.K., C.Ra. and M.F. **Methodology**: M.F., C.Ra., A.L.T., I.La., L.Zh., I.Le., A.Si., F.Gi., S.Y., O.K., A.Sc., N.W., J.S.G., S.K., J.B., L.L., N.Ga., B.Q., E.L.C., L.B., J.P.G., R.D., C.Tr., F.Gh., V.M., D.K., A.M.T., N.S., G.K. and L.Zi. **Software**: M.F., I.La., C.D., K.M., C.Ri., G.V., V.M., D.D. and A.M.T. **Validation**: M.F., C.Ra., C.A.C.S. and L.D. **Formal analysis**: M.F., C.Ra., C.A.C.S., I.La., C.D., M.L., S.D., K.M., S.Y., J.E.F., C.Ri., L.L., G.V., E.L.C., R.D., V.M., D.D., A.M.T. and L.D. **Investigation**: M.F., C.Ra., C.A.C.S., A.L.T., I.La., A.L.M.L.V., L.Zh., C.Th., I.Le., M.M., E.P., R.B., M.D.M.F., S.Z., A.R., M.L., G.F., P.L., A.Si., K.M., C.A.D., M.P.R., M.T.A., J.C., J.B., L.L., R.D., C.Tr., N.C., V.M., L.D., G.K. and L.Zi. **Resources**: A.Si., K.M., C.A.D., F.Gi., M.P.R., S.T., A.Sc., N.W., J.S.G., S.K., E.L.C., L.B., J.P.G., A.J., N.Ge., E.G., N.L., R.K., R.D., B.B., C.Tr., F.Gh., N.C., V.M., D.K., L.A., A.M.T., N.S., F.X.D., A.M., B.R., L.D., G.K. and L.Zi. **Data Curation**: I.La., K.M., G.V., V.M. and A.M.T. **Writing - Original Draft**: L.Zi., G.K., C.Ra and M.F. **Writing - Review & Editing:** L.Zi., G.K., C.Ra, M.F., C.A.C.S., D.D., A.L.T., M.P.R., O.K., E.G., N.L., V.M. and

L.D. **Visualization**: M.F., C.Ra, C.A.C.S., A.L.T., I.La., A.L.M.L.V., R.B. and L.D. **Supervision**: L.Zi., G.K., M.F., C.Ra., L.D., F.Gi., O.K., E.L.C., N.L., D.K. and N.S. **Funding acquisition**: L.Zi., G.K. and L.D.

Data and material availabilities: The raw data that support the findings of this study are available on request from the corresponding author (L.Zi.). Patient data are not publicly available due to restrictions pertaining to information that could compromise the privacy of research participants. An MTA will be necessary to access to intestinal species from everImmune or Gustave Roussy. Bulk RNA seq is publicly available (E-MTAB-12787). Single cell Rhapsody RNA seq is publicly available (E-MTAB-12784). Metabolomics is publicly available (MetaboLights Study - MTBLS7364).

Competing interests: LZ founded everImmune and is the SAB president of everImmune. LZ had grant support from Daichi Sankyo, Kaleido, 9 meters and Pileje. GK has been holding research contracts with Daiichi Sankyo, Eleor, Kaleido, Lytix Pharma, PharmaMar, Osasuna Therapeutics, Samsara Therapeutics, Sanofi, Tollys, and Vascage. GK has been consulting for Reithera. GK is on the Board of Directors of the Bristol Myers Squibb Foundation France. GK is a scientific co-founder of everImmune, Osasuna Therapeutics, Samsara Therapeutics and Therafast Bio. OK is a scientific co-founder of Samsara Therapeutics. LD is member of the SAB of everImmune. LA is advisory or Consulting of Astellas – BMS – Ipsen – Janssen – MSD – Pfizer – EISAI – Roche. Gustave Roussy filed a patent with Registration number EP21305846.4 and Reference B210162EPA/VEM/CPO “Methods for diagnosing a cancer-induced ileopathy and their use for improving cancer treatment by immunotherapy” licensed to everImmune.

Figure Legends

Fig. 0. MAdCAM-1 as a gut immune checkpoint for cancer immunosurveillance. Bacteria from the genus *Enterocloster* genus, for instance following discontinuation of ABX, induce the downregulation of MAdCAM-1 in the ileal LP and mLNs, inducing the exodus of the immunosuppressive $\alpha4\beta7^+$ T_R17 cells, from the gut to cancers and tumor-draining lymph nodes (tdLNs). Disruption of the MAdCAM-1-α4β7 axis compromises the efficacy of immunotherapy in mice and patients.

Fig. 1. Broad-spectrum ABX downregulate MAdCAM-1 expression in the murine ileal vasculature. (**A to D.)** Relative transcription (**A**) (N = 2) and protein (**B to D**) (from N = 3 independent experiments) levels of *Madcam1* gene product obtained with RT-qPCR (**A**), immunohistochemistry staining of MAdCAM-1 in ileal lamina propria (ILP) venules and high endothelial venules (HEV) in Peyer's patch (PP) in ACS-treated and untreated mice (as indicated above micrograph pictures) (Scale bar: 200 µm, 100 µm and 40 µm, respectively) (**B**), flow cytometry gating on $CD45^-$ cells of ILP (**C**), or ELISA (**D**) of ileal (A to D) or colonic (A) tissues in C57BL/6 mice after continuous broad-spectrum antibiotics (ACS: Ampicillin, Colistin, Streptomycin) or after a 4 or 12 days spontaneous recolonization (ACS+4d or ACS+12d) following cessation of ACS. Each dot represents one ileum (A-D) or colon (A). Two (A) to three (B to D) independent experiments were conducted for each graph. (**E**.) Quantitative RT-qPCR of relative *Madcam1* gene expression normalized on the naive specific-pathogen-free (SPF) mice group in ileal mucosae of C57BL/6 mice reared in SPF conditions (no ABX conditioning) which underwent oral gavage with bacteria spp. aligned in the *x*- axis (N = 4). (*Akk*., *Akkermansia muciniphila*; *E. hirae*, *Enterococcus hirae*; *E. clostri*, *Enterocloster clostridioformis*) **(F.)** Same experiments as in C performing flow cytometric analysis of ILP $CD4^+$ T cell subsets ($\alpha4\beta7^+$ vs $CD25^+$ $FoxP3^+$ T_{reg} vs $ROR\gamma t^+$ $CD4^+$ (T_H17) cells) during continuous ACS or at the ACS+4d phase, each dot representing one ileum (n = 5-6 mice per group). (**G.)** Ileal expression levels of *Foxp3* in *Madcam1* gene-deficient mice (left) or phenocopied with an anti-MAdCAM-1 Ab (right) (treated (full dots) or not with anti-PD-1 Ab that did not impact on ileal *Madcam1* expression levels, not shown) without ATB conditioning. Each dot represents the RT-qPCR data of one ileum (n = 6-9 mice per group). Data information: N, the number of times an experiment was independently performed. Comparisons between groups were analyzed using nonparametric

Mann-Whitney U test (2 groups) or Kruskal-Wallis H test (>2 groups) followed by multiple-comparisons test by controlling the FDR. Error bars represent means ± SEM.

Fig. 2. Downregulation of ileal *Madcam1* gene expression in patients taking ABX.

(**A and B.)** RT-qPCR -based transcriptional levels of human *MADCAM1* (**A**) and *RORC* genes (**B**) in intestinal biopsies collected during endoscopic intervention in 21 control (ABX-free) patients and 10 ABX-treated patients (**table S2**). Each dot represents one biopsy either from ileum, caecum and colon, a single patient being represented one to three times. (**C.**) Spearman correlation between ileal *IL17A* and *MADCAM1* gene expressions in ABX-treated or untreated patients. (**D.**) Impact of fecal microbiota transplantation (FMT) in 3 days-ABX-treated recipient mice using feces from NSCLC patients at diagnosis (prior to PD-1 blockade, **table S2**) on ileal *Madcam1* gene expression normalized on the SPF (FMT "−") mice group (log10 axis (D, left panel). Each experiment used a different FMT donor and comprised 6-10 animals per group (N = 4). Each dot represents one ileum. Non supervised hierarchical clustering of the taxonomic composition of human donor feces (defined using shotgun MG sequencing), selecting bacteria of high prevalence >25% and clinically relevant (*10*) (D, middle panel) and volcano plot contrasting significantly different stool taxa of FMT-recipient mice, as assessed using 16S rRNA sequencing, selecting bacteria of high prevalence and, according to ileal expression levels of *Madcam1* (right panel). "Norm": normal levels of MAdCAM-1 (in SPF controls). (**E.**) Shotgun metagenomics-based determination of the relative abundance of fecal species significantly affected by the ABX uptake in lung cancer patients during ABX versus >60 days after ABX discontinuation in a paired analysis including n=13 individuals. Data information: N, number of independent experiments. Comparisons between groups were analyzed using nonparametric Mann-Whitney U test (2 groups) or Kruskal-Wallis H test (>2 groups) followed by multiple-comparisons test by controlling the FDR. For C, nonparametric Spearman correlation was performed. For volcano plot in D, a linear regression was performed to assess *Madcam1* expression as a function of bacteria prevalence in mouse feces and FDR correction was applied. For E, nonparametric Wilcoxon matched-pairs signed rank test was performed. Error bars represent means ± SEM. **fpkm: Fragments per kilo base of transcript per million mapped fragments (gene expression unit)*.

Fig. 3. ABX-induced exodus of enterotropic α4β7$^+$ T$_R$17 CD4$^+$ towards tumor beds.

(**A.**). Flow cytometric analysis of α4β7 expression in PC$^-$ or PC$^+$ CD4$^+$ T cells residing in the tdLN or tumor bed in Kaede mice UV illuminated in the ileum or the "intestine" (ileum+caecum+mLN). (N = 5) (**B.**) Id. as in (A.) but in WT mice subjected to CFSE injection in the mLN and gating on CFSE$^-$ or CFSE$^+$ CD4$^+$ T cells (N = 4). (**C.**) Volcano plot depicting the differential gene transcription in bulk RNA sequencing of α4β7^{hi} versus α4β7$^-$ CD4$^+$ lymphocytes cell-sorted from mLN in four MCA205 tumor-bearing animals. Volcano plots were generated computing the log2 of fold change ratio (FC) of the mean relative abundances of transcripts in α4β7^{hi} versus α4β7$^-$ CD4$^+$ lymphocytes (*x*- axis) with the co-log10 of *P-values* deriving from Mann-Whitney U test for each transcript followed by multiple-comparisons test by controlling the FDR. Blue and orange dots are considered significant ($P<0.05$) while back dots are not ($p>0.05$) (**table S4**). (**D to F.)** Representative gating strategy and dot plots in flow cytometric analyses of the IL-17A secreting α4β7$^+$ T$_{reg}$ (FoxP3$^+$ CD25$^+$) or α4β7$^+$ T$_{conv}$ (FoxP3$^-$) CD4$^+$ T cells within CFSE$^+$ (originating from the mLN, green dots) or CFSE$^-$ cells (tdLN resident cells, black dots) reaching the tdLN during the ACS+4d phase (n = 10-16 mice per group) **(D and E)**. (**F.**) Flow cytometric determination of CFSE$^+$ T$_{reg}$ cells reaching the tdLN (left panel) or the contralateral LN (cLN, right panel) in day 7-established MCA205 bearing WT versus *Madcam1*$^{-/-}$ mice (not treated with ACS), 24 hours after CFSE injection in mLN. Each dot represents one mouse (N = 1). (**G.**) Idem as in (F.) but in Kaede tumor- bearing mice treated or not with anti-MAdCAM-1 Ab (day 8 post-tumor inoculation), photoconverted at day 10 where flow cytometry at day 11 could identify T$_{reg}$-like cells using membrane staining for CD25^{hi}. Each dot represents one mouse (N = 1). (**H.**) Flow cytometric phenotyping of T cells from tdLN in tumor-bearing mice at day 11 post-MCA205 inoculation, gavaged with *E. clostridioformis* (*E. clostri*) at day 8, photoconverted in the ileum at day 10. The percentages of CXCR6$^+$CXCR3$^-$ cells in CD4$^+$ T cells expressing high levels of CD25 (T$_R$17-like, left panel) or CD25$^-$ (right panel) in Kaede mice within PC$^+$ (originating from the mLN) or PC$^-$ cells (tdLN resident cells) reaching the tdLN during the colonization phase with *E. clostridioformis*. Each dot represents one mouse (N = 2). Data information: N, number of independent experiments. Comparisons between groups were analyzed using nonparametric Mann-Whitney U test (2 groups) or Kruskal-Wallis H test (>2 groups) followed by multiple-comparisons test by controlling the FDR. For PC$^+$ vs PC$^-$ or CFSE$^+$ vs CFSE$^-$ comparisons, Wilcoxon matched-pairs signed rank test were performed. Error bars represent mean ± SEM.

Fig. 4. Clonal and functional patterns of emigrating T_{reg} cells according to locations.

(**A.**) Single- cell sorting and RNA sequencing in tumor bearers 11 days after MCA205 implantation using 10X Genomics technology to characterize phenotypic traits of $CFSE^+$ $CD4^+$ and $CD8^+$ T cell subsets emigrating from mLN (CFSE injection at day 10) and reaching tdLN, cLN or tumor bed, or recovered in mLN after oral gavage with water or *E. clostridioformis* at day 5 and day 7. Determination of $CFSE^+$ mLN cells emigrating from the gut to the tdLN or tumor beds (upper and lower panels respectively) by flow cytometry, according to oral gavage with *E. clostridioformis*, depicted in proportions of all $CFSE^+$ cells (N = 2). (**B.**) Single- cell RNA sequencing and cell clustering by mean of *t*-distributed stochastic neighbor embedding (tSNE) of $CFSE^+$ mLN T cells recovered in mLN, cLN, tdLN and tumor bed 24 hrs post inoculation of CFSE in mLN according to transcriptomics patterns (N = 1). (**C.**) Single- cell TCR sequencing was performed on CFSE-stained lymphocytes sampled from the mLN, the cLN, the tumor or the tdLN. Clones were divided into fractions based on their occurrence in the repertoire (clones with an occurrence of one are represented in gray, and ones with counts higher than one in blue. The cumulative frequency of each fraction was calculated within the repertoire of each sample**.** Cumulative frequencies in $FoxP3^+CD127^-$ (upper panels) and $FoxP3^-$ (lower panels) $CD4^+$ T cells according to location are depicted. (**D.**) TCRs from mLN or pooled tumor and tdLN (tumor/tdLN) were clustered with DeepTCR, generating clusters of paired TRA-TRB clonotypes with shared specificities. Clusters were assigned as being mLN (dark blue), tumor/tdLN (black) or shared (cyan) based on the percentage of clonotypes composing them. Proportion of mLN, tumor/tdLN and shared clusters in control (water) and *E. clostridioformis*- gavaged mice (left panel). Percentage of T_{reg} and conventional $CD4^+$ T cells within each compartment-enriched cluster (middle and right panels). (**E.**) Volcano plot of differentially expressed genes in $CFSE^+$ $FoxP3^+$ $CD127^-$ $CD4^+$ T cells in tumors versus mLN (orange versus blue in *x*- axis), in water versus *E. clostridioformis* -treated groups (left and right panels respectively) (**table S5**). (**F.**) Venn diagram comparing control and *E. clostridioformis*-treated groups for genes upregulated in the tumor (versus mLN), highlighting in red, only those upregulated in *E.clostridioformis* -treated mice (**table S5**). Also refer to **fig. S8A** for detailed $CD4^+$ T cell phenotypes and to **fig.S8A** for $CD4^+$ T cell subsets and **fig.S8B, D** and **E** for $CD8^+$ T cell counterparts. Data information: N number of independent experiments.

Fig. 5. Disruption of the MAdCAM-1/ α4β7 axis induced maladaptive responses to anti-PD-1 Abs in mice. (**A.**) Tumor growth kinetics of subcutaneous MCA205 (syngeneic of C57BL/6) implanted in wild- type (WT) versus *Itgb7*- or *Madcam1*- deficient mice (N = 3). (**B to D.**) Tumor growth kinetics or whole-body luminescence-based imaging after implantation of subcutaneous (s.c) MCA205 syngeneic of C57BL/6 (N = 2) (**B**), mammary 4T1 syngeneic of BALB/c (N = 1) (**C**) and orthotopic luciferase-expressing lung TC-1-luc cancer syngeneic of C57BL/6 (N = 2) (**D**) in animals treated with isotype control, anti-α4β7 mAb or anti-MAdCAM-1 mAb while receiving anti-PD-1 therapeutic antibodies (or isotype control Abs). For D, ratios between pre- and post-PD-1 blockade with isotype control mAb, anti-α4β7 mAb or anti-MAdCAM-1 mAb were calculated. Mean±SEM of tumor sizes among five to six mice per group overtime in two treatment groups (anti-PD-1 versus isotype control Ab). (**E.**) Flow cytometric analysis of α4β7 expression on $CD4^+$ T cell splenocytes and tumor- infiltrating lymphocytes (TILs) in WT versus *Madcam1*-deficient mice. Each dot represents one mouse (N = 2). (**F to H.**) Intracellular flow cytometric analysis of RORγt expression in $\alpha4\beta7^+$ or total $CD25^+$ $FoxP3^+$ T_{reg} TILs in anti-MAdCAM-1 or isotype control Ab treated- mice (**F**) or in WT MCA205 tumor bearing mice receiving ACS conditioning regimen (four days post-ACS stop (ACS+4d) or twelve days post-ACS stop (ACS+12d) treated or not with anti-PD-1 Abs (**G, H**)). Each dot represents one mouse (N = 6). (**I.**) Flow cytometric analyses of tumor infiltrating cells (TILs) for $CCR5^+$ $CD8^+$ effector T cells in s.c. MCA205 tumor-bearing mice treated with isotype control mAb, anti-α4β7 mAb or anti-MAdCAM-1 mAb in the setting of PD-1 blockade (N = 2). (**J.**) 4T1 WT or 4T1 *Il22ra1*$^{-/-}$ tumor cell lines were inoculated s.c three days after start of ACS antibiotics that were pursued for 4 days. At ACS discontinuation (after 7 days), neutralizing anti-PD-1 and anti-IL-17A Abs (or isotype control Abs) were i.p injected every 3 days for 5 times until day 12. Tumor sizes of s.c. 4T1 WT or 4T1 *Il22ra1*$^{-/-}$ tumors at sacrifice. In each experiment, four anti-PD-1 i.p. injections were administered every three days during the ACS+12d phase. Each experiment comprised five to eight mice/group and graph depict three pooled independent experiments (N=3). Data information: N, number of independent experiments. Comparisons between groups were analyzed using nonparametric Mann-Whitney U test (2 groups) or Kruskal-Wallis H test (>2 groups) followed by multiple-comparisons test by controlling the FDR. Error bars represent mean ± SEM.

Fig. 6. Interception of immunosuppressive T cells by transfection-enforced overexpression of MAdCAM-1 in the liver. Rapid hydrodynamic iv injection of *Madcam1*- encoding cDNA subcloned into a pLIVE plasmid vector ("plasmid+") or vector alone ("plasmid−") into day 5 tumor- bearing mice, preconditioned with ACS for 3-4 days (or water, from day -3 to day +5)) and treated (**G to J**) or not (**A to F**) with 4 i.p inoculations of anti-PD-1 Ab from day 6 to day 14. (**A and B.**) Liver expression of *Madcam1* mRNA (**A**) or MAdCAM-1 protein (**B**) (assessed in RT-qPCR (**A**) or immunohistochemistry (IHC) (**B**) according to plasmid inoculation and ACS treatment (red dots). Each dot represents one mouse (n = 10-12 mice per group). One representative micrograph picture is shown for IHC (scale bar: 40 μm) (**B, left**). (**C.**) Spearman correlations between liver *Foxp3*/FoxP3 (in RT-qPCR (**left**), in IHC (**right**)) and *Madcam1* mRNA (RT-qPCR) relative expression in plasmid- treated mice, each dot representing one mouse (N = 2) (red dots for ACS treated animals). (**D and E**.) Flow cytometric analysis of $\alpha4\beta7^{+}$ (**D**) or $\alpha4\beta7^{-}$ (**E**) T_{reg} in water or ACS -treated mice according to *Madcam1*- encoding cDNA plasmid injection (or control vector). Concatenated mean±SEM percentages of stained T cells, each dot (black for water, red for ACS) representing one mouse (N = 2). (**F.**) Spearman correlation between liver *Foxp3* in RT-qPCR after normalization of relative expression (*z*-score), and tumor size at sacrifice (D14), each dot representing one mouse (N = 2) (red dots for ACS treated animals). (**G and H**.) Liver expression of *Rorc* and *Madcam1* relative gene expression in RT-qPCR according to PD-1 blockade and *Madcam1*- encoding cDNA plasmid injection (or control vector) as well as ACS (or water). (**H**) Spearman correlations between liver *Rorc* and *Madcam1* relative gene expression in RT-qPCR in plasmid- treated mice, each dot representing one mouse (red dots for ACS treated animals). (**I and J**.) Tumor size in MCA205 bearing-animals treated with anti-PD-1 Abs in water or ACS -treated mice according to *Madcam1*- encoding cDNA plasmid injection (or control vector) (**I, left panel**). Tumor growth kinetics in MCA205 bearing-animals treated with anti-PD-1 Abs with or without ACS in animals inoculated with the vector alone or the *Madcam1*- encoding cDNA plasmid (N=2) (**I, right panel**). (**J**) Spearman correlations between liver *Madcam1* relative expression in RT-qPCR and tumor size at sacrifice (D19), in plasmid- treated mice, each dot representing one mouse (red dots for ACS- treated animals). Data information: N, number of independent experiments. Comparisons between groups were analyzed using nonparametric Mann-Whitney U test (2 groups) or Kruskal-Wallis H test (>2 groups) followed by multiple-comparisons test for controlling the FDR and nonparametric Spearman correlations. Error bars represent means ± SEM.

Fig. 7. Serum soluble MAdCAM-1 is a robust prognosis parameter in cancer patients.

(A). Luminex immunoassay monitoring of serum levels of soluble MAdCAM-1 (sMAdCAM-1) in 299 NSCLC patients belonging to two independent cohorts according to history of recent ABX uptake (**table S7 and S8**). Each dot represents one patient's serum. Error bars represent means ± SEM. (**B to D**.) Overall survival (OS) analysis using the Kaplan Meier estimator and Cox regression to assess the prognostic value of serum levels of sMAdCAM-1, split using the median of the NSCLC patient discovery cohort amenable to PD-1 blockade, according to ABX uptake history (**B**). This cut-off determined from the discovery cohort allowed to split the patients in two groups of different prognosis in the validation cohort (**C**). Both cohorts of NSCLC were pooled and segregated according to tumor PD-L1 expression, and the cut-off value of sMAdCAM-1 (median of the whole cohort) (**D**) (refer to **table S7** for patient description, **fig. S10D** for multivariable analysis and **fig. S10E** for PFS). (**E**.) Idem as in (C) but overall survival in 212 >second line metastatic renal cell carcinoma (RCC) patients amenable to nivolumab. (**F**.) Idem as in (C) but overall survival in 79 patients diagnosed with metastatic bladder cancer (BC) treated with durvalumab (anti-PD-L1). Kaplan-Meier for OS curves were performed and hazard ratios (HR) indicated.

Fig. 8. **Serum sMAdCAM-1 is a proxy for gut dysbiosis.**

(**A and B.**) Alpha (**A**) and beta (**B**) diversity of the taxonomic content of the intestinal microbiota according to the serum sMAdCAM-1 levels in 95 NSCLC patients. (**A**.) MGS Shannon diversity evaluation in shotgun MG sequencing according to the median of sMAdCAM-1 in the whole population composed of 95 NSCLC patients (refer to **table S8** for patient description). The *P*-value was calculated by a Wilcoxon test blocking for cohort. (**B**.) Principal-component analysis (PCA) of species level centered log-ratio-transformed relative abundance. The *P*-value was calculated using ADONIS and 999 permutations. (**C**.) Differentially abundant species according to sMAdCAM-1 serum levels (< (Low) or ≥ (High) according to median), color coded according to the relative abundance of each species detected by at least 3 different methods. (**D.**) Relative abundances of two distinct species from the genus *Enterocloster,* categorizing the patients according to the median of sMAdCAM-1. Each dot represents each patient's stool. Comparisons between groups were analyzed using the nonparametric Mann-Whitney U test (2 groups). Error bars represent means ± SEM.

Supplementary Materials

fig. S1 to S10

Tables S1 to S8

5

Figure 1

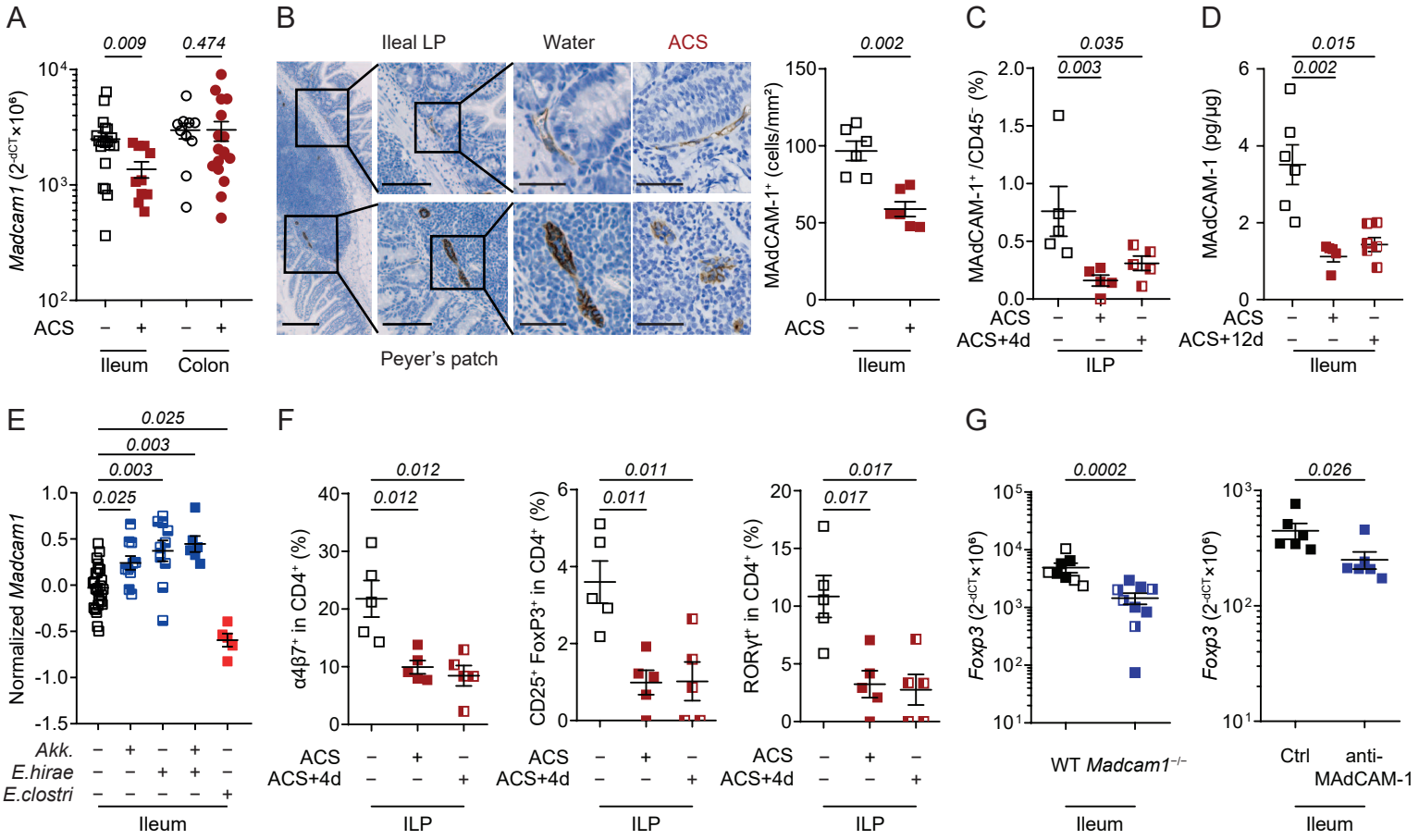
A
B
C
D
Ileal LP
Water
ACS
Peyer's patch
ACS
ACS+4d
ACS+12d
Ileum
Colon
ILP

E
F
G
Akk.
E.hirae
E.clostri
Ileum
ILP
WT Madcam1−/−
Ctrl
anti-MAdCAM-1

Figure 2

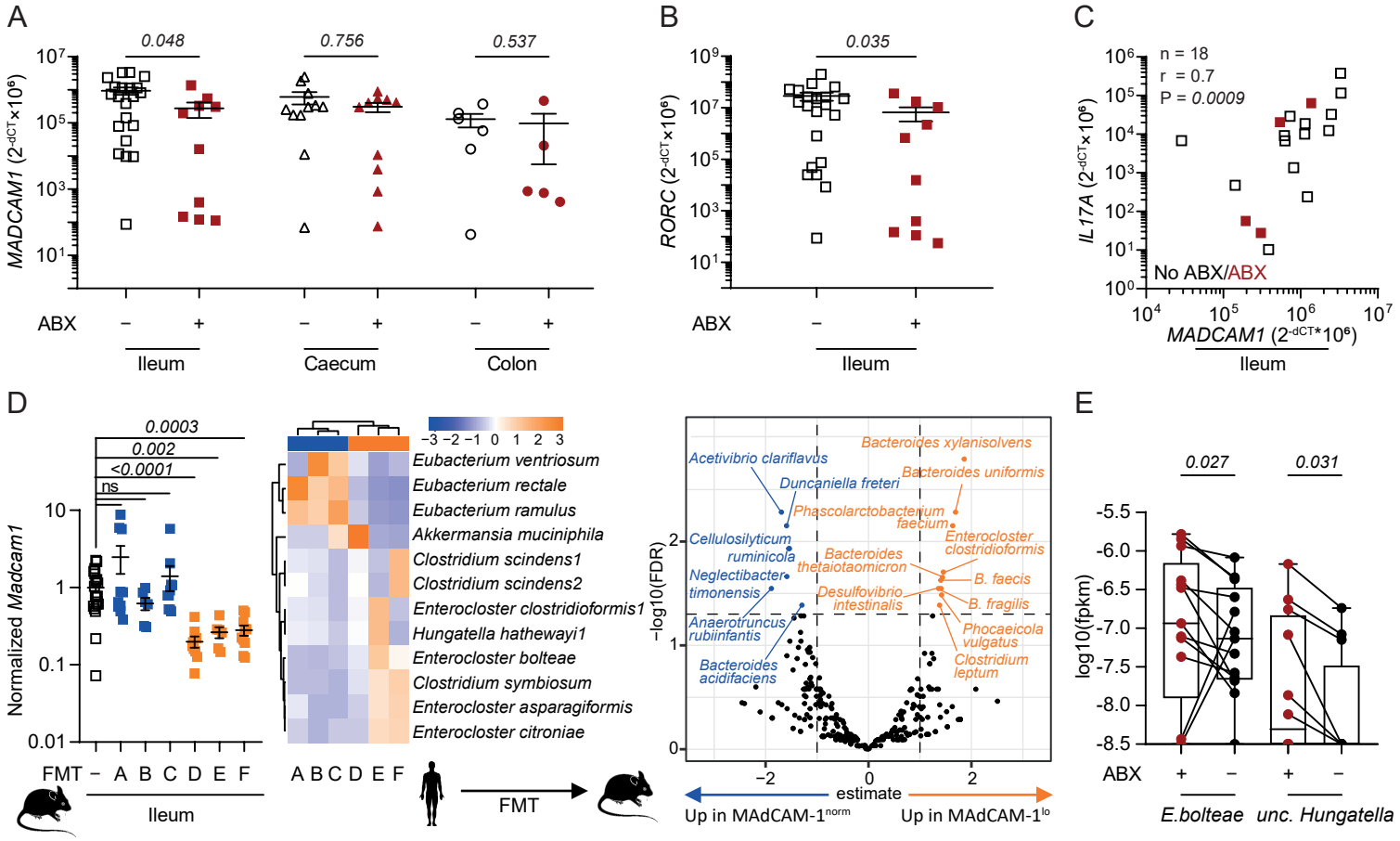
A
0.048
0.756
0.537
MADCAM1 (2-dCT×10⁶)
ABX
Ileum
Caecum
Colon
B
0.035
RORC (2-dCT×10⁶)
C
n = 18
r = 0.7
P = 0.0009
IL17A (2-dCT×10⁶)
No ABX/ABX
MADCAM1 (2-dCT*10⁶)
D
0.0003
0.002
<0.0001
ns
Normalized Madcam1
FMT
Eubacterium ventriosum
Eubacterium rectale
Eubacterium ramulus
Akkermansia muciniphila
Clostridium scindens1
Clostridium scindens2
Enterocloster clostridioformis1
Hungatella hathewayi1
Enterocloster bolteae
Clostridium symbiosum
Enterocloster asparagiformis
Enterocloster citroniae
Acetivibrio clariflavus
Duncaniella freteri
Phascolarctobacterium faecium
Bacteroides xylanisolvens
Bacteroides uniformis
Cellulosilyticum ruminicola
Bacteroides thetaiotaomicron
Enterocloster clostridioformis
Neglectibacter timonensis
B. faecis
Desulfovibrio intestinalis
B. fragilis
Anaerotruncus rubiinfantis
Phocaeicola vulgatus
Bacteroides acidifaciens
Clostridium leptum
−log10(FDR)
estimate
Up in MAdCAM-1norm
Up in MAdCAM-1lo
E
0.027
0.031
log10(fpkm)
E.bolteae
unc. Hungatella

Figure 3

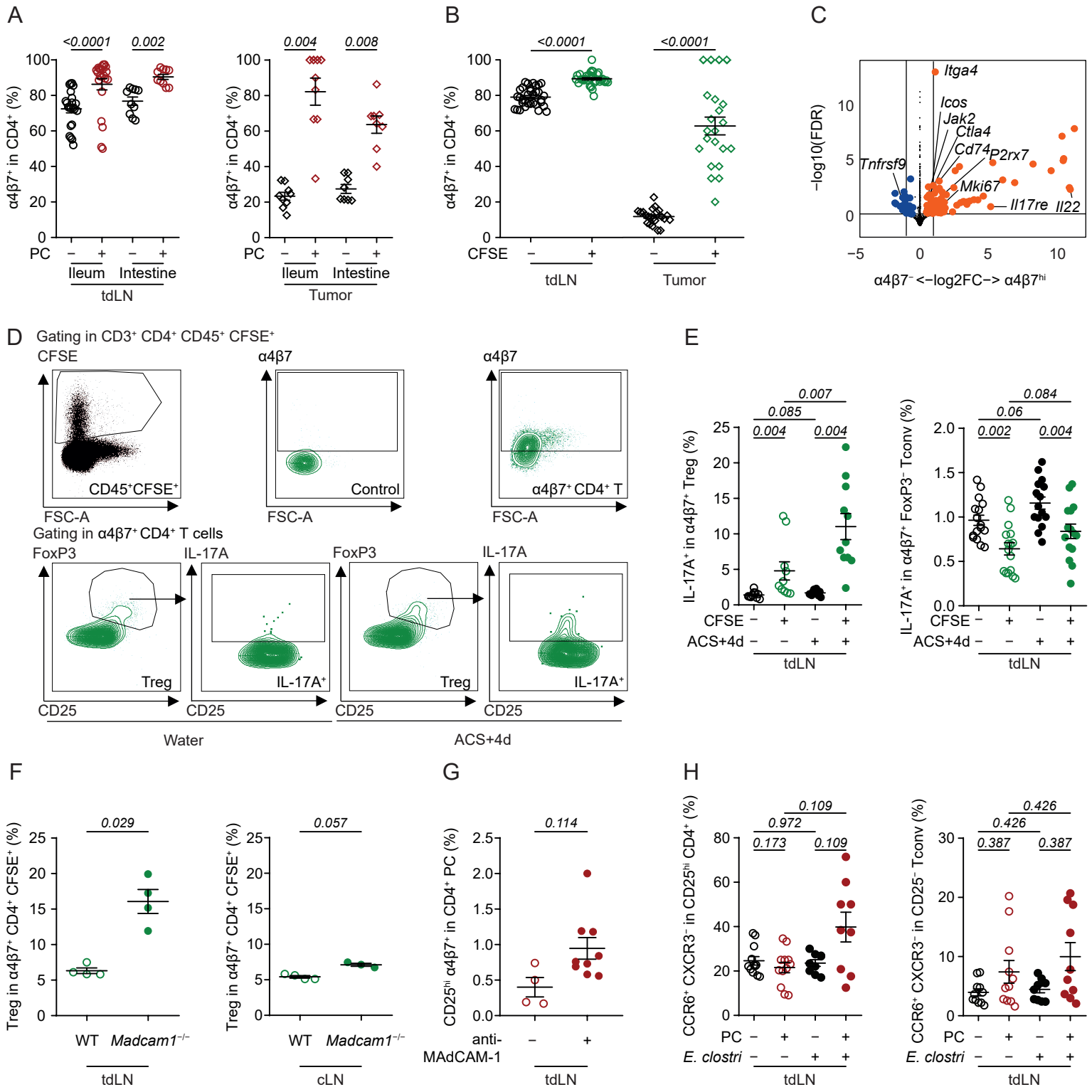
A
<0.0001
0.002
0.004
0.008
α4β7⁺ in CD4⁺ (%)
PC
Ileum
Intestine
tdLN
Tumor
B
<0.0001
<0.0001
CFSE
tdLN
Tumor
C
−log10(FDR)
Itga4
Icos
Jak2
Ctla4
Cd74
P2rx7
Tnfrsf9
Mki67
Il17re
Il22
α4β7⁻ <−log2FC−> α4β7ʰⁱ
D
Gating in CD3⁺ CD4⁺ CD45⁺ CFSE⁺
CFSE
CD45⁺CFSE⁺
FSC-A
α4β7
Control
α4β7⁺ CD4⁺ T
Gating in α4β7⁺ CD4⁺ T cells
FoxP3
IL-17A
Treg
IL-17A⁺
CD25
Water
ACS+4d
E
0.007
0.085
0.004
0.004
IL-17A⁺ in α4β7⁺ Treg (%)
CFSE
ACS+4d
tdLN
0.084
0.06
0.002
0.004
IL-17A⁺ in α4β7⁺ FoxP3⁻ Tconv (%)
F
0.029
0.057
Treg in α4β7⁺ CD4⁺ CFSE⁺ (%)
WT
Madcam1−/−
tdLN
cLN
G
0.114
CD25ʰⁱ α4β7⁺ in CD4⁺ PC (%)
anti-MAdCAM-1
tdLN
H
0.109
0.972
0.173
0.109
CCR6⁺ CXCR3⁻ in CD25ʰⁱ CD4⁺ (%)
PC
E. clostri
tdLN
0.426
0.426
0.387
0.387
CCR6⁺ CXCR3⁻ in CD25⁻ Tconv (%)

Figure 4

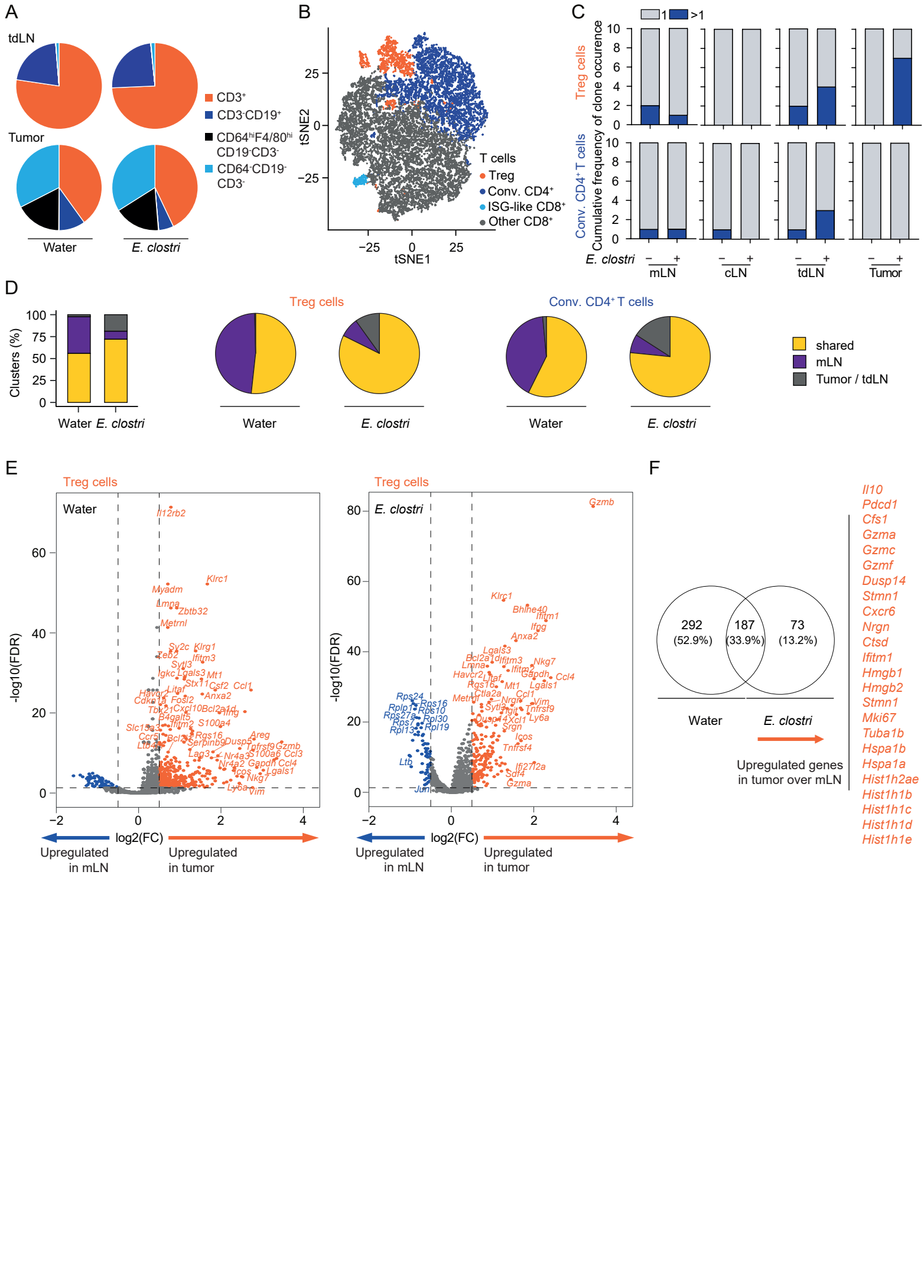
A
tdLN
Tumor
CD3+
CD3-CD19+
CD64hiF4/80hi CD19-CD3-
CD64-CD19- CD3-
Water
E. clostri
B
tSNE2
tSNE1
T cells
Treg
Conv. CD4+
ISG-like CD8+
Other CD8+
C
1
>1
Treg cells
Conv. CD4+ T cells
Cumulative frequency of clone occurence
E. clostri
mLN
cLN
tdLN
Tumor
D
Clusters (%)
Water E. clostri
Treg cells
Conv. CD4+ T cells
shared
mLN
Tumor / tdLN
E
Treg cells
Water
E. clostri
-log10(FDR)
log2(FC)
Upregulated in mLN
Upregulated in tumor
F
292 (52.9%)
187 (33.9%)
73 (13.2%)
Water
E. clostri
Upregulated genes in tumor over mLN
Il10
Pdcd1
Cfs1
Gzma
Gzmc
Gzmf
Dusp14
Stmn1
Cxcr6
Nrgn
Ctsd
Ifitm1
Hmgb1
Hmgb2
Stmn1
Mki67
Tuba1b
Hspa1b
Hspa1a
Hist1h2ae
Hist1h1b
Hist1h1c
Hist1h1d
Hist1h1e

Figure 5

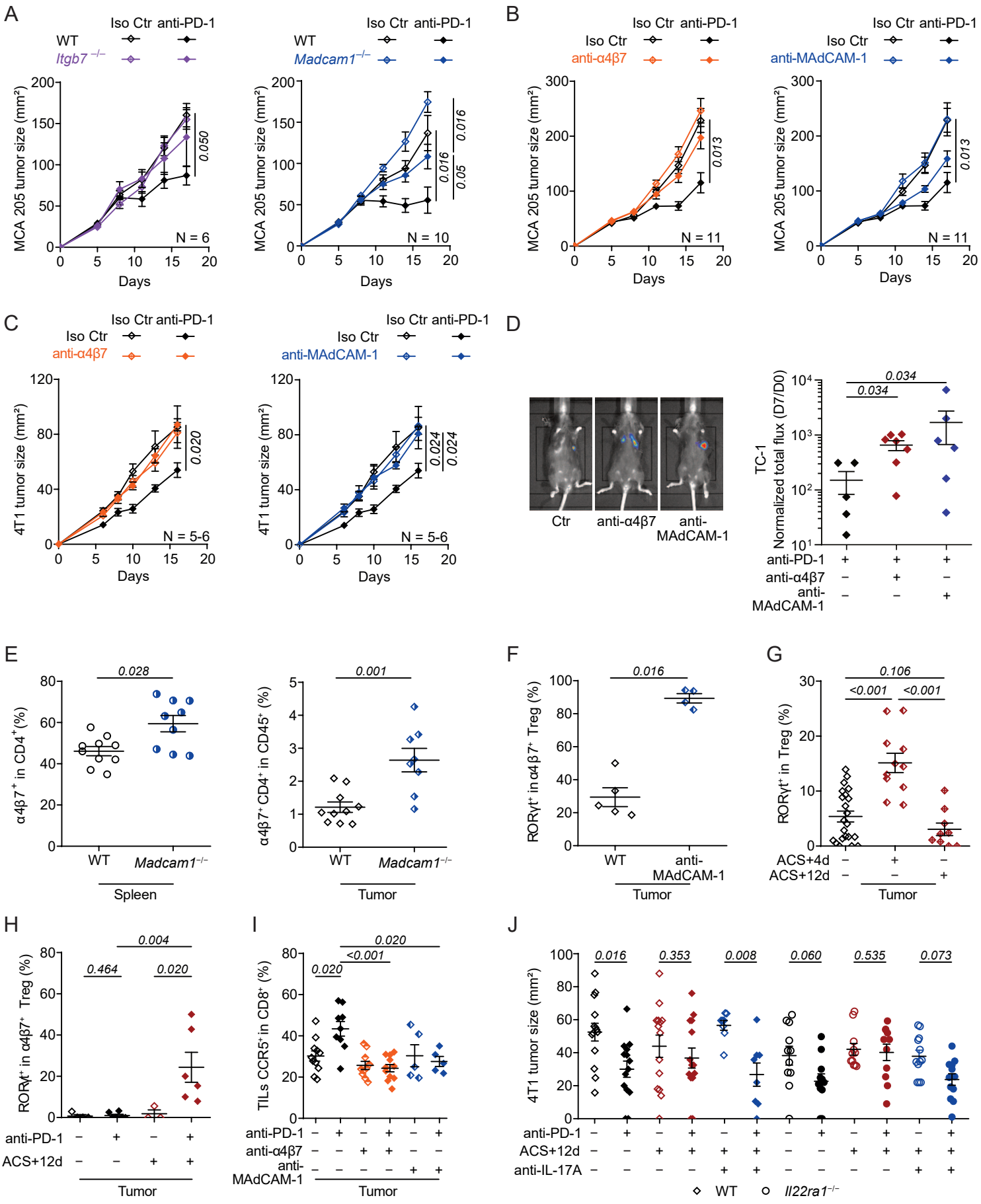
A
Iso Ctr anti-PD-1
WT
Itgb7 −/−
Madcam1−/−
MCA 205 tumor size (mm²)
Days
N = 6
N = 10
0.050
0.016
0.05
0.016
B
Iso Ctr
anti-α4β7
anti-MAdCAM-1
N = 11
0.013
C
4T1 tumor size (mm²)
N = 5-6
0.020
0.024
0.024
D
Ctr
anti-α4β7
anti-MAdCAM-1
TC-1
Normalized total flux (D7/D0)
0.034
0.034
anti-PD-1
anti-α4β7
anti-MAdCAM-1
E
α4β7+ in CD4+ (%)
0.028
WT
Madcam1−/−
Spleen
α4β7+ CD4+ in CD45+ (%)
0.001
Tumor
F
RORγt+ in α4β7+ Treg (%)
0.016
anti-MAdCAM-1
G
RORγt+ in Treg (%)
0.106
<0.001
<0.001
ACS+4d
ACS+12d
H
0.004
0.464
0.020
I
TILs CCR5+ in CD8+ (%)
0.020
<0.001
0.020
J
0.016
0.353
0.008
0.060
0.535
0.073
anti-IL-17A
WT
Il22ra1−/−

Figure 6

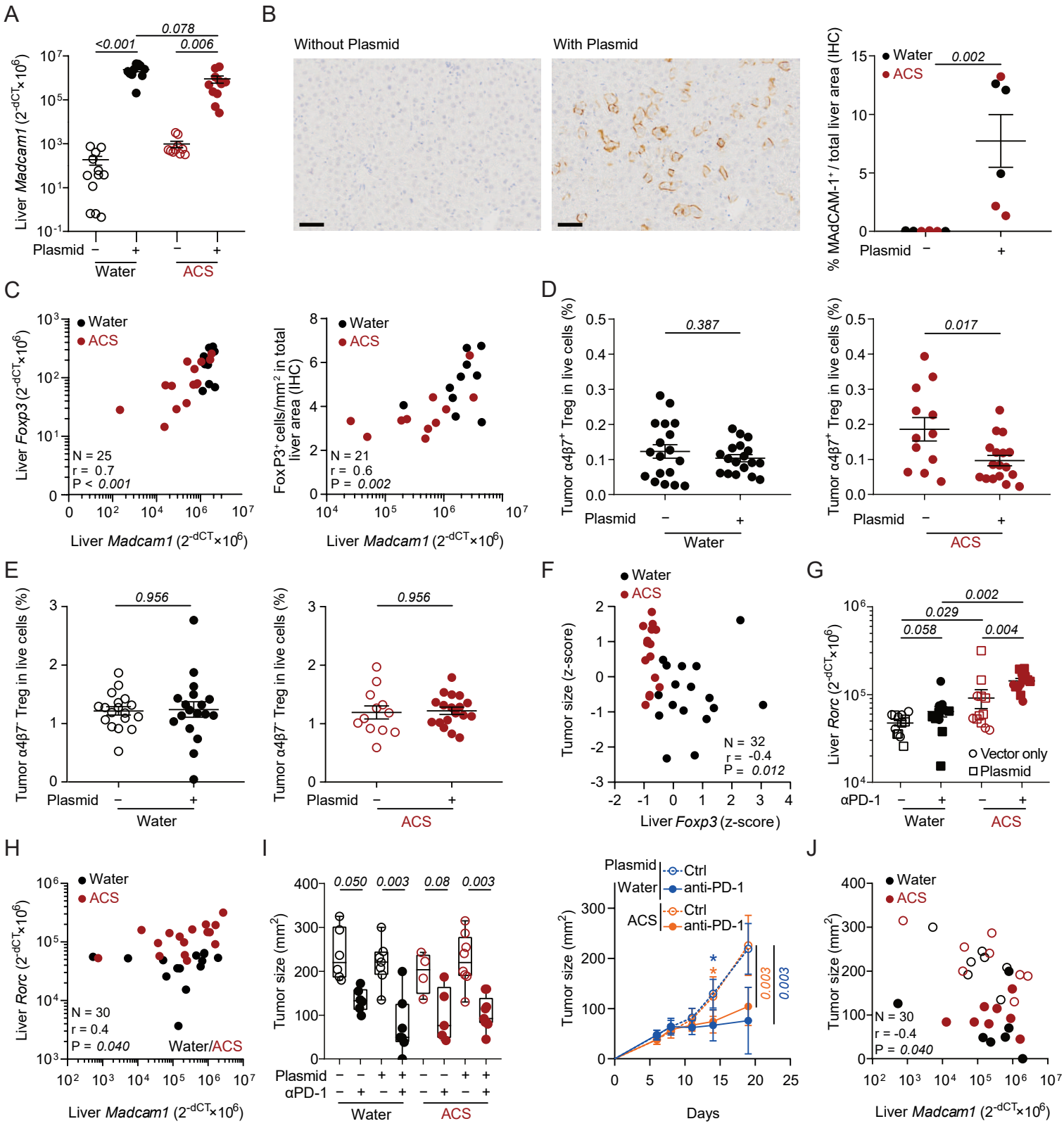
A
B
C
D
E
F
G
H
I
J
Without Plasmid
With Plasmid
Water
ACS
Plasmid
Liver Madcam1 (2-dCT×10^6)
% MAdCAM-1+ / total liver area (IHC)
Liver Foxp3 (2-dCT×10^6)
FoxP3+ cells/mm2 in total liver area (IHC)
Tumor α4β7+ Treg in live cells (%)
Tumor size (z-score)
Liver Rorc (2-dCT×10^6)
Tumor size (mm2)
Vector only
Plasmid
αPD-1
Ctrl
anti-PD-1
Days
N = 25
r = 0.7
P < 0.001
N = 21
r = 0.6
P = 0.002
N = 32
r = -0.4
P = 0.012
N = 30
r = 0.4
P = 0.040
N = 30
r = -0.4
P = 0.040
Water/ACS

Figure 7

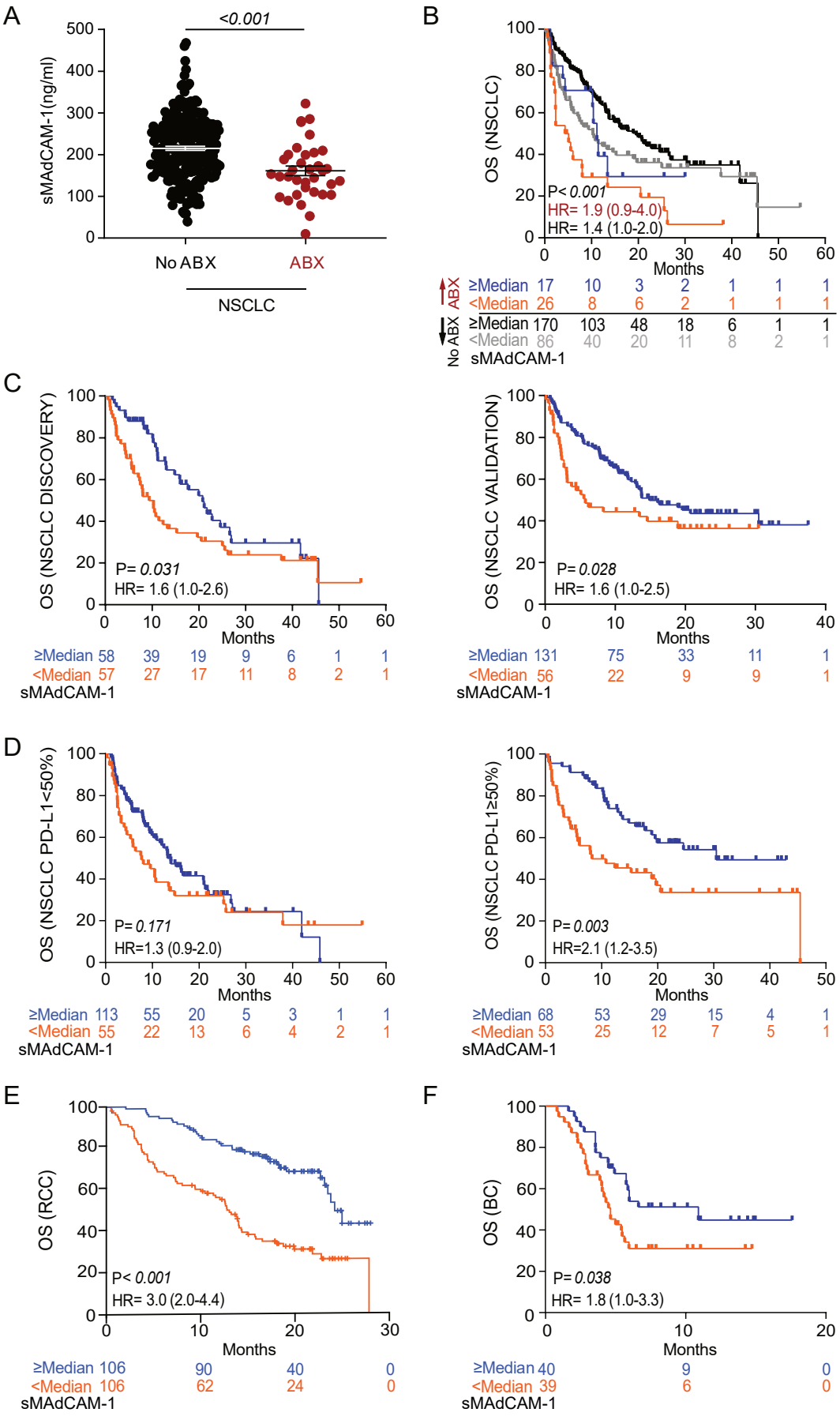
A
<0.001
sMAdCAM-1(ng/ml)
No ABX
ABX
NSCLC
B
OS (NSCLC)
P< 0.001
HR= 1.9 (0.9-4.0)
HR= 1.4 (1.0-2.0)
Months
ABX
≥Median 17 10 3 2 1 1 1
<Median 26 8 6 2 1 1 1
No ABX
≥Median 170 103 48 18 6 1 1
<Median 86 40 20 11 8 2 1
sMAdCAM-1
C
OS (NSCLC DISCOVERY)
P= 0.031
HR= 1.6 (1.0-2.6)
Months
≥Median 58 39 19 9 6 1 1
<Median 57 27 17 11 8 2 1
sMAdCAM-1
OS (NSCLC VALIDATION)
P= 0.028
HR= 1.6 (1.0-2.5)
Months
≥Median 131 75 33 11 1
<Median 56 22 9 9 1
sMAdCAM-1
D
OS (NSCLC PD-L1<50%)
P= 0.171
HR=1.3 (0.9-2.0)
Months
≥Median 113 55 20 5 3 1 1
<Median 55 22 13 6 4 2 1
sMAdCAM-1
OS (NSCLC PD-L1≥50%)
P= 0.003
HR=2.1 (1.2-3.5)
Months
≥Median 68 53 29 15 4 1
<Median 53 25 12 7 5 1
sMAdCAM-1
E
OS (RCC)
P< 0.001
HR= 3.0 (2.0-4.4)
Months
≥Median 106 90 40 0
<Median 106 62 24 0
sMAdCAM-1
F
OS (BC)
P= 0.038
HR= 1.8 (1.0-3.3)
Months
≥Median 40 9 0
<Median 39 6 0
sMAdCAM-1

Figure 8

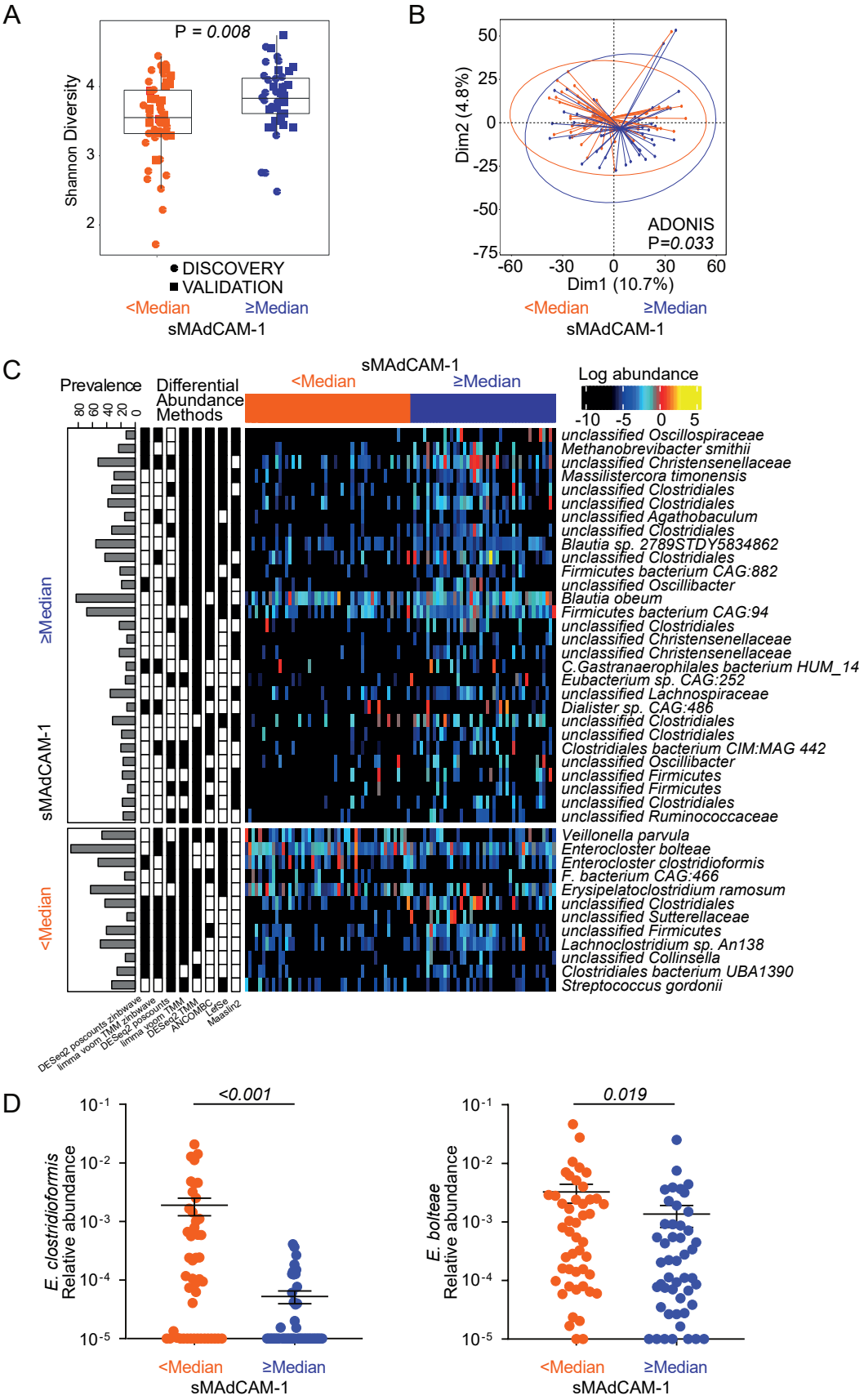
A
P = 0.008
Shannon Diversity
DISCOVERY
VALIDATION
<Median
≥Median
sMAdCAM-1
B
Dim2 (4.8%)
Dim1 (10.7%)
ADONIS
P=0.033
<Median
≥Median
sMAdCAM-1
C
sMAdCAM-1
<Median
≥Median
Prevalence
Differential Abundance Methods
Log abundance
unclassified Oscillospiraceae
Methanobrevibacter smithii
unclassified Christensenellaceae
Massilistercora timonensis
unclassified Clostridiales
unclassified Clostridiales
unclassified Agathobaculum
unclassified Clostridiales
Blautia sp. 2789STDY5834862
unclassified Clostridiales
Firmicutes bacterium CAG:882
unclassified Oscillibacter
Blautia obeum
Firmicutes bacterium CAG:94
unclassified Clostridiales
unclassified Christensenellaceae
unclassified Christensenellaceae
C.Gastranaerophilales bacterium HUM_14
Eubacterium sp. CAG:252
unclassified Lachnospiraceae
Dialister sp. CAG:486
unclassified Clostridiales
unclassified Clostridiales
Clostridiales bacterium CIM:MAG 442
unclassified Oscillibacter
unclassified Firmicutes
unclassified Firmicutes
unclassified Clostridiales
unclassified Ruminococcaceae
Veillonella parvula
Enterocloster bolteae
Enterocloster clostridioformis
F. bacterium CAG:466
Erysipelatoclostridium ramosum
unclassified Clostridiales
unclassified Sutterellaceae
unclassified Firmicutes
Lachnoclostridium sp. An138
unclassified Collinsella
Clostridiales bacterium UBA1390
Streptococcus gordonii
DESeq2 poscounts zinbwave
limma voom TMM zinbwave
DESeq2 poscounts
limma voom TMM
DESeq2 TMM
ANCOMBC
LeFSe
Maaslin2
D
<0.001
0.019
E. clostridioformis Relative abundance
E. bolteae Relative abundance
<Median
≥Median
sMAdCAM-1

Science
AAAS

Supplementary Materials for

A microbiota-modulated checkpoint dictating the traffic of intestinal immunosuppressive T cells into cancers

Marine Fidelle†[1,2,3], Conrad Rauber*†[1,2,3,4], Carolina Alves Costa Silva†[1,2,3], Ai-Ling Tian[1,5,6], Imran Lahmar[1,2,3], Anne-Laure Mallard de La Varende[1,2,3], Liwei Zhao[1,5,6], Cassandra Thélémaque[1,3], Isabelle Lebhar[1,3], Meriem Messaoudene[7], Eugenie Pizzato[1,3], Roxanne Birebent[1,2,3], Maxime Descartes Mbogning Fonkou[1,3], Silvia Zoppi[1,2,8], Anna Reni[1,2,9], Cécile Dalban[10], Marion Leduc[1,5,6], Gladys Ferrere[1,3,11], Sylvère Durand[1,5,6], Pierre Ly[1,3,30], Aymeric Silvin[1,3], Kevin Mulder[1,2,3], Charles-Antoine Dutertre[1,3], Florent Ginhoux[1,3], Satoru Yonekura[1,2,3], Maria Paula Roberti[1,3,12,13], Maryam Tidjani-Alou[1,3], Safae Terrisse[1,2,3], Jianzhou Chen[1,3], Oliver Kepp[1,5,6], Angela Schippers[14], Norbert Wagner[14], Javier Suárez Gosálvez[15], Sebastian Kobold[15,16], Jean-Eudes Fahrner[1,2,3], Corentin Richard[7], Jacques Bosq[17], Leonardo Lordello[1,3], Giacomo Vitali[18], Nathalie Galleron[18], Benoît Quinquis[18], Emmanuelle Le Chatelier[18], Lucas Blanchard[19], Jean-Philippe Girard[19], Anne Jarry[20], Nadine Gervois[20], Emmanuelle Godefroy[20], Nathalie Labarrière[20,21], Ronald Koschny[4], Romain Daillère[11], Benjamin Besse[1,2], Caroline Truntzer[22], François Ghiringhelli[22], Nicolas Coatnoan[23,24], Vanessa Mhanna[23,24], David Klatzmann[23,24], Damien Drubay[1,25,26], Laurence Albiges[1,2], Andrew Maltez Thomas[27], Nicola Segata[27,28], François-Xavier Danlos[1,2,3,29,30], Aurélien Marabelle[1,2,3,29,30], Bertrand Routy[7,31], Lisa Derosa††[1,2,3,30], Guido Kroemer†††*[5,6,32], Laurence Zitvogel†††*.[1,2,3,30]

*Corresponding authors: Laurence Zitvogel or Guido Kroemer or Conrad Rauber. E-mails: laurence.zitvogel@gustaveroussy.fr or kroemer@orange.fr or conrad.rauber@gmx.de
†Shared co-first authorship
††Shared co-last authorship

This PDF file includes:

Supplementary Materials

fig. S1 to S10

Tables S1 to S8

Figure S1

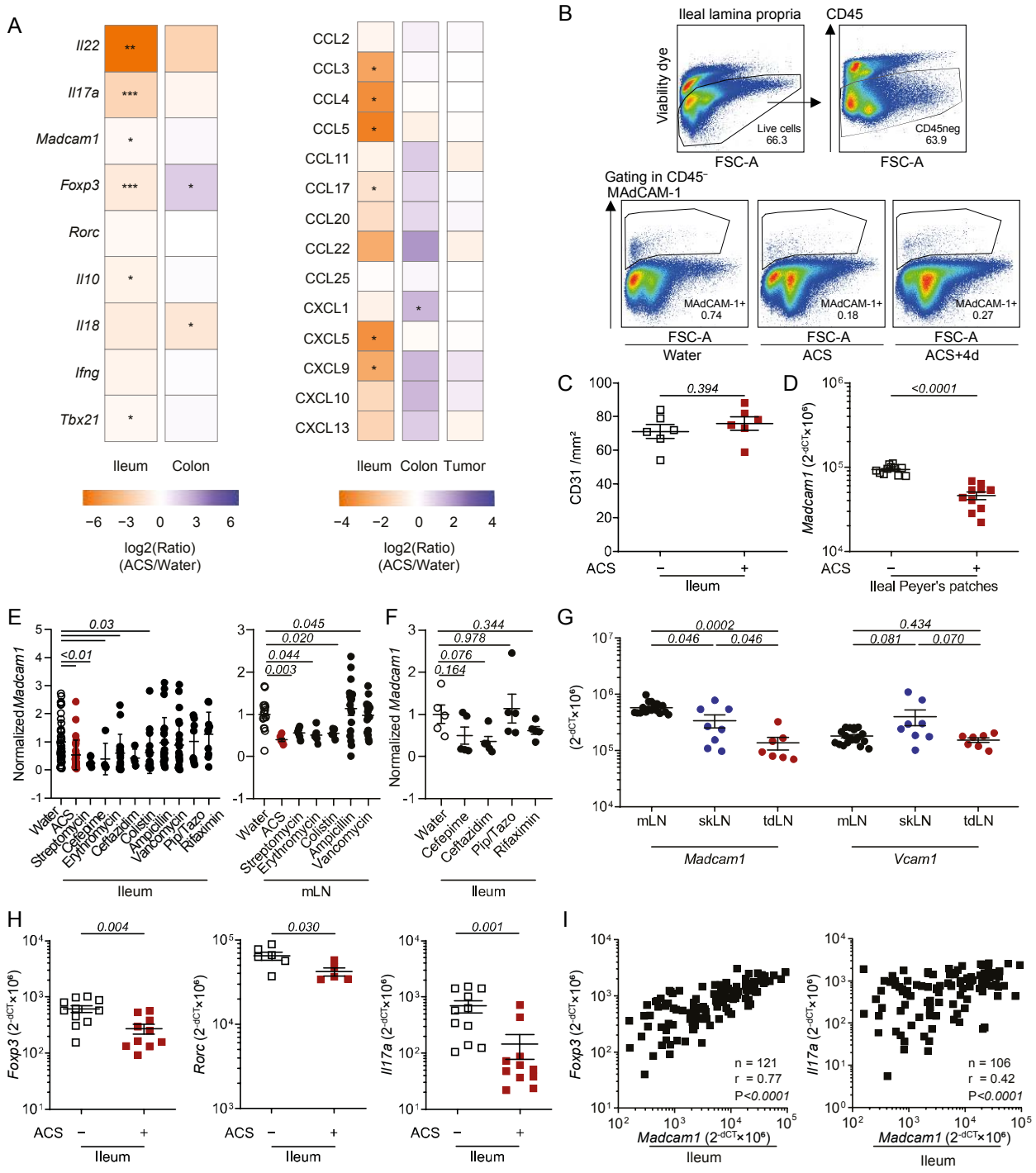

Fig. S1. ACS-induced dysbiosis affects the transcriptional program of immune genes in the intestinal lamina propria. (A.) Heatmap of log2 fold change ratios between ACS-treated and not treated (water) ileum, colon, as well as tumor beds for cytokines/transcription factors (left panel) and chemokines (right panel) expression profiles in RT-qPCR (left panel; N = 5) and ELISA (right

panel; N=1) of the tissue lysates. **(B.)** Representative flow cytometric analysis of MAdCAM-1 protein expression in live CD45 negative cells from the LP in water or ACS conditions (ACS: under antibiotics, ACS+4d: after 4 days of ACS discontinuation). **(C.)** Evaluation of CD31 expression on ileal HEV by IHC in ACS-treated mice **(ref. to Fig. 1B)**. (**D.**) RT-qPCR assessment of the relative expression of *Madcam1* in ileal Peyer's patches (PP) (N=2). **(E.)** RT-qPCR evaluation of the impact of 7 days conditioning with various antibiotic regimens or after ACS+4d on relative transcription levels of *Madcam1* gene in ileal tissue **(left)** or in mesenteric lymph nodes **(right)**. Each dot represents one ileum. The graph gathered N=8 (ileum) and N=3 (mLN) experiments comprising 5-6 mice/group. **(F**.) Idem as in E. but in another animal facility (from CHUM). **(G.**) RT-qPCR assessment of the relative expression of *Madcam1* and *Vcam1* genes in various lymph nodes (LN) (mLN: mesenteric LN, sk: skin LN, td: tumor draining LN). Each dot represents one ileum. **(H and I**.) RT-qPCR evaluation of murine *Foxp3*, *Rorc* and *Il17a* genes in ileal tissue of mice treated or not with ACS (H; N= 2) and Spearman correlations between ileal *Madcam1* and *Foxp3* or *Il17a* expression levels in mice (I; N = 4). Each dot represents one animal. Data information: N, number of independent experiments. Comparisons between groups were analyzed using nonparametric Mann-Whitney U test (2 groups) or Kruskal-Wallis H test (>2 groups) followed by multiple-comparisons test by controlling the FDR. For I, nonparametric Spearman correlations were performed. Error bars represent means ± SEM.

Figure S2

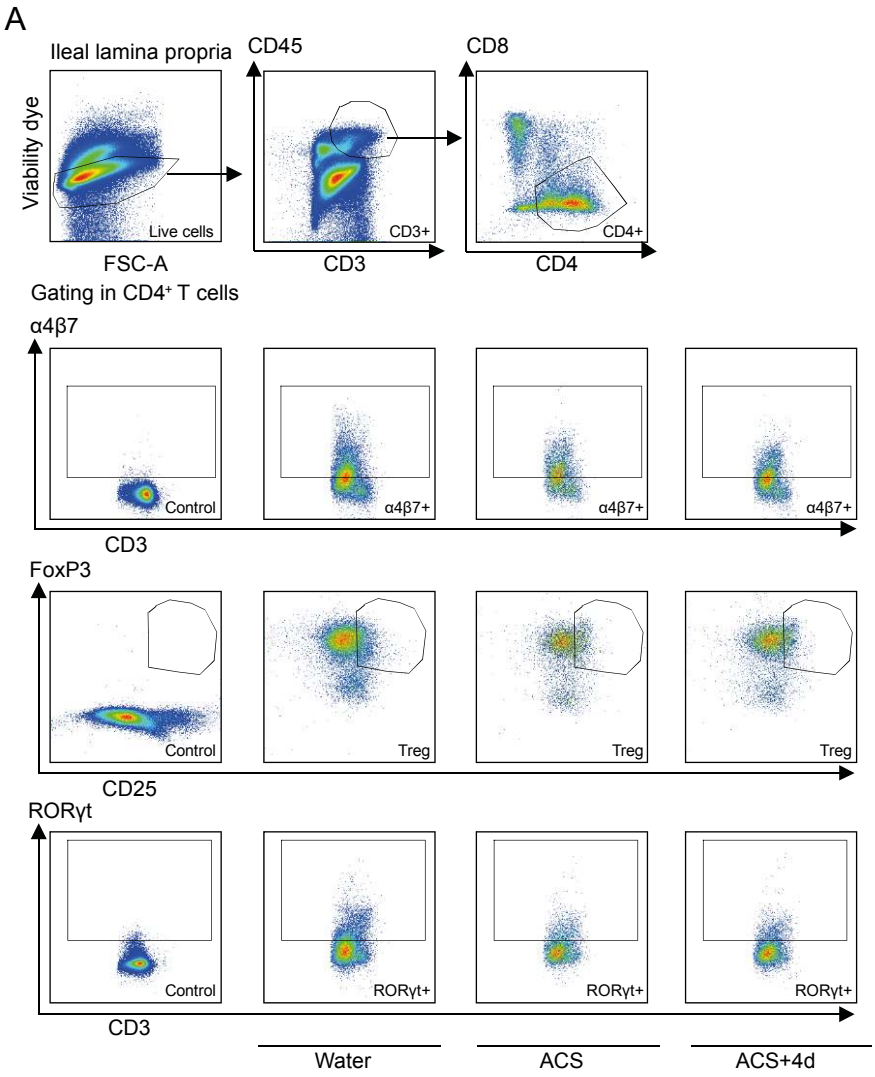

Fig. S2. Representative flow cytometric analysis of T_{reg} and T_R17 in the ileal lamina propria. Representative flow cytometric analysis of T cells of the ileal LP gating on live CD45 positive cells, then T cells (CD3, CD4 or CD8). In the $CD4^+$ T cell gate, we analyzed staining with anti-α4β7 Abs, or anti-FoxP3 and CD25, or RORγt in water or ACS conditions (ACS: under antibiotics, ACS+4d: after 4 days of ACS discontinuation). A typical dot plot is shown for each gating.

Figure S3

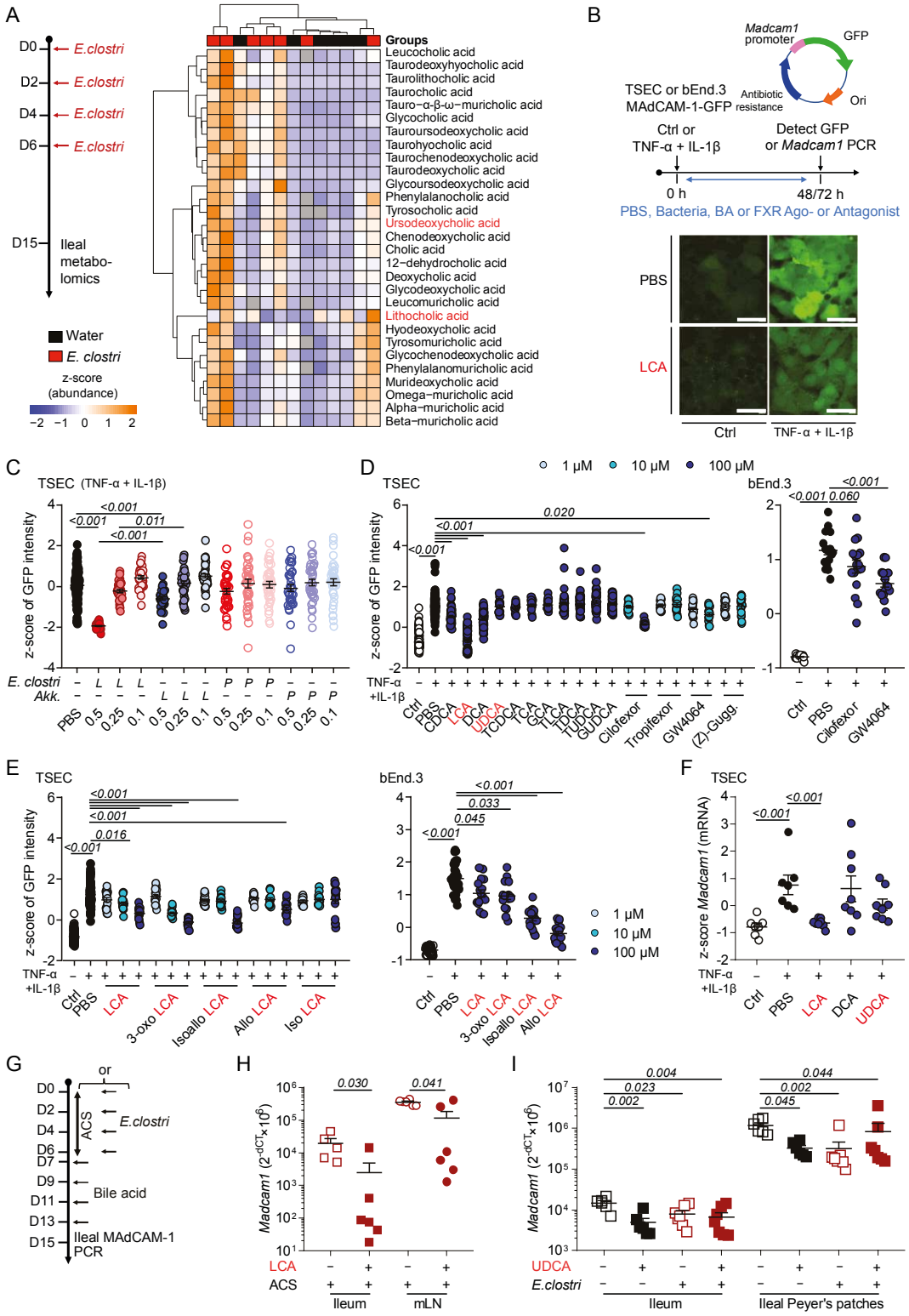
A
D0 E.clostri
D2 E.clostri
D4 E.clostri
D6 E.clostri
D15 Ileal metabo-lomics
Water
E. clostri
z-score (abundance)
−2 −1 0 1 2
Groups
Leucocholic acid
Taurodeoxyhyocholic acid
Taurolithocholic acid
Taurocholic acid
Tauro−α−β−ω−muricholic acid
Glycocholic acid
Tauroursodeoxycholic acid
Taurohyocholic acid
Taurochenodeoxycholic acid
Taurodeoxycholic acid
Glycoursodeoxycholic acid
Phenylalanocholic acid
Tyrosocholic acid
Ursodeoxycholic acid
Chenodeoxycholic acid
Cholic acid
12−dehydrocholic acid
Deoxycholic acid
Glycodeoxycholic acid
Leucomurichólic acid
Lithocholic acid
Hyodeoxycholic acid
Tyrosomurichólic acid
Glycochenodeoxycholic acid
Phenylalanomurichólic acid
Murideoxycholic acid
Omega−muricholic acid
Alpha−muricholic acid
Beta−muricholic acid
B
Madcam1 promoter
GFP
Antibiotic resistance
Ori
TSEC or bEnd.3 MAdCAM-1-GFP
Ctrl or TNF-α + IL-1β
Detect GFP or Madcam1 PCR
0 h
48/72 h
PBS, Bacteria, BA or FXR Ago- or Antagonist
PBS
LCA
Ctrl
TNF-α + IL-1β
C
TSEC (TNF-α + IL-1β)
z-score of GFP intensity
E. clostri
Akk.
PBS 0.5 0.25 0.1 0.5 0.25 0.1 0.5 0.25 0.1 0.5 0.25 0.1
D
1 μM 10 μM 100 μM
TSEC
bEnd.3
TNF-α
+IL-1β
Ctrl PBS CDCA LCA DCA UDCA TCDCA TCA GCA TLCA TUDCA GUDCA Cilofexor Tropifexor GW4064 (Z)-Guggl.
Ctrl PBS Cilofexor GW4064
E
TSEC
bEnd.3
Ctrl PBS LCA 3-oxo LCA Isoallo LCA Allo LCA Iso LCA
1 μM
10 μM
100 μM
F
TSEC
z-score Madcam1 (mRNA)
Ctrl PBS LCA DCA UDCA
G
or
D0
D2
D4
D6
D7
D9
D11
D13
D15
ACS
E.clostri
Bile acid
Ileal MAdCAM-1 PCR
H
Madcam1 (2−dCT×10^6)
LCA
ACS
Ileum
mLN
I
Madcam1 (2−dCT×10^6)
UDCA
E.clostri
Ileum
Ileal Peyer's patches

Fig. S3. *E. clostridioformis*-induced perturbation of ileal biliary acids (BA) and downregulation of MAdCAM-1. (**A.**) Effects of *E. clostridioformis* on ileal metabolites after iterative oral gavage with the bacterium. Targeted metabolomics-profiling of ileal metabolites unveiled a selective and marked alteration of BA composition at one week (D15) in the *E.clostridioformis* group (*E. clostri*) of mice compared with controls. Following gavage with *E. clostri*, and normalization to medium values for each metabolite, we used a non-supervised hierarchical clustering (Euclidean distance, ward linkage method) of z-score-normalized abundances of multiple bile acids (BA) (n = 6-7 mice per group). (**B to E.**) High content confocal microscopy screening using TSEC and bEnd.3 cells stably expressing GFP under the control of the MAdCAM-1 promoter (Scale bar: 40 μm) (**B**) and exposed to live (*L*) and pasteurized (*P*) bacteria at various concentrations (0.5, 0.25 and 0.1 dilutions of 1OD) (**C**) or multiple BA (**D**) and isoforms as well as farnesoid X receptor (FXR) agonists and antagonists (**E**) at various concentrations (1, 10 and 100 μM). Results are depicted as z-score-normalized fluorescence intensity of GFP of triplicate wells. (**F.**) Quantitative PCR analysis of *Madcam1* gene transcripts in TSEC exposed to inflammatory cytokines plus BA (100 μM) (N = 2). (**G to I.**) Experimental setting aimed at assessing the effects of BA orally gavaged with (**H**) or without (**I**) ACS, with (**I**) or without (**H**) *E. clostri* in the presence (LCA, UDCA) or absence of BA, in vivo in naïve animals. The results of ileal *Madcam1* expression assessed by RT-qPCR of LP, mLN or PP of a representative experiment are depicted, each dot representing one mouse. Data information: N, number of independent experiments. Comparisons between groups were analyzed using nonparametric Mann-Whitney U test (2 groups) or Kruskal-Wallis H test (>2 groups) followed by multiple-comparisons test by controlling the FDR. Error bars represent mean ± SEM.

Figure S4

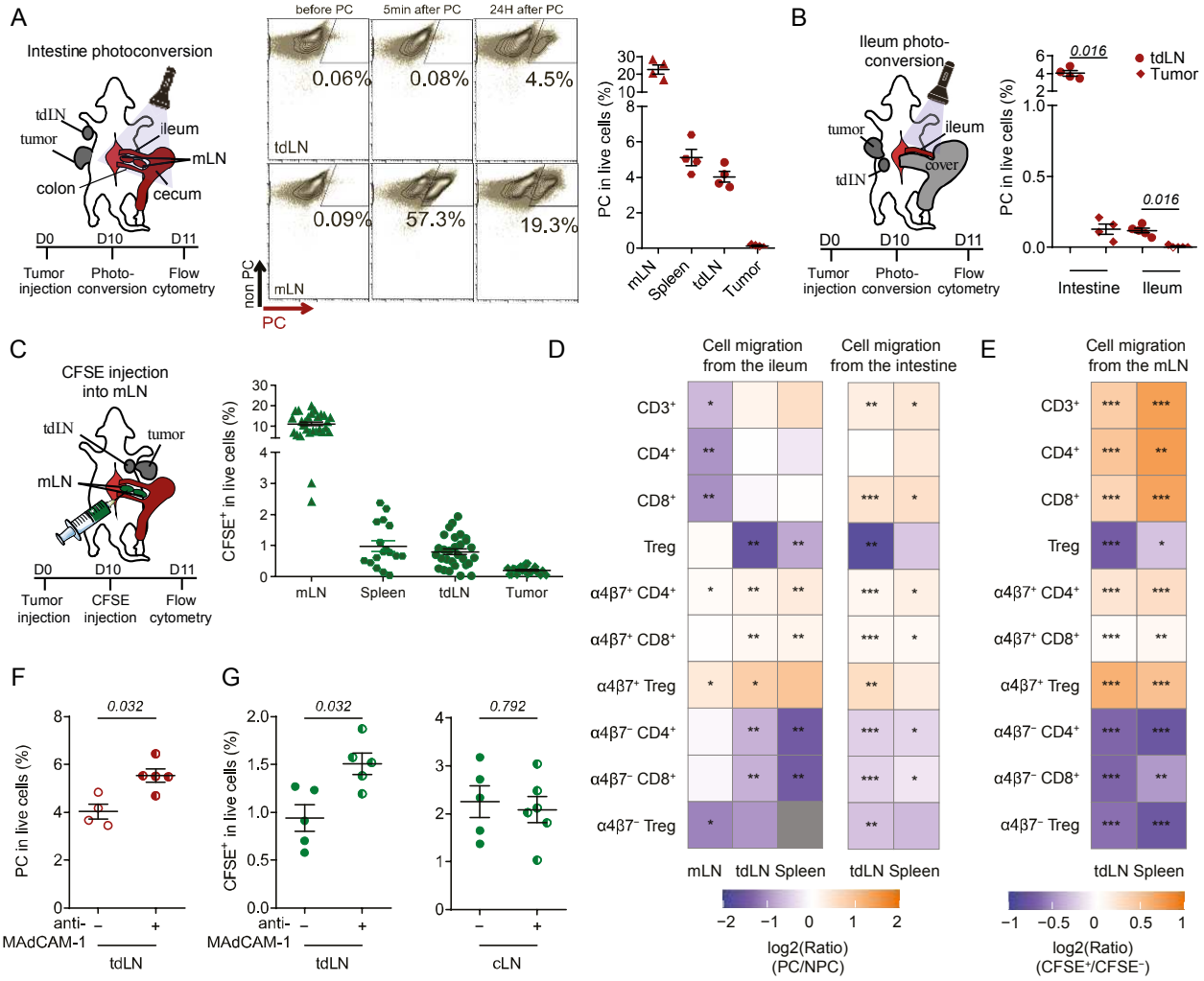

Figure S4. Migratory capacity of enterotropic α4β7 T_{reg} to tdLN and tumors.

(**A**.) Schematic overview of the experimental setup of UV-A illumination of the intestine (ileum, caecum, mesenteric lymph nodes (mLN)) in tumor-bearing Kaede mice (left panel). Flow cytometric gating strategy of photoconverted cells (PC) in tdLN and mLN (right panel) with PC frequencies in target organs before, five min. and 24 hours after laparotomy and UV-A illumination of the intestine compartment (middle panel) as well as detailed percentages of PC cells in mLN, spleen, tdLN and tumor beds at 24 hours, each dot representing one mouse (right panel). A typical experiment out of three yielding similar results is depicted. **(B.)** Flow cytometric determination of photoconverted (PC) gut-originating cells in secondary lymphoid organs (mesenteric LN, spleen, tdLN) and tumors assessed in Kaede mice after UV-A illumination of ileum or "intestine" (ileum+caecum+mLN). The left panel depicts the graphical schema of the experimental setting and the right panel shows the percentages of photoconverted (PC) cells in

tdLN and tumor, each dot representing one mouse (N = 2). (**C.**) Id. as in (A.) in CFSE labeled mLN with detailed percentages of $CFSE^+$ cells in mLN, spleen, tdLN and tumor beds at 24 hours, each dot representing one mouse (right panel) (N = 4). The left panel depicts the graphical schema of the experimental setting. (**D.**) Flow cytometric determination of relative accumulation (log2 Ratio of photoconverted (PC) versus resident (non-photoconverted (NPC)) cells in each cellular subset in various secondary lymphoid organs (SLO) using a color gradient, 24 hours after "intestine" (ileum+caecum+mLN) (right panel, N = 2) or ileum (left panel, N = 3) UV-A illumination. (**E**.) Id. as in D. in CFSE labeled mLN-originated cells model (N = 4). **(F and G).** Effect of the neutralization of MAdCAM-1 using anti-MAdCAM-1 mAb on the recirculation of gut-derived cells towards the tdLN in Kaede (red dots, **F.**) or in mLN- CFSE injected WT mice (green dots, **G. left panel**) or towards a contralateral LN (cLN) (green dots, **G. right panel**). Data information: N, number of independent experiments. Comparisons between groups were analyzed using nonparametric Mann-Whitney U test (2 groups) followed by multiple-comparisons test by controlling the FDR. Error bars represent mean ± SEM. For D and E, **P <0.05, **P <0.01 and ***P <0.001*.

Figure S5

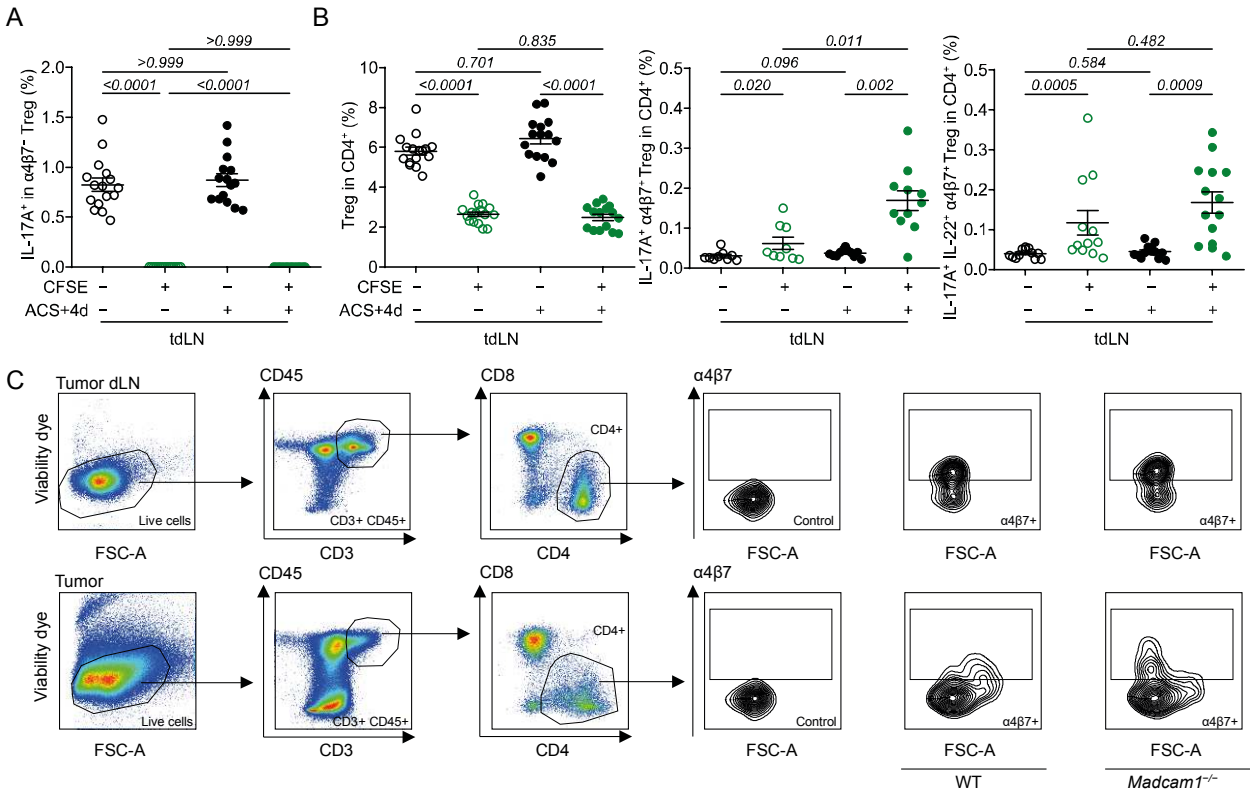

Fig. S5. Tracking enterotropic T_R17 cells during their exodus from mLN to tumor lesions. (**A and B**). Flow cytometric evaluation of different $CD4^+$ T_{reg} cell types (varying in the expression of α4β7, IL-17A, IL-22) in tdLN traced by CFSE labeling in animals treated or not with ASC+4d (*i.e*, 4 days of spontaneous recolonization post ACS-cessation), and bearing subcutaneous MCA205 and subjected to CFSE injection in the mLN 24 hours before (n = 9-16 mice per group). (**C.**) Representative gating strategy to analyze $\alpha4\beta7^+$ $CD4^+$ T cells in the tdLN and tumor beds. Live $CD45^+$ $CD4^+$ T cells were then analyzed for the expression of the heterodimer α4β7 in tdLN and MCA205 sarcomas in wildtype of *Madcam1* deficient mice (**ref. to Fig. 3F**). Data information: N, number of independent experiments. Comparisons between groups were analyzed using nonparametric Kruskal-Wallis H test (>2 groups) followed by multiple-comparisons test by controlling the FDR. For PC^+ vs PC^- or $CFSE^+$ vs $CFSE^-$ comparisons, Wilcoxon matched-pairs signed rank test were performed. Error bars represent mean ± SEM.

Figure S6

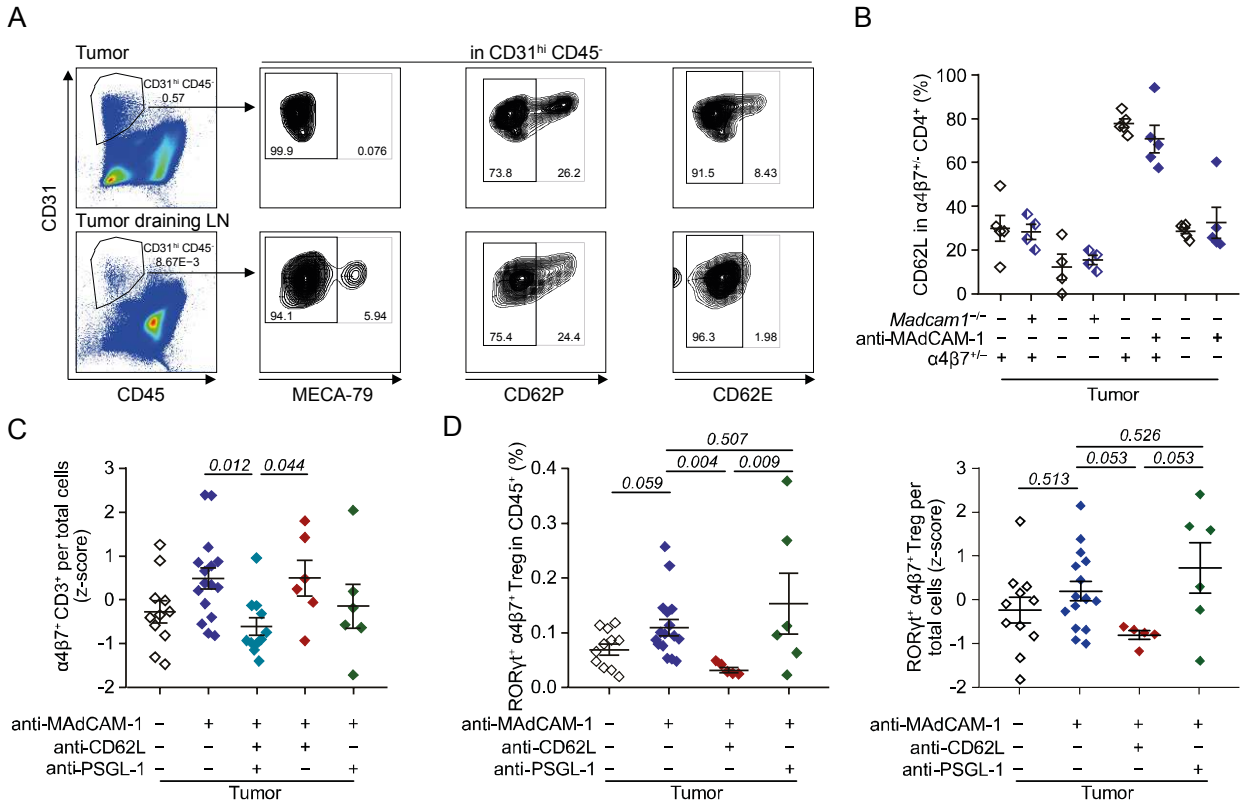

Fig. S6. Role of E/P/L selectins in the accumulation of T cells into tumor-draining LN and sarcomas during MAdCAM-1 blockade.

(A and B.) Flow cytometric analysis of PNAd (MECA-79), P and E-selectins in CD31^{hi} CD45^{-} cells from MCA205 (upper) or tdLN (lower panel) ((**A.**), representative dot plot), as well as CD62L expression in CD4^{+} TILs according to their α4β7 expression and the functionality of MAdCAM-1 (using *Madcam1*$^{+/+}$ or *Madcam1*$^{-/-}$ mice or anti-MAdCAM-1 neutralizing antibodies) (**B**.). Each dot plot represents one mouse (N = 2). (**C to E**.) Flow cytometric analysis of the effects of blocking CD62L or PSGL-1 during antibody-mediated neutralization of MAdCAM-1 in MCA205 tumor-bearing mice on the accumulation of various cell types (indicated in the Y axis) in tumor beds (**D and E**). Each dot represents one mouse (N = 2). Data information: N, number of independent experiments. Results depict absolute numbers z-score normalized (**C and D,** right panel) or percentages (**B and D**, left panel). Comparisons between groups were analyzed using nonparametric Kruskal-Wallis H test (>2 groups) followed by multiple-comparisons test by controlling the FDR. Error bars represent mean ± SEM.

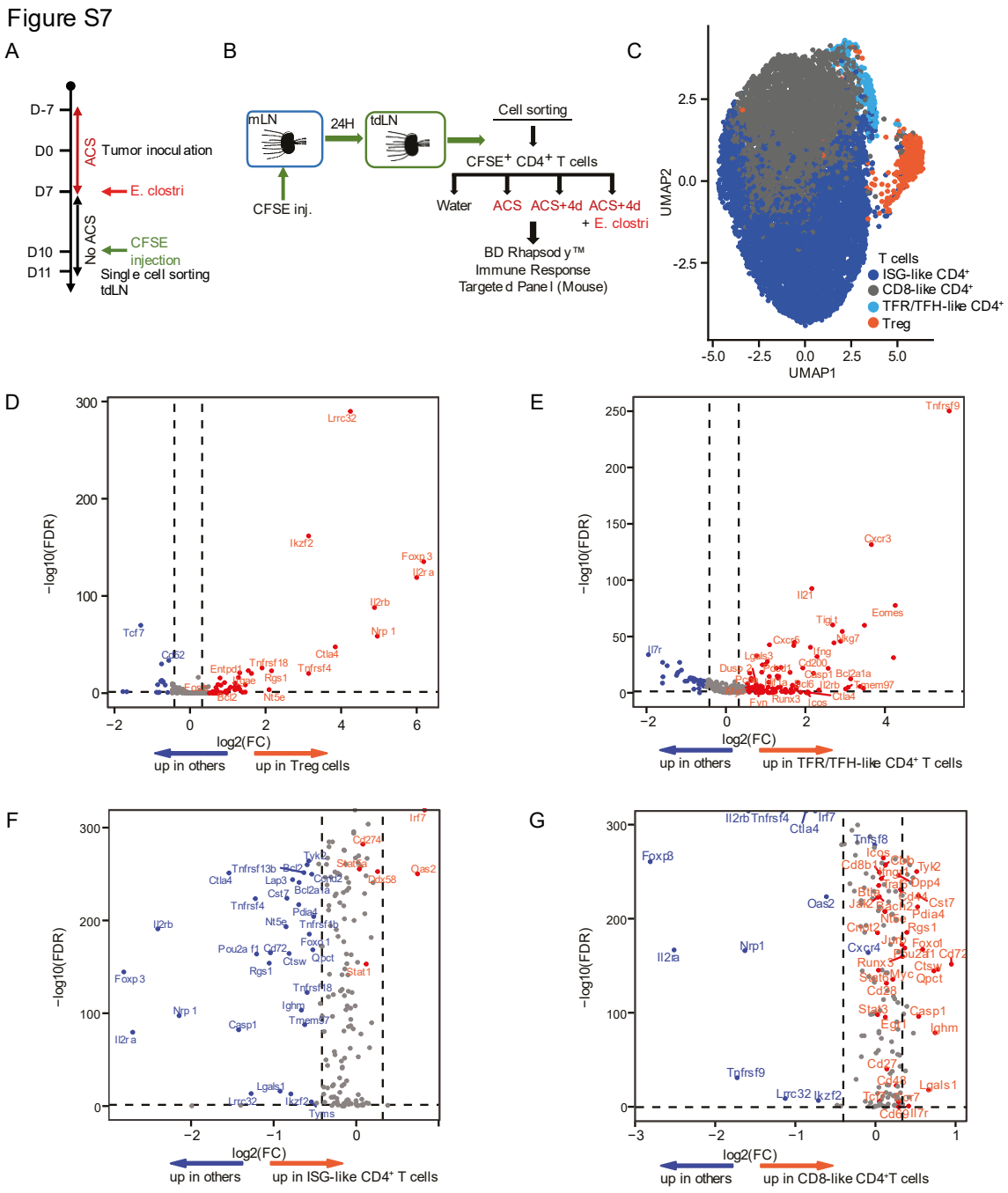

Fig. S7. Characterization of enterotropic CD4$^+$ T cells reaching the tdLN after antibiotics. (**A-B.**) Experimental setting for the single-cell sorting and RNA sequencing using Rhapsody technology to characterize phenotypic traits of CFSE$^+$ CD4$^+$ T cell subsets emigrating from mLN and reaching tdLN after discontinuation of ACS ± *E. clostridioformis* (*E. clostri*). (**C.**) Uniform manifold approximation and projection (UMAP) visualization of 4 clusters of emigrating CFSE$^+$ CD4$^+$ T cells in plate-based full-length single-cell RNA-seq data by unsupervised clustering,

overlaying the four groups of mice. (**D to G.**) Volcano plots of differential gene expression patterns associated with each specific cell type versus the others clustered in (C) according to log10(FDR) and log2 fold change (FC) ratio. Genes are colored if they passed the thresholds for FDR and log2(FC), significant differences being annotated in orange (upregulated) and blue (downregulated).

Figure S8

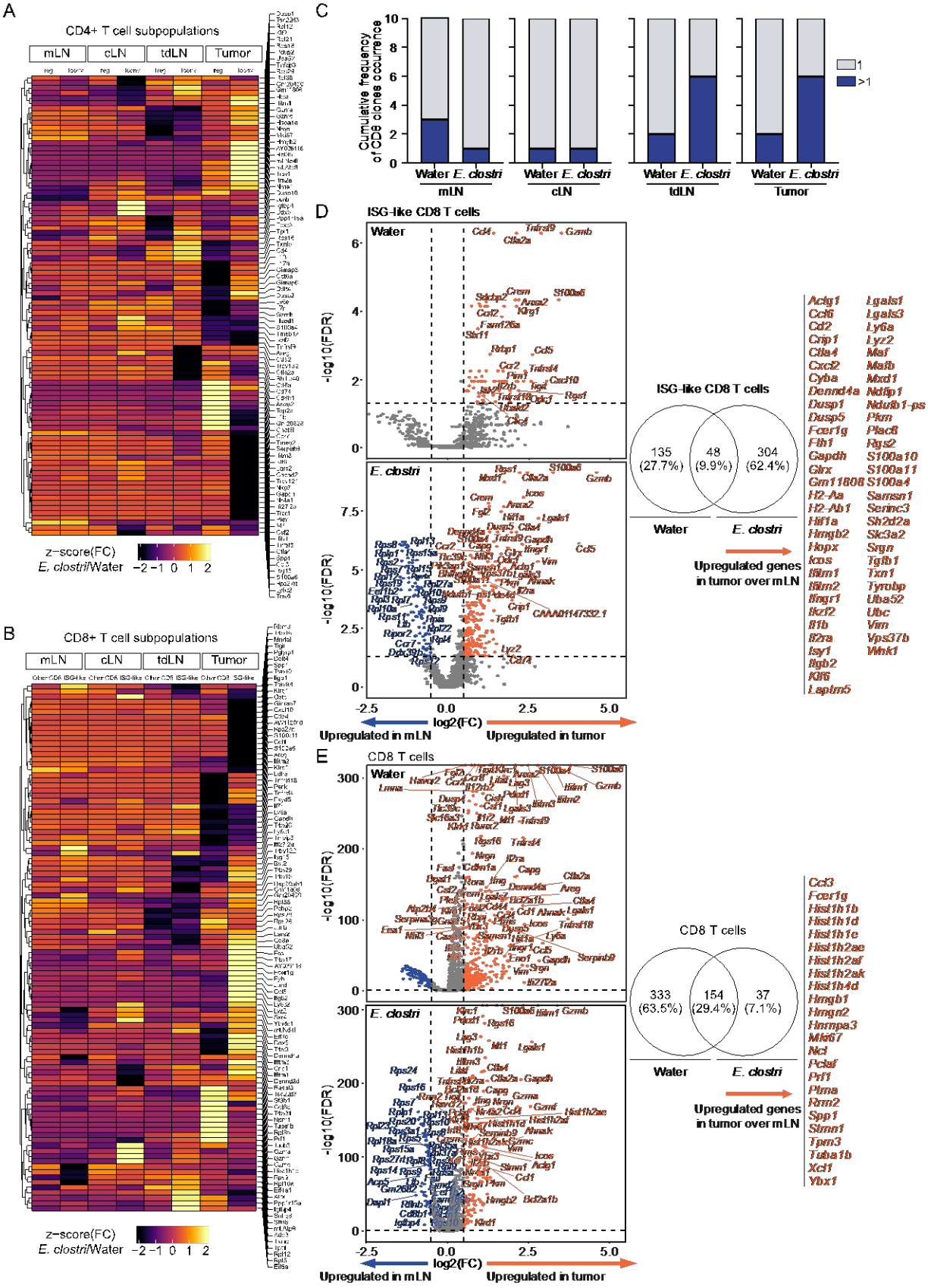
A
CD4+ T cell subpopulations
mLN
cLN
tdLN
Tumor
z−score(FC)
E. clostri/Water −2 −1 0 1 2
B
CD8+ T cell subpopulations
mLN
cLN
tdLN
Tumor
z−score(FC)
E. clostri/Water −2 −1 0 1 2
C
Cumulative frequency of CD8 clones occurrence
1
>1
Water E. clostri
mLN
cLN
tdLN
Tumor
D
ISG-like CD8 T cells
Water
E. clostri
-log10(FDR)
log2(FC)
Upregulated in mLN
Upregulated in tumor
ISG-like CD8 T cells
135 (27.7%)
48 (9.9%)
304 (62.4%)
Water
E. clostri
Upregulated genes in tumor over mLN
Acly1 Lgals1
Ccl6 Lgals3
Cd2 Ly6a
Crip1 Lyz2
Ctla4 Maf
Cxcl2 Mafb
Cyba Mxd1
Dennd4a Ndfip1
Dusp1 Ndufb1-ps
Dusp5 Pkm
Fcer1g Plac8
Fth1 Rgs2
Gapdh S100a10
Glrx S100a11
Gm11808 S100a4
H2-Aa Samsn1
H2-Ab1 Serinc3
Hif1a Sh2d2a
Hmgb2 Slc3a2
Hopx Snn
Icos Tgfb1
Ifitm1 Txn1
Ifitm2 Tyrobp
Ifngr1 Uba52
Ikzf2 Ubc
Il1b Vim
Il2ra Vps37b
Isy1 Wnk1
Itgb2
Klf6
Laptm5
E
CD8 T cells
Water
E. clostri
-log10(FDR)
log2(FC)
Upregulated in mLN
Upregulated in tumor
CD8 T cells
333 (63.5%)
154 (29.4%)
37 (7.1%)
Water
E. clostri
Upregulated genes in tumor over mLN
Ccl3
Fcer1g
Hist1h1b
Hist1h1d
Hist1h1e
Hist1h2ae
Hist1h2af
Hist1h2ak
Hist1h4d
Hmgb1
Hmgn2
Hnrnpa3
Mki67
Ncl
Pclaf
Prf1
Ptma
Rrm2
Spp1
Stmn1
Tpm3
Tuba1b
Xcl1
Ybx1

Fig. S8. Gene patterns and clonal expansion of enterotropic $CD4^+$ and $CD8^+$ T cells associated with target locations and gavaging with *E. clostridioformis*. (**A**.) Heatmap representing the top 10 up- or down-regulated genes between water and *E.clostridioformis (E. clostri)* -treated mice for each $CD4^+$ T cell subpopulations (regulatory $FoxP3^+$ $CD127^-$ $CD4^+$ T cells (T_{reg}) or conventional $FoxP3^-$ $CD4^+$ T cells (T_{conv}) in each organ (mLN, cLN, tdLN and tumor). Genes are arranged in rows and ordered according to unsupervised hierarchical clustering. $CD4^+$ T cell subpopulations are arranged in columns and ordered according to localization and subtypes. Color bars represent the z-scores of the fold changes (FC) (*E.clostridioformis* over water) of average expression for each genes. (**B**.) Idem as in A. for $CD8^+$ T cell subsets. (**C**) Single- cell TCR sequencing was performed on CFSE-stained $CD8^+$ T lymphocytes sampled from the mLN, the cLN, the tumor and tdLN. Cumulative frequencies of $CD8^+$ cell clonal occurrence according to location are depicted. (**D and E.**) Venn diagrams comparing tumor- associated genes in water and *E.clostridioformis*-treated groups for ISG-like $CD8^+$ T cells (**D**) and other $CD8^+$ T cells (**E**). Genes modulated only in *E.clostridioformis*-treated mice are depicted on the right side of each Venn diagram respectively. Genes up- or down-regulated in *E.clostridioformis*-treated mice are depicted in orange and blue, respectively.

Figure S9

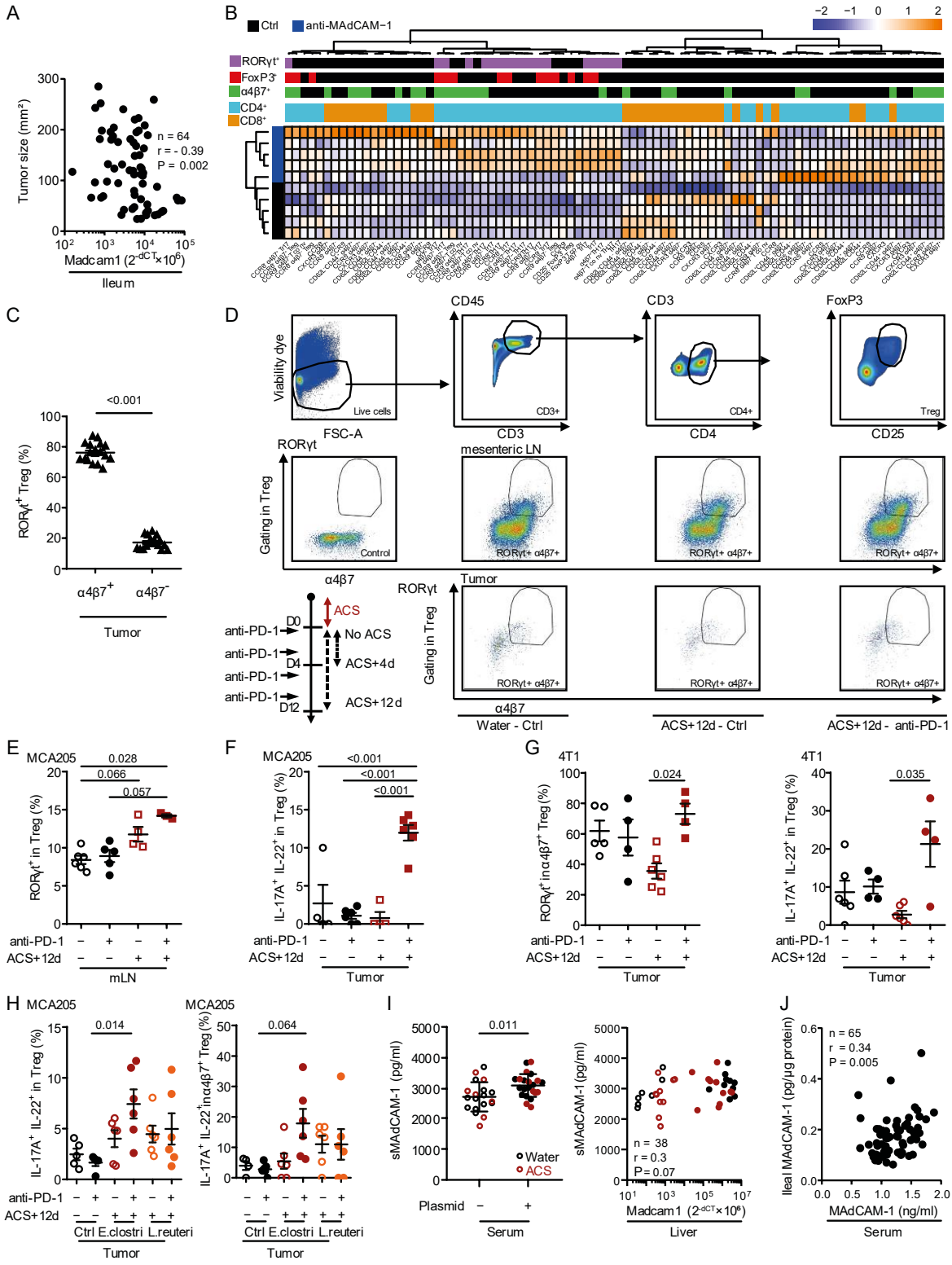
A
Tumor size (mm²)
n = 64
r = - 0.39
P = 0.002
Madcam1 (2^-dCT×10^6)
Ileum
B
Ctrl
anti-MAdCAM-1
RORγt⁺
FoxP3⁺
α4β7⁺
CD4⁺
CD8⁺
C
<0.001
RORγt⁺ Treg (%)
α4β7⁺
α4β7⁻
Tumor
D
Viability dye
Live cells
FSC-A
CD45
CD3+
CD3
CD3
CD4+
CD4
FoxP3
Treg
CD25
RORγt
Gating in Treg
Control
mesenteric LN
RORγt+ α4β7+
α4β7
Tumor
ACS
No ACS
ACS+4d
ACS+12d
anti-PD-1
D0
D4
D12
Water - Ctrl
ACS+12d - Ctrl
ACS+12d - anti-PD-1
E
MCA205
0.028
0.066
0.057
RORγt⁺ in Treg (%)
anti-PD-1
ACS+12d
mLN
F
MCA205
<0.001
<0.001
<0.001
IL-17A⁺ IL-22⁺ in Treg (%)
Tumor
G
4T1
0.024
RORγt⁺ in α4β7⁺ Treg (%)
Tumor
4T1
0.035
IL-17A⁺ IL-22⁺ in Treg (%)
Tumor
H
MCA205
0.014
IL-17A⁺ IL-22⁺ in Treg (%)
Ctrl E.clostri L.reuteri
Tumor
MCA205
0.064
IL-17A⁺ IL-22⁺ in α4β7⁺ Treg (%)
Ctrl E.clostri L.reuteri
Tumor
I
0.011
sMAdCAM-1 (pg/ml)
Water
ACS
Plasmid
Serum
sMAdCAM-1 (pg/ml)
n = 38
r = 0.3
P= 0.07
Madcam1 (2^-dCT×10^6)
Liver
J
n = 65
r = 0.34
P = 0.005
Ileal MAdCAM-1 (pg/µg protein)
MAdCAM-1 (ng/ml)
Serum

Fig. S9. Anti-PD-1 mAb aggravates the accumulation of enterotropic α4β7$^+$ T$_R$17 or IL-22$^+$ T$_R$17 towards tumor lesions caused by ACS-induced dysbiosis. (**A.**) Spearman correlations between ileal *Madcam1* and tumor size in MCA205 tumor bearing and untreated mice. Each dot represents one mouse (N=11). (**B.**) Non supervised hierarchical clustering (Euclidean distance, ward linkage method) represented in a heatmap showing the relative percentages of various immune CD4$^+$ and CD8$^+$ T cell subsets (determined by flow cytometric analyses of TILs dissociated from established s.c. MCA205) in mice treated with neutralizing anti-MAdCAM-1 mAb or isotype control mAb. (**C.**) Flow cytometric assessment of α4β7$^+$ or α4β7$^-$ among RORγt$^+$ Treg (T$_R$17) TIL fractions in subcutaneous MCA205 tumors (n = 18 mice). (**D.**) Experimental setting and flow cytometry gating strategy of PD-1 blockade during ACS intervals of various durations (ACS+4d or +12d) in tumor bearers. (**E to G.**) Flow cytometric assessment of RORγt$^+$ or IL-17A$^+$ IL-22$^+$ cells within T$_{reg}$ in the mLN (**E**) or in subcutaneous MCA205 (N=1) (**F**) or 4T1 (**G**) tumors treated with anti-PD1 Abs in the setting of ACS. (**H**.) Flow cytometric determination of IL-17A$^+$ IL-22$^+$ secreting T$_{reg}$ (**left**) and α4β7$^+$ T$_{reg}$ cells (**right**) in subcutaneous (s.c.) MCA205 tumors treated by PD-1 blockade after ACS+12d stop and enforced gut colonization with *E. clostridioformis* or *L. reuteri* bacteria during anti-PD-1 -based therapy. Each dot represents the tumor size in each animal at sacrifice, in a typical experiment containing 6 mice/group. Refer to Table S4 for detailed phenotypes. (**I.**) Serum sMAdCAM-1 concentrations (assessed by ELISA) at sacrifice (D14, ref to Figure 5A) after hydrodynamic iv inoculation of *Madcam1*- encoding cDNA subcloned into a pLIVE vector (**left panel**) (n = 7-12 mice per group). Spearman correlation between serum sMAdCAM-1 and liver mRNA levels of *Madcam1* gene assessed by RT-qPCR (**right panel**). Each black or red dot representing one mouse conditioned with water or ACS, respectively. (**J.**) Spearman correlation between ileal tissue lysate MAdCAM-1 concentrations (assessed by ELISA) and serum soluble MAdCAM-1 (ELISA) in 65 MCA205 tumor bearers treated or not with anti-PD-1 Abs, each dot representing one mouse (N=2). Data information: N, number of independent experiments. Comparisons between groups were analyzed using nonparametric Mann-Whitney U test (2 groups) or Kruskal-Wallis H test (>2 groups) followed by multiple-comparisons test by controlling the FDR and nonparametric Spearman correlations were performed. For C, Wilcoxon matched-pairs signed rank test was performed. Error bars represent mean ± SEM.

Figure S10

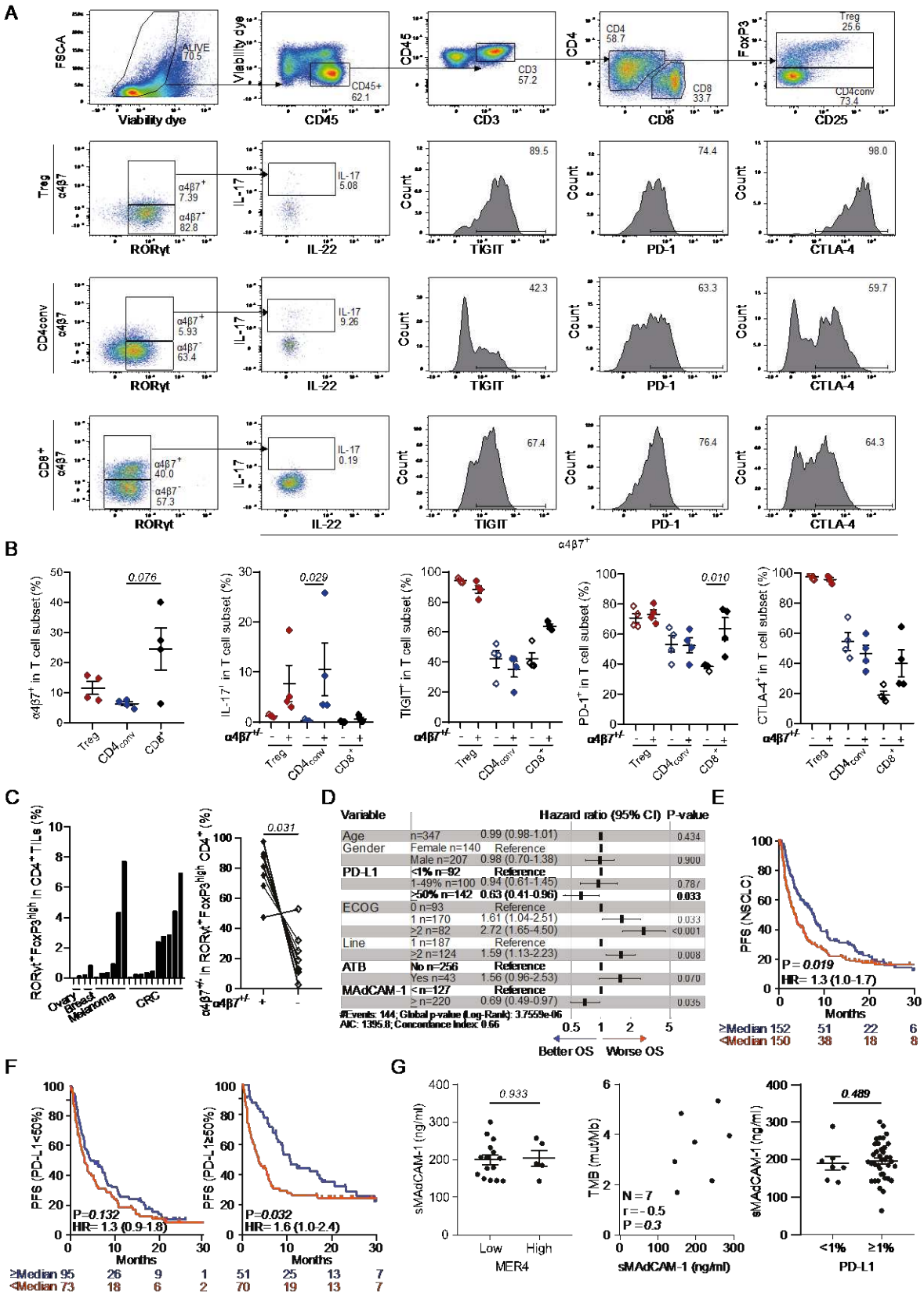
A
FSC-A
ALIVE 70.5
Viability dye
Viability dye
CD45+ 62.1
CD45
CD45
CD3 57.2
CD3
CD4
CD4 58.7
CD8 33.7
CD8
FoxP3
Treg 25.6
CD4conv 73.4
CD25
Treg
α4β7
α4β7+ 7.39
α4β7- 82.8
RORγt
IL-17
IL-17 5.08
IL-22
Count
89.5
TIGIT
74.4
PD-1
98.0
CTLA-4
CD4conv
α4β7+ 5.93
α4β7- 63.4
IL-17 9.26
42.3
63.3
59.7
CD8+
α4β7+ 40.0
α4β7- 57.3
IL-17 0.19
67.4
76.4
64.3
α4β7+
B
α4β7+ in T cell subset (%)
0.076
IL-17+ in T cell subset (%)
0.029
TIGIT+ in T cell subset (%)
PD-1+ in T cell subset (%)
0.010
CTLA-4+ in T cell subset (%)
Treg
CD4conv
CD8+
α4β7+/-
C
RORγt+FoxP3high in CD4+ TILs (%)
Ovary
Breast
Melanoma
CRC
α4β7+/- in RORγt+FoxP3high CD4+ (%)
0.031
D
Variable
Hazard ratio (95% CI)
P-value
Age n=347 0.99 (0.98-1.01) 0.434
Gender Female n=140 Reference
Male n=207 0.98 (0.70-1.38) 0.900
PD-L1 <1% n=92 Reference
1-49% n=100 0.94 (0.61-1.45) 0.787
≥50% n=142 0.63 (0.41-0.96) 0.033
ECOG 0 n=93 Reference
1 n=170 1.61 (1.04-2.51) 0.033
≥2 n=82 2.72 (1.65-4.50) <0.001
Line 1 n=187 Reference
≥2 n=124 1.59 (1.13-2.23) 0.008
ATB No n=256 Reference
Yes n=43 1.56 (0.96-2.53) 0.070
MAdCAM-1 <n=127 Reference
≥n=220 0.69 (0.49-0.97) 0.035
#Events: 144; Global p-value (Log-Rank): 3.7559e-06
AIC: 1395.8; Concordance Index: 0.66
0.5
1
2
5
Better OS
Worse OS
E
PFS (NSCLC)
P = 0.019
HR= 1.3 (1.0-1.7)
Months
≥Median 152 51 22 6
<Median 150 38 18 8
F
PFS (PD-L1<50%)
P=0.132
HR= 1.3 (0.9-1.8)
PFS (PD-L1≥50%)
P=0.032
HR= 1.6 (1.0-2.4)
Months
≥Median 95 26 9 1
<Median 73 18 6 2
≥Median 51 25 13 7
<Median 70 19 13 7
G
sMAdCAM-1 (ng/ml)
0.933
Low
High
MER4
TMB (mut/Mb)
N = 7
r = -0.5
P = 0.3
sMAdCAM-1 (ng/ml)
0.489
<1%
≥1%
PD-L1

Fig. S10. Serum soluble MAdCAM-1 is an independent predictor of clinical benefit to PD-1 blockade. (**A to C.**) Flow cytometric analyses of four fresh NSCLC tumor infiltrating lymphocytes (TIL) focusing of various T cell subsets expressing the integrin α4β7. A representative gating strategy is depicted (**A**.). The activation/exhaustion markers are shown in percentages for each T cell subset for each tumor represented in one dot (**B.**). Same analyses in twenty ex vivo propagated TIL cell lines from ovarian, breast, melanoma and CRC patients. The graph (**C**.) shows the percentages of $FoxP3^{hi}ROR\gamma t^{+}$ $CD4^{+}$ TILs in various cell lines (left panel) and their expression of α4β7 for each tumor with more than 2% of $FoxP3^{hi}ROR\gamma t^{+}$ (right panel). (**D**) Hazard ratios (HR) of the multivariable Cox model for the Overall survival (OS) analysis of the pooled Discovery and Validation NSCLC cohorts. (**E and F.**) Serum soluble MAdCAM-1 as a prognostic factor of progression- free survival (PFS) in the NSCLC discovery and validation cohorts, pooled together, treated with anti-PD-1/PD-L1 Abs (**E**.) Kaplan-Meier PFS curves (HR computed using univariable Cox model) (**E**.) and according to PD-L1 expression (**F**.) (**G.**) Serum levels of sMAdCAM-1 in NSCLC patients according to their tumor expression of endogenous retrovirus MER4 (as determined by tumor RNA sequencing) (**left panel**), the MER4 cut-off value being set up as previously described in a subset (n=20) of patients of the same cohort from Centre George François Leclerc, Dijon. Spearman correlation between TMB and serum sMAdCAM-1 in a subset of NSCLC patients (n=12) (**middle panel**). Serum levels of sMAdCAM-1 in NSCLC patients according to their tumor expression of PD-L1 as determined by EMA-approved routine immunohistochemistry (**right panel**), the cut-off value being 1. Data information: Comparisons between groups were analyzed using the nonparametric Mann-Whitney U test (2 groups).

8.2.1.1 Complementary results: unpublished data.

To validate the prognostic impact of sMAdCAM-1 in patients with advanced RCC and investigate whether the prognostic effect sustained with a different treatment type, we used an independent cohort of patients treated with the RTK Sunitinib in first line therapy (SURF trial, NCT02689167). Clinical characteristics are well balanced between patients with high or low levels of sMAdCAM-1, except for IMDC (Table 4). Patients with lower levels of sMAdCAM-1 had a higher proportion of poor risk IMDC. We confirmed that higher levels of sMadCAM-1 are associated with improved PFS (Fig. 16A) and OS (Fig. 16B). Overall response rates and clinical benefit rates were similar between groups.

Table 4 Clinical characteristics of patients.

	Overall N=170	Low sMAdCAM-1 N=85	High sMAdCAM-1 N=85	*p-value*
Age in years, median (range)	63.7 (29.1-84.2)	63.3 (29.1-84.2)	64.4 (39.2-79)	0.6779
Gender, male – n(%)	136 (80)	67 (79)	69 (81)	0.7014
Albumine, median (range)	41 (21.1-49)	41 (21.1-48)	41.6 (28-49)	0.2996
Brain metastases, yes – n(%)	5 (3)	2 (3)	3 (4)	1
Liver metastases, yes – n(%)	16 (10)	10 (13)	6 (7)	0.2978
Bone metastases, yes – n(%)	25 (15)	16 (20)	9 (11)	0.1279
IMDC risk group – n(%)				
Good	68 (40)	32 (38)	36 (42)	0.0031
Intermediate	79 (47)	34 (40)	45 (53)	
Poor	23 (14)	19 (22)	4 (5)	

International Metastatic renal cell carcinoma Database Consortium (IMDC); Number (n).

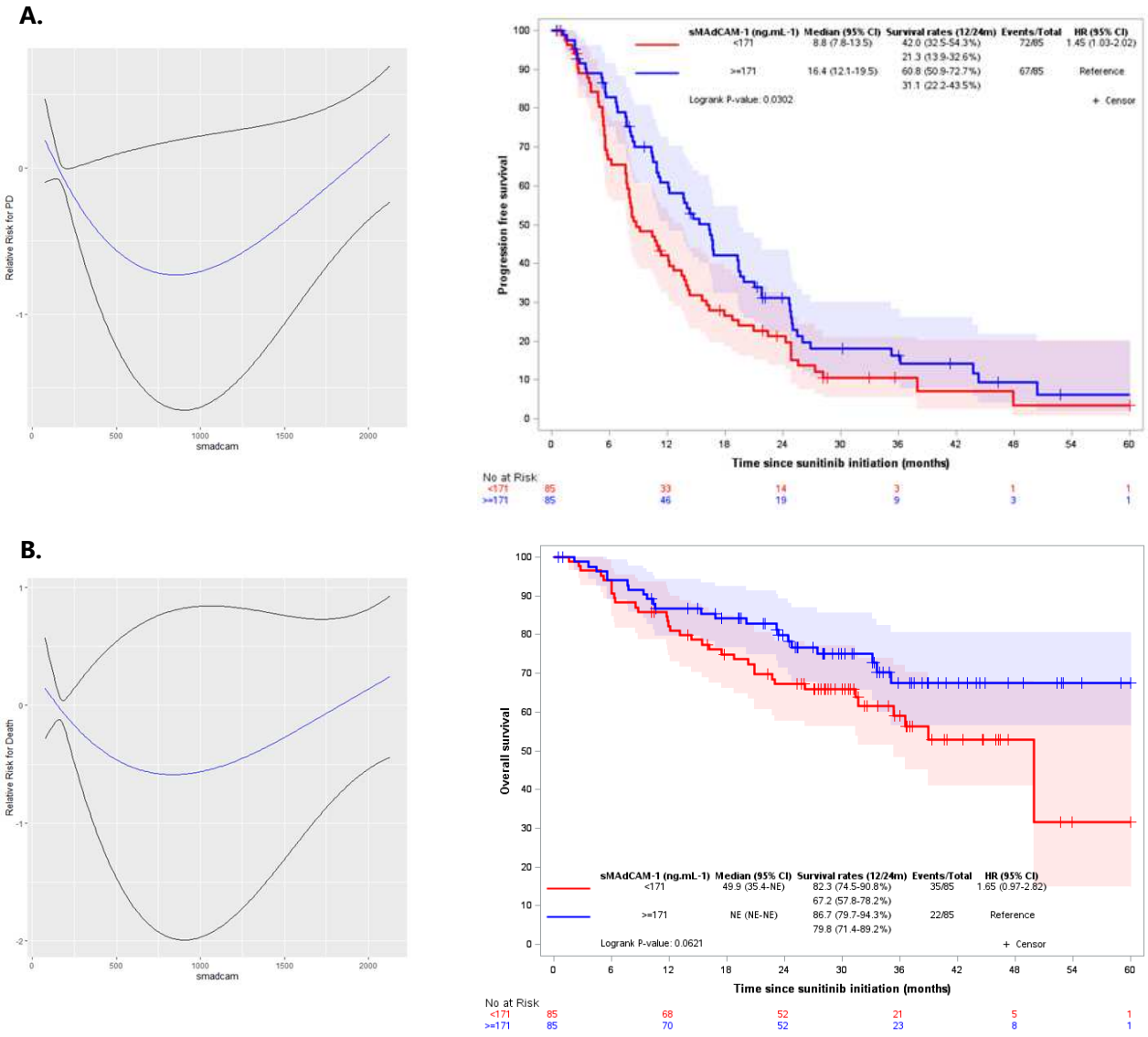

Figure 16 Soluble MAdCAM-1 (sMAdCAM-1) is a prognostic biomarker in patients with advanced renal cell carcinoma. **A-B.** Restricted Cubic Splines method was used to modelize the association between sMADCAM in its continuous form with OS and PFS (left). RCS modelization was used to determine the optimal cut-off. Kaplan–Meier survival curves for progression-free survival (A right) and overall survival (B right).

8.3 HUMORAL RESPONSE AGAINST COMMENSALS

8.3.1 Article V

Title: Escherichia coli–Specific CXCL13-Producing Tfh Are Associated with Clinical Efficacy of Neoadjuvant PD-1 Blockade against Muscle-Invasive Bladder Cancer.

Published on: Cancer Discov (2022) 12 (10): 2280–2307.
https://doi.org/10.1158/2159-8290.CD-22-0201

Anne-Gaëlle Goubet, Leonardo Lordello #, **Carolina Alves Costa Silva** #, Isabelle Peguillet, Marianne Gazzano, Maxime Descartes Mbogning-Fonkou, Cassandra Thelemaque, Cédric Lebacle, Constance Thibault, François Audenet, Géraldine Pignot, Gwenaelle Gravis, Carole Helissey, Luca Campedel, Morgan Roupret, Evanguelos Xylinas, Idir Ouzaid, Agathe Dubuisson, Marine Mazzenga, Caroline Flament, Pierre Ly, Virginie Marty, Nicolas Signolle, Allan Sauvat, Thomas Sbarrato, Mounia Filahi, Caroline Davin, Gabriel Haddad, Jacques Bou Khalil, Camille Bleriot, François-Xavier Danlos, Garett Dunsmore, Kevin Mulder, Aymeric Silvin, Thibault Raoult, Baptiste Archambaud, Shaima Belhechmi, Ivo Gomperts Boneca, Nadège Cayet, Maryse Moya-Nilges, Adeline Mallet, Romain Daillere, Etienne Rouleau, Camelia Radulescu, Yves Allory, Jacques Fieschi, Mathieu Rouanne, Florent Ginhoux, Gwénaël Le Teuff, Lisa Derosa, Aurélien Marabelle, Jeroen Van Dorp, Nick Van Dijk, Michiel S Van Der Heijden, Benjamin Besse, Fabrice Andre, Miriam Merad, Guido Kroemer, Jean-Yves Scoazec, Laurence Zitvogel#, Yohann Loriot#
# contributed equally

ICB have emerged as a promising strategy for patients with bladder cancer, either in metastatic or neoadjuvant settings. In our study, baseline Tfh and post-ICB TLS and activated B cells were associated with improved outcomes. The increase of CXCL13 after 1 cycle of ICB correlated with better outcomes. Uropathogenic *E. coli* was present in tumor and immune cells. Interestingly, release of CXCL13 but not IFNγ in responders after exposure to exogenous *E. coli* (Fig. 17A). Furthermore, exposure of fresh muscle-invasive bladder cancer tissue dissociated right after cystectomy to an exogenous *E. coli* triggered the activation of antibody secreting cells and intratumoral Tfh culminating in the release of CXCL13 and CCL19, TLS- prototypic chemokines (Fig. 17B). Serum IgG directed against urothelium invasive *E. coli* (but not any other urinary commensal) were associated with favorable clinical responses in three independent cohorts of patients with bladder cancer treated with ICB (Fig. 17C).

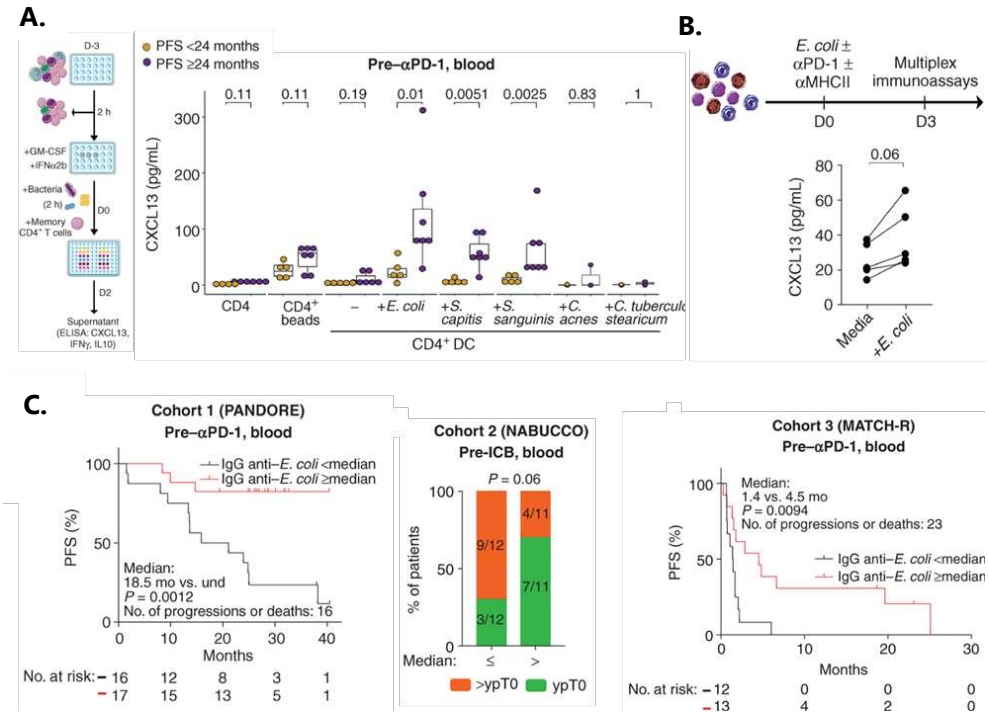

Figure 17 Humoral response against uropathogenic commensal predict response to neoadjuvant immune checkpoint blockade (ICB) in bladder cancer (BC). **A.** Experimental setting of the CD4+ T-cell recall responses against bacteria (left). CXCL13 secretion levels after cocultures of CD4+ T cells isolated before ICB (right) and autologous monocyte-derived dendritic cells (DC) loaded with bacteria for 2 days. Patients with relapse and/or death < 24 months (gold) and without (purple) are shown (left). Unpaired t test (Mann–Whitney U test). **B.** Setting of the "*in sitro*" test with heat-killed bacteria (top). Multiplex immunoassays monitoring of CXCL13 TLS-specific chemokines in *in sitro* stimulation of freshly dissociated BC tissue with *E. coli*. Different culture conditions are annotated as well as the neutralization of MHC class II complexes with specific antibodies. Medians of duplicate–triplicate wells are shown for CXCL13 (each dot, one sample). Paired t test. **C.** Progression-free survival (PFS) Kaplan–Meier curves of ICB-treated patients according to IgG against *E. coli* at baseline. Log-rank tests. Und, undefined. Cohort 1 (left, PANDORE) and Cohort 3 (right, MATCH-R). Percentages of pathological complete response after neoadjuvant ICB in patients with BC from the Cohort 2 (NABUCCO trial) according to IgG against *E. coli* at baseline (middle). IgG titers' median as cutoff value for each cohort.

RESEARCH ARTICLE

Escherichia coli–Specific CXCL13-Producing T_{FH} Are Associated with Clinical Efficacy of Neoadjuvant PD-1 Blockade against Muscle-Invasive Bladder Cancer

Anne-Gaëlle Goubet[1,2,3], Leonardo Lordello[1,3], Carolina Alves Costa Silva[1,2,3,4], Isabelle Peguillet[1,3], Marianne Gazzano[1,3,5], Maxime Descartes Mbogning-Fonkou[1,3], Cassandra Thelemaque[1,3], Cédric Lebacle[6], Constance Thibault[7], François Audenet[8], Géraldine Pignot[9], Gwenaelle Gravis[10], Carole Helissey[11], Luca Campedel[12], Morgan Roupret[13], Evanguelos Xylinas[14], Idir Ouzaid[14], Agathe Dubuisson[1,3], Marine Mazzenga[1,3], Caroline Flament[1,3], Pierre Ly[1,3], Virginie Marty[1,15], Nicolas Signolle[1,15], Allan Sauvat[1,16,17], Thomas Sbarrato[18], Mounia Filahi[18], Caroline Davin[18], Gabriel Haddad[19], Jacques Bou Khalil[19], Camille Bleriot[1,3], François-Xavier Danlos[1,2,3], Garett Dunsmore[1,2,3], Kevin Mulder[1,2,3], Aymeric Silvin[1,3], Thibault Raoult[1,20], Baptiste Archambaud[1,21], Shaima Belhechmi[1,21], Ivo Gomperts Boneca[22], Nadège Cayet[23], Maryse Moya-Nilges[23], Adeline Mallet[23], Romain Daillere[24], Etienne Rouleau[25], Camelia Radulescu[26], Yves Allory[26], Jacques Fieschi[18], Mathieu Rouanne[1,2,3,27], Florent Ginhoux[1,2,28,29], Gwénaël Le Teuff[1,21], Lisa Derosa[1,2,3], Aurélien Marabelle[1,2,3,4,30], Jeroen Van Dorp[31], Nick Van Dijk[32], Michiel S. Van Der Heijden[31,32], Benjamin Besse[1,2,30,33], Fabrice Andre[1,2,30,33,34], Miriam Merad[35,36,37,38,39], Guido Kroemer[1,16,17,40], Jean-Yves Scoazec[1,2,15,41], Laurence Zitvogel[1,2,3,4], and Yohann Loriot[1,2,30,33,34,42]

Illustration by Bianca Dunn

ABSTRACT Biomarkers guiding the neoadjuvant use of immune-checkpoint blockers (ICB) are needed for patients with localized muscle-invasive bladder cancers (MIBC). Profiling tumor and blood samples, we found that follicular helper CD4+ T cells (T_{FH}) are among the best therapeutic targets of pembrolizumab correlating with progression-free survival. T_{FH} were associated with tumoral CD8 and PD-L1 expression at baseline and the induction of tertiary lymphoid structures after pembrolizumab. Blood central memory T_{FH} accumulated in tumors where they produce CXCL13, a chemokine found in the plasma of responders only. IgG4+CD38+ T_{FH} residing in bladder tissues correlated with clinical benefit. Finally, T_{FH} and IgG directed against urothelium-invasive *Escherichia coli* dictated clinical responses to pembrolizumab in three independent cohorts. The links between tumor infection and success of ICB immunomodulation should be prospectively assessed at a larger scale.

SIGNIFICANCE: In patients with bladder cancer treated with neoadjuvant pembrolizumab, *E. coli*–specific CXCL13 producing T_{FH} and IgG constitute biomarkers that predict clinical benefit. Beyond its role as a biomarker, such immune responses against *E. coli* might be harnessed for future therapeutic strategies.

INTRODUCTION

Programmed cell death protein 1 (PD-1) is an immune-checkpoint protein expressed on T cells (1). PD-1 inhibits T-cell responses to cancer after binding to one of its ligands, programmed cell death ligand 1 (PD-L1, B7-H1, CD274) or PD-L2 (B7-DC, CD273; refs. 2, 3). Therapeutic blockade of PD-1 or PD-L1 with monoclonal antibodies (mAb) leads to durable tumor regression in patients with several cancer types (1, 4–6). These clinical observations have spurred the FDA approval of two anti–PD-1 antibodies, pembrolizumab (MK-3475) and nivolumab (BMS-936558), for the treatment of localized and metastatic cancers across numerous indications.

[1]Gustave Roussy, Villejuif, France. [2]Faculté de Médecine, Université Paris-Saclay, Kremlin-Bicêtre, France. [3]Institut National de la Santé Et de la Recherche Médicale (INSERM) U1015, Equipe Labellisée—Ligue Nationale contre le Cancer, Villejuif, France. [4]Center of Clinical Investigations for In Situ Biotherapies of Cancer (BIOTHERIS), INSERM CIC1428, Villejuif, France. [5]Sorbonne Université, Inserm, Centre d'Immunologie et des Maladies Infectieuses (CIMI-Paris), Département d'Immunologie, Assistance Publique Hôpitaux de Paris (AP-HP), Hôpital Pitié-Salpêtrière, Paris, France. [6]Urology Department, University Hospital of Bicêtre-Paris Sud-Saclay University, Le Kremlin Bicêtre, Paris, France. [7]Oncology Department, Hôpital Européen Georges Pompidou, AP-HP, University of Paris, Paris, France. [8]Department of Urology, Hôpital Européen Georges Pompidou, AP-HP Centre, Université de Paris, Paris, France. [9]Department of Surgical Oncology 2, Institut Paoli-Calmettes Cancer Center, Marseille, France. [10]Department of Medical Oncology, Institut Paoli-Calmettes, Aix-Marseille University, CRCM, Marseille, France. [11]Military Hospital Begin, Saint-Mandé, France. [12]Sorbonne Université, AP-HP, Hôpital de La Pitié-Salpêtrière, Institut Universitaire de Cancérologie, Département d'Oncologie Médicale, CLIP2 Galilée, Paris, France. [13]GRC 5 Predictive Onco-Uro, Sorbonne University, Department of Urology, AP-HP, Pitie-Salpetriere Hospital, Paris, France. [14]Department of Urology, Bichat-Claude Bernard Hospital, Paris University, Paris France. [15]Experimental and Translational Pathology Platform (PETRA), AMMICa, INSERM US23/UAR3655, Gustave Roussy, Villejuif, France. [16]Equipe 11 Labellisée par la Ligue Nationale contre le Cancer, Centre de Recherche des Cordeliers, Institut National de la Santé et de la Recherche Médicale U1138, Université de Paris, Sorbonne Université, Paris, France. [17]Metabolomics and Cell Biology Platforms, Gustave Roussy, Villejuif, France. [18]Veracyte, Marseille, France. [19]Aix-Marseille University, IRD, APHM, MEPHI, Institut Hospitalo-Universitaire Méditerranée Infection, Marseille, France. [20]Service de Promotion des Etudes Cliniques (SPEC), Gustave Roussy, Université Paris-Saclay, Villejuif, France. [21]Service de Biostatistiques et d'Epidemiologie, Gustave Roussy, Villejuif, France. [22]Institut Pasteur, Université de Paris, CNRS UMR2001, INSERM U1306, Unité de Biologie et Génétique de la Paroi Bactérienne, Paris, France. [23]Core Facility Ultrastructural BioImaging Core Facility, Institut Pasteur, Paris France. [24]EverImmune, Gustave Roussy, Villejuif, France. [25]Department of Medical Biology and Pathology, Cancer Genetics Laboratory, Gustave Roussy, Villejuif, France. [26]Department of Pathology, Hôpital Foch, UVSQ-Université Paris-Saclay, Suresnes, France. [27]Department of Urology, Hôpital Foch, UVSQ-Université Paris-Saclay, Suresnes, France. [28]Singapore Immunology Network (SIgN), A*STAR, Singapore, Singapore. [29]Shanghai Institute of Immunology, Shanghai Jiao Tong University School of Medicine, Shanghai, China. [30]Cancer Medicine Department, Gustave Roussy, Villejuif, France. [31]Department of Molecular Carcinogenesis, Netherlands Cancer Institute, Amsterdam, the Netherlands. [32]Department of Medical Oncology, Netherlands Cancer Institute, Amsterdam, the Netherlands. [33]INSERM U981, Biomarqueurs Prédictifs et Nouvelles Stratégies Thérapeutiques en Oncologie, Villejuif, France. [34]PRISM Precision Cancer Center, Gustave Roussy, Villejuif, France. [35]The Precision Immunology Institute, Icahn School of Medicine at Mount Sinai, New York, New York. [36]Human Immune Monitoring Center, Icahn School of Medicine at Mount Sinai, New York, New York. [37]The Tisch Cancer Institute, Icahn School of Medicine at Mount Sinai, New York, New York. [38]Department of Oncological Sciences, Icahn School of Medicine at Mount Sinai, New York, New York. [39]Institute for Thoracic Oncology, Icahn School of Medicine at Mount Sinai, New York, New York. [40]Pôle de Biologie, Hôpital Européen Georges Pompidou, AP-HP, Paris, France. [41]Department of Medical Biology and Pathology, Gustave Roussy, Villejuif, France. [42]Early Drug Development Department (DITEP), Gustave Roussy, Villejuif, France.

Note: L. Lordello and C. Alves Costa Silva contributed equally to this article.

L. Zitvogel and Y. Loriot are the co-last authors of this article.

Current address for M. Rouanne: Department of Microbiology and Immunology, Vagelos College of Physicians and Surgeons, Columbia University, New York, New York.

Corresponding Author: Laurence Zitvogel, Clinicobiome, Institut Gustave Roussy, 114 rue Edouard Vaillant, Villejuif 94805, France. Phone: 331-4211-5041; Fax: 331-4211-6094; E-mail: Laurence.zitvogel@gustaveroussy.fr

Cancer Discov 2022;12:2280–307

doi: 10.1158/2159-8290.CD-22-0201

Pembrolizumab targets epitopes on the PD-1 molecule with high affinity and specificity. This mAb is of the IgG4 subclass and hence has low affinity for C1q and Fc receptors (7). Pharmacokinetic studies based on flow-cytometric methods (8) indicated a dose-independent high receptor occupancy at the peak and a plateau reached at 60 days (8). Preclinical studies in immunodeficient NOD/SCID/γ_c^{null} mice transplanted with human CD34$^+$ hematopoietic stem cells and inoculated with partially histocompatible patient-derived xenografts unveiled that pembrolizumab stimulated anticancer T-cell responses (9). Following PD-1 blockade, both CD4$^+$ and CD8$^+$ T cells expanded in blood, but CD8$^+$ T cells were mandatory for the antitumor efficacy of pembrolizumab and migrated from tumor margins to nests (9). In patients, pembrolizumab promotes minor changes in blood while mobilizing not only T cells but also B cells and suppressive monocytes in tumors (10). However, expansion of effector memory CD8$^+$ tumor-infiltrating lymphocytes (TIL) has been recognized as the best pharmacodynamic hallmark of bioactivity of these therapeutic mAbs against melanoma (10).

Urothelial carcinoma (UC) is a highly prevalent malignancy that remains difficult to treat in the case of muscle-invasive tumors (11). Nonmetastatic muscle-invasive bladder cancers (MIBC) are mainly treated with cisplatin-based neoadjuvant chemotherapy followed by radical cystectomy and harbor a poor prognosis, with a 5-year survival of 60% (12). However, a significant subset of patients are ineligible for neoadjuvant cisplatin-based chemotherapy. Since 2017, immune-checkpoint blockers (ICB), such as anti–PD-1/PD-L1 antibodies, have emerged as a successful immunotherapeutic strategy for advanced UC (13–18). Driven by the promising results in advanced diseases, ICB indications have been considered for the treatment of lower stage bladder tumors, including non-MIBC and nonmetastatic MIBC (NCT02844816, NCT02901548, and NCT02792192; refs. 19, 20). To our knowledge, four neoadjuvant trials investigating either anti–PD-1/PD-L1 monotherapy or the combination of anti–CTLA-4 and anti–PD-1/PD-L1 mAbs before cystectomy have been reported for cisplatin-ineligible patients or patients who declined neoadjuvant chemotherapy (21–24). Pathologic complete response (pCR), defined as the absence of tumor cells (ypT0N0; ref. 25), was observed in 31% to 46% of patients. Substantial toxicity (≥grade 3 immune-related adverse events) was reported in 11% and from 21% to 55% of patients treated with anti–PD-1/PD-L1 or combined ICB, respectively. Therefore, there is a need for biomarker discovery to increase the therapeutic index of neoadjuvant immunotherapy in MIBC.

In past trials revealing the efficacy of neoadjuvant ICBs in UC, immune or tumor expression of PD-L1 and tumor mutational burden (TMB) did not represent reliable baseline predictors of clinical benefit (21–24). In fact, responding tumors showed a predominant expression of genes related to tissue repair, whereas resistance was associated with stromal or cell-cycle fingerprints after neoadjuvant PD-L1 mAbs (23). This study also identified preexisting intraepithelial CD8$^+$ T cells and a pro-Th1 signature as predictive biomarkers of pCR to PD-1/PD-L1 blockade. In accordance with previously described biomarkers in melanoma and sarcoma (26–28), tertiary lymphoid structures (TLS) represented the best predictors of clinical responses to neoadjuvant PD-1/PD-L1 plus CTLA-4 blockade in high-grade MIBC (21, 24). Indeed, TLS identified by IHC were associated with a transcriptome blueprint centered around *CD79A*, *LAMP3*, *MS4A1*, and *POU2AF1* predicting pathologic responses (21). In parallel, mutation of *ARID1A* in tumor cells and expression of CXCL13 in tumor tissues at baseline may act as predictors of clinical response for patients receiving ICBs (29). However, these reports did not identify blood immune proxies associated with the local induction of TLS in the bladder (21, 24).

Follicular helper T cells (T_{FH}), a specialized subset of CD4$^+$ effector T (TE) cells involved in germinal center reactions and affinity maturation of B cells, are known to orchestrate TLS formation. In a chronic viral infection, T_{FH} were shown to be mandatory to sustain virus-specific cytotoxic CD8$^+$ T-cell (CTL) immune responses through IL21 production (30). During chronic inflammatory processes of carcinogenesis, the links between T_{FH} and CTL responses have only recently been discussed with the growing awareness of the clinical relevance of TLS (31, 32). For instance, in colon cancers, microbiota-specific T_{FH} responses were indispensable for TLS formation and tumor control in the absence of CTL effectors (33). In contrast, in rodent and human breast cancers, a functional T_{FH} response orchestrated in TILs within active TLS has been associated with cytotoxic CTL responses that governed their prognosis (34). Hence, by bridging the two arms of the adaptive immune system (B cells and CD8$^+$ T cells) within TLS, T_{FH} indirectly contribute to exert an immune pressure against tumor progression in human and rodent ovarian cancers (35, 36).

When investigating the PANDORE single-arm, phase II trial (NCT03212651), which enrolled patients with MIBC treated with neoadjuvant pembrolizumab, we obtained evidence that T_{FH} stand among the main therapeutic targets of neoadjuvant pembrolizumab, both in blood and in the bladder. Baseline blood memory T_{FH} together with B cells became activated by pembrolizumab, facilitating the orchestration of tertiary lymphoid–like (TLS-like) structures and CD8$^+$ TIL accumulation, translating into clinical benefit. Importantly, antibodies (IgG) and CXCL13 producing CD4$^+$ T-cell memory responses against *Escherichia coli* (and not other urinary commensals) emerged as robust biomarkers of clinical benefit.

RESULTS

Clinical Efficacy of Pembrolizumab in the PANDORE Study

Between October 2017 and May 2019, we enrolled 44 cisplatin-ineligible patients with localized MIBC in the PANDORE trial (NCT03212651), but only 39 patients were included in the final analysis (Supplementary Fig. S1A and S1B). Among these patients, 25 (64%) met cisplatin ineligibility and 14 (36%) declined chemotherapy. Following baseline transurethral resection of bladder tumor (TURBT), 39 patients were then treated with pembrolizumab (200 mg) every 3 weeks for a total of three cycles before radical cystectomy (Supplementary Fig. S1B). Clinical and tumor characteristics are summarized in Supplementary Table S1 and Fig. 1. All tumors were UC. Briefly, most patients were men (74.4%), with a median age of 72 years [interquartile range (IQR): 67–78] and presented a clinical-stage cT2 (82.1%) and cN0 (89.7%). Nearly

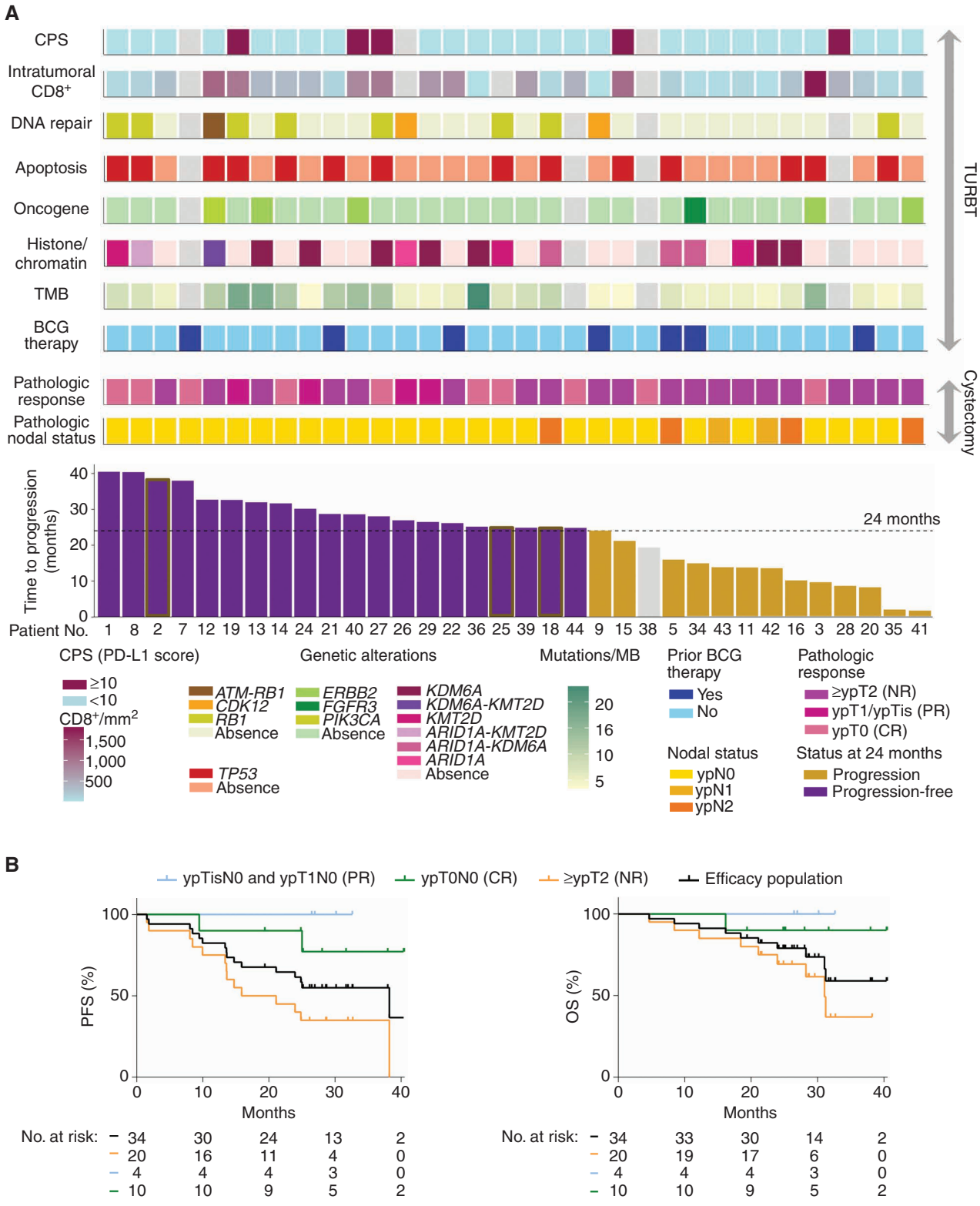

Figure 1. PANDORE patient characteristics and survival after neoadjuvant pembrolizumab. **A,** Clinical, biological, and pathologic characteristics of MIBC-bearing patients. Prior Bacillus Calmette-Guérin (BCG) therapy, PD-L1 combined positive score (CPS; clone: 22C3), intratumoral CD8 (CD8 clone, Veracyte), TMB, and genetic alterations in oncogenes and tumor suppressor genes, in the apoptotic machinery, or in the DNA repair pathway are detailed for each individual, with a color code aligned at the bottom. Time to progression, with a dotted line for the cutoff value (24 months), used throughout the article is indicated. Missing values are shown in gray. CR, complete response; MB, megabase; NR, no response; PR, partial response. **B,** Kaplan–Meier survival curves for PFS (left) and OS (right) in the efficacy population (black) and according to the pathologic response (NR, orange; PR, light blue; and CR, green).

all patients (n = 37/39) received the planned three cycles of pembrolizumab. Patient #11 did not receive the last cycle due to grade 2 keratitis and patient #43 did not receive cycle 2 due to worsening adrenal insufficiency and fatigue. Sixty-two percent of individuals experienced a pembrolizumab-related adverse event, mostly grade 1 (Supplementary Table S2). No deaths related to therapy occurred. The median interval between the first infusion and radical cystectomy was 60 days (IQR: 55–63). Out of 39 patients, 34 proceeded with radical cystectomy (efficacy population; Supplementary Fig. S1A and S1C). The median time between the last cycle and radical cystectomy was 16 days (IQR: 13–21).

Radical cystectomy by open surgery was performed in 12 patients (35%). Postsurgical complications are detailed in Methods and were similar to those reported in other published studies (37, 38). The primary endpoint was pCR, defined as the absence of cancer cells in the bladder and the absence of microscopic lymph node metastases in the cystectomy specimen (ypT0N0). The overall pCR rate was 29.4% [95% confidence interval (CI): 15.1–47.5], and the overall downstaging [i.e., ypT0N0, ypTisN0, ypTaN0, and ypT1N0 and referred to as major pathologic response (MPR); ref. 25] was 41.2% (95% CI: 24.6–59.3; Fig. 1A).

The median follow-up in the efficacy population (n = 34) was 28.7 months (min: 19.4; max: 40.5) at data cutoff. A relapse or a death occurred in 16 patients (Fig. 1B; Supplementary Fig. S1C). The median progression-free survival (PFS) was 38.2 months (95% CI: 15.9–not reached; Fig. 1B, left). With 10 deaths among all 34 patients, overall survival (OS) was 94.1% at 1 year and 78.9% at 2 years. Median OS was not reached (95% CI: 31–not reached; Fig. 1B, right). Somatic DNA sequencing concerned the 450 genes of the Cancer Core Europe panel (39). The most recurrent causal variants are shown in Fig. 1A. The co-occurrence of causal variants *RB1* and *TP53* (observed in n = 8/30 MIBC) was associated with pCR and MPR (P = 0.0042 and P = 0.031, respectively, Fisher exact test) but not with PFS (P = 0.16, log-rank test). As reported earlier (22), high TMB was associated with prolonged PFS (Fig. 1A; Supplementary Fig. S2A).

Hence, the PANDORE study corroborated the efficacy of neoadjuvant ICBs in cisplatin-ineligible MIBC, as previously reported (21–24), with 29.4% and 60.6% of patients who exhibited a pCR and who did not relapse at 2 years after TURBT, respectively. The efficacy population (n = 34 patients; Supplementary Fig. S1A) was analyzed henceforth for biomarker discovery according to PFS with a cutoff value of 24 months (n = 13 with relapse and/or death occurring before 24 months and n = 20 censored at 24 months, excluding one patient whose follow-up did not reach 24 months), as most relapses occur within the first 24 months in trials investigating chemotherapy and ICB (19, 40).

Baseline T_{FH} Are Associated with Clinical Benefit to Neoadjuvant Pembrolizumab

To determine which immune parameter best predicts clinical benefit (MPR and PFS), we performed an exploratory biomarker analysis. We analyzed PD-L1 expression and TILs in tumors obtained through TURBT (pre-pembrolizumab) and on cystectomy (post-pembrolizumab; Supplementary Fig. S2B–S2F). First, we performed IHC staining using anti–PD-L1, anti-CD3, and anti-CD8 antibodies in matched pre- and posttreatment specimens in 34 patients. PD-L1 expression was analyzed in immune and tumor cells using the combined positive score (CPS; clone: PD-L1 22C3; Fig. 1A; Supplementary Fig. S2B) on TURBT samples. Only five patients harbored a CPS ≥10 (16%), and CPS was associated with neither pCR (P = 0.68, χ^2 test) nor MPR (P = 0.82, χ^2 test). CPS failed to predict either PFS or OS (Supplementary Fig. S2B). Density and geodistribution of $CD3^+$ and $CD8^+$ cells, as well as clustering and proximity of $PD\text{-}L1^+$ and $CD8^+$ cells (Immunoscore IC), were evaluated (Fig. 2; Supplementary Fig. S2C and S2D). The density of $CD8^+$ cells, pre- and post-pembrolizumab, was associated with PFS (Supplementary Fig. S2E and S2F, left). After PD-1 blockade, the proximity between $CD8^+$ T and $PD\text{-}L1^+$ cells was associated with prolonged PFS (Supplementary Fig. S2F, right). TLS-like were identified by microscopic morphology in hematoxylin–eosin–safran (HES)–stained tissues in association with CD20 and CD4, CD38, and PD-1 immunolabeling and classified as lymphoid aggregates (LA), resting follicles (RF), and germinal centers (GC). LA were determined as vaguely nodular aggregates of small noncleaved lymphoid cells, usually with more than 250 and fewer than 500 cells, without two or more of the early germinal center elements (follicular dendritic cells, centroblasts, mantle zone, or high endothelial veins); primary follicle–like TLS (RF) were determined as nodular aggregates of predominantly small lymphoid cells, usually with more than 500 cells, with three or more of the follicular elements, but without late germinal center elements (tinged body macrophages or dark/light areas of a clear germinal center, marginal zone); and secondary follicle–like TLS (GC) were determined as lymphoid follicles showing late germinal center structures.

Spearman correlation matrices establishing interconnections between all these pathologic factors are shown in Fig. 2A and B. Thus, the density of $CD4^+PD\text{-}1^+$ cells correlated with the density of $CD8^+$ cells at baseline (Fig. 2A and B, left), and pembrolizumab triggered a coordinated association between the densities of TLS-like (and/or GC, RF, LA) and $CD8^+$ cells (Fig. 2A and B, right). Moreover, the latter coincided with densities of $CD4^+PD\text{-}1^+$ (P = 0.0022 and R = 0.66, Spearman correlation) and anticorrelated with MPR (P = 0.017 and R = –0.53, Spearman correlation; Fig. 2A, right). Finally, although baseline density of TLS-like did not predict PFS (P = 0.24, log-rank test), pembrolizumab-induced TLS-like were associated with PFS (P = 0.01, log-rank test; Fig. 2C).

To investigate the coordination between tumoral TLS-like and CD8 infiltrates with blood immune profiles induced by PD-1 blockade, we performed cytometry by time-of-flight (CyTOF) on paired blood cells before, during, and after (cystectomy) three cycles of pembrolizumab in 38 patients. As mentioned above, the efficacy assessment was available for 34 of 38 patients. One hundred and fifty-three samples were barcoded (one barcode for one time point per patient) and stained with a 38-parameter antibody panel for high-dimensional characterization of the CD4 cell, CD8 cell, and B-cell heterogeneity based on canonical markers of polarization, differentiation, and activation/exhaustion (Supplementary Table S1; Supplementary Fig. S1A and S1B). Using the PhenoGraph algorithm, we analyzed the clinical significance

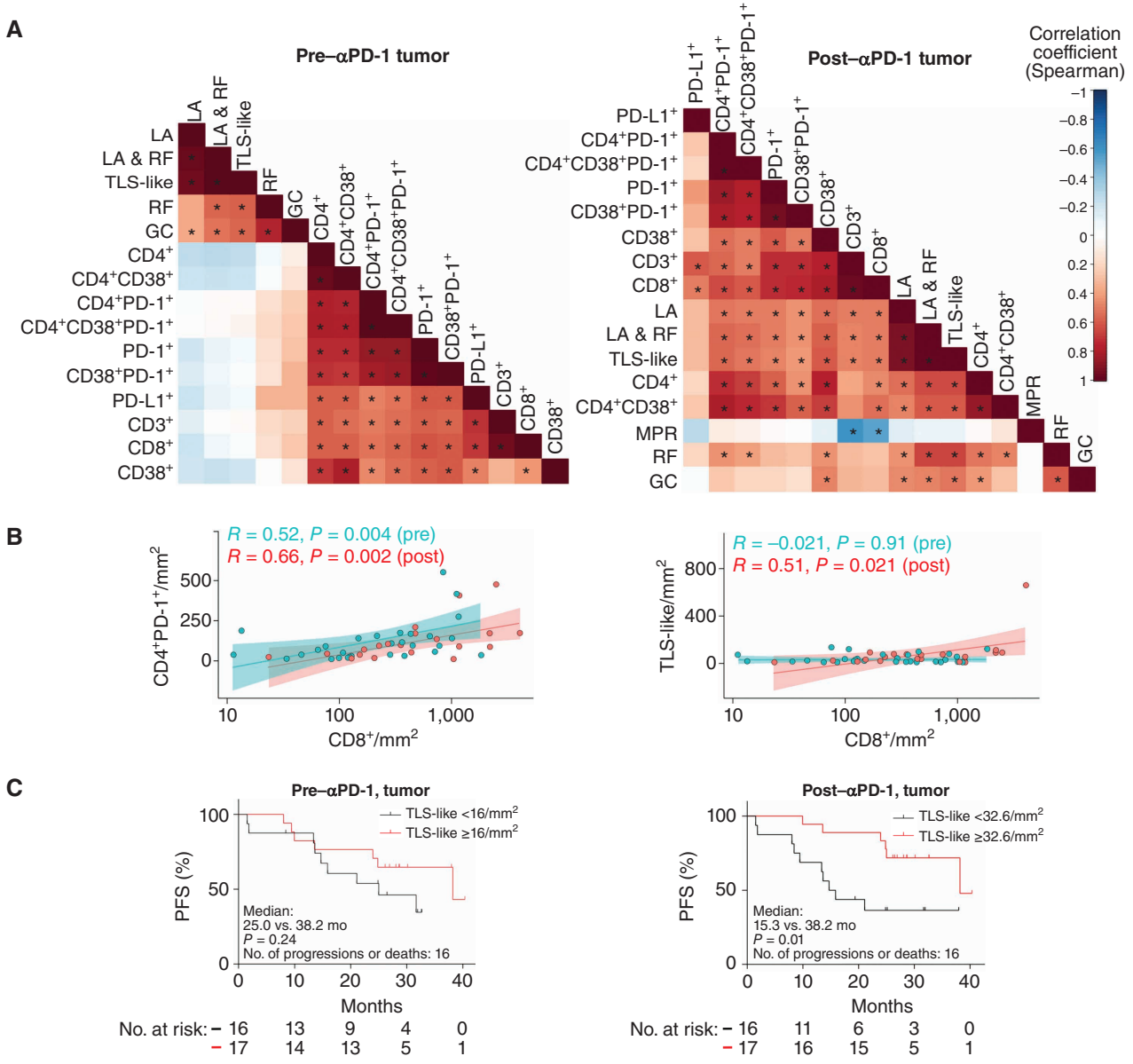

Figure 2. Blood T_{FH} and antibody-secreting cells (ASC) are associated with PFS in PANDORE patients. **A,** Spearman correlation matrices between histopathologic features before (left) and after (right) pembrolizumab in bladder samples. Significant correlations are indicated with a star. TLS-like corresponds to the sum of the densities of each submentioned structure. **B**, Detailed results for the correlations between the densities of $CD8^+$ and $CD4^+PD\text{-}1^+$ TILs (left) or TLS-like (right) at baseline (blue) and after treatment (pink). Each dot represents one patient, and *R* and *P* values are indicated. **C,** Kaplan–Meier curves of PFS according to the density of TLS-like using medians as cutoff values, at baseline (left, median = 16/mm²) and after treatment (right, median = 32.6/mm²). Statistical analyses used the log-rank test. (*continued on next page*)

of different $CD4^+$ T helper (TH) and regulatory T (Treg) subpopulations based on the relative expression of PD-1 and effector/memory markers for the response to pembrolizumab (ref. 41; Supplementary Fig. S3A and S3B). The unsupervised PhenoGraph analysis of the PD-1–expressing clusters revealed that cluster 9 defined as $CD4^+PD\text{-}1^+CD45RA^-CD28^+CD27^+CD127^+$, which are central memory T cells (TCM), and cluster 13 defined as $CD4^+PD\text{-}1^+CD45RA^-CD28^+CD27^+CD127^{low/-}$ cells, which are effector memory T cells (TEM), were the only circulating TH cells associated with PFS at baseline (cluster 9, TCM) and after pembrolizumab (cluster 13, TEM; Supplementary Fig. S3C and S3D). Focusing on specific fingerprints, we found that cluster 9 was selectively enriched for the canonical marker of T_{FH} (19% expressing CXCR5), whereas cluster 13 cells expressed the activation marker CD38 (46% $CD38^+$, 9% $CXCR5^+$; Supplementary Fig. S3B), suggesting that pembrolizumab may preferentially target and activate T_{FH}. Hence, we performed a more biased analysis, applying a manual gating to investigate the clinical significance for PFS of all blood $CD4^+$ TH and B cells, before and after pembrolizumab (Fig. 2D–G; Supplementary Fig. S2G and S2H). Central memory T_{FH} ($CD4^+CXCR5^+PD\text{-}1^+$TCM) and

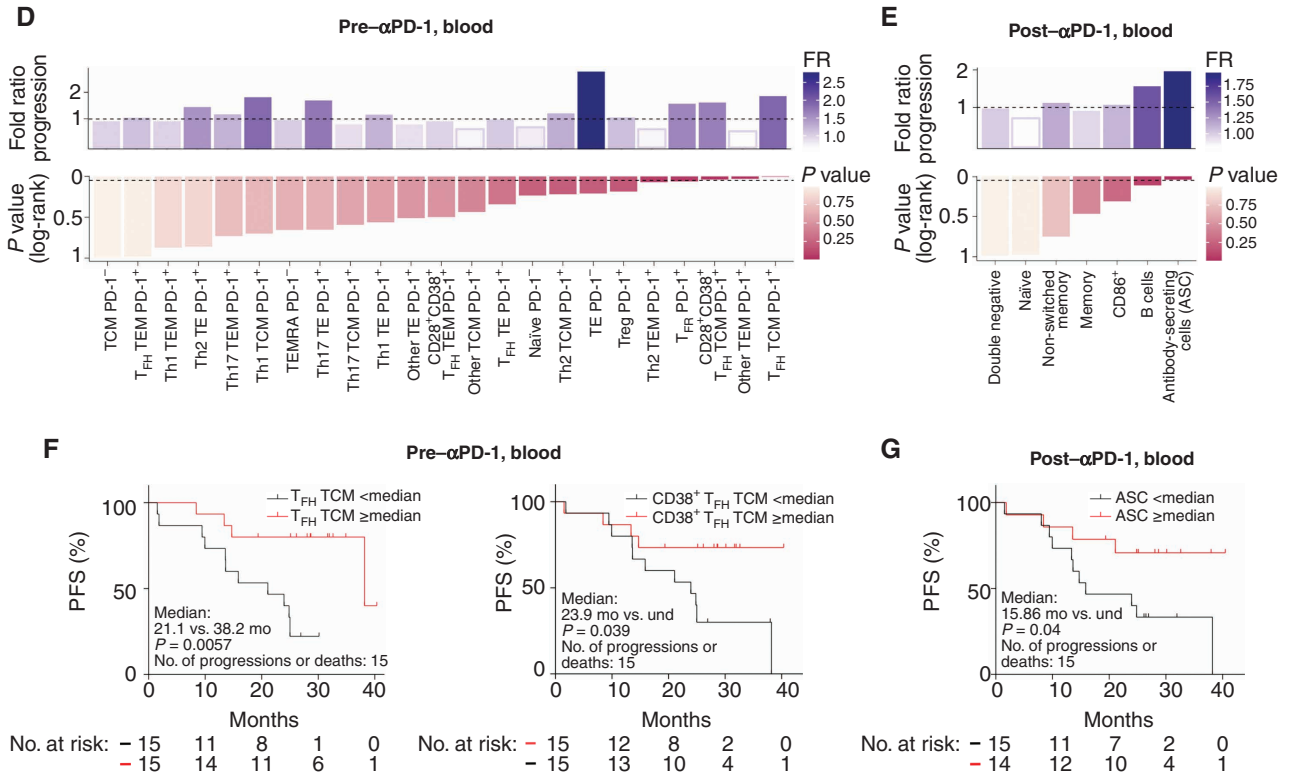

Figure 2. ***(Continued)*** **D** and **E,** Fold ratios (FR) between median values of each PD-1$^+$ T-cell subset (**D**) or B cells (**E**) between nonprogressors versus progressors (top) and *P* values of log-rank tests (bottom) at baseline (**D**; also refer to Supplementary Fig. S2H) or after three cycles of pembrolizumab (**E**; also refer to Supplementary Fig. S2G) assessing the contribution of each CD4$^+$ T-cell subset (**D**) or B cells (**E**) to PFS. CD4$^+$ T-cell subsets were evaluated using mass cytometry ($n = 30$ samples) and a clustering method (PhenoGraph) followed by manual annotation and manual gating (refer to Supplementary Fig. S1A). B-cell subsets were evaluated using mass cytometry ($n = 29$ samples) followed by manual gating (refer to Supplementary Fig. S1B). TEMRA, effector memory T cells reexpressing CD45RA. **F** and **G,** Kaplan–Meier curves of PFS according to circulating T_{FH} TCM (left, median = 3.06%) and CD38$^+$ T_{FH} TCM (right, median = 0.43%) in CD4$^+$ T cells at baseline (**F**) or circulating ASCs (median = 0.05%) in CD45$^+$ cells after three cycles of pembrolizumab (**G**), with medians as cutoff values. Statistical analysis used the log-rank test. und, undefined.

their activated fraction (CD38$^+$CD28$^+$CD4$^+$CXCR5$^+$PD-1$^+$TCM) stood out as the most significant circulating TH cells predicting PFS at baseline (Fig. 2D and F; Supplementary Fig. S2G), whereas CD38^{hi}Blimp1$^+$CD19$^{+/lo}$ antibody-secreting cells (ASC) became associated with PFS only after pembrolizumab (Fig. 2E and G; Supplementary Fig. S2H).

Altogether, neoadjuvant pembrolizumab mostly benefited patients with MIBC who harbored preexisting T_{FH} TCM cells, which could orchestrate TLS-like formation and/or maturation as well as CD8$^+$ T-cell tumor infiltration.

T_{FH} Accumulated within TLS-like and Predicted Prolonged PFS

We next measured the spatial distribution of T_{FH} in tumor lesions using multiplex immunofluorescence staining with mAbs specific for CD20, CD4, CD38, and PD-1 (Fig. 3A). Because T_{FH} are known to reduce CXCR5 expression when they infiltrate the tumor tissue (42), we defined T_{FH}-like cells as CD4$^+$ T cells coexpressing CD38$^+$ and PD-1. We found that the accumulation of T_{FH}-like triple-positive cells in the vicinity of TLS-like at baseline strongly correlated with PFS at 24 months (Fig. 3B; refer to Methods and Supplementary Fig. S2A–S2L). As shown with circulating T_{FH} TCM, the baseline density of intra-TLS T_{FH}-like triple-positive cells was associated with prolonged PFS (Fig. 3C). We corroborated this accumulation using a CD4:Bcl6 costaining and did not observe differences between before and after treatment (Fig. 3D). Moreover, the density of such T_{FH}-like cells within the tissue correlated with TLS-like formation before but not after pembrolizumab (Fig. 3E, bottom vs. top). To further characterize T_{FH}-like cells within the tumor immune atlas after pembrolizumab, we performed CyTOF on 11 available tumors after cystectomy (Supplementary Table S3). As observed in blood, the CD38^{hi}CD28$^+$ subset of nonregulatory PD-1$^+$CD4$^+$ T cells best predicted PFS among all the TIL subsets (Supplementary Fig. S4A and S4B and gating strategy in Supplementary Fig. S3) and correlated with B lymphocytes (Supplementary Fig. S4C).

In addition, we performed single-cell RNA sequencing (RNA-seq) of blood CD45$^+$ cells and tissue leukocytes from two tumor-free bladders, harvested from surgical specimens of a patient with pCR and PFS ≥24 months (P#38) and one MIBC from a nonresponding patient with progressive disease (P#02; Supplementary Table S4). The unsupervised clustering of cell heterogeneity identified one cluster (cluster 2) enriched in CD4$^+$ TILs (Fig. 3F; Supplementary Fig. S5A–S5C). The CD38-, CD28-, and PD-1–specific oligo-conjugated antibodies allowed us to measure the expression of the prototypical transcript of T_{FH} cells, *CXCL13*, only in the CD4$^+$ TIL fraction of the patient exhibiting a pCR (Fig. 3F, right).

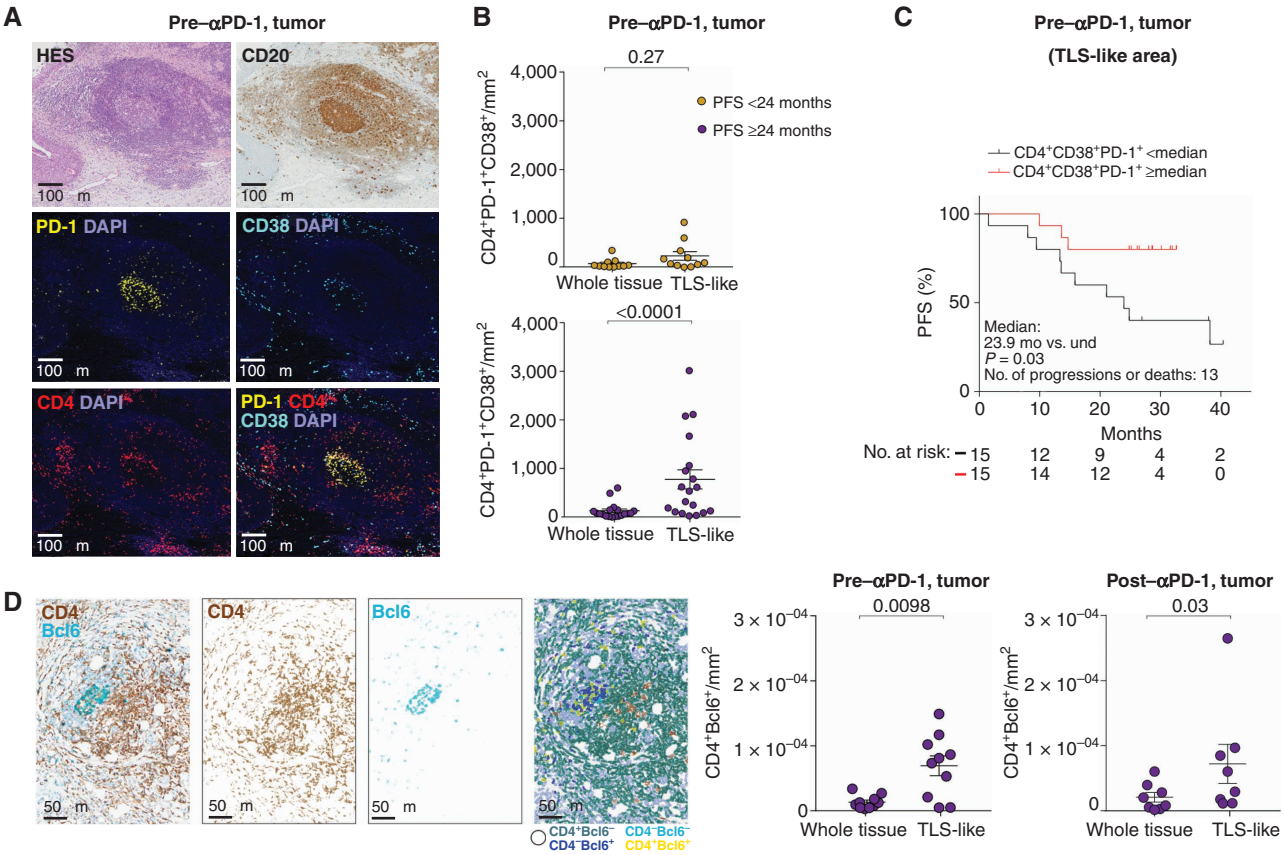

Figure 3. Tumoral T_{FH}-like CD4+ T cells are associated with TLS-like and predict PFS. **A,** Representative micrograph of a mature TLS on HES (top left), constituted by CD20+ cells evidenced by IHC (top right), and of single (middle and bottom left) and triple-positive CD4+CD38+PD-1+ analyzed by immunofluorescence stainings (bottom right) in a radical cystectomy specimen from a patient with PFS ≥24 months (P#39). **B,** Accumulation of CD4+CD38+PD-1+ in TLS-like compared with whole tissue before treatment (refer to Methods). Data are shown as mean ± SEM. Each dot represents one patient, and color indicates the PFS status at 24 months (purple: absence of relapse and/or death at 24 months, gold: relapse and/or death at 24 months). Statistical analysis used paired *t* tests (paired Wilcoxon test). **C,** Kaplan–Meier curve of PFS according to CD4+CD38+PD-1+ cells in TLS-like (median = 222/mm^2) at baseline in TURBT using medians as cutoff values. Statistical analyses used the log-rank test. und, undefined. **D,** Representative micrograph of TLS-like using CD4 and Bcl6 colabeling analyzed by IHC in a specimen pre-pembrolizumab (TURBT) from a patient with PFS ≥24 months (P#24; left). Left, original image for CD4:Bcl6 is shown (10×), followed by color deconvolution for CD4 and Bcl6 channels and a final image corresponding to cell detection done by QuPath based on color deconvolution. Accumulation of CD4+Bcl6+ in TLS-like compared with whole tissue before and after treatment (refer to Methods, "Evaluation of CD4+BCL6+ cells"). Data are shown as mean ± SEM. Each dot represents one patient without relapse and/or death at 24 months (right). Statistical analysis used paired *t* test (paired Wilcoxon test). (*continued on next page*)

To better dissect the T_{FH} phenotype, we set up new panels of multidimensional flow cytometry, including CXCR5, CXCL13, and Bcl6, in addition to CD38, PD-1, CD40L, and ICOS to comprehensively define the T_{FH}-like cells in seven freshly dissociated MIBCs at diagnosis. A representative flow-cytometric analysis and gating strategy are depicted in Supplementary Fig. S4. As outlined in Supplementary Table S5, the subset of conventional (Foxp3$^-$) CD4+ TILs (convCD4+ T cells) coexpressing PD-1 and CD38 is by and large the same as the PD-1+ICOS+ double-positive one [representing 17.5% ± 3.9 and 17.2% ± 3.0% (mean ± SEM) of convCD4+ TILs, respectively], comprising 27% to 73% of CXCL13+ and 64% to 76% CD40L+ cells (IQR; Supplementary Fig. S6A and S6B). The median fluorescence intensity (MFI) of Bcl6 increased gradually—from MFI = 112 for all convCD4+ T cells up to MFI = 149 for PD-1+CD38+ convCD4+ T cells (compared with MFI = 96 in the PD-1$^-$CD38$^-$ double-negative convCD4+ subset), culminating in an MFI = 155 for PD-1+ICOS+ convCD4+ TILs (mean values; Supplementary Fig. S6A and S6B; Supplementary Table S5). In addition, CXCR5 and CXCL13 expressions appeared mutually exclusive, suggesting endocytosis of the receptor upon CXCL13 binding and engagement with CXCR5 (Supplementary Fig. S6C).

Finally, to determine which TH cell–related soluble hallmark could be induced by pembrolizumab, we monitored the dynamic circulating levels of 40 soluble immune and nonimmune factors by bead-based multiplex assay prior to, during, and after pembrolizumab in 38 patients. We found that CXCL13 stood out as the most significant chemokine systemically released in blood after the first cycle, and this early rise was associated with the absence of progression at 24 months, as opposed to other Th1 markers (such as CXCL9) that tended to increase in all patients (Fig. 3G and H; Supplementary Fig. S5D, left). Of note, CCL19, a homeostatic chemokine involved in the architectural organization of TLS (43, 44), accompanied the rise of CXCL13 and was associated with prolonged PFS (Supplementary Fig. S5D, right; Supplementary Fig. S5E, left), whereas CXCL8 predicted

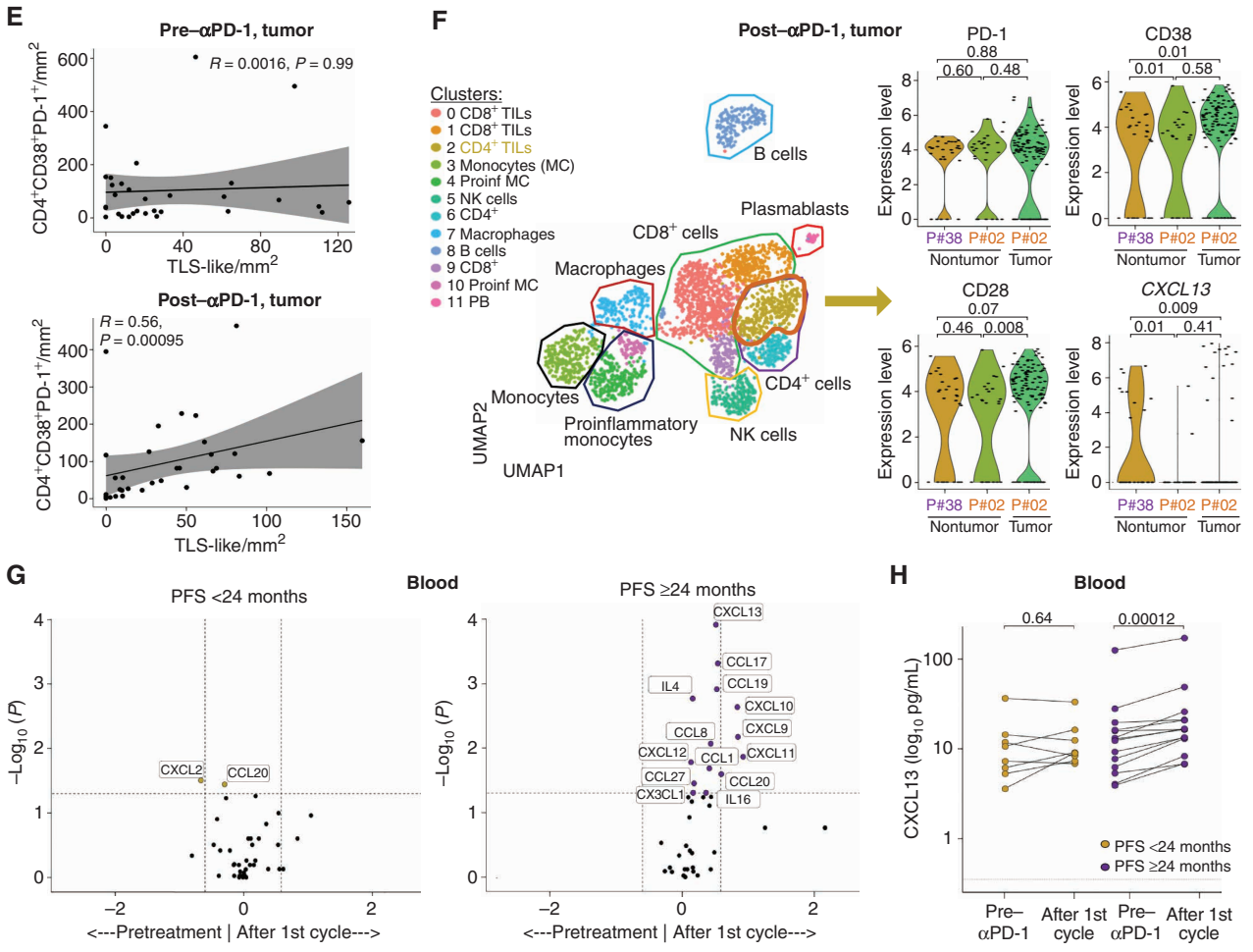

Figure 3. ***(Continued)*** **E,** Spearman correlations between CD4+CD38+PD-1+ cells and TLS-like in bladder tissues at baseline (top) and after 3 cycles of pembrolizumab (bottom). Each dot represents one patient. **F,** Single-cell transcriptomics of CD45+ in four radical cystectomy specimens and two peripheral blood mononuclear cell (PBMC) samples. Analysis of Rhapsody single-cell RNA-seq data, displayed by uniform manifold approximation and projection (UMAP; left). Seurat clustering of 2,432 CD45+ cells from primary bladder tumors, surrounding nontumoral tissue and PBMCs. Expression levels of the *CXCL13* gene product in CD4+ TILs (cluster 2) depicted in violin plots, as well as of PD-1, CD38, and CD28 at the protein level in three specimens collected after anti–PD-1 mAbs [healthy bladder tissue from complete responder (P#38), healthy bladder tissue and bladder cancer from nonresponder (P#02)]. NK, natural killer; PB, plasmablast; Proinf, proinflammatory. **G,** Multiplex array of inflammatory analytes in the plasma. Volcano plots showing differential plasma concentrations of cytokines/chemokines before and after one cycle of pembrolizumab in the group of patients experiencing or not a relapse and/or death before 24 months (left and right, respectively). Volcano plots were generated computing for each soluble factor: (i) the $\log_2$ of fold ratio among the mean values after normalization, after first injection versus preinjection of pembrolizumab (*x*-axis), and (ii) the $\log_{10}$ of *P* values deriving from the paired Wilcoxon test calculated in absolute values (*y*-axis). Black and colored dots are considered nonsignificant ($P < 0.05$) or significant ($P > 0.05$), respectively. **H,** Plasma concentration of CXCL13 ($\log_{10}$) in pre– versus post–first cycle of pembrolizumab in the two groups (according to PFS status at 24 months). Each line represents one patient. The dotted line indicates the lower detection threshold of CXCL13. Statistical analysis used paired *t* test (paired Wilcoxon test).

resistance to therapy (Supplementary Fig. S5E, right), as already described in lung cancer (45).

These results suggest that in patients with prolonged PFS, PD-1 blockade using pembrolizumab may have facilitated the accumulation of T_{FH}-like cells in TLS and induced the release of the T_{FH}-prototypic CXCL13 chemokine in tissue lesions and the bloodstream of patients.

MIBC-Residing T_{FH} Are Associated with *Ex Vivo* Responses to Pembrolizumab

Next, we asked if T_{FH} cell accumulation within TILs is a prerequisite for the immunologic response of MIBC to pembrolizumab. We used the *in vitro/in situ* ("*in sitro*") assay that we recently developed to search for surrogate markers of immune reactivity to ICBs (refs. 46, 47; Fig. 4A). Hence, we assessed the *ex vivo* immunoreactivity to pembrolizumab of 18 surgical resections of MIBC specimens (56% pT3) from treatment-naïve patients (Supplementary Table S6; Fig. 4A). To calculate the index of immune stimulation by anti–PD-1 mAbs, we normalized raw values onto medium values, those being mostly equivalent to isotype control mAb–related values (46). We used nonsupervised hierarchical clustering of *z* score–normalized concentrations of 28 immune- and nonimmune-soluble factors monitored by bead-based multiplex assay and ELISA, as previously described (46). The heat map of this clustering highlighted two categories of patients with MICB: 22% ($n = 4/18$) exhibiting increased levels of most analytes above the mean of

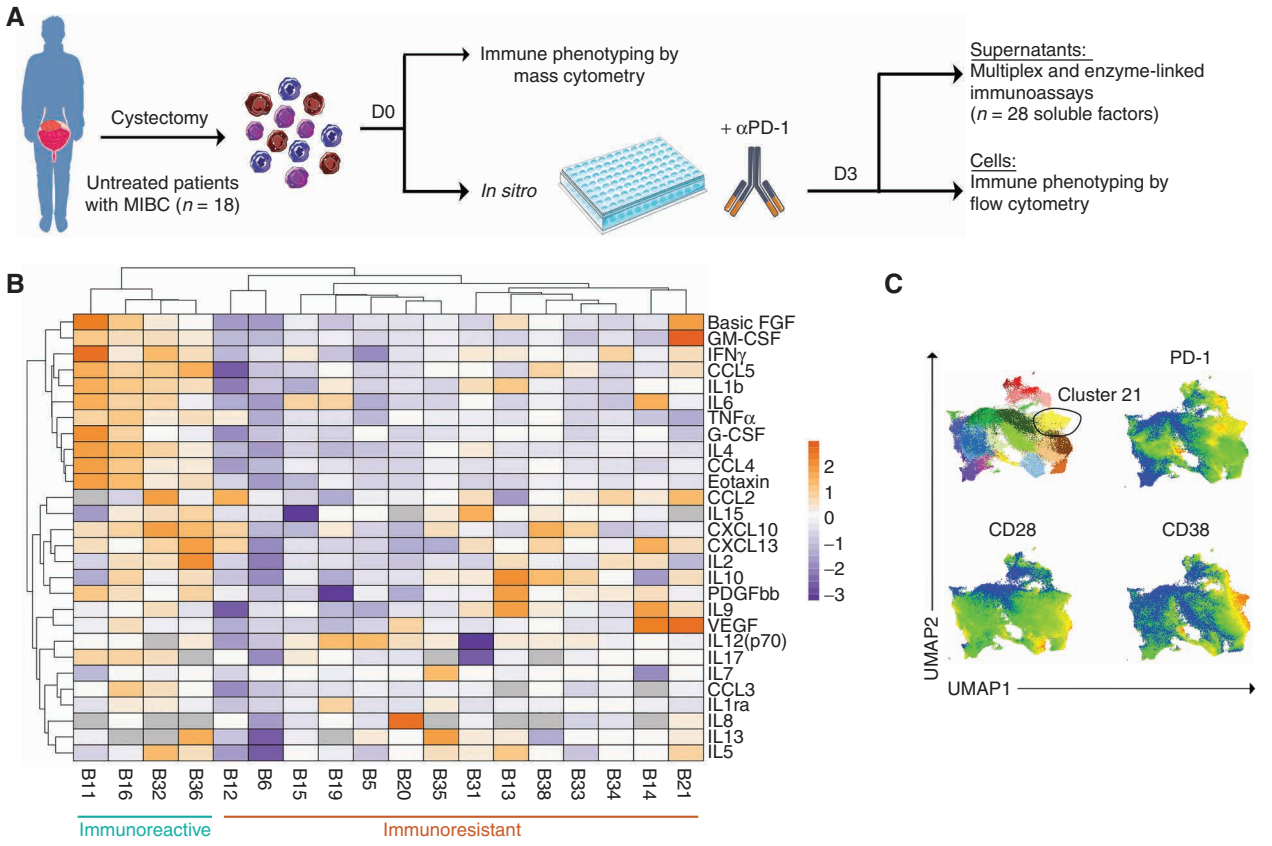

Figure 4. Preexisting T_{FH}-like CD4+ T cells are prerequisites for a functional response of MIBC to pembrolizumab *ex vivo*. **A,** Overview of the *in situ*/*in vitro* (*in sitro*) test. **B,** Heat map of the nonsupervised hierarchical clustering ($n = 18$) of 28 soluble factors (including CXCL13 monitored in ELISA) secreted from MIBC exposed to 72 hours of pembrolizumab. Missing values are shown in gray. Both rows and columns are clustered using correlation distance and average linkage. **C,** Uniform manifold approximation and projection (UMAP) showing the PhenoGraph clusters (refer to Supplementary Fig. S6A) of CD4+ TILs in 18 untreated bladder cancers (mostly MIBC, $n = 17/18$) analyzed by mass cytometry (top left) at day 0. Cluster #21 is surrounded by a circle. Relative expression of PD-1 (top right), CD28 (bottom left), and CD38 (bottom right) in CD4+ TILs at day 0, displayed by UMAP. (*continued on next page*)

the whole cohort after stimulation with anti–PD-1 mAbs (called henceforth "immunoreactive," Fig. 4B), and 88% who failed to do so. The most significant differences between immunoreactive and nonimmunoreactive tumors resided in the release of Th1/Th2 hallmarks (CXCL10, IFNγ, GM-CSF, CCL4, CCL5, eotaxin, and IL4) compatible with the T-cell receptor cross-linking secretory profile (46) as well as inflammatory cytokines (IL1β, TNFα, and IL6; Fig. 4B). We then examined correlates between *in sitro* immunoreactivity and basal CyTOF-based unsupervised clustering using PhenoGraph in these 18 MIBCs. Tumor-infiltrating CD4+ TEM cells ($CD45RA^{-}CD127^{-}CD28^{+/int}$) harboring high expression levels of PD-1, CD38, and CD28 with coexpression of activation markers ($CD69^{+}CD95^{+}CD39^{+}$) belonging to clusters 21 and 28 best predicted *in sitro* responsiveness to PD-1 blockade (Fig. 4C and D; Supplementary Fig. S7A and S7B). We next performed single-cell RNA-seq on two independent MIBC-infiltrating CD45+ leukocyte populations at baseline [harvested from an immunoreactive tumor (B#11) and a tumor at the edge between nonimmunoreactive and nonimmunoreactive (B#12)]. Here again, within the cluster that mostly comprised CD4+ TILs (cluster 2; Supplementary Fig. S5B), membrane expression of CD38, CD28, and PD-1 molecules allowed us to identify the T_{FH} pathognomonic transcript, *CXCL13*, in the CD4+ TILs (Fig. 4E), suggesting that CXCL13-T_{FH}, which expressed PD-1, are critical to potentiate the induction of immune reactivity to *ex vivo* PD-1 blockade. Supporting this finding, the percentages of baseline $CD4^{+}CD38^{hi}CD28^{+}PD\text{-}1^{hi}$ TILs (clusters 21 and 28, differing for their expression of CD103 and relative expression of CD28) and spontaneous CXCL13 release correlated among each other, and all were markedly higher in immunoreactive compared with nonimmunoreactive MIBC (Fig. 4F; Supplementary Fig. S7C). Of note, *CXCL13*-expressing CD8+ T cells were detectable but failed to segregate immunoreactive from nonimmunoreactive tumors (Supplementary Fig. S8A). In parallel, the unsupervised clustering of tumor-infiltrating CD8+ T cells (Supplementary Fig. S8B and S8C) showed positive correlations between T_{FH} TILs (cluster 21) and $CD38^{hi}CD39^{hi}PD\text{-}1^{hi}TIGIT^{+}CD69^{+}CD103^{+}$ tissue-resident CD8+ TILs (TRM; Supplementary Fig. S8C and S8D, top) but not with $CD8^{+}CD38^{-}CD39^{-}PD\text{-}1^{+}$ tissue-resident TILs (clusters CD8+ 24 and 12) or non–tissue-resident CD8+ TILs (cluster CD8+ 30; Supplementary Fig. S8C and S8D, bottom). Although CD38 was used as a proxy marker to identify the CXCL13-expressing PD-1+ T_{FH} CD4+ TIL subset, CD38

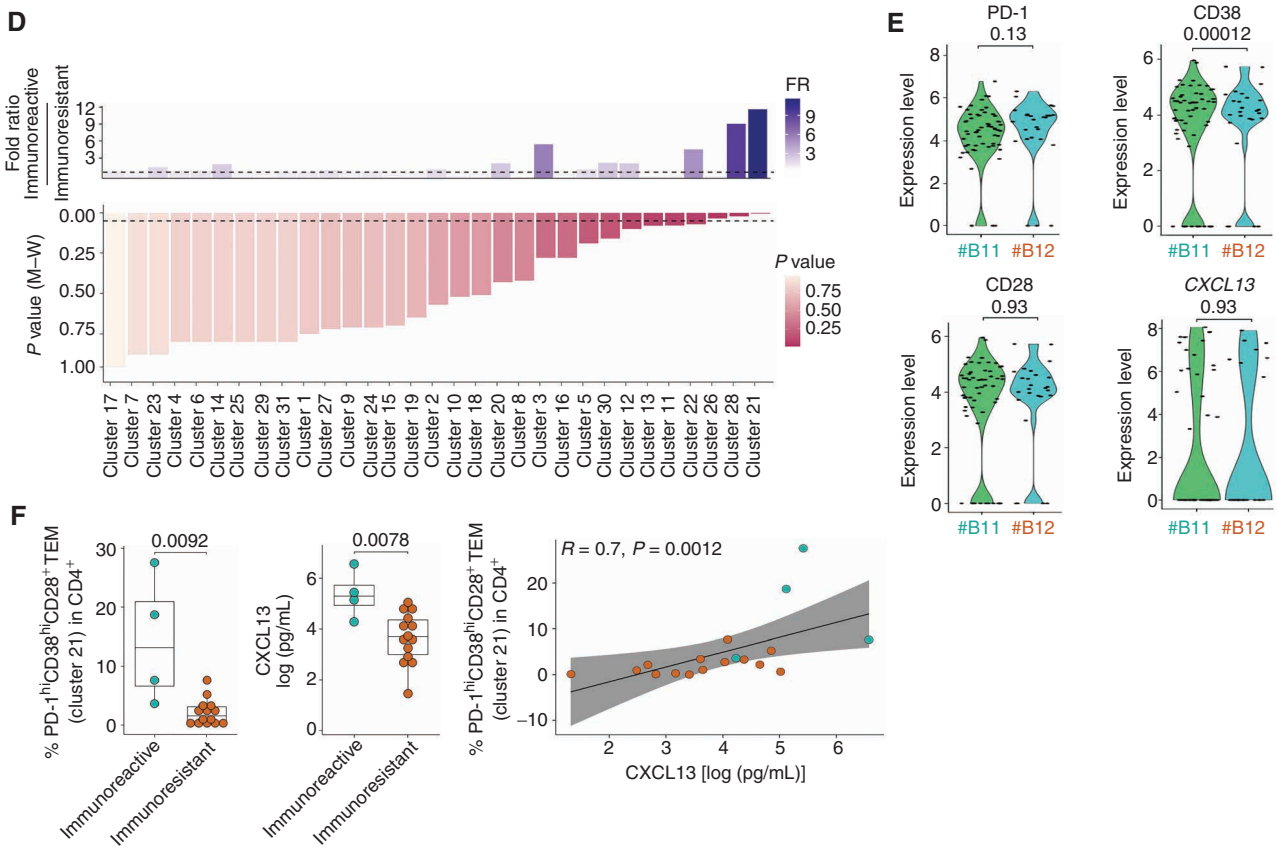

Figure 4. ***(Continued)*** **D,** Bar chart showing fold ratio of median CD4+ TIL cluster values between immunoreactive versus nonimmunoreactive MIBC (top). Increasing blue gradient for increased fold ratios (FR). Bar charts showing the *P* values of unpaired *t* test [Mann–Whitney (M-W) *U* test] for each CD4+ TIL cluster (bottom). **E,** Expression levels of the *CXCL13* gene product in CD4+ TILs (cluster 2, as shown in Fig. 3E) depicted in violin plots, as well as PD-1, CD38, and CD28 at the protein level in two specimens collected before the *in sitro* assay. Samples from untreated patients were utilized (B#11: immune-reactive tumor, B#12: at the edge between immunoresistant and immune-reactive tumors). **F,** Percentages of CD38hiCD28+PD-1hi (cluster 21) in CD4+ TILs (left), quantification of CXCL13 production after 3 days of *in sitro* assay without treatment (middle), and Spearman correlation between both parameters (right). Box plots display a group of numerical data through their third and first quartiles (box), mean (central band), and minimum and maximum (whiskers). Each dot represents one tumor. Statistical analyses used unpaired *t* test (Mann–Whitney *U* test).

did not behave as a checkpoint inhibitory molecule, because we failed to increase or trigger TIL immunoreactivity by combining anti-CD38 with anti–PD-1–neutralizing mAbs in the *in sitro* system (Supplementary Fig. S8E).

Although further work is needed to evaluate the clinical significance of CD8+ TILs during neoadjuvant pembrolizumab, PANDORE and *in sitro* studies both converged in showing that pembrolizumab potentiated the TLS-associated antitumor activity by coordinating T_{FH}, B cells, and CD8+ TRM.

T_{FH} Are Key Targets of Pembrolizumab among CD4+ T Cells

Visualizing the molecular targets of the pembrolizumab IgG4 antibody is of the utmost importance for determining the mechanisms of action of this drug. Although many investigators identified CD8+ cells as the main functional targets of anti–PD-1 mAbs (10, 48, 49), we took a comprehensive approach to study IgG4+ cells in the blood and within cystectomy tissues using CyTOF and immunofluorescence analyses. We confirmed that among blood CD4+PD-1+ cells, CD4+ TEM (cluster 13), as well as TE (clusters 5 + 15) and to a lesser extent TCM (clusters 6 + 9 + 20) exhibited the strongest binding to anti-IgG4 mAbs during pembrolizumab treatment (Fig. 5A and B; Supplementary Fig. S9A–S9C). Moreover, we found a higher proportion of IgG4+ cells in the CD28+CD38+PD-1+ TEM T_{FH}-like subset (cluster 13) before the third injection of pembrolizumab in patients with a prolonged clinical benefit compared with patients with PFS <24 months (Fig. 5C). In tumor beds, IgG4 binding to CD38+ T_{FH}-like was particularly intense within tumor areas enriched in TLS-like (Fig. 5D and E). To better ascribe the IgG4 staining to the therapeutic Ab and not to a local B-cell Ig switch, we compared the dynamics of IgG4 staining in various subsets of MIBC-residing cells before and after pembrolizumab. There was a significant rise only in the CD4+IgG4+ subset after therapy (Fig. 5F). Next, we performed stainings with anti-IgG and anti-IgA antibodies on MIBC samples before and after pembrolizumab and found a preferential labeling of plasma cells with an increase of IgG at the expense of IgA in tumor beds, resulting in a significant pembrolizumab-associated rise in the IgG/IgA ratio (Fig. 5G). In contrast, the IgG/IgA ratio remained stable in the periphery (Fig. 5H). After 3 days of *in sitro* stimulation with anti–PD-1 mAbs, the MFI of IgG4 in

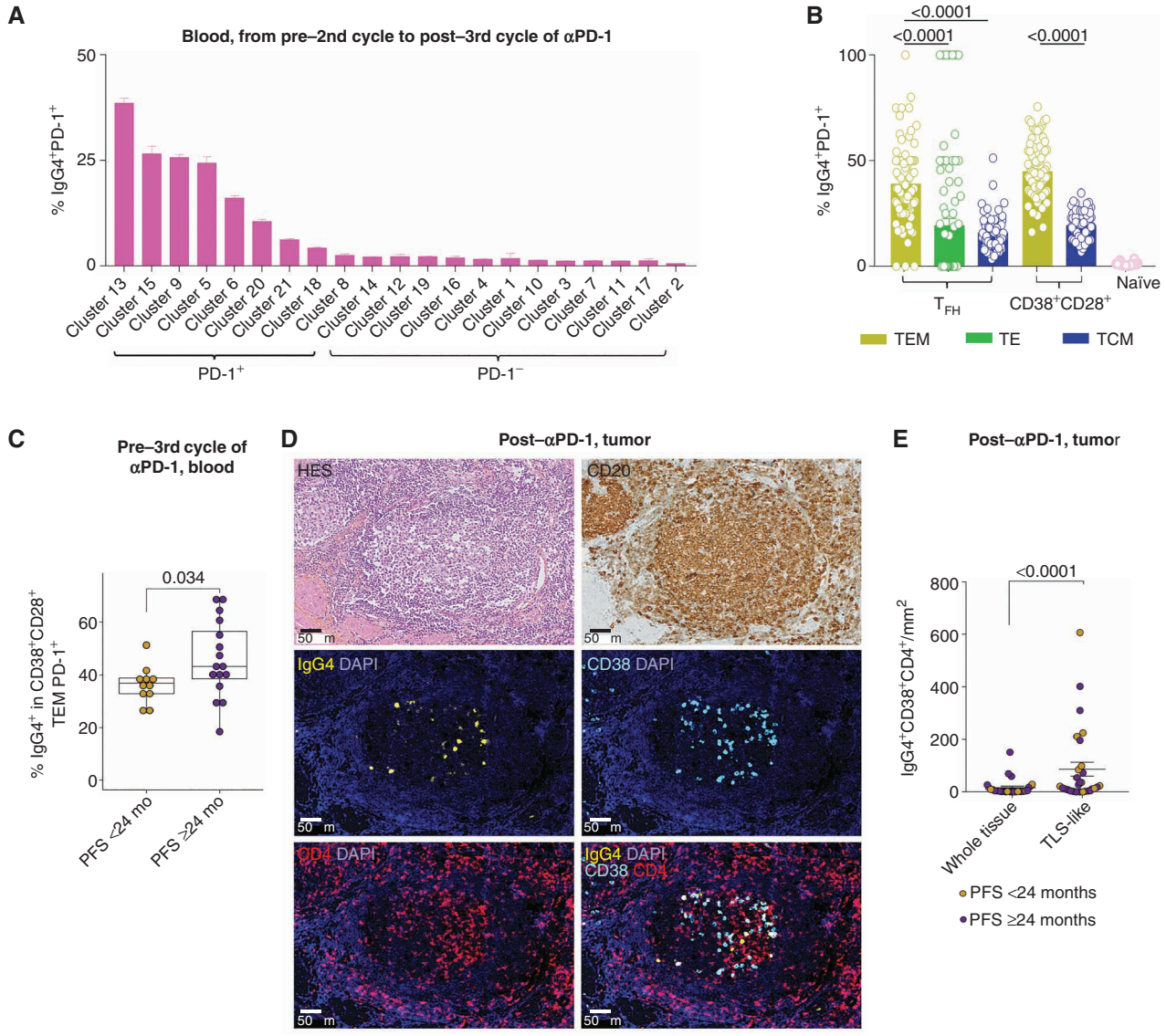

Figure 5. Preferential binding of pembrolizumab to T_{FH} and $CD38^+CD28^+$ T_{FH}-like cells. **A,** Unbiased analyses of $IgG4^+PD\text{-}1^+$ within each cluster of peripheral $CD4^+$ T-cell subset. For each cluster, the average of mean values at three time points for all patients [pre-second, pre-third, post-third cycle (before surgery) of pembrolizumab] as well as the standard error of means are depicted. **B,** Frequencies of peripheral $IgG4^+PD\text{-}1^+$ within activated ($CD38^+$) TCM, TEM, T_{FH} TCM, T_{FH} TEM, and T_{FH} TE as well as in naïve $CD4^+$ T cells as negative control at three time points for all patients [pre-second, pre-third, post-third cycle (before surgery) of pembrolizumab]. Each dot represents one sample. Statistical analysis used the Kruskal–Wallis test. **C,** Frequencies of peripheral $IgG4^+PD\text{-}1^+$ in activated $CD38^+$ TEM before the third injection of pembrolizumab in the group of patients experiencing PFS < or ≥24 months. Box plots display a group of numerical data through their third and first quartiles (box), mean (central band), and minimum and maximum (whiskers). Each dot represents one patient. Statistical analysis used an unpaired *t* test (Mann–Whitney *U* test). **D,** Representative micrograph of TLS-like on HES (top left), constituted predominantly by $CD20^+$ cells evidenced by IHC (top right) and of single (middle and bottom left) and triple-positive $CD4^+CD38^+IgG4^+$ cells by immunofluorescence stainings (bottom right) in a radical cystectomy specimen from a patient with PFS ≥24 months (P#39). **E,** Accumulation of $CD4^+CD38^+IgG4^+$ T_{FH}-like in TLS-like compared with whole tissue after treatment (refer to Methods, "Geodistribution of $CD4^+CD38^+PD\text{-}1^+$ and $CD4^+CD38^+IgG4^+$ in FFPE samples"). Box plots display a group of numerical data through their third and first quartiles (box), mean (central band), and minimum and maximum (whiskers). Each dot represents one patient (gold: relapse and/or death, purple: absence of relapse and/or death). Statistical analysis used paired *t* tests (paired Wilcoxon test). (*continued on next page*)

$CD38^{hi}$ and $CD38^-$ subsets revealed a trend for preferential binding to $CD38^{hi}$-expressing $CD4^+$ TILs in immunoreactive tumors (Supplementary Fig. S9D, top). As expected, there was a correlation between IgG4 and PD-1 positivity on this $CD38^{hi}CD4^+$ T-cell subset after pembrolizumab (Supplementary Fig. S9D, bottom). Of note, supernatants of the *in sitro* studies contained higher baseline levels of IgA and IgG1, IgG2, or IgM than IgE, IgG3, and IgG4 (Supplementary Fig. S10A) that did not increase within 72 hours despite a rise in ASCs after bacterial stimulation (Supplementary Fig. S10B).

Altogether, within $CD4^+$ T cells, pembrolizumab preferentially targeted circulating and tumor-associated T_{FH} expressing CD38 and residing in TLS-like area.

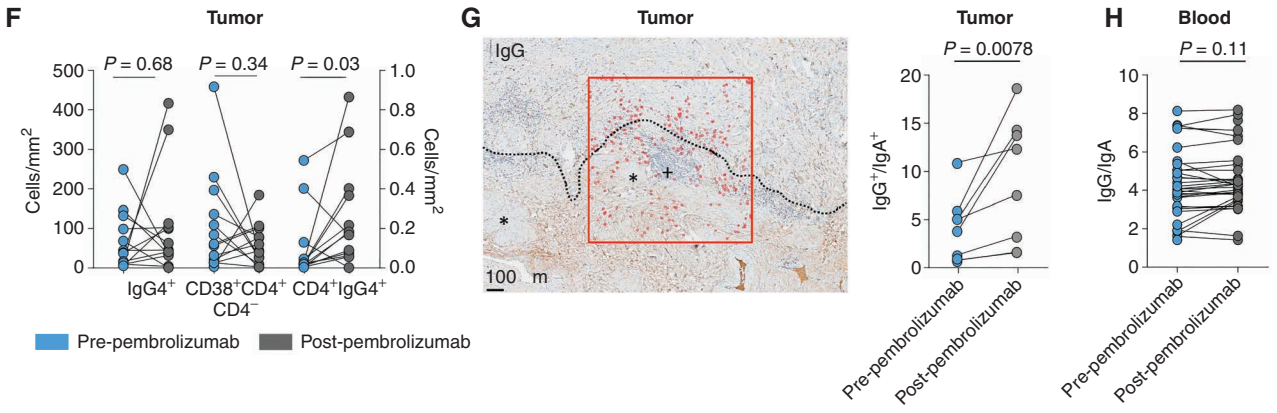

Figure 5. ***(Continued)*** **F,** Densities of IgG4$^+$, CD4$^-$CD38$^+$IgG4$^+$ cells (left y axis of the right) and CD4$^+$IgG4$^+$ cells (right y axis of the right) computed and counted from multiplex-labeled slides before (blue) or after (gray) pembrolizumab in 13 paired patients. Statistical analysis used paired *t* tests (paired Wilcoxon test). **G,** Representative micrograph of IgG$^+$ cells in one out of five regions of interest (red rectangle; magnification 10×). IgG- and IgA-positive cells, mainly corresponding to plasma cells, were counted in five regions of interest in similar peritumoral areas of MIBC in sequential slides in order to generate IgG and IgA density (left). +, TLS; *, smooth muscle. Tumor is delineated by discontinuous line (tumor on the top). Ratio of IgG$^+$/IgA$^+$ cells in bladder tissues before and after treatment evaluated by IHC in eight paired PANDORE cases (right). Statistical analysis used paired *t* tests (paired Wilcoxon test). **H,** Ratio of soluble IgG/IgA in patient serum before and after treatment. Statistical analysis used paired *t* tests (paired Wilcoxon test).

E. coli–Specific Memory T_{FH} and B-cell Responses Are Associated with Clinical Benefit to Neoadjuvant Pembrolizumab

Urine is not sterile, and commensal bacteria are present in the urinary tract of both healthy patients and patients with UC (50, 51). Indeed, patients with UC are commonly diagnosed with urinary tract infections (UTI) or asymptomatic bacteriuria (52). Uropathogenic bacteria have the capacity to invade bladder epithelial cells and can persist for prolonged periods of time (53, 54). Of note, the risk of developing UC in women is inversely correlated with UTIs (55). Additionally, patients diagnosed with noninvasive UC are treated by intravesical bacterial extracts [namely, Bacillus Calmette-Guérin (BCG)], which was the case for 17.9% (n = 7/39) of patients enrolled in the PANDORE study. Recent evidence indicates that local and intratumoral microbiota influence the prognosis of cancers developing at mucosal surfaces (56–59). Therefore, we investigated the presence of tumor-associated bacteria in MIBC using IHC [anti-lipopolysaccharide (LPS) staining], FISH, electron microscopy, qPCR, and culturomics in aerobic and anaerobic conditions. LPS$^+$ structures within UC cells and/or immune cells were observed in up to 70% of TURBT (n = 24/33; Fig. 6A and B), coinciding with cytoplasmic granular structures and exceptionally with neutrophils (Supplementary Fig. S11A). These granular structures were more numerous in tumor cells than in normal urothelial cells from surrounding tumor-free tissues and might correspond, at least partially, to Gram$^+$ bacteria that we isolated in most of the fresh MIBCs that we cultivated (n = 6; Fig. 6C and D). In particular, culturomics of primary bladder tumors and surrounding noncancerous tissues allowed us to identify *Staphylococcus capitis*, *Cutibacterium acnes*, and *Corynebacterium tuberculostearicum* in the tumor tissues but not in the transport supernatant of the tumor, suggesting that these Gram$^+$ bacteria were not contaminants (Fig. 6D; Supplementary Fig. S11B). Given the ability of *E. coli* to invade urothelial cells, we ran qPCR using *E. coli*–specific probe sets (53, 54) and could detect specific signals in 70% of the cases (n = 14/20 of total cases with n = 7/11 untreated specimen and n = 7/9 post-pembrolizumab) without differences between tumors and surrounding "healthy" tissues (Fig. 6E and F). FISH using specific probes for 16s rRNA, *E. coli*, and uropathogenic *E. coli* (UPEC; ref. 60) allowed us to visualize UPEC in tumor, nontumoral urothelium, and immune cells (Fig. 6G). Finally, we confirmed the presence of live bacilli within bladder tissues by scanning and transmission electron microscopy, either intracellularly or in intercellular spaces (Fig. 6H, right and left). Of note, we found a strong correlation between neutrophils and ASCs within tumor-infiltrating CD45$^+$ cells after pembrolizumab (Fig. 6I), suggesting that innate and humoral immune responses against bacteria might cooperate in the tumor beds.

Hence, we addressed whether memory T- or B-cell immune responses directed against *E. coli*, BCG, and other urinary bacterial species such as *Corynebacterium tuberculostearicum* and *Cutibacterium acnes* could be detected before and after pembrolizumab. We first performed a longitudinal study of blood CD4$^+$ T-cell recall responses against urinary tract and tumor bacteria, monitoring cytokines prototypic of Th1 (IFNγ), T_{FH} (CXCL13), and regulatory (IL10) T-cell responses (refs. 61–63; Supplementary Table S7; Fig. 7A). Patients with UC harbored preexisting commensal-specific Th1 and T_{FH} memory T-cell responses that tended to increase and decrease by pembrolizumab for the former and the latter, respectively (Fig. 7B; Supplementary Fig. S11C and S11D). Interestingly, baseline CXCL13-producing T_{FH} but not IFNγ-releasing Th1 memory T-cell responses against *E. coli*, and not *S. capitis*, were associated with the absence of progression at 24 months (Fig. 7B; Supplementary Fig. S11D). Of note, there was no CXCL13 release after stimulation with LPS or lipoteichoic acid (LTA; Supplementary Fig. S11E). We next analyzed the *in situ* reactivity to *E. coli* with or without pembrolizumab in *in sitro* assays on fresh MIBC (Fig. 7C, top). After 72 hours of exposure to heat-inactivated *E. coli*, we observed a release of CXCL13

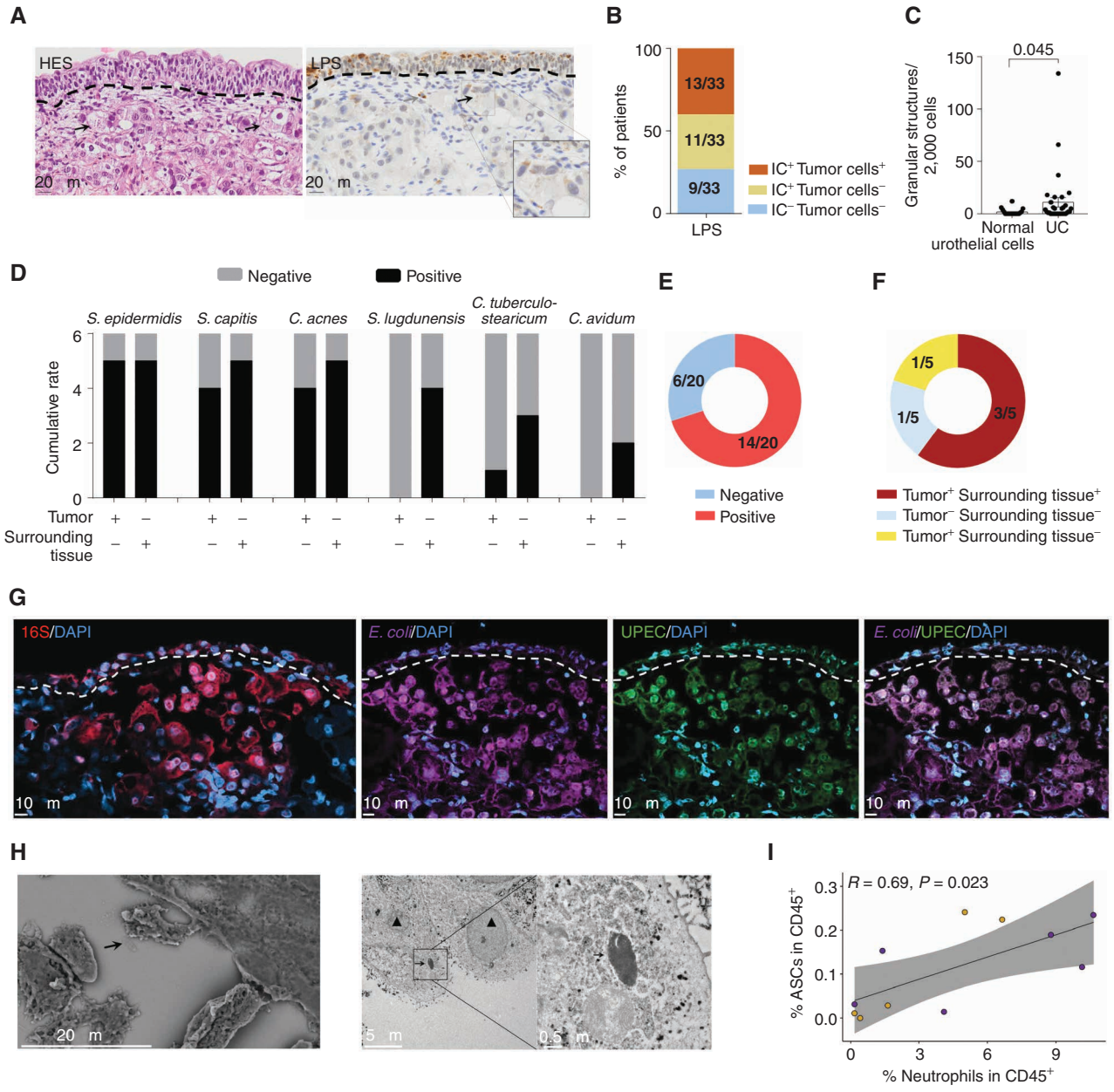

Figure 6. MIBCs contain Gram-negative bacteria with uropathogenic capacities. **A,** Representative micrograph of one bladder showing nontumoral urothelium (above discontinuous line) with invasive cells of UC containing granular cytoplasmic structures (arrows) in P#43 in HES at 20× magnitude (left). LPS IHC staining of the same area highlighting granular cytoplasmic positivity in the normal urothelium, immune cells (gray arrow), and tumor cells (black arrow) at 20× magnitude. **B,** Proportions of patients with positive or negative LPS staining in immune cells (IC) and tumor cells ($n = 33$ patients). **C,** Enumeration of granular cytoplasmic structures in normal and tumoral urothelium. Each dot represents one patient sample. Statistical analysis used unpaired *t* tests (Mann–Whitney *U* test). **D,** Stacked bar chart showing bacteria cultivated by culturomics (refer to Methods) within tumor and nontumor tissues ($n = 6$ patients with paired tissues). Total number of positive (black) or negative (gray) samples is depicted. *C. avidum, Cutibacterium avidum; S. epidermidis, Staphylococcus epidermidis; S. lugdunensis, Staphylococcus lugdunensis.* **E,** Proportions of samples with positive or negative PCR detection of *E. coli* ($n = 20$ bladder specimens, with $n = 9/20$ post-pembrolizumab and $n = 11/20$ untreated). **F,** Proportions of patients with paired samples of tumor and surrounding nontumor tissues ($n = 6$ untreated patients) for PCR detection of *E. coli*. **G,** Distribution of bacteria, *E. coli*, and UPEC by FISH in the same area shown in **A** with *E. coli* (middle left), UPEC-specific probes (middle right) and merge (right) at 40× magnitude. **H,** Scanning (left) and transmission (right) electron microscopy illustrating bacilli (arrow) morphologically compatible with Enterobacteriaceae in the intercellular space (left) or within an urothelial tumor cell (right) in P#08 (left) and P#18 (right). Triangle indicates nucleus. **I,** Spearman correlation between ASCs and neutrophils in tumoral CD45+ cells analyzed by mass cytometry. Each dot represents one tumor, and color indicates the PFS status at 24 months (gold: relapse and/or death, purple: absence of relapse and/or death).

(Fig. 7C, middle) and an MHC class II–restricted release of TLS-associated CCL19 (Fig. 7C, bottom) chemokines, whereas ASC numbers increased in the coculture (Supplementary Fig. S10B). Moreover, this release was amplified by the addition of pembrolizumab (Supplementary Fig. S10B).

Next, we investigated the humoral immune responses against urinary tract and tumor commensals (Supplementary Table S7). Very high serum titers of IgG and IgA antibodies were found against commensals shared between urinary and digestive tracts (such as *E. coli* or *Enterococcus faecalis*;

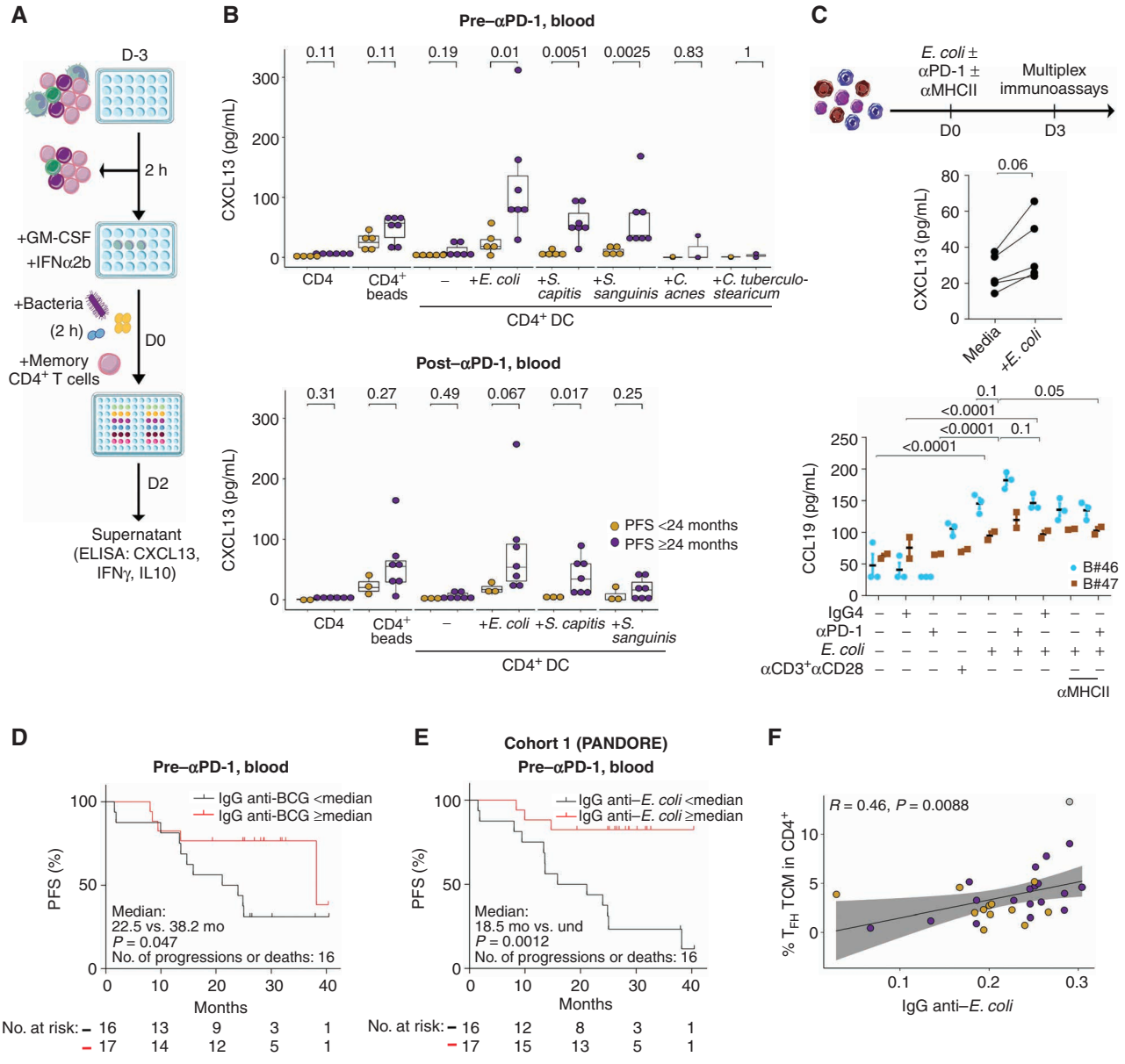

Figure 7. *E. coli*–specific humoral and cellular T_{FH} memory responses are associated with PFS. **A,** Experimental setting of the CD4+ T-cell recall responses against bacteria (refer to Methods). **B,** Quantification of CXCL13 secretion levels in cocultures of CD4+ T cells isolated before treatment (top) or after treatment (bottom) and autologous monocyte-derived dendritic cells (DC) loaded with bacteria for 2 days. Patients with relapse and/or death before 24 months (gold) and without (purple) are shown. Statistical analyses used an unpaired *t* test (Mann–Whitney *U* test). *S. sanguinis, Streptococcus sanguinis.* **C,** Overview of the *in situ*/*in vitro* (*in sitro*) test with heat-killed bacteria (top). Multiplex immunoassays monitoring of CXCL13 (middle) and CCL19 (bottom) TLS-specific chemokines in *in sitro* stimulation of two to 5 freshly dissociated MIBC with *E. coli*. Different culture conditions are annotated as well as the neutralization of MHC class II complexes with specific antibodies. Medians of duplicate–triplicate wells are shown for CXCL13 (each dot corresponds to one MIBC sample) and two independent experiments performed in duplicate–triplicate wells are shown for CCL19 (each dot corresponds to one well). Statistical analyses used paired *t* test (middle) and two-way ANOVA (bottom). **D** and **E,** Cohort 1 (PANDORE). Kaplan–Meier curves of PFS of MIBC patients treated by pembrolizumab according to IgG against BCG (**D**; median = 0.029) and *E. coli* (**E**; median = 0.227) using titer medians as cutoff values at baseline. Statistical analysis used log-rank tests. und, undefined. **F,** Spearman correlation between TCM T_{FH} cells and *E. coli*–specific IgG titers, at baseline, from PANDORE. Each dot represents one patient, and the color indicates the PFS status at 24 months (gold: relapse and/or death, purple: absence of relapse and/or death, gray: unknown). (*continued on next page*)

Supplementary Fig. S11F), contrasting with humoral responses toward skin commensals. Because BCG had been instilled into the bladder of 17.9% of our patients with a history of non-MIBC and given that most patients were vaccinated with BCG, we also found detectable titers of IgG against BCG that tended to decrease with neoadjuvant pembrolizumab (Supplementary Fig. S11G). In fact, preexisting BCG-specific IgG titers were associated with PFS (Fig. 7D). In line with the clinical significance of *E. coli*–specific memory T_{FH} responses, baseline *E. coli*–specific IgG (but not IgA) titers best predicted PFS in the PANDORE study (Fig. 7E; Supplementary Table S7). In addition, there was a correlation

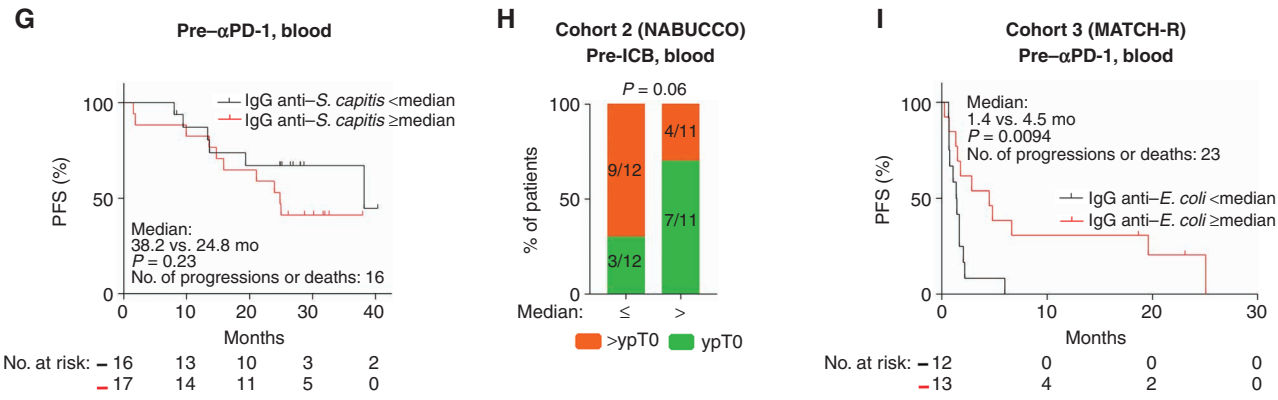

Figure 7. ***(Continued)*** **G,** Cohort 1 (PANDORE). Kaplan–Meier curve of PFS of MIBC patients treated by pembrolizumab according to IgG against *S. capitis* (median = 0.0024) using titer medians as cutoff values at baseline. Statistical analysis used log-rank tests. **H** and **I,** NABUCCO and MATCH-R validation cohorts. Percentages of pCR in response to neoadjuvant ipilimumab and nivolumab in patients with MIBC from the NABUCCO trial according to IgG titers against *E. coli* using titer medians as cutoff values at baseline (**H**). Kaplan–Meier curve of PFS of patients with metastatic MIBC treated with pembrolizumab according to *E. coli*–specific IgG titers using medians as cutoff values at baseline (**I**; median = 7.05). Statistical analyses used the χ^2 test (**H**) and log-rank test (**I**).

between *E. coli*–directed IgG titers and blood TCM T_{FH} cells in PANDORE (Fig. 7F). In contrast, total IgG levels or IgG specific for *S. capitis* (or other commensals) did not have any prognostic value (Fig. 7G; Supplementary Fig. S11H and S11I). In line with the frequent isolation of *S. capitis* from fresh MIBC, we found a potential clinical relevance for *S. capitis*–specific IgA responses (before and after pembrolizumab; Supplementary Table S7). Anti–*E. coli* IgG titers tended to be higher ($P = 0.06$) in patients with pCR in an independent cohort of 23 patients treated with neoadjuvant ipilimumab and nivolumab in the NABUCCO clinical trial (ref. 24; Fig. 7H), thereby supporting the findings obtained through the PANDORE cohort. Of note, Kaplan–Meier survival curves could not be designed for the NABUCCO cohort because only four events were reported at data cutoff (24). In a third independent cohort of 25 patients with metastatic MIBC treated with pembrolizumab in the MATCH-R trial (Supplementary Table S8), we again validated baseline anti–*E. coli* IgG (and not *S. capitis*–specific IgA) as a putative biomarker of PFS (Fig. 7I). We conclude that MIBC contains immunogenic *E. coli* pathobionts eliciting T_{FH} and B-cell responses that predict the clinical outcome of anti–PD-1–based immunotherapy.

DISCUSSION

Here, we showed that circulating and tumor-resident T_{FH} represent prominent (albeit not exclusive) targets for neoadjuvant pembrolizumab. Such T_{FH} cells constitute a critical link with TLS where they preferentially reside and tumor infiltration by $CD8^+$ T cells, culminating in clinical benefit. We used several complementary approaches (immunofluorescence, mass cytometry, functional *in sitro* assay, and flow cytometry) to show that pembrolizumab preferentially binds to effector T_{FH}, which express higher densities of PD-1 (as well as ICOS, CD40L, and Bcl6) than other TH subsets, and induces its bioactivity by promoting CXCL13 release from T_{FH}. Our dynamic study and patient longitudinal follow-up indicated that T_{FH} preexisted in the blood and tumor site prior to therapy, whereas ASCs were induced by immunotherapy and became clinically significant only at this point. In responding patients, CXCL13-producing $CD38^{hi}CD28^+CD4^+$ TILs correlated with B cells that expressed CD86 after pembrolizumab. Although baseline $CD8^+$ TILs were associated with prolonged PFS, TLS-like were induced by pembrolizumab, coinciding with the local accumulation of Bcl6-expressing and $CD38^+$-activated T_{FH}.

In breast cancer, Noël and colleagues highlighted the presence of functional PD-$1^{hi}ICOS^+$ T_{FH} that provided help for the formation of active TLS, characterized by immunoglobulins, proliferating B cells, and cytotoxic $CD8^+$ T-cell effectors (31). Only T_{FH} educated in active TLS had the capacity to provide T-dependent B-cell help and produce IFNγ in *ex vivo* functional assays (31). This is in line with our functional *in sitro* assay showing that preexisting T_{FH} correlated with IFNγ-producing immune-reactive bladder cancers during exposure to pembrolizumab. The functional significance of T_{FH} to instate tumor immunosurveillance has been brought up in three elegant mouse models. Hollem and colleagues dissected the orchestration of immunosurveillance in triple-negative breast cancers harboring a high mutational burden and responding to ICBs (34). The authors showed that IL21-producing T_{FH} activated B cells and stimulated the generation of class-switched plasma cells and tumor-specific IgG—indispensable to control breast tumors. In line with this study, Cui and colleagues deciphered the interplay between T and B cells in a murine lung adenocarcinoma model in which tumor cells expressed neoantigens recognized by T and B cells. Cui and colleagues showed that interactions between T_{FH} and germinal center B cells promoted tumor control by $CD8^+$ T cells through an IL21R-dependent pathway (64). In another preclinical model of colorectal cancer devoid of cancer antigens, bacteria-specific T_{FH} were required for the formation of TLS, bacteria-specific cytotoxic T-cell responses, and control of tumor progression (33).

In the PANDORE study, preexisting memory CXCL13 producing T_{FH} and B-cell cognate immune responses appeared to be directed against commensals common to the digestive and the urinary tracts and/or $Gram^-$ commensals often diagnosed

in UTIs (such as *E. coli*) in these patients. Indeed, *E. coli* IgG titers predicted long-term clinical benefit to pembrolizumab in two independent cohorts of patients. The immunostimulatory capacity of ICBs depends on the taxonomic composition of the intestinal microbiota (62, 63, 65–67). UTI are the most common bacterial infections, preferentially afflicting women, elderly persons, as well as patients with cancer (68). UTIs are typically initiated when certain gut-derived bacteria, such as UPEC, reach the bladder and invade urothelial cells. Several reports identified UPEC antigens evoking robust humoral responses that significantly reduced bladder and kidney infections upon bacterial challenge (69, 70). Cellular Th1 immune responses elicited through mucosal immunization with *E. coli* antigens were shown to be protective against bacterial rechallenge (71). Moreover, urine lymphocytes may reflect the tumor immune landscape in MIBC patients treated with ICBs and could predict recurrence-free survival (72). Although the human tumor microbiome is being deconvoluted (56, 73), new prospects for TIL generation and transfer appear to rely on exploiting MHC-restricted T-cell responses specifically directed toward intratumoral bacteria (74). Bacteria inhabiting the mucus layer close to the intestinal epithelium preferentially induce T_{FH} (75–77). Our study showed that MIBC can be invaded by a distinct commensalism comprising bacteria capable of eliciting specific T_{FH} and B-cell responses. After pembrolizumab therapy, circulating *E. coli*–specific CXCL13-producing T_{FH} tended to decrease, presumably to home to tumor lesions where they are expected to orchestrate the immune landscape of the tumor microenvironment for the long-term clinical protection against relapse. We failed to isolate UTI-related bacteria such as *E. coli* from our fresh bladder samples by culturomics and mass spectrometry but succeeded in isolating $Gram^+$ bacteria (such as *S. capitis*, which was previously isolated from melanoma; ref. 74). Indeed, all patients were treated with cefazolin before radical cystectomy, likely compromising the culture isolation of live *E. coli.* Work is in progress to unveil how antigens from intraurothelial bacteria can be "cross-presented" into tumor MHC molecules to become elective targets of T_{FH} or $CD8^+$ TILs. Pioneering work from Conejo-Garcia's group unraveled the biological significance of transcytosis of tumor antigen–specific and nonspecific IgA for the control of ovarian cancer (35).

These results emphasized that uropathogenic commensals, notably *E. coli* (UPEC) endowed with intrinsic immunogenicity and with tumor-invasive capacities, should be viewed as potential biomarkers of response to ICBs. In addition, UPEC may be harnessed to improve the efficacy of ICBs, for instance, by developing UPEC-based vaccines to elicit a specific T–B cross-talk prior to ICB administration. Along the same lines, extending BCG instillations beyond their current indications (for instance, including MIBC) may be instrumental prior to ICBs to boost BCG vaccine–induced immunity and offer MHC-binding targets for $CD8^+$ effectors.

Regardless of these considerations, monitoring circulating T_{FH} immune responses directed against tumor or commensal antigens should be integrated in the armamentarium of biomarker discovery, in particular in the context of ICB-based therapies of tumors located at cutaneous or mucosal surfaces.

METHODS

Clinical Studies

Study Design and Population

PANDORE. PANDORE is a prospective, single-arm phase II trial testing the antitumor activity of preoperative pembrolizumab monotherapy in patients with histologically confirmed (T2–T4aN0M0) transitional cell carcinoma of the bladder (NCT03212651). Pembrolizumab was given at the recommended dose of 200 mg every 3 weeks for three cycles followed by cystectomy with appropriate lymph node dissection.

Patients were 18 years of age or older, ineligible for cisplatin or refused cisplatin-based chemotherapy, had diagnostic transurethral resection (TURBT) blocks available, and had adequate hematologic and end-organ function. Key exclusion criteria included documented severe autoimmune disease, chronic infectious disease, use of systemic immunosuppressive medications, and prior use of ICBs. Surgery was scheduled 1 to 3 weeks after the last pembrolizumab infusion. Baseline workup included thorax/abdomen/pelvis CT and standard blood analyses (hematology, biochemistry, and coagulation parameters). Neither PET-CT nor MRI was required for baseline imaging. There was no dose modification of pembrolizumab. Patients with grade 2 to 4 pembrolizumab-related toxicity (except for grade 2 infusion reaction) were required to permanently discontinue pembrolizumab administration and to proceed with radical cystectomy.

Thirteen patients (38.2%) had postoperative complications (grades 3–4) such as infection ($n = 3$), metabolism and nutrition disorders ($n = 1$), procedural complications ($n = 2$), renal and urinary disorders ($n = 4$), gastrointestinal disorders ($n = 1$), and musculoskeletal and connective tissue disorders ($n = 1$).

The trial was conducted by the French Genitourinary Group (GETUG) and funded by MSD, which provided the drug. This study was approved by the ethics committee CPP Est-III in December 2017 and the French National Agency for the Safety of Medicines and Health Products (ANSM) in November 2017, and was conducted in accordance with the protocols and Good Clinical Practice Guidelines defined by the International Conference for Harmonisation of Technical Requirements for Pharmaceuticals for Human Use and the principles of the Declaration of Helsinki.

NABUCCO (Validation Cohort). The NABUCCO study enrolled 24 patients with stage III UC treated with ipilimumab (cycle 1), ipilimumab and nivolumab (cycle 2), and nivolumab (cycle 3) followed by resection (24). A baseline serum sample was available for 23 patients who defined the validation cohort 2.

MATCH-R (Validation Cohort). MATCH-R is a prospective trial studying the evolution of the clonal architecture of tumors from patients with advanced cancer and treated with molecular targeted agents to identify mechanisms of acquired resistance (NCT02517892). The design of the study has been reported previously (78). Briefly, the primary objective of this study is to characterize molecular mechanisms of resistance to targeted therapies and immunotherapy by next-generation sequencing and the development of patient-derived xenografts and cell lines.

Patients treated with pembrolizumab with metastatic MIBC were enrolled in our study and define the validation cohort 3. Baseline, on-treatment, and postprogression biopsies were performed in patients treated with pembrolizumab. In addition, blood samples were collected longitudinally throughout the treatment and at progression in patients for collecting serum, plasma, and circulating tumor DNA.

Untreated Bladder Cancers. A cohort of 18 patients with untreated nonmetastatic MIBC was included in this study. Surgeries were performed in the University Paris-Saclay Hôpital Foch between

August 2017 and July 2021, and tumor samples were collected with appropriate written informed consent for use of clinical data and scientific purposes according to protocol reviewed and approved by the institutional ethic committee (number IRB 00012437). Before radical cystectomy, all patients were treated with cefazolin. In case of urinary tract infection, additional antibiotics have been used according to the sensitivity to other antibiotics.

Study Endpoints and Statistics

Outcomes. The primary endpoint was pCR defined as the absence of cancer cells in the bladder and the absence of microscopic lymph node metastases on the final cystectomy specimen (ypT0N0). Histopathologic examination was performed locally in each participating center by expert genitourinary pathologists on the resected primary tumor and lymph node specimens. Pathologic staging was done according to international standards and protocols. Secondary endpoints were: (i) the pathologic response (pR) defined as the absence of muscle-invasive carcinoma (<ypT2 disease) and the absence of microscopic lymph node metastases (ypN0) on the final cystectomy specimen (defined as MPR); (ii) the number of participants with a grade 3 to 4 adverse event according to NCI Common Terminology Criteria for Adverse Events (CTCAE) version 4.0, related or not to pembrolizumab (nonrelated adverse events and immune-related adverse events were graded according to NCI CTCAE version 4.0 and reported throughout the study); and (iii) the number of patients having cystectomy. Survival outcomes were PFS defined as the time from the first dose of pembrolizumab to progression (local relapse or metastases, death, whichever occurred first) and OS defined as the time from the first dose of pembrolizumab to death, whatever the cause.

Statistical Considerations. The sample size was calculated on a precision analysis rather than a power analysis of the main outcome. The sample size was based on the CI and the CI half-width (the CI half-width is the margin of error associated with the CI). For a proportion of pCR equal to 30% and a 95% CI, 36 patients were to be included in order to obtain an estimate with certain precision of 0.15. Considering that a 10% rate of patients did not undergo cystectomy, 40 patients were needed to be recruited.

Response rates were calculated with their 95% CI by using the exact Clopper–Pearson method (based on the exact binomial distribution). PFS and OS were estimated by the Kaplan–Meier method. Median follow-up was estimated using the reverse Kaplan–Meier method. The main analysis included patients who met the eligibility criteria, had at least one cycle of pembrolizumab, and underwent cystectomy. The safety analysis included all patients who met the eligibility criteria and received at least one dose of the study drug. The clinical data cut for analysis occurred in August 2021. Data were analyzed using SAS software v-9.4 and GraphPad Prism version 7 for Windows (GraphPad Software).

Sample Collection and Processing

Sample Collection

PANDORE. Peripheral blood samples from patients enrolled in PANDORE were drawn and collected into sterile vacutainer tubes uncoated and tubes coated with heparin. Blood samples were collected at baseline (before the first cycle of pembrolizumab), right before the second and third cycles of pembrolizumab, and before and 1 month after surgery. Tumors before treatment were collected as formalin-fixed, paraffin-embedded (FFPE) tissues. Tumors after treatment were collected freshly in RPMI and as FFPE tissues. Available and analyzed samples are shown in Supplementary Fig. S5.

MATCH-R (Validation Cohort). Peripheral blood samples from patients enrolled in MATCH-R were drawn and collected into sterile vacutainer tubes uncoated for serum collection.

Untreated Bladder Cancers. Fresh tumors were collected in RPMI at +4°C.

Tissue Digestion. Tumor pieces and noninvolved bladder were collected in RPMI 1640 (GIBCO, Life Technologies, ref: 31870-025), at +4°C. The samples were stored less than 17 hours at +4°C before processing. Tissues were weighed and digested, enzymatically and mechanically. Briefly, tissues were cut into small pieces using scalpels and forceps in a petri dish. The small pieces were then dissociated in a gentleMACS Octo Dissociator (Miltenyi) using the program "37C_h_TDK_1" in a dissociation medium, which consisted of RPMI, Collagenase IV (50 IU/mL, Sigma-Aldrich; cat. #C2139), hyaluronidase (280 IU/mL, Sigma-Aldrich; cat. #H6254), and DNase I (30 IU/mL, Sigma-Aldrich, ref: 260913). Dissociation time lasted 1 hour under mechanical rotation and heating. After digestion, an aliquot of the supernatant was collected for immunoglobulin isotyping (refer to "Immunoglobulin isotyping"). The samples were then filtered through a 100-µm strainer, crushed, and washed in NaCl (Versylene Fresenius Kabi) at 1,500 rpm for 5 minutes. The pellets were resuspended in an adapted volume of NaCl 0.9%. If required, red blood cell lysis was performed using RBC Lysis Buffer 1X (BioLegend; cat. #420301). For untreated samples, an aliquot of 50 µL was used to quantify the total number of cells and the fraction of $CD45^+$ cells with Precision Count Beads (BioLegend; cat. #424902) by flow cytometry following the manufacturer's protocol. For PANDORE samples, the total number of cells was counted using a hemocytometer.

Serum Collection. Uncoated tubes were centrifuged for 10 minutes at 1,800 rpm. Serum was aliquoted and stored at −80°C until measurements.

Peripheral Blood Mononuclear Cell Isolation and Plasma Collection. Whole blood was layered on a Lymphocyte Separation Media (VWR; cat. #25-072-CV) in Leucosep tubes (Dutscher; cat. #227288). Tubes were centrifuged for 15 minutes at 2,000 rpm at room temperature. Plasma was collected and stored at −80°C until measurements. Peripheral blood mononuclear cells (PBMC) were collected, washed in NaCl 0.9%, and counted using a hemocytometer. Cells were washed and resuspended in fetal calf serum containing 10% of dimethyl sulfoxide (DMSO; Sigma-Aldrich; cat. #276855) for storage in liquid nitrogen.

Immunophenotyping

Mass Cytometry

Samples. For PBMCs, after thawing, cells were washed and resuspended in RPMI + 10% FCS + DNase (30 IU/mL). After 1 hour of incubation at 37°C, cells were washed and counted using Vi-Cell XR Cell Viability Analyzer (Beckman Coulter). Two million cells were used. For tumor, at least 1 million cells were used for staining by mass cytometry.

Sample Preparation. Cells were stained for viability and proliferation with rhodium (Rh103, Fluidigm; cat. #201103A; 1:100) and IdU (Fluidigm; cat. #201127; 1:2,000), respectively, in RPMI + 10% FCS for 20 minutes at +37°C. Cells were washed in staining buffer (PBS 1× + BSA 0.2% + EDTA 2 mmol/L). Cells were incubated for 5 minutes with Fc blocker (FcX, BioLegend; cat. #422302) before being stained with extracellular antibodies. For PBMCs, cells from each time point were labeled with a unique barcode by incubating with CD45-antibodies conjugated to distinct metal isotopes (Cadnium 106, 110, 111, 112, 114) before pooling. Antibodies were either purchased preconjugated from Fluidigm or purchased purified and conjugated in-house using the MaxPar X8 Antibody Labeling Kit or the MaxPar MCP9 Antibody Labeling Kit (Fluidigm) according to the manufacturer's instructions. Cells were then stained with PBMCs or a tumor panel of antibodies (Supplementary Table S1) for 30 minutes at +4°C. For PBMCs, samples were washed, fixed, and permeabilized

(Foxp3/Transcription Factor Staining Buffer Set; eBiosciences; cat. #00-55-23-00) for 40 minutes at +4°C before being stained with intracellular antibodies (Supplementary Table S1) for 30 minutes at +4°C. All samples were washed and incubated in Fix and Perm Buffer (Maxpar Fix and Perm Buffer Fluidigm; cat. #201067) for 5 minutes before being fixed in Iridium intercalator (Iridium191/193 Fluidigim; cat. #201192B; 1:4,000) diluted in PBS 1× containing 1.6% formaldehyde for 40 minutes at room temperature. Cells were washed and stored until acquisition at +4°C.

Data Acquisition. Cells were counted, washed, and resuspended in Maxpar Cell Acquisition Solution at 0.5×10^6/mL and mixed with 10% EQ beads immediately before acquisition on a Helios mass cytometer using noise reduction, with event length limits of 10 to 150 pushes. An average of 500,000 events were acquired per sample at a flow rate of 0.03 mL/minute. Mass cytometry standard files were normalized to a global standard determined for each log of EQ beads using CyTOF Software v.6.7.1014 (Fluidigm).

Analyses. Analysis was performed with FlowJo software (Tree Star). Nonevents (doublets and debris, etc.) were removed from the analysis using the Gaussian discrimination channels (center, offset, width and residual) as recommended by Fluidigm. Circulating $CD4^+$ T cells were clustered within and across samples using PhenoGraph (41). One cluster representing less than 0.075% of the total $CD4^+$ T cells (n = 854/1,159,561 cells) was not considered in the following analysis. Clusters were then annotated manually and merged in metaclusters according to their relative expression of PD-1 (relative expression >0: $PD\text{-}1^+$, relative expression = 0: $PD\text{-}1^-$) and effector memory phenotype (Supplementary Table S2). Briefly, naïve, TEMRA, TE, TEM, and TCM were defined as $CD45RA^+CD28^+CD27^+CD127^+$, $CD45RA^+CD28^-$ and/or $CD27^-CD127^{lo}$, $CD45RA^{-/lo}CD28^{-/lo}CD27^{-/lo}CD127^{-/lo}$, $CD45RA^{-/lo}CD28^+CD27^+CD127^{-/lo}$, $CD45RA^{-/lo}CD28^+CD27^{+/lo}CD127^+$, respectively. Then, manual gating was performed on metaclusters to define subsets (helper T cells). Tfh, Th1, Th2, Th17, and other $CD4^+$ T cells were defined as $CXCR5^+CXCR3^{+/-}$, $CXCR3^+CXCR5^-$, $CXCR3^-CXCR5^-CCR4^+$, $CXCR3^-CXCR5^-CCR4^-CCR6^+$, and $CXCR3^-CXCR5^-CCR4^-CCR6^-$, respectively (as illustrated in Supplementary Fig. S1A). Manual gating was performed for the analysis of B cells in PBMC samples (as illustrated in Supplementary Fig. S1B). Briefly, circulating ASCs as well as naïve, memory, nonswitched memory, and double-negative B cells were defined as $CD19^{+/lo}CD38^{hi}Blimp1^+$, IgD^+CD27^-, IgD^-CD27^+, IgD^+CD27^+, and IgD^-CD27^-, respectively. Manual gating was performed for tumor samples from PANDORE (as illustrated in Supplementary Fig. S3). $CD4^+$ TILs and $CD8^+$ TILs from untreated tumors were clustered within and across samples using PhenoGraph.

Flow Cytometry

Sample Preparation after *In Sitro* Tumor Assays. Cells were stained for viability with Zombie Acqua (BioLegend; cat. #423102) for 20 minutes at +4°C. Cells were washed in staining buffer and incubated during 20 minutes at room temperature with a panel of antibodies (Supplementary Table S3, panels 1 and 2) with Brilliant Strain Buffer (BD; cat. #563794). Samples were washed in staining buffer.

Sample Preparation for the Characterization of T_{FH}. Single-cell suspension of dissociated tumor tissue was centrifuged at 1,350 rpm for 5 minutes at +4°C and resuspended with FACS buffer (PBS 1×, 2% BSA, 2 mmol/L EDTA), 50 µL/staining conditions. For blocking nonspecific Fc-mediated interactions, cell suspension was incubated with 5 µL of Human TruStain FcX (Fc Receptor Blocking Solution, BioLegend; cat. #422302) at 4°C for 15 minutes. After the FcR blocking step, anti-human CXCR5 antibody was added to the FcR blocked cell suspension (2 µL/staining condition) and incubated for 20 minutes at +4°C. Combined conjugated antibodies against cell-surface markers (Supplementary Table S3, panels 3 and 4) as well as Zombie Aqua Fixable Viability in an appropriate volume of Brillant Violet staining buffer (BD; cat. #563794) so that the final staining volume was 100 µL (i.e., 50 µL of cell sample + 50 µL of antibody mixture) was added to the cell suspension. Stained cell suspension was incubated for 20 minutes at 4°C and washed twice with FACS buffer. For intracellular staining, after the final wash, cell suspension was fixed with 1× Foxp3 Fixation/Permeabilization working solution (eBioscience Foxp3/Transcription Factor Staining Buffer Set; cat. #00-5523-00) 35 to 40 minutes at room temperature and protected from light. Then, cell suspension was washed twice with 1× Permeabilization Buffer. The cell pellet was resuspended into 100 µL with 1× Permeabilization Buffer combining conjugated antibodies for the detection of intracellular antigens and incubated 20 minutes at 4°C, protected from light. After incubation time, stained cells were washed twice with 1× Permeabilization Buffer and the cell pellet was resuspended with FACS buffer.

Data Acquisition. Samples were acquired on a BD LSRFortessa X-20 Flow Cytometer.

Analyses. Analysis was performed with FlowJo software (Tree Star). The gating strategy is shown in Supplementary Fig. S4.

In Sitro *Tumor Assays*

One out of 18 samples was processed after thawing, and the others were performed freshly. Dissociated bladder cancers were stained for D0 (baseline) with mass cytometry as described in the section.

One hundred thousand $CD45^+$ cells per well were incubated in complete medium [RPMI 1640 supplemented with 10% human AB serum (Institut Jacques Boy; cat. #201021334), 1% penicillin/streptomycin (GIBCO Invitrogen; cat. #15140-122), 1% L-glutamine (GIBCO Life Technologies; cat. #25030-024), and 1% sodium pyruvate (GIBCO Life Technologies; cat. #11360-039)] in a 96-well U-bottom plate. Isotype controls (IgG4 and IgG1; BioLegend; cat. #403702 and #403502, respectively; at 25 µg/mL and 5 µg/mL, respectively), recombinant IL2 (PeproTech; cat. #200-02-11, at 10 µg/mL), and anti-CD3 (Thermo Fisher Scientific, clone OKT3, at 10 µg/mL) + anti-CD28 (Thermo Fisher Scientific, clone CD28.2, at 10 µg/m) were added to control wells. AC anti–PD-1 (pembrolizumab, from Merck, at 25 µg/mL) and AC anti-CD38 (daratumumab, from Janssen-Cilag, at 5 µg/mL) were added to tested wells. Plates were incubated at +37°C with 5% CO_2 for 3 days. After incubation, cells were centrifuged at 1,500 rpm for 5 minutes. The supernatants were collected and stored at −20°C until measurements. The pellets were resuspended in PBS 1× for flow cytometry staining.

For *in sitro* assays using bacteria, cells were resuspended in an appropriate volume of TheraPEAK X-VIVO-15 Serum-free Hematopoietic Cell Medium (TheraPEAK X-VIVO-15, Lonza; cat. #BEBP02-061Q) supplemented with penicillin/streptomycin (Gibco, Invitrogen; cat. #15140-122) extemporaneously and plated at 1×10^5 $CD45^+$ cells/well in a 96-well U-bottom plate. Stimulation agents [heat-killed *E. coli* Q1696 (3×10^6/well), heat-killed *S. capitis* (3×10^6/well), R848 (Invivogen; cat. #tlrl-r848; final concentration: 1 µg/mL) + IL2 (PeproTech; cat. #200-02-11; final concentration: 1×10^3U/mL), and IL21 + IL4 + anti-CD40 (Human B-Poly-SE, Immunospot; cat. #CTL-hBPOLYSE-35)] were prepared extemporaneously and added to cell culture before incubation at 37°C in a humidified atmosphere of 5% CO_2 during 3 days.

Immune Response against Commensals

Bacterial Strains and Culture Conditions. Cultivable bacteria, relevant in bladder cancer patients, *E. coli* (Q1696, IHU Marseille, urine from noncancer patient), *Fusobacterium nucleatum* (P6429), *Bacteroides fragilis* (Ileon6), *E. faecalis* [Gustave Roussy (GR), urine from cancer patient], *S. capitis* (feces from kidney cancer patient nonresponder to

ICBs, EverImmune), *Staphylococcus epidermidis* (GR, urine from cancer patient), *Streptococcus mitis* (GR, urine from healthy volunteer), *Streptococcus sanguinis* (GR, urine from cancer patient), and BCG (Sanofi) were plated onto sheep's blood agar plates (COS, BioMérieux) at 37°C with 5% CO_2 in anaerobic or aerobic conditions for 48 hours and identified by Matrix Assisted Laser Desorption Ionization–Time of Flight (MALDI-TOF) mass spectrometry (Andromas; Beckman Coulter).

Assessing CD4⁺ T-cell Memory Responses. The experiments were performed as much as possible in paired settings assessing the reactivity of pre- and post-memory CD4⁺ T cells during the same experiment.

Generation of Monocyte-Derived Dendritic Cells. Frozen PBMCs were thawed, washed, and resuspended in monocyte-derived dendritic cell (mo-DC) medium (RPMI 1640 supplemented with 10% human AB, 1 mmol/L of glutamine, 1% sodium pyruvate, 1% HEPES, 1% penicillin/streptomycin). Viability and count were evaluated using a Vi-Cell XR Cell Counter. Cells were then cultured at 5 M/mL in 24-well flat-bottom plates (5M cells/well) for 2 hours at 37°C and in 5% CO_2 and separated into adherent and nonadherent cell populations. The nonadherent fraction, containing peripheral blood lymphocytes (PBL), was slowly collected, washed, and resuspended in PBL media [IMDM (Sigma-Aldrich; cat. #I3390-500 mL, supplemented with 10% human AB, 1 mmol/L glutamine, 1% sodium pyruvate, 1% HEPES, 1% penicillin/streptomycin, and 100 IU/mL rhIL2 premium grade (Miltenyi Biotec; cat. #130-097-745)]. PBLs were seeded in 24-well, round-bottom plates and cultured for 3 days at 37°C and in 5% CO_2. The adherent fraction was cultured for 67 hours at 37°C in 5% CO_2 in mo-DC differentiating medium (mo-DC media with GM-CSF (1,000 IU/mL, Miltenyi Biotec; cat. #130-093-867) and IFNα2b (250 IU/mL, Introna, MSD France). The volume defined to get 5 M/mL was used to resuspend PBLs and to add on the adherent fraction.

mo-DC Bacteria Cocultures. After incubation, plates containing mo-DCs were incubated for 20 minutes on ice. mo-DCs (adherent and nonadherent fraction) were harvested by flushing with cold mo-DC medium without antibiotics and washed. Cells were then counted using a hemocytometer, and the suspension was adjusted to 0.125 M/mL of mo-DC. Five thousand mo-DCs were seeded in 96-well, round-bottom plates. Bacterial suspensions containing *E. coli* (IHU Marseille, urine from noncancer patient), *S. sanguinis* (GR, urine from cancer patient), and *S. capitis* (feces from kidney cancer patient nonresponder to ICBs, EverImmune) were prepared by adjusting the turbidity at 0.3 MacFarlan in 2 mL of NaCl 0.9% (200M bacteria). The suspensions were centrifuged at 4,000 rpm for 10 minutes at +4°C and resuspended in 4 mL of mo-DC medium without antibiotics to get 50 M/mL. A multiplicity of infection of 100 was used corresponding to 500,000 bacteria per well. The plates were then centrifuged for 2 minutes at 1,000 rpm and incubated at 37°C and in 5% CO_2 for 2 hours. Wells with mo-DC alone were prepared as negative control. Wells with mo-DCs, LTA (10 ng/mL final, InvivoGen; cat. #tlrl-pstla), or LPS (10 ng/mL final, InvivoGen; cat. #tlrl-3pelps) with memory CD4⁺ T cells were also prepared as negative control. After incubation, mo-DC media with antibiotics were added to each well.

Isolation of Memory CD4⁺ T Cells and Cocultures with Bacteria. Frozen PBMCs obtained before and after pembrolizumab were thawed, washed, and resuspended in an isolation buffer (PBS 1× + 0.5% BSA + 2 mmol/L EDTA). For some experiments, PBL cultured in IL2 were pooled with fresh thawed PBMCs from the same time point. CD4⁺CD45RO⁺ T cells were isolated using the memory CD4⁺ T-cell isolating kit (Miltenyi Biotec; cat. #130-091-893) according to the manufacturer's instructions. All the steps were performed on ice. The fraction of memory CD4⁺ T cells was resuspended at 0.5 M/mL, and 100 μL was added to each well containing the mo-DC loaded with bacteria. Memory CD4⁺ T cells (without mo-DC) alone or with CD3/CD28 beads (10,000 Dynabeads per well, Dynabeads T Activator, Thermo Fisher Scientific; cat. #11131D) were used as negative and positive controls, respectively. mo-DC loaded with bacteria (without memory CD4⁺ T cells) were also cultured. The cocultures were incubated for 48 hours at 37°C in 5% CO_2. Supernatants were harvested and stored at −20°C for the determination of IFNγ, IL10, and CXCL13, as measured by commercial ELISA (details in the "Soluble factor measurements" section).

Bacterial Flow Cytometry Assay. Colonies of bacteria were picked, suspended in 1× PBS–10× glycerol at 10^9 colony-forming units (CFU)/mL using spectrophotometer [optical density (600 nm) = 1] and frozen at −80°C. An accurate quantification of CFUs was then performed by counting bacterial events on a flow cytometer (PANDORE study: Cytoflex, Beckman Coulter; validation cohort: Canto, BD).

The IgG and IgA titers were defined with Optilite analyzer (Binding Site). All buffers were sterilized by filtration with a membrane with 0.22 μm pores. Sera were normalized at 20 μg/mL IgG or IgA in PBS 1×, 2% BSA (Sigma-Aldrich), and 0.02% sodium azide (Sigma-Aldrich). Specific serum antibody levels against purified strains were measured using a flow cytometry assay, as previously described (79). Bacterial strains (10^6) were suspended in PBS 1×, 2% BSA, and 0.02% sodium azide in a 96-well, V-bottom plate. Twenty-five microliters of normalized sera [patients' samples or human normal immunoglobulin (IVIG, Flebogamma, Instituto Grifols) was used as a positive control or PBS as a negative control] were added to the 96-well V-bottom plate at a final concentration of 10 μg/mL, and the plates were incubated for 30 minutes at +4°C. After washing with PBS 1× (10 minutes, 4,000 *g*, +4°C), plates were incubated with secondary conjugated antibodies (1/400e)—either a goat anti-human IgA FITC AffiniPureGoat α chain specific or IgG Alexa Fluor 647 (or 488) AffiniPureGoat Fcγ fragment specific or isotype controls as negative controls (all from Jackson ImmunoResearch; cat. #109-095-011; cat. #709-116-073; cat. #009-090-011; and cat. #005-600-003) for 20 minutes at +4°C. Then, bacteria were washed, fixed in 25 μL paraformaldehyde (4% in PBS 1×; eBioscience) for 10 minutes at room temperature, and resuspended in sterile PBS. We used three different cytometers for three independent experiments; samples were run using a Cytoflex (Beckman Coulter for PANDORE study), another Cytoflex (Beckman Coulter for the validation cohort 2), and a Canto (BD for the validation cohort 3), and 30,000 bacterial events were acquired. Analysis was performed with FlowJo software (Tree Star). MFIs were used to measure mAb binding levels against the specific strains. For each experiment, we calculated stain index (SI) with sample MFI minus negative control MFI divided by twice the standard deviation of batch MFI (SD):

$$\mathrm{SI} = \frac{\text{sample MFI patient} - \text{negative control MFI}}{2 \times \mathrm{SD}}.$$

For each experiment, the SD was defined using the isotype control for each plate and each strain of bacteria.

As we performed three independent experiments, MFI measurement resulted in variation due to flow cytometer variabilities. Normalization of the data was performed intraexperiment, but interexperiment comparisons are therefore impossible.

Soluble Factor Measurements

Multiplex Immunoassays. Plasma from PANDORE was thawed at +4°C overnight and then centrifuged for 15 minutes at 1,000 × *g*. Plasma was monitored using a Bio-Plex Pro Human Cytokine 40-plex Assay (Bio-Rad; cat. #71AK99MR2) according to the manufacturer's instructions. Supernatants from *in sitro* assays were monitored using a Bio-Plex Pro Human Cytokine 27-plex Assay (Bio-Rad; cat.

#M500KCAF0Y) and a Bio-Plex Pro Human Cytokine 40-plex Assay (Bio-Rad; cat. #71AK99MR2; for *in sitro* stimulation with bacteria) according to the manufacturer's instructions.

Acquisitions and analyses were performed on a Bio-Plex 200 system (Bio-Rad) and using Bio-Plex Manager 6.1 Software (Bio-Rad), respectively.

ELISA. CXCL13 in the *in sitro* supernatants was detected using the Human CXCL13/BLC/BCA-1 Quantikine ELISA Kit (R&D Systems; cat. #DCX130) according to the manufacturer's instructions.

Supernatants from *in vitro* stimulations with bacteria were monitored using the Human CXCL13/BLC/BCA-1 Quantikine ELISA Kit (R&D System; cat. #DCX130), ELISA MAX Deluxe Set Human IFNγ (BioLegend; cat. #430116), and ELISA MAX Deluxe Set Human IL10 (BioLegend; cat. #430604) according to the manufacturer's instructions.

Immunoglobulin Isotyping. Supernatants collected immediately after digestion and supernatants from *in sitro* stimulations with bacteria were evaluated for immunologlobulin isotyping using the Procartaplex antibody isotyping panel 7-plex kit (Thermo Fisher Scientific, ProcartaPlex Human Antibody Isotyping Panel 7-Plex Kit; cat. #EPX070-10818-901) according to the manufacturer's recommendations. Supernatants after *in sitro* stimulations were prediluted 1:20 in fresh complete cell culture media.

Tissue Analyses

IHC, Multiplex Immunofluorescence, and PD-L1 Assessment. FFPE samples corresponding to representative slides of TURBT and cystectomies with invasive UC (IUC) were sequentially cut at 3 µm of thickness. HES staining was performed in the first cut, so IHC and immunofluorescence stainings for CD3, CD8, $CD8^-$PD-L1, $CD4^-CD38^-$PD-1, $CD4^-CD38^-$IgG4, CD20, LPS, IgG, IgA, and $CD4^-$BCL6 could be performed in the subsequent ones. CD20 and IgG immunostain was performed by an anti-CD20 (DAKO; cat. #MO755, 1/100 dilution) and an anti-IgG (Abcam, #ab2410, 1/100 dilution) on a Benchmark Ultra (Roche) autostainer system. FFPE sections were deparaffinized, and subsequently antigen retrieval was conducted with CC1 buffer (pH = 8) for 36 and 64 minutes, respectively. IgA and LPS immunostaining was performed by an anti-IgA (Abcam, #ab2411, 1/200 dilution) and an anti-LPS (HycultBiotech; cat. #HM6011, 1/6,000 dilution) on a BOND-RX (Leica) autostainer system. Briefly, FFPE sections were deparaffinized, and subsequently antigen retrieval was conducted with ER1 buffer (pH = 6) for 20 and 30 minutes, respectively. Immunostained slides were revealed with the Ultraview DAB kit from Roche (CD20 and IgG) or Refine DAB from Leica (LPS and IgA). DAB chromogen was used to visualize the immunostain. Double immunostaining for CD4-BCL6 was performed by an anti-BCL6 (Dako, #M7211, 1/500 dilution) and anti-CD4 (Spring, #M3354, 1/30 dilution), in that order, on a Discovery Ultra Roche autostainer. FFPE sections were deparaffinized, and subsequently antigen retrieval was conducted with CC1 buffer (pH = 8) for 92 minutes. BCL-6 was amplified by HQ thyramide and revealed by the HQ-HRP kit, coupled to TEAL chromogen, whereas CD4 was revealed with an anti-rabbit UltraMap, coupled to DAB chromogen. A sequence of denaturation was done between the two immunostains in a CC2 buffer (pH = 6). Slides were mounted with CYTOSEAL (Fisher Scientific, #8312-4). Chromogenic slides were counterstained with hematoxylin (5–8 minutes). Triplex immunofluorescence was performed on a BOND-RX (Leica) autostainer system and an OPAL (Akoya) system. In short, FFPE sections were deparaffinized, and subsequently antigen retrieval was conducted with ER2 buffer (pH = 9) for 20 minutes. First, antibodies were added, starting with PD-1 (R&D Systems; cat. #AF1086, 1/50 dilution), CD38 (Cell Signaling Technology; cat. #51000, 1/6,000), and then CD4 (Spring; cat. #M3364, 1/400). Staining was performed using the OPAL690 polymer with OPAL520 (1/400), OPAL570 (1/1200), and OPAL690 (1/50), respectively. Second, antibodies were added, starting with CD38 (Cell Signaling Technology; cat. #51000, 1/6,000), IgG4 (Epitomics; cat. #AC-0148, 1/3,000), and CD4 (Spring; cat. #M3364, 1/400). Staining was performed using the OPAL690 polymer with OPAL570 (1/500), OPAL520 (1/100), and OPAL690 (1/100), respectively. Baseline PD-L1 IHC was performed by an anti–PD-L1 IHC 22C3 (Dako; cat. #M3653, 1/25 dilution) on a BOND-RX (Leica) autostainer system. In short, FFPE sections were deparaffinized, and subsequently antigen retrieval was conducted with ER2 buffer (pH = 9) for 20 minutes. An experienced pathologist (J.-Y. Scoazec) determined the CPS, and PD-L1 positivity was qualified as CPS≥10.

Evaluation of TLS. Microscopic examination of HES-stained TURBT and cystectomies from patients with IUC was performed by a pathologist (L. Lordello) in order to morphologically identify TLS (LA, primary follicle–like, and secondary follicle–like). The analysis was performed in the single most representative HES slide. LA were determined as vaguely nodular aggregates of small noncleaved lymphoid cells, usually with more than 250 and fewer than 500 cells, without two or more of the early germinal center elements (follicular dendritic cells, centroblasts, mantle zone, or high endothelial veins); primary follicle–like TLS were determined as nodular aggregates of predominantly small lymphoid cells, usually with more than 500 cells, with three or more of the follicular elements, but without late germinal center elements (tinged body macrophages or dark/light areas of a clear germinal center, marginal zone); and secondary follicle–like TLS were determined as lymphoid follicles showing late germinal center structures.

Evaluation of CD20. Evaluation of CD20 was performed in a single slide in order to determine the presence of B cells in more than 50% of LA. Whole slide images (WSI) at magnifications of 20× and 40× were obtained with an Olympus scanner VS120, respectively, for HES and CD20 stainings for TURBT and cystectomies. The images were analyzed by QuPath software, version 0.2.3. TLS were annotated in WSIs in order to determine the best fit for CD20-positive dense areas (Supplementary Fig. S2). Using a simple tissue detection tool (threshold 165, requested pixel size 15, minimum area 10^4 µm^2, max fill area 10^6 µm^2, smooth image, cleanup with median filter, expand boundaries, and smooth coordinates), TLS areas were automatically annotated, whereas artifact areas were manually excluded by a pathologist (L. Lordello). The percentage of TLS area was calculated based on the whole tissue area, which had also been annotated in the WSI. Also, tumor areas were manually annotated on CD20 slides, based on HES, by a pathologist (L. Lordello).

Evaluation of $CD4^+CD38^+PD\text{-}1^+$ and $CD4^+CD38^+IgG4^+$ Populations in FFPE Samples. Immunofluorescence was performed for the identification of triple staining corresponding to $CD4^+CD38^+PD\text{-}1^+$ (one slide for each TURBT and cystectomy) and $CD4^+CD38^+IgG4^+$ (one slide for selected TURBT and each cystectomy) cells in TURBT and cystectomies. WSIs were obtained with an Olympus scanner VS120 for immunofluorescence triple staining (exposure time: 5 ms for DAPI, 30 ms FITC, and 200 ms CY3 and CY5).

Geodistribution of $CD4^+CD38^+PD\text{-}1^+$ and $CD4^+CD38^+IgG4^+$ in FFPE Samples. Tumor and TLS annotated areas on CD20 slides were matched to density maps generated on WSIs from triplex stainings on QuPath in order to define where $CD4^+CD38^+PD\text{-}1^+$ and $CD4^+CD38^+IgG4^+$ populations were located. Populations identified with the IgG4-triplex were counted within three TLS areas. L. Lordello delineated the TLS areas.

Quantification and Phenotyping of Cells. The images were analyzed by QuPath software, version 0.2.3 (80). For each panel (CD38/CD4/PD-1 and CD38/CD4/IgG4), three different classifiers, based on

fluorescence intensities, were then combined to phenotype the cells. In TLS areas, cells were detected on the DAPI channel with the cell detection tool (detection channel: DAPI, requested pixel size 0.5 μm, background radius 12 μm, median filter radius 0.5 μm, sigma 1 μm, minimum area 10 μm^2, maximum area 400 μm^2, threshold 80, split by shape, cell expansion 2 μm, include cell nucleus, smooth boundaries, make measurements). The resulting densities were expressed as the number of cells of each phenotype per square millimeter of tissue.

Immunoscore IC and Assessment of CD3$^+$ and CD8$^+$ Cells

IHC. Immunoscore IC (Veracyte) is an assay designed to measure the densities of PD-L1$^+$ and CD8$^+$ cells as well as the proximity between these cells on a single tissue section with image analysis tools. IHC-based staining was performed on Benchmark XT instrument (Roche-Ventana) as follows: standard deparaffinization, Cell Conditioning 1 for 54 minutes, anti–PD-L1 (clone HDX3) incubation at 37°C for 60 minutes, anti-CD8 (clone HDX1) incubation at 37°C for 60 minutes, and Hematoxylin II counterstaining for 8 minutes. Anti–PD-L1 and anti-CD8 antibodies were revealed with OptiView DAB IHC Detection Kit and ultraView Universal Alkaline Phosphatase Red Detection Kit, respectively. Immune infiltration of tumors by CD8$^+$ and CD3$^+$ cells was assessed on two adjacent tissue sections followed by Digital Pathology analysis with a dedicated software. Staining was adapted from Marliot and colleagues (81).

Digitization. Every stained slide was scanned with a high-resolution scanner (NanoZoomer XR, Hamamatsu) to obtain 20× digital images for subsequent analysis by digital pathology.

Digital Pathology. WSIs were analyzed on the HALO platform (Indica Labs) and consisted of (i) detection of the tissue section and definition of the tumor core and (ii) detection and quantification of stained cells. Subsequently, cell coordinates and phenotypes were exported to analyze their spatial distribution.

The main computed variables were CD3$^+$ cell density (cells/mm^2), CD8$^+$ cell density, PD-L1$^+$ cell density, proximity between CD8$^+$ and PD-L1$^+$ cells, and clustering of CD8$^+$ or PD-L1$^+$ cells. Arbitrarily, cutoff distances used to compute proximity and cluster indexes were set to 20 μm.

Evaluation of Bacteria in FFPE Samples

Morphologic Evaluation. Microscopic evaluation of morphologic structures that could indicate the presence of bacteria in TURBT samples was performed by a pathologist (L. Lordello). Cystic-like structures, sometimes present in cytoplasmic vacuoles filled with round or ovoid basophilic elements, were identified not only in nontumoral urothelial epithelium but also in tumor cells corresponding to IUC. These structures were quantified on the single HES slide corresponding to TURBT (33 slides). After an overview of the slide, the zone with the highest density of structures was evaluated by counting 2,000 urothelial cells, corresponding to either tumor or nontumoral urothelium, when present in the sample. Density was presented as normalized by the total number of structures/2,000 counted cells in either tumoral or nontumoral areas.

LPS Staining. IHC for LPS was performed in order to identify the occasional presence of bacteria in the samples. A group of at least five positive cells showing granular cytoplasmic staining in tumor cells corresponding to IUC was expected for the case to be considered positive. Also, normal urothelial epithelium, immune cells, and cystic-like structures were evaluated for LPS staining when present. Slides corresponding to TURBT were evaluated for LPS (33 slides).

FISH for All Bacteria, *E. coli*, and UPEC. FFPE deparaffinized slides corresponding to representative slides of TURBT with IUC were sequentially cut at 3 μm of thickness. FISH was carried out as previously described (82), with the following modifications. For permeabilization of the tissues, slides were incubated for 5 minutes in a proteinase K solution (10 μg/mL) at 56°C, followed by a distilled water rinsing step. Hybridization was performed at 60°C for 3 hours using 16sRNA Eub338 (GCTGCCTCCCGTAGGAGT) for all bacteria and 5′–3′ probes for *uidA* (F: CGCCGATGCAGATATTCGTA and R: CTGCCAGTTCAGTTCRTTGT) targeting all *E. coli*, *chuA* (F: GCTAC CGCGATAACTGTCAT and R: TGGAGAACCGTTCCACTCTA), *c3686* (F: TTGCACCAACAACGTCTACC and R: TCTGCGTCTTCTACCAT CAC), and *c3509* (F: ACAATCCGCCACCATCCAG and R: CTCTC CACCGGAGAGTGTT) for UPEC (60). The probes for all bacteria and all *E. coli* were coupled to Alexa 647 (Eurogentec), and the ones for UPEC were coupled to Alexa 488 fluorochrome (Eurogentec). Excess probes were removed by rinsing for 5 minutes in degrading series dilutions of saline–sodium citrate solution (4×, 2×, 1×, 0.5×, and water). Slides were then air-dried at room temperature in the dark. DAPI was used for nuclear staining. Slides were observed using the confocal microscope LSM800 with three excitation wavelengths: 595 to 600 nm for all bacteria and all *E. coli* signals, 493 nm for UPEC, and 353 nm for DAPI.

Similarly, FISH for UPEC was positive in four of the five TURBT slides tested, which were selected on the basis of positivity for LPS as well as the highest number of cytoplasmic granular structures and positive cells in different compartments (tumor, nontumor, and immune urothelial cells).

Scanning Electron Microscopy. FFPE deparaffinized slides (see "IHC, multiplex immunofluorescence, and PD-L1 assessment") were stained for 5 minutes using a 10% phosphotungstic acid solution, rinsed using distilled sterile water, and dried at room temperature. Slides were then sputtered with a 5-μm thick platinum layer using ion sputter MC1000 (Hitachi) and imaged on an SU5000 SEM (Hitachi). All acquisition settings are visible on the micrographs.

Transmission Electron Microscopy. A tissue cylinder of 2 mm was obtained from the regions of interest from FFPE blocks and processed as described (83). After rehydration, samples were kept for 4 days in glutaraldehyde 2.5% and HEPES 0.1M at 4°C. Then, samples were washed three times with PHEM 1× for 10 minutes. A second fixation was performed with OsO4 2% and potassium ferricyanide 1.5% in water for 2 hours. Then, samples were washed three times with water. Dehydration was performed with continuous agitation using ethanol 25%, 50%, 75%, and 95% for 15 minutes, ethanol 100% for 20 minutes, three times followed by propylene oxide for 15 minutes. Then, incubation occurred with propylene oxide/Epon A + B + DMP30 using continuous agitation overnight, and biopsies were washed three times with Epon A + B + DMP30 for 2 hours of continuous agitation. Samples were put at 60°C for 48 hours. Sections with a thickness of 70 nm were cut with a Leica UCT microtome and collected on carbon/formvar-coated copper grids. Sections were contrasted with 4% aqueous uranylacetate and Reynold's lead citrate. Stained sections were observed with a Tecnai spirit FEI operated at 120 kV. Images were acquired with an FEI Eagle digital camera. Structures corresponding to bacteria were photographed when showing membrane enhancement and core distinction from mitochondrial or lysosomal contents.

Evaluation of CD4$^+$BCL6$^+$ Cells. Representative cases were selected for immunostaining of CD4-BCL6 (one slide for each selected case), based on clinical and triple staining parameters (highest densities for CD4$^+$CD38$^+$PD-1$^+$ cells). WSIs at a magnification of 20× were obtained with an Olympus scanner VS120 for TURBT and cystectomies. Then, images were analyzed by QuPath software, version 0.3.2. TLS were manually annotated in the WSI corresponding to TURBT or cystectomy from selected cases by a pathologist (L. Lordello). Using the cell detection tool (detection image optical density sum, requested pixel

size 1 μm, background radius 40 μm, median filter radius 0 μm, sigma 1.2 μm, minimum area 5 μm^2, maximum area 100 μm^2, threshold 0.1, max background intensity 2, split by shape, cell expansion 1.5 μm, include cell nucleus, smooth boundaries, make measurements), cells were automatically detected. Best thresholds for DAB (0.371, 0.553, 0.746) and blue (0.982, 0.154, 0.107) chromogens were identified based on the distribution of immunostains compared with morphology for expected CD4- and BCL6-positive areas. Sequentially, a composed classifier was created using channels for CD4 (DAB) and BCL6 (blue), regarding nucleus DAB/blue (residual) optical density mean, with thresholds of 0.15 and 0.2, respectively. The single and double positivity were calculated based on WSI or TLS annotated areas, which matched the original annotated areas on CD20 WSI.

Evaluation of IgG$^+$ and IgA$^+$ Cells. Representative cases were selected for immunostaining of IgG and IgA (one slide each immunoglobulin for all selected cases) based on clinical and serologic parameters. WSIs at a magnification of 20× were obtained with an Olympus scanner VS120 for TURBT and cystectomies. Then, images were analyzed by QuPath software, version 0.3.2. Five regions of interest measuring 1 mm^2 each, representative of similar peritumoral areas with increased immune cell infiltrate, and present in both IgG and IgA slides (sequential slides) were included for each case in paired TURBT and cystectomy. IgG- and IgA-positive cells, mostly corresponding to plasma cells, were automatedly counted by QuPath fast cell counts (DAB, Gaussian sigma 1.5 μm, background radius 15 μm, use difference of Gaussians, cell detection threshold 0.1, DAB threshold 0.2)and then manually corrected by a pathologist (L. Lordello). As blood vessels were commonly stained due to the presence of free immunoglobulin, these areas, including endothelial and some perivascular cells, were not included in the counting. Then, the mean count of IgG$^+$ and IgA$^+$ cells was calculated considering the five regions of interest, and a ratio between IgG$^+$/IgA$^+$ cells was calculated. This ratio was used to evaluate changes between paired RTUV and cystectomies. TLS were manually annotated in the WSI corresponding to TURBT or cystectomy from selected cases by a pathologist (L. Lordello).

Bacteria Identification by qPCR Detection

Total genomic DNA from bladder tissues was extracted with the DNeasy Blood and Tissue Kit (Qiagen; cat. #69506) following the manufacturer's recommendation and using spin-column purification. Measurement of extracted DNA was performed using NanoDrop and normalized to 10 ng/μL. Genomic DNA was analyzed by PowerUp SYBR Green Master Mix (Invitrogen) according to the manufacturer's instructions (2′ 50°C, 10′ 95°C, 45 cycles with 15″ 95°C and 1′ 60°C followed by 15″ 95°C, 1′ 60°C and 15″ 95°C) using Quant Studio 3 (Applied Biosystems). Expression was normalized to the expression of the total bacterial load determined by the Universal 16S RNA gene by means of the $2^{-\Delta Ct}$ method. All primers were from Thermo Fisher Scientific. We used: ACT-CCT-ACG-GGA-GGC-AGC-AGT (all bacteria-F), ATT-ACC-GCG-GCT-GCT-GGC (all bacteria-R), CATGCCGCGTGTATGAAGAA (*E. coli*-F), and CGGG TAACGTCAATGAGCAAA (*E. coli*-R).

Culturomics of MIBC

A trained pathologist (C. Radulescu) processed the tissues in sterile conditions.

The following operations were carried out in a laboratory with Biological Safety Level 2 and under a class II Microbiological Safety Station in order to avoid and limit any contamination. All materials were disinfected with 70°C alcohol.

Sample Preparation

Partitioning. When identifiable, we separated the fresh tissue into layers (muscle, fat, and mucosa) from the tumor and the non-tumor tissues. RPMI used for the transport of the tissues was also analyzed separately.

Processing. Pestle Motor Mixer (Argos Technologies) and Homogen Sys 1.5 mL Pestle (SP Scienceware) were used to mix tissue samples.

We split each sample into 1 g of tissue per 5 mL of NaCl 0.9%.

Culture Conditions

Solid Culture Using Plates. One hundred microliters of each sample were diluted with 900 μL of NaCl; 1/10th and 1/100th dilutions were performed. A total volume of 200 μL of each dilution was used for culturing directly on 5% sheep blood–enriched Columbia Agar (COS; BioMérieux). Plates were incubated in aerobic and anaerobic atmospheres at 37°C.

Liquid Culture. Aerobic and anaerobic blood culture bottles (BD BACTEC Plus Aerobic medium; BD BACTEC Lytic Anaerobic medium) supplemented with sterile a 0.2 μm-filtered rumen (3 mL) and sheep blood defibrinated (Oxoid Limited; 3 mL) were used. Bottles were incubated at 28°C and 37°C. For each sample, 1 mL was inoculated into each of the two bottles using a syringe needle. Supplemented bottles (without samples) were used as negative controls. These vials were then processed according to the specimen to check for any contamination.

The anaerobic atmosphere was generated using an anaerobic jar (W-Zip Plastic*Pouches*, Oxoid Limited) and an atmosphere generator (GENbox aner, BioMérieux).

Isolation and Identification

Isolation. COS plates were routinely checked, and CFUs were identified as below. For liquid cultures, on days 1, 3, 7, 10, 15, and 20, 100 μL of each sample from the BD BACTEC vials was diluted with 900 μL of NaCl 0.9%. A dilution series ranging from 1/10 to 1/100 was performed. A total volume of 200 μL of each dilution was cultured in COS plates and incubated under the same conditions as the initial bottle. Anaerobic conditions were cultivated for 5 days, whereas aerobic conditions were cultivated for 3 days. The colonies were manually subcultured onto COS plates for Matrix Assisted Laser Desorption/Ionization Time-of-Flight (MALDI-TOF) mass spectrometry (MS) identification.

Strain Identification by MALDI-TOF MS. Bacterial colonies were identified using MALDI-TOF MS (Bruker France Daltonics). Each deposit was manually performed and then covered with 2 μL of a matrix solution (HCCA-portioned–Matrix for Maldi-TOF-MS measurements in microorganism identification–(Bremen) with 500 μL of Solution OS (acetinitrile 50%/water 47.5%/trifluoroacetic acid 2.5%; LCH CHIMIE). This analysis was performed using a MicroFlex mass spectrometer (Bruker France Daltonics) according to the manufacturer's recommendations. The acquired spectrum was then loaded into the MALDI Biotyper Software (Bruker France Daltonics) and analyzed using the standard pattern-matching algorithm, which compared the spectrum acquired with that present in the library (Bruker database, constantly updated). Score values of ≥1.7 but <2 indicated identification beyond the genus level, and score values of ≥2.0 indicated identification at the species level. Scores of <1.7 were interpreted as not relevant. An isolate was labeled as correctly identified at the species level when at least one of the colony's spectra had a score ≥1.9 and one other of the colony's spectra had a score ≥1.7 (84).

DNA Extraction, Libraries, and Analyses from TURBT Samples

Six slides of FFPE tissues (TURBT samples) of 10 μm were used per patient.

DNA Extraction. The FFPE samples were extracted with the Maxwell Promega for the extraction of genomic DNA with the Maxwell RSC DNA FFPE Kit (Promega; cat. #AS1450) according to the manufacturer's instructions. Proteinase K treatment was done overnight at 56°C and finalized at 80°C for 4 hours. Samples were then treated with RNAse before the extraction process.

Libraries. The panel targets all tumor suppressors or oncogenes covering the complete sequencing of the codifying region of a total of 411 genes and identifies point mutations, including single-nucleotide variants and small indels. The detection of copy-number variations (gains and losses of chromosomes or complete chromosomal arms) throughout the genome to specific genes and even exons was based on the coverage ratio. The total size of this panel is 1,739,310 bp. The custom panel uses the SureSelect XT HS kit (Agilent) designed for small amounts of FFPE DNA as input and detects low allelic frequencies. After the enzymatic fragmentation of 50 to 200 ng of tumoral gDNA from each sample to an average of 200 to 400 bases, the full preparation was done on Bravo equipment option B (Agilent). Library quality control was performed on Tapestation 2000 and the commercial kits D1000 reagents and D1000 ScreenTape (Agilent). DNA samples were end-repaired, dA-tailed, and ligated to the molecular-barcoded adapter system and purified using AMPure XP beads. Pooled libraries containing captured DNA fragments were subsequently sequenced on a NovaSeq 6000 platform (Illumina) as 2 × 150-bp paired-end reads. Sequences were demultiplexed using an in-house tool.

Analysis. The data analysis pipeline included the following algorithms developed internally: BWA-MEM v-0.7.12 for read alignment to the hg19 human reference genome and Samtools v-1.2 and Picard-tools v-1.139 for PCR duplicate quantification and removal. GATK Haplotype v-3.4-46, snpEff v-4.0, and MutaCaller-1.7 (home pileup internally developed) were used for variant calling and classification. Variants were called with a minimum allelic frequency threshold of 1% for already classified variants (those known in the internal database) and 5% for nonclassified variants, and a read depth threshold of 30× for the total reads at the variant location and at least 10× for the variant.

Several filters were applied to further select for potentially relevant variants among the called variants. The population databases Exac and gnomAd were used to automatically filter out polymorphism as soon as the population frequency was higher than 0.5%. Nonclassified variants (not known in the internal database) were excluded if the intrarun recurrency was superior to 4.

The tumor mutational load was assessed with the Mercury solution (Integragen) calculated by dividing the number of somatic mutations by the number of bases having a depth greater than 10. We used the data published by Lawrence and colleagues (85). The somatic mutations used for the mutational load were filtered as follows: somatic score >3, mutated allele frequency in tumor tissue ≥5%, mutated allele count in tumor tissue ≥3, population heterozygous internal database frequency ≤1%, population homozygous internal database frequency ≤1%, and EVS and 100G and Exac variant frequency ≤0.5% and consequences on protein: stop, start, missense, and splice for the SNPs and in-frame and frameshift for the indels.

Single-cell RNA-seq

Frozen samples were thawed in complete RPMI, counted, and washed in PBS 1× +0.5% BSA+2 mmol/L EDTA. The isolation and enrichment of $CD45^+$ were performed using the REAlease CD45 (TIL) MicroBead Kit, human (Miltenyi Biotec; cat. #130-121-563) according to the manufacturer's instructions.

For the Rhapsody experiment, the process was done by following the manufacturer's (BD Biosciences) protocol. Two thousand four hundred and thirty-two cells were captured in a single run with seven barcoded samples pooled together. The sample was processed according to BD mRNA targeted and sample tag library preparation with the BD Rhapsody targeted mRNA and Abseq amplification kit (Doc ID: 210969 Rev 3.0). The BD Rhapsody Immune Response Targeted Panel (Human; BD; cat. #633750) was used. Samples were then subjected to an indexed paired-end sequencing run of 2 × 151 cycles on an Illumina HiSeq 4000 system (Illumina) with 20% PhiX spike-in.

Targeted transcriptomics Fastq files were processed via the standard Rhapsody analysis pipeline (BD Biosciences) per the manufacturer's recommendations. First, R1 and R2 reads were filtered for high-quality reads, dropping reads too short (fewer than 66 bases for R1 and 64 bases for R2) or having a base quality score of less than 20. R1 reads were annotated to identify cell label sequences and unique molecular identifiers, and R2 reads were mapped to the respective reference sequences using Bowtie2. Finally, all passing R1 and R2 reads were combined and annotated to the respective molecules. For quality control of the reads, recursive substation error correction and distribution-based error correction (DBEC) were applied, which are manufacturer-developed algorithms correcting for PCR and sequencing errors. For determining putative cells (which will contain many more reads than noise cell labels), a filtering algorithm took the number of DBEC-corrected reads into account, calculating the minimum second derivative along with the cumulative reads as the cutoff point. Finally, the expression matrix was obtained from the DBEC-adjusted molecule counts in a CSV format.

A cell was determined as a singlet if the minimum read count of a single sample tag was above the threshold of 75%. A cell was classified as a multiplet if it exceeded the threshold for more than one sample tag. A cell that did not meet the threshold was labeled undetermined. Both multiplets and undetermined cells were excluded from the analysis as described below.

For downstream analysis in Seurat V4 (Hao, Satija Cell 2020), counts were normalized, and principal component analysis (PCA) was performed. To incorporate protein information into the analysis, the Abseq signals were added to the variable genes found by the "FindVariableFeatures" function. Using these variable features and proteins, a uniform manifold approximation and projection (UMAP) was generated. Clustering was performed using shared nearest-neighbor (SNN) analysis. Differentially expressed proteins and genes were identified as FDR <0.05 and log fold change below −0.25 or above 0.25.

Analyses and General Statistical Analysis

Exploratory analyses were performed comparing PFS according to biomarker status using log-rank tests, and *P* values were not corrected for multiple testing.

Flow cytometry and mass cytometry analyses were performed with FlowJo software (Tree Star). Data representation and analyses were performed with either Prism 7 (GraphPad Software) or R v3.6 using readxl, tidyverse, dplyr, ggplot2, ggpubr, ggsignif, pheatmap, corrplot, ggdendro, Hmisc, heatmapply, and survminer packages. Heat maps of normalized marker expression (CyTOF) were generated using heatmapply R package. For *in sitro* assay, soluble factor fold ratios were calculated as $\log_2$ transformation of median values of stimulated versus unstimulated wells and were converted to *z* scores. Heat maps were generated with the R package pheatmap. Hierarchical clustering based on the *z* score was performed using Euclidean distance and ward D2 clustering.

Data Availability

The data generated in this study are available upon request from the corresponding author.

Authors' Disclosures

C. Alves Costa Silva reports grants from MSD Avenir Foundation during the conduct of the study. C. Thibault reports personal fees and nonfinancial support from Pfizer, Merck, MSD, Janssen, and Ipsen, grants, personal fees, and nonfinancial support from AstraZeneca,

Bristol Myers Squibb, and Sanofi, and personal fees from Astellas and AAA during the conduct of the study, as well as personal fees and nonfinancial support from Pfizer, Merck, MSD, Janssen, and Ipsen, grants, personal fees, and nonfinancial support from AstraZeneca, Bristol Myers Squibb, and Sanofi, and personal fees from Astellas and AAA outside the submitted work. F. Audenet reports personal fees from Astellas, Urodiag, Vitadx, and Bristol Myers Squibb, and nonfinancial support from Ipsen outside the submitted work. G. Gravis reports grants from Bristol Myers Squibb, and other support from MSD, Bristol Myers Squibb, and Merck–Pfizer alliance outside the submitted work. C. Helissey reports personal fees from Janssen-Cilag, Roche, Bayer, AstraZeneca, and Astellas outside the submitted work. L. Campedel reports personal fees from MSD, Pfizer, Bristol Myers Squibb, and Bayer outside the submitted work. T. Sbarrato reports personal fees from Veracyte during the conduct of the study. T. Raoult reports grants, personal fees, and nonfinancial support from Merck Sharp & Dohme during the conduct of the study. E. Rouleau reports grants from AstraZeneca, Roche, Clovis, Bristol Myers Squibb, and MSD outside the submitted work. Y. Allory reports other support from AstraZeneca, MSD, and Bristol Myers Squibb outside the submitted work. J. Fieschi reports personal fees from Veracyte during the conduct of the study. A. Marabelle reports grants, personal fees, nonfinancial support, and other support from MSD, Bristol Myers Squibb, and AstraZeneca, and personal fees, nonfinancial support, and other support from Roche/Genentech and Pfizer outside the submitted work. J. Van Dorp reports other support from Bristol Myers Squibb during the conduct of the study. M.S. van der Heijden reports grants from Bristol Myers Squibb during the conduct of the study, as well as grants and personal fees from Bristol Myers Squibb, Roche, and AstraZeneca, grants from 4SC, and personal fees from MSD/Merck, Janssen, Pfizer, and Seagen outside the submitted work. B. Besse reports grants from 4D Pharma, AbbVie, Amgen, Aptitude Health, AstraZeneca, BeiGene, Blueprint Medicines, Boehringer Ingelheim, Celgene, Cergentis, Chugai Pharmaceutical, Cristal Therapeutics, Daiichi Sankyo, Eli Lilly, Eisai, Genzyme Corporation, GSK, Inivata, Ipsen, Janssen, Onxeo, OSE Immunotherapeutics, Pfizer, Roche/Genentech, Sanofi, Takeda, Tolero Pharmaceuticals, and Turning Point Therapeutics during the conduct of the study. F. Andre reports grants and other support from AstraZeneca and Daiichi Sankyo, grants from Lilly and Sanofi, and other support from Novartis and Relay outside the submitted work. M. Merad reports grants and personal fees from Regeneron, personal fees from Compugen, Morphic Therapeutics, Myeloid Therapeutics, Nirogy, DrenBio, Oncoresponse, Asherbio, Pionyr, Owkin, and Larkspur, other support from Innate Pharma, Genenta, DBV, and OSE Immunotherapeutics, and grants from Boehringer outside the submitted work. G. Kroemer reports grants from Daiichi Sankyo, Eleor, Kaleido, Lytix Pharma, PharmaMar, Osasuna Therapeutics, Samsara Therapeutics, Sanofi, Sotio, Tollys, Vascage, and Vasculox/Tioma, and personal fees from Reithera outside the submitted work; is on the Board of Directors for Bristol Myers Squibb Foundation France; and is a scientific cofounder of EverImmune, Osasuna Therapeutics, Samsara Therapeutics, and Therafast Bio. L. Zitvogel reports grants and personal fees from EverImmune, and grants from 9 Meters and Pileje during the conduct of the study; grants from Daiichi Sankyo outside the submitted work; and a patent for B220028EPA pending. Y. Loriot reports grants from MSD and personal fees from MSD during the conduct of the study; personal fees from Bristol Myers Squibb, Pfizer, Merck Serono, AstraZeneca, Seattle Genetics, Gilead, Taiho, and Astellas, grants and personal fees from Janssen, and grants from Roche and Celsius outside the submitted work; and a patent for EP2305181.4 pending. No disclosures were reported by the other authors.

Authors' Contributions

A.-G. Goubet: Conceptualization, formal analysis, supervision, validation, investigation, visualization, methodology, writing–original draft, project administration, writing–review and editing. **L. Lordello:** Formal analysis, validation, investigation, visualization, methodology, writing–original draft, writing–review and editing. **C. Alves Costa Silva:** Investigation, visualization, methodology, writing–review and editing. **I. Peguillet:** Validation, investigation, visualization, methodology, writing–review and editing. **M. Gazzano:** Validation, investigation, visualization, methodology, writing–review and editing. **M.D. Mbogning-Fonkou:** Investigation, visualization, methodology, writing–review and editing. **C. Thelemaque:** Investigation, visualization, methodology. **C. Lebacle:** Resources, project administration. **C. Thibault:** Resources, writing–review and editing. **F. Audenet:** Resources, writing–review and editing. **G. Pignot:** Resources, writing–review and editing. **G. Gravis:** Resources, writing–review and editing. **C. Helissey:** Resources, writing–review and editing. **L. Campedel:** Resources, writing–review and editing. **M. Roupret:** Resources, writing–review and editing. **E. Xylinas:** Resources, writing–review and editing. **I. Ouzaid:** Resources, writing–review and editing. **A. Dubuisson:** Investigation, visualization, methodology, writing–review and editing. **M. Mazzenga:** Investigation, methodology. **C. Flament:** Validation, investigation, visualization, methodology. **P. Ly:** Validation, investigation, methodology. **V. Marty:** Investigation, visualization, methodology. **N. Signolle:** Formal analysis, validation, investigation, visualization, methodology. **A. Sauvat:** Investigation, visualization, methodology. **T. Sbarrato:** Validation, investigation, visualization, methodology, writing–review and editing. **M. Filahi:** Investigation, visualization, methodology, project administration. **C. Davin:** Investigation, visualization, methodology, project administration. **G. Haddad:** Investigation, visualization, methodology. **J. Bou Khalil:** Supervision, validation, investigation, visualization, methodology. **C. Bleriot:** Supervision, validation, investigation, visualization, methodology, writing–review and editing. **F.-X. Danlos:** Investigation, visualization. **G. Dunsmore:** Formal analysis, validation, investigation, visualization, methodology. **K. Mulder:** Formal analysis, validation, investigation, visualization, methodology. **A. Silvin:** Supervision, validation, investigation, visualization, methodology, writing–review and editing. **T. Raoult:** Resources, project administration. **B. Archambaud:** Formal analysis. **S. Belhechmi:** Formal analysis, validation, writing–review and editing. **I. Gomperts Boneca:** Resources, writing–review and editing. **N. Cayet:** Investigation, visualization, methodology, writing–review and editing. **M. Moya-Nilges:** Investigation, visualization, methodology, writing–review and editing. **A. Mallet:** Resources, supervision, investigation, methodology. **R. Daillere:** Resources, writing–review and editing. **E. Rouleau:** Data curation, validation, investigation, visualization, methodology, writing–review and editing. **C. Radulescu:** Resources, project administration, writing–review and editing. **Y. Allory:** Resources, project administration, writing–review and editing. **J. Fieschi:** Supervision, validation, investigation, visualization, methodology, project administration, writing–review and editing. **M. Rouanne:** Resources, writing–review and editing. **F. Ginhoux:** Supervision, validation, writing–review and editing. **G. Le Teuff:** Conceptualization, formal analysis, supervision, validation, investigation, methodology, writing–review and editing. **L. Derosa:** Writing–review and editing. **A. Marabelle:** Conceptualization, resources, writing–review and editing. **J. Van Dorp:** Resources, writing–review and editing. **N. Van Dijk:** Resources, writing–review and editing. **M.S. van der Heijden:** Resources, writing–review and editing. **B. Besse:** Resources, writing–review and editing. **F. Andre:** Resources, writing–review and editing. **M. Merad:** Investigation, writing–review and editing. **G. Kroemer:** Writing–review and editing. **J.-Y. Scoazec:** Supervision, methodology, writing–review and editing. **L. Zitvogel:** Conceptualization, resources, formal analysis, supervision, funding acquisition, investigation, methodology, writing–original draft, project administration, writing–review and editing. **Y. Loriot:** Conceptualization, resources, supervision, funding acquisition, validation, investigation, methodology, writing–original draft, project administration, writing–review and editing.

Acknowledgments

We thank pathologists, nurses, and clinical research associates from Hôpital Européenn George Pompidou, Hôpital Begin, Institut Paoli-Calmettes, Hôpital Bichat, and Hôpital Pitié-Salpétrière for their participation in the PANDORE clinical trial. We are thankful to the flow and mass cytometry facility team of Gustave Roussy (Philippe Rameau and Cyril Catelain). We thank Fluidigm for their support. We are grateful for support for equipment from the French Government Programme Investissements d'Avenir France BioImaging (FBI; No. ANR-10-INSB-04-01) and the French Government (Agence Nationale de la Recherche) Investissement d'Avenir program, Laboratoire d'Excellence "Integrative Biology of Emerging Infectious Diseases" (ANR-10-LABX-62-IBEID). A.-G. Goubet was supported by Fondation pour la Recherche Médicale. C. Alves Costa Silva was supported by MSD Avenir. F.-X. Danlos was supported by Fondation Philantropia. M. Roupret was supported by Fondation Foch and the Association Française d'Urologie (AFU). L. Zitvogel was funded by the RHU Torino Lumière (ANR-16-RHUS-0008). L. Zitvogel and L. Derosa were supported by RHU5 "ANR-21-RHUS-0017" IMMUNOLIFE, SIRIC Stratified Oncology Cell DNA Repair and Tumor Immune Elimination (SOCRATE), as well as the SIGN'IT ARC foundation. L. Zitvogel was supported by European Union's Horizon 2020 research and innovation programme under grant agreement number 825410 [project acronym: ONCOBIOME, project title: Gut OncoMicrobiome Signatures (GOMS) associated with cancer incidence, prognosis, and prediction of treatment response]. L. Zitvogel also received an ANR grant–French-German Ileobiome 19-CE15-0029-01. L. Zitvogel and G. Kroemer received a donation from the Seerave Foundation. L. Zitvogel and G. Kroemer were supported by the Ligue contre le Cancer (équipe labelisée); ANR projets blancs; Cancéropôle Ile-de-France; Fondation pour la Recherche Médicale (FRM); a donation by Elior; Institut National du Cancer (INCa); Inserm (HTE); Institut Universitaire de France; the LabEx Immuno-Oncology; and FHU CARE, Dassault, and Badinter Philantropia.

The costs of publication of this article were defrayed in part by the payment of page charges. This article must therefore be hereby marked *advertisement* in accordance with 18 U.S.C. Section 1734 solely to indicate this fact.

Note

Supplementary data for this article are available at Cancer Discovery Online (http://cancerdiscovery.aacrjournals.org/).

Received February 18, 2022; revised June 21, 2022; accepted August 2, 2022; published first August 5, 2022.

REFERENCES

1. Tumeh PC, Harview CL, Yearley JH, Shintaku IP, Taylor EJM, Robert L, et al. PD-1 blockade induces responses by inhibiting adaptive immune resistance. Nature 2014;515:568–71.
2. Ishida Y, Agata Y, Shibahara K, Honjo T. Induced expression of PD-1, a novel member of the immunoglobulin gene superfamily, upon programmed cell death. EMBO J 1992;11:3887–95.
3. Pardoll DM. The blockade of immune checkpoints in cancer immunotherapy. Nat Rev Cancer 2012;12:252–64.
4. Hamid O, Robert C, Daud A, Hodi FS, Hwu WJ, Kefford R, et al. Safety and tumor responses with lambrolizumab (anti–PD-1) in melanoma. N Engl J Med 2013;369:134–44.
5. Herbst RS, Soria JC, Kowanetz M, Fine GD, Hamid O, Gordon MS, et al. Predictive correlates of response to the anti-PD-L1 antibody MPDL3280A in cancer patients. Nature 2014;515:563–7.
6. Topalian SL, Sznol M, McDermott DF, Kluger HM, Carvajal RD, Sharfman WH, et al. Survival, durable tumor remission, and long-term safety in patients with advanced melanoma receiving nivolumab. J Clin Oncol 2014;32:1020–30.
7. Scapin G, Yang X, Prosise WW, McCoy M, Reichert P, Johnston JM, et al. Structure of full-length human anti–PD-1 therapeutic IgG4 antibody pembrolizumab. Nat Struct Mol Biol 2015;22:953–8.
8. Patnaik A, Kang SP, Rasco D, Papadopoulos KP, Elassaiss-Schaap J, Beeram M, et al. Phase I study of pembrolizumab (MK-3475; anti–PD-1 monoclonal antibody) in patients with advanced solid tumors. Clin Cancer Res 2015;21:4286–93.
9. Wang M, Yao LC, Cheng M, Cai D, Martinek J, Pan CX, et al. Humanized mice in studying efficacy and mechanisms of PD-1-targeted cancer immunotherapy. FASEB J 2018;32:1537–49.
10. Ribas A, Shin DS, Zaretsky J, Frederiksen J, Cornish A, Avramis E, et al. PD-1 blockade expands intratumoral memory T cells. Cancer Immunol Res 2016;4:194–203.
11. Jordan B, Meeks JJ. T1 bladder cancer: current considerations for diagnosis and management. Nat Rev Urol 2019;16:23–34.
12. Alfred Witjes J, Lebret T, Compérat EM, Cowan NC, De Santis M, Bruins HM, et al. Updated 2016 EAU guidelines on muscle-invasive and metastatic bladder cancer. Eur Urol 2017;71:462–75.
13. Balar AV, Castellano D, O'Donnell PH, Grivas P, Vuky J, Powles T, et al. First-line pembrolizumab in cisplatin-ineligible patients with locally advanced and unresectable or metastatic urothelial cancer (KEYNOTE-052): a multicentre, single-arm, phase 2 study. Lancet Oncol 2017;18:1483–92.
14. Balar AV, Galsky MD, Rosenberg JE, Powles T, Petrylak DP, Bellmunt J, et al. Atezolizumab as first-line treatment in cisplatin-ineligible patients with locally advanced and metastatic urothelial carcinoma: a single-arm, multicentre, phase 2 trial. Lancet 2017;389:67–76.
15. Bellmunt J, de Wit R, Vaughn DJ, Fradet Y, Lee JL, Fong L, et al. Pembrolizumab as second-line therapy for advanced urothelial carcinoma. N Engl J Med 2017;376:1015–26.
16. Powles T, Durán I, van der Heijden MS, Loriot Y, Vogelzang NJ, De Giorgi U, et al. Atezolizumab versus chemotherapy in patients with platinum-treated locally advanced or metastatic urothelial carcinoma (IMvigor211): a multicentre, open-label, phase 3 randomised controlled trial. Lancet 2018;391:748–57.
17. Powles T, Park SH, Voog E, Caserta C, Valderrama BP, Gurney H, et al. Avelumab maintenance therapy for advanced or metastatic urothelial carcinoma. N Engl J Med 2020;383:1218–30.
18. Sharma P, Retz M, Siefker-Radtke A, Baron A, Necchi A, Bedke J, et al. Nivolumab in metastatic urothelial carcinoma after platinum therapy (CheckMate 275): a multicentre, single-arm, phase 2 trial. Lancet Oncol 2017;18:312–22.
19. Bajorin DF, Witjes JA, Gschwend JE, Schenker M, Valderrama BP, Tomita Y, et al. Adjuvant nivolumab versus placebo in muscle-invasive urothelial carcinoma. N Engl J Med 2021;384:2102–14.
20. Balar AV, Kamat AM, Kulkarni GS, Uchio EM, Boormans JL, Roumiguié M, et al. Pembrolizumab monotherapy for the treatment of high-risk non-muscle-invasive bladder cancer unresponsive to BCG (KEYNOTE-057): an open-label, single-arm, multicentre, phase 2 study. Lancet Oncol 2021;22:919–30.
21. Gao J, Navai N, Alhalabi O, Siefker-Radtke A, Campbell MT, Tidwell RS, et al. Neoadjuvant PD-L1 plus CTLA-4 blockade in patients with cisplatin-ineligible operable high-risk urothelial carcinoma. Nat Med 2020;26:1845–51.
22. Necchi A, Anichini A, Raggi D, Briganti A, Massa S, Lucianò R, et al. Pembrolizumab as neoadjuvant therapy before radical cystectomy in patients with muscle-invasive urothelial bladder carcinoma (PURE-01): an open-label, single-arm, phase II study. J Clin Oncol 2018;36:3353–60.
23. Powles T, Kockx M, Rodriguez-Vida A, Duran I, Crabb SJ, Van Der Heijden MS, et al. Clinical efficacy and biomarker analysis of neoadjuvant atezolizumab in operable urothelial carcinoma in the ABACUS trial. Nat Med 2019;25:1706–14.
24. van Dijk N, Gil-Jimenez A, Silina K, Hendricksen K, Smit LA, de Feijter JM, et al. Preoperative ipilimumab plus nivolumab in locoregionally advanced urothelial cancer: the NABUCCO trial. Nat Med 2020;26:1839–44.

25. Winoker JS, Liaw CW, Galsky MD, Wiklund P, Mehrazin R. Clinical complete response after neoadjuvant chemotherapy for muscle-invasive bladder cancer: a call for standardized assessments and definitions. Eur Urol Focus 2020;6:627–9.
26. Cabrita R, Lauss M, Sanna A, Donia M, Skaarup Larsen M, Mitra S, et al. Tertiary lymphoid structures improve immunotherapy and survival in melanoma. Nature 2020;577:561–5.
27. Helmink BA, Reddy SM, Gao J, Zhang S, Basar R, Thakur R, et al. B cells and tertiary lymphoid structures promote immunotherapy response. Nature 2020;577:549–55.
28. Petitprez F, de Reyniès A, Keung EZ, Chen TWW, Sun CM, Calderaro J, et al. B cells are associated with survival and immunotherapy response in sarcoma. Nature 2020;577:556–60.
29. Goswami S, Chen Y, Anandhan S, Szabo PM, Basu S, Blando JM, et al. ARID1A mutation plus CXCL13 expression act as combinatorial biomarkers to predict responses to immune checkpoint therapy in mUCC. Sci Transl Med 2020;12:eabc4220.
30. Zander R, Kasmani MY, Chen Y, Topchyan P, Shen J, Zheng S, et al. Tfh-cell-derived interleukin 21 sustains effector CD8+ T cell responses during chronic viral infection. Immunity 2022;55:475–93.
31. Noël G, Langouo Fontsa M, Garaud S, De Silva P, de Wind A, Van den Eynden GG, et al. Functional Th1-oriented T follicular helper cells that infiltrate human breast cancer promote effective adaptive immunity. J Clin Invest 2021;131:e139905.
32. Meylan M, Petitprez F, Becht E, Bougoüin A, Pupier G, Calvez A, et al. Tertiary lymphoid structures generate and propagate antitumor antibody-producing plasma cells in renal cell cancer. Immunity 2022;55:527–41.
33. Overacre-Delgoffe AE, Bumgarner HJ, Cillo AR, Burr AHP, Tometich JT, Bhattacharjee A, et al. Microbiota-specific T follicular helper cells drive tertiary lymphoid structures and anti-tumor immunity against colorectal cancer. Immunity 2021;54:2812–24.
34. Hollern DP, Xu N, Thennavan A, Glodowski C, Garcia-Recio S, Mott KR, et al. B cells and T follicular helper cells mediate response to checkpoint inhibitors in high mutation burden mouse models of breast cancer. Cell 2019;179:1191–206.
35. Biswas S, Mandal G, Payne KK, Anadon CM, Gatenbee CD, Chaurio RA, et al. IgA transcytosis and antigen recognition govern ovarian cancer immunity. Nature 2021;591:464–70.
36. Chaurio RA, Anadon CM, Lee Costich T, Payne KK, Biswas S, Harro CM, et al. TGF-β-mediated silencing of genomic organizer SATB1 promotes Tfh cell differentiation and formation of intratumoral tertiary lymphoid structures. Immunity 2022;55:115–28.
37. Briganti A, Gandaglia G, Scuderi S, Gallina A, Colombo R, Fossati N, et al. Surgical safety of radical cystectomy and pelvic lymph node dissection following neoadjuvant pembrolizumab in patients with bladder cancer: prospective assessment of perioperative outcomes from the PURE-01 Trial. Eur Urol 2020;77:576–80.
38. Szabados B, Rodriguez-Vida A, Durán I, Crabb SJ, Van Der Heijden MS, Pous AF, et al. Toxicity and surgical complication rates of neoadjuvant atezolizumab in patients with muscle-invasive bladder cancer undergoing radical cystectomy: updated safety results from the ABACUS Trial. Eur Urol Oncol 2021;4:456–63.
39. Eggermont AMM, Apolone G, Baumann M, Caldas C, Celis JE, de Lorenzo F, et al. Cancer Core Europe: a translational research infrastructure for a European mission on cancer. Mol Oncol 2019;13:521–7.
40. Pfister C, Gravis G, Flechon A, Chevreau CM, Mahammedi H, Laguerre B, et al. 652O Dose-dense methotrexate, vinblastine, doxorubicin and cisplatin (dd-MVAC) or gemcitabine and cisplatin (GC) as perioperative chemotherapy for patients with muscle-invasive bladder cancer (MIBC): results of the GETUG/AFU VESPER V05 phase III trial. Ann Oncol 2021;32:S678.
41. Levine JH, Simonds EF, Bendall SC, Davis KL, Amir ED, Tadmor MD, et al. Data-driven phenotypic dissection of AML reveals progenitor-like cells that correlate with prognosis. Cell 2015;162:184–97.
42. Gu-Trantien C, Migliori E, Buisseret L, de Wind A, Brohée S, Garaud S, et al. CXCL13-producing TFH cells link immune suppression and adaptive memory in human breast cancer. JCI Insight 2017;2:91487.
43. Jones GW, Hill DG, Jones SA. Understanding immune cells in tertiary lymphoid organ development: it is all starting to come together. Front Immunol 2016;7:401.
44. Sautès-Fridman C, Lawand M, Giraldo NA, Kaplon H, Germain C, Fridman WH, et al. Tertiary lymphoid structures in cancers: prognostic value, regulation, and manipulation for therapeutic intervention. Front Immunol 2016;7:407.
45. Schalper KA, Carleton M, Zhou M, Chen T, Feng Y, Huang SP, et al. Elevated serum interleukin-8 is associated with enhanced intratumor neutrophils and reduced clinical benefit of immune-checkpoint inhibitors. Nat Med 2020;26:688–92.
46. Dubuisson A, Fahrner JE, Goubet AG, Terrisse S, Voisin N, Bayard C, et al. Immunodynamics of explanted human tumors for immunooncology. EMBO Mol Med 2021;13:e12850.
47. Voabil P, de Bruijn M, Roelofsen LM, Hendriks SH, Brokamp S, van den Braber M, et al. An ex vivo tumor fragment platform to dissect response to PD-1 blockade in cancer. Nat Med 2021;27:1250–61.
48. Huang AC, Postow MA, Orlowski RJ, Mick R, Bengsch B, Manne S, et al. T-cell invigoration to tumour burden ratio associated with anti–PD-1 response. Nature 2017;545:60–5.
49. Sade-Feldman M, Yizhak K, Bjorgaard SL, Ray JP, de Boer CG, Jenkins RW, et al. Defining T cell states associated with response to checkpoint immunotherapy in melanoma. Cell 2018;175:998–1013.e20.
50. Dubourg G, Morand A, Mekhalif F, Godefroy R, Corthier A, Yacouba A, et al. Deciphering the urinary microbiota repertoire by culturomics reveals mostly anaerobic bacteria from the gut. Front Microbiol 2020;11:513305.
51. Brubaker L, Wolfe A. The urinary microbiota: a paradigm shift for bladder disorders? Curr Opin Obstet Gynecol 2016;28:407–12.
52. Vermeulen SH, Hanum N, Grotenhuis AJ, Castaño-Vinyals G, van der Heijden AG, Aben KK, et al. Recurrent urinary tract infection and risk of bladder cancer in the Nijmegen bladder cancer study. Br J Cancer 2015;112:594–600.
53. Mulvey MA, Schilling JD, Hultgren SJ. Establishment of a persistent Escherichia coli reservoir during the acute phase of a bladder infection. Infect Immun 2001;69:4572–9.
54. Wu J, Miao Y, Abraham SN. The multiple antibacterial activities of the bladder epithelium. Ann Transl Med 2017;5:35.
55. Jiang X, Castelao JE, Groshen S, Cortessis VK, Shibata D, Conti DV, et al. Urinary tract infections and reduced risk of bladder cancer in Los Angeles. Br J Cancer 2009;100:834–9.
56. Nejman D, Livyatan I, Fuks G, Gavert N, Zwang Y, Geller LT, et al. The human tumor microbiome is composed of tumor type–specific intracellular bacteria. Science 2020;368:973–80.
57. Pushalkar S, Hundeyin M, Daley D, Zambirinis CP, Kurz E, Mishra A, et al. The pancreatic cancer microbiome promotes oncogenesis by induction of innate and adaptive immune suppression. Cancer Discov 2018;8:403–16.
58. Tsay JCJ, Wu BG, Sulaiman I, Gershner K, Schluger R, Li Y, et al. Lower airway dysbiosis affects lung cancer progression. Cancer Discov 2021;11:293–307.
59. Fu A, Yao B, Dong T, Chen Y, Yao J, Liu Y, et al. Tumor-resident intracellular microbiota promotes metastatic colonization in breast cancer. Cell 2022;185:1356–72.
60. Brons JK, Vink SN, de Vos MGJ, Reuter S, Dobrindt U, van Elsas JD. Fast identification of Escherichia coli in urinary tract infections using a virulence gene based PCR approach in a novel thermal cycler. J Microbiol Methods 2020;169:105799.
61. Daillère R, Vétizou M, Waldschmitt N, Yamazaki T, Isnard C, Poirier-Colame V, et al. Enterococcus hirae and barnesiella intestinihominis facilitate cyclophosphamide-induced therapeutic immunomodulatory effects. Immunity 2016;45:931–43.
62. Routy B, Le Chatelier E, Derosa L, Duong CPM, Alou MT, Daillère R, et al. Gut microbiome influences efficacy of PD-1-based immunotherapy against epithelial tumors. Science 2018;359:91–7.
63. Vétizou M, Pitt JM, Daillère R, Lepage P, Waldschmitt N, Flament C, et al. Anticancer immunotherapy by CTLA-4 blockade relies on the gut microbiota. Science 2015;350:1079–84.

64. Cui C, Wang J, Fagerberg E, Chen P-M, Connolly KA, Damo M, et al. Neoantigen-driven B cell and CD4 T follicular helper cell collaboration promotes anti-tumor CD8 T cell responses. Cell 2021;184:6101–18.
65. Gopalakrishnan V, Spencer CN, Nezi L, Reuben A, Andrews MC, Karpinets TV, et al. Gut microbiome modulates response to anti–PD-1 immunotherapy in melanoma patients. Science 2018;359:97–103.
66. Matson V, Fessler J, Bao R, Chongsuwat T, Zha Y, Alegre ML, et al. The commensal microbiome is associated with anti–PD-1 efficacy in metastatic melanoma patients. Science 2018;359:104–8.
67. Sivan A, Corrales L, Hubert N, Williams JB, Aquino-Michaels K, Earley ZM, et al. Commensal Bifidobacterium promotes antitumor immunity and facilitates anti-PD-L1 efficacy. Science 2015;350:1084–9.
68. Flores-Mireles AL, Walker JN, Caparon M, Hultgren SJ. Urinary tract infections: epidemiology, mechanisms of infection and treatment options. Nat Rev Microbiol 2015;13:269–84.
69. Abraham SN, Sun D, Dale JB, Beachey EH. Conservation of the D-mannose-adhesion protein among type 1 fimbriated members of the family Enterobacteriaceae. Nature 1988;336:682–4.
70. Asadi Karam MR, Oloomi M, Mahdavi M, Habibi M, Bouzari S. Vaccination with recombinant FimH fused with flagellin enhances cellular and humoral immunity against urinary tract infection in mice. Vaccine 2013;31:1210–6.
71. Wu J, Bao C, Reinhardt RL, Abraham SN. Local induction of bladder Th1 responses to combat urinary tract infections. Proc Natl Acad Sci U S A 2021;118:e2026461118.
72. Wong YNS, Joshi K, Khetrapal P, Ismail M, Reading JL, Sunderland MW, et al. Urine-derived lymphocytes as a non-invasive measure of the bladder tumor immune microenvironment. J Exp Med 2018;215:2748–59.
73. Sepich-Poore GD, Zitvogel L, Straussman R, Hasty J, Wargo JA, Knight R. The microbiome and human cancer. Science 2021;371:eabc4552.
74. Kalaora S, Nagler A, Nejman D, Alon M, Barbolin C, Barnea E, et al. Identification of bacteria-derived HLA-bound peptides in melanoma. Nature 2021;592:138–43.
75. Ansaldo E, Slayden LC, Ching KL, Koch MA, Wolf NK, Plichta DR, et al. Akkermansia muciniphila induces intestinal adaptive immune responses during homeostasis. Science 2019;364:1179–84.
76. Roberti MP, Yonekura S, Duong CPM, Picard M, Ferrere G, Tidjani Alou M, et al. Chemotherapy-induced ileal crypt apoptosis and the ileal microbiome shape immunosurveillance and prognosis of proximal colon cancer. Nat Med 2020;26:919–31.
77. Xu M, Pokrovskii M, Ding Y, Yi R, Au C, Harrison OJ, et al. c-MAF-dependent regulatory T cells mediate immunological tolerance to a gut pathobiont. Nature 2018;554:373–7.
78. Recondo G, Mahjoubi L, Maillard A, Loriot Y, Bigot L, Facchinetti F, et al. Feasibility and first reports of the MATCH-R repeated biopsy trial at Gustave Roussy. NPJ Precis Oncol 2020;4:27.
79. Moor K, Fadlallah J, Toska A, Sterlin D, Balmer ML, Macpherson AJ, et al. Analysis of bacterial-surface-specific antibodies in body fluids using bacterial flow cytometry. Nat Protoc 2016;11:1531–53.
80. Bankhead P, Loughrey MB, Fernández JA, Dombrowski Y, McArt DG, Dunne PD, et al. QuPath: open source software for digital pathology image analysis. Sci Rep 2017;7:16878.
81. Marliot F, Chen X, Kirilovsky A, Sbarrato T, El Sissy C, Batista L, et al. Analytical validation of the Immunoscore and its associated prognostic value in patients with colon cancer. J Immunother Cancer 2020;8:e000272.
82. Grine G, Terrer E, Boualam MA, Aboudharam G, Chaudet H, Ruimy R, et al. Tobacco-smoking-related prevalence of methanogens in the oral fluid microbiota. Sci Rep 2018;8:9197.
83. Graham L, Orenstein JM. Processing tissue and cells for transmission electron microscopy in diagnostic pathology and research. Nat Protoc 2007;2:2439–50.
84. Seng P, Drancourt M, Gouriet F, La Scola B, Fournier P-E, Rolain JM, et al. Ongoing revolution in bacteriology: routine identification of bacteria by matrix-assisted laser desorption ionization time-of-flight mass spectrometry. Clin Infect Dis 2009;49:543–51.
85. Lawrence MS, Stojanov P, Polak P, Kryukov GV, Cibulskis K, Sivachenko A, et al. Mutational heterogeneity in cancer and the search for new cancer-associated genes. Nature 2013;499:214–8.

8.4 METABOLOMICS HALLMARKS IN PATIENTS WITH CANCER

8.4.1 Article VI

Title: Microbiota-associated metabolic reprogramming influenced clinical outcome in the randomized dendritic cell-based clinical trial in stage III melanoma.

Submitted to: Nature Communications (under revision).

Carolina Alves Costa Silva #, Gianmarco Piccinno #, Mélanie Bourgin #, Déborah Suissa #, Gerty Schreibelt #, Sylvere Durand, Roxanne Birebent, Marine Fidelle, Cissé Sow, Fanny Aprahamian, Paolo Manghi, Michal Punčochář, Francesco Asnicar, Federica Pinto, Federica Armanini, Safae Terrisse, Bertrand Routy, Damien Drubay, Alexander M. M. Eggermont, Guido Kroemer, Nicola Segata, Laurence Zitvogel††, Lisa Derosa†, Kalijn F. Bol† and I. Jolanda M. de Vries†.
# or † contributed equally
†† corresponding author

Microbiota-associated metabolic reprograming influenced clinical outcome in the randomized dendritic cell-based clinical trial in stage III melanoma

Carolina Alves Costa Silva[1,2,3]*, Gianmarco Piccinno[4]*, Mélanie Bourgin[1,5,6]*, Déborah Suissa[1,2,3]*, Gerty Schreibelt[7]*, Sylvere Durand[1,5,6], Roxanne Birebent[1,2,3], Marine Fidelle[1,3], Cissé Sow[1,3], Fanny Aprahamian[1,5,6], Paolo Manghi[4], Michal Punčochář[4], Francesco Asnicar[4], Federica Pinto[4], Federica Armanini[4], Safae Terrisse[8], Bertrand Routy[9,10], Damien Drubay[1,11,12], Alexander M. M. Eggermont[13,14], Guido Kroemer[5,6,15], Nicola Segata[4,16], Laurence Zitvogel[1,2,3,17]††, Lisa Derosa[1,2,3]†, Kalijn F. Bol[7,18]† and I. Jolanda M. de Vries[7]†.

Affiliations :

[1]Gustave Roussy Cancer Campus (GRCC), Clinicobiome, Villejuif Cedex, France

[2] Faculté de Médecine, Université Paris-Saclay, Kremlin-Bicêtre, France.

[3]Institut National de la Santé Et de la Recherche Médicale (INSERM) U1015, Equipe Labellisée—Ligue Nationale contre le Cancer, Villejuif, France.

[4]Department of Computational, Cellular and Integrative Biology, University of Trento, Trento, Italy

[5]Metabolomics and Cell Biology Platforms, Gustave Roussy Cancer Campus, Villejuif, France.

[6]Centre de Recherche des Cordeliers, INSERM U1138, Équipe Labellisée – Ligue Nationale contre le Cancer, Université Paris Cité, Sorbonne Université, Paris, France.

[7]Medical BioSciences, Radboud university medical center, Nijmegen, the Netherlands

[8]Oncology Department, Assistance Publique Hôpitaux de Paris (AP-HP), Hôpital Saint-Louis, Paris, France

[9]Centre de Recherche du Centre Hospitalier de l'Université de Montréal (CRCHUM), Montréal, QC, Canada.

[10]Hematology-Oncology Division, Department of Medicine, Centre Hospitalier de l'Université de Montréal (CHUM), Montréal, QC, Canada.

[11]Office of Biostatistics and Epidemiology, Gustave Roussy Cancer Campus, Université Paris-Saclay, Villejuif, France.

[12]Inserm, Université Paris-Saclay, CESP U1018, Oncostat, labeled Ligue Contre le Cancer, Villejuif, France.

[13]Princess Máxima Center and University Medical Center Utrecht, 3584 CS Utrecht, the Netherlands

[14]Comprehensive Cancer Center Munich, Technical University Munich & Ludwig Maximiliaan University, Munich, Germany
[15]Institut du Cancer Paris CARPEM, Department of Biology, Hôpital Européen Georges Pompidou, AP-HP, Paris, France
[16]Istituto Europeo di Oncologia (IEO), National Cancer Institute (IRCCS), Milan, Italy
[17]Center of Clinical Investigations BIOTHERIS, INSERM CIC1428, Villejuif, France.
[18]Department of Medical Oncology, Radboud university medical center, Nijmegen, the Netherlands

†These co-last authors contributed equally to this work.

*C.A.C.S. & G.P. & M.B. & D.S. & G.S are co-first authors.
††Corresponding author: laurence.zitvogel@gustaveroussy.fr (L.Zi.)
Gustave Roussy, 114 rue Edouard Vaillant, 94805 Villejuif Cedex France
ORCID 0000-0003-1596-0998 (L.Zi.)

Keywords: cancer, microbiota, immune response, metabolomics, metagenomics, melanoma, dendritic cells, vaccines

List of abbreviations:

2-year recurrence-free survival rate: 2Y-RFS; 2-year recurrence: 2Y-R; Antigen-presenting cell: APC; Arcsin-sqrt: AST; Biliary acids: BA; Body mass index: BMI; Branched-chain amino acids: BCAAs; Centered-log-ratio: CLR; Dendritic cell: DC; Delayed type hypersensitivity: DTH; Eastern Cooperative Oncology Group performance status: ECOG-PS; Fatty acids: FA; Fold change: FC; US Food and Drug Administration: FDA; Healthy volunteers: HV; Interleukin: IL ; Immune checkpoint inhibitors: ICI ; Kyoto Encyclopedia of Genes and Genomes Orthology: KEGG; Keyhole limpet hemocyanin: KLH; Kaplan-Meier: KM; Liquid chromatography coupled with mass spectrometers: LC/MS; Melanoma: MEL; Metabolomics: MB; Metagenomics: MG; Metagenomic species: MGS; Metastatic melanoma: MM; Natural dendritic cell: nDC; No recurrence at 2 years: 2Y-noR; Overall survival: OS; Placebo: PL; Principal Component analyses: PCA; Programmed death 1: PD-1; Recurrence-free survival: RFS; Species-level genome bin: SGB; Tumor- associated antigens: TAA.

Abstract

Background: Melanoma is a malignancy where tumor immunosurveillance plays a major prognostic role, prompting the development of immunotherapy strategies, dominated earlier on by dendritic cell (DC)-based immunotherapy and recently, by immune checkpoint inhibitors (ICI). The taxonomic composition of the gut microbiome earned its credentials among predictors of survival in melanoma, by influencing the peripheral and tumoral immune tonus.
Methods: In the MIND-DC phase III clinical trial (NCT02993315), 148 stage IIIB/IIIC cutaneous melanoma patients were randomized in a 2:1 ratio to adjuvant treatment with autologous conventional and plasmacytoid mature natural DC (nDC) versus placebo. Serum and stool samples were collected in 144 patients before (T1) and after (T2) 2 biweekly nDC injections to perform longitudinal metabolomics (MB) and metagenomics (MG), with the aim of finding predictors of 2-year recurrence-free survival (RFS).
Results: Different microbial species were associated with prognosis in these patients with stage III melanoma, with the health-related *Faecalibacterium prausnitzii* standing out as the main beneficial taxon for no recurrence at 2 years (p=0.008 à T1, p=0.007 at T2, nDC arm). Therapy coincided with major perturbations of serum acylcarnitines, as well as carboxylic and fatty acids (FA). Incidentally, despite randomization, patients in the nDC treatment arm exhibited a bias in their MG and MB baseline profiles, with a relative under-representation of *F. prausnitzii*, and perturbations of primary biliary acids (BA), compared to the control arm. Stool *F. prausnitzii* anticorrelated with serum BA, as well as medium and long chain acylcarnitines and the combination of these MG and MB biomarkers markedly determined RFS.
Conclusions: Altogether, the host-microbial interaction may play a role in the prognosis of stage III melanoma. We value the systematic MG and MB profiling in 2:1 randomized trials to avoid bias in baseline differences attributed to host-microbe interactions.

Background

The rise in incidence of melanoma worldwide has led to an increasing number of patients with regional positive lymph nodes (stage III) being diagnosed each year, especially in the western world [1]. Over the last decade, there has been tremendous progress in the clinical management of stage III melanoma with the advent of adjuvant and neoadjuvant immune checkpoint inhibitors (ICI). Before the era of (neo)adjuvant ICI in localized melanoma, patients with operable clinically positive nodes underwent full lymphadenectomy of the involved sites [2,3]. Surgery alone is insufficient to achieve a cure in most patients with high-risk stage III

melanoma. Thus, systemic adjuvant therapy has been investigated over the last decades in patients with high-risk melanoma. The development of effective adjuvant therapies for patients with high-risk melanoma has included ipilimumab (an anti-CTLA-4 antibody), pembrolizumab, and nivolumab (both monoclonal antibodies against programmed death 1 [PD-1]), and combination of BRAF and MEK inhibitors for patients whose tumors harbor a BRAF mutation [1,4–12], leading to US Food and Drug Administration (FDA) approvals. More recently, pembrolizumab and the combination of anti-CTLA-4 and PD-1 antibodies showed benefit in the neoadjuvant setting in patients with high-risk node-positive melanoma in early phase clinical trials [13–16].

Prior to the modern era of ICI, vaccination involving dendritic cells (DC) has been developed owing to the special properties of these cells in coordinating innate and adaptive immune responses. The aim of DC immunization was to induce tumor-specific effector T cells that can exhibit a tumoricidal activity in a tumor antigen-specific manner through induction of a protective immunological memory to cancer antigens. Across the world, many investigators showed that DC-based vaccines were safe and induced the expansion of circulating $CD4^+$ T cells and $CD8^+$ T cells that were tumor antigen-specific. Objective clinical responses have been observed in 5-8% of patients [17–21]. Long term follow-up of DC vaccinated metastatic melanoma (MM) (stage IV) reported up to 19% survival rates at 11 years, comparable to ipilimumab-treated patients. Survival significantly correlated with intense reactivities at the dermal injection site, and with eosinophilia [22]**.** In the past years, DC-based immunotherapy was performed in stage IV HLA-A2.1 positive melanoma patients using intravenous, intradermal, and intranodal routes of administration of mature DC loaded with tumor-associated antigens (TAA) such as tyrosinase and gp100, and keyhole limpet hemocyanin (KLH) as a control antigen. All vaccinated patients showed a pronounced proliferative T cell or humoral response against KLH. TAA-specific T cell reactivities were monitored in post-treatment delayed-type hypersensitivity (DTH) skin biopsies by tetramer staining and functional analyses. Patients harboring peptide-specific T cell immunity exhibited the best clinical response, with eventually complete responses in a minority of MM patients while rIL-2 or modified TAA did not further increase vaccine efficacy [23,24]. A direct correlation between DC- induced tumor-specific T cells detected in DTH skin biopsies and a favorable clinical outcome was observed in patients with MM [25,26].

The ”Melanoma Patients Immunized With Natural DenDritic Cells (MIND-DC)” trial was the first randomized phase III clinical trial testing adjuvant natural DC (nDC) therapy in high-risk stage III melanoma. The trial showed that adjuvant nDC treatment generated specific immune

responses and was well tolerated, but did not translate into survival benefit (K. Bol, co-submitted, NCOMMS-23-20360A). Here, we investigated whether nDC loaded with TAA *ex vivo* could modulate fecal metagenomics (MG) and serum metabolomics (MB) profiles that might in turn, influence clinical outcomes. Indeed, shotgun MG-based taxonomic composition of feces at baseline was associated with objective response rates in stage IV melanoma treated with anti-PD-1 alone or combined to anti-CTLA-4 in several independent cohorts [27–30]. In a meta-analysis incorporating new cohorts, McCulloch et al. confirmed that baseline microbiota composition was associated with 1-year progression-free survival. Bacteria associated with favorable response during ICI belonged to *Lachnospiraceae* and *Bifidobacteriaceae* families including *Ruminococcus* spp*, Mediterraneibacter* spp., and *Blautia* spp. [31]We unveiled that a relative deficiency in the primary biliary acid (BA) cholic acid or *F. prausnitzii*, or high levels of fatty acids (FA) and acylcarnitines were all associated with reduced recurrence-free survival (RFS), especially in the nDC treatment arm. Moreover, the relative abundance of stool *F. prausnitzii* anti-correlated with serum BA and FA at 4 weeks post-therapy start. Therefore, we hypothesize that the pharmacodynamic effects of the nDC might have been influenced by the host-microbiome dialogue in patients harboring a deviated lipid metabolism (including carboxylic acids, BA and acylcarnitines) and gut microbiota.

Results

Metagenomics-based profiles at baseline (T1) and at 4 weeks (T2) are associated with 2 year-RFS (2Y-RFS)

MIND-DC trial (NCT02993315) randomized 148 eligible patients with resected stage IIIB and IIIC melanoma between 2018 and 2021 of which 144 patients were included in this translational cohort (n=95 in the nDC arm, versus n=49 in the placebo (PL) arm) (Table S1). Five patients had not received any injection (all in the nDC arm), three being related to tumor recurrence. One was censured (because of a follow up inferior to 1 month). The clinical results are described in the companion manuscript (K. Bol, co-submitted, NCOMMS-23-20360A). Shotgun MG sequencing of stools at baseline (pre-therapy, T1) and after 4 weeks of therapy start (2 biweekly injections of nDC or PL, T2) was undertaken, and an estimate of the presence and abundance of species-level genome bins (SGBs) was estimated [32]. Here, we describe a longitudinal follow up of the shotgun MG-based stool composition in 91 and 92 patients with stage IIIB/C melanoma at T1 and at T2, respectively (Table S2). Secondly, we correlated the microbiota

composition of the T1 (Figure 1A-B) and T2 (Figure 1C-D) samples with 2Y-RFS. While the alpha-diversity was not associated with prognosis, the beta-diversity (between sample variability) significantly differed between those patients prone to stay cancer-free (no recurrence at 2 years, 2Y-noR) versus those who will experience a 2-year recurrence (2Y-R) at both time points (Figures 1A and 1C, $p<0.01$). We focused on differentially abundant SGBs and functional pathways according to 2Y-RFS and found a relative overrepresentation of *Faecalibacterium prausnitzii* (whether considering SGB 15318 or SGB15322), in patients with favorable prognosis, not only at T1 (Figure 1B, Table S3A) but also at T2 (Figure 1D, Table S3A). Next, we analyzed the intraindividual variations of this taxonomic composition at T1 and T2 considering each treatment arm (Figures S1 and S2A-B), and its clinical relevance for 2Y-RFS (Figure S3).

By splitting the whole cohort into 4 groups according to treatment arm and outcomes, we obtained small sample size (Table S2): 40/60 (67%) and 15/31 (48%) experiencing 2Y-R, and 9/60 (15%) and 1/31 (3%) experiencing 2Y-death for nDC and PL, respectively. This prevented any significant associations to pass the FDR correction for the MG analyses (all Q-values>0.2). Linear model coefficients (MaAsLin2, coefficient) for microbial SGBs that were found associated either after arcsin-sqrt (AST) or centered-log-ratio (CLR) transformation with 2Y-R with $p<0.05$ (i.e. without FDR correction) at T1 and T2 are detailed in Figures S1, S2 and S3. In brief, *F. prausnitzii* SGB15318 was relatively over-represented in 2Y-noR in the nDC arm (Figures S1 and S2A-B, $p<0.05$), while this species was not significantly impacted by the nDC therapy (Figures S3A-D and S4). Of note, *Streptococcus salivarius* SGB8007 and *Streptococcus parasanguinis* SGB8071 followed the same behavior only in the nDC arm (Figures S1, $p<0.05$ after AST, and S2A-B). In addition, the prevalence and relative abundances of distinct strains of *F. prausnitzii* tended to be reduced in the nDC arm compared with the PL arm (Figure S2C-D). Moreover, few and weak ($p<0.05$, but $Q>0.2$) additional changes occurred at microbiome levels overtime during nDC therapy. Patients classified 2Y-noR at T2 tended to harbor a relative over-overabundance of metagenomic species (MGS) that are associated with no recurrence in the PL arm (such as *Bacteroides ovatus*), the arm associated with better RFS (Figure S3C). In contrast, patients with 2Y-R receiving nDC tended to lose beneficial MGS like *Barnesiella intestinihominis* (that was associated with 2Y-noR in the PL arm) (Figure S3D). The set of MGS associated with 2Y-R in the PL arm was different (with *B. ovatus* and *Lachnospira pectinoschiza* positively and negatively associated with 2Y-noR, respectively).

The MG biomarker evolution between the two timepoints was assessed using linear regression adjusted for the clinical features treatment arm, age, gender, tumor stage (IIIB vs IIIC), Eastern Cooperative Oncology Group performance status (ECOG-PS), and body mass index (BMI) (Figure S4). We concluded that the nDC treatment arm barely impacted on the evolution of the MG taxonomic composition, except for a few taxa, such as the *Lachnospiraceae unclassified* (SGB4894) that increased in the PL arm (P=0.030) and the *Senegalimassilia anaerobia* that increased in the nDC arm (P=0.024), both remaining stable in the other arm, independently of clinical features (Figure S4). Of note, these dynamics did not pass the FDR correction. We may impute these weak associations to the small sample size (limiting the power of the analysis) and to the lack of clear effect of the treatment arm in this negative trial.

We concluded that gut microbiota composition was associated, albeit weakly, with the prognosis of stage III melanoma with *F. prausnitzii* (SGB15318 and SGB15322), referenced for its homeostatic [33,34] and antitumor properties in MM [29,35], as the most prominent MGS found at T1 and T2 in this MIND-DC cohort.

Serum metabolic changes following the first cycle of immunization

In parallel to MG, the mass spectrometry-based serum MB was serially assessed at T1 and T2 in 95 patients in the nDC arm and 49 patients in the PL arm. The Volcano plot and principal component analysis (PCA) revealed major differences between the two time points overruling those observed between the treatment groups (Figures 2A-B and S5A, Table S5A). In particular, the lipid metabolism became very perturbed at T2, with the accumulation of very long and long chain saturated FA (such as the carboxylic acids docosanoid acid (also called "behenic" acid), nonadecanoic acid, the tetradecanedioic acid, arachidonic acid, hexacosanoic acid, palmitic acid), and mono- or poly-unsaturated FA (such as 10-nonadecenoic acid, oleic acid, linoleic acid, linolenic acid, stearidonic acid, docosenoic acid) as well as acylcarnitines (glutarylcarnitine, carnitine C4:0, C4:0 (OH), C6:0, C8:1, C10:1, C12:0, C14:2) (Figure 2B, $p<0.05$, Mann–Whitney). Besides the massive shift in circulating FA and in the acylcarnitine shuttle found at T2, we observed perturbations of polyamine biosynthesis and acetylation between T1 and T2 (N-acetylputrescine, spermidine, N1-acetylspermine) (Figure 2B, $p<0.05$, Mann–Whitney). In addition, branched-chain amino acids (BCAAs) (valine/leucine/isoleucine), and γ-glutamyl dipeptides involved in inflammation, oxidative stress, and glucose regulation were significantly increased at T2 (Figure 2B, $p<0.05$, Mann–Whitney) [36]. Analysis adjustments for these shifts were done based on the trial arm, age, gender,

tumor stage (IIIB vs IIIC), ECOG-PS, and BMI (as detailed in the methods section). These metabolic shifts could not be explained by clinical events between the two time points (Table S4) since few patients experienced flu-like symptoms (19%) or started new medications (12%) between T1 and T2 (Table S4).

To assess the clinical relevance of these early changes, we investigated which metabolic profiles were associated with 2Y-RFS using an unsupervised hierarchical clustering across all metabolites (Figure 2C). We concluded that the above-mentioned medium and long chain-acylcarnitines and FA linolenic acid (Figure 2D, $p<0.05$ Mann-Whitney), acetylated polyamines (Figure S5B, $p<0.05$ Mann-Whitney), as well as BCAAs and γ-glutamyl dipeptides (Figure S5C, $p<0.05$ Mann-Whitney) were negatively associated with 2Y-RFS at T1 in univariate analyses. In contrast, serum levels of ornithine, a precursor of spermidine, were higher in patients with favorable prognosis (Figure S5D, $p<0.05$ Mann-Whitney) in univariate analyses.

The significance of FA in the temporal metabolic shift and clinical recurrence prompted us to evaluate the RFS according to median of the 13 most relevant FA abundances' sum. Levels above the FA median at T2 ($p=0.025$) and to a lesser extent at T1 ($p=0.055$) were associated with shorter RFS (Figure 2E).

Attempting to ascribe these lipid profiles to the gut microbiome, we used the MG data, and annotated the organism-specific gene hits according to the Kyoto Encyclopedia of Genes and Genomes Orthology (KEGG)[37]. Based on these annotations, reads from each sample were reconstructed into metabolic pathways using the MetaCyc hierarchy of pathway classifications [38]. The Linear model-based analysis contrasting hits separating patients who recurred and/or died of their melanoma from the others showed that the FA beta-oxidation and biosynthesis pathways at T1 were associated with overall recurrence (Figure S6A).

Hence, these findings suggest that time and/or therapy have perturbed a delicate and preexisting disbalance of lipid synthesis or degradation, at the level of the mono- and poly-unsaturated and saturated fatty and carboxylic acid metabolism, coinciding with melanoma recurrence.

Taxonomic and metabolomic differences between treatment arms at randomization

Our findings indicate that the gut taxonomic composition at T1 and the serum metabolic profile shift after only 2 injections of nDC treatment were associated with the 2Y-RFS. Although we did not anticipate any significant difference in clinical characteristics between the two treatment arms at baseline given the process of randomization (Table S1), we took a deeper dive into

potential pre-existing differences in the fecal microbial ecosystem defined by shotgun MG-based sequencing. Strikingly, while the stool compositional richness did not differ between the two arms, the beta-diversity (assessed with Bray-Curtis dissimilarity)[39] of the taxa present in feces from stage III melanoma randomized to PL was significantly different from that of individuals about to receive nDC (Figure 3A, p=0.001 Wilcoxon). Patients randomized in the PL arm exhibited a relative over-representativity of health-related and immunogenic MGS (*F. prausnitzii SGB15322, Blautia massiliensis SGB4826*, and *Lachnospiraceae* family members (such as *Dorea longicatena, Dorea formicigenerans, Eubacterium rectale*) compared with the nDC arm that presented with a relative overabundance of bacteria associated with resistance to immunotherapy (*Bacteroides uniformis*) [40] or poor prognosis in MM (*Alistipes* spp.) [31] (Figure 3B, Table S3B). Indeed, the nDC treatment arm tended to harbor higher proportions of individuals lacking *F. prausnitzii* spp. (Figure 3C) and more specifically distinct strains of *F. prausnitzii* or bearing lower relative abundance of these strains compared to the PL arm (Figure S2C-D). The same observation could be made comparing stage IV melanoma from publicly available databases with healthy volunteers (HV) (Figure S2C-D).

When we analyzed the effect of nDC (versus PL) on the RFS according to the relative abundance of several MGS associated with survival, using Kaplan-Meier (KM) analyses, we observed that the presence of higher relative abundances of commensals associated with recurrence aligned in Figure 1B (such as *Gemmiger formicilis*, p=0.333, and *L. pectinoschiza*, p=0.006, Log-Rank (Mantel Cox) test) (Figure 3D) and the absence or low abundances of bacteria associated with good prognosis (such as *F. prausnitzii*, p=0.077, Log-Rank (Mantel Cox) test) (Figure 3E) were associated with a poor prognosis in the nDC arm. Of note, many other commensals appeared irrelevant to predict RFS with or without nDC (Figure 3F).

Next, to evaluate if this MG bias also translated into different MB patterns between the two treatment arms at T1, we re-analyzed the mass-spectrometry-based MB profiles of PL and DC arms using a supervised hierarchical clustering (Figure 4A, Table S5B). Strikingly, there was a highly significant bias in the cluster corresponding to primary conjugated biliary acids at T1 (Figure 4B, $p<0.05$ Mann–Whitney) that was confirmed at T2 (Figure 4C, $p<0.001$ Mann–Whitney) in the nDC arm. Another cluster composed of mono-unsaturated and long chain FA separated nDC from PL groups at T1 (Figure 4A). To identify whether these perturbations in BA and FA translated into clinically relevant differences, we compared the most significant concentration differences between 2Y-noR and 2Y-R in PL and nDC groups for each of these metabolites and performed RFS KM curves. High levels of acylcarnitines C12:0 and C14:1, as well as linolenic acid were markedly associated with recurrence in the nDC arm only (Figure

4D, p<0.05 Mann–Whitney) in contrast to the primary BA cholic acid, that was associated with prolonged RFS (Figure 4D, p<0.05, Mann–Whitney, and Figure 4E, p=0.057, Log-Rank Mantel Cox test), but not in the PL arm (Figure S6B).

Hence, despite randomization, patients assigned to the two treatment arms appeared to differ as to the relative representativity of *F. prausnitzii* strains and primary BA composition.

Dynamic and integrative pathways

Using the XGBoost algorithm, coupled to a model explainer based on SHapley Additive exPlanations (SHAP) values for model interpretability [41], we corroborated that patients assigned to nDC arm differed from patients in the PL arm as to primary BA and polyamines (Figure S7).

Next, we re-analyzed the clinical relevance of all biological and clinical features to reduce dimension and allow prediction of 2Y-R taking into account their interactions and their slope of evolution overtime. We corroborated that BA (in particular chenodeoxycholic and cholic acid), FA and acetylcarnitines as well as a few pathways meaningful in other studies including tryptophan metabolism, vitamin B3 (trigonelline, 1-methylnicotinamide) and polyamines (acetylated metabolites of spermine/spermidine) were predictors of 2Y-RFS at T1 (Figure 5A, AUC=0.73 (CI 95%: 0.66-0.80)). Next, the metabolite evolution between the two timepoints (T2-T1/T1) was added to the baseline value (T1) to identify if biomarker drifts could improve the prediction of the 2Y-RFS (model T2-T1/T1) and if treatment arms influenced this evolution (Figure S8A-C). The SHAP analysis indicated that the increase of FA (oleic acid) and acetylated polyamines and the decrease of ornithine (upstream of the polyamine pathway) and primary BA (glyco-cholic acid, chenodeoxycholic acid) were associated with an increased risk of 2Y-R (Figure S8A, T2-T1/T1: AUC=0.72 (CI 95%: 0.66-0.78). Even if the trajectory of BA and polyamines was associated with the prognosis of stage III melanoma, we could not conclude that nDC significantly alter their levels overtime (Figure S8B showing the most significant features among all SHAP parameters). We applied the same analysis integrating MG and clinical features at T1 (Figure 5B), but obtaining better prediction at T2 for 2Y-RFS (Figure S8C) and confirming the prognostic impact of *F. prausnitzii* SGB15332. The circosplot highlights the anticorrelations between these MGS and primary BA as well as positive correlations between factors associated with dismal prognosis at T1 (Figure 5C). The multi-omics integrative model depicted in Figure 5D (AUC=0.75, CI 95%: 0.68-0.80), where the

MGS *Ruminococcaceae bacterium* SGB14899, *S. parasanguinis* SGB8071 and *F. prausnitzii* SGB15332 are consistently associated with better prognosis. Furthermore, the multi-omics integrative model corroborate MB signatures such as polyamines, FA (oleic acid), BA (chenodeoxycholic acid), acetylcarnitines and pathways including tryptophan metabolism (kynurenine), vitamin B3 (1-methylnicotinamide) are predictors of 2Y-RFS at T1.

We next performed Metabolic pathway-enrichment analysis performed in MetaboAnalyst using a KEGG database[37] and Spearman correlations[42] between fecal relative abundance of *F. prausnitzii* (SGB15318 and SGB15322) and serum MB at T1 (Figures 6A and S9A-B) and T2 (Figure S9C-D) in the whole cohort. Both *F. prausnitzii* strains markedly anticorrelated with many acylcarnitines, most specifically with medium chain (C6:0, C8:0, C10:0) and long chain saturated (C14:1) acylcarnitines, as well as many fatty and carboxylic acids (linoleic and linolenic acids) at T1 and/or T2, mainly in the nDC arm (Figure 6A left and right, Figure S9A-D). The 13 serum FA abundance were clinically relevant after 2 injections of treatment. Indeed, levels above the median at T2 were associated with earlier relapse in the nDC arm (p=0.013, Log-Rank (Mantel Cox) test) but not in the PL arm (p=0.640, Log-Rank (Mantel Cox) test) (Figure 6B). Low levels of acylcarnitines, i.e lauroyl-L-carnitine (C12:0) or myristoylcarnitine (C14:1) at T1 were associated with prolonged RFS in the PL arm (Figure 6C left, p=0.049 and Figure 6C right, p=0.099, Log-Rank (Mantel Cox) test), with less of an effect in the nDC arm (Figure 6C left, p=0.126 and Figure 6C right, p=0.269, Log-Rank (Mantel Cox) test). In fact, taking into account both *F. prausnitzii* relative abundance and acylcarnitine estimates, we could identify a subgroup of nDC-treated patients with improved RFS. Patients in the nDC arm harboring high relative abundance of *F. prausnitzii* (*F. prausnitzii*^{high}) and low levels of acylcarnitines (either carnitine C12:0^{low} or C14:1^{low}) representing up to 37% (22/60) of the nDC arm exhibited a prolonged RFS (Figure 6D left, p=0.016 and Figure 6D right, p=0.044, Log-Rank (Mantel Cox) test). The survival advantage of this subgroup of individuals based on these two biomarkers could be generalized to all patients (Figure S10A-B). Figure S10C-D depicts distinct strains of *F. prausnitzii*.

Altogether, a number of biological serum soluble markers independent from clinical parameters impacted the survival of this cohort of stage III melanoma, that may not be directly inferred to the nDC treatment, including *F. prausnitzii* strains, FA, acylcarnitines, BA and polyamines, that interact together.

Discussion

This ancillary prospective study attempted to infer a prognostic impact of serum biomarkers analyzed at two time points in the treatment efficacy. Due to treatment failure and to relatively small subgroup of patients, it aims at drawing new hypothesis on how systemic pathological deviations in the host-microbiome interaction may be clinically relevant. We conclude that, despite the randomization process, a bias was inadvertently introduced in the MIND-DC trial with the nDC treatment arm skewed at baseline towards a relative under-representation of health-associated commensals, dominated by but not limited to distinct strains of *F. prausnitzii* [31,43]. This bias also translated into a relative increase of the conjugated primary BA in the nDC arm (compared with the PL arm), likely at the expense of the unconjugated BA (namely cholic acid harboring a favorable prognostic value). Interestingly, the *F. prausnitzii* strains anticorrelated with fatty and carboxylic acids, as well as acylcarnitines, especially in the nDC arm. Last but not least, both *F. prausnitzii* and FA metabolites (acylcarnitines) cooperated to predict RFS in the whole cohort, identifying a subset of patients with better prognosis in the nDC arm.

This unexpected randomization bias was not due to artefactual deviations in serum sample storage or freezing troubleshooting with center of enrollment (Zwolle versus Nijmegen) effects or co-medications to the best of our appreciation. *F. prausnitzii* is one of the main members of the *Faecalibacterium* genus within the Firmicutes phylum, described as a health-related gut homeostatic bacterium [44]. Defects in the relative abundance of *F. prausnitzii* have also been associated with an increased risk of post-operative recurrence of Crohn disease [45]. *F. prausnitzii* exerts anti-inflammatory effects both *in vitro* and *in vivo* in specific pathogen-free and gnotobiotic mice subjected to experimental acute colitis [33,46–48]. The health-beneficial effects of *F. prausnitzii* stem from various mechanisms affecting the epithelial barrier, the local and systemic metabolism, and the immune system. *F. prausnitzii* can stimulate goblet cells to produce mucus glycans, dampens the activation of the NF-κB pathway through the secretion of a 15kDa soluble microbial anti-inflammatory molecule [49], as well as several metabolites (including short-chain fatty acids [50,51], 4-Hydroxy-butyrate [52], the anti-inflammatory shikimic and salicylic acids, and the osmoprotective raffinose [52]). Importantly, the human colonic mucosa contains *F. prausnitzii*-specific regulatory type 1-like IL-10-secreting and Foxp3-negative T cells that are characterized by a double expression of CD4 and CD8α (DP8α) endowed with potent anti-inflammatory functions [53]. The adoptive transfer of a HLA-DR*0401-restricted DP8α Treg clone combined with *F. prausnitzii* oral supplementation

conferred a protective effect against acute colitis in HLA-DR*0401 transgenic NSG model [53]. *F. prausnitzii* directly acted on antigen presenting cells (APC), inducing DC to express anti-inflammatory mediators (such as IL-10, IL-27, CD39, IDO-1, and PDL-1) reducing overt TLR4 signaling [34]. We surmise that these homeostasis-promoting effects of *F. prausnitzii* are seminal to prevent or compensate for the cancer-associated stress ileopathy observed in patients diagnosed with solid tumors [54]. Indeed, the β2 adrenergic receptor-dependent ileal atrophy described in tumor-bearing mice and patients culminates in intestinal dysbiosis (dominated by the *Enterocloster* genus) that contributes to tumor incidence and severity [54].

Besides maintaining homeostasis, *F. prausnitzii* was correlated with the immunostimulatory effects of ICI, increasing blood $ICOS^+CD4^+$ T cells and sCD25 serum levels as well as reprogramming of the tumor microenvironment [27,29]. Of note, *F. prausnitzii* could increase α-ketoglutarate release [52] that in turn, was shown to induce PDL-1 and to synergize with anti-PD-1 antibody [55]. *F. prausnitzii* might also exert direct cytostatic activity on tumor cells *in vitro*. Its supernatant could inhibit the autocrine secretion of IL-6 and the phosphorylation of JAK2/STAT3 in the breast cancer cell line MCF-7 [56]. This effect was ascribed to *F. prausnitzii* metabolites. In a study comparing stool MG and serum MB in 50 patients diagnosed with breast malignant or benign nodules, the authors showed a significant reduction in the relative abundance of *F. prausnitzii* in the breast cancer group. The MB profiles of patients with breast cancer differed from that of controls in the linoleic acid metabolism, and biosynthesis of unsaturated FA [56]. *F. prausnitzii* was also negatively correlated with the levels of phospholipid metabolites, such as 1-stearoyl-2-hydroxy-sn-glycero-3-phosphocholine, 1-Oleoyl-sn-glycero-3-phosphocholine and sphingomyelin.

In fact, accumulating evidence points to a role of *F. prausnitzii* in regulating lipid metabolism. FA are involved in energy metabolism and cell membrane structural components involved in wound healing and cancer cell metabolism [57]. In tumor tissues, free FA are esterified to fatty acyl-CoAs and then transported into the mitochondria by the carnitine shuttling, while in normal tissue, they undergo beta-oxidation as fatty acyl-CoAs to feed into the TCA cycle [58,59]. Nonalcoholic fatty liver disease (NAFLD) patients exhibit a decreased relative abundance or prevalence of *F. prausnitzii* compared with HV [60]. Approximately 20–80% of NAFLD patients have dyslipidemia [61]. Treatment with distinct *F. prausnitzii* strains reversed dyslipidemia symptoms in NAFLD mice [51]. Oral gavage with *F. prausnitzii* in high fat diet-treated mice appeared to increase FA oxidation and adiponectin signaling in liver and increased adiponectin expression in visceral adipose tissue [62]. Gas chromatography analyses of hepatic lipid classes revealed a drop in several FA (such as stearic acid, arachidonic acid,

eicosapentaenoic acid, and docosahexanoic acid) in *F. prausnitzii*-treated mice [62]. Our findings highlight the potential critical impact of lipid metabolism in melanoma aggressiveness [63,64]. The contribution of adipose tissue and lipid metabolism, in particular glycerophospholipids, sphingolipids, sterols and eicosanoids in melanoma plasticity has been reviewed [65]. There is a *de novo* synthesis (of cholesterol, glycerophospholipids, sphingolipids, droplets of neutral lipids), an elongation and desaturation of FA cells as well as importation of FA from neighboring adipocytes that can fuel FA β-oxidation in mitochondria of melanoma cells. De novo lipogenesis together with hypoxia and driver mutations cooperate in melanoma cells to meet their energetic demands. In addition to cell intrinsic pathways, melanoma cells secretes the immunosuppressive PGE2 and the S1P lipids to escape cancer immunosurveillance. Lipid metabolites have a major impact on APC and macrophages. Macrophages are a rich source of bioactive lipids, including FA and their oxygenated forms, oxylipins, following incorporation of lipoproteins or non-esterified FA bound to albumin as well as phagocytosis and efferocytosis. Saturated FA and oxylipins strongly contribute to type 1 inflammation by macrophages (associated with their tumoricidal and proinflammatory phenotype) while IL-4 -mediated M2 polarization tends to dampen FA and oxylipin synthesis [66]. Inhibition of FA synthesis by DC, albeit reducing their differentiation, enhanced their T cell stimulatory capacities, inducing an endoplasmic reticulum stress response associated with MHC class II, costimulatory molecule and cytokine expression [67]. Further, blockade of FA synthesis increased the DC/NK cell cross-talk leading to IFNγ secretion [67]. Two other studies demonstrated that saturated FA activated TLR4, whereas n-3 and n-6 polyunsaturated FA inhibited LPS activation, resulting in altered DC surface molecule expression of CD40 and reduced TNF-α or IL-12p40 release [68,69]. Finally, the liver could also be a source of FA and account for BA deregulation. In addition to absorbing circulating FA, hepatocytes synthesize FA from dietary carbohydrates that reach the hepatocytes via the portal vein [70]. The enterohepatic recirculation of BA exerts important regulatory effects on many hepatic, biliary, and intestinal functions. Dysbiosis can modulate biliary salt composition, leading to a downregulation of MAdCAM-1 and the exodus of immunosuppressive enterotropic T cells promoting tumor growth [71].

Hence, our findings allow to postulate that patients with stage III melanoma of dismal prognosis harbored major deviations in lipid metabolism at diagnosis, likely originating from a diseased enterohepatic axis, that corrupted the immunostimulatory potential and/or exacerbated the tolerogenic functions of autologous nDC in certain patients. These data support the use of distinct biomarkers belonging to specific pathways (listed in the circosplot Figure 5C) to better select the patient population to immunize. Prospective trials assessing immunotherapy

strategies involving patients with melanoma should validate the clinical relevance of these biomarkers.

Material and methods

Medical centers and regulatory approvals for translational research. The MIND-DC trial (NCT02993315) was performed in 2 centers in the Netherlands.

Ethics approval and consent to participate. This study involves human participants, was approved by the Dutch Central Committee on Research Involving Human Subjects, and is in concordance with the Declaration of Helsinki. Written informed consent was obtained from all patients.

Trial design. Double-blind, randomized, placebo-controlled phase III clinical trial. Patients with resected stage IIIB and IIIC cutaneous melanoma were randomized in a 2:1 ratio to nDC treatment or placebo (Figure S1A). Patients received either intranodal injections of nDC (3-8x10^6/injection) or placebo every 2 weeks for 3 doses, repeated after 6 and 12 months. The primary endpoint was the 2Y-RFS. One patient was excluded due to insufficient follow-up to avoid censoring bias using binary classifiers. Treatment was stopped in case of disease recurrence (including both loco-regional and distant metastases), unacceptable toxicity, or withdrawn from the study. Details are described in the companion manuscript (K. Bol, co-submitted).

Dendritic cell isolation and vaccine preparation. Patients in the nDC arm were vaccinated with autologous DC loaded with tumor peptides and overlapping peptide pools. Cells were harvested by apheresis and conventional and serumcytoid DC were isolated with the fully automated and enclosed immunomagnetic CliniMACS Prodigy® isolation system (Miltenyi Biotec). DC were pulsed with MACS® GMP-grade PepTivators®, overlapping peptide pools of the CTA MAGE-A3 and NY-ESO-1 (Miltenyi Biotec) covering the sequence of the entire antigen, and a mix of fourteen peptides of TAA gp100 and tyrosinase and CTA MAGE-C2, MAGE-A3 and NY-ESO-1 (all Leiden University Medical Center, Leiden, the Netherlands) and matured with protamine/mRNA (Meda Pharma, Amstelveen, the Netherlands) and Universitätsklinikum Erlangen, Erlangen, Germany).

Collection of stool and blood samples. Stool samples were prospectively collected at different time points (T1: pre-treatment, T2: 4 weeks after treatment start, before the 3rd injection) at each center following the International Human Microbiome Standards (IHMS) guidelines. Both T1 and T2 samples were considered for this analysis. Blood samples were collected at the same timepoints.

Metagenomic analysis of patient stools. Overall, 185 fecal samples from 93 patients were sequenced with whole genome sequencing technology. Aliquots of stool samples were stored with DNA/RNA Shield Buffer (Zymo) at –20 °C until use. DNA was extracted from aliquots of fecal samples using the DNeasy PowerSoil Pro Kit (Qiagen) following the manufacturer's instructions. Sequencing libraries were prepared using the Illumina® DNA Prep, (M) Tagmentation kit (Illumina), following the manufacturer's guidelines. A cleaning step on the pool with 0.7x Agencourt AMPure XP beads was implemented. Sequencing was performed on a Novaseq600 S4 flow cell (Illumina) at the internal sequencing facility at University of Trento, Trento, Italy. Libraries were multiplexed using dual indexing and sequenced for 150bp paired-end reads using the Illumina NovaSeq6000 platform according to manufacturer's protocols. Subsequently, sequenced metagenomes were QCed using the pre-processing pipeline implemented by Segata's lab and available on https://github.com/SegataLab/preprocessing. This preprocessing pipeline consists of three steps: i) Initial quality control by removing low-quality reads (quality score Q20), fragmented short reads (75 bp), and reads with 2 or more ambiguous nucleotides; ii) contaminant DNA removal by using Bowtie 2 with the --sensitive-local parameter, for both the phiX174 Illumina spike-in and human-associated reads (hg19); iii) Sorting and splitting for the creation of paired forward and reverse output files and the unpaired reads in a separate output file for each metagenome. After preprocessing, we obtained an average of 48M reads per sample. Microbial relative abundances were then generated using MetaPhlAn-4 [32], while functional profiles were obtained applying HumanN-3.6 [72]. For alpha and beta-diversity, we computed the per-sample Shannon index [73] and the between-samples Bray-Curtis dissimilarities using the implementation available in the Vegan R package [74]. Differences in the distributions of alpha and beta diversity for samples collected at diagnosis with respect to recurrence at 2 years were then evaluated using an unpaired two-sample Wilcoxon test [75]. For the comparisons concerning response variables (recurrence, 2-year recurrence-free survival) and treatment arms, we fitted a generalized linear model for each feature for each considered task (2 year relapse) via the MaAsLin2 R package [76]. Microbial features are first AST or CLR transformed after being converted to pseudo-counts. FDR

correction is applied via Benjamini-Hochberg procedure. Only features with at least 30% prevalence have been considered in the analysis for 2-year relapse and 2-year death to guarantee at least 10 positive samples for each feature. A threshold of 20% prevalence is used when comparing samples from nDC versus PL arms at baseline.

Metabolomics analyses

Serum sample preparation and widely targeted detection by GC-MS and LC-MS. Fifty (50) µl of collected sera were mixed with 500 µl of ice-cold extraction mixture (methanol/water, 9/1, -20°C, with labelled internal standard). To facilitate endogenous metabolites extraction, samples were then completely homogenized (vortexed 5 minutes at 2500 rpm) and then centrifuged (10 min at 15000 g, 4°C). Supernatants were collected and several fractions were split to be analyzed by different Liquid chromatography coupled with mass spectrometers (LC/MS) [77]. Polyamines and biliary acids analyses were performed by LC-MS/MS with a 1260 UHPLC (Ultra-High Performance Liquid Chromatography) (Agilent Technologies) coupled to a QQQ 6410 (Agilent Technologies) and were previously described [78]. Pseudo-targeted analysis by UHPLC-HRAM (Ultra-High Performance Liquid Chromatography – High Resolution Accurate Mass) was performed on a U3000 (Dionex) / Orbitrap q-Exactive (Thermo) coupling, previously described [78,79]. All targeted treated data were merged and cleaned with a dedicated R (version 4.0) package (@Github/Kroemerlab/GRMeta).

Data processing and statistical analysis. Raw data were preprocessed and analyzed with R using the GRMeta package (@Github/Kroemerlab/GRMeta). This software included statistical analysis using a multivariate method approach, as PCA, Heatmap and data visualization, as volcano plots. Area intensity levels were corrected with a quality control pooled sample based algorithm and normalized area were then log2-transformed prior to heatmaps, boxplots and volcano plots visualizations. A total of 152 metabolites were finally analyzed for sera samples at T1 and at T2. The best significant metabolites were presented with boxplots with metabolite levels log scaled. Mann-Whitney U-test with no adjustment were conducted on data gathered by two groups on processed data with R. In cases when data treatments were performed on more than two groups of patients, Kruskal-Wallis test followed by a Dunn's test with no adjustment were used on processed data. Pearson correlation analysis was applied on log2 transformed data from metabolite normalized profiles and *F. prausnitzii* SGB15318 and 15322 abundances. Relevant metabolites correlating with *F. prausnitzii* strains were selected and analyzed by enrichment functional analysis with Metaboanalyst

(https://www.metaboanalyst.ca) using the KEGG Database[37] for significant metabolites annotation and visualization.

Statistical analyses

Data analyses analyses were performed with the Prism 8 (GraphPad, San Diego, CA, USA) and the R software. The prevalence of MGS was calculated using microbial relative abundances (MetaPhlAn-4) and considered absent if relative abundance equal to 0 and present if relative abundance superior to 0. Chi-square test was used for comparison of unpaired groups, considered significant at $p<0.05$. For MGS, two groups of patients were defined by reference values of relative abundances (MetaPhlAn-4) from publicly available HV cohort: high if $\geq$ median and low if < median of the MGS relative abundance from HV. For key metabolites, two groups of patients were defined by its abundance median in the overall MIND-DC cohort: high if $\geq$ median and low if < median. RFS analyses were performed using KM estimator. As the analysis of compositional data can lead to missleading results due to spurious correlation, we used the CLR transform to project the MGS relative abundances from the simplex to the more usual Euclidean space using the *clr* function of the compositions R package.

Longitudinal analysis. The analysis of the metabolite or CLR transformed microbial SGB evolution between T1, M_{T1}, and T2, M_{T2}, was performed using the following linear regression adjusted for the clinical covariables $\boldsymbol{X}$ (age, sex, BMI, stage, and ECOG-PS), considering M_{T2} as response and M_{T1} as offset: $M_{T2} = M_{T1} + \beta_0 + \beta_{DC} + \boldsymbol{\beta X}$. The intercept β_0 represents evolution of M ($M_{T2} - M_{T1}$) in the placebo arm, and β_{DC} represents the impact of the DC (i.e. the difference of the evolution between the two arms). The Wald test p-values of β_0 and β_{DC} were provided and considered as statistically significant when $p<0.05$. The evolution in the DC arm was estimated by β_0 reversing the arm reference (i.e. from the model $M_{T2} = M_{T1} + \beta_0 + \beta_{PL} + \boldsymbol{\beta X}$).

Machine Learning. All ML models were developed using R. Feature selection and prediction were based alternatively on two different outcomes: the 2Y-R and treatment arm (nDC versus PL arms). For each type of outcome, three datasets per omic (clinical features only, MB, MGS, or MB and MGS) were defined from the timepoint that was used: T1, T2, and T2-T1/T1 (pre treatment + evolution until T2 i.e. T2-T1) and a third dataset constructed by joining T2-T1 and T1 values. For each of these 18 models, clinical features were always included in both feature

609 selection and prediction phases. For each model, clinical features were always included in both
610 feature selection and prediction phases. The ML pipeline is based on a first step of feature
611 selection using Boruta feature selection algorithm based on XGboost (eXtreme Gradient
612 Boosting) algorithm [80] to identify most relevant features among clinical and biological markers
613 (both in metabolomics or and metagenomics). A second step consisted in re-training the model
614 from the subset of selected features re-including clinical variables in order to control potential
615 confounding bias. A last fit of the model using selected biomarkers was applied on our training
616 data, enabling the model to prepare for future label predictions on new data. For the multi-omics
617 model, we performed a second step of feature selection from the metabolites and MGS selected
618 in each omics in the first step (+ clinical variables) to obtain our final model. Missing values of
619 metabolites were imputed using the multiple imputation by chained equations (MICE) method
620 using the mice R package [81]. We performed 50 imputations with 50 iterations to capture the
621 uncertainty of the imputation procedure. The feature selection procedure described above was
622 repeated using the 50 imputed datasets, and the metabolites selected in more than 75% of these
623 50 iterations were retained for the final step (assuming that they are robust to the randomness
624 of the imputation). A single last imputation was performed to retrain the model in the final step.
625 The model explainer of the different final model was based on the SHAP (Shapley Additive
626 exPlanations) analysis, which is a visualization tool based on the following construction: SHAP
627 values are weights associated to features for each patient, positive when the value of a marker
628 for this patient tends to increase the prediction as class 1 (2Y-relapse), negative otherwise (2Y-
629 no-relapse). The more the absolute value of SHAP value increases, the more the feature is likely
630 to impact the prediction (as class 1 if SHAP_value>0, class 0 otherwise). SHAP values are thus
631 positive or negative continuous values.
632 Correlations between biomarkers were analyzed via the mixOmics package in R [82], using the
633 DIABLO multiblock sPLS-DA method to display explanatory relationship between pathways
634 and then displayed into a circosplot. The prediction performance of the whole model pipeline
635 (feature selection to model fitting) was evaluated using the bootstrap optimism corrected area
636 under the receiver operating characteristic (AUROC) curve. Due to the lack of external
637 validation cohort, the optimism of the AUROC was corrected using the 0.632+ bootstrap
638 method [83]. The confidence interval of these optimism corrected AUROC was obtained using
639 two-stage bootstrap methods proposed by Noma et al [84]. (50 internal samples, 500 external
640 samples). The 0.632+ estimators are displayed on each figure.
641

642 **Availability of data and material.** Metagenomics (bioprojects PRJEB66197) and
643 metabolomics (Elsevier/Mendeley DOI: 10.17632/nzb653783h.1) data are all publicly
644 available.
645
646 **References**
647 1. Eggermont, A. M., Spatz, A. & Robert, C. Cutaneous melanoma. *The Lancet* **383**, 816–
648 827 (2014).
649 2. Reijers, I. L. M. *et al.* Personalized response-directed surgery and adjuvant therapy after
650 neoadjuvant ipilimumab and nivolumab in high-risk stage III melanoma: the PRADO
651 trial. *Nat Med* **28**, 1178–1188 (2022).
652 3. Morton, D. L. *et al.* Sentinel-Node Biopsy or Nodal Observation in Melanoma. *N Engl J*
653 *Med* **355**, 1307–1317 (2006).
654 4. Eggermont, A. M. M. *et al.* Adjuvant ipilimumab versus placebo after complete resection
655 of high-risk stage III melanoma (EORTC 18071): a randomised, double-blind, phase 3
656 trial. *Lancet Oncol* **16**, 522–530 (2015).
657 5. Eggermont, A. M. M. *et al.* Prolonged Survival in Stage III Melanoma with Ipilimumab
658 Adjuvant Therapy. *N Engl J Med* **375**, 1845–1855 (2016).
659 6. Robert, C. *et al.* Improved Overall Survival in Melanoma with Combined Dabrafenib and
660 Trametinib. *N Engl J Med* **372**, 30–39 (2015).
661 7. Robert, C. *et al.* Nivolumab in previously untreated melanoma without BRAF mutation. *N*
662 *Engl J Med* **372**, 320–330 (2015).
663 8. Robert, C. *et al.* Pembrolizumab versus Ipilimumab in Advanced Melanoma. *N Engl J*
664 *Med* **372**, 2521–2532 (2015).
665 9. Hodi, F. S. *et al.* Improved survival with ipilimumab in patients with metastatic
666 melanoma. *N Engl J Med* **363**, 711–723 (2010).
667 10. Ugurel, S. *et al.* Survival of patients with advanced metastatic melanoma: the impact of
668 novel therapies-update 2017. *Eur J Cancer* **83**, 247–257 (2017).

669 11. Long, G. V. *et al.* Adjuvant Dabrafenib plus Trametinib in Stage III BRAF-Mutated
670 Melanoma. *N Engl J Med* **377**, 1813–1823 (2017).
671 12. Weber, J. *et al.* Adjuvant Nivolumab versus Ipilimumab in Resected Stage III or IV
672 Melanoma. *N Engl J Med* **377**, 1824–1835 (2017).
673 13. Versluis, J. M. *et al.* Neoadjuvant ipilimumab plus nivolumab in synchronous clinical
674 stage III melanoma. *Eur J Cancer* **148**, 51–57 (2021).
675 14. Patel, S. P. *et al.* Neoadjuvant-Adjuvant or Adjuvant-Only Pembrolizumab in Advanced
676 Melanoma. *N Engl J Med* **388**, 813–823 (2023).
677 15. Amaria, R. N. *et al.* Neoadjuvant systemic therapy in melanoma: recommendations of the
678 International Neoadjuvant Melanoma Consortium. *Lancet Oncol* **20**, e378–e389 (2019).
679 16. Menzies, A. M. *et al.* Pathological response and survival with neoadjuvant therapy in
680 melanoma: a pooled analysis from the International Neoadjuvant Melanoma Consortium
681 (INMC). *Nat Med* **27**, 301–309 (2021).
682 17. Palucka, K., Ueno, H., Roberts, L., Fay, J. & Banchereau, J. Dendritic cells: are they
683 clinically relevant? *Cancer J* **16**, 318–324 (2010).
684 18. Palucka, K. & Banchereau, J. Cancer immunotherapy via dendritic cells. *Nat Rev Cancer*
685 **12**, 265–277 (2012).
686 19. Draube, A. *et al.* Dendritic cell based tumor vaccination in prostate and renal cell cancer:
687 a systematic review and meta-analysis. *PLoS One* **6**, e18801 (2011).
688 20. Bol, K. F., Schreibelt, G., Gerritsen, W. R., de Vries, I. J. M. & Figdor, C. G. Dendritic
689 Cell–Based Immunotherapy: State of the Art and Beyond. *Clinical Cancer Research* **22**,
690 1897–1906 (2016).
691 21. Anguille, S., Smits, E. L., Lion, E., Van Tendeloo, V. F. & Berneman, Z. N. Clinical use
692 of dendritic cells for cancer therapy. *The Lancet Oncology* **15**, e257–e267 (2014).

693 22. Gross, S. *et al.* Twelve-year survival and immune correlates in dendritic cell-vaccinated
694 melanoma patients. *JCI Insight* **2**, e91438, 91438 (2017).
695 23. Lesterhuis, W. J. *et al.* Wild-type and modified gp100 peptide-pulsed dendritic cell
696 vaccination of advanced melanoma patients can lead to long-term clinical responses
697 independent of the peptide used. *Cancer Immunol Immunother* **60**, 249–260 (2011).
698 24. Lesterhuis, W. J. *et al.* Route of administration modulates the induction of dendritic cell
699 vaccine-induced antigen-specific T cells in advanced melanoma patients. *Clin Cancer Res*
700 **17**, 5725–5735 (2011).
701 25. de Vries, I. J. M. *et al.* Immunomonitoring tumor-specific T cells in delayed-type
702 hypersensitivity skin biopsies after dendritic cell vaccination correlates with clinical
703 outcome. *J Clin Oncol* **23**, 5779–5787 (2005).
704 26. Aarntzen, E. H. J. G. *et al.* Skin-Test Infiltrating Lymphocytes Early Predict Clinical
705 Outcome of Dendritic Cell–Based Vaccination in Metastatic Melanoma. *Cancer Research*
706 **72**, 6102–6110 (2012).
707 27. Gopalakrishnan, V. *et al.* Gut microbiome modulates response to anti–PD-1
708 immunotherapy in melanoma patients. *Science* **359**, 97–103 (2018).
709 28. Matson, V. *et al.* The commensal microbiome is associated with anti–PD-1 efficacy in
710 metastatic melanoma patients. *Science* **359**, 104–108 (2018).
711 29. Chaput, N. *et al.* Baseline gut microbiota predicts clinical response and colitis in
712 metastatic melanoma patients treated with ipilimumab. *Ann Oncol* **28**, 1368–1379 (2017).
713 30. Lee, K. A. *et al.* Cross-cohort gut microbiome associations with immune checkpoint
714 inhibitor response in advanced melanoma. *Nat Med* **28**, 535–544 (2022).
715 31. McCulloch, J. A. *et al.* Intestinal microbiota signatures of clinical response and immune-
716 related adverse events in melanoma patients treated with anti-PD-1. *Nat Med* **28**, 545–556
717 (2022).

718 32. Blanco-Míguez, A. *et al.* Extending and improving metagenomic taxonomic profiling
719 with uncharacterized species using MetaPhlAn 4. *Nat Biotechnol* (2023)
720 doi:10.1038/s41587-023-01688-w.
721 33. Miquel, S. *et al.* Faecalibacterium prausnitzii and human intestinal health. *Curr Opin*
722 *Microbiol* **16**, 255–261 (2013).
723 34. Alameddine, J. *et al.* Faecalibacterium prausnitzii Skews Human DC to Prime IL10-
724 Producing T Cells Through TLR2/6/JNK Signaling and IL-10, IL-27, CD39, and IDO-1
725 Induction. *Front Immunol* **10**, 143 (2019).
726 35. Routy, B. *et al.* The gut microbiota influences anticancer immunosurveillance and general
727 health. *Nature Reviews Clinical Oncology* **15**, 382–396 (2018).
728 36. Sivanand, S. & Vander Heiden, M. G. Emerging Roles for Branched-Chain Amino Acid
729 Metabolism in Cancer. *Cancer Cell* **37**, 147–156 (2020).
730 37. Kanehisa, M. & Goto, S. KEGG: kyoto encyclopedia of genes and genomes. *Nucleic*
731 *Acids Res* **28**, 27–30 (2000).
732 38. Caspi, R. *et al.* The MetaCyc database of metabolic pathways and enzymes - a 2019
733 update. *Nucleic Acids Research* **48**, D445–D453 (2020).
734 39. Bray, J. R. & Curtis, J. T. An Ordination of the Upland Forest Communities of Southern
735 Wisconsin. *Ecological Monographs* **27**, 325–349 (1957).
736 40. Derosa, L. *et al.* Intestinal Akkermansia muciniphila predicts clinical response to PD-1
737 blockade in patients with advanced non-small-cell lung cancer. *Nat Med* **28**, 315–324
738 (2022).
739 41. Chen, T. & Guestrin, C. XGBoost: A Scalable Tree Boosting System. in *Proceedings of*
740 *the 22nd ACM SIGKDD International Conference on Knowledge Discovery and Data*
741 *Mining* 785–794 (ACM, 2016). doi:10.1145/2939672.2939785.

742 42. Spearman Rank Correlation Coefficient. in *The Concise Encyclopedia of Statistics* 502–
743 505 (Springer New York, 2008). doi:10.1007/978-0-387-32833-1_379.
744 43. Derosa, L. *et al.* Microbiota-Centered Interventions: The Next Breakthrough in Immuno-
745 Oncology? *Cancer Discovery* **11**, 2396–2412 (2021).
746 44. Sokol, H. *et al.* Low counts of Faecalibacterium prausnitzii in colitis microbiota:
747 *Inflammatory Bowel Diseases* **15**, 1183–1189 (2009).
748 45. Sokol, H. *et al.* Faecalibacterium prausnitzii is an anti-inflammatory commensal
749 bacterium identified by gut microbiota analysis of Crohn disease patients. *Proc Natl Acad*
750 *Sci U S A* **105**, 16731–16736 (2008).
751 46. Zhang, M. *et al.* Faecalibacterium prausnitzii inhibits interleukin-17 to ameliorate
752 colorectal colitis in rats. *PLoS One* **9**, e109146 (2014).
753 47. Wrzosek, L. *et al.* Bacteroides thetaiotaomicron and Faecalibacterium prausnitzii
754 influence the production of mucus glycans and the development of goblet cells in the
755 colonic epithelium of a gnotobiotic model rodent. *BMC Biol* **11**, 61 (2013).
756 48. Martín, R. *et al.* The commensal bacterium Faecalibacterium prausnitzii is protective in
757 DNBS-induced chronic moderate and severe colitis models. *Inflamm Bowel Dis* **20**, 417–
758 430 (2014).
759 49. Quévrain, E. *et al.* Identification of an anti-inflammatory protein from Faecalibacterium
760 prausnitzii, a commensal bacterium deficient in Crohn's disease. *Gut* **65**, 415–425 (2016).
761 50. Zhang, M. *et al. Faecalibacterium prausnitzii* produces butyrate to decrease c-Myc-
762 related metabolism and Th17 differentiation by inhibiting histone deacetylase 3.
763 *International Immunology* **31**, 499–514 (2019).
764 51. Hu, W. *et al.* Specific Strains of Faecalibacterium prausnitzii Ameliorate Nonalcoholic
765 Fatty Liver Disease in Mice in Association with Gut Microbiota Regulation. *Nutrients* **14**,
766 2945 (2022).

767 52. Miquel, S. *et al.* Identification of metabolic signatures linked to anti-inflammatory effects
768 of Faecalibacterium prausnitzii. *mBio* **6**, e00300-15 (2015).
769 53. Touch, S. *et al.* Human CD4+CD8α+ Tregs induced by Faecalibacterium prausnitzii
770 protect against intestinal inflammation. *JCI Insight* **7**, e154722 (2022).
771 54. Yonekura, S. *et al.* Cancer Induces a Stress Ileopathy Depending on β-Adrenergic
772 Receptors and Promoting Dysbiosis that Contributes to Carcinogenesis. *Cancer Discovery*
773 **12**, 1128–1151 (2022).
774 55. Liu, N. *et al.* Supplementation with α-ketoglutarate improved the efficacy of anti-PD1
775 melanoma treatment through epigenetic modulation of PD-L1. *Cell Death Dis* **14**, 170
776 (2023).
777 56. Ma, J. *et al.* Alter between gut bacteria and blood metabolites and the anti-tumor effects
778 of Faecalibacterium prausnitzii in breast cancer. *BMC Microbiol* **20**, 82 (2020).
779 57. Serhan, C. N., Chiang, N. & Van Dyke, T. E. Resolving inflammation: dual anti-
780 inflammatory and pro-resolution lipid mediators. *Nat Rev Immunol* **8**, 349–361 (2008).
781 58. Liu, X. *et al.* LC-MS-Based Plasma Metabolomics and Lipidomics Analyses for
782 Differential Diagnosis of Bladder Cancer and Renal Cell Carcinoma. *Front. Oncol.* **10**,
783 717 (2020).
784 59. Wettersten, H. I. *et al.* Grade-Dependent Metabolic Reprogramming in Kidney Cancer
785 Revealed by Combined Proteomics and Metabolomics Analysis. *Cancer Res* **75**, 2541–
786 2552 (2015).
787 60. Zhu, L. *et al.* Characterization of gut microbiomes in nonalcoholic steatohepatitis
788 (NASH) patients: A connection between endogenous alcohol and NASH. *Hepatology* **57**,
789 601–609 (2013).

790 61. Zhang, Q.-Q. & Lu, L.-G. Nonalcoholic Fatty Liver Disease: Dyslipidemia, Risk for
791 Cardiovascular Complications, and Treatment Strategy. *J Clin Transl Hepatol* **3**, 78–84
792 (2015).
793 62. Munukka, E. *et al.* Faecalibacterium prausnitzii treatment improves hepatic health and
794 reduces adipose tissue inflammation in high-fat fed mice. *ISME J* **11**, 1667–1679 (2017).
795 63. Kamphorst, J. J. *et al.* Hypoxic and Ras-transformed cells support growth by scavenging
796 unsaturated fatty acids from lysophospholipids. *Proc Natl Acad Sci U S A* **110**, 8882–
797 8887 (2013).
798 64. Kuzu, O. F., Noory, M. A. & Robertson, G. P. The Role of Cholesterol in Cancer. *Cancer*
799 *Res* **76**, 2063–2070 (2016).
800 65. Pellerin, L. *et al.* Lipid metabolic Reprogramming: Role in Melanoma Progression and
801 Therapeutic Perspectives. *Cancers (Basel)* **12**, 3147 (2020).
802 66. Balestrieri, B., Di Costanzo, D. & Dwyer, D. F. Macrophage-Mediated Immune
803 Responses: From Fatty Acids to Oxylipins. *Molecules* **27**, 152 (2021).
804 67. Rehman, A. *et al.* Role of Fatty-Acid Synthesis in Dendritic Cell Generation and
805 Function. *The Journal of Immunology* **190**, 4640–4649 (2013).
806 68. Weatherill, A. R. *et al.* Saturated and polyunsaturated fatty acids reciprocally modulate
807 dendritic cell functions mediated through TLR4. *J Immunol* **174**, 5390–5397 (2005).
808 69. Zeyda, M. *et al.* Polyunsaturated Fatty Acids Block Dendritic Cell Activation and
809 Function Independently of NF-κB Activation. *Journal of Biological Chemistry* **280**,
810 14293–14301 (2005).
811 70. Bechmann, L. P. *et al.* The interaction of hepatic lipid and glucose metabolism in liver
812 diseases. *J Hepatol* **56**, 952–964 (2012).
813 71. Fidelle, M. *et al.* A microbiota-modulated checkpoint directs immunosuppressive
814 intestinal T cells into cancers. *Science* **380**, eabo2296 (2023).

72. Beghini, F. *et al. Integrating taxonomic, functional, and strain-level profiling of diverse microbial communities with bioBakery 3*. http://biorxiv.org/lookup/doi/10.1101/2020.11.19.388223 (2020) doi:10.1101/2020.11.19.388223.

73. Shannon, C. E. A Mathematical Theory of Communication. *Bell System Technical Journal* **27**, 379–423 (1948).

74. Oksanen J, Blanchet FG, Friendly M, Kindt R, Legendre P, McGlinn D, Minchin PR, O'Hara RB, Simpson GL, Solymos P, Stevens MHH, Szoecs E, Wagner H (2018) vegan: Community Ecology Package. R package version 2.5-2.

75. Rey, D. & Neuhäuser, M. Wilcoxon-Signed-Rank Test. in *International Encyclopedia of Statistical Science* (ed. Lovric, M.) 1658–1659 (Springer Berlin Heidelberg, 2011). doi:10.1007/978-3-642-04898-2_616.

76. Mallick, H. *et al.* Multivariable association discovery in population-scale meta-omics studies. *PLoS Comput Biol* **17**, e1009442 (2021).

77. Grajeda-Iglesias, C. *et al.* Oral administration of Akkermansia muciniphila elevates systemic antiaging and anticancer metabolites. *Aging (Albany NY)* **13**, 6375–6405 (2021).

78. Durand, S. *et al.* The intracellular metabolome of starving cells. in *Methods in Cell Biology* vol. 164 137–156 (Elsevier, 2021).

79. Abdellatif, M. *et al.* Nicotinamide for the treatment of heart failure with preserved ejection fraction. *Sci. Transl. Med.* **13**, eabd7064 (2021).

80. Kursa, M. B. & Rudnicki, W. R. Feature Selection with the **Boruta** Package. *J. Stat. Soft.* **36**, (2010).

81. Buuren, S. V. & Groothuis-Oudshoorn, K. **mice** : Multivariate Imputation by Chained Equations in *R*. *J. Stat. Soft.* **45**, (2011).

82. Rohart, F., Gautier, B., Singh, A. & Lê Cao, K.-A. mixOmics: An R package for 'omics feature selection and multiple data integration. *PLoS Comput Biol* **13**, e1005752 (2017).
83. Efron, B. & Tibshirani, R. Improvements on Cross-Validation: The .632+ Bootstrap Method. *Journal of the American Statistical Association* **92**, 548 (1997).
84. Noma, H., Shinozaki, T., Iba, K., Teramukai, S. & Furukawa, T. A. Confidence intervals of prediction accuracy measures for multivariable prediction models based on the bootstrap-based optimism correction methods. *Statistics in Medicine* **40**, 5691–5701 (2021).

Acknowledgments. We would like to particularly thank the patients who participated in the trial and all employees at the Radboud university medical center and Isala hospital who were involved in the trial execution.

Authors' contributions. Conceptualization: C.A.C.S., G.K., L.Zi., L.D. K.F.B., and I.J.M.V. **Methodology**: D.D, D.S, G.S., C.A.C.S., M.B., G.P., S.D., F.A., N.S., G.K. and L.Zi. **Software**: M.B., G.P., S.D. and D.D. **Validation**: D.D, D.S, C.A.C.S., G.S., M.B., G.P. and S.D. **Formal analysis**: C.A.C.S., M.B., G.P., S.D., D.D. and L.D. **Investigation**: G.S., C.A.C.S., M.B., G.P., K.F.B., S.D., M.F., R.B. **Resources**: K.F.B., I. J.M.V., G.S., G.K., L.Zi. and L.D. **Data Curation**: M.B., G.P., S.D., G.S., K.F.B. and I.J.M.V. **Writing - Original Draft**: L.Zi. and C.A.C.S. **Writing - Review & Editing:** all but in particular C.A.C.S., M.B., G.P., K.F.B., S.D., M.F., C.S., B.R., A.M.M.E., G.K., J.M.V., L.Zi. and L.D. **Visualization**: C.A.C.S. **Supervision**: L.Zi., K.F.B., and L.D. **Project administration:** C.A.C.S., C.S., N.S., G.K., K.F.B., I.J.M.V., L.Zi. and L.D. **Funding acquisition**: G.K., I.J.M.V., L.Zi. and L.D.

Competing interests. L.Zi. founded EverImmune and is the SAB president of everImmune. L.ZI. had grant support from Daichi Sankyo, Kaleido, 9 meters and Pileje. A.M.M.E.: consulting fees from Acetra, Agenus, BioInvent, Brenus, CatalYm, Epics, Ellipses, Galecto, GenOway, IO Biotech, IQVIA, ISA Pharmaceuticals, Merck&Co, MSD, Pierre Fabre, Sairopa, Scorpion, Sellas, SkylineDX, TigeTx, Trained Immunity TX. A.M.M.E.: participation on a Data Safety Monitoring Board: Boehringer Ingelheim, BioNTech, and Pfizer. A.M.M.E.: lectures for BMS, MSD. A.M.M.E.: stock or stock options for IO Biotech, SkylineDx and

Sairopa. G.K. has been holding research contracts with Daiichi Sankyo, Eleor, Kaleido, Lytix Pharma, PharmaMar, Osasuna Therapeutics, Samsara Therapeutics, Sanofi, Tollys, and Vascage. G.K. is on the Board of Directors of the Bristol Myers Squibb Foundation France. G.K. is a scientific co-founder of EverImmune, Osasuna Therapeutics, Samsara Therapeutics and Therafast Bio. G.K. is in the scientific advisory boards of Hevolution, Institut Servier and Longevity Vision Funds. G.K. is the inventor of patents covering therapeutic targeting of aging, cancer, cystic fibrosis and metabolic disorders. G.K.'s brother, Romano Kroemer, was an employee of Sanofi and now consults for Boehringer-Ingelheim. B.R. is co-founder of Science Curebiota. L.D. is a SAB member of EverImmune. K.F.B.: consulting fees (institutional) from MSD and Pierre Fabre. All other authors have declared no conflicts of interest. The funders had no role in the design of the study, in the writing of the manuscript, or in the decision to publish the results.

Funding. The MIND-DC trial was funded by ZonMw, Ministry of Health, Welfare and Sport (VWS), Stichting ATK, Miltenyi Biotec (in-kind). This work was supported by SEERAVE Foundation, European Union Horizon 2020:Project Number: 825410 and Project Acronym: ONCOBIOME, Institut National du Cancer (INCa), ANR Ileobiome - 19-CE15-0029-01, ANR RHU5 "ANR-21-RHUS-0017" IMMUNOLIFE", MAdCAM INCA_ 16698, Ligue contre le cancer, LABEX OncoImmunology, la direction generale de l'offre de soins (DGOS), Universite Paris-Sud, SIRIC SOCRATE (INCa/DGOS/INSERM 6043), and PACRI network. G.K. is supported by the Ligue contre le Cancer (équipe labellisée); Agence National de la Recherche (ANR) – Projets blancs; AMMICa US23/CNRS UMS3655; Association pour la recherche sur le cancer (ARC); Cancéropôle Ile-de-France; Fondation pour la Recherche Médicale (FRM); a donation by Elior; Equipex Onco-Pheno-Screen; European Joint Programme on Rare Diseases (EJPRD); European Research Council Advanced Investigator Award (ERC-2021-ADG, ICD-Cancer, Grant No. 101052444), European Union Horizon 2020 Projects Oncobiome, Prevalung (grant No. 101095604) and Crimson; Fondation Carrefour; Institut National du Cancer (INCa); Institut Universitaire de France; LabEx Immuno-Oncology (ANR-18-IDEX-0001); a Cancer Research ASPIRE Award from the Mark Foundation; the RHU Immunolife; Seerave Foundation; SIRIC Stratified Oncology Cell DNA Repair and Tumor Immune Elimination (SOCRATE); and SIRIC Cancer Research and Personalized Medicine (CARPEM). This study contributes to the IdEx Université de Paris ANR-18-IDEX-0001. This work is supported by the Prism project funded by the Agence Nationale de la Recherche under grant number ANR-18-IBHU-0002. CACS is funded by MSD Avenir. MF is

904 funded by SEERAVE Foundation and MERCK Foundation. LD and BR were supported by
905 Philantropia at Gustave Roussy Foundation.

Tables

Table S1. Clinical characteristics of patients included in the translational analysis.

Table S2. Patient accrual for each omics and treatment arm in the MIND-DC ancillary study.

Table S3. A-C. Linear model coefficients (MaAsLin2, coefficient) for microbial SGBs that are found associated after arcsin-sqrt (AST) with outcome (recurrence at 2 years, Figure 1) (A) or treatment arm (nDC versus PL, Figure 3) (B) or outcome (recurrence at 2 years) according to treatment arm (Figure S1) (C).

Table S4. Comedications and flu-like symptoms between T1 and T2.

Table S5. A-B. List of metabolites monitored by targeted metabolomics between T1 versus T2 according to treatment arm (A) and between treatment arm (nDC versus PL) according to timepoints (B).

Figure Legends

Figure 1. Metagenomics-based profiles show taxonomic signatures associated with recurrence at 2 years (2Y-R) in two different time points.

A and C. Shannon index and between-samples Bray-Curtis dissimilarities distributions for patients with recurrence at 2 years (2Y-R, orange, n=55) compared to patients with no recurrence at 2 years (2Y-noR, blue, n=36) at baseline (T1, **A**) and for patients with recurrence at 2 years (2Y-R, orange, n=56) compared to patients with no recurrence at 2 years (2Y-noR, blue, n=36) after 2 biweekly injections (T2, **C**). P-values for differences between the two classes for both alpha- and beta-diversities have been computed through the Wilcoxon signed-rank test. **B and D.** Linear model coefficients for 2y-R and 2y-noR, corrected for age, gender and treatment arm at T1 (B) or T2 (D). Positive values indicate species-level genome bin (SGB) association with 2Y-R (orange), while negative values indicate a positive association for the corresponding SGB with 2Y-noR (blue). Only associations with $p<=0.05$ are reported since no association has $Q<0.2$. Q-values have been computed via Benjamini-Hochberg procedure. Refer to Table S3A for linear model coefficients (MaAsLin2, coefficient) for microbial SGBs after arcsin-sqrt (AST).

Figure 2. Longitudinal metabolic patterns showing a shift in lipid metabolism associated with recurrence at 2 years (2Y-R).

A. Principal component analysis (PCA) analysis plot representing the distribution of serum metabolomics (MB) overtime and according to clinical outcome no recurrence at 2 years (2y-noR, blue) versus recurrence at 2 years (2y-R, orange). Light gray circle: 2y-noR at baseline (T1); Blue triangle: 2y-noR after 2 biweekly injections (T2); Dark gray square: 2y-R at T1; Orange crosses: 2y-R at T2. **B.** Volcano-plots based on MB data showing significant ($p < 0.05$) differences between T1 (green dots) and T2 (yellow dots) with a cut -off in the T2/T1 fold change (FC) ≥ 0.3. Metabolites with T2/T1 FC$\geq$0.3 with a $p < 0.05$ were colored green. X-axis: log2 fold change of metabolites; Y-axis: fold change of –log10. The p-value was determined by the Mann–Whitney test. **C.** Hierarchical clustering of metabolites according to the clinical outcome (2y-noR versus 2y-R at baseline (T1) and after 2 injections (T2)) and treatment arm. Dark grey: 2y-R at T1; Light orange: 2y-R at T2; Light grey: 2y-noR at T1; Light blue: 2y-noR at T2. Dark blue: PL arm; Dark orange: nDC arm. Targeted metabolomic data on 140 serum samples computed as normalized areas of identified metabolites. Heatmap illustrating the changes in metabolite abundances according to the median of each metabolite in the two subgroups of opposite prognosis, highlighting the fatty acids (FA) fingerprint. Rows are samples, columns are metabolites. Heatmap data are log2 normalized and centered around the average abundance computed from all the samples for each metabolite. Red/green colors are ion signal higher/lower than average and missing values are displayed as grey. Samples are sorted following biological conditions and metabolites are cluterized following the ward.D2 algorithm, with euclidean distance. **D.** Relative abundance of distinct FA or acylcarnitine in both patient groups (2y-noR, blue: n = 56, 2y-R, orange: n = 83 at T1). All boxplot indicates the interquartile range Q1 to Q3 with Q2 (median) in the center. The range of outliers is depicted by whiskers. The p-value are related to the group comparison using the Mann–Whitney test. **E.** Recurrence-free survival (RFS) analysis using the Kaplan-Meier estimator (Log-Rank (Mantel Cox) test) to assess the prognostic value of low FA (calculated based on the sum of estimates of 24 FA or carboxylic acids) versus high FA relative abundances at T1 (left panel) and at T2 (right panel).

Figure 3. Significant differences in the microbiota taxonomic profiles at randomization. **A.** Shannon index and between-samples Bray-Curtis dissimilarities distributions for patients into placebo arm (PL, blue, n=31) compared to patients into natural dendritic cell arm (nDC, orange, n=60)) at baseline (T1). P-values for differences between the two classes for both alpha- and beta-diversities have been computed through the Wilcoxon signed-rank test. **B.** Linear model coefficients for nDC and PL, corrected for age and gender. Positive values indicate SGB

association with nDC (orange), while negative values indicate a positive association for the corresponding SGB with PL (blue). Only associations with p<=0.05 are reported since no association has Q<0.2. Q-values have been computed via Benjamini-Hochberg procedure. Refer to Table S3B for linear model coefficients (MaAsLin2, coefficient) for microbial SGBs after arcsin-sqrt (AST). **C.** Prevalence of *Faecalibacterium prausnitzii*, i.e proportion of individuals with its absence between healthy volunteers (HV, n=5345), patients into PL arm (n=31), all patients with melanoma into MIND-DC trial (MEL, n=91) and nDC arm (n=60). **D-E.** Recurrence-free survival (RFS) analysis using the Kaplan-Meier estimator (Log-Rank (Mantel Cox) test) to assess the predictive value of *Gemmiger formicilis* (D, left panel) and *Lachnospira pectinoschiza* (D, right panel) and *Faecalibacterium prausnitzii* (E) using relative abundances at T1. The numbers per group are depicted under the plots. **F.** Heatmap illustrating the p-values (upper panel) and hazard ratios (HR, lower panel) of comparisons between high and low relative abundances of MGS in PL and nDC arms.

Figure 4. Significant differences in metabolomics (MB) profiles at randomization.
A. Hierarchical clustering of metabolites according to the randomization arm: placebo (PL, n=49) versus natural dendritic cell (nDC, n=94) at baseline (T1)). Targeted MB data on 140 serum samples computed as normalized areas of identified metabolites. Heatmap illustrating the changes in metabolite abundances according to the median of each metabolite in the two arms. Rows are samples, columns are metabolites. Heatmap data are log2 normalized and centered around the average abundance computed from all the samples for each metabolite. Red/green colors are ion signal higher/lower than average and missing values are displayed as grey. Samples and metabolites are cluterized following the ward.D2 algorithm, with euclidean distance. **B.** Volcano-plots based on metabolomic data showing significant (p<0.05) differences between PL (blue dots) and nDC (orange dots) with a cut -off in the fold change (FC (DC/Placebo)) ≥ 0.5. X-axis: log2 fold change of metabolites; Y-axis: fold change of –log10 P value determined by the Mann–Whitney test. **C.** Relative abundances of key metabolites (glycoconjugated primary bile acids) from significant perturbations detected in B. between nDC (orange) and PL (blue) arms at T1 and T2. **D.** Volcano-plots based on metabolite significant differences in the nDC arm at T1 associated with recurrence (R) (orange, left) versus no recurrence (noR) (blue, right). Metabolites with FC (R-nDC/noR-nDC)) ≥ 0.5 and p<0.05 were colored in red dots, while those with FC (R-nDC /noR-DC) ≤ 0.5 and p<0.05 were colored in green dots. X-axis: log2 fold change of metabolites; Y-axis: fold change of –log10 P value determined by the Mann–Whitney test. **E.** Recurrence-free survival (RFS) analysis using the

Kaplan-Meier estimator (Log-Rank (Mantel Cox) test) to assess the predictive value of Cholic acid at T1.

Figure 5. Machine learning (ML, XGBoost) algorithm to identify biomarkers and their interaction predicting survival in stage III melanoma.

A-B. ML model summary. Features are clinical parameters and MB (A) or MG (B) monitored in serum at T1. SHAP values for each feature per patient are positive when the value of the feature increases the prediction of relapse, negative otherwise. Each dot represents one patient and the color represents the value of each feature. The importance of the feature is depicted with the number on the left column. **C.** Circosplot indicating correlations between common features described in A. and B., thickness of lines indicating an increasing positive (pink) or negative (blue) correlation. **D.** ML model summary. Features are clinical parameters and MB+MG monitored in serum at T1. SHAP values for each feature per patient are positive when the value of the feature increases the prediction of relapse, negative otherwise. Each dot represents one patient and the color represents the value of each feature. The importance of the feature is depicted with the number on the left column.

Figure 6. Patient RFS according to *Faecalibacterium prausnitzii* and fatty acids.

A. Metabolic pathway- enrichment analysis performed in MetaboAnalyst using a KEGG database of a set of metabolites found to be significantly correlated with *Faecalibacterium prausnitzii* SGB15318 and 15322 in patients into natural dendritic cell (nDC, n=60) and placebo (PL, n=31) arms at baseline (T1). **B.** Recurrence-free survival (RFS) analysis using the Kaplan-Meier (KM) estimator (Log-Rank (Mantel Cox) test) to assess the predictive value of low abundance of fatty acids (low FA) versus high abundance of fatty acids (high FA) after 2 biweekly injections (T2) in PL (left panel) and nDC (right panel) arms. **C.** Same as in B. for Carnitine C12:0 (left panel) and Carnitine C14:1 (right panel) at T1. **D.** Same as in C. for Carnitine C12:0 (left panel) and Carnitine C14:1 (right panel) associated with relative abundances of *Faecalibacterium prausnitzii* at T1. The numbers per group are depicted under the KM plots.

Supplemental Figure Legends

Figure S1. Metagenomics analyses of MIND-DC patient stools according to 2Y-R for each treatment arm at 2 time points.

A-D. Linear model coefficients (MaAsLin2, coefficient) for microbial SGBs that are found associated either after arcsin-sqrt (AST, left columns) or centered-log-ratio (CLR, middle columns) transformation with recurrence at 2 years (2Y-R) and no recurrence at 2 years (2Y-noR), with $p<0.05$, at T1 (A-B) and at T2 (C-D) in the placebo (PL, A and C) and in the natural dendritic cell (nDC, B and D) groups. The right columns represent the number of samples where each SGB was present (with direction to the left for 2Y-noR and with direction to the right for 2Y-R). The numbers of patients considered in this analysis are detailed in Table S2. Refer to Table S3C for linear model coefficients (MaAsLin2, coefficient) for microbial SGBs after arcsin-sqrt (AST).

Figure S2. Relative abundances of distinct bacterial species associated with relapse or survival including strains of *Faecalibacterium prausnitzii.*

A-B. Boxplots showing relative abundances of distinct Species-level genome bins (SGBs) that accounted for significant differences according to recurrence at 2 years (2Y-R) versus no recurrence at 2 years (2Y-noR) at T1 (A) and T2 (B). All boxplots indicate the interquartile range Q1 to Q3 with Q2 (median levels) in the center. The range of outliers is depicted by whiskers. The p-value are related to the group comparison using the Student's t-test. **C-D.** Prevalence (C) of *Faecalibacterium prausnitzii* SGB15316 & SGB15318 (left panels), SGB15322 (middle panel) and SGB15323 (right panel) between healthy volunteers (HV, n=6048), publicly available patients with melanoma (n=1036) together with patients into MIND-DC trial (MEL, n=1127 in total), placebo (PL, n=31) and natural dendritic cell (nDC, n=60) arms from MIND-DC. Boxplots showing relative abundances (D) of distinct *Faecalibacterium prausnitzii* SGBs according to treatment arms at T1 (left) and T2 (right). All boxplots indicate the interquartile range Q1 to Q3 with Q2 (median levels) in the center. The range of outliers is depicted by whiskers. The p-value are related to the group comparison using the linear models reported in Figure S1.

Figure S3. Metagenomics-based differences between T1 and T2 according to treatment arms.

A-D. Longitudinal differential abundant species (Paired Wilcoxon test, on Arcsin-sqrt (AST) transformed relative abundances) in the natural dendritic cell (nDC) and placebo (PL) arms considering recurrence at 2 years (2Y-R) and no recurrence at 2 years (2Y-noR) separately. Only associations with $P < 0.05$ are reported. Box plots show the raw relative abundances of the most significant bacteria SGB under each graph.

Figure S4. Natural dendritic cells (nDC)-induced modulations of MGS overtime and metabolomics principal component analysis for MIND-DC.

Short list of the statistically significant (without FDR correction) MGS differential evolution between the treatment arms (nDC vs PL), modeled using linear regression adjusted for the age, gender, melanoma stage, ECOG PS, and BMI. The square represents the point estimate of the evolution of the MGB between T1 and T2, and the horizontal segments represent their 95% confidence intervals. The first column of p-values is related to the Wald test that the evolution is different from 0. The last column of p-values is related to the Wald test of the difference of the evolution between the two arms.

Figure S5. Metabolic modulations during therapy.

A. Principal component analysis (PCA) plots representing the circulating metabolome according to treatment arms (natural dendritic cell, nDC, versus placebo, PL), recurrence or no recurrence at 2 years (2Y-R or 2Y-noR, respectively), and time points baseline (T1, right) or after 2 biweekly injections (T2, left). Blue circle: PL 2Y-noR at T1; Orange triangle: 2Y-noR at T2; Yellow crosses: nDC 2Y-noR at T2; Pink cross: nDC 2Y-R at T2; Purple diamond: nDC 2Y-R at T1; Green upside triangle: nDC 2Y-noR at T1; Red crossed square: PL 2Y-R at T2; Blue asterisk: PL 2Y-noR at T2. **B-D**. Boxplots showing the relative abundances of metabolites according to 2Y-R or 2Y-noR.

Figure S6. Associations of functional gene pathways with overall recurrence.

A. Linear model coefficients for the comparisons in overall recurrence at baseline (T1) for microbial gene functional pathways corrected for age, gender and treatment. Q values have been computed via Benjamini-Hochberg procedure. Any association with either p<=0.05 or Q<=0.3 has been selected. Q-values have been computed via Benjamini-Hochberg procedure. **B.** Volcano-plots based on metabolomics data highlighting no significant difference between), recurrence at 2 years (2Y-R, left side, orange) and no recurrence at 2 years (2Y-noR, right side, blue) at T1 in placebo (PL) arm. Controls of panels depicted in Figure 5D. X-axis: log2 fold change of metabolites; Y-axis: fold change of –log10 P value determined by the Mann–Whitney test.

Figure S7. Identification of the most representative metabolites differentiating the two treatment arms by machine learning approach.

A feature selection was conducted using Boruta feature selection algorithm based on XGboost to identify most relevant features in the metabolomics analysis at T1. (Left) Selected features ranked by importance in the prediction of treatment arm attribution (natural dendritic cell (nDC) versus placebo (PL)) status. Features are clinical parameters, and 152 metabolites. (Right) SHAP values for each feature per patient are positive when the value of the feature increases the prediction of nDC randomization, negative otherwise. Each dot represents one patient and the color depicts the value of each feature.

Figure S8. Identification of the most relevant baseline values and trajectory of metagenomics (MG) and metabolomics (MB) for the prediction of the 2Y-R.

A. A feature selection was conducted using Boruta feature selection algorithm based on XGboost to identify most relevant feature evolution in between T1 and T2 in the MB analysis. Selected features ranked by importance in the prediction of treatment arm attribution (2Y-R versus 2Y-noR) status, pooling the two treatment arms. Features are clinical parameters, and 152 metabolites. SHAP values for each feature per patient are positive when the value of the feature increases the prediction of 2Y-R, negative otherwise. Each dot represents one patient and the color depicts the value of each feature. **B.** Short list of the statistically significant (without FDR correction) metabolite differential evolution between the treatment arm (nDC vs PL), modeled using linear regression adjusted for the age, gender, melanoma stage, ECOG-PS, and BMI. The square represents the point estimate of the evolution of the metabolite between T1 and T2, and the horizontal segments represent their 95% confidence intervals. The first column of p-values is related to the Wald test that the evolution is different from 0. The last column of p-values is related to the Wald test of the difference of the evolution between the two arms**. C.** Machine learning performance using Boruta feature selection algorithm based on XGboost for 2Y-R prediction. Representation of the AUC values for each treatment arm and feature (clinical, MB or MGS parameters) according to T1 and T2-T1 slope of the trajectory.

Figure S9. Associations between *Faecalibacterium prausnitzii* SGB15318 and 15322 strain abundances with FA for each treatment arms at both time points.

A-B. Pairwise Pearson correlations of concentration-fitted metabolites and *F. prausnitzii* SGB15318 and 15322 strains prevalence at T1 in placebo (PL, A) and natural dendritic cell (nDC, B) arms. **C-D.** Pairwise Spearman correlation of concentration-fitted metabolites and *F. prausnitzii* SGB15318 and 15322 strains prevalence at T2 in PL (C) and nDC (D) arms. Green color stands for inverse associations. Red color denotes positive associations. Symbols on the

plot represent the level of significance denoting Spearman's correlation test significant associations at p value < 0.05 (Spearman's correlation test). DC, dendritic cell; PL, placebo.

Figure S10. Acylcarnitines and *Faecalibacterium prausnitzii* segregate MIND-DC into patient subsets of different prognosis.

A-B. Recurrence-free survival (RFS) analysis using the Kaplan-Meier estimator (Log-Rank (Mantel Cox) test) to assess the prognostic value of abundances of Carnitine C12:0 (A) or Carnitine C14:1 (B) and relative abundances of *Faecalibacterium prausnitzii* at baseline (T1) for all MIND-DC cohort (nDC+PL) (left panels) or the placebo (PL) arm only (right panels). PL, placebo; RFS, relapse-free survival. **C-D.** Idem but considering only Carnitine C12:0 and various strains of *F. prausnitzii* SGB described in Figure S2C-D.

Figure 1

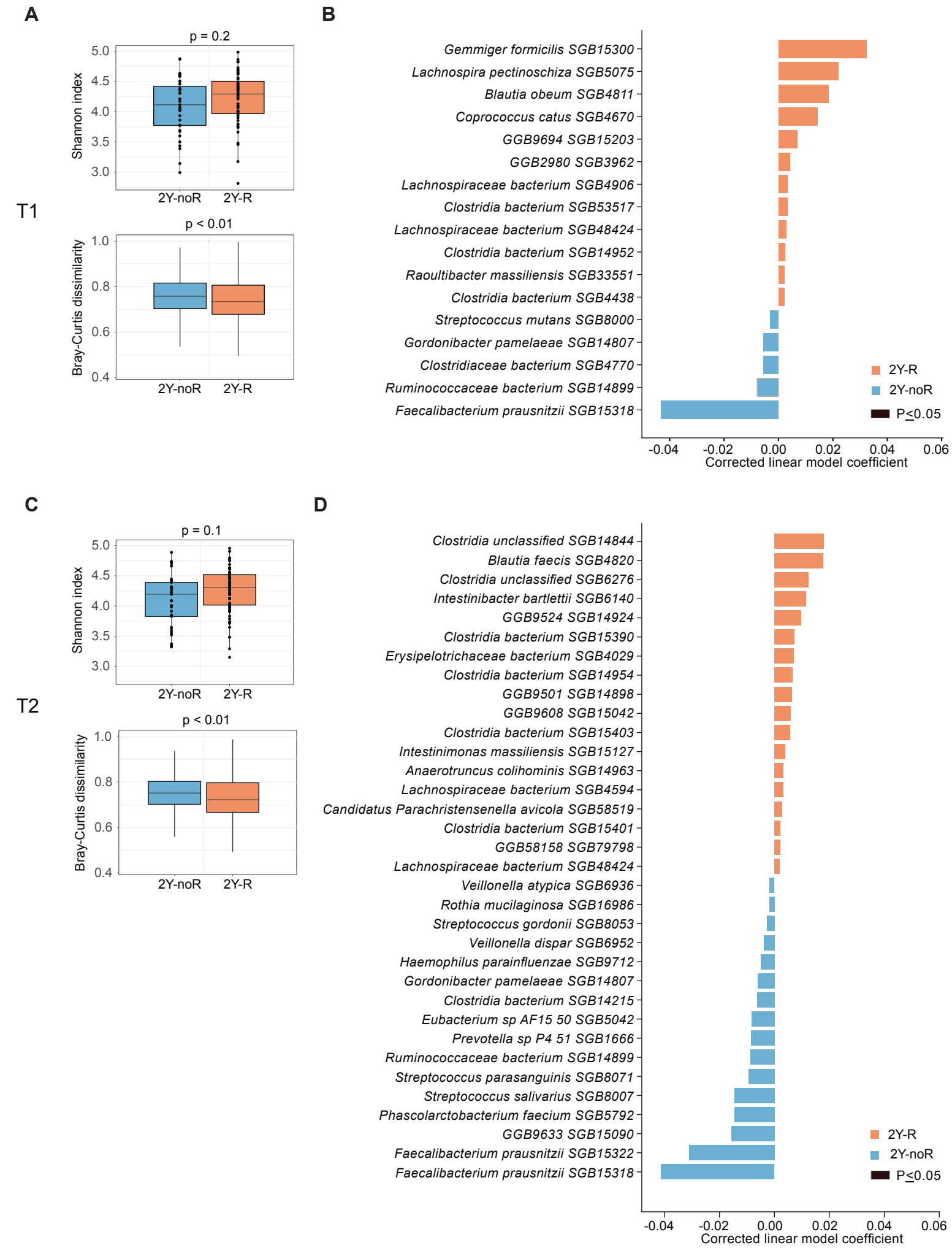
A
T1
p = 0.2
Shannon index
5.0
4.5
4.0
3.5
3.0
2Y-noR
2Y-R
p < 0.01
Bray-Curtis dissimilarity
1.0
0.8
0.6
0.4
2Y-noR
2Y-R
B
Gemmiger formicilis SGB15300
Lachnospira pectinoschiza SGB5075
Blautia obeum SGB4811
Coprococcus catus SGB4670
GGB9694 SGB15203
GGB2980 SGB3962
Lachnospiraceae bacterium SGB4906
Clostridia bacterium SGB53517
Lachnospiraceae bacterium SGB48424
Clostridia bacterium SGB14952
Raoultibacter massiliensis SGB33551
Clostridia bacterium SGB4438
Streptococcus mutans SGB8000
Gordonibacter pamelaeae SGB14807
Clostridiaceae bacterium SGB4770
Ruminococcaceae bacterium SGB14899
Faecalibacterium prausnitzii SGB15318
2Y-R
2Y-noR
P≤0.05
-0.04
-0.02
0.00
0.02
0.04
0.06
Corrected linear model coefficient
C
T2
p = 0.1
Shannon index
5.0
4.5
4.0
3.5
3.0
2Y-noR
2Y-R
p < 0.01
Bray-Curtis dissimilarity
1.0
0.8
0.6
0.4
2Y-noR
2Y-R
D
Clostridia unclassified SGB14844
Blautia faecis SGB4820
Clostridia unclassified SGB6276
Intestinibacter bartlettii SGB6140
GGB9524 SGB14924
Clostridia bacterium SGB15390
Erysipelotrichaceae bacterium SGB4029
Clostridia bacterium SGB14954
GGB9501 SGB14898
GGB9608 SGB15042
Clostridia bacterium SGB15403
Intestinimonas massiliensis SGB15127
Anaerotruncus colihominis SGB14963
Lachnospiraceae bacterium SGB4594
Candidatus Parachristensenella avicola SGB58519
Clostridia bacterium SGB15401
GGB58158 SGB79798
Lachnospiraceae bacterium SGB48424
Veillonella atypica SGB6936
Rothia mucilaginosa SGB16986
Streptococcus gordonii SGB8053
Veillonella dispar SGB6952
Haemophilus parainfluenzae SGB9712
Gordonibacter pamelaeae SGB14807
Clostridia bacterium SGB14215
Eubacterium sp AF15 50 SGB5042
Prevotella sp P4 51 SGB1666
Ruminococcaceae bacterium SGB14899
Streptococcus parasanguinis SGB8071
Streptococcus salivarius SGB8007
Phascolarctobacterium faecium SGB5792
GGB9633 SGB15090
Faecalibacterium prausnitzii SGB15322
Faecalibacterium prausnitzii SGB15318
2Y-R
2Y-noR
P≤0.05
-0.04
-0.02
0.00
0.02
0.04
0.06
Corrected linear model coefficient

Figure 2

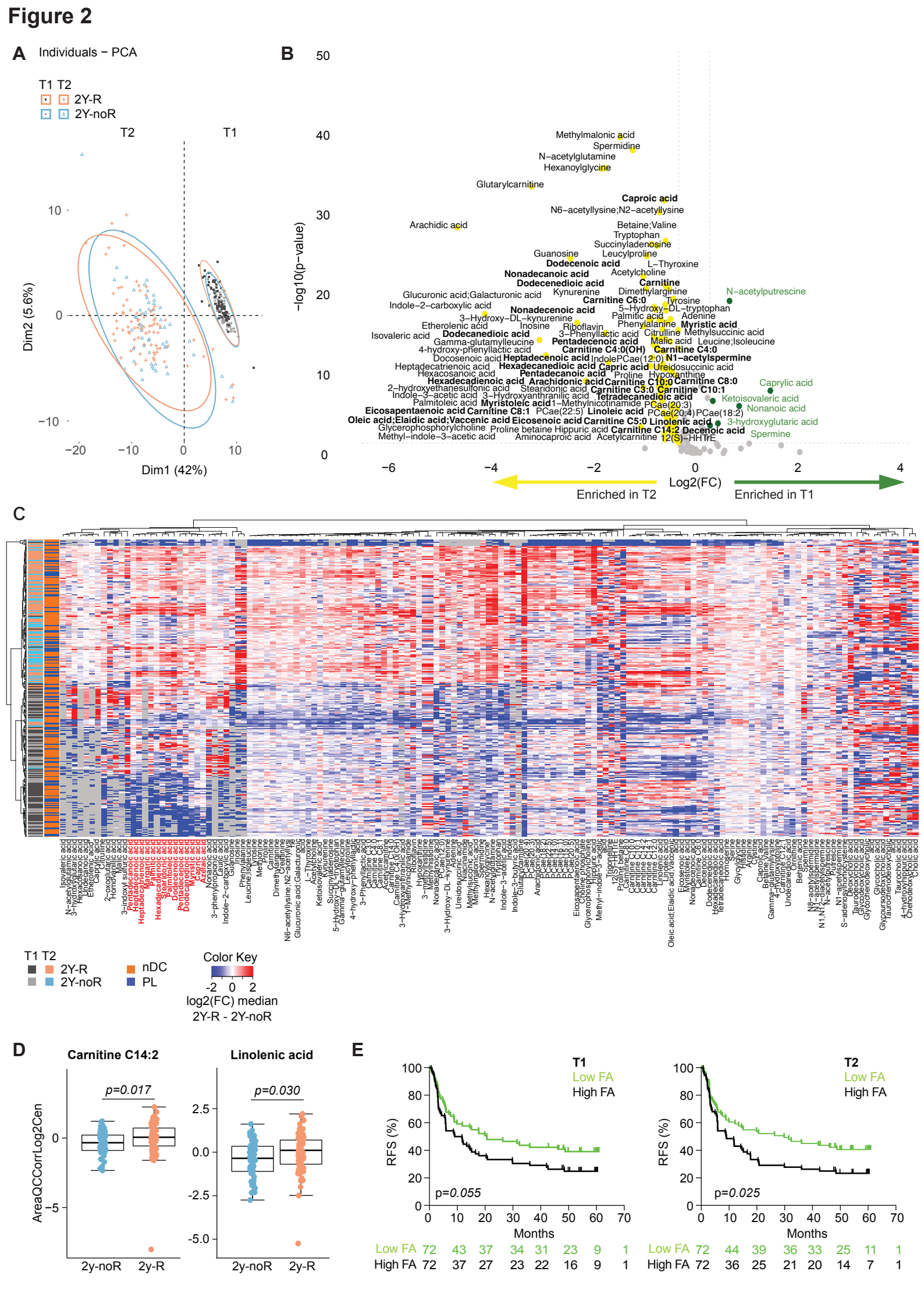
A
Individuals − PCA
T1 T2
2Y-R
2Y-noR
T2
T1
Dim2 (5.6%)
Dim1 (42%)
B
−log10(p−value)
Log2(FC)
Enriched in T2
Enriched in T1
Methylmalonic acid
Spermidine
N−acetylglutamine
Hexanoylglycine
Glutarylcarnitine
Caproic acid
N6−acetyllysine;N2−acetyllysine
Arachidic acid
Betaine;Valine
Tryptophan
Succinyladenosine
Guanosine
Leucylproline
Dodecenoic acid
L−Thyroxine
Nonadecanoic acid
Acetylcholine
Dodecenedioic acid
Carnitine
Glucuronic acid;Galacturonic acid
Kynurenine
Dimethylarginine
N−acetylputrescine
Indole−2−carboxylic acid
Carnitine C6:0
Tyrosine
Nonadecenoic acid
5−Hydroxy−DL−tryptophan
3−Hydroxy−DL−kynurenine
Palmitic acid
Adenine
Etherolenic acid
Inosine
Riboflavin
Phenylalanine
Myristic acid
Isovaleric acid
Dodecanedioic acid
3−Phenyllactic acid
Citrulline
Methylsuccinic acid
Gamma−glutamylleucine
Pentadecenoic acid
Malic acid
Leucine;Isoleucine
4−hydroxy−phenyllactic acid
Carnitine C4:0(OH)
Carnitine C4:0
Docosenoic acid
Heptadecenoic acid
IndolePCae(12:0)
N1−acetylspermine
Heptadecatrienoic acid
Hexadecanedioic acid
Capric acid
Ureidosuccinic acid
Hexacosanoic acid
Pentadecanoic acid
Proline
Hypoxanthine
Hexadecadienoic acid
Arachidonic acid
Carnitine C10:0
Carnitine C8:0
Caprylic acid
2−hydroxyethanesulfonic acid
Stearidonic acid
Carnitine C3:0
Carnitine C10:1
Indole−3−acetic acid
3−Hydroxyanthranilic acid
Tetradecanedioic acid
Ketoisovaleric acid
Palmitoleic acid
Myristoleic acid
1−Methylnicotinamide
PCae(20:3)
Nonanoic acid
Eicosapentaenoic acid
Carnitine C8:1
PCae(22:5)
Linoleic acid
PCae(20:4)
PCae(18:2)
Oleic acid;Elaidic acid;Vaccenic acid
Eicosenoic acid
Carnitine C5:0
Linolenic acid
3−hydroxyglutaric acid
Glycerophosphorylcholine
Proline betaine
Hippuric acid
Carnitine C14:2
Decenoic acid
Spermine
Methyl−indole−3−acetic acid
Aminocaproic acid
Acetylcarnitine
12(S)−HHTrE
C
T1 T2
2Y-R
2Y-noR
nDC
PL
Color Key
-2 0 2
log2(FC) median
2Y-R - 2Y-noR
D
Carnitine C14:2
Linolenic acid
p=0.017
p=0.030
AreaQCCorrLog2Cen
2y-noR
2y-R
E
T1
T2
Low FA
High FA
RFS (%)
p=0.055
p=0.025
Months
Low FA 72 43 37 34 31 23 9 1
High FA 72 37 27 23 22 16 9 1
Low FA 72 44 39 36 33 25 11 1
High FA 72 36 25 21 20 14 7 1

Figure 3

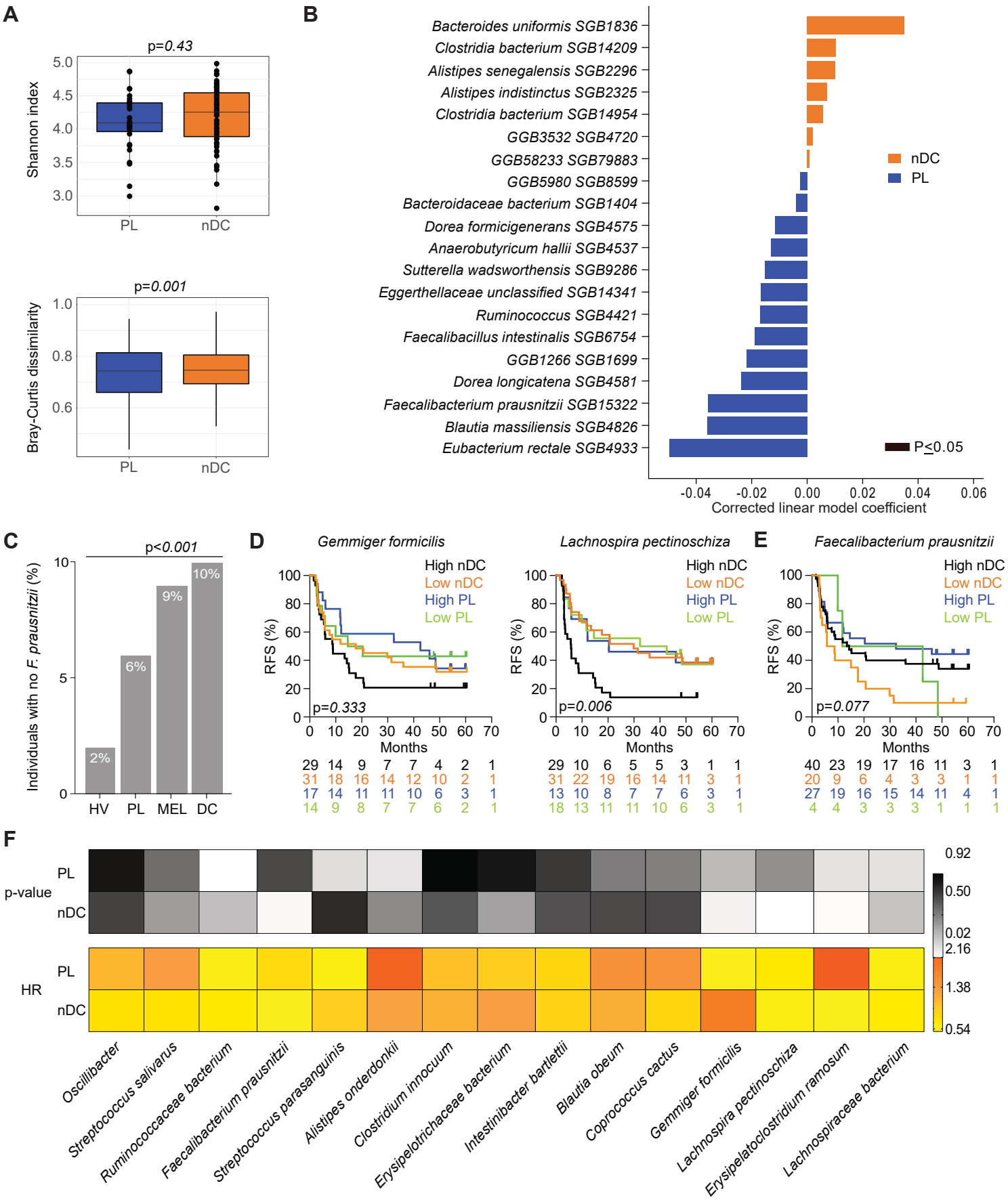
A
p=0.43
Shannon index
PL
nDC
p=0.001
Bray-Curtis dissimilarity
B
Bacteroides uniformis SGB1836
Clostridia bacterium SGB14209
Alistipes senegalensis SGB2296
Alistipes indistinctus SGB2325
Clostridia bacterium SGB14954
GGB3532 SGB4720
GGB58233 SGB79883
GGB5980 SGB8599
Bacteroidaceae bacterium SGB1404
Dorea formicigenerans SGB4575
Anaerobutyricum hallii SGB4537
Sutterella wadsworthensis SGB9286
Eggerthellaceae unclassified SGB14341
Ruminococcus SGB4421
Faecalibacillus intestinalis SGB6754
GGB1266 SGB1699
Dorea longicatena SGB4581
Faecalibacterium prausnitzii SGB15322
Blautia massiliensis SGB4826
Eubacterium rectale SGB4933
nDC
PL
P≤0.05
Corrected linear model coefficient
C
p<0.001
Individuals with no F. prausnitzii (%)
2%
6%
9%
10%
HV
PL
MEL
DC
D
Gemmiger formicilis
Lachnospira pectinoschiza
High nDC
Low nDC
High PL
Low PL
RFS (%)
p=0.333
p=0.006
Months
E
Faecalibacterium prausnitzii
p=0.077
F
p-value
HR
PL
nDC
Oscillibacter
Streptococcus salivarus
Ruminococcaceae bacterium
Faecalibacterium prausnitzii
Streptococcus parasanguinis
Alistipes onderdonkii
Clostridium innocuum
Erysipelotrichaceae bacterium
Intestinibacter bartlettii
Blautia obeum
Coprococcus cactus
Gemmiger formicilis
Lachnospira pectinoschiza
Erysipelatoclostridium ramosum
Lachnospiraceae bacterium

Figure 4

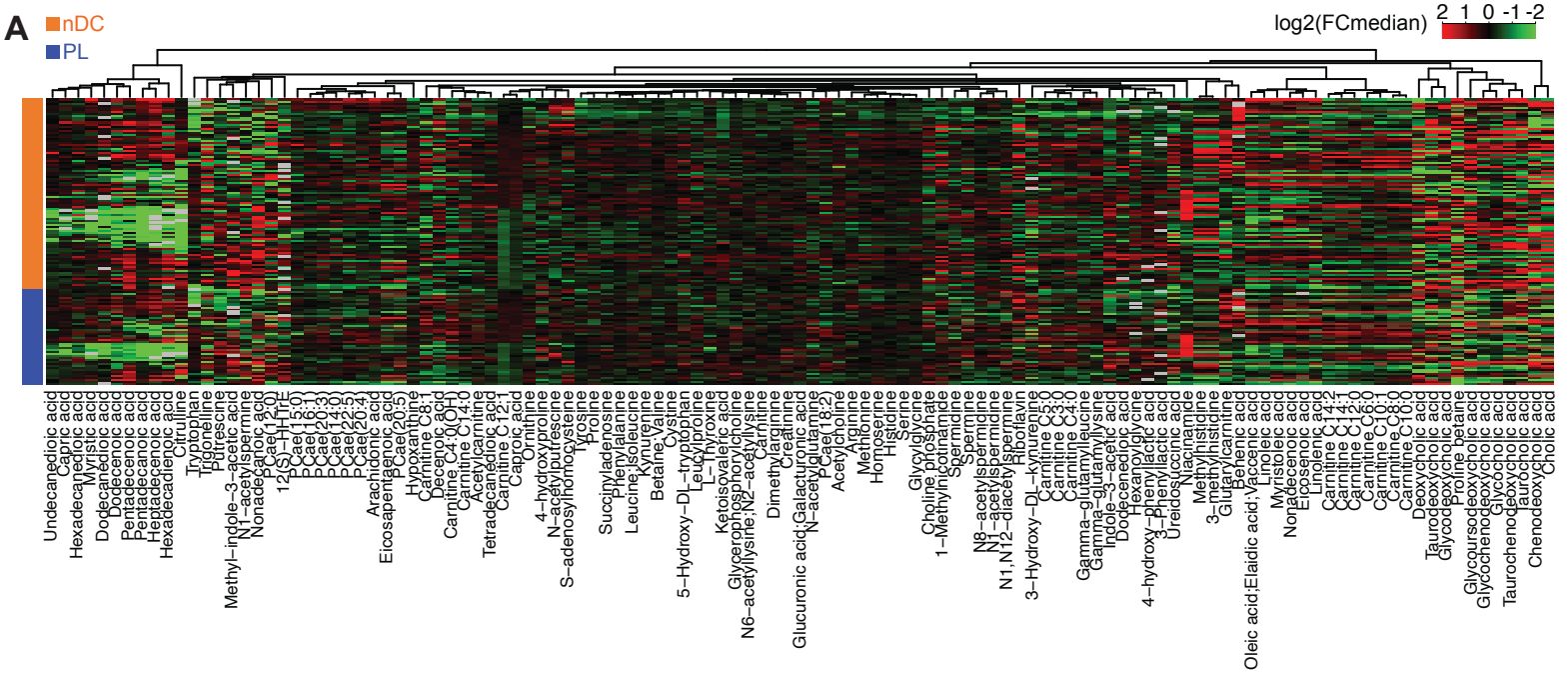
A
nDC
PL
log2(FCmedian) 2 1 0 -1 -2
Undecanedioic acid
Capric acid
Hexadecanedioic acid
Myristic acid
Dodecanedioic acid
Decanedioic acid
Pentadecenoic acid
Pentadecanoic acid
Heptadecenoic acid
Hexadecadienoic acid
Citrulline
Tryptophan
Trigonelline
Putrescine
Methyl-indole-3-acetic acid
N1-acetylspermine
Nonadecanoic acid
Palmitic acid
12(S)-HETE
PCae(15:0)
PCae(16:1)
PCae(20:3)
PCae(14:0)
PCae(22:5)
PCae(20:4)
Arachidonic acid
Eicosapentaenoic acid
PCae(20:5)
Hypoxanthine
Carnitine C8:1
Caprylic acid
Carnitine C14:1
Acetylcarnitine
Tetradecanedioic acid
Carnitine C12:1
Caproic acid
Ornithine
4-hydroxyproline
N-acetylputrescine
S-adenosylhomocysteine
Tyrosine
Proline
Succinyladenosine
Phenylalanine
Leucine,Isoleucine
Kynurenine
Betaine,Valine
Cystine
5-Hydroxy-DL-tryptophan
Leucylproline
L-Thyroxine
Ketoisovaleric acid
Glycerophosphorylcholine
N6-acetyllysine,N2-acetyllysine
Carnitine
Dimethylarginine
Glucuronic acid;Galacturonic acid
N-acetylglutamine
PCae(18:2)
Acetylcholine
Arginine
Methionine
Homoserine
Histidine
Serine
Glycylglycine
Choline phosphate
1-Methylnicotinamide
Spermine
N8-acetylspermidine
N1-acetylspermidine
N1,N12-diacetylspermine
Riboflavin
3-Hydroxy-DL-kynurenine
Carnitine C5:0
Carnitine C3:0
Carnitine C4:0
Gamma-glutamylleucine
Gamma-glutamylysine
Indole-3-acetic acid
Dodecanoic acid
Hexanoylglycine
4-hydroxy-3-Phenyllactic acid
3-Phenyllactic acid
Ureidosuccinic acid
Niacinamide
Methylhistidine
3-methylhistidine
Glutarylcarnitine
Behenic acid
Oleic acid;Elaidic acid;Vaccenic acid
Linoleic acid
Myristoleic acid
Nonadecanoic acid
Eicosenoic acid
Linolenic acid
Carnitine C14:2
Carnitine C12:0
Carnitine C6:0
Carnitine C10:1
Carnitine C8:0
Carnitine C10:0
Deoxycholic acid
Taurodeoxycholic acid
Glycodeoxycholic acid
Glycochenodeoxycholic acid
Glycocholic acid
Taurocholic acid
Chenodeoxycholic acid
Cholic acid

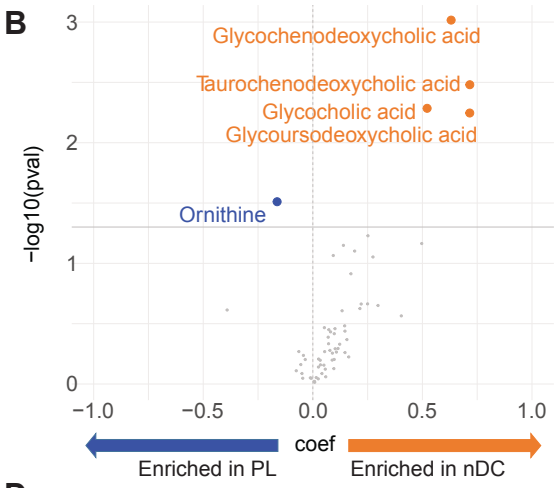
B
Glycochenodeoxycholic acid
Taurochenodeoxycholic acid
Glycocholic acid
Glycoursodeoxycholic acid
Ornithine
−log10(pval)
coef
Enriched in PL
Enriched in nDC

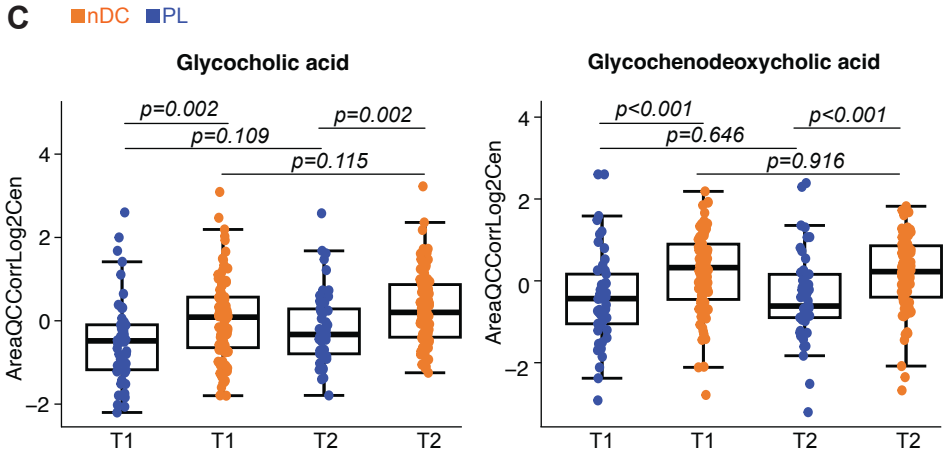
C
nDC
PL
Glycocholic acid
Glycochenodeoxycholic acid
p=0.002
p=0.109
p=0.002
p=0.115
p<0.001
p=0.646
p<0.001
p=0.916
AreaQCCorrLog2Cen
T1
T1
T2
T2

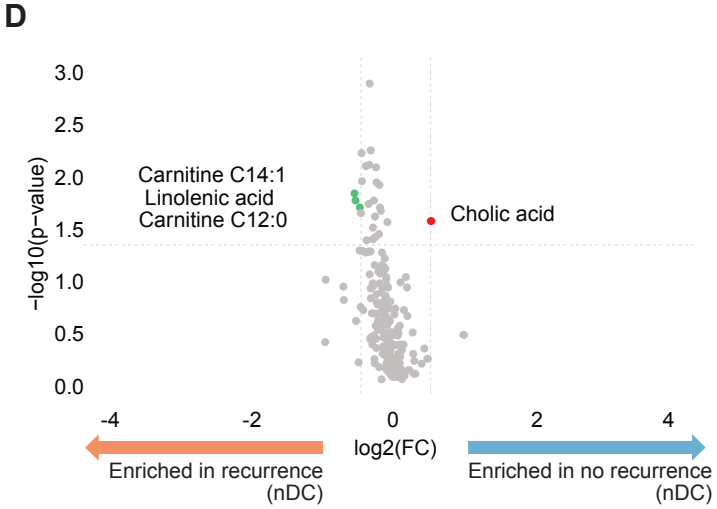
D
Carnitine C14:1
Linolenic acid
Carnitine C12:0
Cholic acid
−log10(p-value)
log2(FC)
Enriched in recurrence (nDC)
Enriched in no recurrence (nDC)

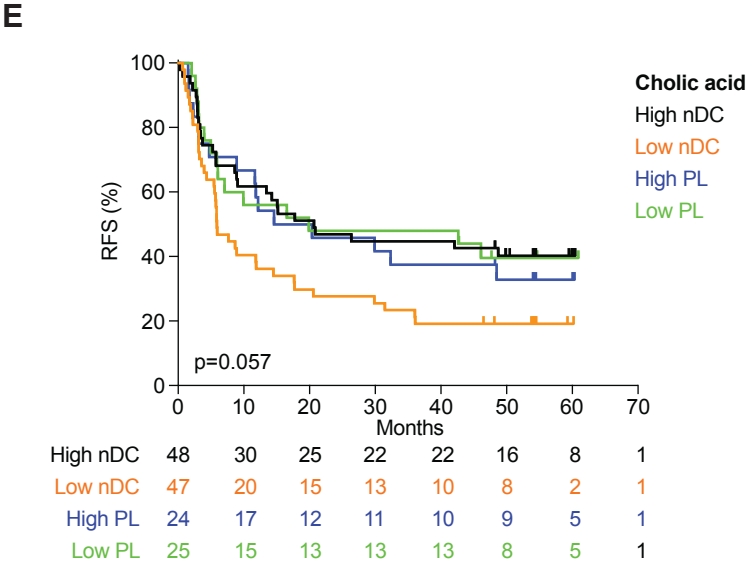
E
Cholic acid
High nDC
Low nDC
High PL
Low PL
RFS (%)
p=0.057
Months
High nDC 48 30 25 22 22 16 8 1
Low nDC 47 20 15 13 10 8 2 1
High PL 24 17 12 11 10 9 5 1
Low PL 25 15 13 13 13 8 5 1

Figure 5

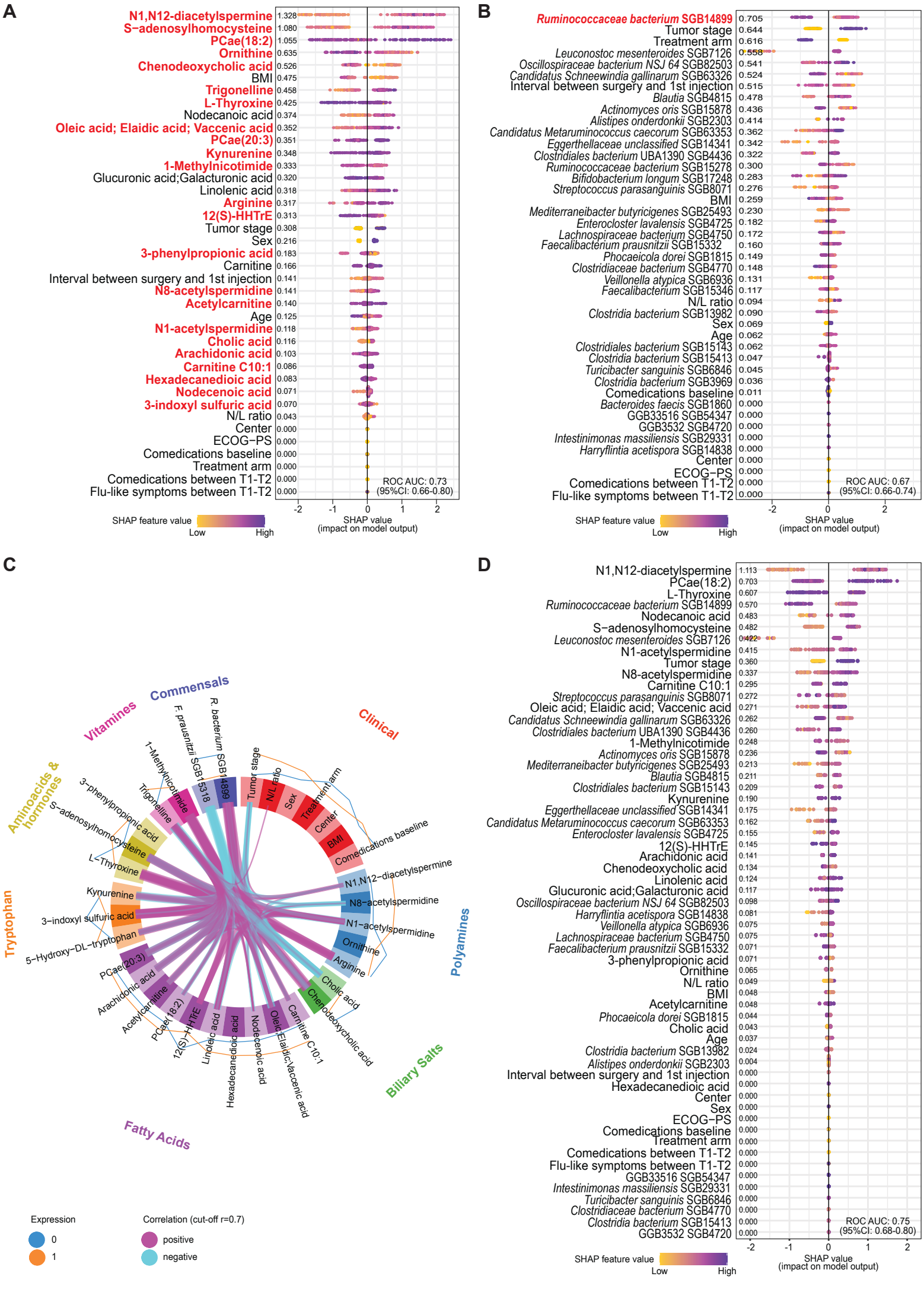
A
N1,N12-diacetylspermine
S−adenosylhomocysteine
PCae(18:2)
Ornithine
Chenodeoxycholic acid
BMI
Trigonelline
L-Thyroxine
Nodecanoic acid
Oleic acid; Elaidic acid; Vaccenic acid
PCae(20:3)
Kynurenine
1-Methylnicotimide
Glucuronic acid;Galacturonic acid
Linolenic acid
Arginine
12(S)-HHTrE
Tumor stage
Sex
3-phenylpropionic acid
Carnitine
Interval between surgery and 1st injection
N8-acetylspermidine
Acetylcarnitine
Age
N1-acetylspermidine
Cholic acid
Arachidonic acid
Carnitine C10:1
Hexadecanedioic acid
Nodecenoic acid
3-indoxyl sulfuric acid
N/L ratio
Center
ECOG−PS
Comedications baseline
Treatment arm
Comedications between T1-T2
Flu-like symptoms between T1-T2
ROC AUC: 0.73
(95%CI: 0.66-0.80)
SHAP feature value
Low
High
SHAP value
(impact on model output)
B
Ruminococcaceae bacterium SGB14899
Tumor stage
Treatment arm
Leuconostoc mesenteroides SGB7126
Oscillospiraceae bacterium NSJ 64 SGB82503
Candidatus Schneewindia gallinarum SGB63326
Interval between surgery and 1st injection
Blautia SGB4815
Actinomyces oris SGB15878
Alistipes onderdonkii SGB2303
Candidatus Metaruminococcus caecorum SGB63353
Eggerthellaceae unclassified SGB14341
Clostridiales bacterium UBA1390 SGB4436
Ruminococcaceae bacterium SGB15278
Bifidobacterium longum SGB17248
Streptococcus parasanguinis SGB8071
BMI
Mediterraneibacter butyricigenes SGB25493
Enterocloster lavalensis SGB4725
Lachnospiraceae bacterium SGB4750
Faecalibacterium prausnitzii SGB15332
Phocaeicola dorei SGB1815
Clostridiaceae bacterium SGB4770
Veillonella atypica SGB6936
Faecalibacterium SGB15346
N/L ratio
Clostridia bacterium SGB13982
Sex
Age
Clostridiales bacterium SGB15143
Clostridia bacterium SGB15413
Turicibacter sanguinis SGB6846
Clostridia bacterium SGB3969
Comedications baseline
Bacteroides faecis SGB1860
GGB33516 SGB54347
GGB3532 SGB4720
Intestinimonas massiliensis SGB29331
Harryflintia acetispora SGB14838
Center
ECOG−PS
Comedications between T1-T2
Flu-like symptoms between T1-T2
ROC AUC: 0.67
(95%CI: 0.66-0.74)
SHAP feature value
Low
High
SHAP value
(impact on model output)
C
Vitamines
Commensals
Clinical
Aminoacids & hormones
Polyamines
Tryptophan
Biliary Salts
Fatty Acids
F. prausnitzii SGB15318
R. bacterium SGB14899
1-Methylnicotimide
Trigonelline
3-phenylpropionic acid
S−adenosylhomocysteine
L−Thyroxine
Kynurenine
3−indoxyl sulfuric acid
5−Hydroxy−DL−tryptophan
PCae(20:3)
Arachidonic acid
Acetylcarnitine
PCae(18:2)
12(S)−HHTrE
Linoleic acid
Hexadecanedioic acid
Nodecenoic acid
Oleic acid
Elaidic acid
Vaccenic acid
Carnitine C10:1
Chenodeoxycholic acid
Cholic acid
Arginine
Ornithine
N1−acetylspermidine
N8−acetylspermidine
N1,N12−diacetylspermine
Comedications baseline
BMI
Center
Treatment arm
Sex
N/L ratio
Tumor stage
Expression
0
1
Correlation (cut-off r=0.7)
positive
negative
D
N1,N12-diacetylspermine
PCae(18:2)
L-Thyroxine
Ruminococcaceae bacterium SGB14899
Nodecanoic acid
S−adenosylhomocysteine
Leuconostoc mesenteroides SGB7126
N1-acetylspermidine
Tumor stage
N8-acetylspermidine
Carnitine C10:1
Streptococcus parasanguinis SGB8071
Oleic acid; Elaidic acid; Vaccenic acid
Candidatus Schneewindia gallinarum SGB63326
Clostridiales bacterium UBA1390 SGB4436
1-Methylnicotimide
Actinomyces oris SGB15878
Mediterraneibacter butyricigenes SGB25493
Blautia SGB4815
Clostridiales bacterium SGB15143
Kynurenine
Eggerthellaceae unclassified SGB14341
Candidatus Metaruminococcus caecorum SGB63353
Enterocloster lavalensis SGB4725
12(S)-HHTrE
Arachidonic acid
Chenodeoxycholic acid
Linolenic acid
Glucuronic acid;Galacturonic acid
Oscillospiraceae bacterium NSJ 64 SGB82503
Harryflintia acetispora SGB14838
Veillonella atypica SGB6936
Lachnospiraceae bacterium SGB4750
Faecalibacterium prausnitzii SGB15332
3-phenylpropionic acid
Ornithine
N/L ratio
BMI
Acetylcarnitine
Phocaeicola dorei SGB1815
Cholic acid
Age
Clostridia bacterium SGB13982
Alistipes onderdonkii SGB2303
Interval between surgery and 1st injection
Hexadecanedioic acid
Center
Sex
ECOG−PS
Comedications baseline
Treatment arm
Comedications between T1-T2
Flu-like symptoms between T1-T2
GGB33516 SGB54347
Intestinimonas massiliensis SGB29331
Turicibacter sanguinis SGB6846
Clostridiaceae bacterium SGB4770
Clostridia bacterium SGB15413
GGB3532 SGB4720
ROC AUC: 0.75
(95%CI: 0.68-0.80)
SHAP feature value
Low
High
SHAP value
(impact on model output)

Figure 6

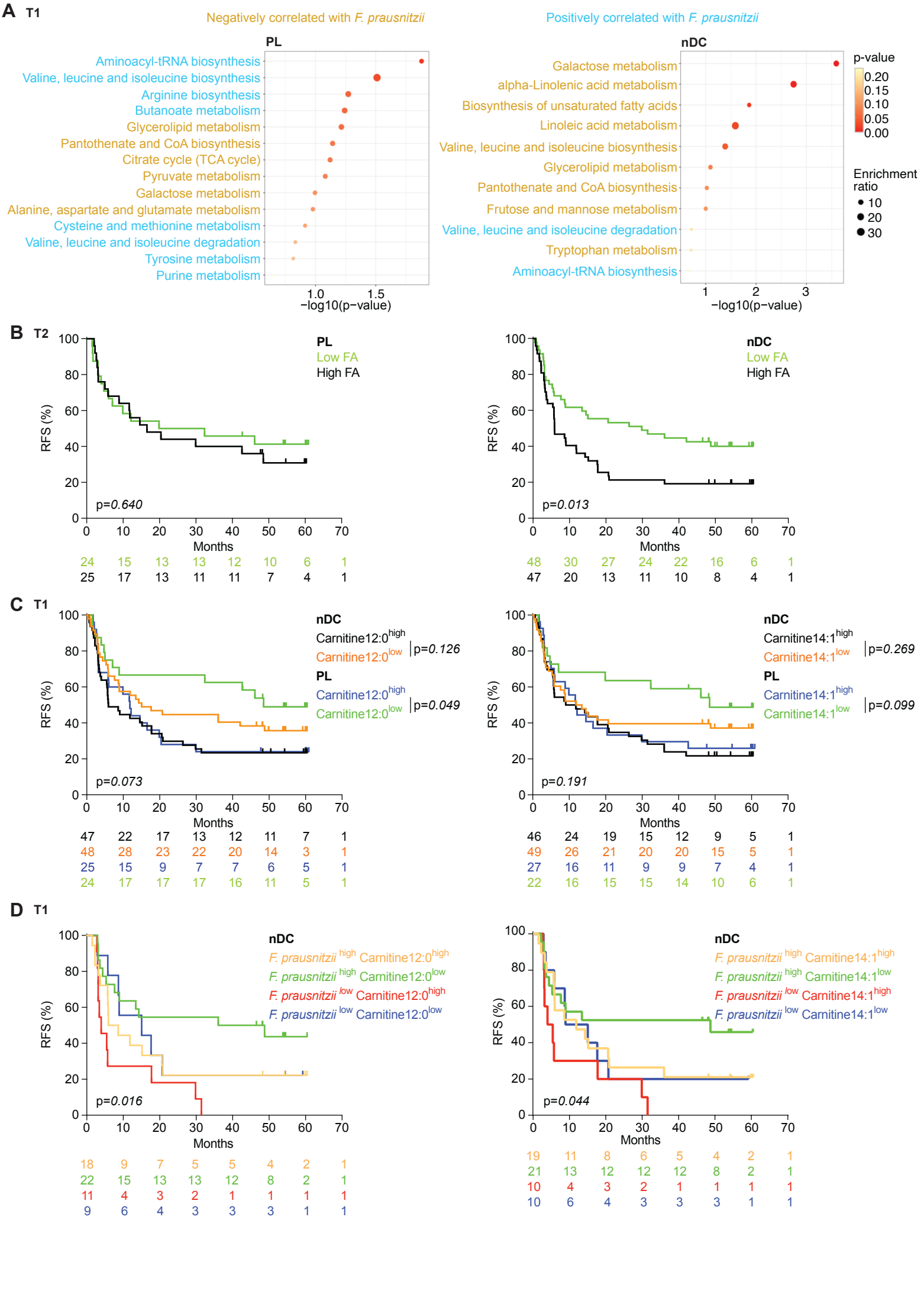
A T1
Negatively correlated with F. prausnitzii
Positively correlated with F. prausnitzii
PL
Aminoacyl-tRNA biosynthesis
Valine, leucine and isoleucine biosynthesis
Arginine biosynthesis
Butanoate metabolism
Glycerolipid metabolism
Pantothenate and CoA biosynthesis
Citrate cycle (TCA cycle)
Pyruvate metabolism
Galactose metabolism
Alanine, aspartate and glutamate metabolism
Cysteine and methionine metabolism
Valine, leucine and isoleucine degradation
Tyrosine metabolism
Purine metabolism
1.0
1.5
−log10(p−value)
nDC
Galactose metabolism
alpha-Linolenic acid metabolism
Biosynthesis of unsaturated fatty acids
Linoleic acid metabolism
Valine, leucine and isoleucine biosynthesis
Glycerolipid metabolism
Pantothenate and CoA biosynthesis
Frutose and mannose metabolism
Valine, leucine and isoleucine degradation
Tryptophan metabolism
Aminoacyl-tRNA biosynthesis
1
2
3
−log10(p−value)
p-value
0.20
0.15
0.10
0.05
0.00
Enrichment ratio
10
20
30
B T2
PL
Low FA
High FA
RFS (%)
p=0.640
Months
24 15 13 13 12 10 6 1
25 17 13 11 11 7 4 1
nDC
Low FA
High FA
RFS (%)
p=0.013
Months
48 30 27 24 22 16 6 1
47 20 13 11 10 8 4 1
C T1
nDC
Carnitine12:0high
Carnitine12:0low
p=0.126
PL
Carnitine12:0high
Carnitine12:0low
p=0.049
RFS (%)
p=0.073
Months
47 22 17 13 12 11 7 1
48 28 23 22 20 14 3 1
25 15 9 7 7 6 5 1
24 17 17 17 16 11 5 1
nDC
Carnitine14:1high
Carnitine14:1low
p=0.269
PL
Carnitine14:1high
Carnitine14:1low
p=0.099
RFS (%)
p=0.191
Months
46 24 19 15 12 9 5 1
49 26 21 20 20 15 5 1
27 16 11 9 9 7 4 1
22 16 15 15 14 10 6 1
D T1
nDC
F. prausnitzii high Carnitine12:0high
F. prausnitzii high Carnitine12:0low
F. prausnitzii low Carnitine12:0high
F. prausnitzii low Carnitine12:0low
RFS (%)
p=0.016
Months
18 9 7 5 5 4 2 1
22 15 13 13 12 8 2 1
11 4 3 2 1 1 1 1
9 6 4 3 3 3 1 1
nDC
F. prausnitzii high Carnitine14:1high
F. prausnitzii high Carnitine14:1low
F. prausnitzii low Carnitine14:1high
F. prausnitzii low Carnitine14:1low
RFS (%)
p=0.044
Months
19 11 8 6 5 4 2 1
21 13 12 12 12 8 2 1
10 4 3 2 1 1 1 1
10 6 4 3 3 3 1 1

Figure S1

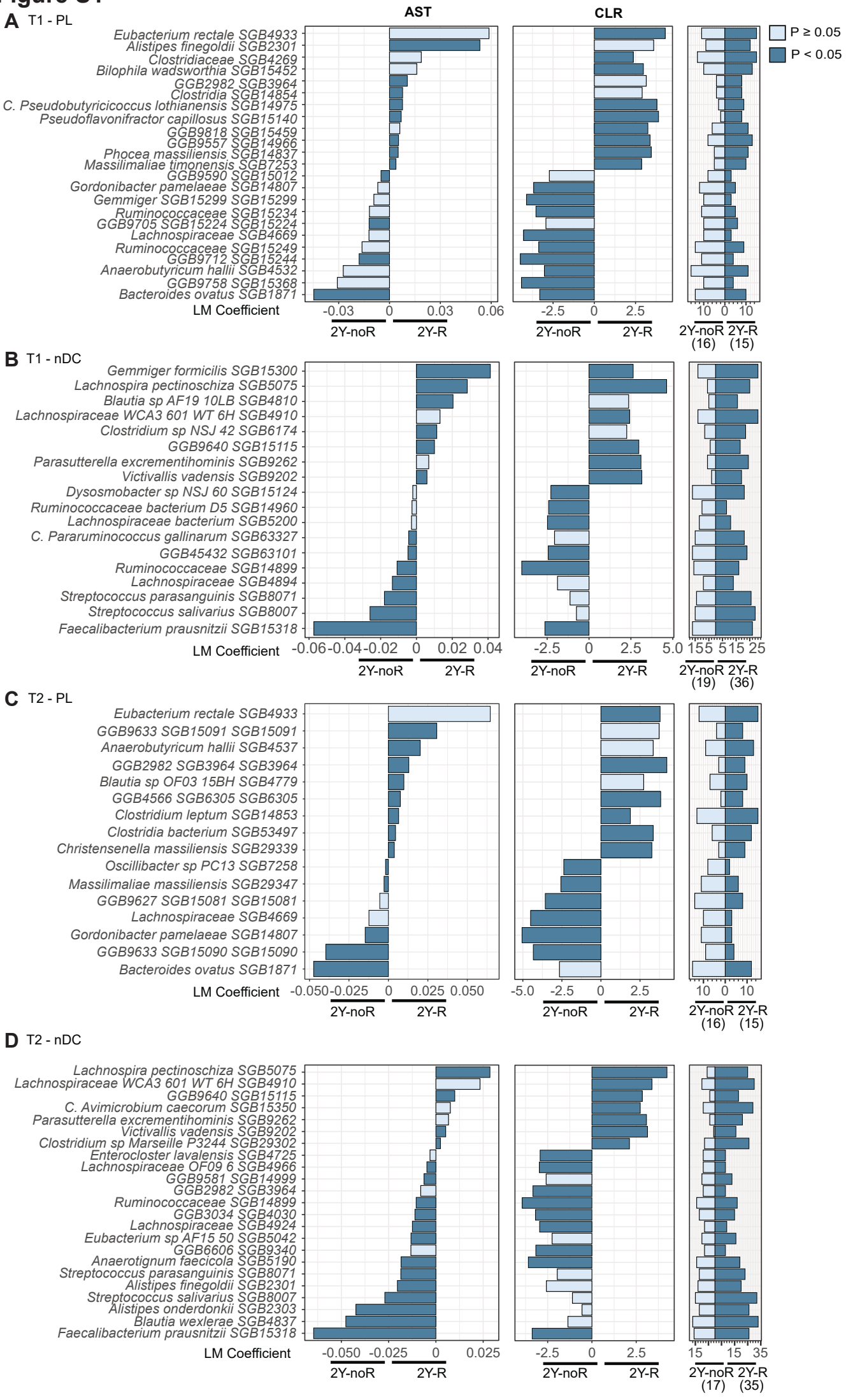
A T1 - PL
AST
CLR
P ≥ 0.05
P < 0.05
Eubacterium rectale SGB4933
Alistipes finegoldii SGB2301
Clostridiaceae SGB4269
Bilophila wadsworthia SGB15452
GGB2982 SGB3964
Clostridia SGB14854
C. Pseudobutyricicoccus lothianensis SGB14975
Pseudoflavonifractor capillosus SGB15140
GGB9818 SGB15459
GGB9557 SGB14966
Phocea massiliensis SGB14837
Massilimaliae timonensis SGB7253
GGB9590 SGB15012
Gordonibacter pamelaeae SGB14807
Gemmiger SGB15299 SGB15299
Ruminococcaceae SGB15234
GGB9705 SGB15224 SGB15224
Lachnospiraceae SGB4669
Ruminococcaceae SGB15249
GGB9712 SGB15244
Anaerobutyricum hallii SGB4532
GGB9758 SGB15368
Bacteroides ovatus SGB1871
LM Coefficient
-0.03 0 0.03 0.06
-2.5 0 2.5
10 0 10
2Y-noR
2Y-R
2Y-noR (16)
2Y-R (15)
B T1 - nDC
Gemmiger formicilis SGB15300
Lachnospira pectinoschiza SGB5075
Blautia sp AF19 10LB SGB4810
Lachnospiraceae WCA3 601 WT 6H SGB4910
Clostridium sp NSJ 42 SGB6174
GGB9640 SGB15115
Parasutterella excrementihominis SGB9262
Victivallis vadensis SGB9202
Dysosmobacter sp NSJ 60 SGB15124
Ruminococcaceae bacterium D5 SGB14960
Lachnospiraceae bacterium SGB5200
C. Pararuminococcus gallinarum SGB63327
GGB45432 SGB63101
Ruminococcaceae SGB14899
Lachnospiraceae SGB4894
Streptococcus parasanguinis SGB8071
Streptococcus salivarius SGB8007
Faecalibacterium prausnitzii SGB15318
LM Coefficient
-0.06 -0.04 -0.02 0 0.02 0.04
-2.5 0 2.5 5.0
15 5 15 25
2Y-noR
2Y-R
2Y-noR (19)
2Y-R (36)
C T2 - PL
Eubacterium rectale SGB4933
GGB9633 SGB15091 SGB15091
Anaerobutyricum hallii SGB4537
GGB2982 SGB3964 SGB3964
Blautia sp OF03 15BH SGB4779
GGB4566 SGB6305 SGB6305
Clostridium leptum SGB14853
Clostridia bacterium SGB53497
Christensenella massiliensis SGB29339
Oscillibacter sp PC13 SGB7258
Massilimaliae massiliensis SGB29347
GGB9627 SGB15081 SGB15081
Lachnospiraceae SGB4669
Gordonibacter pamelaeae SGB14807
GGB9633 SGB15090 SGB15090
Bacteroides ovatus SGB1871
LM Coefficient
-0.050 -0.025 0 0.025 0.050
-5.0 -2.5 0 2.5
10 0 10
2Y-noR
2Y-R
2Y-noR (16)
2Y-R (15)
D T2 - nDC
Lachnospira pectinoschiza SGB5075
Lachnospiraceae WCA3 601 WT 6H SGB4910
GGB9640 SGB15115
C. Avimicrobium caecorum SGB15350
Parasutterella excrementihominis SGB9262
Victivallis vadensis SGB9202
Clostridium sp Marseille P3244 SGB29302
Enterocloster lavalensis SGB4725
Lachnospiraceae OF09 6 SGB4966
GGB9581 SGB14999
GGB2982 SGB3964
Ruminococcaceae SGB14899
GGB3034 SGB4030
Lachnospiraceae SGB4924
Eubacterium sp AF15 50 SGB5042
GGB6606 SGB9340
Anaerotignum faecicola SGB5190
Streptococcus parasanguinis SGB8071
Alistipes finegoldii SGB2301
Streptococcus salivarius SGB8007
Alistipes onderdonkii SGB2303
Blautia wexlerae SGB4837
Faecalibacterium prausnitzii SGB15318
LM Coefficient
-0.050 -0.025 0 0.025
-2.5 0 2.5
15 15 35
2Y-noR
2Y-R
2Y-noR (17)
2Y-R (35)

Figure S2

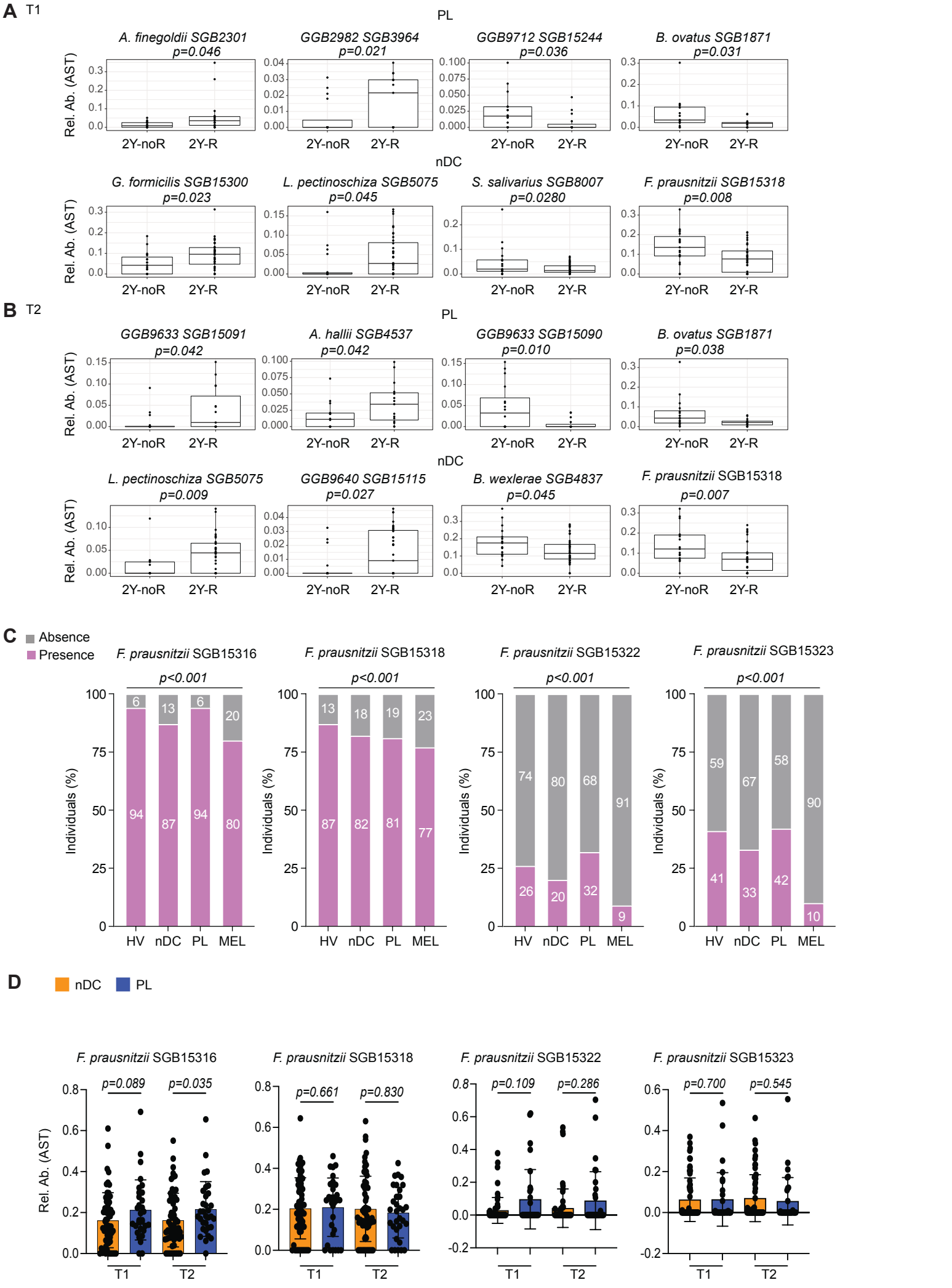
A T1
PL
A. finegoldii SGB2301
p=0.046
GGB2982 SGB3964
p=0.021
GGB9712 SGB15244
p=0.036
B. ovatus SGB1871
p=0.031
nDC
G. formicilis SGB15300
p=0.023
L. pectinoschiza SGB5075
p=0.045
S. salivarius SGB8007
p=0.0280
F. prausnitzii SGB15318
p=0.008
B T2
PL
GGB9633 SGB15091
p=0.042
A. hallii SGB4537
p=0.042
GGB9633 SGB15090
p=0.010
B. ovatus SGB1871
p=0.038
nDC
L. pectinoschiza SGB5075
p=0.009
GGB9640 SGB15115
p=0.027
B. wexlerae SGB4837
p=0.045
F. prausnitzii SGB15318
p=0.007
Rel. Ab. (AST)
2Y-noR
2Y-R
C
Absence
Presence
F. prausnitzii SGB15316
F. prausnitzii SGB15318
F. prausnitzii SGB15322
F. prausnitzii SGB15323
p<0.001
Individuals (%)
HV
nDC
PL
MEL
D
nDC
PL
F. prausnitzii SGB15316
F. prausnitzii SGB15318
F. prausnitzii SGB15322
F. prausnitzii SGB15323
p=0.089
p=0.035
p=0.661
p=0.830
p=0.109
p=0.286
p=0.700
p=0.545
Rel. Ab. (AST)
T1
T2

Figure S3

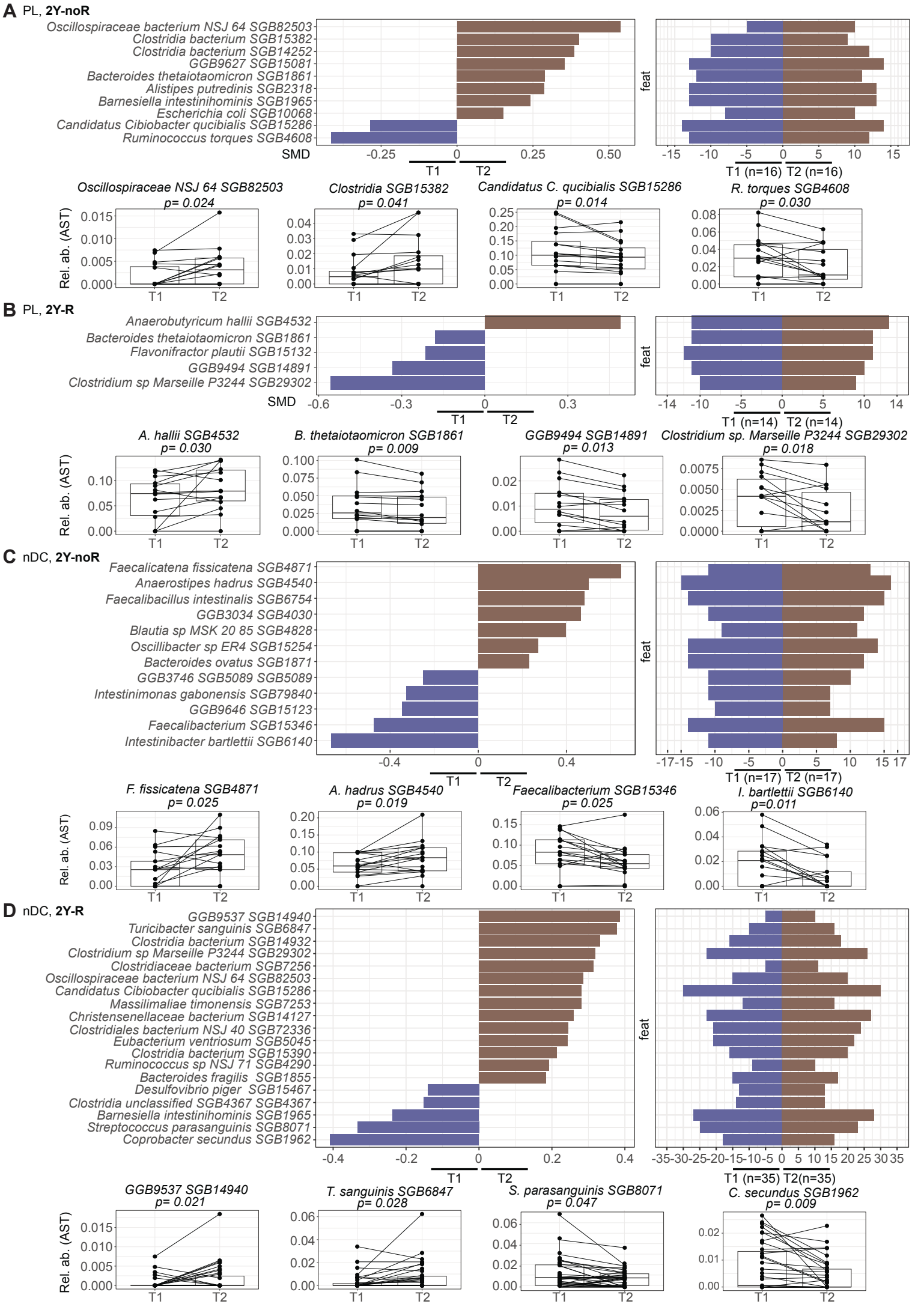
A PL, 2Y-noR
Oscillospiraceae bacterium NSJ 64 SGB82503
Clostridia bacterium SGB15382
Clostridia bacterium SGB14252
GGB9627 SGB15081
Bacteroides thetaiotaomicron SGB1861
Alistipes putredinis SGB2318
Barnesiella intestinihominis SGB1965
Escherichia coli SGB10068
Candidatus Cibiobacter qucibialis SGB15286
Ruminococcus torques SGB4608
SMD
T1
T2
feat
T1 (n=16) T2 (n=16)
Oscillospiraceae NSJ 64 SGB82503 p= 0.024
Clostridia SGB15382 p= 0.041
Candidatus C. qucibialis SGB15286 p= 0.014
R. torques SGB4608 p= 0.030
Rel. ab. (AST)
B PL, 2Y-R
Anaerobutyricum hallii SGB4532
Bacteroides thetaiotaomicron SGB1861
Flavonifractor plautii SGB15132
GGB9494 SGB14891
Clostridium sp Marseille P3244 SGB29302
T1 (n=14) T2 (n=14)
A. hallii SGB4532 p= 0.030
B. thetaiotaomicron SGB1861 p= 0.009
GGB9494 SGB14891 p= 0.013
Clostridium sp. Marseille P3244 SGB29302 p= 0.018
C nDC, 2Y-noR
Faecalicatena fissicatena SGB4871
Anaerostipes hadrus SGB4540
Faecalibacillus intestinalis SGB6754
GGB3034 SGB4030
Blautia sp MSK 20 85 SGB4828
Oscillibacter sp ER4 SGB15254
Bacteroides ovatus SGB1871
GGB3746 SGB5089 SGB5089
Intestinimonas gabonensis SGB79840
GGB9646 SGB15123
Faecalibacterium SGB15346
Intestinibacter bartlettii SGB6140
T1 (n=17) T2 (n=17)
F. fissicatena SGB4871 p= 0.025
A. hadrus SGB4540 p= 0.019
Faecalibacterium SGB15346 p= 0.025
I. bartlettii SGB6140 p=0.011
D nDC, 2Y-R
GGB9537 SGB14940
Turicibacter sanguinis SGB6847
Clostridia bacterium SGB14932
Clostridium sp Marseille P3244 SGB29302
Clostridiaceae bacterium SGB7256
Oscillospiraceae bacterium NSJ 64 SGB82503
Candidatus Cibiobacter qucibialis SGB15286
Massilimaliae timonensis SGB7253
Christensenellaceae bacterium SGB14127
Clostridiales bacterium NSJ 40 SGB72336
Eubacterium ventriosum SGB5045
Clostridia bacterium SGB15390
Ruminococcus sp NSJ 71 SGB4290
Bacteroides fragilis SGB1855
Desulfovibrio piger SGB15467
Clostridia unclassified SGB4367 SGB4367
Barnesiella intestinihominis SGB1965
Streptococcus parasanguinis SGB8071
Coprobacter secundus SGB1962
T1 (n=35) T2(n=35)
GGB9537 SGB14940 p= 0.021
T. sanguinis SGB6847 p= 0.028
S. parasanguinis SGB8071 p= 0.047
C. secundus SGB1962 p= 0.009

Figure S4

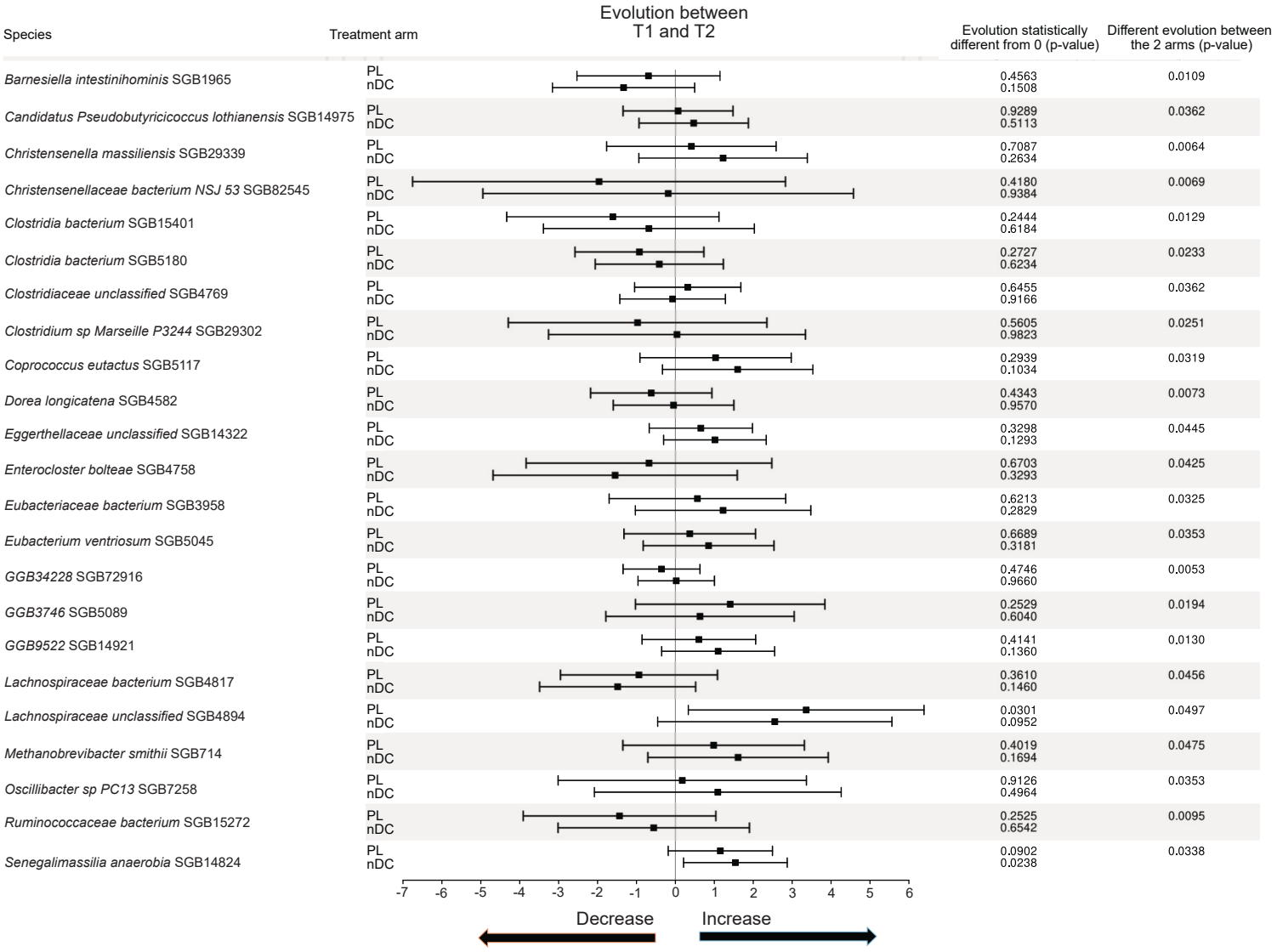
Species
Treatment arm
Evolution between T1 and T2
Evolution statistically different from 0 (p-value)
Different evolution between the 2 arms (p-value)
Barnesiella intestinihominis SGB1965
PL 0.4563
nDC 0.1508
0.0109
Candidatus Pseudobutyricicoccus lothianensis SGB14975
PL 0.9289
nDC 0.5113
0.0362
Christensenella massiliensis SGB29339
PL 0.7087
nDC 0.2634
0.0064
Christensenellaceae bacterium NSJ 53 SGB82545
PL 0.4180
nDC 0.9384
0.0069
Clostridia bacterium SGB15401
PL 0.2444
nDC 0.6184
0.0129
Clostridia bacterium SGB5180
PL 0.2727
nDC 0.6234
0.0233
Clostridiaceae unclassified SGB4769
PL 0.6455
nDC 0.9166
0.0362
Clostridium sp Marseille P3244 SGB29302
PL 0.5605
nDC 0.9823
0.0251
Coprococcus eutactus SGB5117
PL 0.2939
nDC 0.1034
0.0319
Dorea longicatena SGB4582
PL 0.4343
nDC 0.9570
0.0073
Eggerthellaceae unclassified SGB14322
PL 0.3298
nDC 0.1293
0.0445
Enterocloster bolteae SGB4758
PL 0.6703
nDC 0.3293
0.0425
Eubacteriaceae bacterium SGB3958
PL 0.6213
nDC 0.2829
0.0325
Eubacterium ventriosum SGB5045
PL 0.6689
nDC 0.3181
0.0353
GGB34228 SGB72916
PL 0.4746
nDC 0.9660
0.0053
GGB3746 SGB5089
PL 0.2529
nDC 0.6040
0.0194
GGB9522 SGB14921
PL 0.4141
nDC 0.1360
0.0130
Lachnospiraceae bacterium SGB4817
PL 0.3610
nDC 0.1460
0.0456
Lachnospiraceae unclassified SGB4894
PL 0.0301
nDC 0.0952
0.0497
Methanobrevibacter smithii SGB714
PL 0.4019
nDC 0.1694
0.0475
Oscillibacter sp PC13 SGB7258
PL 0.9126
nDC 0.4964
0.0353
Ruminococcaceae bacterium SGB15272
PL 0.2525
nDC 0.6542
0.0095
Senegalimassilia anaerobia SGB14824
PL 0.0902
nDC 0.0238
0.0338
-7 -6 -5 -4 -3 -2 -1 0 1 2 3 4 5 6
Decrease
Increase

Figure S5

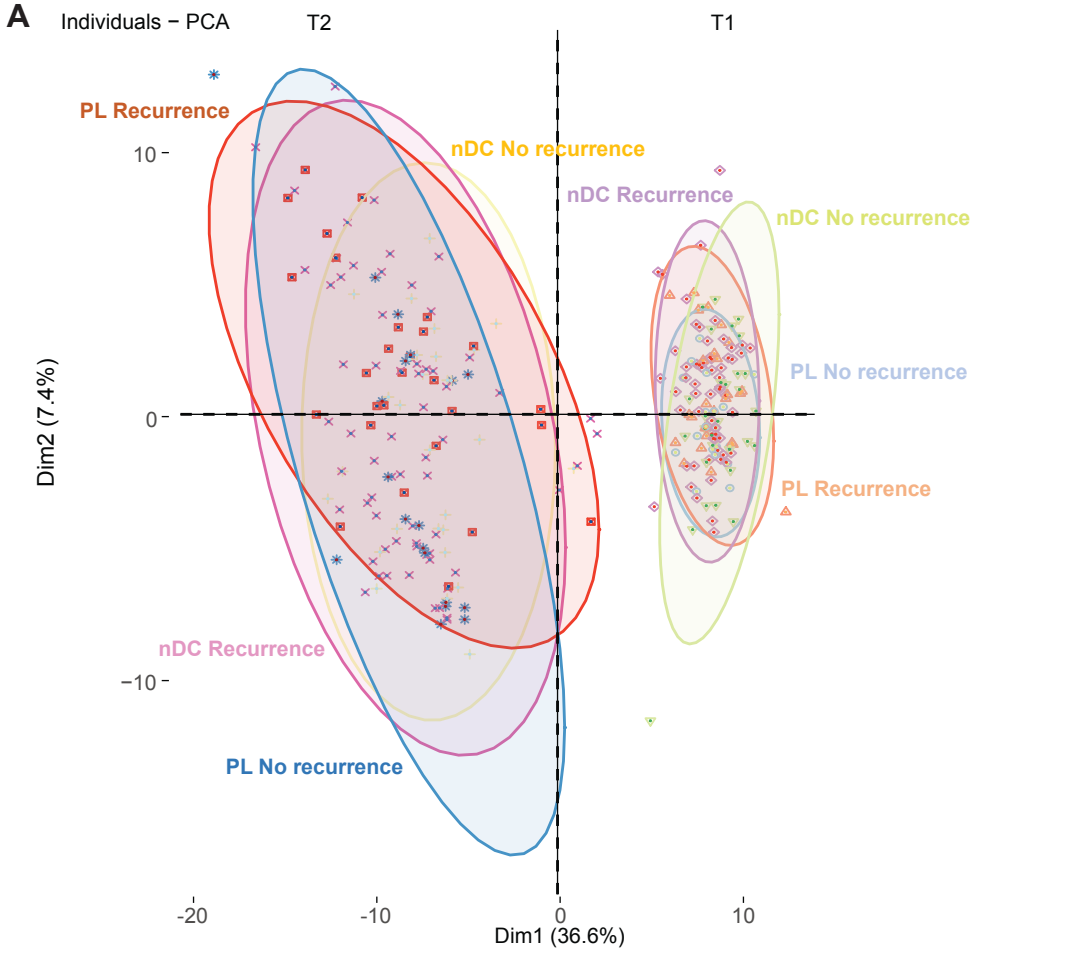
A
Individuals − PCA
T2
T1
PL Recurrence
nDC No recurrence
nDC Recurrence
nDC No recurrence
PL No recurrence
PL Recurrence
nDC Recurrence
PL No recurrence
Dim2 (7.4%)
Dim1 (36.6%)
10
0
−10
-20
-10
0
10

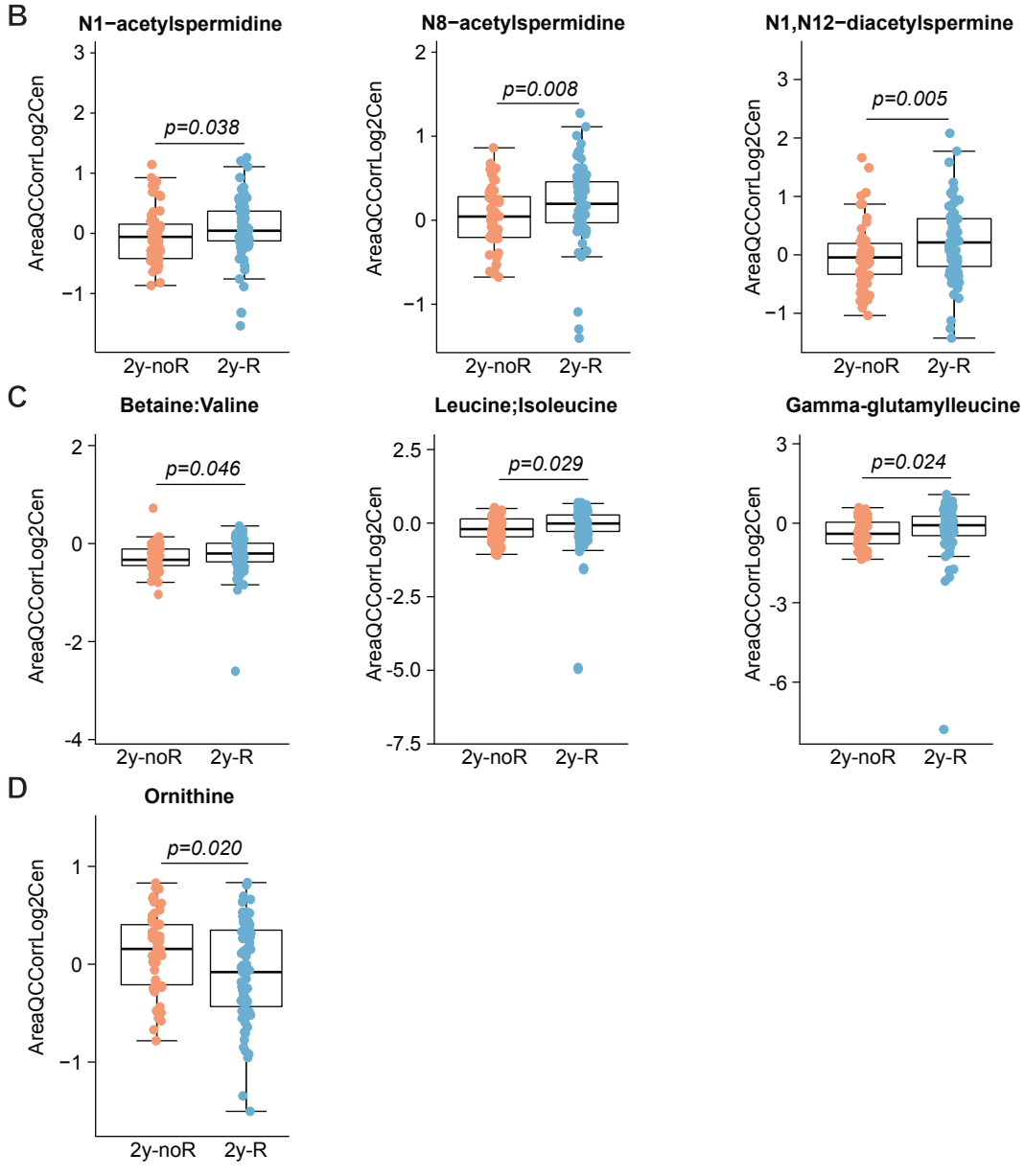
B
N1−acetylspermidine
N8−acetylspermidine
N1,N12−diacetylspermine
AreaQCCorrLog2Cen
p=0.038
p=0.008
p=0.005
2y-noR
2y-R
C
Betaine:Valine
Leucine;Isoleucine
Gamma-glutamylleucine
p=0.046
p=0.029
p=0.024
D
Ornithine
p=0.020

Figure S6

A T1

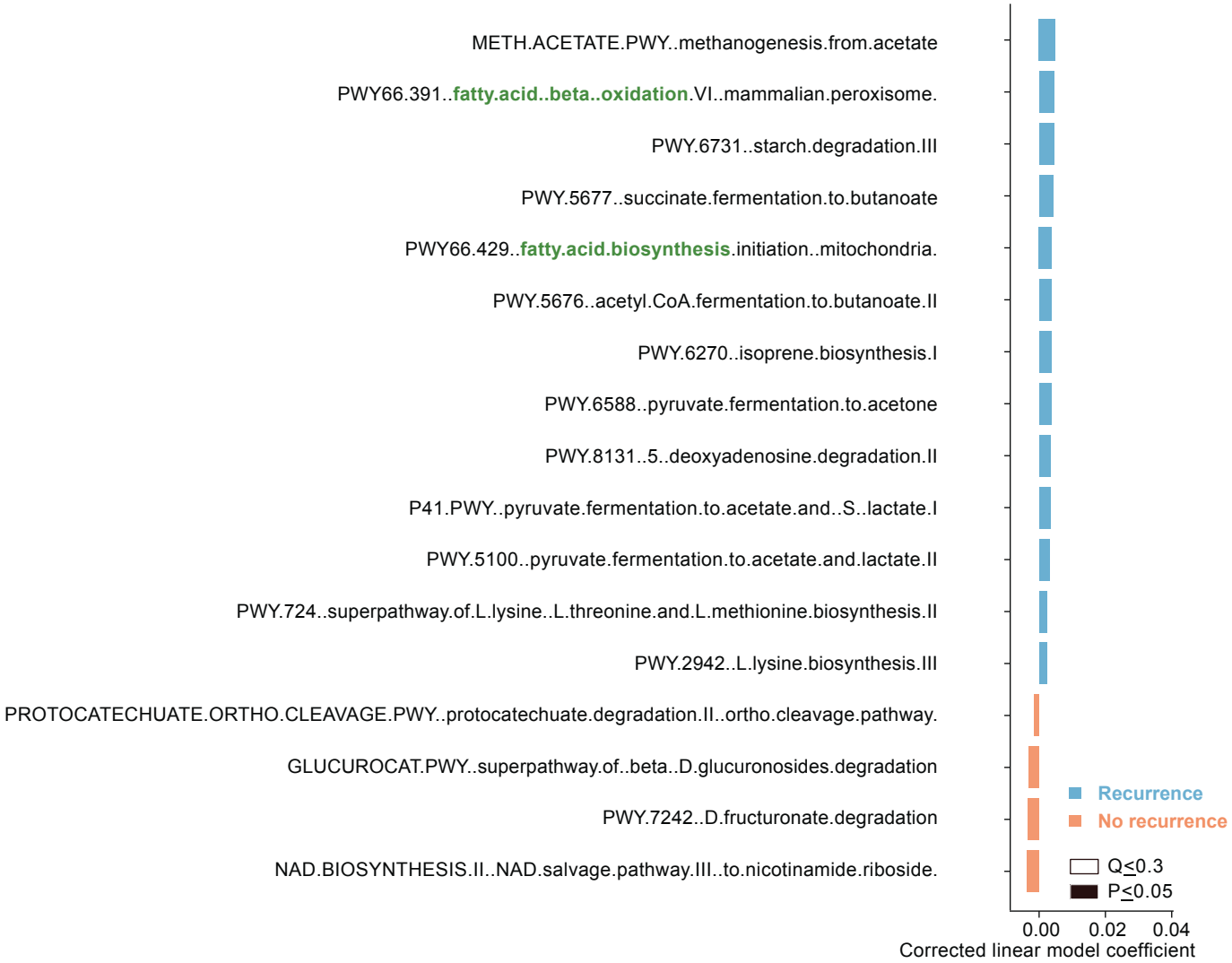

B

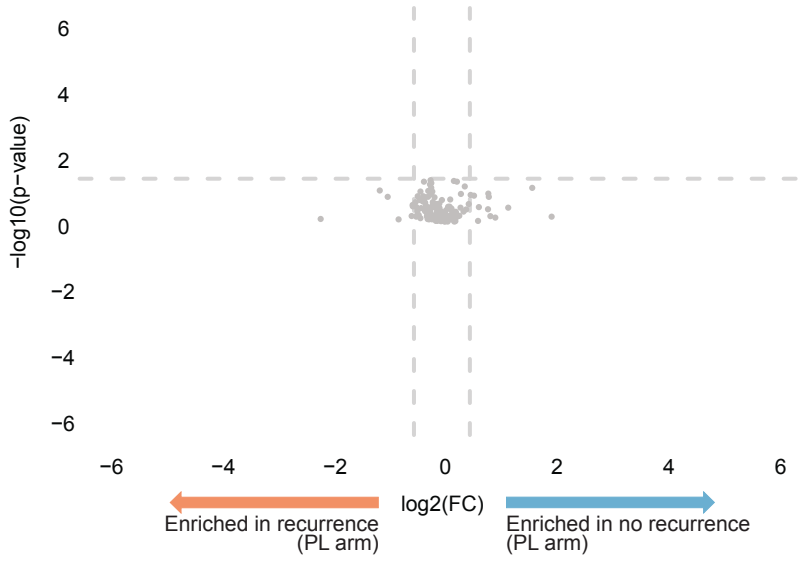

Figure S7

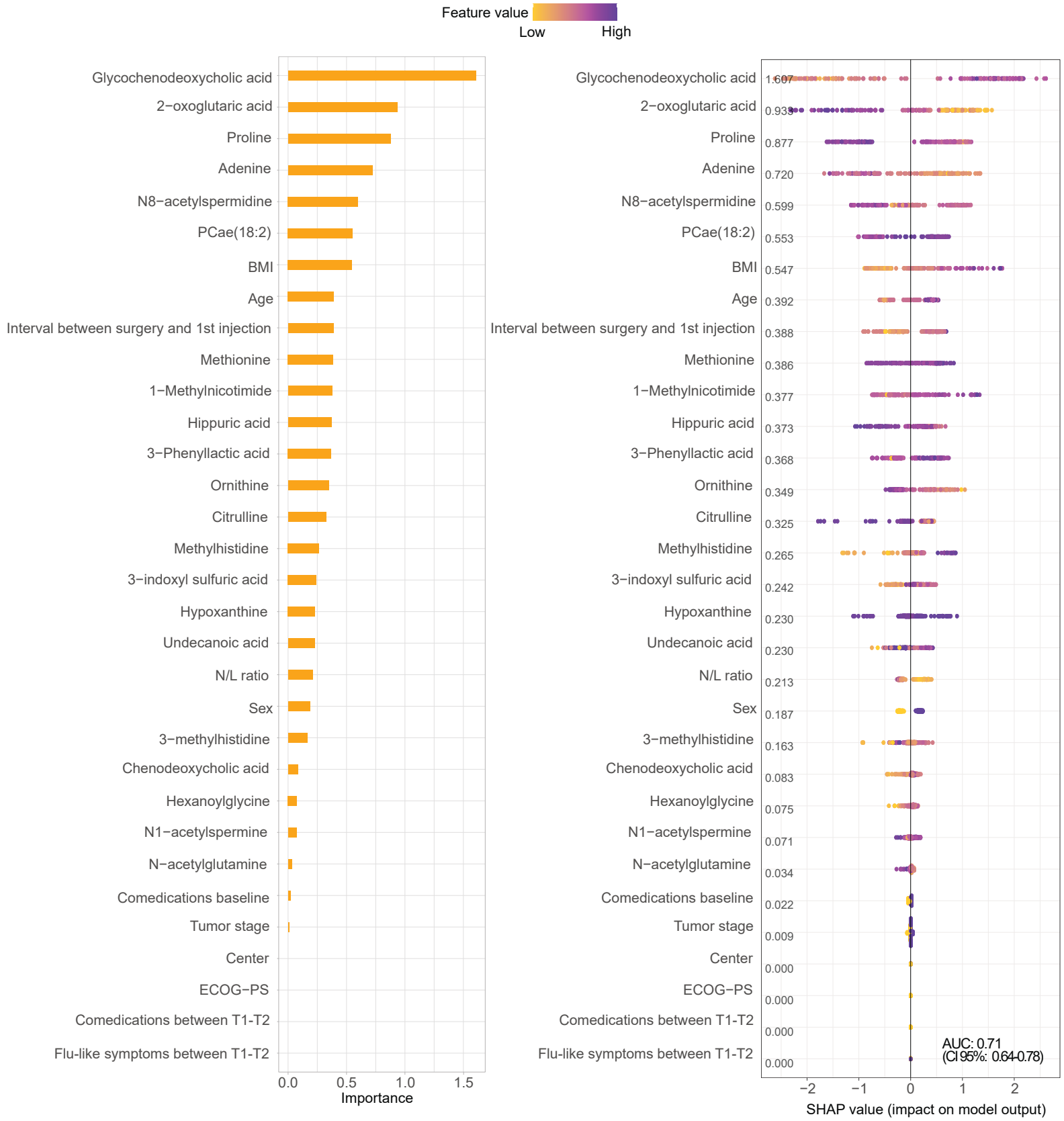
Feature value
Low
High
Glycochenodeoxycholic acid
2−oxoglutaric acid
Proline
Adenine
N8−acetylspermidine
PCae(18:2)
BMI
Age
Interval between surgery and 1st injection
Methionine
1−Methylnicotimide
Hippuric acid
3−Phenyllactic acid
Ornithine
Citrulline
Methylhistidine
3−indoxyl sulfuric acid
Hypoxanthine
Undecanoic acid
N/L ratio
Sex
3−methylhistidine
Chenodeoxycholic acid
Hexanoylglycine
N1−acetylspermine
N−acetylglutamine
Comedications baseline
Tumor stage
Center
ECOG−PS
Comedications between T1-T2
Flu-like symptoms between T1-T2
0.0
0.5
1.0
1.5
Importance
1.607
0.939
0.877
0.720
0.599
0.553
0.547
0.392
0.388
0.386
0.377
0.373
0.368
0.349
0.325
0.265
0.242
0.230
0.230
0.213
0.187
0.163
0.083
0.075
0.071
0.034
0.022
0.009
0.000
0.000
0.000
0.000
AUC: 0.71
(CI 95%: 0.64-0.78)
−2
−1
0
1
2
SHAP value (impact on model output)

Figure S8

A

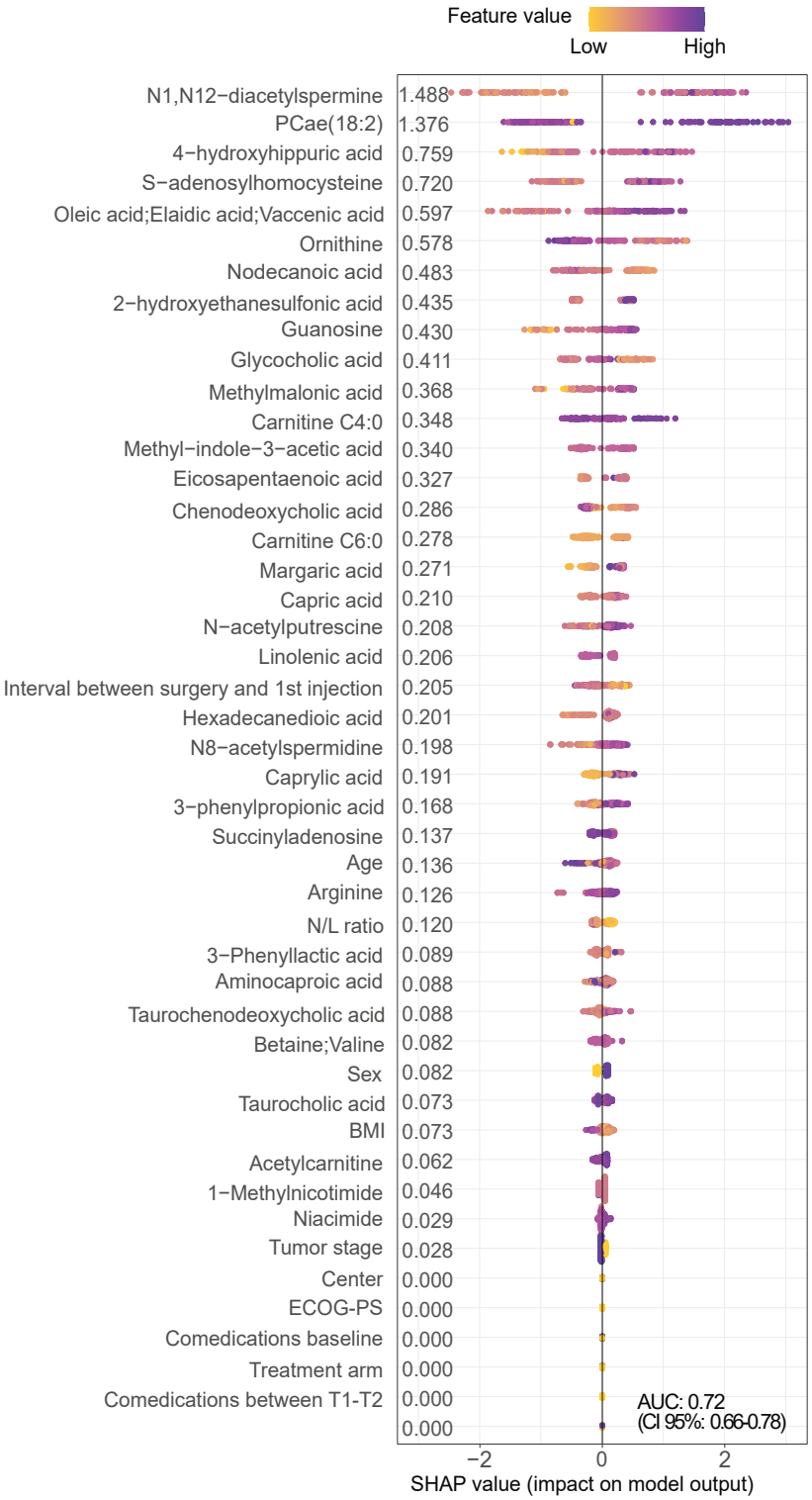

B

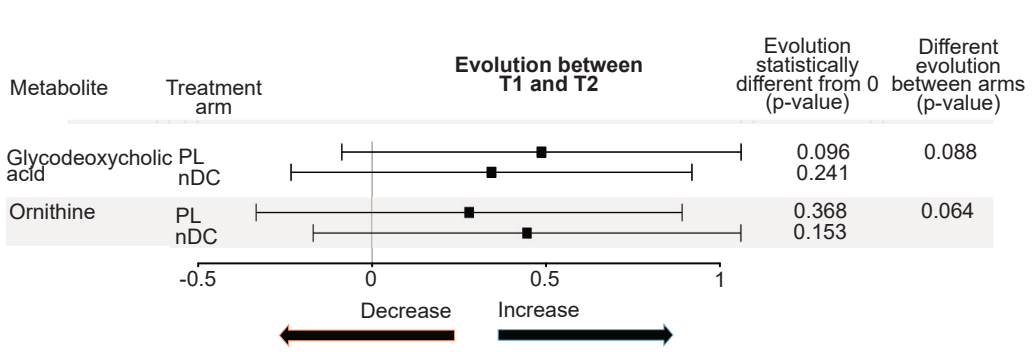

C

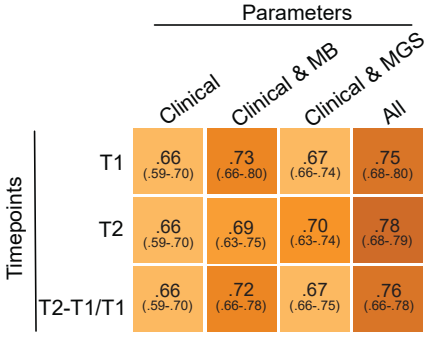

Figure S9

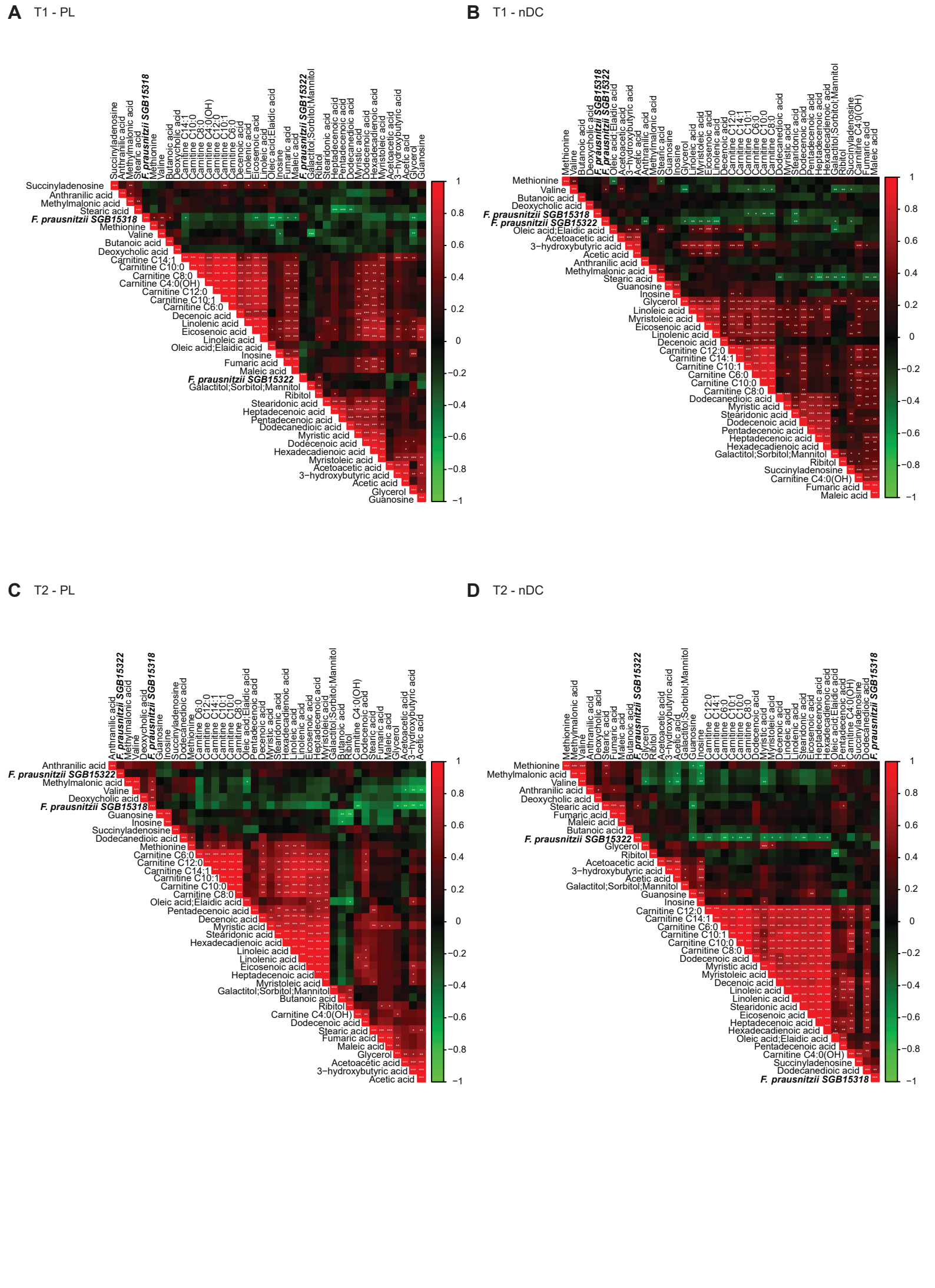
A
T1 - PL
B
T1 - nDC
C
T2 - PL
D
T2 - nDC
F. prausnitzii SGB15318
F. prausnitzii SGB15322
1
0.8
0.6
0.4
0.2
0
−0.2
−0.4
−0.6
−0.8
−1

Figure S10

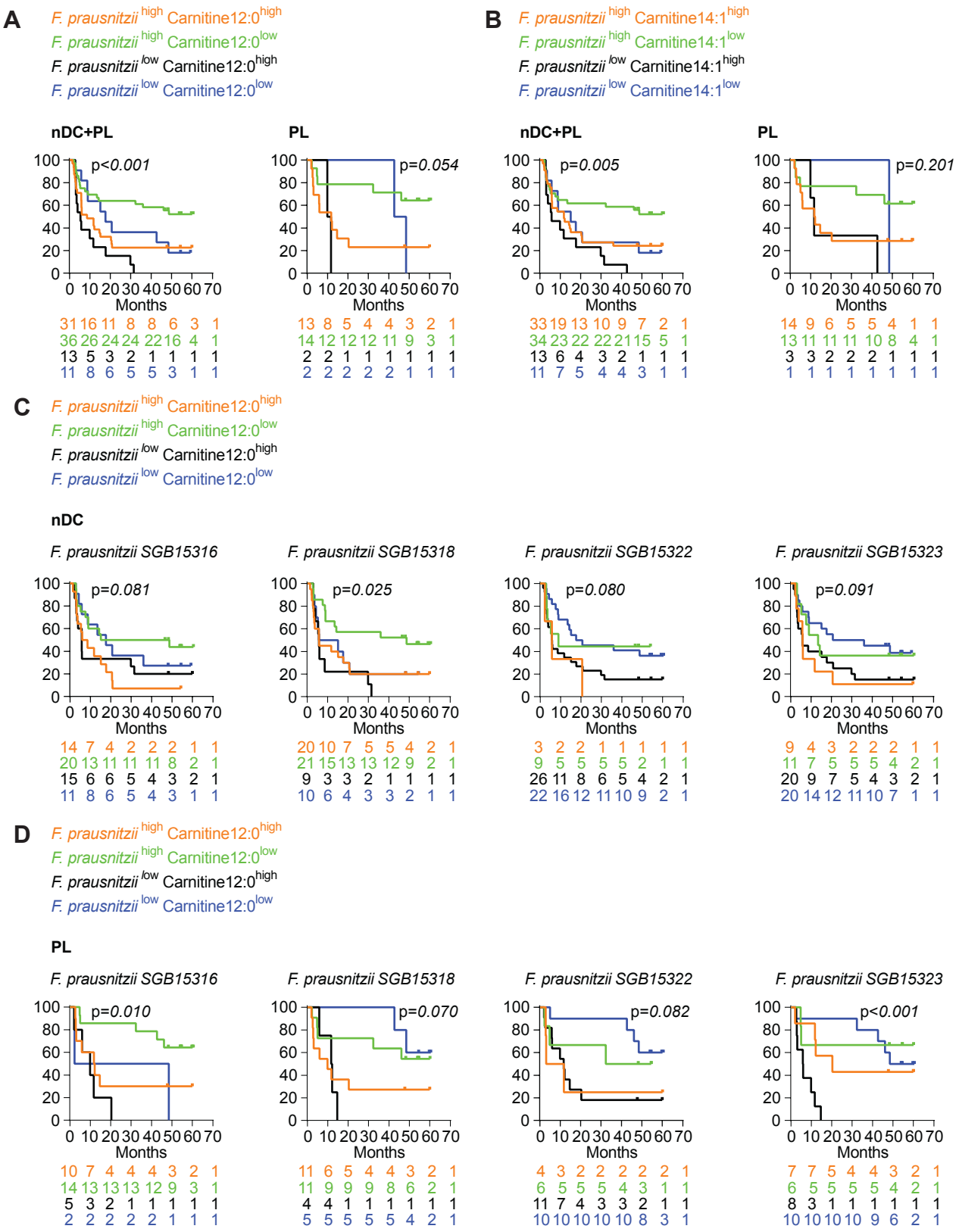
A
F. prausnitzii high Carnitine12:0high
F. prausnitzii high Carnitine12:0low
F. prausnitzii low Carnitine12:0high
F. prausnitzii low Carnitine12:0low
nDC+PL
p<0.001
31 16 11 8 8 6 3 1
36 26 24 24 22 16 4 1
13 5 3 2 1 1 1 1
11 8 6 5 5 3 1 1
PL
p=0.054
13 8 5 4 4 3 2 1
14 12 12 12 11 9 3 1
2 2 1 1 1 1 1 1
2 2 2 2 2 1 1 1
B
F. prausnitzii high Carnitine14:1high
F. prausnitzii high Carnitine14:1low
F. prausnitzii low Carnitine14:1high
F. prausnitzii low Carnitine14:1low
nDC+PL
p=0.005
33 19 13 10 9 7 2 1
34 23 22 22 21 15 5 1
13 6 4 3 2 1 1 1
11 7 5 4 4 3 1 1
PL
p=0.201
14 9 6 5 5 4 1 1
13 11 11 11 10 8 4 1
3 3 2 2 2 1 1 1
1 1 1 1 1 1 1 1
C
F. prausnitzii high Carnitine12:0high
F. prausnitzii high Carnitine12:0low
F. prausnitzii low Carnitine12:0high
F. prausnitzii low Carnitine12:0low
nDC
F. prausnitzii SGB15316
p=0.081
14 7 4 2 2 2 1 1
20 13 11 11 11 8 2 1
15 6 6 5 4 3 2 1
11 8 6 5 4 3 1 1
F. prausnitzii SGB15318
p=0.025
20 10 7 5 5 4 2 1
21 15 13 13 12 9 2 1
9 3 3 2 1 1 1 1
10 6 4 3 3 2 1 1
F. prausnitzii SGB15322
p=0.080
3 2 2 1 1 1 1 1
9 5 5 5 5 2 1 1
26 11 8 6 5 4 2 1
22 16 12 11 10 9 2 1
F. prausnitzii SGB15323
p=0.091
9 4 3 2 2 2 1 1
11 7 5 5 5 4 2 1
20 9 7 5 4 3 2 1
20 14 12 11 10 7 1 1
D
F. prausnitzii high Carnitine12:0high
F. prausnitzii high Carnitine12:0low
F. prausnitzii low Carnitine12:0high
F. prausnitzii low Carnitine12:0low
PL
F. prausnitzii SGB15316
p=0.010
10 7 4 4 4 3 2 1
14 13 13 13 12 9 3 1
5 3 2 1 1 1 1 1
2 2 2 2 2 1 1 1
F. prausnitzii SGB15318
p=0.070
11 6 5 4 4 3 2 1
11 9 9 9 8 6 2 1
4 4 1 1 1 1 1 1
5 5 5 5 5 4 2 1
F. prausnitzii SGB15322
p=0.082
4 3 2 2 2 2 2 1
6 5 5 5 4 3 1 1
11 7 4 3 3 2 1 1
10 10 10 10 10 8 3 1
F. prausnitzii SGB15323
p<0.001
7 7 5 4 4 3 2 1
6 5 5 5 5 4 2 1
8 3 1 1 1 1 1 1
10 10 10 10 9 6 2 1
0 10 20 30 40 50 60 70
Months

9 DISCUSSION

In the past years, immune checkpoint blockade became the backbone therapy for patients with solid tumors. The reason why the tumor microenvironment leads to immune failure can be explained by the cancer-immune phenotypes (5). The better understanding of the tumor microenvironment led to the development of biomarkers in IO. Nowadays, only three of these IO biomarkers have FDA approval: TMB, PD-L1 expression and MSI/MMR (10). Cancer is not just a genetic or epigenetic disease resulting from cell autonomous aberrations but is the cumulative outcome of functional failures of the meta-organism. Increasing evidence support the impact of the microbiota on cancer immune-surveillance, and we actively participated in the evolution from the state-of-the-art MGS to MCI and user-friendly diagnostic tools of gut dysbiosis. Here, we demonstrate that cancer has taxonomic and metabolomics hallmarks that contribute to progression and may be used as biomarkers in immuno-oncology.

Cancers induce a stress ileopathy, characterized by ectopic proliferation of enteroendocrine cells and disbalance between sympathetic and cholinergic, and protracted intestinal dysbiosis dominated by tolerogenic *Enterocloster* spp. We demonstrated the causal role of microbiota in cancer-associated ileopathy using different approaches (targeted ABX or cohousing tumor-bearer mice with healthy littermates). The presence of a distinct gut microbiota composition in patients with cancer (versus HV) dominated by tolerogenic commensals, previously associated with resistance to ICB, highlights the need to define gut dysbiosis in order to better select donors and recipients to MCI. So, we explored taxonomic signatures towards a definition of gut dysbiosis in cancer immunotherapy. More than predicting benefit to ICB, normal levels of *Akk* is associated with richer commensalism and may be used as a proxy of dysbiosis. Due to the limitations in predicting clinical outcome across cohorts and cancer types using single MGS species, we focused on a different approach, based on an ecological distribution of stool MGS species into two opposite SIGs. From a whole-population-based network we could de-

escalate to a unidimensional score calculated at an individual level: the TOPOSCORE. TOPOSCORE is independently associated with outcomes in three independent cohorts, outperforming PD-L1, and may be the first agnostic biomarker of gut dysbiosis. By selecting the most prevalent bacteria, TOPOSCORE could be translated into a qPCR-based user-friendly diagnosis tool of gut dysbiosis. Interestingly, when applied to a publicly available cohort of HV, we identified that 21% of these individuals harbor the SIG1+ signature. As a limitation, the cohorts of patients with cancer and HV were not paired for geopraphic site or clinical characteristics. ABX stop lead to a gut microbiota shift towards tolerogenic bacteria (including *Enterocloster* spp.), impairing ICB outcomes. *Enterocloster* spp. induce MB deviations (biliary salt perturbation), leading to downregulation of ileal MAdCAM-1 by secondary biliary acids and exodus of intestinal Tr17 toward tumor beds. Soluble MAdCAM-1 (correlating ileal transcripts) is an independent prognostic biomarker in IO and proxy of gut dysbiosis. Cancer-associated gut dysbiosis is not cancer-specific, but related to distinct inflammatory conditions, opening an opportunity to explore our gut-related biomarkers in an interception setting (184).

From a negative and prematurely closed two-arm randomized clinical trial using a non-standard protocol, we identified MB signatures associates with recurrence in patients with high-risk localized melanoma. Early deviations in MB profiling, months before recurrence, towards lipid metabolism, carboxylic acids, middle and long chain acetylcarnitines, acetylated polyamines and aberrations in biliary salt composition may play a central role in tumor recurrence and progression. As small molecules that act as intermediates or end products of cellular metabolism, some metabolites are mediators of either beneficial or harmful effects of probiotics or diet, paving the way for theurapetic interventions (259–261). We faced hurdles and challenges in analyzing MB data, mostly related to normalization in data preprocessing to avoid batch effect.

Furthermore, we demonstrated that immune responses directed against the uropathogenic *E. coli* (either Tfh or humoral) dictated benefit to ICB in patients with bladder cancer. Microbial tissue colonization can exert

antitumor effects and immune stimulation through TLS and these microbes might be harnessed for future therapeutic strategies (227,260,261). Wang and colleagues showed that the protumoral anaerobic *F. nucleatum* induced an immunosuppressive TME in CRC models (262). Patients with localized CRC that received anaerobe-targeting ABX (nitroimidazole or lincomycin classes) prior to surgery had longer disease-free survival when compared to patients receiving other classes or any ABX. ABX-loaded liposomes to target CRC induced the release of cancer-specific microbial neoantigens and elicited microbial-specific T cell immunity (262).

Our research evolved into Clinicobiome, a medical-scientific program that aim to leverage the microbiota to improve quality in clinical care. This program enable the prospective validation of these gut-related biomarkers in cancer immunotherapy across different histologies. In addition, ongoing international consortiums and collaborations allow us to validate these biomarkers in patients from different geographic regions and ethnic groups. Based on our work, two multicentric clinical trials are currently enrolling patients in France. The Oncobax®-AK (NCT05865730) clinical trial evaluate the use of a live bacterial product (specific strain of *Akkermansia*) as an adjuvant treatment for ICB in selected patients with RCC and NSCLC. Patients are selected based on a qPCR test to detect the presence of *Akk* in feces. The KETOREIN trial (NCT05119010) is a non-randomized four-arm pilot study evaluating the use of ketogenic diet or its mediator metabolite 3- hydroxybutyrate as MCI in non-selected patients with advanced RCC treated with dual ICB in first-line setting.

As a summary, Table 5 depicts emerging IO biomarkers, including our recently described gut-related markers, showing their current clinical use and limitations. Taken together, our results show that mechanistic insights towards understanding the role of microbiota open opportunities to the development of novel prevention and treatment strategies of various cancer types (Table 5) (263).

Table 5 *Emerging biomarkers in immuno-oncology.*

Category	Biomarker	Current clinical use	Limitations
Blood	NLR and LIPI	Enable identify high-risk patients who may require intensive therapeutic schema.	Prognostic rather than predictive value, since these scores do not select patients that would benefit from targeted therapy.
	ctDNA	FDA-approved NGS and PCR tests enable qualitative assessment to identify targetable genetic aberrations.	Restricted panel of genetic aberrations. Require validation as strategy for screening, assessment of residual disease after definitive treatment or response to systemic therapy (264).
	sMAdCAM-1	ELISA kit is available, but still not used outside of research context.	Require prospective validation as a proxy of dysbiosis.
	sCD27	ELISA kit is available, but still not used outside of research context.	Require further validation as a predictive biomarker in ICB combination strategies.
	Metabolites (such as fatty acids, acetylated polyamines, conjugated	Not recommended outside of research context.	High cost and time-consuming technique. Data variability. To date, a normal threshold is not defined.

	biliary acids).		
Tumor	TMB	FDA-approved WES and NGS panels.	There is no consensus on threshold. High cost and time-consuming technique (10).
	PD-L1	FDA-approved PD-Ll tests as companion diagnostic tests for PD-(L)1 mAbs.	Multiple testing methods, staining Abs clones, and interpretation protocols (scoring system, threshold, and type of cells, see Table 4). Low predictive value (29%) (35).
	MSI-H and dMMR	FDA-approved MMR (PMS2, MLH1, MSH6 and MSH2) PCR-based or IHC tests and NGS.	dMMR does not always reflect MSI intensity / mutational load (265). It could explain why some patients with dMMR do not respond to ICB.
	POLE mutations	Molecular classification for risk assessment of endometrial cancer (266). Although requiring prospective validaton, the presence of POLE mutations in routine DNA sequencing may favor ICB-based therapy in other tumor types.	DNA sequencing techniques can be high cost and time-consuming methods. PCR-based assays are promising strategies in endometrial cancer (267).
	T-cell–inflamed GEP	Nowadays, this finding in routine NGS	High cost and time-consuming

		test may favor ICB-based therapy.	technique.
Fecal	Alpha diversity	Not recommended outside of research context.	Require cost and time-consuming methods. Do not reflect gut microbiota composition. It is not a robust biomarker across studies.
	Akkermansia muciniphila	PCR-based assay to test *Akk* presence in stool is available, but not used outside of research context. Ongoing clinical trial using PCR-based test to select patients for Oncobax®-AK (NCT05865730).	Require further validation as a predictive biomarker and proxy of dysbiosis.
	TOPOSCORE	Not recommended outside of research context.	Require prospective validation of MGS- and PCR-based assays (ongoing).

Immune-checkpoint blockade (ICB); Lung Immune Prognostic Index (LIPI); Neutrophil-lymphocite ratio (NLR); Polymerase Chain Reaction (PCR); Polymerase-epsilon (POLE); Tumor mutation burden (TMB).

10 REFERENCES

1. Bray F, Laversanne M, Weiderpass E, Soerjomataram I. The ever-increasing importance of cancer as a leading cause of premature death worldwide. Cancer. 2021 Aug 15;127(16):3029–30.

2. Sung H, Ferlay J, Siegel RL, Laversanne M, Soerjomataram I, Jemal A, et al. Global Cancer Statistics 2020: GLOBOCAN Estimates of Incidence and Mortality Worldwide for 36 Cancers in 185 Countries. CA A Cancer J Clin. 2021 May;71(3):209–49.

3. Wu Q, Qian W, Sun X, Jiang S. Small-molecule inhibitors, immune checkpoint inhibitors, and more: FDA-approved novel therapeutic drugs for solid tumors from 1991 to 2021. J Hematol Oncol. 2022 Oct 8;15(1):143.

4. De Visser KE, Joyce JA. The evolving tumor microenvironment: From cancer initiation to metastatic outgrowth. Cancer Cell. 2023 Mar;41(3):374–403.

5. Chen DS, Mellman I. Elements of cancer immunity and the cancer–immune set point. Nature. 2017 Jan;541(7637):321–30.

6. Rozenblatt-Rosen O, Regev A, Oberdoerffer P, Nawy T, Hupalowska A, Rood JE, et al. The Human Tumor Atlas Network: Charting Tumor Transitions across Space and Time at Single-Cell Resolution. Cell. 2020 Apr;181(2):236–49.

7. Pylaeva E, Korschunow G, Spyra I, Bordbari S, Siakaeva E, Ozel I, et al. During early stages of cancer, neutrophils initiate anti-tumor immune responses in tumor-draining lymph nodes. Cell Reports. 2022 Aug;40(7):111171.

8. Gil Del Alcazar CR, Huh SJ, Ekram MB, Trinh A, Liu LL, Beca F, et al. Immune Escape in Breast Cancer During *In Situ* to Invasive Carcinoma Transition. Cancer Discovery. 2017 Oct 1;7(10):1098–115.

9. Mascaux C, Angelova M, Vasaturo A, Beane J, Hijazi K, Anthoine G, et al. Immune evasion before tumour invasion in early lung squamous carcinogenesis. Nature. 2019 Jul;571(7766):570–5.

10. Lei Y, Li X, Huang Q, Zheng X, Liu M. Progress and Challenges of Predictive Biomarkers for Immune Checkpoint Blockade. Front Oncol. 2021 Mar 11;11:617335.

11. De Plaen E, Lurquin C, Van Pel A, Mariamé B, Szikora JP, Wölfel T, et al. Immunogenic (tum-) variants of mouse tumor P815: cloning of the gene of tum- antigen P91A and identification of the tum- mutation. Proc Natl Acad Sci USA. 1988 Apr;85(7):2274–8.

12. Stauss HJ, Van Waes C, Fink MA, Starr B, Schreiber H. Identification of a unique tumor antigen as rejection antigen by molecular cloning and gene transfer. Journal of Experimental Medicine. 1986 Nov 1;164(5):1516–30.

13. Fratta E, Coral S, Covre A, Parisi G, Colizzi F, Danielli R, et al. The biology of cancer testis antigens: Putative function, regulation and therapeutic potential. Molecular Oncology. 2011 Apr;5(2):164–82.

14. Gjerstorff MF, Andersen MH, Ditzel HJ. Oncogenic cancer/testis antigens: prime candidates for immunotherapy. Oncotarget. 2015 Jun 30;6(18):15772–87.

15. Bol KF, Schreibelt G, Gerritsen WR, de Vries IJM, Figdor CG. Dendritic Cell–Based Immunotherapy: State of the Art and Beyond. Clinical Cancer Research. 2016 Apr 15;22(8):1897–906.

16. Bol K, Bloemendal M, van Willigen W, Schreibelt G, Bree SH de, de Goede A, et al. 1078MO MIND-DC: A randomized phase III trial to assess the efficacy of adjuvant dendritic cell vaccination in comparison to placebo in stage IIIB and IIIC melanoma patients. Annals of Oncology. 2020 Sep;31:S732.

17. Ostroverkhova D, Przytycka TM, Panchenko AR. Cancer driver

mutations: predictions and reality. Trends in Molecular Medicine. 2023 Apr;S1471491423000679.

18. Mok TS, Wu YL, Thongprasert S, Yang CH, Chu DT, Saijo N, et al. Gefitinib or Carboplatin–Paclitaxel in Pulmonary Adenocarcinoma. N Engl J Med. 2009 Sep 3;361(10):947–57.

19. Chapman PB, Hauschild A, Robert C, Haanen JB, Ascierto P, Larkin J, et al. Improved Survival with Vemurafenib in Melanoma with BRAF V600E Mutation. N Engl J Med. 2011 Jun 30;364(26):2507–16.

20. Calles A, Riess JW, Brahmer JR. Checkpoint Blockade in Lung Cancer With Driver Mutation: Choose the Road Wisely. American Society of Clinical Oncology Educational Book. 2020 May;(40):372–84.

21. Saxena M, Van Der Burg SH, Melief CJM, Bhardwaj N. Therapeutic cancer vaccines. Nat Rev Cancer. 2021 Jun;21(6):360–78.

22. Boudewijns S, Bloemendal M, De Haas N, Westdorp H, Bol KF, Schreibelt G, et al. Autologous monocyte-derived DC vaccination combined with cisplatin in stage III and IV melanoma patients: a prospective, randomized phase 2 trial. Cancer Immunol Immunother. 2020 Mar;69(3):477–88.

23. Boudewijns S, Bol KF, Schreibelt G, Westdorp H, Textor JC, Van Rossum MM, et al. Adjuvant dendritic cell vaccination induces tumor-specific immune responses in the majority of stage III melanoma patients. OncoImmunology. 2016 Jul 2;5(7):e1191732.

24. Aarntzen EHJG, Schreibelt G, Bol K, Lesterhuis WJ, Croockewit AJ, De Wilt JHW, et al. Vaccination with mRNA-Electroporated Dendritic Cells Induces Robust Tumor Antigen-Specific CD4+ and CD8+ T Cells Responses in Stage III and IV Melanoma Patients. Clinical Cancer Research. 2012 Oct 1;18(19):5460–70.

25. Lesterhuis WJ, de Vries IJM, Schreibelt G, Lambeck AJA, Aarntzen EHJG, Jacobs JFM, et al. Route of administration modulates the induction

of dendritic cell vaccine-induced antigen-specific T cells in advanced melanoma patients. Clin Cancer Res. 2011 Sep 1;17(17):5725–35.

26. Adotévi O, Vernerey D, Jacoulet P, Meurisse A, Laheurte C, Almotlak H, et al. Safety, Immunogenicity, and 1-Year Efficacy of Universal Cancer Peptide–Based Vaccine in Patients With Refractory Advanced Non–Small-Cell Lung Cancer: A Phase Ib/Phase IIa De-Escalation Study. JCO. 2023 Jan 10;41(2):373–84.

27. Carpentier AF, Verlut C, Ghiringhelli F, Bronnimann C, Ursu R, Fumet JD, et al. Anti-telomerase vaccine in patients with newly diagnosed, unmethylated MGMT glioblastoma: A phase II study. JCO. 2023 Jun 1;41(16_suppl):2005–2005.

28. He M, Chai Y, Qi J, Zhang CWH, Tong Z, Shi Y, et al. Remarkably similar CTLA-4 binding properties of therapeutic ipilimumab and tremelimumab antibodies. Oncotarget. 2017 Sep 15;8(40):67129–39.

29. Cha E, Klinger M, Hou Y, Cummings C, Ribas A, Faham M, et al. Improved Survival with T Cell Clonotype Stability After Anti–CTLA-4 Treatment in Cancer Patients. Sci Transl Med [Internet]. 2014 May 28 [cited 2023 Jun 14];6(238). Available from: https://www.science.org/doi/10.1126/scitranslmed.3008211

30. Triebel F, Jitsukawa S, Baixeras E, Roman-Roman S, Genevee C, Viegas-Pequignot E, et al. LAG-3, a novel lymphocyte activation gene closely related to CD4. Journal of Experimental Medicine. 1990 May 1;171(5):1393–405.

31. Huo JL, Wang YT, Fu WJ, Lu N, Liu ZS. The promising immune checkpoint LAG-3 in cancer immunotherapy: from basic research to clinical application. Front Immunol. 2022 Jul 26;13:956090.

32. Tawbi HA, Schadendorf D, Lipson EJ, Ascierto PA, Matamala L, Castillo Gutiérrez E, et al. Relatlimab and Nivolumab versus Nivolumab in Untreated Advanced Melanoma. N Engl J Med. 2022 Jan 6;386(1):24–34.

33. Translational Research | OncologyPRO [Internet]. [cited 2023 Jun 25]. Available from: https://oncologypro.esmo.org/education-library/esmo-books/esmo-handbooks/translational-research/predictive-biomarkers

34. Litchfield K, Reading JL, Puttick C, Thakkar K, Abbosh C, Bentham R, et al. Meta-analysis of tumor- and T cell-intrinsic mechanisms of sensitization to checkpoint inhibition. Cell. 2021 Feb;184(3):596-614.e14.

35. Davis AA, Patel VG. The role of PD-L1 expression as a predictive biomarker: an analysis of all US Food and Drug Administration (FDA) approvals of immune checkpoint inhibitors. j immunotherapy cancer. 2019 Dec;7(1):278.

36. El-Khoueiry AB, Sangro B, Yau T, Crocenzi TS, Kudo M, Hsu C, et al. Nivolumab in patients with advanced hepatocellular carcinoma (CheckMate 040): an open-label, non-comparative, phase 1/2 dose escalation and expansion trial. The Lancet. 2017 Jun;389(10088):2492–502.

37. Sharma P, Callahan MK, Bono P, Kim J, Spiliopoulou P, Calvo E, et al. Nivolumab monotherapy in recurrent metastatic urothelial carcinoma (CheckMate 032): a multicentre, open-label, two-stage, multi-arm, phase 1/2 trial. The Lancet Oncology. 2016 Nov;17(11):1590–8.

38. Itoh S, Yoshizumi T, Yugawa K, Imai D, Yoshiya S, Takeishi K, et al. Impact of Immune Response on Outcomes in Hepatocellular Carcinoma: Association With Vascular Formation. Hepatology. 2020 Dec;72(6):1987–99.

39. Wolf Y, Bartok O, Patkar S, Eli GB, Cohen S, Litchfield K, et al. UVB-Induced Tumor Heterogeneity Diminishes Immune Response in Melanoma. Cell. 2019 Sep;179(1):219-235.e21.

40. McGranahan N, Furness AJS, Rosenthal R, Ramskov S, Lyngaa R, Saini SK, et al. Clonal neoantigens elicit T cell immunoreactivity and sensitivity to immune checkpoint blockade. Science. 2016 Mar 25;351(6280):1463–9.

41. Liu D, Schilling B, Liu D, Sucker A, Livingstone E, Jerby-Arnon L, et al. Integrative molecular and clinical modeling of clinical outcomes to PD1 blockade in patients with metastatic melanoma. Nat Med. 2019 Dec;25(12):1916–27.

42. Yarchoan M, Hopkins A, Jaffee EM. Tumor Mutational Burden and Response Rate to PD-1 Inhibition. N Engl J Med. 2017 Dec 21;377(25):2500–1.

43. Gunjur A. Nivolumab plus ipilimumab in advanced renal-cell carcinoma. The Lancet Oncology. 2018 May;19(5):e232.

44. Crisafulli G, Sartore-Bianchi A, Lazzari L, Pietrantonio F, Amatu A, Macagno M, et al. Temozolomide Treatment Alters Mismatch Repair and Boosts Mutational Burden in Tumor and Blood of Colorectal Cancer Patients. Cancer Discovery. 2022 Jul 6;12(7):1656–75.

45. Overman MJ, McDermott R, Leach JL, Lonardi S, Lenz HJ, Morse MA, et al. Nivolumab in patients with metastatic DNA mismatch repair-deficient or microsatellite instability-high colorectal cancer (CheckMate 142): an open-label, multicentre, phase 2 study. The Lancet Oncology. 2017 Sep;18(9):1182–91.

46. Marabelle A, Le DT, Ascierto PA, Di Giacomo AM, De Jesus-Acosta A, Delord JP, et al. Efficacy of Pembrolizumab in Patients With Noncolorectal High Microsatellite Instability/Mismatch Repair–Deficient Cancer: Results From the Phase II KEYNOTE-158 Study. JCO. 2020 Jan 1;38(1):1–10.

47. Azad NS, Gray RJ, Overman MJ, Schoenfeld JD, Mitchell EP, Zwiebel JA, et al. Nivolumab Is Effective in Mismatch Repair–Deficient Noncolorectal Cancers: Results From Arm Z1D—A Subprotocol of the NCI-MATCH (EAY131) Study. JCO. 2020 Jan 20;38(3):214–22.

48. Chalabi M, Fanchi LF, Dijkstra KK, Van Den Berg JG, Aalbers AG, Sikorska K, et al. Neoadjuvant immunotherapy leads to pathological responses in MMR-proficient and MMR-deficient early-stage colon

cancers. Nat Med. 2020 Apr;26(4):566–76.

49. Dong ZY, Zhong WZ, Zhang XC, Su J, Xie Z, Liu SY, et al. Potential Predictive Value of *TP53* and *KRAS* Mutation Status for Response to PD-1 Blockade Immunotherapy in Lung Adenocarcinoma. Clinical Cancer Research. 2017 Jun 15;23(12):3012–24.

50. Garmezy B, Gheeya J, Lin HY, Huang Y, Kim T, Jiang X, et al. Clinical and Molecular Characterization of *POLE* Mutations as Predictive Biomarkers of Response to Immune Checkpoint Inhibitors in Advanced Cancers. JCO Precision Oncology. 2022 May;(6):e2100267.

51. Girardin SE, Boneca IG, Viala J, Chamaillard M, Labigne A, Thomas G, et al. Nod2 Is a General Sensor of Peptidoglycan through Muramyl Dipeptide (MDP) Detection. Journal of Biological Chemistry. 2003 Mar;278(11):8869–72.

52. Barnet MB, Masle-Farquhar E, Russell A, Burnett DL, Jackson KJL, Brink R, et al. Association of common inherited *NOD2* mutations with exceptional response to immune checkpoint inhibitors. JCO. 2023 Jun 1;41(16_suppl):2514–2514.

53. Sade-Feldman M, Jiao YJ, Chen JH, Rooney MS, Barzily-Rokni M, Eliane JP, et al. Resistance to checkpoint blockade therapy through inactivation of antigen presentation. Nat Commun. 2017 Oct 26;8(1):1136.

54. Liu XD, Kong W, Peterson CB, McGrail DJ, Hoang A, Zhang X, et al. PBRM1 loss defines a nonimmunogenic tumor phenotype associated with checkpoint inhibitor resistance in renal carcinoma. Nat Commun. 2020 May 1;11(1):2135.

55. Carril-Ajuria L, Santos M, Roldán-Romero JM, Rodriguez-Antona C, De Velasco G. Prognostic and Predictive Value of PBRM1 in Clear Cell Renal Cell Carcinoma. Cancers. 2019 Dec 19;12(1):16.

56. Vano YA, Rioux-Leclercq N, Dalban C, Sautes-Fridman C, Bougoüin A, Chaput N, et al. NIVOREN GETUG-AFU 26 translational study:

Association of PD-1, AXL, and PBRM-1 with outcomes in patients (pts) with metastatic clear cell renal cell carcinoma (mccRCC) treated with nivolumab (N). JCO. 2020 Feb 20;38(6_suppl):618–618.

57. Gorbachev AV, Kobayashi H, Kudo D, Tannenbaum CS, Finke JH, Shu S, et al. CXC Chemokine Ligand 9/Monokine Induced by IFN-γ Production by Tumor Cells Is Critical for T Cell-Mediated Suppression of Cutaneous Tumors. The Journal of Immunology. 2007 Feb 15;178(4):2278–86.

58. Ayers M, Lunceford J, Nebozhyn M, Murphy E, Loboda A, Kaufman DR, et al. IFN-γ–related mRNA profile predicts clinical response to PD-1 blockade. Journal of Clinical Investigation. 2017 Jun 26;127(8):2930–40.

59. Zhao B, Sedlak JC, Srinivas R, Creixell P, Pritchard JR, Tidor B, et al. Exploiting Temporal Collateral Sensitivity in Tumor Clonal Evolution. Cell. 2016 Mar;165(1):234–46.

60. Chen Y, Huang Y, Gao X, Li Y, Lin J, Chen L, et al. CCND1 Amplification Contributes to Immunosuppression and Is Associated With a Poor Prognosis to Immune Checkpoint Inhibitors in Solid Tumors. Front Immunol. 2020 Aug 10;11:1620.

61. Montalto FI, De Amicis F. Cyclin D1 in Cancer: A Molecular Connection for Cell Cycle Control, Adhesion and Invasion in Tumor and Stroma. Cells. 2020 Dec 9;9(12):2648.

62. Rampioni Vinciguerra GL, Sonego M, Segatto I, Dall'Acqua A, Vecchione A, Baldassarre G, et al. CDK4/6 Inhibitors in Combination Therapies: Better in Company Than Alone: A Mini Review. Front Oncol. 2022 May 27;12:891580.

63. Avelumab, Palbociclib and Axitinib in Advanced RCC - Full Text View - ClinicalTrials.gov [Internet]. [cited 2023 Jun 23]. Available from: https://clinicaltrials.gov/ct2/show/NCT05176288

64. Shi AP, Tang XY, Xiong YL, Zheng KF, Liu YJ, Shi XG, et al. Immune

Checkpoint LAG3 and Its Ligand FGL1 in Cancer. Front Immunol. 2022 Jan 17;12:785091.

65. Ros-Martínez S, Navas-Carrillo D, Alonso-Romero JL, Orenes-Piñero E. Immunoscore: a novel prognostic tool. Association with clinical outcome, response to treatment and survival in several malignancies. Critical Reviews in Clinical Laboratory Sciences. 2020 Oct 2;57(7):432–43.

66. Kümpers C, Jokic M, Haase O, Offermann A, Vogel W, Grätz V, et al. Immune Cell Infiltration of the Primary Tumor, Not PD-L1 Status, Is Associated With Improved Response to Checkpoint Inhibition in Metastatic Melanoma. Front Med. 2019 Mar 13;6:27.

67. Mlecnik B, Bifulco C, Bindea G, Marliot F, Lugli A, Lee JJ, et al. Multicenter International Society for Immunotherapy of Cancer Study of the Consensus Immunoscore for the Prediction of Survival and Response to Chemotherapy in Stage III Colon Cancer. JCO. 2020 Nov 1;38(31):3638–51.

68. Anitei MG, Zeitoun G, Mlecnik B, Marliot F, Haicheur N, Todosi AM, et al. Prognostic and Predictive Values of the Immunoscore in Patients with Rectal Cancer. Clinical Cancer Research. 2014 Apr 1;20(7):1891–9.

69. Li F, Li C, Cai X, Xie Z, Zhou L, Cheng B, et al. The association between CD8+ tumor-infiltrating lymphocytes and the clinical outcome of cancer immunotherapy: A systematic review and meta-analysis. eClinicalMedicine. 2021 Nov;41:101134.

70. Remark R, Alifano M, Cremer I, Lupo A, Dieu-Nosjean MC, Riquet M, et al. Characteristics and Clinical Impacts of the Immune Environments in Colorectal and Renal Cell Carcinoma Lung Metastases: Influence of Tumor Origin. Clinical Cancer Research. 2013 Aug 1;19(15):4079–91.

71. Thommen DS, Koelzer VH, Herzig P, Roller A, Trefny M, Dimeloe S, et al. A transcriptionally and functionally distinct PD-1+ CD8+ T cell pool with predictive potential in non-small-cell lung cancer treated with PD-1 blockade. Nat Med. 2018 Jul;24(7):994–1004.

72. Medioni J, Arakelian N, Fournier L, Helley D, Thiam R, Banu E, et al. Relation between lactate dehydrogenase (LDH) during two first cycles in patients with metastatic renal cell carcinoma (mRCC) treated with sunitinib (SU). JCO. 2007 Jun 20;25(18_suppl):14079–14079.

73. Tjokrowidjaja A, Lord SJ, John T, Lewis CR, Kok P, Marschner IC, et al. Pre- and on-treatment lactate dehydrogenase as a prognostic and predictive biomarker in advanced non–small cell lung cancer. Cancer. 2022 Apr 15;128(8):1574–83.

74. Benhamouda N, Sam I, Epaillard N, Gey A, Phan L, Pham HP, et al. Plasma CD27, a Surrogate of the Intratumoral CD27–CD70 Interaction, Correlates with Immunotherapy Resistance in Renal Cell Carcinoma. Clinical Cancer Research. 2022 Nov 14;28(22):4983–94.

75. Schalper KA, Carleton M, Zhou M, Chen T, Feng Y, Huang SP, et al. Elevated serum interleukin-8 is associated with enhanced intratumor neutrophils and reduced clinical benefit of immune-checkpoint inhibitors. Nat Med. 2020 May;26(5):688–92.

76. Yuen KC, Liu LF, Gupta V, Madireddi S, Keerthivasan S, Li C, et al. High systemic and tumor-associated IL-8 correlates with reduced clinical benefit of PD-L1 blockade. Nat Med. 2020 May;26(5):693–8.

77. Kagamu H, Kitano S, Yamaguchi O, Yoshimura K, Horimoto K, Kitazawa M, et al. CD4+ T-cell Immunity in the Peripheral Blood Correlates with Response to Anti-PD-1 Therapy. Cancer Immunology Research. 2020 Mar 1;8(3):334–44.

78. Fairfax BP, Taylor CA, Watson RA, Nassiri I, Danielli S, Fang H, et al. Peripheral CD8+ T cell characteristics associated with durable responses to immune checkpoint blockade in patients with metastatic melanoma. Nat Med. 2020 Feb;26(2):193–9.

79. Rodriguez-Abreu D, Budde PI, Zucht HD, Shrivastava D, Kilian AL, Höglander E, et al. Baseline autoantibody profiling in patients with NSCLC with pre-existing autoimmune diseases or who had received prior anti-

PD-1 therapy before enrolling in the TAIL study. JCO. 2023 Jun 1;41(16_suppl):2512–2512.

80. Gonzalez-Kozlova E, Del Valle D, Tuballes K, Barcessat V, King S, Huang HH, et al. Serum cytokines and autoantibodies to GM-CSF and immune-related colitis in ipilimumab-treated patients with cancer. JCO. 2023 Jun 1;41(16_suppl):12080–12080.

81. De Jonge H, Iamele L, Maggi M, Pessino G, Scotti C. Anti-Cancer Auto-Antibodies: Roles, Applications and Open Issues. Cancers. 2021 Feb 15;13(4):813.

82. Fridman WH, Meylan M, Petitprez F, Sun CM, Italiano A, Sautès-Fridman C. B cells and tertiary lymphoid structures as determinants of tumour immune contexture and clinical outcome. Nat Rev Clin Oncol. 2022 Jul;19(7):441–57.

83. Ma SJ, Yu H, Khan M, Gill J, Santhosh S, Chatterjee U, et al. Evaluation of Optimal Threshold of Neutrophil-Lymphocyte Ratio and Its Association With Survival Outcomes Among Patients With Head and Neck Cancer. JAMA Netw Open. 2022 Apr 15;5(4):e227567.

84. Buonacera A, Stancanelli B, Colaci M, Malatino L. Neutrophil to Lymphocyte Ratio: An Emerging Marker of the Relationships between the Immune System and Diseases. IJMS. 2022 Mar 26;23(7):3636.

85. Mezquita L, Auclin E, Charrier M, Ferrara R, Remon Masip J, Planchard D, et al. The Lung Immune Prognostic Index (LIPI), a predictive score for immune checkpoint inhibitors in advanced non-small cell lung cancer (NSCLC) patients. Annals of Oncology. 2017 Sep;28:v473.

86. Aldea M, Benitez JC, Mezquita L. The Lung Immune Prognostic Index (LIPI) stratifies prognostic groups in advanced non-small cell lung cancer (NSCLC) patients. Transl Lung Cancer Res. 2020 Aug;9(4):967–70.

87. Carril-Ajuria L, Motzer RJ, Tannir NM, McDermott DF, Hammers HJ, Plimack ER, et al. Prognostic value of the lung immune prognostic index

in patients with untreated advanced renal cell carcinoma (aRCC) receiving nivolumab plus ipilimumab (N+I) or sunitinib (SUN) in the CheckMate 214 trial. JCO. 2022 Jun 1;40(16_suppl):4538–4538.

88. Carril-Ajuria L, Desnoyer A, Meylan M, Dalban C, Naigeon M, Cassard L, et al. Baseline circulating unswitched memory B cells and B-cell related soluble factors are associated with overall survival in patients with clear cell renal cell carcinoma treated with nivolumab within the NIVOREN GETUG-AFU 26 study. J Immunother Cancer. 2022 May;10(5):e004885.

89. Luo P, Wu S, Yu Y, Ming X, Li S, Zuo X, et al. Current Status and Perspective Biomarkers in AFP Negative HCC: Towards Screening for and Diagnosing Hepatocellular Carcinoma at an Earlier Stage. Pathol Oncol Res. 2020 Apr;26(2):599–603.

90. Dall'Olio FG, Vasseur D, Karimi M, Michiels S, Lacroix L, Tomasini P, et al. Association of ctDNA tumor fraction with survival in advanced non-small cell lung cancer (NSCLC) treated with maintenance durvalumab in the UNICANCER SAFIR02-Lung/IFCT1301 trial. JCO. 2023 Jun 1;41(16_suppl):2516–2516.

91. Lee JH, Long GV, Boyd S, Lo S, Menzies AM, Tembe V, et al. Circulating tumour DNA predicts response to anti-PD1 antibodies in metastatic melanoma. Annals of Oncology. 2017 May;28(5):1130–6.

92. Albiges L, Hakimi AA, Xie W, McKay RR, Simantov R, Lin X, et al. Body Mass Index and Metastatic Renal Cell Carcinoma: Clinical and Biological Correlations. Journal of Clinical Oncology. 2016 Oct 20;34(30):3655–63.

93. Colomba E, Alves Costa Silva C, Le Teuff G, Elmawieh J, Afonso D, Benchimol-Zouari A, et al. Weight and skeletal muscle loss with cabozantinib in metastatic renal cell carcinoma. J cachexia sarcopenia muscle. 2022 Oct;13(5):2405–16.

94. Macek Jilkova Z, Aspord C, Kurma K, Granon A, Sengel C, Sturm N, et al. Immunologic Features of Patients With Advanced Hepatocellular

Carcinoma Before and During Sorafenib or Anti-programmed Death-1/Programmed Death-L1 Treatment. Clin Transl Gastroenterol. 2019 Jul 1;10(7):e00058.

95. Zhang Y, Chen L. Classification of Advanced Human Cancers Based on Tumor Immunity in the MicroEnvironment (TIME) for Cancer Immunotherapy. JAMA Oncol. 2016 Nov 1;2(11):1403.

96. Jiang P, Gu S, Pan D, Fu J, Sahu A, Hu X, et al. Signatures of T cell dysfunction and exclusion predict cancer immunotherapy response. Nat Med. 2018 Oct;24(10):1550–8.

97. Paik S, Shak S, Tang G, Kim C, Baker J, Cronin M, et al. A multigene assay to predict recurrence of tamoxifen-treated, node-negative breast cancer. N Engl J Med. 2004 Dec 30;351(27):2817–26.

98. Henry NL, Somerfield MR, Abramson VG, Ismaila N, Allison KH, Anders CK, et al. Role of Patient and Disease Factors in Adjuvant Systemic Therapy Decision Making for Early-Stage, Operable Breast Cancer: Update of the ASCO Endorsement of the Cancer Care Ontario Guideline. J Clin Oncol. 2019 Aug 1;37(22):1965–77.

99. van 't Veer LJ, Dai H, van de Vijver MJ, He YD, Hart AAM, Mao M, et al. Gene expression profiling predicts clinical outcome of breast cancer. Nature. 2002 Jan 31;415(6871):530–6.

100. Heng DYC, Xie W, Regan MM, Warren MA, Golshayan AR, Sahi C, et al. Prognostic Factors for Overall Survival in Patients With Metastatic Renal Cell Carcinoma Treated With Vascular Endothelial Growth Factor–Targeted Agents: Results From a Large, Multicenter Study. JCO. 2009 Dec 1;27(34):5794–9.

101. Ernst MS, Navani V, Wells JC, Donskov F, Basappa N, Labaki C, et al. Outcomes for International Metastatic Renal Cell Carcinoma Database Consortium Prognostic Groups in Contemporary First-line Combination Therapies for Metastatic Renal Cell Carcinoma. European Urology. 2023 Jul;84(1):109–16.

102. Escudier B, Porta C, Schmidinger M, Rioux-Leclercq N, Bex A, Khoo V, et al. Renal cell carcinoma: ESMO Clinical Practice Guidelines for diagnosis, treatment and follow-up. Annals of Oncology. 2019 May;30(5):706–20.

103. Drubay D, Van Calster B, Michiels S. Development and Validation of Risk Prediction Models. In: Piantadosi S, Meinert CL, editors. Principles and Practice of Clinical Trials [Internet]. Cham: Springer International Publishing; 2020 [cited 2023 Jul 10]. p. 1–22. Available from: http://link.springer.com/10.1007/978-3-319-52677-5_138-1

104. André T, Lonardi S, Wong KYM, Lenz HJ, Gelsomino F, Aglietta M, et al. Nivolumab plus low-dose ipilimumab in previously treated patients with microsatellite instability-high/mismatch repair-deficient metastatic colorectal cancer: 4-year follow-up from CheckMate 142. Annals of Oncology. 2022 Oct;33(10):1052–60.

105. Doki Y, Ajani JA, Kato K, Xu J, Wyrwicz L, Motoyama S, et al. Nivolumab Combination Therapy in Advanced Esophageal Squamous-Cell Carcinoma. N Engl J Med. 2022 Feb 3;386(5):449–62.

106. Yau T, Kang YK, Kim TY, El-Khoueiry AB, Santoro A, Sangro B, et al. Efficacy and Safety of Nivolumab Plus Ipilimumab in Patients With Advanced Hepatocellular Carcinoma Previously Treated With Sorafenib: The CheckMate 040 Randomized Clinical Trial. JAMA Oncol. 2020 Nov 12;6(11):e204564.

107. Peters S, Scherpereel A, Cornelissen R, Oulkhouir Y, Greillier L, Kaplan MA, et al. First-line nivolumab plus ipilimumab versus chemotherapy in patients with unresectable malignant pleural mesothelioma: 3-year outcomes from CheckMate 743. Annals of Oncology. 2022 May;33(5):488–99.

108. Eggermont AMM, Chiarion-Sileni V, Grob JJ, Dummer R, Wolchok JD, Schmidt H, et al. Adjuvant ipilimumab versus placebo after complete resection of high-risk stage III melanoma (EORTC 18071): a randomised,

double-blind, phase 3 trial. Lancet Oncol. 2015 May;16(5):522–30.

109. Larkin J, Chiarion-Sileni V, Gonzalez R, Grob JJ, Rutkowski P, Lao CD, et al. Five-Year Survival with Combined Nivolumab and Ipilimumab in Advanced Melanoma. N Engl J Med. 2019 Oct 17;381(16):1535–46.

110. Robert C, Thomas L, Bondarenko I, O'Day S, Weber J, Garbe C, et al. Ipilimumab plus Dacarbazine for Previously Untreated Metastatic Melanoma. N Engl J Med. 2011 Jun 30;364(26):2517–26.

111. Hodi FS, O'Day SJ, McDermott DF, Weber RW, Sosman JA, Haanen JB, et al. Improved survival with ipilimumab in patients with metastatic melanoma. N Engl J Med. 2010 Aug 19;363(8):711–23.

112. Hellmann MD, Paz-Ares L, Bernabe Caro R, Zurawski B, Kim SW, Carcereny Costa E, et al. Nivolumab plus Ipilimumab in Advanced Non–Small-Cell Lung Cancer. N Engl J Med. 2019 Nov 21;381(21):2020–31.

113. Paz-Ares L, Ciuleanu TE, Cobo M, Schenker M, Zurawski B, Menezes J, et al. First-line nivolumab plus ipilimumab combined with two cycles of chemotherapy in patients with non-small-cell lung cancer (CheckMate 9LA): an international, randomised, open-label, phase 3 trial. The Lancet Oncology. 2021 Feb;22(2):198–211.

114. Motzer RJ, Tannir NM, McDermott DF, Arén Frontera O, Melichar B, Choueiri TK, et al. Nivolumab plus Ipilimumab versus Sunitinib in Advanced Renal-Cell Carcinoma. New England Journal of Medicine. 2018 Apr 5;378(14):1277–90.

115. Abou-Alfa GK, Chan SL, Kudo M, Lau G, Kelley RK, Furuse J, et al. Phase 3 randomized, open-label, multicenter study of tremelimumab (T) and durvalumab (D) as first-line therapy in patients (pts) with unresectable hepatocellular carcinoma (uHCC): HIMALAYA. JCO. 2022 Feb 1;40(4_suppl):379–379.

116. Johnson ML, Cho BC, Luft A, Alatorre-Alexander J, Geater SL, Laktionov K, et al. Durvalumab With or Without Tremelimumab in

Combination With Chemotherapy as First-Line Therapy for Metastatic Non–Small-Cell Lung Cancer: The Phase III POSEIDON Study. JCO. 2023 Feb 20;41(6):1213–27.

117. D'Angelo SP, Bhatia S, Brohl AS, Hamid O, Mehnert JM, Terheyden P, et al. Avelumab in patients with previously treated metastatic Merkel cell carcinoma: long-term data and biomarker analyses from the single-arm phase 2 JAVELIN Merkel 200 trial. J Immunother Cancer. 2020 May;8(1):e000674.

118. Motzer RJ, Penkov K, Haanen J, Rini B, Albiges L, Campbell MT, et al. Avelumab plus Axitinib versus Sunitinib for Advanced Renal-Cell Carcinoma. New England Journal of Medicine. 2019 Mar 21;380(12):1103–15.

119. Powles T, Park SH, Voog E, Caserta C, Valderrama BP, Gurney H, et al. Avelumab Maintenance Therapy for Advanced or Metastatic Urothelial Carcinoma. N Engl J Med. 2020 Sep 24;383(13):1218–30.

120. Patel MR, Ellerton J, Infante JR, Agrawal M, Gordon M, Aljumaily R, et al. Avelumab in metastatic urothelial carcinoma after platinum failure (JAVELIN Solid Tumor): pooled results from two expansion cohorts of an open-label, phase 1 trial. The Lancet Oncology. 2018 Jan;19(1):51–64.

121. Testing Atezolizumab Alone or Atezolizumab Plus Bevacizumab in People With Advanced Alveolar Soft Part Sarcoma - Full Text View - ClinicalTrials.gov [Internet]. [cited 2023 Jul 1]. Available from: https://clinicaltrials.gov/ct2/show/NCT03141684

122. Finn RS, Qin S, Ikeda M, Galle PR, Ducreux M, Kim TY, et al. Atezolizumab plus Bevacizumab in Unresectable Hepatocellular Carcinoma. N Engl J Med. 2020 May 14;382(20):1894–905.

123. Gutzmer R, Stroyakovskiy D, Gogas H, Robert C, Lewis K, Protsenko S, et al. Atezolizumab, vemurafenib, and cobimetinib as first-line treatment for unresectable advanced BRAFV600 mutation-positive melanoma (IMspire150): primary analysis of the randomised, double-

blind, placebo-controlled, phase 3 trial. The Lancet. 2020 Jun;395(10240):1835–44.

124. Felip E, Altorki N, Zhou C, Csőszi T, Vynnychenko I, Goloborodko O, et al. Adjuvant atezolizumab after adjuvant chemotherapy in resected stage IB–IIIA non-small-cell lung cancer (IMpower010): a randomised, multicentre, open-label, phase 3 trial. The Lancet. 2021 Oct;398(10308):1344–57.

125. Herbst RS, Giaccone G, De Marinis F, Reinmuth N, Vergnenegre A, Barrios CH, et al. Atezolizumab for First-Line Treatment of PD-L1–Selected Patients with NSCLC. N Engl J Med. 2020 Oct 1;383(14):1328–39.

126. Socinski MA, Jotte RM, Cappuzzo F, Orlandi F, Stroyakovskiy D, Nogami N, et al. Atezolizumab for First-Line Treatment of Metastatic Nonsquamous NSCLC. N Engl J Med. 2018 Jun 14;378(24):2288–301.

127. West H, McCleod M, Hussein M, Morabito A, Rittmeyer A, Conter HJ, et al. Atezolizumab in combination with carboplatin plus nab-paclitaxel chemotherapy compared with chemotherapy alone as first-line treatment for metastatic non-squamous non-small-cell lung cancer (IMpower130): a multicentre, randomised, open-label, phase 3 trial. The Lancet Oncology. 2019 Jul;20(7):924–37.

128. Rittmeyer A, Barlesi F, Waterkamp D, Park K, Ciardiello F, Von Pawel J, et al. Atezolizumab versus docetaxel in patients with previously treated non-small-cell lung cancer (OAK): a phase 3, open-label, multicentre randomised controlled trial. The Lancet. 2017 Jan;389(10066):255–65.

129. Horn L, Mansfield AS, Szczęsna A, Havel L, Krzakowski M, Hochmair MJ, et al. First-Line Atezolizumab plus Chemotherapy in Extensive-Stage Small-Cell Lung Cancer. N Engl J Med. 2018 Dec 6;379(23):2220–9.

130. Oh DY, Ruth He A, Qin S, Chen LT, Okusaka T, Vogel A, et al. Durvalumab plus Gemcitabine and Cisplatin in Advanced Biliary Tract Cancer. NEJM Evidence [Internet]. 2022 Jul 26 [cited 2023 Jul 2];1(8). Available from: https://evidence.nejm.org/doi/10.1056/EVIDoa2200015

131. Antonia SJ, Villegas A, Daniel D, Vicente D, Murakami S, Hui R, et al. Durvalumab after Chemoradiotherapy in Stage III Non–Small-Cell Lung Cancer. N Engl J Med. 2017 Nov 16;377(20):1919–29.

132. Paz-Ares L, Dvorkin M, Chen Y, Reinmuth N, Hotta K, Trukhin D, et al. Durvalumab plus platinum–etoposide versus platinum–etoposide in first-line treatment of extensive-stage small-cell lung cancer (CASPIAN): a randomised, controlled, open-label, phase 3 trial. The Lancet. 2019 Nov;394(10212):1929–39.

133. Schmid P, Cortes J, Pusztai L, McArthur H, Kümmel S, Bergh J, et al. Pembrolizumab for Early Triple-Negative Breast Cancer. N Engl J Med. 2020 Feb 27;382(9):810–21.

134. Cortes J, Rugo HS, Cescon DW, Im SA, Yusof MM, Gallardo C, et al. Pembrolizumab plus Chemotherapy in Advanced Triple-Negative Breast Cancer. N Engl J Med. 2022 Jul 21;387(3):217–26.

135. Colombo N, Dubot C, Lorusso D, Caceres MV, Hasegawa K, Shapira-Frommer R, et al. Pembrolizumab for Persistent, Recurrent, or Metastatic Cervical Cancer. N Engl J Med. 2021 Nov 11;385(20):1856–67.

136. Chung HC, Ros W, Delord JP, Perets R, Italiano A, Shapira-Frommer R, et al. Efficacy and Safety of Pembrolizumab in Previously Treated Advanced Cervical Cancer: Results From the Phase II KEYNOTE-158 Study. JCO. 2019 Jun 10;37(17):1470–8.

137. Hughes BGM, Munoz-Couselo E, Mortier L, Bratland Å, Gutzmer R, Roshdy O, et al. Pembrolizumab for locally advanced and recurrent/metastatic cutaneous squamous cell carcinoma (KEYNOTE-629 study): an open-label, nonrandomized, multicenter, phase II trial. Annals of Oncology. 2021 Oct;32(10):1276–85.

138. Makker V, Colombo N, Casado Herráez A, Santin AD, Colomba E, Miller DS, et al. Lenvatinib plus Pembrolizumab for Advanced Endometrial Cancer. N Engl J Med. 2022 Feb 3;386(5):437–48.

139. Choi MC, Kim YM, Lee JW, Lee YJ, Suh DH, Lee SJ, et al. Real-World Experience of Pembrolizumab Monotherapy in Patients with Recurrent or Persistent Cervical Cancer: A Korean Multi-Center Retrospective Study (KGOG1041). Cancers. 2020 Oct 29;12(11):3188.

140. Frenel JS, Le Tourneau C, O'Neil B, Ott PA, Piha-Paul SA, Gomez-Roca C, et al. Safety and Efficacy of Pembrolizumab in Advanced, Programmed Death Ligand 1–Positive Cervical Cancer: Results From the Phase Ib KEYNOTE-028 Trial. JCO. 2017 Dec 20;35(36):4035–41.

141. Sun JM, Shen L, Shah MA, Enzinger P, Adenis A, Doi T, et al. Pembrolizumab plus chemotherapy versus chemotherapy alone for first-line treatment of advanced oesophageal cancer (KEYNOTE-590): a randomised, placebo-controlled, phase 3 study. The Lancet. 2021 Aug;398(10302):759–71.

142. Fuchs CS, Doi T, Jang RW, Muro K, Satoh T, Machado M, et al. Safety and Efficacy of Pembrolizumab Monotherapy in Patients With Previously Treated Advanced Gastric and Gastroesophageal Junction Cancer: Phase 2 Clinical KEYNOTE-059 Trial. JAMA Oncol. 2018 May 10;4(5):e180013.

143. Janjigian YY, Kawazoe A, Yañez P, Li N, Lonardi S, Kolesnik O, et al. The KEYNOTE-811 trial of dual PD-1 and HER2 blockade in HER2-positive gastric cancer. Nature. 2021 Dec 23;600(7890):727–30.

144. Burtness B, Harrington KJ, Greil R, Soulières D, Tahara M, De Castro G, et al. Pembrolizumab alone or with chemotherapy versus cetuximab with chemotherapy for recurrent or metastatic squamous cell carcinoma of the head and neck (KEYNOTE-048): a randomised, open-label, phase 3 study. The Lancet. 2019 Nov;394(10212):1915–28.

145. Muro K, Chung HC, Shankaran V, Geva R, Catenacci D, Gupta S, et al. Pembrolizumab for patients with PD-L1-positive advanced gastric cancer (KEYNOTE-012): a multicentre, open-label, phase 1b trial. The Lancet Oncology. 2016 Jun;17(6):717–26.

146. Zhu AX, Finn RS, Edeline J, Cattan S, Ogasawara S, Palmer D, et al.

Pembrolizumab in patients with advanced hepatocellular carcinoma previously treated with sorafenib (KEYNOTE-224): a non-randomised, open-label phase 2 trial. The Lancet Oncology. 2018 Jul;19(7):940–52.

147. Eggermont AMM, Blank CU, Mandalà M, Long GV, Atkinson VG, Dalle S, et al. Adjuvant pembrolizumab versus placebo in resected stage III melanoma (EORTC 1325-MG/KEYNOTE-054): distant metastasis-free survival results from a double-blind, randomised, controlled, phase 3 trial. The Lancet Oncology. 2021 May;22(5):643–54.

148. Luke JJ, Rutkowski P, Queirolo P, Del Vecchio M, Mackiewicz J, Chiarion-Sileni V, et al. Pembrolizumab versus placebo as adjuvant therapy in completely resected stage IIB or IIC melanoma (KEYNOTE-716): a randomised, double-blind, phase 3 trial. The Lancet. 2022 Apr;399(10336):1718–29.

149. Hamid O, Robert C, Daud A, Hodi FS, Hwu WJ, Kefford R, et al. Five-year survival outcomes for patients with advanced melanoma treated with pembrolizumab in KEYNOTE-001. Annals of Oncology. 2019 Apr;30(4):582–8.

150. Robert C, Schachter J, Long GV, Arance A, Grob JJ, Mortier L, et al. Pembrolizumab versus Ipilimumab in Advanced Melanoma. N Engl J Med. 2015 Jun 25;372(26):2521–32.

151. Nghiem P, Bhatia S, Lipson EJ, Sharfman WH, Kudchadkar RR, Brohl AS, et al. Durable Tumor Regression and Overall Survival in Patients With Advanced Merkel Cell Carcinoma Receiving Pembrolizumab as First-Line Therapy. JCO. 2019 Mar 20;37(9):693–702.

152. Le DT, Kim TW, Van Cutsem E, Geva R, Jäger D, Hara H, et al. Phase II Open-Label Study of Pembrolizumab in Treatment-Refractory, Microsatellite Instability–High/Mismatch Repair–Deficient Metastatic Colorectal Cancer: KEYNOTE-164. JCO. 2020 Jan 1;38(1):11–9.

153. André T, Shiu KK, Kim TW, Jensen BV, Jensen LH, Punt C, et al. Pembrolizumab in Microsatellite-Instability–High Advanced Colorectal

Cancer. N Engl J Med. 2020 Dec 3;383(23):2207–18.

154. Mok TSK, Wu YL, Kudaba I, Kowalski DM, Cho BC, Turna HZ, et al. Pembrolizumab versus chemotherapy for previously untreated, PD-L1-expressing, locally advanced or metastatic non-small-cell lung cancer (KEYNOTE-042): a randomised, open-label, controlled, phase 3 trial. The Lancet. 2019 May;393(10183):1819–30.

155. Gandhi L, Rodríguez-Abreu D, Gadgeel S, Esteban E, Felip E, De Angelis F, et al. Pembrolizumab plus Chemotherapy in Metastatic Non–Small-Cell Lung Cancer. N Engl J Med. 2018 May 31;378(22):2078–92.

156. Paz-Ares L, Luft A, Vicente D, Tafreshi A, Gümüş M, Mazières J, et al. Pembrolizumab plus Chemotherapy for Squamous Non–Small-Cell Lung Cancer. N Engl J Med. 2018 Nov 22;379(21):2040–51.

157. O'Brien M, Paz-Ares L, Marreaud S, Dafni U, Oselin K, Havel L, et al. Pembrolizumab versus placebo as adjuvant therapy for completely resected stage IB–IIIA non-small-cell lung cancer (PEARLS/KEYNOTE-091): an interim analysis of a randomised, triple-blind, phase 3 trial. The Lancet Oncology. 2022 Oct;23(10):1274–86.

158. Herbst RS, Baas P, Kim DW, Felip E, Pérez-Gracia JL, Han JY, et al. Pembrolizumab versus docetaxel for previously treated, PD-L1-positive, advanced non-small-cell lung cancer (KEYNOTE-010): a randomised controlled trial. The Lancet. 2016 Apr;387(10027):1540–50.

159. Rini BI, Plimack ER, Stus V, Gafanov R, Hawkins R, Nosov D, et al. Pembrolizumab plus Axitinib versus Sunitinib for Advanced Renal-Cell Carcinoma. New England Journal of Medicine. 2019 Mar 21;380(12):1116–27.

160. Choueiri TK, Tomczak P, Park SH, Venugopal B, Ferguson T, Chang YH, et al. Adjuvant Pembrolizumab after Nephrectomy in Renal-Cell Carcinoma. N Engl J Med. 2021 Aug 19;385(8):683–94.

161. Balar AV, Kamat AM, Kulkarni GS, Uchio EM, Boormans JL,

Roumiguié M, et al. Pembrolizumab monotherapy for the treatment of high-risk non-muscle-invasive bladder cancer unresponsive to BCG (KEYNOTE-057): an open-label, single-arm, multicentre, phase 2 study. The Lancet Oncology. 2021 Jul;22(7):919–30.

162. Balar AV, Castellano D, O'Donnell PH, Grivas P, Vuky J, Powles T, et al. First-line pembrolizumab in cisplatin-ineligible patients with locally advanced and unresectable or metastatic urothelial cancer (KEYNOTE-052): a multicentre, single-arm, phase 2 study. The Lancet Oncology. 2017 Nov;18(11):1483–92.

163. Bellmunt J, De Wit R, Vaughn DJ, Fradet Y, Lee JL, Fong L, et al. Pembrolizumab as Second-Line Therapy for Advanced Urothelial Carcinoma. N Engl J Med. 2017 Mar 16;376(11):1015–26.

164. Lenz HJ, Van Cutsem E, Luisa Limon M, Wong KYM, Hendlisz A, Aglietta M, et al. First-Line Nivolumab Plus Low-Dose Ipilimumab for Microsatellite Instability-High/Mismatch Repair-Deficient Metastatic Colorectal Cancer: The Phase II CheckMate 142 Study. JCO. 2022 Jan 10;40(2):161–70.

165. Overman MJ, Lonardi S, Wong KYM, Lenz HJ, Gelsomino F, Aglietta M, et al. Durable Clinical Benefit With Nivolumab Plus Ipilimumab in DNA Mismatch Repair–Deficient/Microsatellite Instability–High Metastatic Colorectal Cancer. JCO. 2018 Mar 10;36(8):773–9.

166. Kelly RJ, Ajani JA, Kuzdzal J, Zander T, Van Cutsem E, Piessen G, et al. Adjuvant Nivolumab in Resected Esophageal or Gastroesophageal Junction Cancer. N Engl J Med. 2021 Apr 1;384(13):1191–203.

167. Janjigian YY, Shitara K, Moehler M, Garrido M, Salman P, Shen L, et al. First-line nivolumab plus chemotherapy versus chemotherapy alone for advanced gastric, gastro-oesophageal junction, and oesophageal adenocarcinoma (CheckMate 649): a randomised, open-label, phase 3 trial. The Lancet. 2021 Jul;398(10294):27–40.

168. Kato K, Cho BC, Takahashi M, Okada M, Lin CY, Chin K, et al.

Nivolumab versus chemotherapy in patients with advanced oesophageal squamous cell carcinoma refractory or intolerant to previous chemotherapy (ATTRACTION-3): a multicentre, randomised, open-label, phase 3 trial. The Lancet Oncology. 2019 Nov;20(11):1506–17.

169. Weber J, Mandala M, Del Vecchio M, Gogas HJ, Arance AM, Cowey CL, et al. Adjuvant Nivolumab versus Ipilimumab in Resected Stage III or IV Melanoma. N Engl J Med. 2017 Nov 9;377(19):1824–35.

170. Robert C, Long GV, Brady B, Dutriaux C, Maio M, Mortier L, et al. Nivolumab in previously untreated melanoma without BRAF mutation. N Engl J Med. 2015 Jan 22;372(4):320–30.

171. Forde PM, Spicer J, Lu S, Provencio M, Mitsudomi T, Awad MM, et al. Neoadjuvant Nivolumab plus Chemotherapy in Resectable Lung Cancer. N Engl J Med. 2022 May 26;386(21):1973–85.

172. Borghaei H, Paz-Ares L, Horn L, Spigel DR, Steins M, Ready NE, et al. Nivolumab versus Docetaxel in Advanced Nonsquamous Non–Small-Cell Lung Cancer. N Engl J Med. 2015 Oct 22;373(17):1627–39.

173. Choueiri TK, Powles T, Burotto M, Escudier B, Bourlon MT, Zurawski B, et al. Nivolumab plus Cabozantinib versus Sunitinib for Advanced Renal-Cell Carcinoma. N Engl J Med. 2021 Mar 4;384(9):829–41.

174. Motzer RJ, Escudier B, McDermott DF, George S, Hammers HJ, Srinivas S, et al. Nivolumab versus Everolimus in Advanced Renal-Cell Carcinoma. N Engl J Med. 2015 Nov 5;373(19):1803–13.

175. Bajorin DF, Witjes JA, Gschwend JE, Schenker M, Valderrama BP, Tomita Y, et al. Adjuvant Nivolumab versus Placebo in Muscle-Invasive Urothelial Carcinoma. N Engl J Med. 2021 Jun 3;384(22):2102–14.

176. Sharma P, Retz M, Siefker-Radtke A, Baron A, Necchi A, Bedke J, et al. Nivolumab in metastatic urothelial carcinoma after platinum therapy (CheckMate 275): a multicentre, single-arm, phase 2 trial. The Lancet Oncology. 2017 Mar;18(3):312–22.

177. Stratigos AJ, Sekulic A, Peris K, Bechter O, Prey S, Kaatz M, et al. Cemiplimab in locally advanced basal cell carcinoma after hedgehog inhibitor therapy: an open-label, multi-centre, single-arm, phase 2 trial. The Lancet Oncology. 2021 Jun;22(6):848–57.

178. Migden MR, Rischin D, Schmults CD, Guminski A, Hauschild A, Lewis KD, et al. PD-1 Blockade with Cemiplimab in Advanced Cutaneous Squamous-Cell Carcinoma. N Engl J Med. 2018 Jul 26;379(4):341–51.

179. Sezer A, Kilickap S, Gümüş M, Bondarenko I, Özgüroğlu M, Gogishvili M, et al. Cemiplimab monotherapy for first-line treatment of advanced non-small-cell lung cancer with PD-L1 of at least 50%: a multicentre, open-label, global, phase 3, randomised, controlled trial. The Lancet. 2021 Feb;397(10274):592–604.

180. Gogishvili M, Melkadze T, Makharadze T, Giorgadze D, Dvorkin M, Penkov K, et al. Cemiplimab plus chemotherapy versus chemotherapy alone in non-small cell lung cancer: a randomized, controlled, double-blind phase 3 trial. Nat Med. 2022 Nov;28(11):2374–80.

181. Berton D, Banerjee SN, Curigliano G, Cresta S, Arkenau HT, Abdeddaim C, et al. Antitumor activity of dostarlimab in patients with mismatch repair-deficient/microsatellite instability–high tumors: A combined analysis of two cohorts in the GARNET study. JCO. 2021 May 20;39(15_suppl):2564–2564.

182. Grignani G, Rutkowski P, Lebbe C, Prinzi N, Grob J jaques, Tanda ET, et al. 545 A phase 2 study of retifanlimab in patients with advanced or metastatic merkel cell carcinoma (MCC) (POD1UM-201). J Immunother Cancer. 2021 Nov;9(Suppl 2):A574–5.

183. Hanahan D. Hallmarks of Cancer: New Dimensions. Cancer Discovery. 2022 Jan 1;12(1):31–46.

184. Gacesa R, Kurilshikov A, Vich Vila A, Sinha T, Klaassen MAY, Bolte LA, et al. Environmental factors shaping the gut microbiome in a Dutch population. Nature. 2022 Apr 28;604(7907):732–9.

185. Rothschild D, Weissbrod O, Barkan E, Kurilshikov A, Korem T, Zeevi D, et al. Environment dominates over host genetics in shaping human gut microbiota. Nature. 2018 Mar;555(7695):210–5.

186. Song SJ, Lauber C, Costello EK, Lozupone CA, Humphrey G, Berg-Lyons D, et al. Cohabiting family members share microbiota with one another and with their dogs. eLife. 2013 Apr 16;2:e00458.

187. Xie H, Guo R, Zhong H, Feng Q, Lan Z, Qin B, et al. Shotgun Metagenomics of 250 Adult Twins Reveals Genetic and Environmental Impacts on the Gut Microbiome. Cell Systems. 2016 Dec;3(6):572-584.e3.

188. Wu H, Esteve E, Tremaroli V, Khan MT, Caesar R, Mannerås-Holm L, et al. Metformin alters the gut microbiome of individuals with treatment-naive type 2 diabetes, contributing to the therapeutic effects of the drug. Nat Med. 2017 Jul;23(7):850–8.

189. Floris Imhann, Marc Jan Bonder, Arnau Vich Vila, Jingyuan Fu, Zlatan Mujagic, Lisa Vork, et al. Proton pump inhibitors affect the gut microbiome. Gut. 2016 May 1;65(5):740.

190. Spencer CN, McQuade JL, Gopalakrishnan V, McCulloch JA, Vetizou M, Cogdill AP, et al. Dietary fiber and probiotics influence the gut microbiome and melanoma immunotherapy response. Science. 2021 Dec 24;374(6575):1632–40.

191. Derosa L, Hellmann MD, Spaziano M, Halpenny D, Fidelle M, Rizvi H, et al. Negative association of antibiotics on clinical activity of immune checkpoint inhibitors in patients with advanced renal cell and non-small-cell lung cancer. Annals of Oncology. 2018 Jun;29(6):1437–44.

192. Derosa L, Zitvogel L. Antibiotics impair immunotherapy for urothelial cancer. Nature Reviews Urology [Internet]. 2020 Sep 8 [cited 2020 Oct 21]; Available from: http://www.nature.com/articles/s41585-020-0373-1

193. Elkrief A, Derosa L, Kroemer G, Zitvogel L, Routy B. The negative

impact of antibiotics on outcomes in cancer patients treated with immunotherapy: a new independent prognostic factor? Annals of Oncology. 2019 Oct;30(10):1572–9.

194. Yang Z, Wei S, Liu L. Antibiotic Treatment and Immune Checkpoint Inhibitor Therapy in Patients With Cancer. JAMA Oncology. 2020 Apr 1;6(4):587.

195. Serpas V, Rogers JE, Xiao L, Mola-Rudd K, Dasari A, Kee BK, et al. Impact of antibiotic exposure on the efficacy of immune checkpoint blockade in MSI-H metastatic CRC. JCO. 2020 Feb 1;38(4_suppl):161–161.

196. Pinato DJ, Howlett S, Ottaviani D, Urus H, Patel A, Mineo T, et al. Association of Prior Antibiotic Treatment With Survival and Response to Immune Checkpoint Inhibitor Therapy in Patients With Cancer. JAMA Oncology. 2019 Dec 1;5(12):1774.

197. Routy B, Le Chatelier E, Derosa L, Duong CPM, Alou MT, Daillère R, et al. Gut microbiome influences efficacy of PD-1–based immunotherapy against epithelial tumors. Science. 2018 Jan 5;359(6371):91–7.

198. Derosa L, Routy B, Desilets A, Daillère R, Terrisse S, Kroemer G, et al. Microbiota-Centered Interventions: The Next Breakthrough in Immuno-Oncology? Cancer Discovery. 2021 Oct 1;11(10):2396–412.

199. Albiges L, Negrier S, Dalban C, Chevreau C, Gravis G, Oudard S, et al. Safety and efficacy of nivolumab in metastatic renal cell carcinoma (mRCC): Final analysis from the NIVOREN GETUG AFU 26 study. JCO. 2019 Mar 1;37(7_suppl):542–542.

200. Derosa L, Routy B, Fidelle M, Iebba V, Alla L, Pasolli E, et al. Gut Bacteria Composition Drives Primary Resistance to Cancer Immunotherapy in Renal Cell Carcinoma Patients. European Urology [Internet]. 2020 May [cited 2020 May 8]; Available from: https://linkinghub.elsevier.com/retrieve/pii/S0302283820303079

201. Viaud S, Saccheri F, Mignot G, Yamazaki T, Daillere R, Hannani D, et

al. The Intestinal Microbiota Modulates the Anticancer Immune Effects of Cyclophosphamide. Science. 2013 Nov 22;342(6161):971–6.

202. Vetizou M, Pitt JM, Daillere R, Lepage P, Waldschmitt N, Flament C, et al. Anticancer immunotherapy by CTLA-4 blockade relies on the gut microbiota. Science. 2015 Nov 27;350(6264):1079–84.

203. Routy B, Gopalakrishnan V, Daillère R, Zitvogel L, Wargo JA, Kroemer G. The gut microbiota influences anticancer immunosurveillance and general health. Nat Rev Clin Oncol. 2018 Jun;15(6):382–96.

204. Tanoue T, Morita S, Plichta DR, Skelly AN, Suda W, Sugiura Y, et al. A defined commensal consortium elicits CD8 T cells and anti-cancer immunity. Nature. 2019 Jan;565(7741):600–5.

205. Matson V, Fessler J, Bao R, Chongsuwat T, Zha Y, Alegre ML, et al. The commensal microbiome is associated with anti–PD-1 efficacy in metastatic melanoma patients. Science. 2018 Jan 5;359(6371):104–8.

206. Park EM, Chelvanambi M, Bhutiani N, Kroemer G, Zitvogel L, Wargo JA. Targeting the gut and tumor microbiota in cancer. Nat Med. 2022 Apr;28(4):690–703.

207. Sivan A, Corrales L, Hubert N, Williams JB, Aquino-Michaels K, Earley ZM, et al. Commensal Bifidobacterium promotes antitumor immunity and facilitates anti-PD-L1 efficacy. Science. 2015 Nov 27;350(6264):1084–9.

208. Spiliopoulou P, Rooney A, Genta S, Kulikova M, Wang BX, Tsao MS, et al. Intestinal microbiome characterization in immune checkpoint inhibition (ICI) resistant disease. JCO. 2023 Jun 1;41(16_suppl):2515–2515.

209. Chaput N, Lepage P, Coutzac C, Soularue E, Le Roux K, Monot C, et al. Baseline gut microbiota predicts clinical response and colitis in metastatic melanoma patients treated with ipilimumab. Ann Oncol. 2017 Jun 1;28(6):1368–79.

210. Frankel AE, Coughlin LA, Kim J, Froehlich TW, Xie Y, Frenkel EP, et al. Metagenomic Shotgun Sequencing and Unbiased Metabolomic Profiling Identify Specific Human Gut Microbiota and Metabolites Associated with Immune Checkpoint Therapy Efficacy in Melanoma Patients. Neoplasia. 2017 Oct;19(10):848–55.

211. Gopalakrishnan V, Spencer CN, Nezi L, Reuben A, Andrews MC, Karpinets TV, et al. Gut microbiome modulates response to anti–PD-1 immunotherapy in melanoma patients. Science. 2018 Jan 5;359(6371):97–103.

212. Chau J, Yadav M, Liu B, Furqan M, Dai Q, Shahi S, et al. Prospective correlation between the patient microbiome with response to and development of immune-mediated adverse effects to immunotherapy in lung cancer. BMC Cancer. 2021 Dec;21(1):808.

213. McCulloch JA, Davar D, Rodrigues RR, Badger JH, Fang JR, Cole AM, et al. Intestinal microbiota signatures of clinical response and immune-related adverse events in melanoma patients treated with anti-PD-1. Nat Med. 2022 Mar;28(3):545–56.

214. Xu L, Ma Y, Fang C, Peng Z, Gao F, Moll JM, et al. Genomic and microbial factors affect the prognosis of anti-pd-1 immunotherapy in nasopharyngeal carcinoma. Front Oncol. 2022 Aug 17;12:953884.

215. Lee KA, Thomas AM, Bolte LA, Björk JR, de Ruijter LK, Armanini F, et al. Cross-cohort gut microbiome associations with immune checkpoint inhibitor response in advanced melanoma. Nat Med. 2022 Mar;28(3):535–44.

216. Cascone T, Leung CH, Weissferdt A, Pataer A, Carter BW, Godoy MCB, et al. Neoadjuvant chemotherapy plus nivolumab with or without ipilimumab in operable non-small cell lung cancer: the phase 2 platform NEOSTAR trial. Nat Med. 2023 Mar;29(3):593–604.

217. Dora D, Ligeti B, Kovacs T, Revisnyei P, Galffy G, Dulka E, et al. Non-small cell lung cancer patients treated with Anti-PD1 immunotherapy

show distinct microbial signatures and metabolic pathways according to progression-free survival and PD-L1 status. OncoImmunology. 2023 Dec 31;12(1):2204746.

218. Golčić M, Simetić L, Herceg D, Blažičević K, Kenđel Jovanović G, Dražić I, et al. Analysis of the Gut Microbiome and Dietary Habits in Metastatic Melanoma Patients with a Complete and Sustained Response to Immunotherapy. Cancers. 2023 Jun 4;15(11):3052.

219. Baruch EN, Youngster I, Ben-Betzalel G, Ortenberg R, Lahat A, Katz L, et al. Fecal microbiota transplant promotes response in immunotherapy-refractory melanoma patients. Science. 2021 Feb 5;371(6529):602–9.

220. Davar D, Dzutsev AK, McCulloch JA, Rodrigues RR, Chauvin JM, Morrison RM, et al. Fecal microbiota transplant overcomes resistance to anti–PD-1 therapy in melanoma patients. Science. 2021 Feb 5;371(6529):595–602.

221. Routy B, Lenehan JG, Miller WH, Jamal R, Messaoudene M, Daisley BA, et al. Fecal microbiota transplantation plus anti-PD-1 immunotherapy in advanced melanoma: a phase I trial. Nat Med [Internet]. 2023 Jul 6 [cited 2023 Jul 9]; Available from: https://www.nature.com/articles/s41591-023-02453-x

222. Park SR, Kim G, Kim Y, Cho B, Kim SY, Do EJ, et al. Fecal microbiota transplantation combined with anti-PD-1 inhibitor for unresectable or metastatic solid cancers refractory to anti-PD-1 inhibitor. JCO. 2023 Jun 1;41(16_suppl):105–105.

223. Ebrahimi H, Meza LA, Lee K, Malhotra J, Alcantara M, Zengin ZB, et al. Effect of CBM588 in combination with cabozantinib plus nivolumab for patients (pts) with metastatic renal cell carcinoma (mRCC): A randomized clinical trial. JCO. 2023 Jun 10;41(17_suppl):LBA104–LBA104.

224. Dizman N, Meza L, Bergerot P, Alcantara M, Dorff T, Lyou Y, et al. Nivolumab plus ipilimumab with or without live bacterial

supplementation in metastatic renal cell carcinoma: a randomized phase 1 trial. Nat Med. 2022 Apr;28(4):704–12.

225. Gupta VK, Kim M, Bakshi U, Cunningham KY, Davis JM, Lazaridis KN, et al. A predictive index for health status using species-level gut microbiome profiling. Nat Commun. 2020 Sep 15;11(1):4635.

226. Boulate D, Fidelle M, Caramella C, Issard J, Planché O, Pradère P, et al. Epidemiological Study to Assess the Prevalence of Lung Cancer in patients with smoking-associated atherosclerotic cardiovascular diseases: PREVALUNG study protocol. BMJ Open. 2022 Dec;12(12):e067191.

227. Nejman D, Livyatan I, Fuks G, Gavert N, Zwang Y, Geller LT, et al. The human tumor microbiome is composed of tumor type–specific intracellular bacteria. Science. 2020 May 29;368(6494):973–80.

228. Goubet AG. Could the tumor-associated microbiota be the new multi-faceted player in the tumor microenvironment? Front Oncol. 2023 May 23;13:1185163.

229. Cullin N, Azevedo Antunes C, Straussman R, Stein-Thoeringer CK, Elinav E. Microbiome and cancer. Cancer Cell. 2021 Oct;39(10):1317–41.

230. List of Classifications – IARC Monographs on the Identification of Carcinogenic Hazards to Humans [Internet]. [cited 2023 Jun 14]. Available from: https://monographs.iarc.who.int/list-of-classifications

231. Fluckiger A, Daillère R, Sassi M, Sixt BS, Liu P, Loos F, et al. Cross-reactivity between tumor MHC class I–restricted antigens and an enterococcal bacteriophage. Science. 2020 Aug 21;369(6506):936–42.

232. Koebel CM, Vermi W, Swann JB, Zerafa N, Rodig SJ, Old LJ, et al. Adaptive immunity maintains occult cancer in an equilibrium state. Nature. 2007 Dec;450(7171):903–7.

233. Dridi B, Henry M, El Khéchine A, Raoult D, Drancourt M. High prevalence of Methanobrevibacter smithii and Methanosphaera

stadtmanae detected in the human gut using an improved DNA detection protocol. PLoS One. 2009 Sep 17;4(9):e7063.

234. Angelakis E, Bachar D, Henrissat B, Armougom F, Audoly G, Lagier JC, et al. Glycans affect DNA extraction and induce substantial differences in gut metagenomic studies. Sci Rep. 2016 18;6:26276.

235. Million M, Tidjani Alou M, Khelaifia S, Bachar D, Lagier JC, Dione N, et al. Increased Gut Redox and Depletion of Anaerobic and Methanogenic Prokaryotes in Severe Acute Malnutrition. Sci Rep. 2016 17;6:26051.

236. Discovery of Microbiome-based Biomarkers for Patients With Cancer Using Metagenomic Approach - Full Text View - ClinicalTrials.gov [Internet]. [cited 2023 Jun 30]. Available from: https://clinicaltrials.gov/ct2/show/NCT04567446

237. Sonpavde GP, Sternberg CN, Loriot Y, Marabelle A, Lee JL, Fléchon A, et al. Primary results of STRONG: An open-label, multicenter, phase 3b study of fixed-dose durvalumab monotherapy in previously treated patients with urinary tract carcinoma. European Journal of Cancer. 2022 Mar;163:55–65.

238. Recondo G, Mahjoubi L, Maillard A, Loriot Y, Bigot L, Facchinetti F, et al. Feasibility and first reports of the MATCH-R repeated biopsy trial at Gustave Roussy. npj Precis Onc. 2020 Sep 8;4(1):27.

239. Pasolli E, Schiffer L, Manghi P, Renson A, Obenchain V, Truong DT, et al. Accessible, curated metagenomic data through ExperimentHub. Nat Methods. 2017 Oct 31;14(11):1023–4.

240. Terrisse S, Derosa L, Iebba V, Ghiringhelli F, Vaz-Luis I, Kroemer G, et al. Intestinal microbiota influences clinical outcome and side effects of early breast cancer treatment. Cell Death Differ. 2021 Sep;28(9):2778–96.

241. Thomas AM, Manghi P, Asnicar F, Pasolli E, Armanini F, Zolfo M, et al. Metagenomic analysis of colorectal cancer datasets identifies cross-cohort microbial diagnostic signatures and a link with choline

degradation. Nature Medicine. 2019 Apr;25(4):667–78.

242. Beghini F, McIver LJ, Blanco-Míguez A, Dubois L, Asnicar F, Maharjan S, et al. Integrating taxonomic, functional, and strain-level profiling of diverse microbial communities with bioBakery 3 [Internet]. Microbiology; 2020 Nov [cited 2021 Apr 17]. Available from: http://biorxiv.org/lookup/doi/10.1101/2020.11.19.388223

243. https://human-microbiome.org/index.php?id=Sop&num=007 [Internet]. [cited 2023 Jun 25]. Available from: https://human-microbiome.org/index.php?id=Sop&num=007

244. Love MI, Huber W, Anders S. Moderated estimation of fold change and dispersion for RNA-seq data with DESeq2. Genome Biol. 2014 Dec;15(12):550.

245. Ritchie ME, Phipson B, Wu D, Hu Y, Law CW, Shi W, et al. limma powers differential expression analyses for RNA-sequencing and microarray studies. Nucleic Acids Research. 2015 Apr 20;43(7):e47–e47.

246. Lin H, Peddada SD. Analysis of compositions of microbiomes with bias correction. Nat Commun. 2020 Jul 14;11(1):3514.

247. Mallick H, Rahnavard A, McIver LJ, Ma S, Zhang Y, Nguyen LH, et al. Multivariable association discovery in population-scale meta-omics studies. Coelho LP, editor. PLoS Comput Biol. 2021 Nov 16;17(11):e1009442.

248. Segata N, Izard J, Waldron L, Gevers D, Miropolsky L, Garrett WS, et al. Metagenomic biomarker discovery and explanation. Genome Biology. 2011;12(6):R60.

249. Blanco-Míguez A, Beghini F, Cumbo F, McIver LJ, Thompson KN, Zolfo M, et al. Extending and improving metagenomic taxonomic profiling with uncharacterized species using MetaPhlAn 4. Nat Biotechnol [Internet]. 2023 Feb 23 [cited 2023 May 9]; Available from: https://www.nature.com/articles/s41587-023-01688-w

250. Shannon CE. A Mathematical Theory of Communication. Bell System Technical Journal. 1948 Jul;27(3):379–423.

251. Oksanen J, Blanchet FG, Friendly M, Kindt R, Legendre P, McGlinn D, Minchin PR, O'Hara RB, Simpson GL, Solymos P, Stevens MHH, Szoecs E, Wagner H (2018) vegan: Community Ecology Package. R package version 2.5-2. [Internet]. Available from: https://cran.r-project.org/web/packages/vegan/index.html

252. Rey D, Neuhäuser M. Wilcoxon-Signed-Rank Test. In: Lovric M, editor. International Encyclopedia of Statistical Science [Internet]. Berlin, Heidelberg: Springer Berlin Heidelberg; 2011 [cited 2023 Jul 30]. p. 1658–9. Available from: http://link.springer.com/10.1007/978-3-642-04898-2_616

253. Grajeda-Iglesias C, Durand S, Daillère R, Iribarren K, Lemaitre F, Derosa L, et al. Oral administration of Akkermansia muciniphila elevates systemic antiaging and anticancer metabolites. Aging (Albany NY). 2021 Mar 2;13(5):6375–405.

254. Durand S, Grajeda-Iglesias C, Aprahamian F, Nirmalathasan N, Kepp O, Kroemer G. The intracellular metabolome of starving cells. In: Methods in Cell Biology [Internet]. Elsevier; 2021 [cited 2023 Apr 2]. p. 137–56. Available from: https://linkinghub.elsevier.com/retrieve/pii/S0091679X21000431

255. Abdellatif M, Trummer-Herbst V, Koser F, Durand S, Adão R, Vasques-Nóvoa F, et al. Nicotinamide for the treatment of heart failure with preserved ejection fraction. Sci Transl Med. 2021 Feb 10;13(580):eabd7064.

256. Kanehisa M, Goto S. KEGG: kyoto encyclopedia of genes and genomes. Nucleic Acids Res. 2000 Jan 1;28(1):27–30.

257. Seethaler B, Nguyen NK, Basrai M, Kiechle M, Walter J, Delzenne NM, et al. Short-chain fatty acids are key mediators of the favorable effects of the Mediterranean diet on intestinal barrier integrity: data from

the randomized controlled LIBRE trial. The American Journal of Clinical Nutrition. 2022 Oct;116(4):928–42.

258. Ferrere G, Tidjani Alou M, Liu P, Goubet AG, Fidelle M, Kepp O, et al. Ketogenic diet and ketone bodies enhance the anticancer effects of PD-1 blockade. JCI Insight. 2021 Jan 25;6(2):e145207.

259. Liu N, Zhang J, Yan M, Chen L, Wu J, Tao Q, et al. Supplementation with α-ketoglutarate improved the efficacy of anti-PD1 melanoma treatment through epigenetic modulation of PD-L1. Cell Death Dis. 2023 Feb 28;14(2):170.

260. Kalaora S, Nagler A, Nejman D, Alon M, Barbolin C, Barnea E, et al. Identification of bacteria-derived HLA-bound peptides in melanoma. Nature. 2021 Apr 1;592(7852):138–43.

261. Overacre-Delgoffe AE, Bumgarner HJ, Cillo AR, Burr AHP, Tometich JT, Bhattacharjee A, et al. Microbiota-specific T follicular helper cells drive tertiary lymphoid structures and anti-tumor immunity against colorectal cancer. Immunity. 2021 Dec;54(12):2812-2824.e4.

262. Wang M, Rousseau B, Qiu K, Huang G, Zhang Y, Su H, et al. Killing tumor-associated bacteria with a liposomal antibiotic generates neoantigens that induce anti-tumor immune responses. Nat Biotechnol [Internet]. 2023 Sep 25 [cited 2023 Oct 8]; Available from: https://www.nature.com/articles/s41587-023-01957-8

263. Thomas AM, Fidelle M, Routy B, Kroemer G, Wargo JA, Segata N, et al. Gut OncoMicrobiome Signatures (GOMS) as next-generation biomarkers for cancer immunotherapy. Nat Rev Clin Oncol [Internet]. 2023 Jun 26 [cited 2023 Jul 3]; Available from: https://www.nature.com/articles/s41571-023-00785-8

264. Dang DK, Park BH. Circulating tumor DNA: current challenges for clinical utility. Journal of Clinical Investigation. 2022 Jun 15;132(12):e154941.

265. Mandal R, Samstein RM, Lee KW, Havel JJ, Wang H, Krishna C, et al. Genetic diversity of tumors with mismatch repair deficiency influences anti–PD-1 immunotherapy response. Science. 2019 May 3;364(6439):485–91.

266. Oaknin A, Bosse TJ, Creutzberg CL, Giornelli G, Harter P, Joly F, et al. Endometrial cancer: ESMO Clinical Practice Guideline for diagnosis, treatment and follow-up. Annals of Oncology. 2022 Sep;33(9):860–77.

267. Van Den Heerik ASVM, Ter Haar NT, Vermij L, Jobsen JJ, Brinkhuis M, Roothaan SM, et al. *QPOLE*: A Quick, Simple, and Cheap Alternative for *POLE* Sequencing in Endometrial Cancer by Multiplex Genotyping Quantitative Polymerase Chain Reaction. JCO Global Oncology. 2023 May;(9):e2200384.

11 APPENDIX

11.1 ARTICLES

11.1.1 Article VII

Published at J Cachexia Sarcopenia Muscle. 2022 Oct;13(5):2405-2416. doi: 10.1002/jcsm.13021. Epub 2022 Jul 28.

Weight and skeletal muscle loss with cabozantinib in metastatic renal cell carcinoma.

Colomba E#, Alves Costa Silva C#, Le Teuff G, Elmawieh J, Afonso D, Benchimol-Zouari A, Guida A, Derosa L, Flippot R, Raynard B, Escudier B, Bidault F, Albiges L.
# contributed equally

Background: Cabozantinib, a standard of care metastatic renal cell carcinoma (mRCC), may be associated with weight and muscle loss. These effects of new generation VEGFR tyrosine kinase inhibitor on muscle mass loss are poorly described.
Methods: All cabozantinib-treated mRCC patients from January 2014 to February 2019 in our institution were included. Clinical data including weight were collected during therapy. Computed tomography images were centrally reviewed for response assessment, and axial sections at the third lumbar vertebrae were used to measure the total muscle area. Toxicities and cabozantinib outcomes were evaluated. Co-primary endpoints included skeletal muscle loss and weight loss (WL), longitudinally evaluated during treatment. WL has been classified according to CTCAEv5.0: Grade 1 (loss of 5 to <10% of baseline body weight), Grade 2 (loss of 10% to <20% of baseline body weight), and Grades 3-4 (loss >20% of baseline body weight).
Results: Patients were mostly men (70.3%), median age was 59.2 (range: 22.0-78.0) years, and median baseline body mass index was 25.0 (range: 16.4-49.3) kg/cm2 . Prognosis according to International Metastatic RCC Database Consortium score was good, intermediate, and poor for 13 (13.0%), 63 (63.0%), and 24 (24.0%) patients,

respectively. Out of a total of 120 patients, 101 patients with a median follow-up of 22.3 months (range: 4.5-62.2) were eligible for analysis; 85 experienced muscle loss and muscle loss >10% increased during cabozantinib exposition, especially after 6 months of treatment. At cabozantinib baseline, 71 patients (70.3%) had sarcopenia, and 16/30 (53.3%) non-sarcopenic patients developed sarcopenia during treatment. Baseline sarcopenia was associated with lower response rates (P = 0.031) and higher grades 3-4 toxicities (P = 0.001). Out of 92 patients included in the WL analysis, 44 (47.8%) and 12 (13.0%) experienced grades 2 and 3 WL, respectively.
Conclusions: We report a high incidence of grades 3-4 WL, fourth times higher than reported in prior pivotal trials, and half of the patients developed sarcopenia while on cabozantinib treatment. Weight and muscle mass loss with cabozantinib are underreported and may require further investigations and early management.

11.1.2 Article VIII

Published at Cancer Discov. 2022 Apr 1;12(4):958-983. doi: 10.1158/2159-8290.CD-21-1441.

The Polarity and Specificity of Antiviral T Lymphocyte Responses Determine Susceptibility to SARS-CoV-2 Infection in Patients with Cancer and Healthy Individuals.

Fahrner JE, Lahmar I, Goubet AG, Haddad Y, Carrier A, Mazzenga M, Drubay D, **Alves Costa Silva C**; Lyon COVID Study Group; de Sousa E, Thelemaque C, Melenotte C, Dubuisson A, Geraud A, Ferrere G, Birebent R, Bigenwald C, Picard M, Cerbone L, Lérias JR, Laparra A, Bernard-Tessier A, Kloeckner B, Gazzano M, Danlos FX, Terrisse S, Pizzato E, Flament C, Ly P, Tartour E, Benhamouda N, Meziani L, Ahmed-Belkacem A, Miyara M, Gorochov G, Barlesi F, Trubert A, Ungar B, Estrada Y, Pradon C, Gallois E, Pommeret F, Colomba E, Lavaud P, Deloger M, Droin N, Deutsch E, Gachot B, Spano JP, Merad M, Scotté F, Marabelle A, Griscelli F, Blay JY, Soria JC, Merad M, André F, Villemonteix J, Chevalier MF, Caillat-Zucman S, Fenollar F, Guttman-Yassky E, Launay O, Kroemer G, La Scola B, Maeurer M, Derosa L, Zitvogel L.

Abstract: Vaccination against coronavirus disease 2019 (COVID-19) relies on the in-depth understanding of protective immune responses to severe acute respiratory syndrome coronavirus-2 (SARS-CoV-2). We characterized the polarity and specificity of memory T cells directed against SARS-CoV-2 viral lysates and peptides to determine correlates with spontaneous, virus-elicited, or vaccine-induced protection against COVID-19 in disease-free and cancer-bearing individuals. A disbalance between type 1 and 2 cytokine release was associated with high susceptibility to COVID-19. Individuals susceptible to infection exhibited a specific deficit in the T helper 1/T cytotoxic 1 (Th1/Tc1) peptide repertoire affecting the receptor binding domain of the spike protein (S1-RBD), a hotspot of viral mutations. Current vaccines triggered Th1/Tc1 responses in only a fraction of all subject categories, more effectively against the original sequence of S1-RBD than that from viral variants. We speculate that the next generation of vaccines should elicit Th1/Tc1 T-cell responses against the S1-RBD domain of emerging viral variants.

11.1.3 Article IX

Published at Clin Genitourin Cancer. 2022 Feb;20(1):80-87. doi: 10.1016/j.clgc.2021.09.001.

Activity of Systemic Treatments After Cabozantinib Failure in Advanced Metastatic Renal Cell Carcinoma.

Cerbone L, Nunno VD, Carril Ajuria L, Alves Costa Silva C, Colomba E, Guida A, Salviat F, Hirsch L, Benchimol-Zouari A, Flippot R, Escudier B, Albiges L.

Background: Cabozantinib, a potent multityrosine kinases inhibitor (TKI), has demonstrated overall survival (OS) benefit over everolimus in patients previously treated with VEGFR TKI for metastatic Renal Cell Carcinoma (mRCC). The efficacy of systemic treatments after cabozantinib failure has not been investigated.
Materials and methods: We conducted a retrospective study on patients receiving systemic treatment after cabozantinib failure in

heavily pretreated patient with mRCC. We assessed Time to Treatment Failure (TTF), OS and objective response rate (ORR).
Results: Among 150 patients treated with cabozantinib in our institution, 56 (37.3%) received subsequent systemic therapy and were eligible for the analysis. IMDC prognostic group was good, intermediate and poor in 11 (19.6%), 24 (42.9%) and 11 (19.6%) patients, respectively. Cabozantinib was administered mainly as a second (41.1%), or third (33.9%) line treatment. axitinib or immune-checkpoint inhibitors were the subsequent treatment in 18 (34.8%) patients for each everolimus (n:16, 28.6%), other angiogenesis inhibitors (n:4, 7.1%) TTF and OS from subsequent systemic therapy after cabozantinib failure were 2.8 months (95%CI 1.9-3.7) and 7.7 months (95%CI 4.4-10.8), respectively. ORR was 8.7% and 2 patients with axitinib and 2 patients treated with Immune checkpoint inhibitors achieved a partial response.
Conclusion: Overall, activity of systemic therapies after cabozantinib was limited.

11.1.4 Article X

Published at JCI Insight. 2021 Jan 25;6(2):e145207. doi: 10.1172/jci.insight.145207.

Ketogenic diet and ketone bodies enhance the anticancer effects of PD-1 blockade.

Ferrere G, Tidjani Alou M, Liu P, Goubet AG, Fidelle M, Kepp O, Durand S, Iebba V, Fluckiger A, Daillère R, Thelemaque C, Grajeda-Iglesias C, **Alves Costa Silva C**, Aprahamian F, Lefevre D, Zhao L, Ryffel B, Colomba E, Arnedos M, Drubay D, Rauber C, Raoult D, Asnicar F, Spector T, Segata N, Derosa L, Kroemer G, Zitvogel L.

Abstract: Limited experimental evidence bridges nutrition and cancer immunosurveillance. Here, we show that ketogenic diet (KD) - or its principal ketone body, 3-hydroxybutyrate (3HB), most specifically in intermittent scheduling - induced T cell-dependent tumor growth retardation of aggressive tumor models. In conditions in which anti-PD-1 alone or in combination with anti-CTLA-4 failed to reduce tumor

growth in mice receiving a standard diet, KD, or oral supplementation of 3HB reestablished therapeutic responses. Supplementation of KD with sucrose (which breaks ketogenesis, abolishing 3HB production) or with a pharmacological antagonist of the 3HB receptor GPR109A abolished the antitumor effects. Mechanistically, 3HB prevented the immune checkpoint blockade-linked upregulation of PD-L1 on myeloid cells, while favoring the expansion of CXCR3+ T cells. KD induced compositional changes of the gut microbiota, with distinct species such as Eisenbergiella massiliensis commonly emerging in mice and humans subjected to carbohydrate-low diet interventions and highly correlating with serum concentrations of 3HB. Altogether, these results demonstrate that KD induces a 3HB-mediated antineoplastic effect that relies on T cell-mediated cancer immunosurveillance.

11.1.5 Article XI

Published at Eur Urol. 2020 Aug;78(2):195-206. doi: 10.1016/j.eururo.2020.04.044.

Gut Bacteria Composition Drives Primary Resistance to Cancer Immunotherapy in Renal Cell Carcinoma Patients.

Derosa L, Routy B, Fidelle M, Iebba V, Alla L, Pasolli E, Segata N, Desnoyer A, Pietrantonio F, Ferrere G, Fahrner JE, Le Chatellier E, Pons N, Galleron N, Roume H, Duong CPM, Mondragón L, Iribarren K, Bonvalet M, Terrisse S, Rauber C, Goubet AG, Daillère R, Lemaitre F, Reni A, Casu B, Alou MT, **Alves Costa Silva C**, Raoult D, Fizazi K, Escudier B, Kroemer G, Albiges L, Zitvogel L.

Background: The development of immune checkpoint blockade (ICB) has revolutionized the clinical outcome of renal cell carcinoma (RCC). Nevertheless, improvement of durability and prediction of responses remain unmet medical needs. While it has been recognized that antibiotics (ATBs) decrease the clinical activity of ICB across various malignancies, little is known about the direct impact of distinct intestinal nonpathogenic bacteria (commensals) on therapeutic outcomes of ICB in RCC.
Objective: To evaluate the predictive value of stool bacteria composition for ICB efficacy in a cohort of advanced RCC patients.
Design, setting, and participants: We prospectively collected fecal samples from 69 advanced RCC patients treated with nivolumab and enrolled in the GETUG-AFU 26 NIVOREN microbiota translational substudy phase 2 trial (NCT03013335) at Gustave Roussy. We recorded patient characteristics including ATB use, prior systemic therapies, and response criteria. We analyzed 2994 samples of feces from healthy volunteers (HVs). In parallel, preclinical studies performed in RCC-bearing mice that received fecal transplant (FMT) from RCC patients resistant to ICB (NR-FMT) allowed us to draw a cause-effect relationship between gut bacteria composition and clinical outcomes for ICB. The influence of tyrosine kinase inhibitors (TKIs) taken before starting nivolumab on the microbiota composition has also been assessed.

Outcome measurements and statistical analysis: Metagenomic data (MG) from whole genome sequencing (WGS) were analyzed by multivariate and pairwise comparisons/fold ratio to identify bacterial fingerprints related to ATB or prior TKI exposure and patients' therapeutic response (overall response and progression-free survival), and compared with the data from cancer-free donors.

Results and limitations: Recent ATB use (n=11; 16%) reduced objective response rates (from 28% to 9%, $p<0.03$) and markedly affected the composition of the microbiota, facilitating the dominance of distinct species such as *Clostridium hathewayi*, which were also preferentially over-represented in stools from RCC patients compared with HVs. Importantly, TKIs taken prior to nivolumab had implications in shifting the microbiota composition. To establish a cause-effect relationship between gut bacteria composition and ICB efficacy, NR-FMT mice were successfully compensated with either FMT from responding RCC patients or beneficial commensals identified by WGS-MG (*Akkermansia muciniphila* and *Bacteroides salyersiae*).

Conclusions: The composition of the microbiota is influenced by TKIs and ATBs, and impacts the success of immunotherapy. Future studies will help sharpen the role of these specific bacteria and their potential as new biomarkers.

11.2 Abstracts

11.2.1 Abstract I

Oral presentation at ESMO Congress 2021 (Mini oral session - Genitourinary tumours, non-prostate)

Annals of Oncology (2021) 32 (suppl_5): S678-S724. 10.1016/annonc/annonc675

657MO - Antibiotic (ATB) therapy and outcome from nivolumab (N) in metastatic renal cell carcinoma (mRCC) patients (pts): Results of the GETUG-AFU 26 NIVOREN multicentric phase II study

L. Derosa, **C. Alves Costa Silva**, C. Dalban, E. Colomba, S. Negrier, C.M. Chevreau, G. Gravis, S.M. Oudard, B. Laguerre, P. Barthelemy, D. Borchiellini, M. Gross-Goupil, L. Geoffrois, F. Rolland, A. Thiery-Vuillemin, F. Joly, S. Ladoire1, F. Tantot, B. Escudier, L. Albiges

Background: Previous studies examined the impact of ATB on immune checkpoint inhibitor efficacy across a wide range of tumors, including genitourinary neoplasms. Perturbation of the gut microbiota has been indicated as a putative mechanism to explain this influence. We aimed to assess the impact of ATB in refractory mRCC pts.
Methods: The GETUG-AFU 26 NIVOREN phase II trial (NCT 0301335) assessed the activity and safety of N in metastatic ccRCC pts who failed anti-angiogenic regimen. Pts who received ATB between 60 days before until 42 days after N initiation were compared with those who did not. Progression-free survival (PFS), overall survival (OS), overall response rate (ORR) and toxicities were assessed. Multivariate Cox analysis was used to adjust for established risk factors: sex, age, international Metastatic RCC Database Consortium (IMDC) score, number of previous lines, hypoalbuminemia, and brain, bone and liver metastasis.
Results: Among 707 pts included between February 2016 and June 2017, 104 (14.7%) received ATB. Characteristics were well balanced except for IMDC score: 12% vs 19% good, 49% vs 57% intermediate, 39% vs 24% poor in ATB users vs non-users, respectively. Median OS

was 13.0 (95%CI 8.1-19.8; 67/104) months for ATB users vs 25.0 (95%CI 22.4-28.4; 284/603) months in non-users [HR 1.77 (95%CI 1.36-2.31), p<.0001]. In multivariate analysis, ATB was still associated with worse OS [HR 1.59 (1.22-2.09), p=0.0008]. Median PFS was 2.6 (95%CI 2.4-4.1; 90/104) months in ATB users vs 3.8 (95%CI 2.9-4.6; 504/603) months in non-users [HR 1.24 (0.99-1.55), p=0.0564]. ORR was 15.1% for ATB users vs 21.1% for non-users (p=0.176). Among ATB users, there was no complete response (CR) and 53 (57.0%) had progressive disease (PD), while 9 (1.5%) and 275 (47.3%) of non-users had CR and PD, respectively. The incidence of grades 3-5 toxicity leading to treatment stop was 26.9% among ATB vs 17.9% of non-users (p=0.031).
Conclusions: ATB severely compromise OS and PFS in N-treated mRCC pts. We confirm the potential deleterious effect for ATB in pts treated with anti-PD1, and the suspected impact of microbiota lay the ground for interventional study.

11.2.2 Abstract II

Poster display session at ESMO Congress 2021

Annals of Oncology (2021) 32 (suppl_5): S678-S724. 10.1016/annonc/annonc675

697P - Impact of β-blockers (BB) on outcomes of metastatic renal cell carcinoma (mRCC) patients treated with nivolumab (N)

C. Alves Costa Silva, L. Derosa, C. Dalban, E. Colomba, S. Negrier, C.M. Chevreau, G. Gravis, S.M. Oudard, B. Laguerre, P. Barthelemy, D. Borchiellini, M. Gross-Goupil, L. Geoffrois, F. Rolland, A. Thiery-Vuillemin, F. Joly, S. Ladoire, F. Tantot, B. Escudier, L. Albiges

Background: Beta-blockers have been associated with improved survival and immune checkpoint inhibitors (ICI) efficacy in cancer patients. We aimed to evaluate whether BB has an impact on outcomes of mRCC patients treated with N.
Methods: The multicentric and prospective study NIVOREN GETUG AFU 26 evaluated the safety and efficacy of N in mRCC patients after failure of 1 or 2 tyrosine kinase inhibitors. Patients were treated

between February 2016 and June 2017. Patients who were treated with BB at N start were compared with those who did not. Progression-free survival (PFS), overall survival (OS), overall response rate (ORR) and toxicities were assessed. Multivariate Cox analysis was used to adjust for age and BMI.

Results: Overall, 698 patients were enrolled. One hundred and fifty-seven (22.5%) patients were treated with BB. From these, 143 (91.1%) received β1-selective blocker and 14 (8.9%) received pan β-blocker. Clinical characteristics were similar between both groups, except for median age and BMI (Table). Median OS was 22.8 (95%CI: 17.5-28.7; 82 events) months for BB users versus 24.1 (95%CI: 20.7-27.8; 263 events) months in non-users [HR 1.07 (0.83-1.37), p=0.6004]. Median PFS was 3.8 (95%CI: 2.8-5.2; 133 events) months in BB users versus 3.1 (95%CI: 2.8-4.4; 455 events) months in non-users [HR 0.99 (0.82-1.20), p=0.9409]. In multivariate analysis, both endpoints were not associated to BB at nivolumab start. The groups did not differ for ORR: 20.0% for BB users versus 20.1% for BB non-users (p=0.975). Toxicity was similar between groups.

Table: Patient characteristics

		ALL (n=698)	BB (n=157)	No BB (n=541)
Age(year)	Median (range)	64 (22; 90)	68 (33; 86)	62 (22; 90)
Gender–no(%)	Male	540 (77)	123 (78)	417 (77)
BMI–no(%)	<25 kg/m ^{2}	333 (49)	62 (40)	271 (51)
	≥25 kg/m ^{2}	353 (51)	94 (60)	259 (49)
	Missing	12	1	11
Histology–no(%)	Clear Cell	695 (100)	157 (100)	538 (100)
	Missing	3	0	3
IMDC score–no(%)	Good	126 (18)	28 (18)	98 (18)
	Intermediate	391 (56)	91 (58)	300 (56)
	Poor	179 (26)	38 (24)	141 (26)
	Missing	2	0	2

ECOG PS–no(%)	≥2	102 (16)	23 (15)	79 (15)
	Missing	36	7	29
Previous lines–no(%)	1-2	541 (78)	119 (76)	422 (78)
	≥3	157 (22)	38 (24)	119 (22)

Conclusions: There is no impact of BB in mRCC patients treated with N in our study.

11.2.3 Abstract III

Oral presentation at ESMO Congress 2022 (Mini-oral session 2: GU tumours, non-prostate)

Annals of Oncology (2022) 33 (suppl_7): S660-S680. 10.1016/annonc/annonc1072

1452MO - Longitudinal analysis reveals gut microbiota shift during standard therapies in metastatic renal cell carcinoma (mRCC)

C. Alves Costa Silva, G. Piccinno, L. Cerbone, V. Iebba, E. Colomba, R. Flippot, C. sow, I. Darik, A. Maltez Thomas, N. Naoun, A. Bernard-Tessier, A. Reni, N. Segata, B. Escudier, L. Zitvogel, L. Albiges, L. Derosa

Background: Baseline GM composition is associated with pts outcomes in immune-checkpoint blockade (ICB)-treated mRCC. GM shift during mRCC therapies has never been described. We report IMDC risk and tyrosine kinase inhibitors (TKI)'s GM signatures and changes during ICB and TKI treatment.
Methods: We prospectively collected fecal samples of all comers mRCC pts who started a 1st or >2nd line (ICB or TKI or combinations) in the NCT04567446 trial at Gustave Roussy. Fecal samples were collected before and during treatment (within 1, 3, 6 and 12 months of treatment start). Shot gun metagenomic sequencing (MGS) data were analyzed by multivariate and pair-wise/fold ratio. Patients under TKI were classified as either responders (R) (CR+PR+SD and OS>12

months) or non-responders (NR) (PD and OS<12 months). Patients under ICB were classified as elite if CR+PR with PFS>12 months and OS>24 months by RECIST1.1.

Results: From February 2016 to July 2021, 160 mRCC pts were screened for enrollment and 127 met inclusion criteria. TKI-ORR was 48%, more than a half experienced related diarrhea and ICB-ORR was 31%. Overall, we observed significant differences in alpha and beta diversity of GM between IMDC risk groups, intermediate IMDC harboring immunogenic commensals (Faecalibacterium, Akkermansia spp, Ruminococcaceae), and between TKI R versus NR, NR harboring pro-TH17 bacteria such as Veillonella parvula. Interestingly, both ICB and TKI induced significant and opposite GM shifts during treatment. While TKI induced pro-Treg tolerogenic bacteria (belonging to Enterocloster genus or diarrhea-associated B. intestinalis and Klebsiella), at the expense of health-related Eubacteriaceae and Bifidobacteria in R patients, ICB promoted the loss of tolerogenic Enterocloster gen. in elite and the loss of health-relatred bacteria in NR.

Conclusions: In this largest longitudinal MGS study, we conclude that in contrast to ICB, TKI favor the over-representation of harmful commensals despite treatment success. TKI increased bacteria related to carcinogenesis, weight loss, sarcopenia and inflammation as a possible consequence of gastrointestinal toxicity. Our data provide new rationale for decision making in first line and treatment sequencing in mRCC.

11.2.4 Abstract IV

Oral presentation at ESMO Asia 2022 (Mini-oral session: Developmental and precision medicine)

Annals of Oncology (2022) 33 (suppl_9): S1533-S1539. 10.1016/annonc/annonc1130

259MO – A predictive score of cancer immunotherapy responses based on ecological analysis of gut microbiota

L. Derosa, **C. Alves Costa Silva**, V. Iebba, B. Routy, A. Reni, C. Audigier-

Valette, G. Zalcman, J. Mazieres, S. Friard, F. Goldwasser, D. Moro-Sibilot, A. Scherpereel, H. Pegliasco, S. Martinez, B. Escudier, D. Planchard, L. Albiges, B. Besse, F. Barlesi, L. Zitvogel

Background: Accumulating evidence points to the clinical relevance of the gut microbiota on outcome of immune checkpoint inhibitors (ICI). Recent work identified a gut oncomicrobiome signature centered by Akkermansia muciniphila (Akk) associated with favorable outcomes to ICI in advanced lung (NSCLC) and kidney (RCC) cancer patients.
Methods: ONCOBIOTICS (NCT04567446) provided shotgun metagenomics sequencing (MGS) of fecal samples from NSCLC and RCC during ICI in France and Canada. We reconstructed topological pearson networks within the microbial ecosystem of patients with overall survival >12 (responders: R) and <12 months (non-responders: NR). Networks of species interacting groups (SIG), notably two highly enriched in harmful (SIG1) or beneficial (SIG2) bacteria, were identified. Then, we computed TOPOSCORE, a monodimensional score based on SIG1/SIG2 ratio combined with Akk relative abundance. Multivariate analysis (MVA) was used to adjust for established prognostic factors.
Results: In two different cohorts with a total of 393 NSCLC, we could classify patients in R or NR using TOPOSCORE. The sensitivity, specificity, positive and negative predictive value were 80%, 47%, 67% and 63%, respectively. The MVA revealed that the TOPOSCORE was an independent prognostic factor (Table). In new cohorts of NSCLC (n=50) and RCC (n=83), TOPOSCORE outperformed PD-L1 and the International Metastatic RCC Database Consortium (IMDC) risk model for RCC in estimating R respectively. Then, we exploited the publicly available datasets of MGS (n=641; NSCLC, RCC and melanoma) to validate TOPOSCORE across different cancer populations. Finally, we developed a friendly user PCR-based score test for SIG bacterial detection allowing the diagnosis of gut dysbiosis within 48 hrs.

Table: Multivariate analysis for overall survival.

Prognostic factors	Variables	Hazard ratio (range)	p-value
TOPOSCORE	SIG1 + Grey Akk high or 0 (n=131)	ref	
	SIG2 + Grey Akk low	0.55 (0.41-0.73)	<0.001

Prognostic factors	Variables (n=250)	Hazard ratio (range)	p-value
ECOG-PS	0 (n=133)	ref	
	1 (n=169)	1.81 (1.30-2.52)	<0.001
	>2 (n=47)	1.85 (1.19-2.88)	0.006
	Unknown (n=32)	0.66 (0.32-1.34)	0.246
PD-L1	0 (n=69)	ref	
	1-49 (n=58)	1.09 (0.66-1.79)	0.746
	>50 (n=120)	0.83 (0.54-1.29)	0.417
	Unknown (n=134)	1.06 (0.71-1.57)	0.774
BMI	<25 (n=241)	ref	
	>25 (n=140)	0.67 (0.50-0.90)	0.008
LIPI	0 (n=81)	ref	
	1 (n=81)	1.85 (1.20-2.86)	0.005
	2 (n=20)	3.25 (1.76-6.01)	<0.001
	Unknown (n=199)	1.63 (1.12-2.39)	0.011

Conclusions: TOPOSCORE represents the first easy-to-use and cost-effective tool capable of detecting intestinal dysbiosis associated with longer OS after ICI across cancers on an individual basis. This TOPOSCORE has several implementations, to select donors and recipients of fecal microbial transplantations and follow any microbiota-centered interventions.

11.2.5 Abstract V

Poster presented at ASCO Genitourinary Symposium 2023

J Clin Oncol 41, 2023 (suppl 6; abstr 719). DOI: 10.1200/JCO.2023.41.6_suppl.719

The Lung Immune Prognostic Index (LIPI) stratifies prognostic groups and correlates with gut microbiota (GM) in patients with advanced renal cell carcinoma (RCC).

Carolina Alves Costa Silva, Silvia Zoppi, Anna Reni, Gianmarco

Piccinno, Imran Lahmar, Luigi Cerbone, Lucía Carril-Ajuria, Emeline Colomba, Ronan Flippot, Cissé Sow, Nicola Segata, Bernard Escudier, Laurence Zitvogel, Laurence Albiges, Lisa Derosa

Background: The LIPI score has been reported as an independent prognostic factor in RCC patients treated with immune checkpoint inhibitors (ICI) or tyrosine kinase inhibitors (TKI). Here, we aimed to correlate LIPI score and GM composition in patients with RCC.
Methods: We prospectively collected fecal samples of all comers RCC patients who started a 1st or beyond line therapy (standard or clinical trial) in the NCT0457446 at Gustave Roussy. Neutrophil to lymphocyte ratio (dNLR) and lactate dehydrogenase (LDH) were obtained from routine blood tests. Shot gun metagenomic sequencing (MGS) data were analyzed by multivariate and pair-wise/fold ratio. Clinical benefit ratio (CBR, complete response + partial response + stable disease, RECIST1.1) and overall survival (OS, from treatment start) were evaluated. Multivariate analysis (MVA) for OS included age, gender, therapy line, IMDC, histology, hypoalbuminemia.
Results: From February 2016 to July 2021, 160 patients were screened and 102 were included. Median age was 61 years (22-89), patients were mostly males (75%) and clear cell histology (90%). Patients were treated in 1st (15%), 2nd (53%) and beyond (32%) lines. Treated with ICI monotherapy (65%), followed by TKI or mTOR (20%) and ICI combination (19%). IMDC was 32% good (G), 54% intermediate (I) and 14% poor (P) and LIPI was 69% G, 25% I and 6% P. Median OS was 42.9, 17.7 and 8.3 months in patients with LIPI G, I and P, respectively ($p<0.0001$). Among IMDC risk groups, IMDC G + LIPI G had better OS compared to other subgroups ($p=0.017$), and those with IMDC P + LIPI P had the worse OS. Overall, LIPI G had higher rates of CBR than I+P LIPI (74% vs 50%; $p=0.0158$). At MVA, LIPI was independently associated with OS (HR 6.25, 2.02-24.34; $p=0.0187$). Overall, *Parabacteroides merdae* and *Veillonella parvula* were enriched in LIPI I+P, while LIPI G harbored *Faecalibacterium prausnitzii*. In patients treated with ICI monotherapy, LIPI I+P were enriched with Bacteroides spp (*P. merdae, Phocaeicola vulgatus*), and LIPI G had an overrepresentation of *Ruminococcaceae unclass* bacterium.
Conclusions: We report the first MGS study correlating LIPI score and GM composition in RCC patients. LIPI score correlates with clinical

outcomes (OS and CBR) and helped to better-stratified IMDC risk groups. Patients LIPI G harbor health-related commensals, while I and P groups are associated with harmful ones. LIPI score could represent a clinically relevant score to stratify mRCC patients. Clinical trial information: NCT04567446.

11.2.6 Abstract VI

Oral presentation at ASCO 2023 (Clinical Science Symposium)

J Clin Oncol 41, 2023 (suppl 16; abstr 103). DOI: 10.1200/JCO.2023.41.16_suppl.103

Friendly-user score assessing gut dysbiosis and resistance to immune checkpoint inhibitors (ICI).

Lisa Derosa, **Carolina Alves Costa Silva,** Valerio Iebba, Bertrand Routy, Anna Reni, Clarisse Audigier-Valette, Gerard Zalcman, Julien Mazieres, Sylvie Friard, François Goldwasser, Denis Lucien MORO SIBILOT, Arnaud Scherpereel, Herve Pegliasco, Stéphanie Martinez, Bernard Escudier, David Planchard, Laurence Albiges, Benjamin Besse, Fabrice Barlesi, Laurence Zitvogel

Background: Accumulating evidence pointed to the impact of the intestinal microbiota on ICI outcomes across various cancers. Although specific gut microbial species have been associated with beneficial responses (i.e. *Akkermansia muciniphila* (Akk)), no consensus exists on a gut fingerprint predicting immunoresistance to clinical routine use.
Methods: NCT04567446 provided whole genome sequencing (WGS) of longitudinal fecal samples from patients (pts) with advanced non-small cell lung cancer (NSCLC) during ICI (alone or with chemotherapy) in France and Canada. Topological Pearson networks clustered into species interacting groups (SIG) correlating with overall survival (OS; OS<12=NR; OS>12=R). Forty harmful (SIG1) and thirty-four beneficial (SIG2) WGS species were associated with NR and R to ICI. A monodimensional score (TOPOSCORE) based on SIG1/SIG2 ratio combined with Akk relative abundance was calculated and compared to machine-learning (ML) algorithms. Multivariate Cox analysis (MVA)

adjusted for established risk factors (ATB, gender, age, ECOG, PD-L1, LIPI score). Intraindividual dynamics of the TOPOSCORE was evaluated in pts with at least two fecal samples. Three independent cohorts of NSCLC and genitourinary (GU) cancers pts validated the data.
Results: In n=245 and n=148 NSCLC pts, we could classify pts into dysbiotic (SIG1+,33%) and eubiotic (SIG2+, 67%), using the TOPOSCORE. Pts falling within the SIG2+ exhibited a significantly prolonged OS than pts falling into SIG1+ (HR: (95% CI), 0.50 (0.36-0.71), p<0.0001). TOPOSCORE also predicted OS in 277 ICI-treated NSCLC and GU pts and compared to the state-of-the-art ML algorithms, held the highest percentage of correct predictions (63%). At MVA, TOPOSCORE was independently associated with OS (HR: 0.56 (0.39-0.81), p=0.002). Analyzing the intraindividual dynamics of the TOPOSCORE (n=67), we found that 74% of SIG2+ and 68% of SIG1+ individuals remained in their initial classification during ICI treatment. We finally scaled the calculation of the TOPOSCORE down to 24WGS (instead 75WGS) and set up a qPCR-based friendly-user test capable of accurately identifying the fecal presence of the bacteria of interest within 48 hrs. We confirmed (n=323) that OS was superior in those pts harboring a 24-bacteria-qPCR-based TOPOSCORE falling within the SIG2+ category (HR: 0.65 (0.48 to 0.87), p=0.0005).
Conclusions: TOPOSCORE represents a robust biomarker predicting and following the dynamic of the immunoresistance to ICI across cancers on an individual basis. By converting the WGS TOPOSCORE to a qPCR-based test with a rapid turnaround time, it will be possible to adopt this score in routine clinical practice to improve pts stratification and ICI success rates guiding the selection of dysbiotic pts amenable to microbiota-centered interventions and eubiotic fecal microbiota transplantation donors. Clinical trial information: NCT04567446.

11.2.7 Abstract VII

Poster presented at ASCO 2023 (Genitourinary Cancer—Kidney and Bladder session)

J Clin Oncol 41, 2023 (suppl 16; abstr 4548). DOI: 10.1200/JCO.2023.41.16_suppl.4548

Serum soluble MAdCAM-1: A new biomarker for cancer immunotherapy.

Carolina Alves Costa Silva, Marine Fidelle, Roxanne Birebent, Cécile Dalban, Silvia Zoppi, Anna Reni, Conrad Rauber, Imran Lahmar, Anne-Laure Mallard de La Varende, Nathalie Rioux-Leclercq, Catherine Sautès-Fridman, Maxime Meylan, Yann-Alexandre Vano, Benoit Beusenlick, Salem Chouaib, Florence Tantot, Bernard Escudier, Laurence Zitvogel, Lisa Derosa, Laurence Albiges

Background: ABX deviate the gut taxonomic microbiota composition and have a deleterious impact on survival in ICI-treated pts. ABX downregulate the ileal mucosal addressin cell adhesion molecule-1 (MAdCAM-1), leading to the recirculation of immunosuppressive enterotropic T cells into the tumor and ICI resistance. Here, we aimed to assess the prognostic impact of MAdCAM-1 in ICI-treated RCC pts.
Methods: The GETUG-AFU 26 NIVOREN phase II trial (NCT 0301335) is a multicentric study that assessed the activity and safety of Nivolumab in pts with clear cell mRCC after anti-angiogenic therapy. We measured serum soluble MAdCAM-1 (sMAdCAM-1) levels (correlating ileal MAdCAM-1 transcripts) using Human Luminex Discovery Assay in the available plasma. Progression-free survival (PFS), overall survival (OS) and clinical benefit rate (CBR) were assessed using sMAdCAM-1 median as a cut off value (high if >median and low if <median). Multivariate Cox analysis adjusted for established risk factors: ATB, gender, age, international Metastatic RCC Database Consortium (IMDC) score, number of previous lines, hypoalbuminemia, and brain, bone and liver metastasis. Two independent cohorts of metastatic lung and bladder cancer patients validated the data.
Results: Overall, 212 pts were included. Median age was 64 years (22-87), and pts were mostly male (82%). ATB users had lower levels of sMadCAM-1. Low sMadCAM-1 pts had diminished OS compared to high sMadCAM-1 pts [HR 2.97 (95%CI 1.99-4.44), p<.0001]: 13.3 (95%CI 9.8-14.9; 72/106) versus 25.3 (95%CI 24.1-NR; 36/106) months. Also, low sMadCAM-1 pts had diminished PFS [HR 1.92 (1.43-2.57), p<.0001]: 2.6 (95%CI 2.4-2.8; 99/106) versus 5.2 (95%CI 4.6-5.7; 86/106) months. Interestingly, sMAdCAM-1 was independently associated with OS [HR 2.40 (1.52-3.80), p=0.0002] and PFS [HR 1.55

(1.13-2.13), p=0.0071] in multivariate analysis. Low sMadCAM-1 pts had lower CBR (37% versus 63%, p=0.0004). Serum sMAdCAM-1 also predicted OS in 381 ICI-treated patients with lung and bladder cancer. **Conclusions:** Low sMAdCAM-1 is associated with ABX intake, ABX-independent gut dysbiosis and worse outcomes, in ICI-treated pts with metastatic lung, bladder and RCC cancer. ELISA determination of sMAdCAM-1 might guide the selection of patients amenable to microbiota-centered interventions, such as *Akkermansia* sp., and fecal microbiota transplantation.

11.3 Merit Awards

11.3.1 ESMO Merit Award
ESMO Congress 2022

11.3.2 Conquer Cancer Foundation Merit Award
ASCO Genitourinary Symposium 2023